D 3715

[03]

Eur. J. Inorg. Chem. **2010**, 337–496

EurJIC
European Journal of
Inorganic Chemistry

3/2010
3rd January Issue

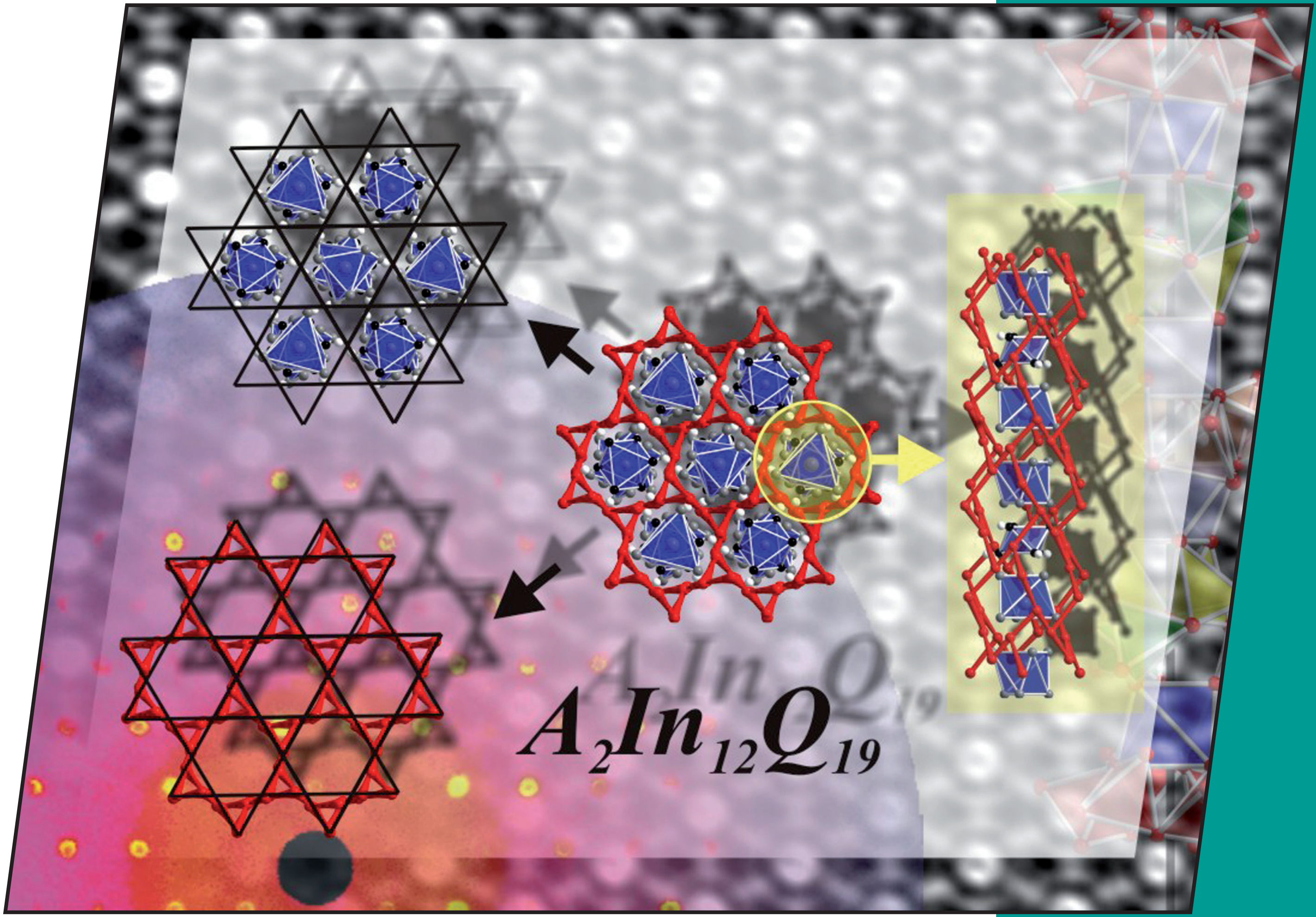

Cover Picture

Hans-Jörg Deiseroth et al.

Ordering Phenomena in Complex Chalcogenides

A Journal of
ChemPubSoc Europe

WILEY-VCH

www.eurjic.org

EJICFK (3) 337–496 (2010) · ISSN 1434-1948 · No. 3/2010

Hungary
Italy
Germany
Greece
Czech Republic
France
Sweden
Belgium
Austria
Portugal
Poland
Spain
Netherlands

EurJIC is co-owned by 11 societies of ChemPubSoc Europe, a union of European chemical societies for the purpose of publishing high-quality science. All owners merged their national journals to form two leading chemistry journals, the *European Journal of Inorganic Chemistry* and the *European Journal of Organic Chemistry*. Three further members of ChemPubSoc Europe (Austria, Czech Republic and Sweden) are Associates of the two journals.

Other ChemPubSoc Europe journals are *Chemistry – A European Journal*, *ChemBioChem*, *ChemPhysChem*, *ChemMedChem*, *ChemSusChem* and *ChemCatChem.*

COVER PICTURE

The cover picture shows the structural complexity of the $A_2In_{12}Q_{19}$ phases, which was unravelled by a combined methodical approach including state-of-the-art XRD and HRTEM techniques (background). An ordered arrangement of the atoms is limited to nanodomains built from the extended structural fragments (foreground) that constitute these crystalline solids as a whole. Details are discussed in the article by H.-J. Deiseroth et al. on p. 367ff.

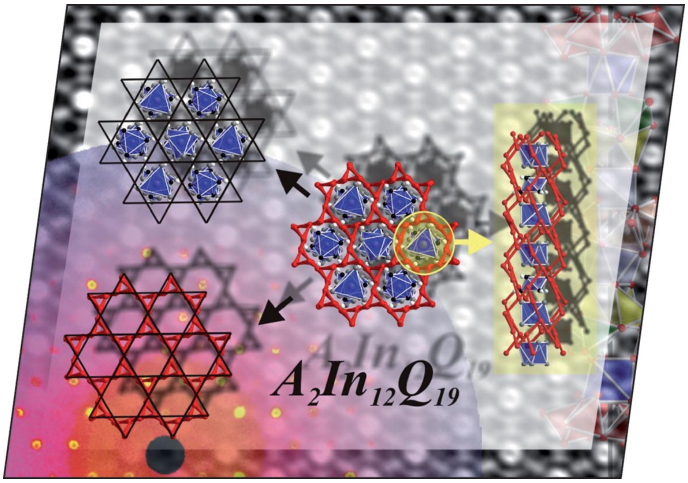

Hungary
Italy
Germany
Greece
Czech Republic
France
Sweden
Belgium
Austria
Portugal
Poland
Spain
Netherlands

EurJIC is co-owned by 11 societies of ChemPubSoc Europe, a union of European chemical societies for the purpose of publishing high-quality science. All owners merged their national journals to form two leading chemistry journals, the *European Journal of Inorganic Chemistry* and the *European Journal of Organic Chemistry*. Three further members of ChemPubSoc Europe (Austria, Czech Republic and Sweden) are Associates of the two journals.

Other ChemPubSoc Europe journals are *Chemistry – A European Journal*, *ChemBioChem*, *ChemPhysChem*, *ChemMedChem*, *ChemSusChem* and *ChemCatChem.*

COVER PICTURE

The cover picture shows the structural complexity of the $A_2In_{12}Q_{19}$ phases, which was unravelled by a combined methodical approach including state-of-the-art XRD and HRTEM techniques (background). An ordered arrangement of the atoms is limited to nanodomains built from the extended structural fragments (foreground) that constitute these crystalline solids as a whole. Details are discussed in the article by H.-J. Deiseroth et al. on p. 367ff.

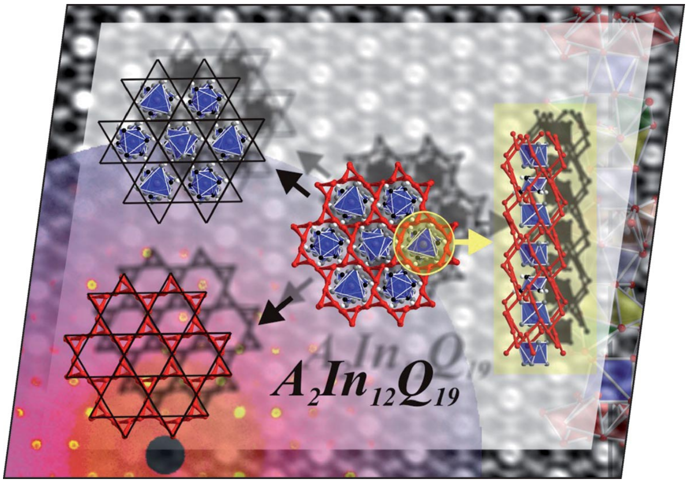

SHORT COMMUNICATIONS

Hydroxylase Mechanism

E. Olsson, A. Martinez, K. Teigen,
V. R. Jensen* 351–356

Water Dissociation and Dioxygen Binding in Phenylalanine Hydroxylase

Keywords: Enzymes / Phenylalanine hydroxylase / Tetrahydrobiopterin cofactor / Dioxygen ligands / Density functional calculations

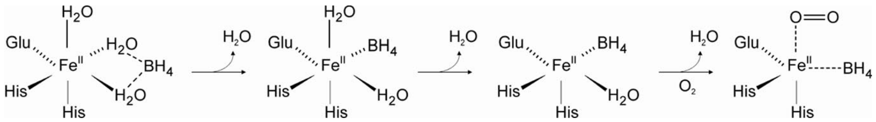

A density-functional theory study of the pterin-dependent non-heme iron(II) enzyme phenylalanine hydroxylase shows that dissociation of the initial ligating water molecules and the subsequent binding of O_2 to form a water-free, catalytic iron–O_2 complex is facile and accompanied by entrance of the tetrahydrobiopterin (BH_4) cofactor into the first coordination sphere of iron.

Hollow Nanostructures

J. Shin, T.-L. Ha, I. S. Lee* 357–360

Generation of Hollow $MnSiO_3$ Nanostructures through the Solid-State Reaction of Mn_3O_4 and Pd/PdO Nanocrystals Dimensionally Confined within Nanosized Silica Spheres

Keywords: Nanoparticles / Hollow structures / Solid-state reactions / Manganese / Palladium

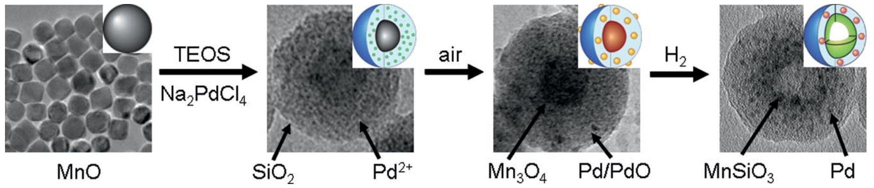

In the course of annealing Mn_3O_4 and Pd/PdO nanocrystals co-encapsulated within a nanosized silica sphere under the reducing environment, the Mn_3O_4 nanocrystals were reduced and transformed into a hollow $MnSiO_3$ nanostructure through a process facilitated by the adjacent Pd nanocrystals.

A Diamidocarbene Ligand

V. César,* N. Lugan,
G. Lavigne* 361–365

Reprogramming of a Malonic N-Heterocyclic Carbene: A Simple Backbone Modification with Dramatic Consequences on the Ligand's Donor Properties

Keywords: Heterocyclic carbenes / Diamidocarbene / Organometallic chemistry / Electronic properties / Rhodium

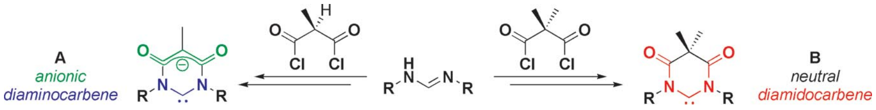

The formal introduction of a second substituent on the malonate unit of the NHC ligand **A** blocks the electronic communication between backbone atoms, thereby inducing a reorganization of the electron distribution within the heterocycle. The resulting diamidocarbene **B** exhibits significantly reduced donor properties, but can still be complexed with transition metal ions as illustrated here for the case of rhodium.

FULL PAPERS

Complex Chalcogenides

L. Kienle, M. Schlosser, M. J. Manos,
C. D. Malliakas, V. Duppel, C. Reiner,
H.-J. Deiseroth,* M. G. Kanatzidis,
K. Kelm, A. Simon 367–378

Ordering Phenomena in Complex Chalcogenides – the Showcase of $A_2In_{12}Q_{19}$ (A = K, Tl, NH_4; Q = Se, Te) and Pseudobinary In_2Q_3

Keywords: Electron microscopy / Real structure / X-ray diffraction / Disordered structure / Diffuse scattering / Chalcogens / Solid-state structures

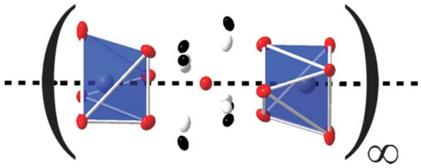

From order to disorder and back: A combined approach of electron microscopy and X-ray diffraction was applied for the characterization of highly complex chalcogenide phases. In the course of observations, a new structural variant of $(NH_4)_2$-$In_{12}Se_{19}$ was produced in situ, and the mechanism of structure formation was analyzed by electron microscopy.

Magnetostructural Correlations

The paper offers theoretical analysis of the factors governing the exchange interaction in hybrid-spin systems chosen as models of molecular magnets. The effect of molecular conformation and the importance of symmetry are brought up for the first time.

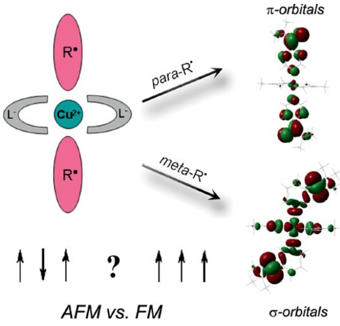

T. Miteva, J. Romanova, A. Ivanova, A. Tadjer,* M. Baumgarten 379–390

Theoretical Study on the Structural Aspects of Cu^{II} Hybrid-Spin Complexes

Keywords: Hybrid-spin molecular systems / Conformation analysis / Nitroxide radicals / Magnetic properties / Density functional calculations

Stereochemistry at Rhenium

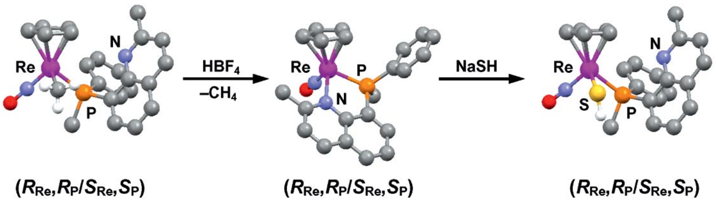

Diastereomerically pure rhenium complexes [CpRe(NO)(P*–N)(R)] have been obtained through a highly diastereoselective intramolecular proton-transfer reaction. The stereochemistry of chelate ring closure/opening was followed by X-ray crystallography for each step. The Re–SH complex reacts with aldehydes to give diastereomerically pure thioaldehyde complexes which add nucleophiles with 42–89% *de.*

F. Bock, F. Fischer, K. Radacki, W. A. Schenk* 391–402

Diastereoselective Protonation, Substitution and Addition Reactions at Pseudotetrahedral Rhenium Complexes

Keywords: Rhenium / Chiral resolution / N,P ligands / S ligands

Chemoselective Nickel Coordination

Primary amines react reversibly with unsaturated Ni=Mo or Ni=W complexes to give adducts in which the amine is N-coordinated to the nickel atom. This contrasts with previously reported results with P-donor ligands where always coordination to the group 6 metal is observed.

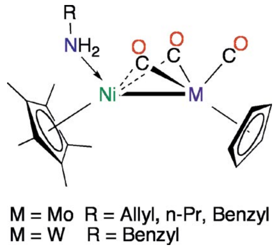

C. C. Carmona, S. Clapham, M. Gonidec, V. Ritleng, P. Braunstein, R. Welter, M. J. Chetcuti* 403–409

Reactions of Unsaturated Nickel–Molybdenum and –Tungsten Complexes with Primary Amines: Chemoselective N-Coordination to Nickel To Give the First Structurally Characterised Primary Amine–Organonickel Complexes

Keywords: Nickel / Amines / Hydrogen bonding / Heterodimetallic compounds / Group 6 metals

1D Tin Coordination Compounds

Single crystalline 1-D-tin(II) phenylchalcogenolato complexes ${}^{1}_{\infty}[Sn(EPh)_2]$ (E = S, Se, Te) were synthesized in high yields and their bonding situation rationalized by DFT. Thermal investigations partially reveal their suitability as precursors for the synthesis of the corresponding binary SnE phases.

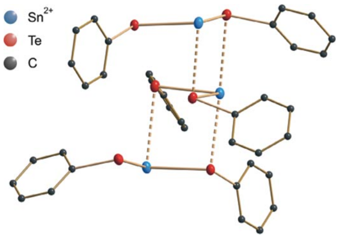

A. Eichhöfer,* J.-J. Jiang, H. Sommer, F. Weigend, O. Fuhr, D. Fenske, C.-Y. Su, G. Buth 410–418

1-D-Tin(II) Phenylchalcogenolato Complexes ${}^{1}_{\infty}[Sn(EPh)_2]$ (E = S, Se, Te) – Synthesis, Structures, Quantum Chemical Studies and Thermal Behaviour

Keywords: Tin / Chalcogens / Complexes / X-ray diffraction / TGA / Density functional calculations

CONTENTS

Cobalt Ferrite Octahedra

X. A. Fan, J. G. Guan,* X. F. Cao, W. Wang, F. Z. Mou **419–426**

Low-Temperature Synthesis, Magnetic and Microwave Electromagnetic Properties of Substoichiometric Spinel Cobalt Ferrite Octahedra

Keywords: Cobalt / Ferrites / Coprecipitation / Oxidation / Octahedral morphology / Magnetic properties / Microwave electromagnetic properties

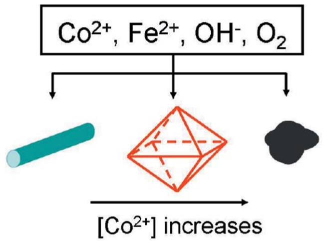

Substoichiometric cobalt ferrite octahedra were prepared by controlling the nucleation and selective crystallographic direction growth by a simple optimization of [Co^{2+}]. As this method is carried out in a low-temperature (45 °C) aqueous system and does not need any directing agents, it can be easily generalized in a large-scale synthesis of spinel $M_xFe_2O_4$ ($0 \leq x \leq 1$) octahedra.

Cluster-Based Cu–Azido Polymers

C.-B. Tian, Z.-H. Li, J.-D. Lin, S.-T. Wu, S.-W. Du,* P. Lin* **427–437**

Cluster-Based Cu^{II}–Azide Polymers: Synthesis, Structure, Magnetic Properties, and Effect of Polyamines on Crystal Structures

Keywords: Copper / Polynuclear compounds / Magnetic properties / Solid-state structures / Amines

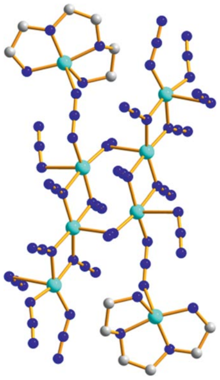

Four new copper(II)–azide polymers $[Cu_8(N_3)_{16}(222\text{-tet})_2]_n$ (**1**), $[Cu_{10}(N_3)_{20}(dien)_2]_n$ (**2**), $[Cu_{12}(N_3)_{24}(Me_5dien)_2]_n$ (**3**), and $[Cu_3(N_3)_6(dien)]_n$ (**4**) were synthesized by using different kinds of polyamines under hydrothermal conditions. Their magnetic properties were studied.

Multinuclear Pt Complexes

M.-E. Moret, P. Chen* **438–446**

Mononuclear Platinum(II) Complexes of a Bis(bidentate) Ligand Based on 1,3,4-Oxadiazole and Their Reactions with Copper(I) Salts

Keywords: Platinum / Copper / N ligands / Metal–metal interactions / Bridging ligands

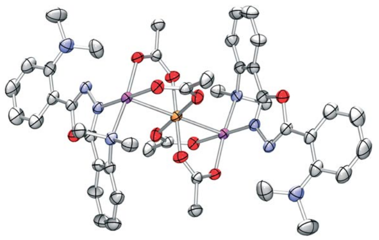

A series of mononuclear platinum(II) complexes of the bis(bidentate) ligand 2,5-bis[2-(dimethylamino)phenyl]-1,3,4-oxadiazole were synthesized, and their reaction with Cu^I salts was studied. In one case, a complex containing an acetate-supported, linear Pt^{II}–Cu^{II}–Pt^{II} chain was obtained.

Heterobimetallic Complexes

N. Nakata, M. Sakashita, C. Komatsubara, A. Ishii* **447–453**

Synthesis, Structure, and Catalytic Activity of Bimetallic Pt^{II}–Ir^{III} Complexes Bridged by Cyclooctane-1,2-dithiolato Ligands

Keywords: Heterometallic complexes / Platinum / Iridium / S ligands / Hydrosilylation

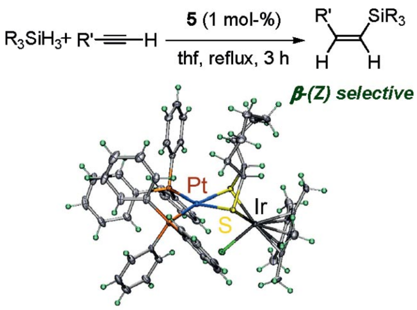

Pt–Ir bimetallic complex **5**

Cationic Pt^{II}–Ir^{III} bimetallic complexes bridged by cyclooctane-1,2-dithiolato ligands were synthesized by reaction of (cyclooctane-1,2-dithiolato)Pt^{II} complexes with $[IrCl(\mu\text{-}Cl)(\eta^5\text{-}Cp^*)]_2$ in thf in the presence of $AgSbF_6$. The bimetallic complexes serve as a catalyst in the hydrosilylation of terminal alkynes with tertiary hydrosilanes to afford selectively the β-(*Z*)-vinylsilanes in high yields.

Ln–Nitrile Frameworks

Solvent-free melt reactions of anhydrous rare earth trichlorides with molten 1,3-benzodinitrile result in isophthalonitrile frameworks of the rare earth elements. The particle size of the products can be varied from the millimeter to the nanometer scale (50–400 nm) depending on the synthesis conditions. A constitution of 1:1 concerning $\mathrm{LnCl_3/1,3\text{-}C_6H_4(CN)_2}$ is found for Y, Dy, Ho, Er and Yb in isotypic $^{3}_{\infty}[\mathrm{LnCl_3}\{1,3\text{-}\mathrm{C_6H_4(CN)_2}\}]$.

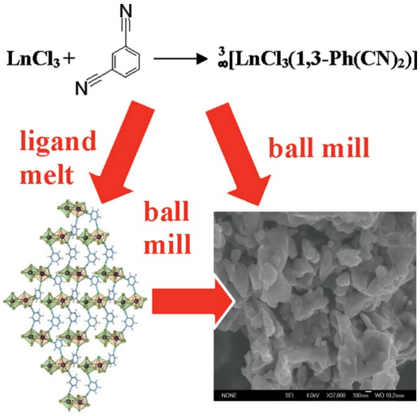

C. J. Höller, K. Müller-Buschbaum* 454–460

Frameworks by Solvent-Free Synthesis of Rare Earth Chlorides with Molten 1,3-Benzodinitrile and Tailoring of the Particle Size: $^{3}_{\infty}[\mathrm{LnCl_3}\{1,3\text{-}\mathrm{C_6H_4(CN)_2}\}]$, Ln = Y, Dy, Ho, Er, Yb

Keywords: Lanthanides / 1,3-Benzodinitrile / Framework structures / Nanoparticles / Solvent-free synthesis / Metal–organic frameworks

Silicon Hypercoordination

The *N*-silylated ureato ligand **1**, accessible via insertion of phenyl isocyanate into the Si–N bond of $\mathrm{Me_3SiNEt_2}$, proved an interesting κ(*O*,*N*) chelator, capable of setting up distorted trigonal antiprismatic coordination spheres about silicon. The ^{29}Si CSA tensor of a silicon tris-chelate of this ligand was found to exhibit pronounced axiality and remarkably narrow span.

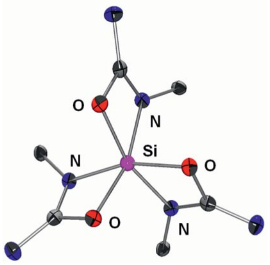

D. Schöne, D. Gerlach, C. Wiltzsch, E. Brendler, T. Heine, E. Kroke,* J. Wagler* 461–467

A Distorted Trigonal Antiprismatic Cationic Silicon Complex with Ureato Ligands: Syntheses, Crystal Structures and Solid State ^{29}Si NMR Properties

Keywords: Silicon / Chelates / Density-functional calculations / Hypercoordination

Tricarbonyliron Chalcogenolates

The tricarbonyliron thiolate and selenolate $[(\mathrm{OC})_3\mathrm{Fe}(\mu\text{-}\mathrm{ESi}t\mathrm{Bu_3})]_2$ (E = S, Se) were synthesized photochemically by the reaction of pentacarbonyliron with the dichalcogenides $t\mathrm{Bu_3Si{-}E_2{-}Si}t\mathrm{Bu_3}$ (E = S, Se).

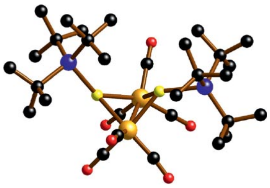

T. Kückmann, F. Schödel, I. Sänger, M. Bolte, M. Wagner, H.-W. Lerner* 468–475

The Tricarbonyliron Chalcogenolates $[(\mathrm{OC})_3\mathrm{Fe}(\mu\text{-}\mathrm{ESi}t\mathrm{Bu_3})]_2$ (E = S, Se, Te)

Keywords: Sulfur / Selenium / Iron / Supersilyl chalcogenolates / [FeFe]-Hydrogenase

Fibrous Titania Hybrids

The biomimetic construction of belt-like $\mathrm{TiO_2}$-LPEI fibrous hybrids was successfully achieved in an aqueous solution by using linear poly(ethyleneimine) (LPEI) aggregates as a catalytic mediator.

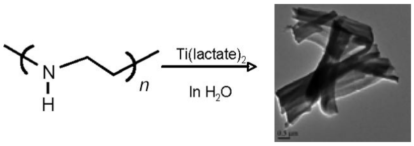

P.-X. Zhu, R.-H. Jin* 476–482

Simple and Efficient Aqueous Process for Nanostructured Fibrous $\mathrm{TiO_2}$ Regulated by Linear Polyethyleneimine Aggregates

Keywords: Biomimetic synthesis / Titanium oxide / Photocatalysts / Nanostructures

CONTENTS

“Naked” Manganese Triangles

Keywords: Manganese / Oximes / Magnetic properties / Ligand effects

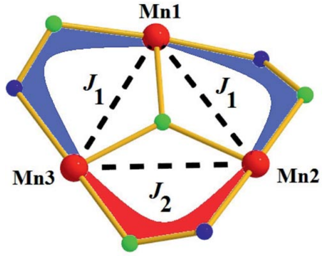

Capping ligands on $[Mn_3]$ triangles induce a small but vital effect on magnetic exchange properties. Although the bridging/capping ligand has little effect on the magnitude of the magnetic interactions, its presence is vital in achieving maximal structural distortion, and, therefore, interesting magnetic properties.

---

* Author to whom correspondence should be addressed.

💻 Supporting information on the WWW (see article for access details).

On these pages, we feature a selection of the excellent work that has recently been published in our sister journals. If you are reading these pages on a computer, click on any of the items to read the full article. Otherwise please see the DOIs for easy online access through Wiley InterScience.

Main Group Chemistry

A. Weickgenannt, M. Oestreich*

Silicon- and Tin-Based Cuprates: Now Catalytic in Copper!

Go catalytic! Simple transmetalation from lithium to zinc attenuates the basicity and nucleophilicity of silicon and tin main group organometallics, thereby rendering the stoichiometric use of copper superfluous. All common carbon–silicon and selected carbon–tin bond formations are now catalytic in copper.

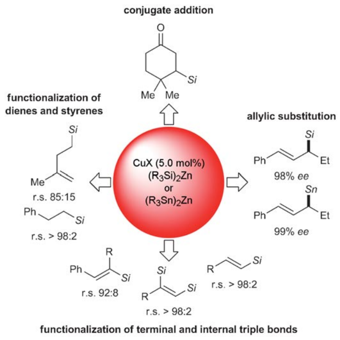

Chem. Eur. J.
DOI: **10.1002/chem.200902222**

Photovoltaic Cells

J.-L. Wang, C. Zhong, Z.-M. Tang, H. Wu, Y. Ma,* Y. Cao,* J. Pei*

Solution-Processed Bulk Heterojunction Photovoltaic Cells from Gradient π-Conjugated Thienylene Vinylene Dendrimers

A series of gradient π-conjugated dendrimers and their corresponding models based on 5,5,10,10,15,15-hexahexyltruxene moieties as nodes and oligo(thienylene vinylene) (OTVs) units with different lengths as branching arms was developed as active materials for photovoltaic cells. The power conversion efficiency of the devices based on **G0-4-2** (see picture) was 0.40 %, which is the highest recorded value for OTV-based materials to date.

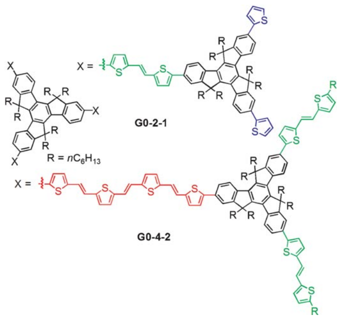

Chem. Asian J.
DOI: **10.1002/asia.200900245**

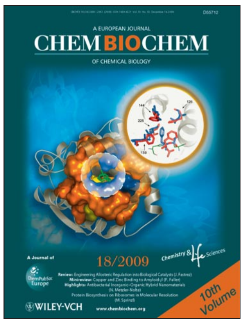

Biocatalysts

J. Fastrez*

Engineering Allosteric Regulation into Biological Catalysts

'Allo 'Allo! Enzymes or ribozymes have been engineered to incorporate allosteric sites that bind ligands unrelated to their substrates. Random mutagenesis of surface residues followed by selection or appendage of ligand-binding modules to biocatalysts affords enzymes or ribozymes with activity that can be regulated by allosteric ligand binding.

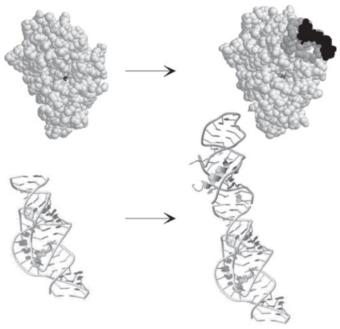

ChemBioChem
DOI: **10.1002/cbic.200900590**

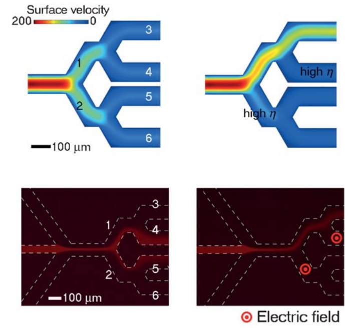

ChemPhysChem
DOI: **10.1002/cphc.200900778**

Microfluidics

Y.-J. Na, T.-Y. Yoon, S. Park, B. Lee, S.-D. Lee*

Electrically Programmable Nematofluidics with a High Level of Selectivity in a Hierarchically Branched Architecture

Go with the flow: A concept of *nematofluidics* that provides a simple, programmable, and hierarchically branched architecture of microfluidics where a nematic liquid crystal (LC) is used as an anisotropic fluid (see picture) is presented. Based on anisotropic flow resistance this method provides a fast and hierarchical channel selection in microfluidics.

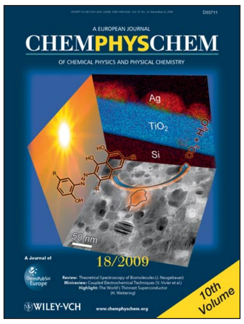

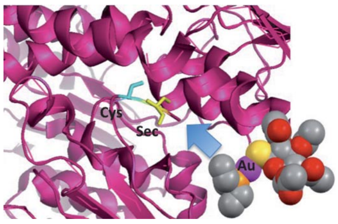

ChemMedChem
DOI: **10.1002/cmdc.200900370**

Antitumor Agents

E. Vergara, A. Casini, F. Sorrentino, O. Zava, E. Cerrada, M. P. Rigobello, A. Bindoli, M. Laguna,* P. J. Dyson*

Anticancer Therapeutics That Target Selenoenzymes: Synthesis, Characterization, in vitro Cytotoxicity, and Thioredoxin Reductase Inhibition of a Series of Gold(I) Complexes Containing Hydrophilic Phosphine Ligands

Several studies indicate that thioredoxin reductases represent effective druggable targets for the development of new anticancer drugs. We report herein the inhibitory properties of gold(I) complexes with water-soluble phosphine ligands. Biochemical studies suggest binding of gold atoms to both cysteine and selenocysteine residues that are catalytically essential.

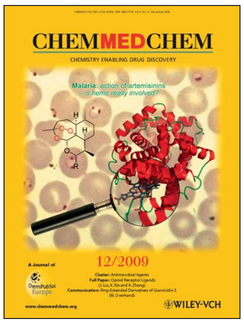

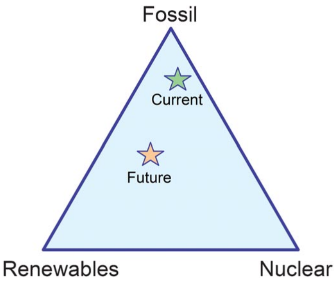

ChemSusChem
DOI: **10.1002/cssc.200900190**

Energy Materials

V. L. Kuznetsov, P. P. Edwards*

Functional Materials for Sustainable Energy Technologies: Four Case Studies

Functional energy materials are recognized as a top priority in providing many of the key technological solutions for next-generation energy conversion and storage systems. We highlight four areas of activity in which functional materials are already a significant element of world-wide research efforts: transparent conducting oxides, solar energy materials, materials for thermoelectric energy conversion, and hydrogen storage materials.

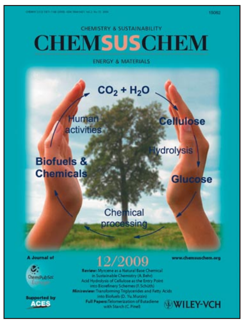

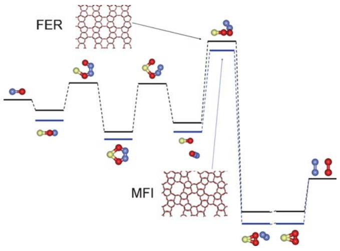

ChemCatChem
DOI: **10.1002/cctc.200900219**

Heterogeneous Catalysis

A. Pulido, P. Nachtigall*

Correlation Between Catalytic Activity and Metal Cation Coordination:
NO Decomposition Over Cu/Zeolites

Just say NO: The catalytic activity of Cu/zeolites for NO removal depends on the metal cation coordination to the framework. The most active catalysts are those with Cu^I loosely coordinated to the framework. The catalytic cycle is investigated using a periodic DFT model to account for the effect of the zeolite on the stability of reaction intermediates.

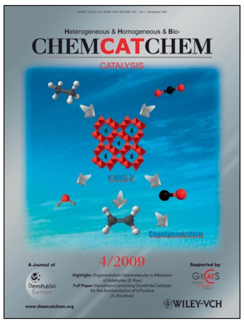

Soft Nanoparticle Crystals

W. L. Cheng, M. R. Hartman, D.-M. Smilgies, R. Long, M. J. Campolongo, R. Li, K. Sekar, C.-Y. Hui, D. Luo*

Probing in Real Time the Soft Crystallization of DNA-Capped Nanoparticles

The crystallization events occurring in a drying droplet containing DNA-capped nanoparticles were probed by means of small-angle X-ray scattering (SAXS; the picture shows a series of 1D SAXS patterns recorded over time). Unusual nanoparticle supracrystals form that are both soft and elastic with continuously scalable crystalline states over a wide range of lattice constants.

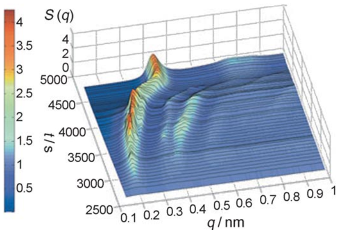

Angew. Chem. Int. Ed.
DOI: **10.1002/anie.200904066**

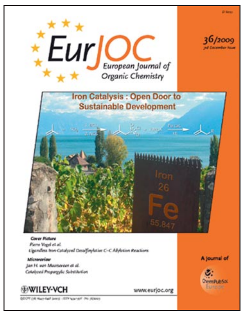

Carbohydrate Recognition

A. Ardá, C. Venturi, C. Nativi, O. Francesconi, F. J. Cañada, J. Jiménez-Barbero,* S. Roelens*

Selective Recognition of β-Mannosides by Synthetic Tripodal Receptors: A 3D View of the Recognition Mode by NMR

A 3D model of the complex of a synthetic tripodal receptor with octyl β-D-mannoside based on molecular mechanics calculations and NMR experimental data is proposed. The structure explains the observed selectivity for β-mannosyl in terms of hydrogen bonding, intermolecular van der Waals interactions and conformational bias

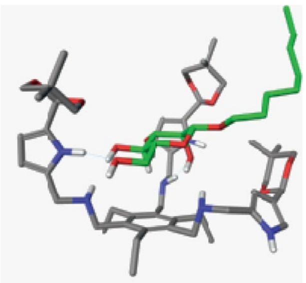

Eur. J. Org. Chem.
DOI: **10.1002/ejoc.200901024**

DOI: 10.1002/ejic.200900489

Water Dissociation and Dioxygen Binding in Phenylalanine Hydroxylase

Elaine Olsson,[a] Aurora Martinez,[b] Knut Teigen,[b] and Vidar R. Jensen*[a]

Keywords: Enzymes / Phenylalanine hydroxylase / Tetrahydrobiopterin cofactor / Dioxygen ligands / Density functional calculations

Phenylalanine hydroxylase (PAH) catalyzes the hydroxylation of L-phenylalanine to L-tyrosine and is dependent on the contribution of electrons from the reduced cofactor tetrahydrobiopterin (BH_4). Whereas three ligating water molecules are bound to the central iron atom in the existing crystal structures of binary complexes of the catalytic domain of both the inactive, PAH–Fe^{III}–BH_2, and active, PAH–Fe^{II}–BH_4, forms of the human enzyme, previous spectroscopic studies show that the water molecules dissociate prior to the onset of the catalytic reaction. In the present study, starting from a cluster model of the active Fe^{II} center of PAH, three successive water ligand dissociations followed by dioxygen coordination have been investigated by using density functional theory. The calculations show that the formation of the active, water-free O_2 complex from the water-ligated complex of the PAH–Fe^{II}–BH_4 crystal structure is remarkably facile (ΔG = 1.5 kcal/mol). Moreover, the initial water dissociation is accompanied by entrance of the cofactor into the first coordination sphere of iron.

Introduction

Phenylalanine hydroxylase (PAH) is a tetrahydropterin-dependent non-heme iron enzyme responsible for the conversion of the essential amino acid L-phenylalanine (L-Phe) into the amino acid L-tyrosine (L-Tyr); see Scheme 1. This reaction is the first step in the catabolism of L-Phe, obtained from food, to carbon dioxide and water. PAH is located mainly in the liver and to a less extent in the kidneys. A defected PAH leads to phenylketonuria (PKU), an inborn genetic disease that prevents a normal development of the brain. PAH is, together with tyrosine hydroxylase (TH) and the tryptophan hydroxylases 1 and 2 (TPH1-2), a member of the family of aromatic amino acid hydroxylases (AAHs).[1–3]

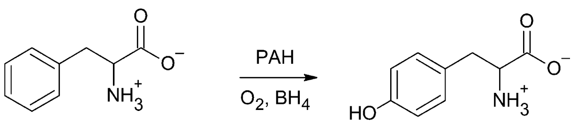

Scheme 1. The hydroxylation of L-phenylalanine catalyzed by PAH with molecular oxygen as additional substrate. The cofactor tetrahydrobiopterin (BH_4) is also hydroxylated in the reaction.

The enzymes in the AAH family are all dependent on the cofactor (6*R*)-L-*erythro*-5,6,7,8-tetrahydrobiopterin (BH_4) to be able to catalyze their respective reactions. The cofactor is hydroxylated into pterin-4a-carbinolamine during the catalytic cycle, and is subsequently transformed to quinoid dihydropterin by 4a-carbinolamine dehydratase. The product is then converted back to reduced active BH_4, either directly by dihydropteridine reductase or via 7,8-dihydropterin (BH_2) by dihydrofolate reductase.[2] In addition to the aromatic amino acid substrate (L-Phe, L-Tyr or L-Trp) and the pterin cofactor, the enzymes use molecular oxygen, the atoms of which are incorporated into both the cofactor and the substrate.[4]

The enzymes in the AAH family consist of three domains; an N-terminal regulatory, a catalytic and a C-terminal tetramerization domains. The catalytic domain includes the active site where the substrates and co-substrates bind and where the reaction takes place. Because of high sequence identity in the catalytic domain of the AAH enzymes, they have been assumed to share a common mechanism of hydroxylation.[2,5] The iron atom, which has been shown to be necessary for catalytic activity,[6,7] is in the ferric form (Fe^{III}) in the resting state of PAH, and is reduced by BH_4 to the active ferrous form (Fe^{II}). The general mechanism is typically thought to consist of two steps, the first starting with molecular oxygen activation by iron to form an iron-bound peroxopterin intermediate. Next, O–O heterolytic bond cleavage leads to a ferryl (Fe^{IV} = O) species which is responsible for the hydroxylation of L-Phe in the second step.[6,8–10]

In the active site, the iron atom is anchored by one carboxylate and two imidazole ligands, provided by one

---

[a] Department of Chemistry, University of Bergen,
Allégaten 41, 5007 Bergen, Norway
Fax: +47-55589490
E-mail: Vidar.Jensen@kj.uib.no
[b] Department of Biomedicine, University of Bergen,
Jonas Lies vei 91, 5009 Bergen, Norway

Supporting information for this article is available on the WWW under http://dx.doi.org/10.1002/ejic.200900489.

glutamic acid (Glu) and two histidine (His) residues, respectively. The 2-His-1-carboxylate (from Glu or aspartic acid) binding motif, which is found among many metalloenzymes, e.g., α-ketoglutarate-dependent enzymes, Rieske dioxygenases, 1-aminocyclopropane-1-carboxylic acid oxidase, and isopenicillin N synthase,[11–13] is conserved in all existing X-ray crystal structures of the catalytic domain of human PAH (hPAH).[14–17] Whereas crystal structures of binary complexes of the catalytic domain of both the inactive, hPAH–Fe^{III}–BH_2[15,17] and active, hPAH–Fe^{II}–BH_4[14] form of the enzyme show an essentially octahedral coordination geometry of the central iron atom, with three ligating water molecules, the corresponding crystal structures of the ternary complexes involving substrate analogues display none[16] or only one water ligand.[15,16] Although the distance between iron and BH_4 differs significantly between the various X-ray crystal structures (see Table 1 in the discussion of Teigen et al.[18]), Fe–BH_4 bond formation is not supported by the crystallographic analyzes.

The difference in the iron coordination between the crystal structures of binary and ternary complexes indicates that the binding of cofactor and substrate triggers dissociation of water molecules from iron.[14–17] This structural modification is also suggested by a number of additional observations.[6,19] In particular, electron paramagnetic resonance (EPR) and ultraviolet-visible (UV/Vis) spectroscopic studies show that, when the cofactor and substrate are bound in the active site, the last iron-bound water molecule is displaced by an oxygen mimic (nitric oxide) and a pentacoordinate iron complex is formed.[19] Furthermore, studies of the heme enzyme cytochrome P450, which also catalyzes hydroxylation reactions, show that there is a risk of forming hydrogen peroxide if water and O_2 are coordinated simultaneously to iron, and water molecules are thus dissociated prior to the coordination of molecular oxygen.[20,21] Moreover, tryptophan 2,3-dioxygenase has a single water molecule coordinated to heme iron and this is also dissociated prior to coordination of O_2. A water-free first coordination sphere thus seems to stabilize the Fe–O–O complex by making the environment less hydrophilic.[22]

Although much mechanistically relevant information on the AAHs has been gained in recent years, through, e.g., solution NMR,[23,24] X-ray absorption spectroscopy[25,26] and quantum chemical modeling,[18,27–29] the details of the mechanism of hydroxylation still remain elusive.[30] The thorough density functional theory (DFT) based investigation of Bassan et al.[27,28] has, in particular, offered insight into a likely reaction route. The latter study, as well as other quantum-chemical investigations of the mechanism of hydroxylation[23,29] have been based on models of the X-ray crystal structures of the ferric or ferrous binary complexes from which only a single water molecule has been dissociated prior to dioxygen binding. However, regardless of the true number of ligating water molecules present during catalysis, the study of Bassan et al.[27,28] is important as it indicates that the assumed two-step reaction route (vide supra) should be energetically feasible. One study reported briefly on DFT geometry optimizations on models of the active site based on an X-ray structure of a ternary complex (PDB: 1MMK)[16] containing no water ligands, but did not explicitly investigate dissociation of water and the potential mechanistic connection to the structures of the binary complexes.[18] Furthermore, the latter DFT optimizations lead to iron–cofactor bond formation. These computational results are commensurate with NMR spectroscopic analyses of PAH with L-Phe and an inactive form of the cofactor (BH_2) that place the latter firmly in the first coordination sphere of iron[23] and also with the fact that coordination of the cofactor, or cofactor analogues, to the metal has been observed in other biopterin-dependent metalloenzymes such as PAH from *Chromobacterium violaceum*.[31] Nevertheless, cofactor coordination to iron has so far not been observed or verified in other molecular-level computational studies, for example by starting from hexacoordinate iron complexes.

The goal of the present work is to uncover the structural and energetical changes associated with successive water dissociation in AAHs, and thus to connect the three-water octahedral iron geometries of the binary X-ray crystal structures with a complex containing no water ligands. Such a study will also give the opportunity to monitor the position of the cofactor in the course of water dissociation and thus to investigate potential iron–cofactor bond formation. The establishment of a likely route to water-free complexes will form a sound basis for subsequent investigations of the full catalytic cycle and also for studies directly including the surrounding protein (e.g., QM/MM).

To this end, starting from a cluster model of the X-ray crystal structure of the binary complex hPAH–Fe^{II}–BH_4[14] we have studied successive water ligand dissociation using DFT including effects of polarization from the surrounding protein as well as dispersion.

Computational Details

The models used in this study were based on the X-ray crystal structure of the catalytic domain of hPAH–Fe^{II}–BH_4.[14] The iron atom and its six coordinating ligands [His285, His290, Glu330, H_2O1250 (Wat1), H_2O1251 (Wat3) and H_2O1253 (Wat2)] were extracted from the X-ray crystal structure together with the cofactor, H_2O1142 (Wat 4), and Glu286 of the second coordination sphere (Figure 1). Histidine was modeled by imidazole and glutamic acids by formate. The diol chain on the cofactor was substituted by a hydrogen atom. This strategy with respect to model building in quantum chemical studies of enzyme catalysis is well tested.[27,28,32,33] Geometry optimizations were performed using the B3LYP three-parameter hybrid functional[34] in combination with basis sets of valence double-ζ quality and the located stationary points were characterized by calculation of the second derivatives. Several conformations were located for each point on the reaction path, and only the most stable ones are reported here. The energy was re-evaluated at the optimized geometries, in single-point energy calculations for which the basis sets were augmented with single sets of diffuse and polarization functions. Polarization from the surrounding protein was treated as electrostatic solvent effects using a continuum solvent model. An empirical term accounting for long-range dispersion was also added, meaning that our final energy evaluations are those of B3LYP-D.[35] Complete computational details are given in the Supporting Information.

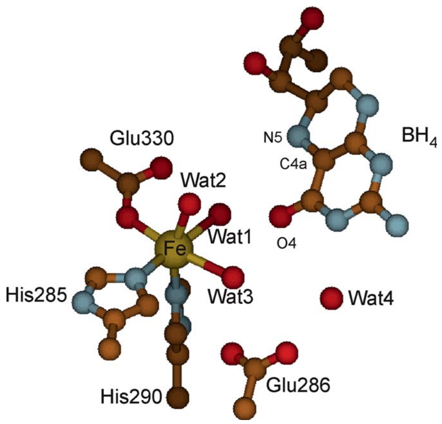

Figure 1. The iron center of the crystal structure of the catalytic domain of hPAH (PDB: 1J8U). The numbering scheme for the amino acid residues and water molecules is that used by Andersen et al.[14]

Results and Discussion

A model including the hexacoordinate iron(II) complex, the cofactor, Glu286 and Wat4 (see Figure 1) was extracted from the X-ray crystal structure (PDB: 1J8U)[14] and modified as described in the Computational Details section. The geometry-optimized model structure (**1b**) has a spin quintet ground state (M = 5) for which the spin density is almost entirely located on iron (spin population of 3.85 on Fe). The optimized cluster model and the corresponding atoms of the X-ray structure could be superimposed with an RMS deviation of 0.73 Å (Figure S2, cf. the Supporting Information).[36] In the minimized structure, the distance between the cofactor carbonyl oxygen and the iron atom is somewhat shorter (3.54 Å) than in the crystal structure (3.81 Å). Furthermore, Wat1 hydrogen bonds to the carbonyl oxygen in the cofactor and to the oxygen atom in Glu330. Wat3 is also interacting with the cofactor carbonyl oxygen and with Glu286, as in the X-ray crystal structure. The overall agreement between the X-ray crystal structure and the minimized structure must be described as good considering the fact that the latter is a gas-phase cluster model without secondary interactions to the surrounding protein. Our model is thus expected to be a reasonable starting point for investigation of the catalytic mechanism. A 0.5 kcal/mol more stable conformation, with His290 rotated 180° compared to the X-ray crystal structure, was also found (**1a**). The two rotational conformations of His290 lead to near degeneration also in structures **2** and **3**, whereas for **4**–**6**, a more pronounced preference for the conformation of **1a** is seen; see the overview in Figure 2.

In the X-ray crystal structure,[14] the water molecules distal to His285 (Wat1) and distal to His290 (Wat2) have been identified as the ones that are most weakly bound to iron.[14] Our calculations show that the water molecule which is the thermodynamically most feasible to remove first is Wat1. Dissociation of Wat1 from **1a** leads to **2a** (ΔG_{diss} = –5.3 kcal/mol, ΔH_{diss} = 4.2 kcal/mol) and is associated with a free energy barrier of 4.4 kcal/mol (**TS[1a-2a]**‡, in the Supporting Information). The free energy dissociation barrier for Wat1 from **1b** is higher (6.9 kcal/mol) (**TS[1b-2b]**‡, in the Supporting Information) and leads to

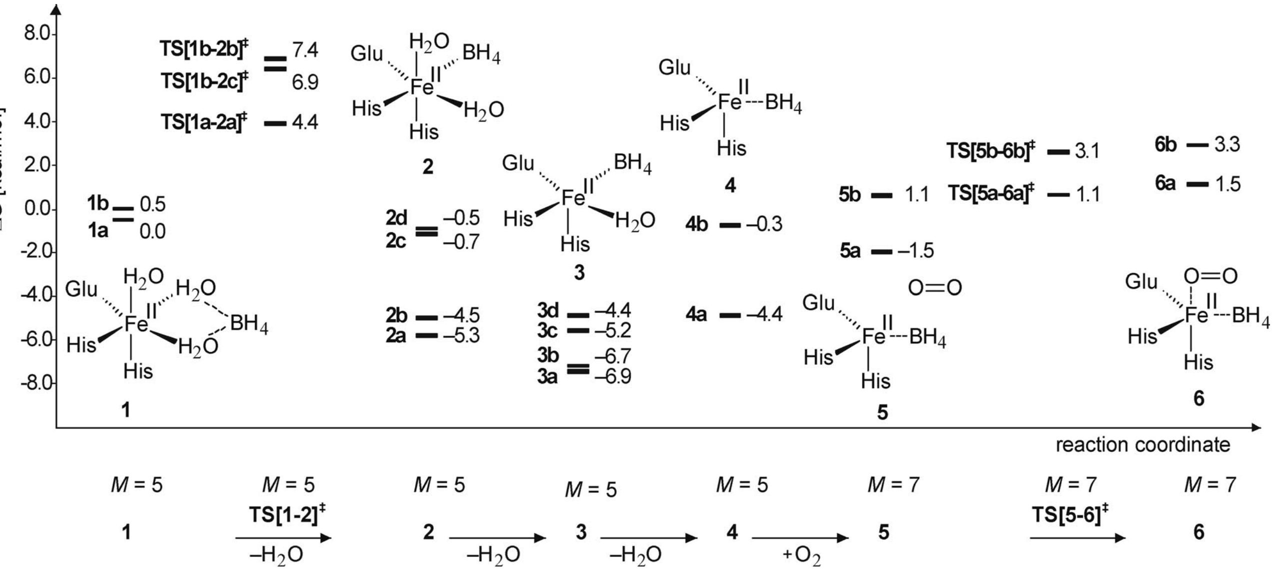

Figure 2. Minima and transition states of water dissociation and O_2 binding for the Fe^{II} model complex. Free energies are given relative to **1a**. Structure **1a** is similar to the crystal structure shown in Figure 1. See Figure 3, 4, 5, and 6 for images of **2a**, **3a**, **4a**, and **6a**, and the Supporting Informations for the other structures and conformations.

structure **2b** which is slightly less stable than **2a**. In the hexacoordinate complex (**2a**; Figure 3) resulting from geometry optimization starting from **1a** with Wat1 removed, the cofactor is bound to iron through the carbonyl oxygen (O4), with an iron–oxygen distance of 2.13 Å. This is not much shorter than the distance found in analysis of NMR spectroscopic data from measurements on PAH with phenylalanine and a cofactor analogue (BH_2) bound in the active site [2.6(±0.3) Å].[23]

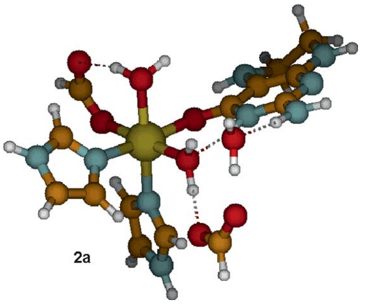
2a

Figure 3. Minimum energy structure of the model of the hPAH Fe^{II} complex with the water molecule distal to His285 (Wat1) dissociated from Fe (**2a**: M = 5, ΔG_{total} = –5.3 kcal/mol).

Removing instead the water molecule distal to His290 (Wat2) turns out to be slightly less facile. Removing Wat2 from **1a** leads to **2d** (cf. the Supporting Information),[37] a pentacoordinate iron complex with the pterin cofactor still placed in the second coordination sphere, interacting with Wat1, Wat3, Wat4 and Glu286. Removing Wat2 from **1b** leads to **2c** (cf. the Supporting Information) (ΔG_{diss} = –0.7 kcal/mol, ΔH_{diss} = 9.6 kcal/mol) and is associated with a free energy dissociation barrier of 6.4 kcal/mol (**TS[1b-2c]**‡, in the Supporting Information). Bassan et al.[28] reported a significantly higher bond dissociation energy (22.5 kcal/mol) upon removal of the water molecule distal to His290 in their DFT study. These authors derived their model system from a different crystal structure of the inactive Fe^{III} form of the enzyme (PDB: 1DMW)[17] than the one forming the basis of the present study (PDB: 1J8U).[14] Some differences in the active site region between the two crystal structures can be noticed, in particular relating to the position of the water molecule in the second coordination sphere (Wat4, cf. Figure 1) and the conformation of Glu330; compare structure **2c** with Wat2 removed (cf. the Supporting Information) and Figure 2 in Bassan et al.[28] The coordinates of the optimized structures of ref.[28] are no longer available.[38] We have thus started calculations from the same X-ray crystal structure[17] as in ref.[28] and obtained a dissociation enthalpy of 11.8 kcal/mol (using our standard methods; see the Computational Details section)[37] and 7.0 kcal/mol (excluding dispersion corrections, to facilitate comparison with the results of ref.[28]) for the water distal to His290. The geometry obtained (**2f**, in the Supporting Information) appears to be similar to the pentacoordinate complex shown in Figure 2 in Bassan et al.,[28] indicating that geometry differences account for a relatively small fraction of the large discrepancy in dissociation energy. Next, calculation of single-point energies according to the methodological approach in ref.[28] results in an increase in the calculated dissociation enthalpy, to 11.4 kcal/mol including continuum solvent effects to mimic the surrounding protein. Omitting the solvent effects leads to dissociation energies ($\Delta H_{diss,gas}$ = 19.5 kcal/mol and $\Delta E_{diss,gas}$ = 21.3 kcal/mol) close to that reported by Bassan et al. In conclusion, the details of the methods applied seem to be more important than variation in the geometries for explaining the large differences in calculated dissociation energies, the single largest contribution possibly being solvent effects.

Returning now to the hexacoordinate complex resulting from the most facile, initial water dissociation (**2a**), it turns out that a second water molecule (Wat2) easily can be removed starting from this structure (ΔG_{diss} = –1.6 kcal/mol). The resulting complex (**3a** in Figure 4) is pentacoordinate and has an iron–O4(BH_4) distance (2.10 Å) slightly shorter than that of **2a**. The bond dissociation free energy for abstraction of the cofactor from this iron complex is 5.9 kcal/mol. Thus, judged from the present gas-phase cluster model, an iron-bound cofactor is favored. In addition, assuming that all three iron-bound water molecules of the initial crystal structure must be dissociated prior to binding of molecular oxygen,[19–21] the resulting complex would appear to be both coordinatively and electronically unsaturated, in particular taking into account the fact that the present complex is charged (balanced by a glutamate in the second coordination sphere) and must be considered relatively Lewis acidic. Alternative structures resulted from optimizations started from geometries in which the cofactor was shifted somewhat in order to probe coordination of N5 to the iron. The iron–nitrogen interaction is preserved in the optimized structures (**3c** and **3d**; cf. the Supporting Information), with a Fe–N5 distance of 2.39 Å and 2.45 Å respectively. The structures **3c** and **3d** are 1.5 kcal/mol and 2.5 kcal/mol less stable than their corresponding carbonyl-bound counterparts with the same rotational conformations of His290, **3b** and **3a**, correspondingly.

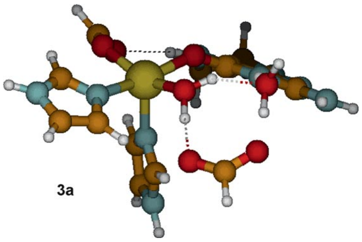
3a

Figure 4. Optimized Fe^{II} complex with one water molecule and BH_4 coordinated through the carbonyl oxygen (**3a**: M = 5, ΔG_{total} = –6.9 kcal/mol).

In the next step, the remaining water molecule in **3a**, distal to Glu330 (Wat3 in Figure 1), was removed. The resulting water-free four-coordinate complex (**4a** in Figure 5) has an iron–oxygen(BH_4) distance of 1.92 Å and is 4.4 kcal/mol more stable than **1a**. The crystal structure-like conformation of His290 leads to a complex (**4b**; cf the Supporting Information) which is 4.1 kcal/mol less stable than **4a**. In both **4a** and **4b**, hydrogen bonds from a carbon atom next to the iron-bound imine nitrogen to Glu286 and Wat4 exist, and the O–H distances involved are somewhat shorter in **4a** where the hydrogen bonds originate from a carbon atom bound to two nitrogen atoms.

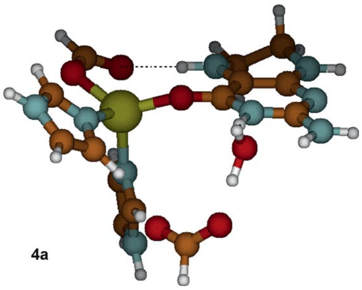

4a

Figure 5. Geometry optimized Fe^{II} complex with all water molecules dissociated from Fe (**4a**: M = 5, ΔGtotal = –4.4 kcal/mol).

Binding of dioxygen to the water-free complex **4a** results in a complex (**5a**), 2.9 kcal/mol less stable than **4a**, in which dioxygen does not coordinate to the metal but is placed above the cofactor (**5a**, in the Supporting Information) with the closest oxygen 4.63 Å from iron. Coordination of dioxygen to iron from this weakly bound complex proceeds with a free energy barrier of 2.6 kcal/mol (**TS[5a-6a]**‡, in the Supporting Information) and results in a complex (**6a** in Figure 6) in which O_2 coordinates to iron in a end-on fashion with a distance between iron and the closest oxygen of 2.55 Å. The distal oxygen is oriented towards the carbonyl group on the cofactor. The iron–O_2 complex is pentacoordinate, which is consistent with spectroscopic results,[6,19] and has a septet ground state due to the triplet molecular oxygen.

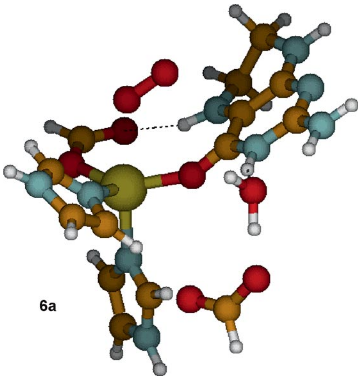

6a

Figure 6. Optimized Fe^{II} complex with molecular oxygen coordinated to iron (**6a**: M = 7, ΔG_{total} = 1.5 kcal/mol).

Structure **6a** is located 1.5 kcal/mol above the hexacoordinate starting complex **1a**, implying that the overall water dissociation and oxygen coordination is weakly endergonic. Water dissociation does not seem to involve significant barriers. The overall effective free energy barrier (8.0 kcal/mol, from **3a** to **TS[5a-6a]**‡) includes the binding of dioxygen. The present results are thus consistent with the observed rapid equilibrium binding of oxygen in TH.[39] The mechanism of water dissociation and oxygen coordination as obtained using the present cluster model should be further investigated and verified in hybrid quantum mechanic/molecular mechanics (QM/MM) calculations including explicit treatment of the surrounding protein.[29]

Supporting Information (see also the footnote on the first page of this article): Complete computational details; total energies, thermochemical corrections, dispersion corrections, solvent corrections, relative energies and enthalpies, and Cartesian coordinates calculated for the stationary points and conformations located along the reaction coordinate path.

Acknowledgments

The University of Bergen is acknowledged for financial support through the Nanoscience program. The Norwegian Research Council is acknowledged for CPU resources granted through the NOTUR supercomputing program. We are grateful to Dr. Giovanni Occhipinit and Prof. Karl Wilhelm Törnroos for helpful discussions.

---

[1] P. F. Fitzpatrick, *Annu. Rev. Biochem.* **1999**, *68*, 355–381.
[2] T. J. Kappock, J. P. Caradonna, *Chem. Rev.* **1996**, *96*, 2659–2756.
[3] E. I. Solomon, T. C. Brunold, M. I. Davis, J. N. Kemsley, S. K. Lee, N. Lehnert, F. Neese, A. J. Skulan, Y. S. Yang, J. Zhou, *Chem. Rev.* **2000**, *100*, 235–349.
[4] T. A. Dix, S. J. Benkovic, *Acc. Chem. Res.* **1988**, *21*, 101–107.
[5] W. A. Francisco, G. C. Tian, P. F. Fitzpatrick, J. P. Klinman, *J. Am. Chem. Soc.* **1998**, *120*, 4057–4062.
[6] J. N. Kemsley, N. Mitic, K. L. Zaleski, J. P. Caradonna, E. I. Solomon, *J. Am. Chem. Soc.* **1999**, *121*, 1528–1536.
[7] D. W. Gottschall, R. F. Dietrich, S. J. Benkovic, R. Shiman, *J. Biol. Chem.* **1982**, *257*, 845–849.
[8] T. A. Dix, S. J. Benkovic, *Biochemistry* **1985**, *24*, 5839–5846.
[9] B. E. Eser, E. W. Barr, P. A. Frantorn, L. Saleh, J. M. Bollinger, C. Krebs, P. F. Fitzpatrick, *J. Am. Chem. Soc.* **2007**, *129*, 11334–11335.
[10] J. A. Pavon, P. F. Fitzpatrick, *J. Am. Chem. Soc.* **2009**, *131*, 4582–4583.
[11] A. Bassan, M. R. A. Blomberg, T. Borowski, P. E. M. Siegbahn, *J. Inorg. Biochem.* **2006**, *100*, 727–743.
[12] E. L. Hegg, L. J. Que, *Eur. J. Biochem.* **1997**, *250*, 625–629.
[13] L. Que, *Nat. Struct. Biol.* **2000**, *7*, 182–184.
[14] O. A. Andersen, T. Flatmark, E. Hough, *J. Mol. Biol.* **2001**, *314*, 279–291.
[15] O. A. Andersen, T. Flatmark, E. Hough, *J. Mol. Biol.* **2002**, *320*, 1095–1108.
[16] O. A. Andersen, A. J. Stokka, T. Flatmark, E. Hough, *J. Mol. Biol.* **2003**, *333*, 747–757.
[17] H. Erlandsen, E. Bjørgo, T. Flatmark, R. C. Stevens, *Biochemistry* **2000**, *39*, 2208–2217.
[18] K. Teigen, V. R. Jensen, A. Martinez, *Pteridines* **2005**, *16*, 27–34.
[19] A. Y. Han, A. Q. Lee, M. M. Abu-Omar, *Inorg. Chem.* **2006**, *45*, 4277–4283.
[20] P. J. Loida, S. G. Sligar, *Biochemistry* **1993**, *32*, 11530–11538.
[21] T. I. Oprea, G. Hummer, A. E. Garcia, *Proc. Natl. Acad. Sci. USA* **1997**, *94*, 2133–2138.
[22] F. Forouhar, J. L. R. Anderson, C. G. Mowat, S. M. Vorobiev, A. Hussain, M. Abashidze, C. Bruckmann, S. J. Thackray, J. Seetharaman, T. Tucker, R. Xiao, L. C. Ma, L. Zhao, T. B. Acton, G. T. Montelione, S. K. Chapman, L. Tong, *Proc. Natl. Acad. Sci. USA* **2007**, *104*, 473–478.
[23] K. Teigen, N. A. Frøystein, A. Martinez, *J. Mol. Biol.* **1999**, *294*, 807–823.
[24] H. Erlandsen, J. Y. Kim, M. G. Patch, A. Han, A. Volner, M. M. Abu-Omar, R. C. Stevens, *J. Mol. Biol.* **2002**, *320*, 645–661.

[25] E. C. Wasinger, N. Mitic, B. Hedman, J. Caradonna, E. I. Solomon, K. O. Hodgson, *Biochemistry* **2002**, *41*, 6211–6217.
[26] K. E. Loeb, T. E. Westre, T. J. Kappock, N. Mitic, E. Glasfeld, J. P. Caradonna, B. Hedman, K. O. Hodgson, E. I. Solomon, *J. Am. Chem. Soc.* **1997**, *119*, 1901–1915.
[27] A. Bassan, M. R. A. Blomberg, P. E. M. Siegbahn, *Chem. Eur. J.* **2003**, *9*, 4055–4067.
[28] A. Bassan, M. R. A. Blomberg, P. E. M. Siegbahn, *Chem. Eur. J.* **2003**, *9*, 106–115.
[29] Y. Shiota, K. Yoshizawa, *J. Phys. Chem. B* **2004**, *108*, 17226–17237.
[30] M. M. Abu-Omar, A. Loaiza, N. Hontzeas, *Chem. Rev.* **2005**, *105*, 2227–2252.
[31] S. O. Pember, S. J. Benkovic, J. J. Villafranca, M. Pasenkiewiczgierula, W. E. Antholine, *Biochemistry* **1987**, *26*, 4477–4483.
[32] P. E. M. Siegbahn, *J. Comput. Chem.* **2001**, *22*, 1634–1645.
[33] P. E. M. Siegbahn, F. Himo, *J. Biol. Inorg. Chem.* **2009**, *14*, 643–651.
[34] P. J. Stevens, F. J. Devlin, C. F. Chablowski, M. J. Frisch, *J. Phys. Chem.* **1994**, *98*, 11623–11627.
[35] S. Grimme, *J. Comput. Chem.* **2006**, *27*, 1787–1799.
[36] Quatfit. D. J. Heisterberg, unpublished results. The iron atoms of the two structures were constrained to coincide.
[37] Solvent and dispersion effects contribute –7.8 kcal/mol and 5.8 kcal/mol to these dissociation energies, respectively.
[38] A. Bassan, M. R. A. Blomberg, P. E. M. Siegbahn, personal communication.
[39] P. F. Fitzpatrick, *Biochemistry* **1991**, *30*, 3658–3662.

Received: May 31, 2009

DOI: 10.1002/ejic.200900946

Generation of Hollow $MnSiO_3$ Nanostructures through the Solid-State Reaction of Mn_3O_4 and Pd/PdO Nanocrystals Dimensionally Confined within Nanosized Silica Spheres

Jongmin Shin,[a] Tae-Lin Ha,[a] and In Su Lee*[a]

Keywords: Nanoparticles / Hollow structures / Solid-state reactions / Manganese / Palladium

In the course of annealing Mn_3O_4 and Pd/PdO nanocrystals co-encapsulated within a nanosized silica sphere under a reducing environment, we observed that the reduction of Mn_3O_4 into MnO was facilitated by the Pd/PdO nanocrystals. Successive annealing at high temperatures induced the MnO nanocrystals to react with the silica matrix, resulting in the formation of hollow nanostructures composed of a polycrystalline $MnSiO_3$ shell.

Introduction

There is growing interest in the synthesis and fabrication of nanosized colloidal particles with a hollow interior structure based on their wide range of potential applications.[1,2] For instance, we previously demonstrated the potential utility of hollow manganese oxide nanoparticles as a multifunctional agent for simultaneous MR imaging and drug delivery.[2a] Hollow nanoparticles are often synthesized by sacrificing the template that defines the interior structure through chemical etching or galvanic replacement processes.[3] Recently, a template-free method was developed by using the nanoscale Kirkendall effect to synthesize several hollow nanostructures composed of metal sulfide, selenide, and phosphide from preformed metal nanoparticles.[4] However, despite the recent development of synthetic methods, precise control of their phase, structure, and consequent properties is still a significant challenge. Most reported methods employ solution-based reactions to synthesize hollow nanoparticles rather than solid-state reactions due to the high temperatures required in the latter process that cause coalescence and coarsening of the nanostructures.[5]

In this context, our research efforts have focused on developing a novel approach to manipulate hollow nanoparticles based on an the understanding of the solid-state reactions between nanoparticles. Mn_3O_4 and Pd/PdO nanocrystals were co-encapsulated within nanosized silica spheres to preserve their nanostructural characteristics, even at high temperatures, and to induce interactions between adjacent nanoparticles.[5a,6] In the course of annealing the nanocrystals under a hydrogen environment, the Mn_3O_4 nanocrystals were reduced and transformed into hollow $MnSiO_3$ nanostructures through a process facilitated by the adjacent Pd nanocrystals (Scheme 1). Moreover, we found that the conversion between nanostructures could be achieved only by reactions dimensionally confined within the nanosized matrix. To the best of our knowledge, this is the first report of the generation of hollow nanostructures through a novel solid-state approach using nanoparticles co-encapsulated within silica nanospheres.

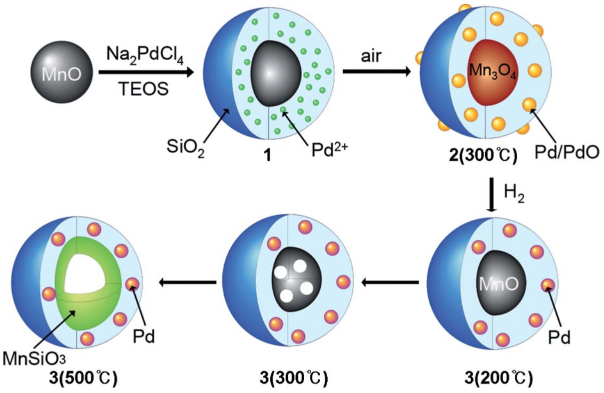

Scheme 1. Formation of hollow $MnSiO_3$ nanoparticle in silica sphere.

Results and Discussion

The 39(±4) nm-sized silica nanospheres, **1**, containing a 19(±3) nm-sized MnO nanocore passivated with Mn_3O_4 and tiny aggregates of Pd^{2+} complexes distributed homogeneously over the silica shell, were prepared by modification of a previously reported reverse microemulsion technique.[6b,7] Nanospheres **1** were then annealed in air at vari-

---

[a] Department of Applied Chemistry, College of Applied Science, Kyung Hee University,
Gyeonggi-do 449-701, Korea
Fax: +82-31-202-7337
E-mail: insulee97@khu.ac.kr

Supporting information for this article is available on the WWW under http://dx.doi.org/10.1002/ejic.200900946.

ous temperatures between 300 and 700 °C. Transmission electron microscopy (TEM), X-ray diffraction (XRD), and X-ray photoelectron spectroscopy (XPS) analyses of resulting nanospheres **2** revealed oxidation of the MnO nanocrystals to Mn_3O_4 with preservation of their initial shape and size (Figure 1). In addition, the Pd^{2+} complexes were converted into small, mixed-phase Pd/PdO nanocrystals during annealing at 300 °C. Although further research is required to understand this process fully, the formation of metallic Pd species might be coupled with the oxidation of Mn^{2+} into Mn^{3+}. As the annealing temperature was increased to 700 °C, the Pd/PdO nanoparticles diffused outward and coalesced into larger PdO grains at the silica surface.

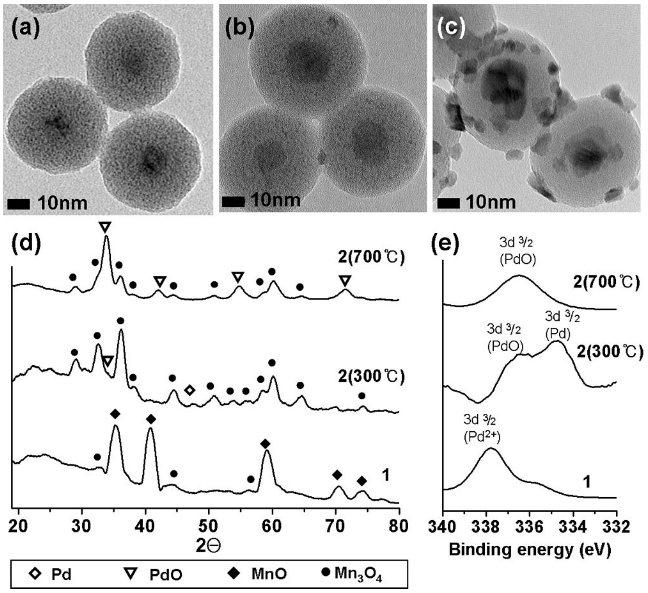

Figure 1. TEM images of the silica nanospheres containing a MnO nanocore and Pd^{2+} complexes before and after the annealing in air at different temperatures: (a) **1**, (b) **2**(300 °C), and (c) **2**(700 °C), and their (d) XRD and (e) XPS data.

The transformation of nanocrystals under a reducing environment was examined by using nanospheres **2**(300 °C) encapsulating 19(±3) nm-sized Mn_3O_4 particles and small Pd/PdO nanocrystals. Nanospheres **3**, obtained after annealing **2**(300 °C) under flowing Ar + 4% H_2 at various temperatures, revealed the steps involved in the solid-state transformation of the nanocrystals into hollow nanostructures (Figure 2). Reductive annealing of **2**(300 °C) at 200 °C did not cause any significant changes in the shape and size of the Mn_3O_4 nanocrystals during the reaction. XRD and XPS revealed the reduction of Mn_3O_4 and Pd/PdO, even at 200 °C, resulting in nanospheres containing a MnO nanocore and small Pd nanocrystals distributed around the silica shell. While several studies have reported the ready reduction of PdO nanocrystals at temperatures as low as 200 °C, the reduction of Mn_3O_4 at this low temperature is quite unusual.[8] When silica nanospheres containing Mn_3O_4 nanoparticles were prepared without the addition of a Pd^{2+} complex, or their physical mixture with silica nanospheres containing PdO was annealed under a hydrogen atmosphere, the reduction of Mn_3O_4 was not observed even at 500 °C (see Supporting Information). This suggests that the Pd/PdO nanocrystals co-confined within the nanospheres facilitated Mn_3O_4 reduction. The enhanced reducibility of Mn_3O_4 can be understood by a process involving the spillover of hydrogen atoms from prereduced Pd nanocrystal surfaces and their migration for nanometer distances over the silica matrix to reach and reduce Mn_3O_4.[9] Enhanced reducibility via a hydrogen spillover effect has previously been reported for bulk Pd or Pt materials supported by metal oxides.[10]

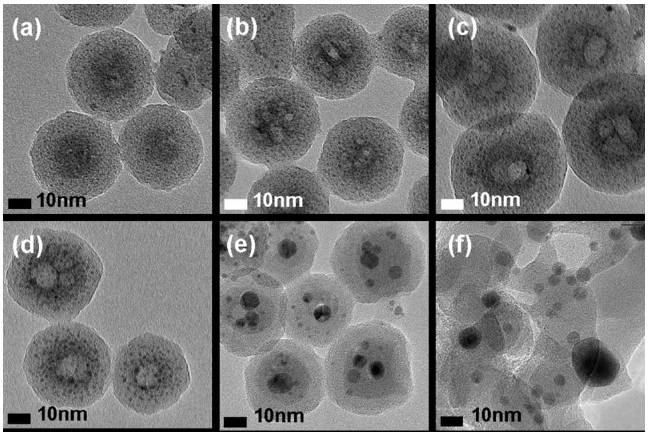

Figure 2. TEM images of the silica nanospheres containing a MnO nanocore and Pd/PdO nanocrystals after annealing under the reductive environment at different temperatures: (a) **3**(200 °C), (b) **3**(300 °C), (c) **3**(400 °C), (d) **3**(500 °C), (e) **3**(600 °C), and (f) **3**(700 °C).

When nanospheres **2**(300 °C) were annealed at high temperatures, the Mn_3O_4 nanoparticles were converted into porous structures. TEM of the nanospheres treated at 300 °C, **3**(300 °C), revealed the formation of MnO nanocrystals with interior voids and an average diameter of 4(±2) nm. Increasing the annealing temperature to 400 °C induced further development of the void space with the expansion of the nanocrystal. When nanospheres **2**(300 °C) were further annealed at 500 °C, the voids merged into a spherical cavity within the nanoparticle, resulting in the formation of a hollow nanostructure within the silica nanospheres containing Pd nanoparticles. The nitrogen adsorption/desorption isotherm of **2**(300 °C) and **3**(500 °C) revealed the increase in BET surface area from 33 to 63 m^2/g and the generation of a porous system with a pore size distribution centered at 21.3 nm during the reductive annealing process (see Supporting Information). Energy dispersive X-ray spectroscopy (EDX) of the nanospheres annealed at 500 °C, **3**(500 °C), showed the localization of Mn at the hollow shell. The annealing of **2**(300 °C) at 400 and 500 °C caused an increase and narrowing of the Pd peaks in the XRD patterns, which is consistent with the coalescence and growth of Pd grains at high temperatures as observed by TEM. A marked decrease in the MnO peaks in the XRD patterns of **3**(400 °C) and **3**(500 °C) was observed upon the appearance of new broad peaks corresponding to a $MnSiO_3$

phase (Figure 3). XPS revealed the presence of Mn^{2+} species in **3**(400 °C) and **3**(500 °C) (see Supporting Information).

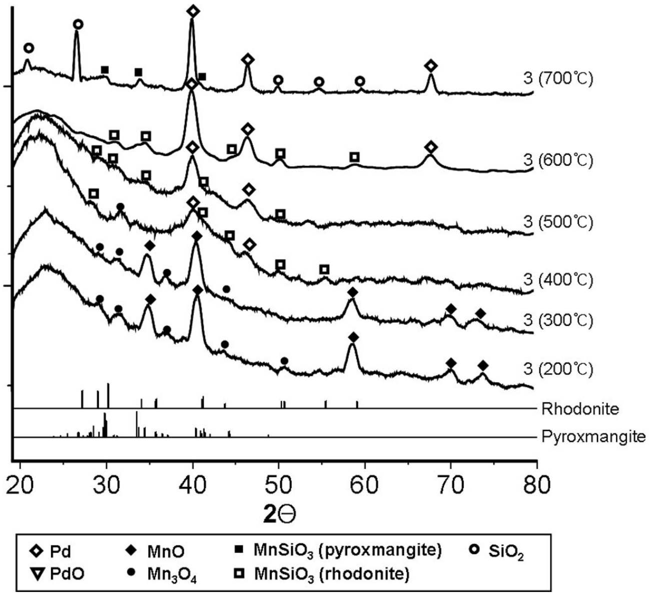

Figure 3. (a) XRD patterns of the silica nanospheres before and after the reductive annealing at different temperature.

These observations suggest that successive annealing at high temperatures induced the reaction of MnO nanoparticles with the silica matrix, resulting in their conversion into hollow nanostructures composed of a polycrystalline $MnSiO_3$ shell. The development of voids inside the nanocrystals and the formation of a hollow structure can be explained by a mechanism based on the nanoscale Kirkendall effect, in which the outward flow of fast-moving MnO species rather than the inward transport of SiO_2 species is dominant during the formation of $MnSiO_3$.[4e] The diffusion of Mn species into SiO_2 and consequent formation of $MnSiO_3$ has been observed at the interface between Cu–Mn alloy and SiO_2 layers.[11] A comparison of the EDX elementary maps for the nanospheres also provides evidence for the outward diffusion of Mn species from the nanoparticle core (Figure 4). The smaller cavity diameter of the resulting hollow structures than the size of the starting Mn_3O_4 nanocrystals suggests that the inward transport of SiO_2 can occur at a moderate rate during $MnSiO_3$ formation. No significant change was detected in the nanocrystals when the silica nanospheres encapsulating only MnO nanoparticles without Pd nanoparticles were annealed under reducing conditions at 500 °C (see Supporting Information). Although the reaction mechanism is not yet fully understood, the presence of Pd nanoparticles within the nanosphere could be responsible for the formation of hollow Mn_3O_4 nanoparticles. When nanospheres **2**(300 °C) were annealed reductively at higher temperatures, such as 600 and 700 °C, the hollow Mn_3O_4 nanostructures collapsed and the Pd nanoparticles coalesced into much larger grains. At 700 °C, the crystalline phase of Mn_3O_4 was transformed from rhodonite into pyroxmangite.[12]

Conclusions

The ready reduction of Mn_3O_4 nanoparticles occurred during the reductive annealing of silica nanospheres co-en-

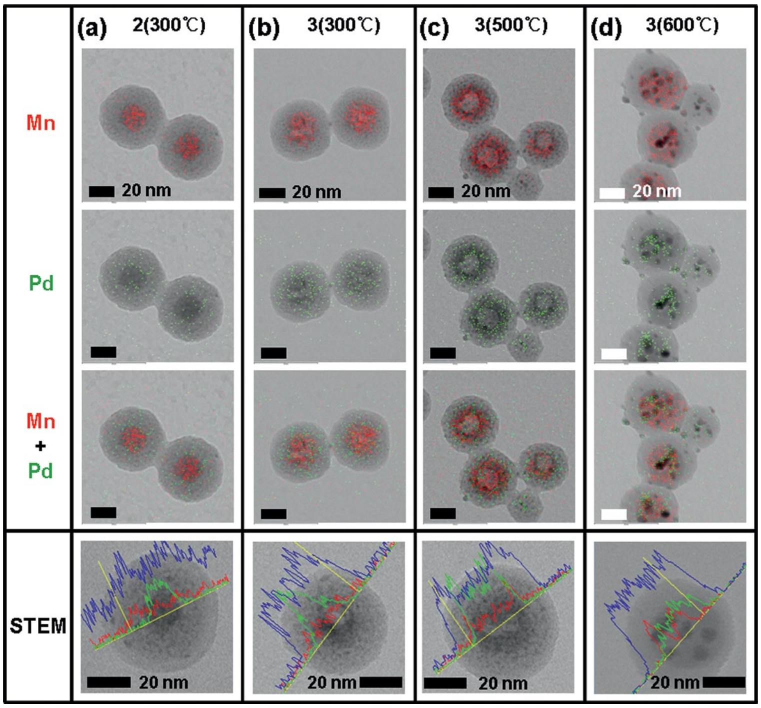

Figure 4. EDX elementary maps and STEM images of the silica nanospheres before and after reductive annealing at different temperatures: (a) **2**(300 °C), (b) **3**(300 °C), (c) **3**(500 °C), and (d) **3**(600 °C).

capsulating a Mn_3O_4 nanocore and small Pd/PdO nanoparticles, resulting in hollow $MnSiO_3$ nanostructures. This solid-state conversion of nanoparticles into a hollow structure was induced by a process facilitated by the adjacent Pd nanoparticles and was achieved by a reaction confined dimensionally within a nanosized matrix. This novel approach can be used to fabricate porous nanoparticles for catalytic, biosensing, and drug delivery applications.

Experimental Section

Synthesis: MnO nanoparticles having an average core size of 19 nm were prepared through the previously reported procedure.[13] Polyoxyethylene(5)nonylphenyl ether (1.54 mg, 3.49 mmol, Igepal® CO-520, containing 50 mol-% hydrophilic group, Aldrich) was dispersed in a round-bottomed flask containing cyclohexane (34 mL) by sonication. Next, MnO nanoparticles (4 mg) dispersed in cyclohexane were added to the reaction solution. The resulting mixture was vortexed until the mixture became transparent. An aqueous solution of Na_2PdCl_4 (0.285 M, 0.2 mL) and ammonium hydroxide solution (30%, 0.26 mL) were successfully added to the reaction mixture to form a transparent suspension. Lastly, tetraethylorthosilicate (0.3 mL, TEOS) was added, and the mixture was stirred for 48 h. Resulting silica nanospheres **1** containing MnO nanocores and tiny aggregates of Pd^{2+} complexes were collected by centrifugation. The collected nanospheres of **1** were redispersed in EtOH and recovered by centrifugation. The dispersion of **1** into EtOH suspension and the centrifugation was repeated three times for the purification to yield 34 mg of **1**. The powder of **1** (20 mg) was heated with a heating rate of 5 °C/min in a furnace and annealed in air condition for 5 h at 300, 500, and 700 °C, generating 18.1 mg of nanospheres **2** (91% yield). For the generation of **3** (17.7 mg, 89% yield), nanospheres **2**(300 °C) (20 mg) was annealed under a flow of Ar + 4% H_2 at 200, 300, 400, 500, 600, and 700 °C for 5 h.

Characterization: Analyses of transmission electron microscopy (TEM), scanning transmission electron microscopy (STEM), energy dispersive x-ray spectroscopy (EDX), and electron energy loss spectroscopy (EELS) were conducted with JEOL JEM-2010 and JEOL JEM 2100F. Scanning tunneling microscopy (SEM) was carried out with LEO SUPRA 55 (Carl Zeiss, Germany). X-ray photoelectron spectroscopy (XPS) was obtained using K_α (Thermo Electron, UK). UV absorption was observed by using V670 UV/Vis/NIR spectrophotometer (JASCO). The nitrogen adsorption/desorption isotherm experiment was carried out by using BELSORP-max (BEL JAPAN, Japan).

Supporting Information (see footnote on the first page of this article): TEM and XRD data for the control experiment, SEM and XPS data, diagrams for showing particle and pore size distribution for **2** and **3**, additional TEM images and N_2 sorption isotherms of **2**(300 °C) and **3**(500 °C), EELS image of **3**(500 °C), and STEM image and EDX elementary map of **3**(700 °C).

Acknowledgments

This research was supported by the Basic Science Research Program through the National Research Foundation of Korea (NRF) funded by the Ministry of Education, Science and Technology (2009-0071362).

---

[1] a) C. N. Rao, A. Govindaraj, *Adv. Mater.* **2009**, *21*, 4208–4233; b) X. W. Lou, L. A. Archer, Z. Yang, *Adv. Mater.* **2008**, *20*, 3987–4019.

[2] a) J. Shin, R. M. Anisur, M. K. Ko, G. H. Im, J. H. Lee, I. S. Lee, *Angew. Chem. Int. Ed.* **2009**, *48*, 321–324; b) J. Zhou, H. Song, X. Chen, L. Zhi, S. Yang, J. Huo, W. Yang, *Chem. Mater.* **2009**, *21*, 2935–2940; c) C.-C. Huang, W. Huang, C.-H. Su, C.-N. Feng, W.-S. Kuoa, C.-S. Yeh, *Chem. Commun.* **2009**, 3360–3362; d) P. M. Arnal, M. Comotti, F. Schüth, *Angew. Chem. Int. Ed.* **2006**, *45*, 8224–8227.

[3] a) X. W. Lou, L. A. Archer, *Adv. Mater.* **2008**, *20*, 1853–1858; b) X. Lu, H.-Y. Tuan, J. Chen, Z.-Y. Li, B. A. Korgel, Y. Xia, *J. Am. Chem. Soc.* **2007**, *129*, 1733–1742; c) Y. Yin, C. Erdonmez, S. Aloni, A. P. Alivisatos, *J. Am. Chem. Soc.* **2006**, *128*, 12671–12673; d) A. N. Zelikin, O. Li, F. Caruso, *Angew. Chem. Int. Ed.* **2006**, *45*, 7743–7745; e) Y. Sun, B. Mayers, Y. Xia, *Adv. Mater.* **2003**, *15*, 641–646; f) F. Caruso, *Chem. Eur. J.* **2000**, *6*, 413–419.

[4] a) X. Liang, X. Wang, Y. Zhuang, B. Xu, S. Kuang, Y. Li, *J. Am. Chem. Soc.* **2008**, *130*, 2736–2737; b) S. Peng, S. Sun, *Angew. Chem. Int. Ed.* **2007**, *46*, 4155–4158; c) A. E. Henkes, Y. Vasquez, R. E. Schaak, *J. Am. Chem. Soc.* **2007**, *129*, 1896–1897; d) J. Gao, B. Zhang, X. Zhang, B. Xu, *Angew. Chem. Int. Ed.* **2006**, *45*, 1220–1223; e) Y. Yin, R. M. Rioux, C. K. Erdonmez, S. Hughes, G. A. Somorjai, A. P. Alivisatos, *Science* **2004**, *304*, 711–714.

[5] a) Y. Piao, J. Kim, H. B. Na, D. Kim, J. S. Baek, M. K. Ko, J. H. Lee, M. Shokouhimehr, T. Hyeon, *Nat. Mater.* **2008**, *7*, 242–247; b) H. J. Fan, M. Knez, R. Scholz, K. Nielsch, E. Pippel, D. Hesse, M. Zacharias, U. Gösele, *Nat. Mater.* **2006**, *5*, 627–631.

[6] a) J. Kim, C. Rong, J. P. Liu, S. Sun, *Adv. Mater.* **2009**, *21*, 906–909; b) J. Shin, H. Kim, I. S. Lee, *Chem. Commun.* **2008**, 5553–5555; c) S. Yamamoto, Y. Morimoto, T. Ono, M. Takano, *Appl. Phys. Lett.* **2005**, *87*, 032503/1–032503/3.

[7] a) D. C. Lee, F. V. Mikulec, J. M. Pelaez, B. Koo, B. A. Korgel, *J. Phys. Chem. Part B* **2006**, *110*, 11160–11166; b) D. K. Yi, S. T. Selvan, S. S. Lee, G. C. Papaefthymiou, D. Kundaliya, J. Y. Ying, *J. Am. Chem. Soc.* **2005**, *127*, 4990–4991.

[8] a) L. S. F. Feio, C. E. Hori, S. Damyanova, F. B. Noronha, W. H. Cassinelli, C. M. P. Marques, J. M. C. Bueno, *Appl. Catal. A* **2007**, *316*, 107–116; b) A. Baylet, S. Royer, C. Labrugère, H. Valencia, P. Marécot, J. M. Tatibouët, D. Duprez, *Phys. Chem. Chem. Phys.* **2008**, *10*, 5983–5992.

[9] a) W. C. Conner Jr., J. L. Falconer, *Chem. Rev.* **1995**, *95*, 759–788; b) W. C. Conner Jr., G. M. Pajonk, S. J. Teichner, *Adv. Catal.* **1986**, *34*, 1–79.

[10] a) W. K. Jozwiak, E. Kaczmarek, T. P. Maniecki, W. Ignaczak, W. Maniukiewicz, *Appl. Catal. A: Gen.* **2007**, *326*, 17–27; b) T. Matsuda, A. Hanai, F. Uchijima, H. Sakagami, N. Takahashi, *Microporous Mesoporous Mater.* **2002**, *51*, 155–164; c) G. Fröhlich, W. M. H. Sachtler, *J. Chem. Soc. Faraday Trans.* **1998**, *94*, 1339–1346; d) D. Martin, D. Duprez, *J. Phys. Chem. B* **1997**, *101*, 4428–4436.

[11] a) J. M. Ablett, J. C. Woicik, Zs. Tökei, S. List, E. Dimasi, *Appl. Phys. Lett.* **2009**, *94*, 042112/1–042112/3; b) J. Koike, M. Haneda, J. Iijima, Y. Otsuka, H. Sako, K. Neishi, *J. Appl. Phys.* **2007**, *102*, 043527/1–043527/7; c) J. Koike, M. Wada, *Appl. Phys. Lett.* **2005**, *87*, 041911/1–041911/3.

[12] H. Narita, K. Koto, N. Morimoto, *Mineral. J.* **1977**, *8*, 329–342.

[13] H. B. Na, J. H. Lee, K. An, Y. I. Park, I. S. Lee, D.-H. Nam, S. T. Kim, S.-H. Kim, S.-W. Kim, K.-H. Lim, K.-S. Kim, S.-O. Kim, T. Hyeon, *Angew. Chem. Int. Ed.* **2007**, *46*, 5397–5401.

Received: September 22, 2009

DOI: 10.1002/ejic.200901113

Reprogramming of a Malonic N-Heterocyclic Carbene: A Simple Backbone Modification with Dramatic Consequences on the Ligand's Donor Properties

Vincent César,*[a,b] Noël Lugan,[a,b] and Guy Lavigne*[a,b]

Keywords: Heterocyclic carbenes / Diamidocarbene / Organometallic chemistry / Electronic properties / Rhodium

Reaction of *N*,*N*′-dimesitylformamidine with dimethylmalonyl dichloride in dichloromethane in the presence of an excess of triethylamine gives the 2-chloro-4,5-dioxohexahydropyrimidine **1**. The corresponding diamidocarbene **3** is generated in situ by further deprotonation with KHMDS at –40 °C and identified by trapping with S_8 to give the fully characterized (including X-ray structure) sulfur adduct **4**. It also reacts with $[RhCl(cod)]_2$ to yield the NHC complex [RhCl(**3**)(cod)] (**5**) (characterized also by X-ray structure). The donor properties of **3** were evaluated against the established IR [ν(CO)] scale from [RhCl(**3**)$(CO)_2$] (**6**). The average value of ν(CO) = 2045 cm^{-1} indicates that the diamidocarbene **3** is much less nucleophilic than structurally relevant six-membered NHCs including the anionic diaminocarbenes previously reported in our group.

Introduction

N-Heterocyclic carbenes (NHCs)[1,2] have gained valuable significance over the past fifteen years, both as organocatalysts[3] and as "universal" ligands for organometallic catalysis.[4] Due to the presence of at least one amino-type nitrogen atom (two nitrogen atoms directly connected to the carbene atom for the most studied cyclic diaminocarbenes) in the vicinity of the carbene centre, they are typically classified as *nucleophilic* carbenes and, by consequence, behave as strong electron-donor ligands, particularly in comparison with phosphanes.[5] So, whereas the successful design of highly nucleophilic NHCs has received considerable attention,[6] the alternate possibility of reducing their donor properties has been only reported in a few cases.[7]

Our recent disclosure of a modulable synthetic strategy[8] leading to the six-membered anionic NHC **A** incorporating a malonate backbone (Figure 1) offered further possibilities to devise structurally related derivatives exhibiting different donor properties.[8] Indeed, we reasoned that a slightly modified approach based on dimethylmalonyl chloride as a coupling partner (vide infra) would allow the introduction of a second substituent at the position 5 of the heterocycle, thereby blocking the electronic delocalisation through the malonate skeleton, ultimately producing the neutral carbene of type **B**, being much less nucleophilic due to the incorporation of nitrogen atoms as amide groups.

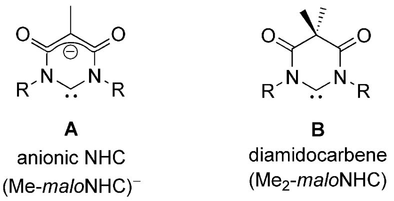

Figure 1. Anionic N-heterocyclic carbene and diamidocarbene based on the same six-membered skeleton.

During the course of this work, we became aware of the very recent independent publication by Bielawski and coworkers of a slightly different synthetic approach leading to the first diamidocarbene of type **B**.[9] This prompted us to disclose our parallel results giving additional insight into the chemistry of this fascinating new type of N-heterocyclic carbene incorporating amide-type nitrogen atoms.[10]

Results and Discussion

In a logical transposition of our synthesis of **A**,[8] the precursor of **B** was prepared by coupling *N*,*N*′-dimesitylformamidine with dimethylmalonyl dichloride in dichloromethane in the presence of an excess of triethylamine as a base (Scheme 1). Surprisingly, the product did not display any salt-like character but behaved as a neutral compound, with a relative good solubility in aromatic solvents (toluene or benzene) as well as in nonpolar mixtures usually unable to dissolve chloride salts. Such properties facilitated the isolation of the product by simple selective extraction from a CH_2Cl_2/Et_2O mixture (1:2, v/v). Considering that the attachment of two electron-withdrawing carbonyl functionalities on the nitrogen atoms renders the formamid-

---

[a] CNRS, LCC (Laboratoire de Chimie de Coordination),
205 route de Narbonne, 31077 Toulouse Cedex 4, France
[b] Université de Toulouse, UPS, INPT,
31077 Toulouse Cedex 4, France
E-mail: vincent.cesar@lcc-toulouse.fr
guy.lavigne@lcc-toulouse.fr

inium unit sufficiently electrophilic to undergo a nucleophilic attack by the chloride counteranion, a formulation of the compound as a 2-chloro-4,5-dioxohexahydropyrimidine **1** – a "masked" form for a formamidinium – was reasonably anticipated.[11] Such a structure was confirmed by ^{1}H and ^{13}C NMR spectra, where the proton and carbon resonances at the position 2 of the heterocycle appeared at δ = 6.93 ppm (singlet) and δ = 90.5 ppm, respectively. Such signals are in agreement with the chemical shifts reported for 4,6-dioxo-1,3-diazine with an sp^3-hybridized carbon atom at the position 2.[12]

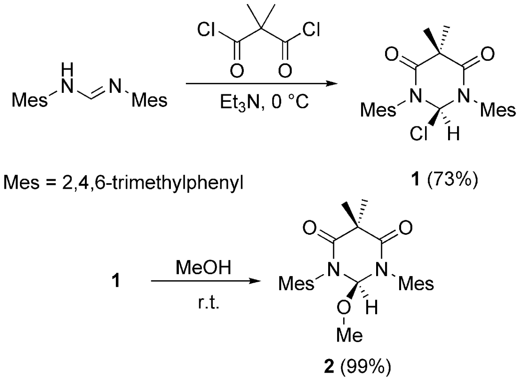

Scheme 1. Synthesis of compound **1** and its subsequent methanolysis.

The chloride adduct **1** proved to be extremely moisture-sensitive, thus requiring manipulation under an inert gas. Typically, the chlorine atom in position 2 of the heterocycle could be readily replaced by better nucleophiles, as exemplified by the reaction of **1** with methanol to produce the air-stable, methoxy-substituted heterocycle **2** (Scheme 1), exhibiting a shift of the ^{1}H NMR signal at position 2 to δ = 5.28 ppm, consistent with a reduced electrophilicity.

The free *N*,*N*′-diamidocarbene **3** could be generated by treatment of **1** with potassium bis(trimethylsilyl)amide (KHMDS) in thf at low temperature (–40 °C) (Scheme 2).

Whereas **3** appears to be viable only at low temperature, its formulation as a carbene was established by its trapping with S_8 to form the thiourea **4**. The architecture of the new heterocycle was confirmed by the crystal structure of **4**, depicted in Figure 2. Very characteristically, the cycle exhibits boat conformation, with the sp^3-hydridized carbon atom C3 lying out of the plane of the cycle in contrast to the previously reported case of a planar pyrimidinium betaine.[8] This clearly reflects the disappearance of the electron-delocalisation along the malonate unit, as also corroborated by a concomitant lengthening of interatomic distances C2–C3 and C3–C6, now appearing as C–C single bonds [1.514(3) Å and 1.516(3) Å, respectively].

The reaction between the in situ generated carbene **3** and [RhCl(cod)]$_2$ (cod = 1,5-cyclooctadiene) led to the formation of the expected NHC complex [RhCl(**3**)(cod)] (**5**) in good yield (68%), confirming Bielawski's original observation (in the case of iridium) that the carbene **3** is still a suitable ligand for transition metal complexes in spite of its reduced nucleophilicity. The latter characteristics can be illustrated by the carbene's ^{13}C NMR resonance appearing at δ = 245.2 ppm (d, J_{RhC} = 49 Hz), which is significantly downfield-shifted compared to those observed in related (NHC)rhodium complexes reported in the literature (δ = 175–225 ppm),[13] and in particular the (4-oxoimidazolin-2-ylidene)rhodium complex reported by us (δ = 229.7 ppm).[10a] Such a high chemical shift can be attributed to a decrease of the electron density on the carbene centre due to the electron-withdrawing effect of the two carbonyl groups.

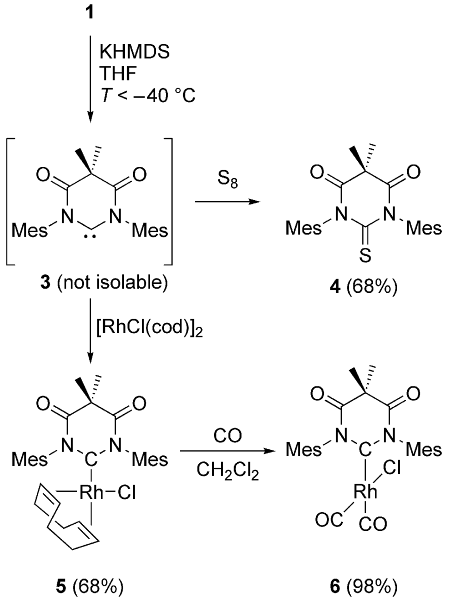

Scheme 2. Generation of diamidocarbene **3**, its trapping with S_8 and complexation with a rhodium(I) center.

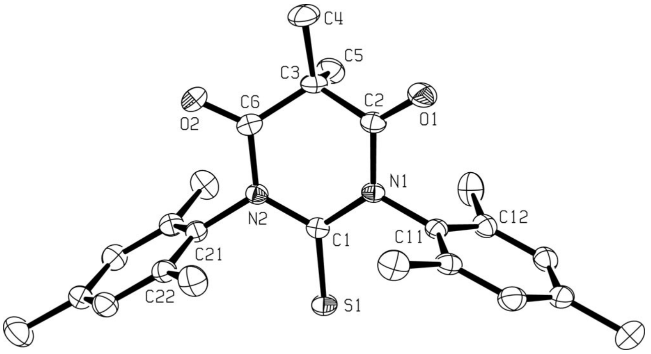

Figure 2. Perspective view of **4**. Anisotropic displacement parameter ellipsoids are shown at the 50% probability level, whereas hydrogen atoms were omitted for clarity. Selected bond lengths [Å]: C1–S1 1.640(2), C1–N1 1.397(3), C1–N2 1.391(3), C2–O1 1.210(3), C6–02 1.205(3), C2–C3 1.514(3), C3–C6 1.516(3).

A perspective view of the molecular structure of complex **5** established by X-ray diffraction is depicted in Figure 3 along with the principal interatomic distances and bond angles. The complex exhibits a square-planar arrangement of ligands around the rhodium centre, with the carbene ring being orthogonal to the mean coordination plane [torsion angle: N1–C1–Rh1–Cl1 83.9(2)°]. Again, the heterocycle is not planar and exhibits a half-chair conformation in which the sp^3-hybridized carbon atom C3 is pointing towards the chloride atom, C3 being off the mean plane defined by C2–N1–C1–N2–C4 (average deviation from mean plane 0.004 Å) by 0.486(2) Å. Most importantly, the Rh1–C1 bond [2.0107(19) Å] is considerably shorter than those reported for six-membered (NHC)RhCl(cod) complexes [2.036(2) Å $<$ Rh–$C_{carbene}$ $<$ 2.090(3) Å].[14] This reflects a stronger interaction between the carbene and the rhodium center, probably due to a greater level of π-backdonation from the metal centre to the carbene ligand. Further studies are currently carried out in order to completely understand the real nature of the metal–carbene bonding.

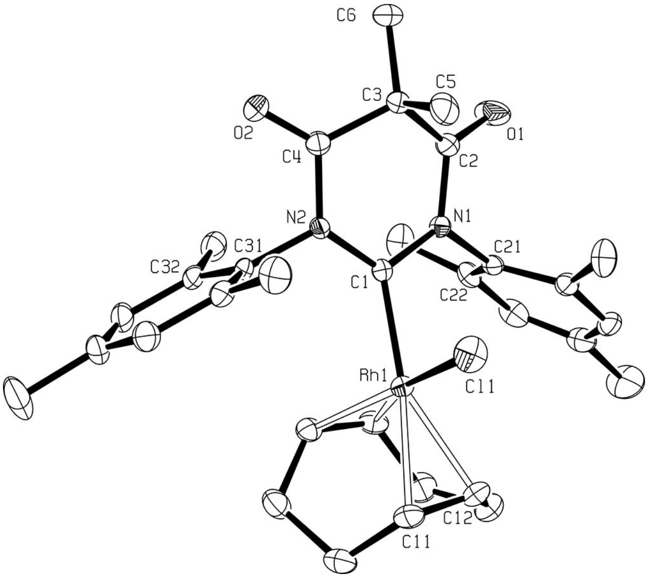

Figure 3. Perspective view of complex **5**. Anisotropic displacement parameter ellipsoids are shown at 50% probability level, whereas hydrogen atoms were omitted for clarity. Selected bond lengths [Å]: Rh1–C1 2.0107(19), C1–N1 1.374(2), C1–N2 1.380(3), N1–C2 1.410(3), N2–C4 1.416(3), C2–O1 1.201(3), C4–O2 1.204(3). Selected bond angles [°]: Rh1–C1–N1 117.71(13), Rh1–C1–N2 125.77(14), N1–C1–N2 115.49(16).

Due to the adjunction of the two carbonyl groups in its core, the electron-donating properties of the carbene **3** were also expected to be significantly reduced. In order to quantify this, complex **5** was converted into its dicarbonyl analogue [RhCl(**3**)(CO)$_2$] by bubbling CO gas into a solution of **5** in CH_2Cl_2. The outcome of the reaction was observable by a colour change of the solution from dark red to pale yellow. Complex **6** was obtained in excellent yields (99%) and was fully characterized.[15] As for complex **5**, the ^{13}C NMR carbene signal at δ = 230.8 ppm is found at much higher field than those reported for known [RhCl(NHC)(CO)$_2$] complexes (δ $<$ 219.6 ppm).[16] The electron deficiency of the carbene **3** was confirmed by the IR spectra of complex **6** in CH_2Cl_2. Two strong bands at 2005.3 and 2086.1 cm^{-1} were indeed observed, corresponding to the asymmetric and symmetric normal vibrations of the two CO ligands, respectively. The average value of ν_{av} = 2045.4 cm^{-1} is much higher than those reported for other six-membered NHCs, which typically are in the range 2029 $< \nu_{av} <$ 2038 cm^{-1}. This result points out the critical role of the two carbonyl groups on the electronic structure of the carbene, which renders carbene ligand **3** much less of an electron donor than typical NHCs. Moreover, the Tolman electronic parameter (TEP) of the carbene **3** could be calculated by the two linear regressions developed by Plenio and Nolan,[17] and was found to be equal to 2055 cm^{-1}. Considering the approximations due to the linear regressions, this value confirms that of 2057 cm^{-1} obtained by Bielawski et al.

Conclusions

It is hoped that this and earlier reports from several groups cited above will draw growing attention on the rich chemistry of functional six-membered N-heterocyclic carbenes. Indeed, with one more skeletal atom than for five-membered NHCs, they offer not only different steric properties, but also a broader variability in the number and nature of the functionalities that can be introduced as integral parts of their heterocyclic backbone. This is particularly important, since we see growing evidence that such remote functionalities can very significantly modify the intrinsic properties of the carbene ligand.

Experimental Section

General: All manipulations were performed under dry nitrogen by using standard vacuum-line and Schlenk-tube techniques. Glassware was dried at 120 °C in an oven for at least 3 h. Solvents were dried and distilled by classical methods. NMR spectra were recorded with Bruker ARX250 or AV300 spectrometers. Chemical shifts are reported in ppm (δ) compared to TMS (^{1}H and ^{13}C) by using the residual peak of the deuterated solvent as internal standard. IR spectra were obtained with a Perkin–Elmer Spectrum 100 FT-IR spectrometer. Microanalyses were performed by the Laboratoire de Chimie de Coordination Microanalytical Service, and mass spectra were obtained from the Mass Spectrometry Service of the Paul Sabatier University. *N,N′*-dimesitylformamidine[18] was synthesized according to a literature procedure.

2-Chloro-1,3-dimesityl-5,5-dimethyl-4,6-dioxohexahydropyrimidine (1): Dimethylmalonyl dichloride (0.75 mL, 5.6 mmol, 1.05 equiv.) was added dropwise to a well-stirred solution of *N,N′*-dimesitylformamidine (1.5 g, 5.35 mmol) and Et_3N (1.1 mL, 8.0 mmol, 1.5 equiv.) in CH_2Cl_2 (15 mL) at 0 °C. After stirring at this temperature for 1 h, all volatiles were removed in vacuo, and the residue was taken up in CH_2Cl_2/Et_2O (1:2, v/v; 18 mL) and filtered through a pad of Celite to remove triethylammonium chloride. After washing the solid a second time with CH_2Cl_2/Et_2O (1:2, v/v; 6 mL), the solvents were evaporated, which afforded the desired product as a white, fluffy solid (1.6 g, 73%); m.p. 212–214 °C (dec.). ^{1}H NMR (300 MHz, $CDCl_3$): δ = 6.96 (s, 4 H, CH_{Mes}), 6.93 (s, 1 H, N_2CHCl), 2.30 (s, 12 H, $CH_{3\,ortho}$), 2.29 (s, 6 H, $CH_{3\,para}$), 1.79 [s, 6 H, $C(CH_3)_2$] ppm. $^{13}C\{^1H\}$ NMR (75.4 MHz, $CDCl_3$): δ = 170.8 (C=O), 139.0 (C_{Mes}), 136.0 (C_{Mes}), 132.2 (C_{Mes}), 130.2 (CH_{Mes}), 90.5 (N_2CHCl), 48.2 [$C(CH_3)_2$], 23.6 [$C(CH_3)_2$], 20.9

($\mathit{C}H_{3\,\mathit{para}}$), 19.2 ($\mathit{C}H_{3\,\mathit{ortho}}$) ppm. IR (ATR): ṽ = 2975, 2925, 1713, 1682, 1665, 1608, 1459, 1401, 1356, 1261, 1249, 1189, 1167, 1103, 1034, 974, 910, 856, 763, 739, 720 cm^{-1}. MS (ESI): *m*/*z* (%) = 412 (100) [M]$^+$, 395 (98) [M – Cl + H_2O]$^+$.

1,3-Dimesityl-2-methoxy-5,5-dimethyl-4,6-dioxohexahydropyrimidine (2): To a solution of *N*,*N′*-dimesitylformamidine (373 mg, 1.33 mmol) and Et_3N (0.28 mL, 2.0 mmol, 1.5 equiv.) in CH_2Cl_2 (5 mL) was added dimethylmalonyl dichloride (186 µL, 1.39 mmol, 1.05 equiv.) at 0 °C. The resulting solution was then stirred for 1 h, before MeOH (1 mL) was added. After 5 min, all volatiles were removed in vacuo, and the residue was purified by flash chromatography (SiO_2; CH_2Cl_2/MeOH, 95:5) to afford the expected product as a white solid (540 mg, 99 %); m.p. 185 °C. ^{1}H NMR (300 MHz, $CDCl_3$): δ = 6.94 (s, 4 H, $C\mathit{H}_{\mathrm{Mes}}$), 5.28 [s, 1 H, $N_2C\mathit{H}(OMe)$], 2.83 (s, 3 H, $OC\mathit{H}_3$), 2.28 (s, 12 H, $C\mathit{H}_{3\,\mathit{ortho}}$), 2.27 (s, 6 H, $C\mathit{H}_{3\,\mathit{para}}$), 1.83 [s, 3 H, $C(C\mathit{H}_3)_2$], 1.58 [s, 3 H, $C(C\mathit{H}_3)_2$] ppm. $^{13}C\{^1H\}$ NMR (75.4 MHz, $CDCl_3$): δ = 170.8 (C=O), 138.3, 138.0, 134.5, 133.4 ($\mathit{C}_{\mathrm{Mes}}$), 129.9, 129.5 ($\mathit{C}H_{\mathrm{Mes}}$), 98.5 [$N_2\mathit{C}H(OMe)$], 59.6 ($O\mathit{C}H_3$), 47.0 [$\mathit{C}(CH_3)_2$], 28.1 [$C(\mathit{C}H_3)_2$], 21.2 [$C(\mathit{C}H_3)_2$], 20.9 ($\mathit{C}H_{3\,\mathit{para}}$), 18.5 ($\mathit{C}H_{3\,\mathit{ortho}}$), 18.3 ($\mathit{C}H_{3\,\mathit{ortho}}$) ppm. IR (ATR): ṽ = 2984, 2918, 2859, 1696 (C=O), 1666, 1606, 1484, 1456, 1422, 1366, 1353, 1238, 1167, 1108, 1059, 957, 862, 776, 725, 684 cm^{-1}. MS (ESI): *m*/*z* (%) = 431 (100) [M + Na]$^+$, 281 (26) [$HC(NHMes)_2$]$^+$. $C_{25}H_{32}N_2O_3$ (408.53): calcd. C 73.50, H 7.90, N 6.86; found C 73.39, H 8.00, N 6.79.

1,3-Dimesityl-5,5-dimethylhexahydropyrimidin-4,6-dione-2-thione (4): A solution of **1** (856 mg, 2.07 mmol) in thf (15 mL) was cooled to –80 °C, and KHMDS (0.5 M in toluene, 4.6 mL, 1.1 equiv.) was added dropwise. The very pale yellow solution was stirred for 30 min, and S_8 (139 mg, 4.35 mmol) was added as a solid all at once. After 1 h of stirring at –80 °C, the cooling bath was removed, and the solution was warmed to room temperature. After evaporation of all volatiles, the crude product was purified by flash chromatography (SiO_2; hexane/CH_2Cl_2, 1:1 then 1:2) to yield **4** as a bright orange crystalline solid (573 mg, 68 %); m.p. 282 °C (dec.). ^{1}H NMR (300 MHz, $CDCl_3$): δ = 6.97 (s, 4 H, $C\mathit{H}_{\mathrm{Mes}}$), 2.32 (s, 6 H, $C\mathit{H}_{3\,\mathit{para}}$), 2.13 (s, 12 H, $C\mathit{H}_{3\,\mathit{ortho}}$), 1.79 [s, 6 H, $C(C\mathit{H}_3)_2$] ppm. $^{13}C\{^1H\}$ NMR (75.4 MHz, $CDCl_3$): δ = 177.4 (C=S), 170.3 (C=O), 138.7, 134.4, 134.3 ($\mathit{C}_{\mathrm{Mes}}$), 129.6 ($\mathit{C}H_{\mathrm{Mes}}$), 48.6 [$\mathit{C}(CH_3)_2$], 25.0 [$C(\mathit{C}H_3)_2$], 21.2 ($\mathit{C}H_{3\,\mathit{para}}$), 17.5 ($\mathit{C}H_{3\,\mathit{ortho}}$) ppm. IR (ATR): ṽ = 2971, 2916, 1855, 1731, 1701, 1671, 1658, 1608, 1480, 1459, 1382, 1330, 1305, 1263, 1222, 1144, 1121, 1034, 1011, 963, 856, 818, 762 cm^{-1}. MS (ESI): *m*/*z* (%) = 431 (100) [M + Na]$^+$, 409 (18) [M + H]$^+$. $C_{24}H_{28}N_2O_2S$ (408.56): calcd. C 70.55, H 6.91, N 6.86; found C 70.53, H 6.96, N 6.78.

Chlorido(1,5-cyclooctadiene)(1,3-dimesityl-5,5-dimethyl-4,6-dioxotetrahydropyrimidin-2-ylidene)rhodium(I) (5): Compound **1** (143 mg, 0.346 mmol) was dissolved in thf (6 mL), and the solution was cooled to –40 °C. A solution of KHMDS in toluene (0.5 M, 0.73 mL, 0.36 mmol, 1.05 equiv.) was then added dropwise, and, after stirring for 30 min, $[RhCl(cod)]_2$ (85 mg, 0.17 mmol, 0.5 equiv.) was added as a solid all at once. After 15 min at that temperature, the cooling bath was removed and the reaction mixture warmed up to room temperature, during which time the solution gradually turned from yellow to dark red. After 30 min at room temperature, all volatiles were evaporated in vacuo, and the crude product was directly purified by flash chromatography (neutral Al_2O_3 type III; CH_2Cl_2) to leave the desired complex as a red powder (147 mg, 68 %). Single crystals suitable for an X-ray diffraction experiment were obtained by slow diffusion of pentane into a solution of **5** in thf; m.p. 197 °C. ^{1}H NMR (300 MHz, $CDCl_3$): δ = 7.11 (s, 2 H, $C\mathit{H}_{\mathrm{Mes}}$), 6.98 (s, 2 H, $C\mathit{H}_{\mathrm{Mes}}$), 4.71 (br., 2 H, $C\mathit{H}_{\mathrm{cod}}$), 3.23 (br., 2 H, $C\mathit{H}_{\mathrm{cod}}$), 2.54 (s, 6 H, $C\mathit{H}_{3\,\mathrm{Mes}}$), 2.39 (s, 6 H, $C\mathit{H}_{3\,\mathrm{Mes}}$), 1.99 [s, 3 H, $C(C\mathit{H}_3)_2$], 1.98 (s, 6 H, $C\mathit{H}_{3\,\mathrm{Mes}}$), 1.58–1.44 (m, 8 H, $C\mathit{H}_{2\,\mathrm{cod}}$), 1.55 [s, 3 H, $C(C\mathit{H}_3)_2$] ppm. $^{13}C\{^1H\}$ NMR (75.4 MHz, $CDCl_3$): δ = 245.2 (d, $^1J_{\mathrm{RhC}}$ = 49.1 Hz, $N_2\mathit{C}$), 169.1 (d, $^3J_{\mathrm{RhC}}$ = 2.2 Hz, C=O), 139.0, 137.4, 135.8, 135.1 ($\mathit{C}_{\mathrm{Mes}}$), 130.5 ($\mathit{C}H_{\mathrm{Mes}}$), 128.4 ($\mathit{C}H_{\mathrm{Mes}}$), 101.3 (d, J_{RhC} = 6.3 Hz, $\mathit{C}H_{\mathrm{cod}}$), 72.7 (d, J_{RhC} = 13.9 Hz, $\mathit{C}H_{\mathrm{cod}}$), 50.8 [$\mathit{C}(CH_3)_2$], 31.8 ($\mathit{C}H_{2\,\mathrm{cod}}$), 29.8 [$C(\mathit{C}H_3)_2$], 27.2 ($\mathit{C}H_{2\,\mathrm{cod}}$), 21.0 ($\mathit{C}H_{3\,\mathrm{Mes}}$), 20.1 ($\mathit{C}H_{3\,\mathrm{Mes}}$), 19.6 ($\mathit{C}H_{3\,\mathrm{Mes}}$), 18.8 [$C(\mathit{C}H_3)_2$] ppm. IR (ATR): ṽ = 2919, 2877, 1738, 1711, 1697, 1668, 1460, 1429, 1384, 1365, 1351, 1322, 1306, 1226, 1104, 1071, 1053, 1037, 1016, 957, 941, 848, 783, 767 cm^{-1}. MS (ESI): *m*/*z* (%) = 769 (39), 683 (69), 624 (22) [M + H]$^+$, 587 (100) [M – Cl]$^+$, 566 (30), 413 (18), 286 (28). $C_{32}H_{40}ClN_2O_2Rh$ (623.03): calcd. C 61.69, H 6.47, N 4.50; found C 61.78, H 6.57, N 4.44.

Dicarbonyl(chlorido)(1,3-dimesityl-5,5-dimethyl-4,6-dioxotetrahydropyrimidin-2-ylidene)rhodium(I) (6): CO was bubbled into a solution of **5** (43 mg, 69 mmol) in CH_2Cl_2 (3 mL) for 10 min. From dark red, the solution gradually turned pale yellow. After 1 h of stirring, all volatiles were removed in vacuo. In order to thoroughly remove the liberated cyclooctadiene, pentane (2 × 3 mL) was added to the crude product, the mixture was sonicated and concentrated again. This procedure gave pure **6** as a pale yellow powder (39 mg, 98 %); m.p. 235 °C (dec.). ^{1}H NMR (250 MHz, $CDCl_3$): δ = 7.00 (s, 4 H, $C\mathit{H}_{\mathrm{Mes}}$), 2.36 (s, 6 H, $C\mathit{H}_{3\,\mathrm{Mes}}$), 2.34 (s, 6 H, $C\mathit{H}_{3\,\mathrm{Mes}}$), 2.20 (s, 6 H, $C\mathit{H}_{3\,\mathrm{Mes}}$), 1.92 [s, 3 H, $C(C\mathit{H}_3)_2$], 1.69 [s, 3 H, $C(C\mathit{H}_3)_2$] ppm. $^{13}C\{^1H\}$ NMR (63 MHz, $CDCl_3$): δ = 230.8 (d, $^1J_{\mathrm{RhC}}$ = 43.4 Hz, $N_2\mathit{C}$), 184.6 (d, J_{RhC} = 53.9 Hz, $Rh\mathit{C}O$), 182.4 (d, J_{RhC} = 75.7 Hz, $Rh\mathit{C}O$), 169.9 (C=O), 139.8, 136.1, 134.9, 134.1 ($\mathit{C}_{\mathrm{Mes}}$), 130.4 ($\mathit{C}H_{\mathrm{Mes}}$), 129.4 ($\mathit{C}H_{\mathrm{Mes}}$), 51.5 [$\mathit{C}(CH_3)_2$], 28.7 [$C(\mathit{C}H_3)_2$], 21.1 ($\mathit{C}H_{3\,\mathrm{Mes}}$), 20.4 ($\mathit{C}H_{3\,\mathrm{Mes}}$), 19.5 ($\mathit{C}H_{3\,\mathrm{Mes}}$), 18.5 [$C(\mathit{C}H_3)_2$] ppm. IR (ATR): ṽ = 2923, 2077, 1994, 1768, 1736, 1697, 1667, 1469, 1411, 1389, 1315, 1289, 1243, 1172, 1096, 1036, 1008, 870, 848, 782, 767, 678 cm^{-1}. IR (CH_2Cl_2): ṽ = 2086.1 (CO), 2005.3 (CO), 1764.5, 1735.2 cm^{-1}. MS (ESI): *m*/*z* (%) = 611 (43) [M – 2 CO + 2 CH_3CN + H]$^+$, 507 (65) [M – Cl – CO]$^+$, 415 (100) [M – Cl – Mes]$^+$. $C_{26}H_{28}ClN_2O_4Rh$ (570.87): calcd. C 54.70, H 4.94, N 4.91; found C 55.13, H 4.99, N 4.75.

X-ray Diffraction Studies: Crystals of **4** and **5**, suitable for X-ray diffraction, were obtained through crystallization from CH_2Cl_2/pentane and thf/pentane, respectively. Data were collected at 180 K with a Bruker D8 Apex II diffractomer and an Oxford Diffraction Xcalibur diffractometer, respectiveley. All calculations were performed with a PC-compatible computer by using the WinGX system.[19] The structures were solved by using the SIR92 program,[20] which revealed in each instance the position of most of the non-hydrogen atoms. All remaining non-hydrogen atoms were located by the usual combination of full-matrix least-squares refinement and difference electron-density syntheses by using the SHELXL97 program.[21] Atomic scattering factors were taken from the usual tabulations. Anomalous dispersion terms for Rh, S, and Cl atoms were included in F_c. All non-hydrogen atoms were allowed to vibrate anisotropically. All the hydrogen atoms – except for olefinic H atoms of the cod ligand in **5** – were set in idealized positions [R_3CH: C–H = 0.96 Å; R_2CH_2: C–H = 0.97 Å; RCH_3: C–H = 0.98 Å; C(sp^2)–H = 0.93 Å; U_{iso} = 1.2 or 1.5 times that of the U_{eq} of the carbon atom to which the hydrogen atom is attached], and their position were refined as "riding" atoms. The olefinic H atoms of the cod ligand in **5** were located from a difference electron-density synthesis; their positions and isotropic thermal parameters (arbitrarily set to 0.05 Å^2) were kept fixed during the final refinement. CCDC-755193 (**4**) and CCDC-755194 (**5**) contain the supplementary crystallographic data for this paper. These data can be obtained free of charge from The Cambridge Crystallographic Data Centre via www.ccdc.cam.ac.uk/data_request/cif.

Acknowledgments

Support from the Centre National de la Recherche Scientifique (CNRS) and from the Agence Nationale de la Recherche (ANR) (programme blanc, ANR-08-BLAN-0137-01) is gratefully acknowledged.

---

[1] For monographs, see: a) *N-Heterocyclic Carbenes in Transition Metal Catalysis* (Ed.: F. Glorius), *Top. Organomet. Chem.* **2007**, *21*; b) *N-Heterocyclic Carbenes in Synthesis* (Ed.: S. P. Nolan), Wiley-VCH, Weinheim, **2006**.

[2] For general reviews, see: a) O. Schuster, L. Yang, H. G. Raubenheimer, M. Albrecht, *Chem. Rev.* **2009**, *109*, 3445–3478; b) F. E. Hahn, M. C. Jahnke, *Angew. Chem. Int. Ed.* **2008**, *47*, 3122–3172; c) D. Bourissou, O. Guerret, F. Gabbaï, G. Bertrand, *Chem. Rev.* **2000**, *100*, 39–91.

[3] a) D. Enders, O. Niemeier, A. Henseler, *Chem. Rev.* **2007**, *107*, 5606–5655; b) N. Marion, S. Díez-González, S. P. Nolan, *Angew. Chem. Int. Ed.* **2007**, *46*, 2–15.

[4] a) S. Díez-González, N. Marion, S. P. Nolan, *Chem. Rev.* **2009**, *109*, 3612–3676; b) C. Samojlowicz, M. Bieniek, K. Grela, *Chem. Rev.* **2009**, *109*, 3708–3742; c) M. Poyatos, J. A. Mata, E. Peris, *Chem. Rev.* **2009**, *109*, 3677–3707; d) E. A. B. Kantchev, C. J. O'Brien, M. G. Organ, *Angew. Chem. Int. Ed.* **2007**, *46*, 2768–2813; e) V. César, S. Bellemin-Laponnaz, L. H. Gade, *Chem. Soc. Rev.* **2004**, *33*, 619–636; f) C. M. Crudden, D. P. Allen, *Coord. Chem. Rev.* **2004**, *248*, 2247–2273; g) W. A. Herrmann, *Angew. Chem. Int. Ed.* **2002**, *41*, 1290–1309.

[5] a) S. Díez-González, S. P. Nolan, *Coord. Chem. Rev.* **2007**, *251*, 874–883; b) A. Fürstner, M. Alcarazo, H. Krause, C. W. Lehmann, *J. Am. Chem. Soc.* **2007**, *129*, 12676–12678.

[6] a) A. Fürstner, M. Alcarazo, K. Radkowski, C. W. Lehmann, *Angew. Chem. Int. Ed.* **2008**, *47*, 8302–8306; b) S. Nakafuji, J. Kobayashi, T. Kawashima, *Angew. Chem. Int. Ed.* **2008**, *47*, 1141–1144; c) V. Lavallo, Y. Canac, C. Präsang, B. Donnadieu, G. Bertrand, *Angew. Chem. Int. Ed.* **2005**, *44*, 5705–5709; d) M. Mayr, K. Wurst, K.-H. Ongania, M. R. Buchmeiser, *Chem. Eur. J.* **2004**, *10*, 1256–1266; e) P. Bazinet, G. P. A. Yap, D. S. Richeson, *J. Am. Chem. Soc.* **2003**, *125*, 13314–13315.

[7] a) U. Siemeling, C. Färber, C. Bruhn, *Chem. Commun.* **2009**, 98–100; b) D. M. Khramov, E. L. Rosen, V. M. Lynch, C. W. Bielawski, *Angew. Chem. Int. Ed.* **2008**, *47*, 2267–2270; c) D. M. Khramov, E. L. Rosen, J. A. V. Er, P. D. Vu, V. M. Lynch, C. W. Bielawski, *Tetrahedron* **2008**, *64*, 6853–6862; d) M. Alcarazo, R. Fernández, E. Alvarez, J. M. Lassaletta, *J. Organomet. Chem.* **2005**, *690*, 5979–5988; e) M. Viciano, E. Mas-Marza, M. Sanau, E. Peris, *Organometallics* **2006**, *25*, 3063–3069.

[8] V. César, N. Lugan, G. Lavigne, *J. Am. Chem. Soc.* **2008**, *130*, 11286–11287.

[9] T. W. Hudnall, C. W. Bielawski, *J. Am. Chem. Soc.* **2009**, *131*, 16039–16041.

[10] We and others have also disclosed very recently a mixed amino/amidocarbene, see: a) L. Benhamou, V. César, H. Gornitzka, N. Lugan, G. Lavigne, *Chem. Commun.* **2009**, 4720–4722; b) A. T. Biju, K. Hirano, R. Fröhlich, F. Glorius, *Chem. Asian J.* **2009**, *4*, 1786–1789.

[11] Such an attack was already reported leading to a similar structure, see: E. A. Barsa, R. Richter, *J. Org. Chem.* **1986**, *51*, 4483–4485.

[12] a) K.-U. Fulda, E. Maassen, H. Ritter, R. Sperber, B. Tieke, *Langmuir* **1996**, *12*, 854–856; b) H. Gotthardt, M. Riegels, *Chem. Ber.* **1987**, *120*, 445–447; c) H. Gotthardt, J. Blum, *Chem. Ber.* **1987**, *120*, 109–114.

[13] For a compilation, see: a) D. Tapu, D. A. Dixon, C. Roe, *Chem. Rev.* **2009**, *109*, 3385–3407.

[14] a) Ref.[8]; b) M. Mayr, K. Wurst, K.-H. Ongania, M. R. Buchmeiser, *Chem. Eur. J.* **2004**, *10*, 1256–1266; c) C. Präsang, B. Donnadieu, G. Bertrand, *J. Am. Chem. Soc.* **2005**, *127*, 10182–10183; d) P. Bazinet, T.-G. Ong, J. S. O'Brien, N. Lavoie, E. Bell, G. P. A. Yap, I. Korobkov, D. S. Richeson, *Organometallics* **2007**, *26*, 2885–2895; e) H. Arslan, D. VanDerveer, I. Ozdemir, S. Demir, B. Cetinkaya, *Acta Crystallogr., Sect. E* **2007**, *63*, m770–m771.

[15] In particular, no decomposition and no loss of carbon monoxide were observed during the workup of the reaction mixture, contrary to other reports dealing with poor-donating NHC systems, see: a) M. D. Sanderson, J. W. Kamplain, C. W. Bielawski, *J. Am. Chem. Soc.* **2007**, *128*, 16514–16515; b) S. Wolf, H. Plenio, *J. Organomet. Chem.* **2009**, *694*, 1487–1492.

[16] The most downfield carbene ^{13}C chemical shift in [RhCl(NHC)(CO)$_2$] was found in ref.[14c]

[17] For Plenio's linear regression, see ref.[15b]; for Nolan's method, see: R. A. I. Kelly, H. Clavier, S. Giudice, N. M. Scott, E. D. Stevens, J. Bordner, I. Samardjiev, C. D. Hoff, L. Cavallo, S. P. Nolan, *Organometallics* **2008**, *27*, 202–210.

[18] K. E. Krahulic, G. D. Enright, M. Parvez, R. Roesler, *J. Am. Chem. Soc.* **2005**, *127*, 4142–4143.

[19] L. J. Farrugia, *J. Appl. Crystallogr.* **1999**, *32*, 837–838.

[20] A. Altomare, G. Cascarano, C. Giacovazzo, A. Guagliardi, *J. Appl. Crystallogr.* **1993**, *26*, 343–350.

[21] G. M. Sheldrick, *Acta Crystallogr., Sect. A* **2008**, *64*, 112–122.

Received: November 17, 2009

DOI: 10.1002/ejic.200900721

Ordering Phenomena in Complex Chalcogenides – the Showcase of $A_2In_{12}Q_{19}$ (A = K, Tl, NH_4; Q = Se, Te) and Pseudobinary In_2Q_3

Lorenz Kienle,[a] Marc Schlosser,[b] Manolis J. Manos,[c] Christos D. Malliakas,[c] Viola Duppel,[d] Christof Reiner,[b] Hans-Jörg Deiseroth,*[b] Mercouri G. Kanatzidis,[c] Klemens Kelm,[e] and Arndt Simon[d]

Dedicated to Professor Martin Jansen on the occasion of his 65th birthday

Keywords: Electron microscopy / Real structure / X-ray diffraction / Disordered structure / Diffuse scattering / Chalcogens / Solid-state structures

A group of solids with the general composition $A_2In_{12}Q_{19}$ (A = K, Tl, NH_4; Q = Se, Te) is characterized by combined X-ray single-crystal and high-resolution transmission-electron microscopy (HRTEM). Similar nanosize domains with variable sizes and complex internal structures are common to all three compounds. Although a partial ordering of domains for the bulk of $K_2In_{12}Se_{19}$ is dominating, the observed ordering patterns in microdomains range from total random orientation to a pattern with a ninefold superstucture (rare precursor phase not stable under HRTEM conditions). In spite of testing various synthesis conditions it was not possible to avoid these unusual structural features for $K_2In_{12}Se_{19}$, which are apparently intrinsic. The formation of significantly larger domains is observed for $K_2In_{12}Se_{19-x}Te_x$ and $K_{2-y}Tl_yIn_{12}Se_{19}$ and results in a twofold superstructure that can be observed with X-ray diffraction also on a macroscopic scale. $(NH_4)_2In_{12}Se_{19}$ is a special case where an initial weak ordering is observed that is characterized by ring X-ray reflections forming hexagons around certain reciprocal lattice positions. This pattern has apparent similarities to $K_2In_{12}Se_{19}$ but is not stable in the HRTEM. Instead, it disappears rapidly and is finally replaced by a twofold superstructure similar to $K_2In_{12}Se_{19-x}Te_x$ and $K_{2-y}Tl_yIn_{12}Se_{19}$. The reason was identified as a combined process of domain broadening and NH_3 evaporation. As observed for $K_2In_{12}Se_{19}$ at $T > 473$ K, the superstructure reflections disappear. Surprisingly, the pseudobinary phase In_2Q_3 (Q: chalcogen) shows strong structural similarities to $K_2In_{12}Se_{19}$ with respect to the internal structure of the nanodomains. Their three-dimensional arrangement, however, and the resulting superstructure are closer related to $K_2In_{12}Se_{19-x}Te_x$ and $K_{2-y}Tl_yIn_{12}Se_{19}$.

Introduction

The variability of main-group chalcogenides with respect to chemical composition, chemical bonding, morphology and structure, as well as their useful materials properties, has been referenced in several earlier papers. Among those are systematic synthetic and structural aspects ranging from molecular chalcogenides to ionic solids,[1] zeolite-type framework structures,[2,3] and highly porous chalcogenide aerogels.[4] Due to their physical properties, semiconducting glassy and crystalline chalcogenides are interesting candidates for optical applications[5,6] as phase-change materials,[7,8] nanowires,[9] nanosensors,[10] or photocatalysts.[11] Mixed main-group transition-metal chalcogenides are important thermoelectric materials[12] and useful for thin-film solar cells.[13] Moreover, the material $(NH_4)_4In_{12}Se_{20}$, closely related in chemical composition to the title compounds, is an open-framework semiconductor and has facile ion-exchange properties, which result in excellent selectivity for the capture of heavy metal ions.[14] It has also been shown recently that a group of new main-group chalcogenides exhibits unusual high Li ionic conductivity.[15]

In this paper a small group of complex new main-group chalcogenides with unusual structures apparently outside the framework of the above-mentioned materials is presented with a pronounced focus on details of their micro-

---

[a] Christian Albrechts University Kiel, Institute for Materials Science, Synthesis and Real Structure,
Kaiserstr. 2, 24143 Kiel, Germany
[b] University of Siegen, Inorganic Chemistry I,
Adolf-Reichwein-Straße 2, 57068 Siegen, Germany
Fax: +49-271-740-2555
E-mail: deiseroth@chemie.uni-siegen.de
[c] Department of Chemistry, Northwestern University,
2145 Sheridan Rd, Evanston, IL 60208, USA
[d] Max Planck Institute for Solid State Research,
Heisenbergstraße 1, 70569 Stuttgart, Germany
[e] German Aerospace Center,
Linder Höhe, 51147 Köln, Germany

Supporting information for this article is available on the WWW under http://dx.doi.org/10.1002/ejic.200900721.

and nanostructure. Although not yet visible completely, the title compounds might be useful candidates for some of the above-mentioned applications.

Two initial series of experiments using a combined methodical approach of high-resolution transmission-electron microscopy (HRTEM) and temperature-dependent single-crystal X-ray diffraction on $K_2In_{12}Se_{19}$[16,17] revealed the first details of their complex crystal structures. In particular the inevitable presence of *disordered* nanosize domains in $K_2In_{12}Se_{19}$ and complex internal order/disorder patterns associated with variable domain sizes gave rise to the reversible appearance of diffuse ring-shaped intensities in X-ray diagrams and complicated the investigations considerably. But in a first step, a macroscopic *average model* of *disordered* nanosize rods inserted in an *ordered* Kagomé-like host structure could be developed (cf. Figure 1). Further group-theoretical considerations and electron-diffraction studies of nanosize areas point to local deviations from the average model leading to a doubled repeat unit in the longitudinal extension [001] of the rods. It was shown that the translational symmetry of the host structure allows *two* distinct rod positions (A, B), such that a relative shift of A and/or B by 0.5c leads to antiphase domains (APD) restricted to areas of several nanometers. Taking into account such a model of the real structure, the initial macroscopic average structure derived from the X-ray analysis could be refined and simulated by a superposition of nanoscale APDs, a model that was strongly supported by HRTEM investigations.

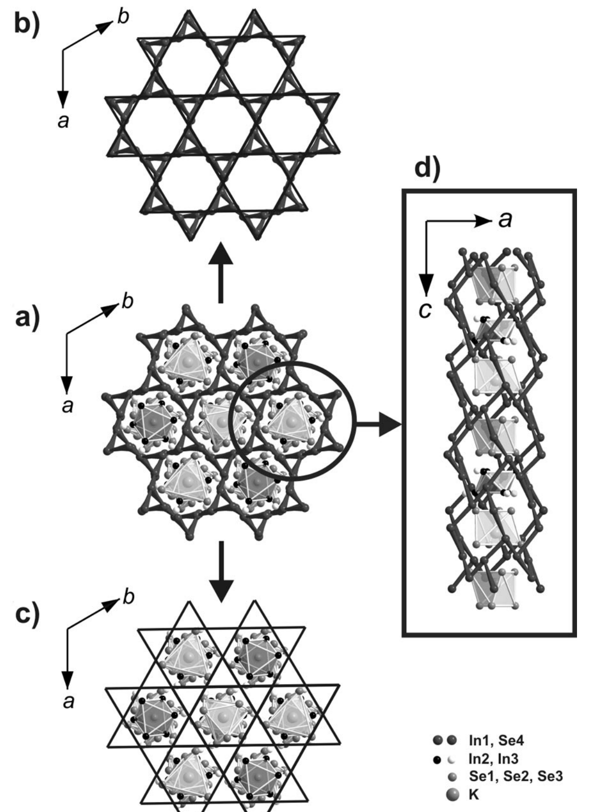

Figure 1. Separation of the crystal structure of $K_2In_{12}Se_{19}$ (a) by dint of a Kagomé net (black lines) in a framework structure as host (b) with inserted disordered rods (c); side view of a single channel of the host structure with an inserted rod (d).

In this paper, we compare $K_2In_{12}Se_{19}$ with the closely related solids $K_2In_{12}Se_{19-x}Te_x$ and $K_{2-y}Tl_yIn_{12}Se_{19}$ and the recently described $(NH_4)_2In_{12}Se_{19}$. These compounds can formally be seen as chemical substitution products of $K_2In_{12}Se_{19}$ and are discussed with respect to domain-size variations and structural differences. Surprisingly, also the pseudobinary compound In_2Q_3[18] (Q = S, Se, Te) can be structurally assigned to this group of compounds.

Results and Discussion

Indications for Complex Ordering in $K_2In_{12}Se_{19}$

In order to facilitate the understanding of the new results, a short summary based on an earlier paper[17] is given, but it also anticipates a few results reported subsequently in this paper.

The above-mentioned model of a Kagomé-like *host* structure for $K_2In_{12}Se_{19}$ (Figure 1) is also suitable for a basic description of $K_2In_{12}Se_{19-x}Te_x$ and $K_{2-y}Tl_yIn_{12}Se_{19}$. The inserted rods, however, show significant differences. In this respect the rods of the average structure of $K_2In_{12}Se_{19}$ (Figure 2, a) suffering from internal disorder of In atoms serve as a reference with K1 and Se1 located on the rod axis K1 is coordinated by six Se atoms forming a distorted Se_6 octahedron ("metaprism"). Se1 is formally coordinated by 12 *disordered* In atoms [*sof* = 0.5; d(In2–In3) = 1.033(2) Å] of which only six can be simultaneously present. Thus, an ordering of the indium positions inside the rods leads to a *twofold superstructure* (Figure 2, b and c) with two distinct types ("A" and "B") of rods.

The important tendency to establish reasonable interatomic distances d(In–In) between *adjacent* rods associated to an inevitably structural frustration problem has been discussed in detail in ref.[17] and could be identified as one of the main reasons for the unique structural chemistry of the title compounds. In simple words, the formation of nanosize domains seems to minimize the just mentioned "structure-distance dilemma". In the language of thermodynamics an unfavorable positive ΔG contribution [repulsion due to short d(In–In)] is overcompensated by a negative $T\Delta S$ contribution (pronounced disorder of nanosize domains).

The direct comparison of the ordered rods of $K_2In_{12}Se_{19}$ with those in $K_2In_{12}Se_{19-x}Te_x$ and $K_{2-y}Tl_yIn_{12}Se_{19}$ (Figure 2, d and e) clearly visualizes the significant differences between their internal structures. A comparison of relevant internal interatomic distances within the rods in the three solids is shown in Table 4.

Several attempts to enlarge the sizes of the nanosized APDs in $K_2In_{12}Se_{19}$ into a macroscopic scale, e.g. by optimizing the temperature treatment of the samples, gave no significant effect. HRTEM micrographs recorded on long-term (two years) annealed and rapidly quenched samples display similar real structures based on the above-men-

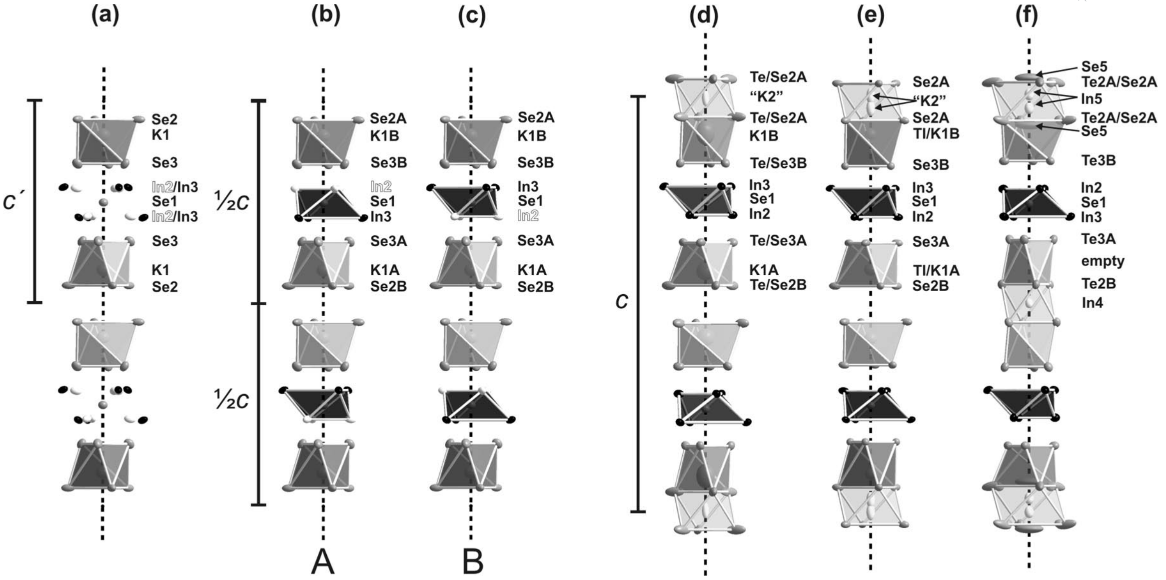

Figure 2. Comparison of rods: (a) average structure of $K_2In_{12}Se_{19}$ with disordered indium (In2/In3) atoms, (b, c) ordered structure variants A and B of $K_2In_{12}Se_{19}$, simulated based on group-theoretical considerations, (d, e) $K_2In_{12}Se_{19-x}Te_x$ and $K_{2-y}Tl_yIn_{12}Se_{19}$.

tioned nanoscale APDs. However, when probing sequentially inside selected nanoareas of the same microcrystal considerable local variations of the structural ordering were identified. They can be categorized with respect to the intensities on or next to positions *hkl*, $l = 2n + 1$ of electron-diffraction patterns and fast Fourier transforms (FFTs) of HRTEM micrographs.

(I) Regions with faint intensity on *hkl*, $l = 2n + 1$ (Figure 3, a, 1). These areas are produced by superposition of the APDs along the zone axis. The HRTEM micrographs can be well reproduced by a random superposition of APDs with twofold superstructure. Such real structure is denominated as "superposition structure" (SPS) below.

(II) Selected areas with diffuse double spots or streaks (Figure 3, a, 2) on *hkl*, $l = 2n + 1$, which are aligned perpendicular to c^*. These regions contain several separated and nanoscale APDs.

(III) Regions containing larger single APDs, thus exhibiting superstructure reflections on *hkl*, $l = 2n + 1$ (cf. FFT in Figure 3, a, 3).

As category (II) with *diffuse* double spots or streaks is dominant for $K_2In_{12}Se_{19}$, *sharp* Bragg peaks on *hkl*, $l = 2n + 1$ could only be obtained when analyzing selected *small* areas in such samples by FFTs. When transmitting *larger* areas, for example, with the aid of the SAED technique, diffuse scattering preferably occurs.

(IV) In one single case (of about 1000 examined crystallites), domains of a new and complex structural variant was observed, which is embedded within nanoscale APDs. The higher structural complexity of this rare variant according to the APDs is indicated by a ninefold superstructure ($c_{\text{complex}} = 9c$, see Figure 3, a, 4). The peculiar superstructure of this variant is well seen by characteristic changes of the contrast in HRTEM micrographs, i.e. every ninth bright spot along c is imaged with discernible contrast (see arrows in Figure 3, b). Interestingly, a further analysis is inhibited by rapid structural changes forced by electron-beam impact. Even when applying low-dose settings, the complex ninefold ordering changes within seconds via a disordered interme-

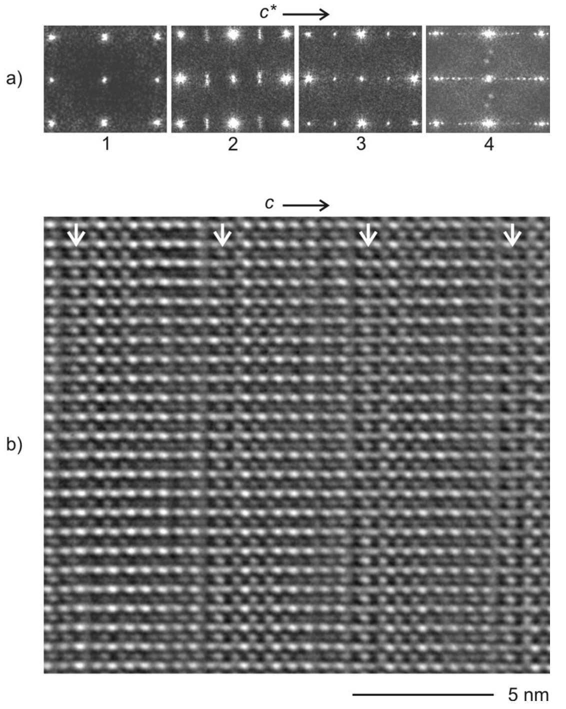

Figure 3. (a) FFTs calculated within circular cutouts of HRTEM micrographs recorded on $K_2In_{12}Se_{19}$, zone axis [210]. Position 1: no significant intensity on *hkl*, $l = 2n + 1$ [cf. (I), see text], 2: diffuse peaks on *hkl*, $l = 2n + 1$ [cf. (II), see text], 3: superstructure peaks on *hkl*, $l = 2n + 1$ [cf. (III), see text], 4: complex superstructure with $c = 9c'$ [cf. (IV), see text]. (b) HRTEM micrograph of complex ordered $K_2In_{12}Se_{19}$, zone axis [210], $\Delta f \approx + 5$ nm [cf. (IV), see text].

diate exhibiting diffuse streaks along c^*. The final products of the transformation are large APDs with superstructure reflections on *hkl*, $l = 2n + 1$ [cf. (III)], which stay unaffected even after extended times of irradiation. Careful X-ray analysis on many single crystals gave no indication for the just mentioned ninefold superstructure to occur on a macroscopic scale. Thus, we assume that it represents a precursor phase, which always coexists with the type (II) real structure of APDs.

These observations, together with the above-mentioned nonresponsiveness of the samples to thermal treatment conditions, prompted us to investigate isostructural samples of $K_2In_{12}Se_{19}$ in the hope of initiating a suitable change of the structural conditions towards a reproducible macroscopic superstructure.

Domain Broadening: Substituted Derivatives

We observed that partial substitution of selenium with tellurium ($K_2In_{12}Se_{19-x}Te_x$) or potassium with thallium ($K_{2-y}Tl_yIn_{12}Se_{19}$) in $K_2In_{12}Se_{19}$ causes the reproducible occurrence of twofold macroscopic superstructures [category (III)] indicated by reflections *hkl*, $l = 2n + 1$ in powder X-ray patterns (Figure 4).

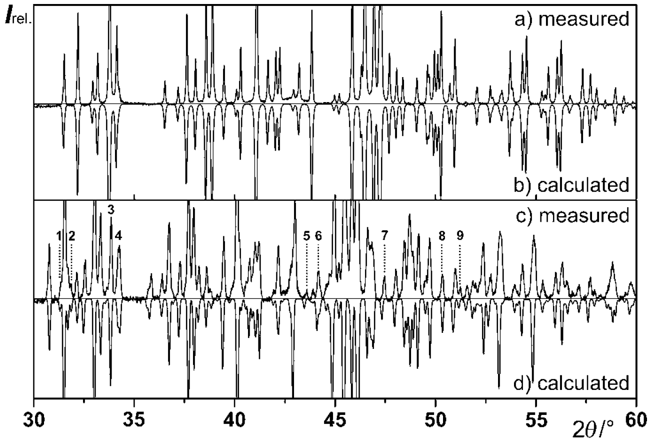

Figure 4. Measured and calculated (based on single-crystal data) X-ray powder diagram of $K_2In_{12}Se_{19}$ (a, b) and $K_{2.08}In_{12}Se_{11.44}Te_{7.56}$ (c, d). A selection of superstructure reflections *hkl*, $l = 2n + 1$ are marked. 1: 0 3 9; 2: –3 5 1; 3: 2 2 9; 4: 2 5 5 and 4 1 3; 5: 0 1 17; 6: 4 0 13; 7: 1 2 17; 8: 6 1 5; 9: 3 1 17.

In the case of $K_2In_{12}Se_{19-x}Te_x$ the twofold superstructure (category III) is stable between $x = 2$ and 12 ($\Delta x = 2$), whereas in $K_{2-y}Tl_yIn_{12}Se_{19}$ samples it clearly shows up in X-ray powder patterns with $y = 0.2$, 0.4, and 0.6.

In order to confirm these results at a more detailed level, the Tl and Te derivatives were examined by means of single-crystal X-ray analyses (see Tables 1, 2, and 3). It was shown that all observed crystals of both derivatives can be assigned to space group $R\bar{3}$ with an approximately doubled $c \approx 2c'$ axis in comparison to the *average structure* of $K_2In_{12}Se_{19}$ [$K_2In_{12}Se_{19}$; av.: $a' = 13.9318(5)$ Å, $c' = 17.7226(9)$ Å[16]]. The presence of sharp Bragg peaks on *hkl*, $l = 2n + 1$ (Figures 4 and 5, b and c) serve as strong arguments for this statement.

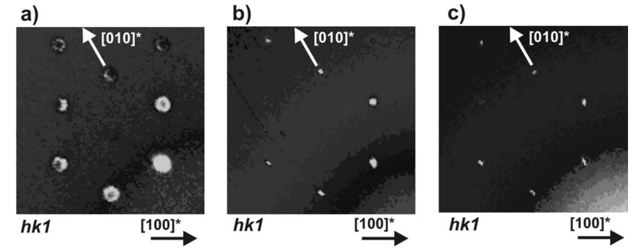

Figure 5. Precession photographs calculated from image plate data of the reciprocal planes *hk*1 of $K_2In_{12}Se_{19}$ (a, with diffuse rings), $K_2In_{12}Se_{19-x}Te_x$ (b), and $K_{2-y}Tl_yIn_{12}Se_{19}$ (c). The last two show sharp Bragg peaks on *hkl*, $l = 2n + 1$ in contrast to the diffuse rings of (a).

A comparison of the relevant structure parameters (Table 2) of both derivatives with one of the *ordered* structure models of $K_2In_{12}Se_{19}$, which were derived from group-theoretical considerations and electron-diffraction studies,[17] shows a good agreement. Thus, a stabilization of this superstructure within larger, at least micron-sized domains has succeeded.

Crystal Structure Description of the Substituted Derivatives

Significant variations of the interatomic distances are mainly observed in the case of the *A*1a and *A*1b *centered* Q_6 metaprisms (*A* = K or K/Tl; *Q* = Se/Te or Se). Whereas the *A*1a–*Q*2b distances are about 0.12 Å longer than those in the average structure of $K_2In_{12}Se_{19}$, the distances *A*1b–*Q*2a are about 0.28 Å and 0.19 Å shorter than those in the Se/Te and K/Tl derivatives, respectively. All other interatomic distances within the inserted rods show only minor differences (Table 4). A still unexplained residual electron density on the rod axis inside the distorted octahedron (metaprism) at position 3*a* ("K2" in Tables 2 and 3, cf. Figure 2, d) of $K_2In_{12}Se_{19-x}Te_x$ has to be mentioned here.

In the K/Tl derivative a similar residual electron density occurs, however, split into two maxima closely above and below position 3*a* (Figure 2, e).

Real Structure of Substituted Derivatives

According to simulations distinct ordering schemes of the cations inside the Q_6 metaprisms (see above) cannot be determined by HRTEM. However, even for the substituted crystals electron microscopy allows one to identify a characteristic domain structure. HRTEM examinations of samples of $K_{2-y}Tl_yIn_{12}Se_{19}$ and $K_2In_{12}Se_xTe_{19-x}$ fully confirm the twofold superstructure (category III, see above) observed by XRD. SAED patterns did not contain diffuse scattering, but superstructure reflections *hkl*, $l = 2n + 1$ (cf. experimental and simulated pattern in Figure 6, a for the showcase of an approximate composition $K_2In_{12}Se_{12}Te_7$).

Table 1. Crystallographic data and details of the structure determination for $K_{2.08}In_{12}Se_{11.44}Te_{7.56}$, $K_{1.50}Tl_{0.72}In_{12}Se_{19}$, and "$In_{\approx 2}Q_3$, Q = S, Se, Te".

Empirical formula	$K_{2.08}In_{12}Se_{11.44}Te_{7.56}$	$K_{1.50}Tl_{0.72}In_{12}Se_{19}$	"$In_{\approx 2}Q_3$, Q = S, Se, Te"
Formula mass	M = 3327.12 g/mol	M = 3083.88 g/mol	M = 1032.06 g/mol
Color	deep red	deep red	silver metallic
Crystal system	trigonal	trigonal	trigonal
Space group	$R\bar{3}$ (No. 148)	$R\bar{3}$ (No. 148)	$R\bar{3}$ (No. 148)
Unit cell dimensions	a = 14.1702(5) Å c = 35.883(2) Å	a = 13.801(1) Å c = 35.113(3) Å	a = 14.0212(4) Å c = 35.346(2) Å
Volume	V = 6239.9(5) Å^3	V = 5792.0(8) Å^3	V = 6017.8(4) Å^3
Formula units/unit cell	Z = 6	Z = 6	Z = 18
Calculated density	ρ = 5.264 g/cm^3	ρ = 5.370 g/cm^3	ρ = 5.126 g/cm^3
Diffractometer	IPDS (STOE)	IPDS (STOE)	IPDS (STOE)
Wavelength	λ = 0.71073 Å (Mo-K_α)	λ = 0.71073 Å (Mo-K_α)	λ = 0.71073 Å (Mo-K_α)
Monochromator	graphite	graphite	graphite
Crystal size	0.20 × 0.19 × 0.18 mm	0.24 × 0.23 × 0.14 mm	0.24 × 0.19 × 0.12 mm
Measuring temperature	T = 296(2) K	T = 296(2) K	T = 296(2) K
Scan type	ϕ-scan	ϕ-scan	ϕ-scan
Measured θ range	$2.01° \le \theta \le 25.82°$	$2.06° \le \theta \le 26.04°$	$2.03° \le \theta \le 25.98°$
Index ranges	$-17 \le h \le 17$ $-17 \le k \le 17$ $-43 \le l \le 43$	$-16 \le h \le 16$ $-16 \le k \le 17$ $-43 \le l \le 43$	$-17 \le h \le 17$ $-17 \le k \le 17$ $-43 \le l \le 43$
Reflections collected	19261	19460	23210
Independent reflections	2641	2537	2636
Observed reflections	2223 [$I > 2\sigma(I)$]	2073 [$I > 2\sigma(I)$]	2485 [$I > 2\sigma(I)$]
Data averaging[a]	R_{int} = 0.0754 R_σ = 0.0338	R_{int} = 0.0641 R_σ = 0.0315	R_{int} = 0.0530 R_σ = 0.0200
Completeness to θ_{max}	98.3%	99.5%	99.8%
Absorption coefficient	μ = 22.029 mm^{-1}	μ = 29.192 mm^{-1}	μ = 18.770 mm^{-1}
Absorption correction	numerical[20,21]	numerical[20,21]	numerical[20,21]
Transmission factors	$0.0507 \le T \le 0.0916$	$0.0139 \le T \le 0.0838$	$0.0488 \le T \le 0.1355$
Extinction coefficient	–	ε = 0.000023(3)	ε = 0.000026(4)
Structure solution	direct methods[22]	direct methods[22]	direct methods[22]
Structure refinement	full-matrix least squares on F^2	full-matrix least squares on F^2	full-matrix least squares on F^2
Number of parameters	112	107	127
Number of restraints	0	0	0
GooF on F^2	1.029	0.923	1.121
F(000)	8388	8004	7848
Weighting scheme[b]	A = 0.0414, B = 165.0150	A = 0.0197, B = 0	A = 0.0162, B = 77.3336
Figure of merit[a] [$I > 2\sigma(I)$]	R_1 = 0.0327, wR_2 = 0.0791	R_1 = 0.0208, wR_2 = 0.0403	R_1 = 0.0238, wR_2 = 0.0529
Figure of merit[a] (all data)	R_1 = 0.0411, wR_2 = 0.0818	R_1 = 0.0309, wR_2 = 0.0420	R_1 = 0.0261, wR_2 = 0.0538
Residual electron density	$-3.513 \le \rho \le 3.373$ e/Å^3	$-1.477 \le \rho \le 1.244$ e/Å^3	$-0.983 \le \rho \le 1.783$ e/Å^3

[a] Definition of R factors see ref.[22] [b] $w = 1/[\sigma^2(F_o^2) + (AP)^2 + BP]$, $P = (F_o^2 + 2F_c^2)/3$.

Additionally, HRTEM supports the significance of the ordering when selecting optimum focusing conditions. The simulated micrographs in Figure 6, b were calculated on the basis of the SPS (left) and the twofold superstructure (right). Because of the complexity of the structure, single rows of atoms are not resolved in any zone axis orientation of HRTEM micrographs. Therefore, the characteristic superposition of atoms must be interpreted. For zone axis [100] the bright ovals represent structural motifs containing the In atoms ordered within the twofold superstructure. For the SPS (see Figure 6, b, left), all ovals are equivalent; hence, no superstructure along c is observed. The ordering of the atoms in terms of the twofold superstructure (Figure 6, b, right) is indicated by significant and periodic variations of the ovals. The latter is also seen in the experimental and simulated micrographs of Figure 6, c. In accordance with the simulations, the significance of the ordering fades in underfocused images, as shown in the series of HRTEM micrographs in the Supporting Information (Figure S1).

Like $K_2In_{12}Se_{19}$, the crystals of $K_2In_{12}Se_{12}Te_7$ are built from APDs; however, the sizes of the APDs differ considerably (see Figure 7). For $K_2In_{12}Se_{12}Te_7$ they show dimensions of several microns in all zone axes; hence, the FFTs (Figure 7, a, right) and SAED patterns clearly show the superstructure peaks on *hkl*, $l = 2n + 1$. The HRTEM micrograph of Figure 7, a was recorded at the boundary of two shifted APDs (see arrows). As substantiated by simulations, the superstructure ordering inside the APDs is indicated by the dark spots which are arranged on hexagons [see mark in Figure 7, a and attached simulated micrograph (top right)]. Between the APDs the signs of ordering fade, and the contrasts approximate the image expected for the SPS (cf. simulated micrograph in Figure 7, a, top left). The focusing conditions of the micrograph recorded for $K_2In_{12}Se_{19}$ (Figure 7, b) were selected similarly to those for Figure 7, a. In this case, the areas with clear superstructure ordering are within the nanoscale, and the attached FFT contains diffuse intensities on *hkl*, $l = 2n + 1$ [category (II), see above].

Table 2. Atomic coordinates, occupancies, and equivalent isotropic displacement parameters, U_{eq}/Å^2, for $K_{2.08}In_{12}Se_{11.44}Te_{7.56}$, $K_{1.50}Tl_{0.72}In_{12}Se_{19}$, and "$In_{\approx 2}Q_3$, Q = S, Se, Te". For comparison, the ordered superstructure model of $K_2In_{12}Se_{19}$ is added.

Atom	*f*	Compound	*x*/*a*	*y*/*b*	*z*/*c*	*sof*	U_{eq}
K1a/Tl1a		$K_2In_{12}Se_{19}$	0	0	0.41673	1	–
		$K_{2.08}In_{12}Se_{11.44}Te_{7.56}$	0	0	0.4204(2)	1.02(3)/–	0.101(4)
		$K_{1.50}Tl_{0.72}Se_{12}Te_{19}$	0	0	0.41513(4)	0.821(3)/0.179(3)	0.0504(7)
	A(In)	$In_{\approx 2}Q_3$ (Q = S, Se, Te)	0	0	0.5	0.75(1)	0.0233(4)
K1b/Tl1b		$K_2In_{12}Se_{19}$	0	0	0.08327	1	–
		$K_{2.08}In_{12}Se_{11.44}Te_{7.56}$	0	0	0.0840(9)	0.37(3)/–	0.13(1)
		$K_{1.50}Tl_{0.72}Se_{12}Te_{19}$	0	0	0.07920(2)	0.455(3)/0.545(3)	0.0403(3)
	A(Se)	$In_{\approx 2}Q_3$ (Q = S, Se, Te)	0	0	0.0581(2)	0.282(9)	0.178(7)
K2		$K_2In_{12}Se_{19}$	–	–	–	–	–
		$K_{2.08}In_{12}Se_{11.44}Te_{7.56}$	0	0	0	1.38(2)	0.036(2)
		$K_{1.50}Tl_{0.72}Se_{12}Te_{19}$	0	0	0.0150(4)	0.23(1)	0.043(5)
	A(In)	$In_{\approx 2}Q_3$ (Q = S, Se, Te)	0	0	0.01704(9)	0.215(4)	0.033(1)
In1a		$K_2In_{12}Se_{19}$	0.31565	0.20621	0.00829	1	–
		$K_{2.08}In_{12}Se_{11.44}Te_{7.56}$	0.31699(5)	0.20451(5)	0.00644(2)	1	0.0230(2)
		$K_{1.50}Tl_{0.72}Se_{12}Te_{19}$	0.31580(3)	0.20798(3)	0.00567(1)	1	0.0198(1)
		$In_{\approx 2}Q_3$ (Q = S, Se, Te)	0.31923(4)	0.19875(4)	0.01402(1)	0.73(1)	0.0290(2)
In1b		$K_2In_{12}Se_{19}$	0.22389	0.35101	0.17495	1	–
		$K_{2.08}In_{12}Se_{11.44}Te_{7.56}$	0.21717(5)	0.34765(5)	0.17881(2)	1	0.0227(2)
		$K_{1.50}Tl_{0.72}Se_{12}Te_{19}$	0.22136(3)	0.35053(3)	0.17789(1)	1	0.0188(1)
		$In_{\approx 2}Q_3$ (Q = S, Se, Te)	0.21923(3)	0.34991(3)	0.17372(1)	0.76(1)	0.0237(2)
In2		$K_2In_{12}Se_{19}$	0.11607	0.19577	0.28446	1	–
		$K_{2.08}In_{12}Se_{11.44}Te_{7.56}$	0.11189(5)	0.18915(5)	0.28324(2)	1	0.0244(2)
		$K_{1.50}Tl_{0.72}Se_{12}Te_{19}$	0.11514(3)	0.19495(4)	0.28459(1)	1	0.0238(1)
		$In_{\approx 2}Q_3$ (Q = S, Se, Te)	0.10988(3)	0.18612(4)	0.78304(1)	0.75(1)	0.0236(2)
In3		$K_2In_{12}Se_{19}$	0.28953	0.11134	0.21268	1	–
		$K_{2.08}In_{12}Se_{11.44}Te_{7.56}$	0.29352(5)	0.11269(5)	0.21395(2)	1	0.0224(2)
		$K_{1.50}Tl_{0.72}Se_{12}Te_{19}$	0.29291(3)	0.11237(3)	0.213314(9)	1	0.0191(1)
		$In_{\approx 2}Q_3$ (Q = S, Se, Te)	0.29508(4)	0.11462(3)	0.71455(1)	0.75(1)	0.0249(2)
Se1/Te1		$K_2In_{12}Se_{19}$	0	0	0.25000	1	–
		$K_{2.08}In_{12}Se_{11.44}Te_{7.56}$	0	0	0.24739(4)	0.92(2)/0.08(2)	0.0231(6)
		$K_{1.50}Tl_{0.72}Se_{12}Te_{19}$	0	0	0.24916(3)	1	0.0233(2)
	Q(Se)	$In_{\approx 2}Q_3$ (Q = S, Se, Te)	0	0	0.25320(4)	0.538(9)	0.0210(5)
Se2a/Te2a		$K_2In_{12}Se_{19}$	0.18522	0.25044	0.04513	1	–
		$K_{2.08}In_{12}Se_{11.44}Te_{7.56}$	0.1645(1)	0.2182(1)	0.04594(3)	0.51(1)/0.49(1)	0.0584(5)
		$K_{1.50}Tl_{0.72}Se_{12}Te_{19}$	0.18005(5)	0.23890(5)	0.04566 (2)	1	0.0259(1)
	Q(Se)	$In_{\approx 2}Q_3$ (Q = S, Se, Te)	0.1936(6)	0.2690(7)	0.04762(4)	0.66(2)	0.066(2)
	Q(Te)		0.1537(2)	0.2158(4)	0.0451(1)	0.232(9)	0.0238(9)
Se2b/Te2b		$K_2In_{12}Se_{19}$	0.14811	0.41623	0.12154	1	–
		$K_{2.08}In_{12}Se_{11.44}Te_{7.56}$	0.14498(7)	0.40689(8)	0.12092(2)	0.51(1)/0.49(1)	0.0378(3)
		$K_{1.50}Tl_{0.72}Se_{12}Te_{19}$	0.14513(5)	0.40687(6)	0.12217(2)	1	0.0271(1)
	Q(Te)	$In_{\approx 2}Q_3$ (Q = S, Se, Te)	0.18731(4)	0.47087(4)	0.11973(1)	0.655(9)	0.0240(2)
Se3a/Te3a		$K_2In_{12}Se_{19}$	0.03597	0.19029	0.34566	1	–
		$K_{2.08}In_{12}Se_{11.44}Te_{7.56}$	0.03291(6)	0.18912(6)	0.35025(2)	0.40(1)/0.60(1)	0.0290(3)
		$K_{1.50}Tl_{0.72}Se_{12}Te_{19}$	0.03462(5)	0.19370(5)	0.34884(2)	1	0.0247(1)
	Q(Te)	$In_{\approx 2}Q_3$ (Q = S, Se, Te)	0.03592(4)	0.17413(4)	0.34268(1)	0.69(1)	0.0263(2)
Se3b/Te3b		$K_2In_{12}Se_{19}$	0.19029	0.15431	0.15434	1	–
		$K_{2.08}In_{12}Se_{11.44}Te_{7.56}$	0.17753(5)	0.14018(5)	0.15727(2)	0.33(1)/0.67(1)	0.0250(3)
		$K_{1.50}Tl_{0.72}Se_{12}Te_{19}$	0.18597(4)	0.14765(4)	0.15847(1)	1	0.0184(1)
	Q(Te)	$In_{\approx 2}Q_3$ (Q = S, Se, Te)	0.17938(4)	0.15210(3)	0.14737(1)	0.73(1)	0.0264(2)
Se4a/Te4a		$K_2In_{12}Se_{19}$	0.34780	0.09822	0.06516	1	–
		$K_{2.08}In_{12}Se_{11.44}Te_{7.56}$	0.35380(6)	0.09769(6)	0.06201(2)	0.918(9)/0.082(9)	0.0198(3)
		$K_{1.50}Tl_{0.72}Se_{12}Te_{19}$	0.34925(4)	0.09575(4)	0.06205(1)	1	0.0163(1)
	Q(Se)	$In_{\approx 2}Q_3$ (Q = S, Se, Te)	0.34484(6)	0.09282(6)	0.07195(2)	0.69(1)	0.0269(3)

Table 2. *(Continued)*

Atom	*f*	Compound	*x*/*a*	*y*/*b*	*z*/*c*	*sof*	U_{eq}
Se4b/Te4b		$K_2In_{12}Se_{19}$	0.08375	0.31886	0.23182	1	–
		$K_{2.08}In_{12}Se_{11.44}Te_{7.56}$	0.08513(6)	0.32112(6)	0.23656(2)	0.83(1)/0.17(1)	0.0226(3)
		$K_{1.50}Tl_{0.72}Se_{12}Te_{19}$	0.08727(4)	0.32231(4)	0.23528(1)	1	0.0172(1)
	Q(Se)	$In_{\approx 2}Q_3$ (Q = S, Se, Te)	0.07464(6)	0.31084(6)	0.22858(2)	0.574(8)	0.0224(3)

Table 3. Anisotropic displacement parameters, U_{ij}/Å^2, for $K_{2.08}In_{12}Se_{11.44}Te_{7.56}$, $K_{1.50}Tl_{0.72}In_{12}Se_{19}$, and "$In_{\approx 2}Q_3$, Q = S, Se, Te".

Atom	*f*	Compound	U_{11}	U_{22}	U_{33}	U_{12}	U_{13}	U_{23}
K1a/Tl1a		$K_{2.08}In_{12}Se_{11.44}Te_{7.56}$	0.104(4)	0.104(4)	0.095(7)	0	0	0.052(2)
		$K_{1.50}Tl_{0.72}Se_{12}Te_{19}$	0.0546(9)	0.0546(9)	0.042(1)	0	0	0.0273(5)
	A(In)	$In_{\approx 2}Q_3$ (Q = S, Se, Te)	0.0197(4)	0.0197(4)	0.0305(6)	0	0	0.0098(2)
K1b/Tl1b		$K_{2.08}In_{12}Se_{11.44}Te_{7.56}$	0.105(13)	0.105(13)	0.18(3)	0	0	0.053(7)
		$K_{1.50}Tl_{0.72}Se_{12}Te_{19}$	0.0413(4)	0.0413(4)	0.0383(5)	0	0	0.0207(2)
	A(Se)	$In_{\approx 2}Q_3$ (Q = S, Se, Te)	0.26(1)	0.26(1)	0.026(3)	0	0	0.127(5)
K2		$K_{2.08}In_{12}Se_{11.44}Te_{7.56}$	0.0152(13)	0.0152(13)	0.078(4)	0	0	0.0076(7)
		$K_{1.50}Tl_{0.72}Se_{12}Te_{19}$	0.023(5)	0.023(5)	0.082(9)	0	0	0.012(2)
	A(In)	$In_{\approx 2}Q_3$ (Q = S, Se, Te)	0.027(1)	0.027(1)	0.044 (2)	0	0	0.0133(6)
In1a		$K_{2.08}In_{12}Se_{11.44}Te_{7.56}$	0.0197(3)	0.0236(3)	0.0258(4)	–0.0035(2)	–0.0024(2)	0.0108(2)
		$K_{1.50}Tl_{0.72}Se_{12}Te_{19}$	0.0196(2)	0.0195(2)	0.0206(2)	–0.0033(1)	–0.0021(1)	0.0099(2)
		$In_{\approx 2}Q_3$ (Q = S, Se, Te)	0.0339(3)	0.0265(3)	0.0276(3)	–0.0006(2)	–0.0022(2)	0.0158(2)
In1b		$K_{2.08}In_{12}Se_{11.44}Te_{7.56}$	0.0201(3)	0.0241(3)	0.0230(4)	0.0016(3)	0.0008(2)	0.0104(2)
		$K_{1.50}Tl_{0.72}Se_{12}Te_{19}$	0.0171(2)	0.0213(2)	0.0189(2)	0.0013(1)	0.0001(1)	0.0103(2)
		$In_{\approx 2}Q_3$ (Q = S, Se, Te)	0.0218(2)	0.0182(2)	0.0294(3)	0.0022(2)	0.0000(2)	0.0086(2)
In2		$K_{2.08}In_{12}Se_{11.44}Te_{7.56}$	0.0228(3)	0.0337(4)	0.0209(4)	0.0012(3)	0.0019(2)	0.0173(3)
		$K_{1.50}Tl_{0.72}Se_{12}Te_{19}$	0.0235(2)	0.0374(3)	0.0172(2)	0.0034(2)	0.0030(2)	0.0203(2)
		$In_{\approx 2}Q_3$ (Q = S, Se, Te)	0.0213(2)	0.0308(3)	0.0227(2)	–0.0004(2)	0.0011(2)	0.0159(2)
In3		$K_{2.08}In_{12}Se_{11.44}Te_{7.56}$	0.0283(3)	0.0210(3)	0.0186(4)	0.0017(2)	0.0050(2)	0.0126(3)
		$K_{1.50}Tl_{0.72}Se_{12}Te_{19}$	0.0268(2)	0.0177(2)	0.0138(2)	0.0012(1)	0.0039(1)	0.0119(2)
		$In_{\approx 2}Q_3$ (Q = S, Se, Te)	0.0303(3)	0.0223(2)	0.0206(2)	0.0026(2)	0.0056(2)	0.0120(2)
Se1/Te1		$K_{2.08}In_{12}Se_{11.44}Te_{7.56}$	0.0235(6)	0.0235(6)	0.022(1)	0	0	0.0117(3)
		$K_{1.50}Tl_{0.72}Se_{12}Te_{19}$	0.0249(3)	0.0249(3)	0.0202(4)	0	0	0.0124(2)
	Q(Se)	$In_{\approx 2}Q_3$ (Q = S, Se, Te)	0.0201(6)	0.0201(6)	0.0230(8)	0	0	0.0100(3)
Se2a/Te2a		$K_{2.08}In_{12}Se_{11.44}Te_{7.56}$	0.0876(9)	0.113(1)	0.0273(6)	–0.0014(5)	–0.0051(5)	0.0892(8)
		$K_{1.50}Tl_{0.72}Se_{12}Te_{19}$	0.0317(3)	0.0406(4)	0.0167(3)	0.0035(2)	0.0021(2)	0.0264(3)
	Q(Se)	$In_{\approx 2}Q_3$ (Q = S, Se, Te)	0.103(3)	0.125(4)	0.0290(6)	–0.0206(9)	–0.0212(8)	0.102(3)
	Q(Te)		0.026(1)	0.028(2)	0.021(1)	–0.0006(7)	–0.0011(6)	0.016(1)
Se2b/Te2b		$K_{2.08}In_{12}Se_{11.44}Te_{7.56}$	0.0492(6)	0.0604(6)	0.0251(5)	0.0008(4)	–0.0034(4)	0.0434(5)
		$K_{1.50}Tl_{0.72}Se_{12}Te_{19}$	0.0357(3)	0.0432(4)	0.0165(2)	0.0012(2)	0.0003(2)	0.0303(3)
	Q(Te)	$In_{\approx 2}Q_3$ (Q = S, Se, Te)	0.0227(3)	0.0241(3)	0.0281(3)	0.0000(2)	–0.0033(2)	0.0140(2)
Se3a/Te3a		$K_{2.08}In_{12}Se_{11.44}Te_{7.56}$	0.0291(4)	0.0392(5)	0.0236(5)	–0.0011(3)	0.0025(3)	0.0208(3)
		$K_{1.50}Tl_{0.72}Se_{12}Te_{19}$	0.0276(3)	0.0375(4)	0.0160(2)	0.0026(2)	0.0022(2)	0.0215(3)
	Q(Te)	$In_{\approx 2}Q_3$ (Q = S, Se, Te)	0.0243(3)	0.0233(3)	0.0305(3)	–0.0054(2)	–0.0007(2)	0.0112(2)
Se3b/Te3b		$K_{2.08}In_{12}Se_{11.44}Te_{7.56}$	0.0252(4)	0.0256(4)	0.0265(4)	0.0034(3)	0.0047(3)	0.0145(3)
		$K_{1.50}Tl_{0.72}Se_{12}Te_{19}$	0.0187(3)	0.0192(3)	0.0174(2)	–0.0004(2)	0.0002(2)	0.0095(2)
	Q(Te)	$In_{\approx 2}Q_3$ (Q = S, Se, Te)	0.0342(3)	0.0238(2)	0.0224(2)	0.0020 (2)	0.0020 (2)	0.0155(2)
Se4a/Te4a		$K_{2.08}In_{12}Se_{11.44}Te_{7.56}$	0.0207(5)	0.0219(5)	0.0190(5)	–0.0026(3)	–0.0023(3)	0.0122(3)
		$K_{1.50}Tl_{0.72}Se_{12}Te_{19}$	0.0171(3)	0.0177(3)	0.0148(2)	–0.0024(2)	–0.0013(2)	0.0094(2)
	Q(Se)	$In_{\approx 2}Q_3$ (Q = S, Se, Te)	0.0347(4)	0.0274(4)	0.0272(4)	–0.0059(3)	–0.0070(3)	0.0220(3)
Se4b/Te4b		$K_{2.08}In_{12}Se_{11.44}Te_{7.56}$	0.0179(4)	0.0258(5)	0.0222(5)	0.0045(3)	0.0003(3)	0.0095(3)
		$K_{1.50}Tl_{0.72}Se_{12}Te_{19}$	0.0153(3)	0.0189(3)	0.0159(2)	0.0007(2)	0.0005(2)	0.0076(2)
	Q(Se)	$In_{\approx 2}Q_3$ (Q = S, Se, Te)	0.0164(4)	0.0223(4)	0.0243(4)	0.0034(3)	–0.0014(3)	0.0067(3)

Table 4. Comparison of selected interatomic distances found in $K_2In_{12}Se_{19}$ (average structure), $K_2In_{12}Se_{19-x}Te_x$ and $K_{2-y}Tl_y$-$In_{12}Se_{19}$.

No.	Atom1	Atom2	d/Å $K_2In_{12}Se_{19}$, av.	Se/Te mix.	K/Tl mix.
1	K1a–	Se3a	3.482(2)–3.483(2)	3 × 3.535(5)	3 × 3.394(1)
2	K1a–	Se2b	*3.393(1)–3.394(1)*	*3 × 3.511(3)*	*3 × 3.5069(9)*
3	Se1–	In2	6 × 2.6538(7)	3 × 2.665(1)	3 × 2.6527(8)
4	Se1–	In3	6 × 3.7408(6)	3 × 3.827(1)	3 × 3.7499(5)
5	K1b–	Se3b	3.482(2)–3.483(2)	3 × 3.49(2)	3 × 3.6409(8)
6	K1b–	Se2a	*3.393(1)–3.394(1)*	*3 × 3.11(1)*	*3 × 3.1999(9)*
7	In3–	In3	*3.5271(8)*	*3.6609(9)*	*3.5426(5)*

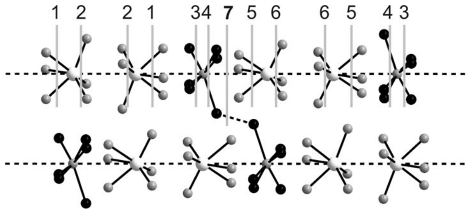

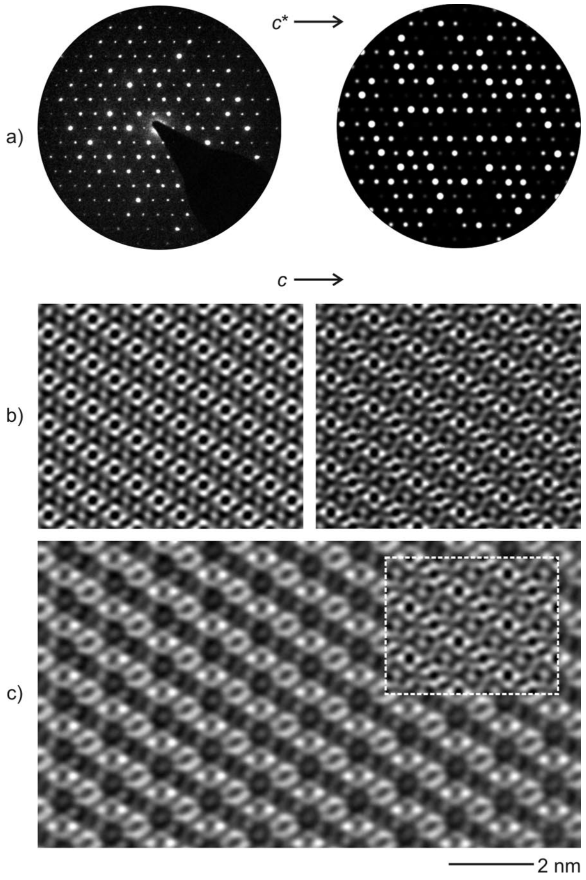

Figure 6. Electron microscopy performed on $K_2In_{12}Se_{12}Te_7$, zone axis [100]. (a) Experimental (left) and calculated (kinematical approximation, right) SAED pattern. (b) Simulated micrographs (Δf = +5 nm, t = 5.5 nm) for the SPS (left, see text) and the twofold superstructure [(III), right]. (c) Experimental micrograph with inserted simulation (Δf = +5 nm, t = 5.5 nm).

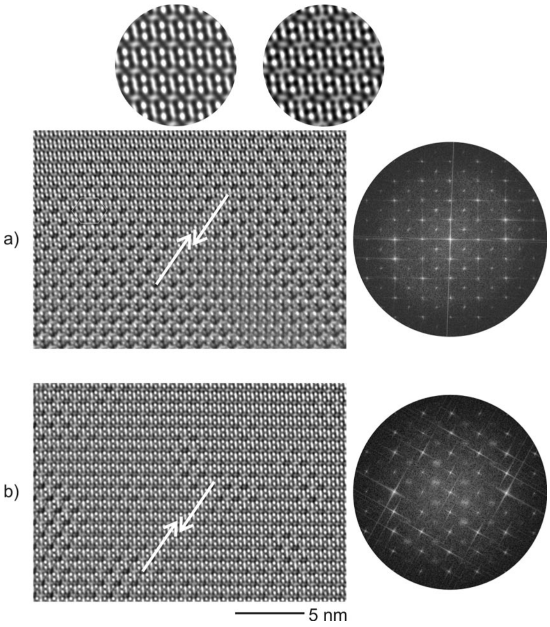

Figure 7. (a) HRTEM micrographs displaying APDs for K_2In_{12}-$Se_{12}Te_7$ and attached FFT, zone axis [–111]. Top: simulated micrographs for the SPS (left) and the twofold superstructure (right). Parameters for simulations: Δf = +5 nm, t = 4.3 nm. Both simulations are scaled by 200% with respect to the experimental micrograph (bottom). (b) HRTEM micrograph for $K_2In_{12}Se_{19}$ (zone axis [–111], $\Delta f \approx$ +5 nm) with attached FFT.

Complex Ordering of $(NH_4)_2In_{12}Se_{19}$

The first structural analyses performed on $(NH_4)_2$-$In_{12}Se_{19}$ were restricted to the Bragg reflections hkl, with $l = 2n$. They resulted in an average structure strongly related to the one initially determined for $K_2In_{12}Se_{19}$, particularly exhibiting the disorder of the In atoms inside the rods. However, a close analysis of layers hkl with $l = 2n + 1$ revealed the presence of complex ordering in all examined single crystals. At room temperature, the layers hkl, $l = 2n + 1$ (see $hk1$ in Figure 8, a and the attached enlarged section) contain Bragg intensities forming hexagons around the positions hkl, with $–h + k = n –1$ and $l = 2n + 1$. Note that the diameter of the hexagons coincides with the one of the diffuse rings observed for $K_2In_{12}Se_{19}$. The ordering of the structure changes at higher temperatures. Simulated X-ray precession photographs (based on imaging-plate data) of the reciprocal layer $hk1$ (related to the twofold superstructure) at 297, 373, 423 and 473 K are shown in Figure 8. At higher temperatures the reflections of the sharp hexagons are blurred to diffuse rings (cf. diffuse rings in $K_2In_{12}Se_{19}$) with a decrease in intensity. At around 473 K all diffuse intensities disappeared.

HRTEM was selected to determine the structure models of the new complex ordered phase; however, rapid structural transformations in two consecutive steps occur under the conditions of HRTEM experiments. The complex ordering is so rapidly transformed that even the observation of the complex ordered phase was inhibited. Therefore, all SAED patterns show broad diffuse intensity on hkl, $l = 2n$

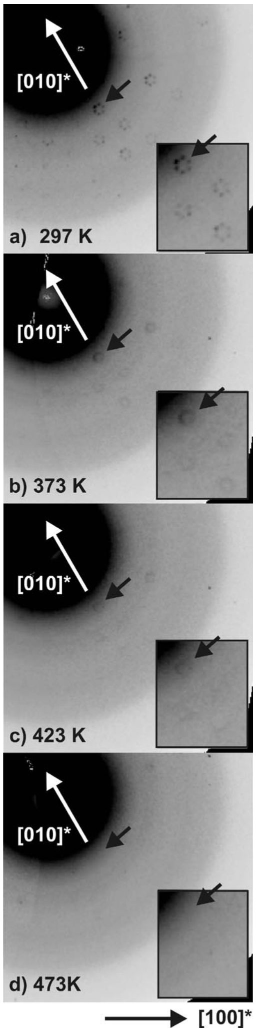

Figure 8. Simulated precession photographs of $(NH_4)_2In_{12}Se_{19}$ at different temperatures measured with a STOE imaging-plate diffractometer system (IPDS). Each simulation shows the reciprocal layer *hk*1.

+ 1 instead of the expected hexagons associated with the complex ordering. In a second and continuous step, the twofold superstructure (category III) is formed.

For the detection of intensities in higher-order Laue zones, the SAED technique is not suitable. The [001] SAED pattern (Figure 9, a, left) and the corresponding precession electron-diffraction (PED) pattern (Figure 9, a, right) were recorded directly after adjusting the zone axis. Only the PED pattern shows broad diffuse intensities, *hk*1 and *hk*2, superimposed on the zero-order Laue zone. Even the SAED pattern after extended exposure did not show any information about the structural transformation; however, the PED pattern now contains the sharp superstructure reflection expected for the twofold superstructure.

The continuous development of structural ordering by electron-beam irradiation is demonstrated by the cutouts of the [100] PED patterns (Figure 9, b), which were recorded sequentially within a time slice of 30 s. After the initial loss of structural complexity (cf. diffuse spots in Figure 9, b, left), the increase of ordering is evident from the concentration (Figure 9, b, center) of the diffuse intensities on *hkl*, $l = 2n + 1$, finally forming sharp Bragg intensities (Figure 9, b, right).

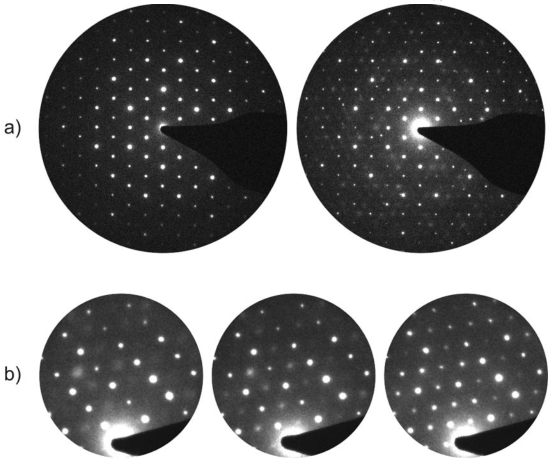

Figure 9. Ordering in $(NH_4)_2In_{12}Se_{19}$. (a) Left: SAED pattern recorded immediately after adjusting the zone axis [001], right: corresponding PED pattern. (b) PED patterns recorded within an exposure series within a time slice of 30 s (see text).

The development of structural ordering is based on the growth of APDs as verified by in situ HRTEM observations. Images with strong contrast can be calculated from Fourier filtering techniques, which allow to limit the image information to the intensities *hkl* with $l = 2n + 1$. According to this procedure, the micrograph recorded directly after adjusting the zone axis (Figure 10, a, left) exhibits considerably smaller APDs compared to the image recorded after 1 min of irradiation (Figure 10, a, right). As in the categories (II) and (III) of $K_2In_{12}Se_{19}$ (see above), the inserted Fourier transforms show diffuse scattering (Figure 10, a, left) and superstructure peaks (Figure 10, a, right) on *hkl* with $l = 2n + 1$, respectively.

The whole scenario of disordering and subsequent ordering is reminiscent of the structural transformation of complex ordered $K_2In_{12}Se_{19}$ (see above). However, the complex orderings in $K_2In_{12}Se_{19}$ and $(NH_4)_2In_{12}Se_{19}$ are different. The first points to a complex ordering along *c*, the latter perpendicular to *c*. For the identification of the final product, PED and HRTEM were applied. The PED patterns in Figure 10, b convincingly match simulated patterns when constructing the twofold superstructure from the initial model of the X-ray analysis. In particular, for the intensities inside the zero-order Laue zones the agreement is perfect; however, slight deviations occur for the superimposed higher-order Laue zones (Figure 10, b, top). In a future project, a quantification of the data needs to clarify whether these deviations correlate with structural variations. The experimental micrographs shown in Figure 11 were recorded after several minutes of irradiation. For zone axis [100] (Figure 11, a), the characteristic variations of the oval bright contrasts are visible and correlate with the twofold superstructure (cf. Figure 6, b and c and inserted simulation). Figure 11, b shows the ordering of the structure for zone axis [–111]. The superstructure is evident from the experimental micrographs (cf. characteristic contrast on hexagons, Figure 7, a). Furthermore, such ordering can also be identified when selecting underfocus conditions for the imaging (see Figure 7, b and inserted simulation).

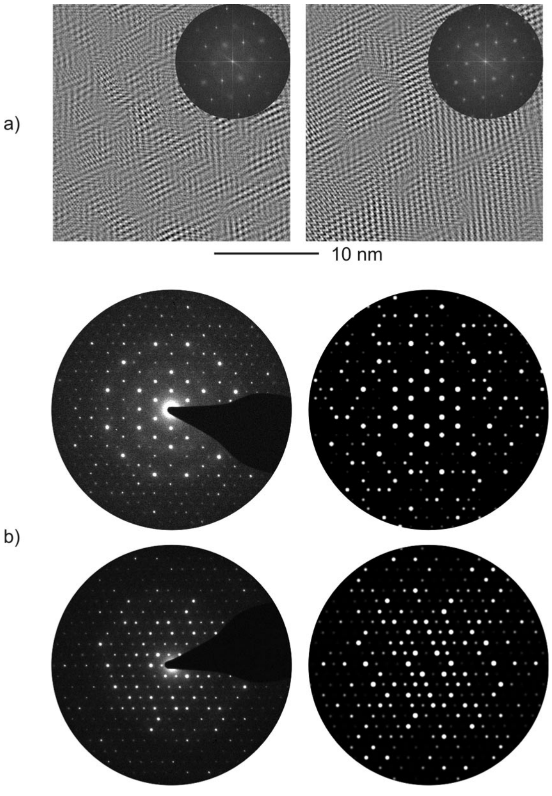

Figure 10. (a) Visualization of APDs by Fourier filtering, zone axis [–111] directly after adjusting the zone axis and after 1 min of irradiation. (b) Left: PED patterns of the final product, right: simulated PED patterns (top: zone axis [001]; bottom: zone axis [–111]).

In order to derive information about the in situ transformation, EELS measurements were performed with a Tecnai F30 microscope. Actually, the irradiation within the time slice needed for adjusting the crystals and the microscope already produces structural ordering as shown by a concentration of the diffuse intensity inside SAED patterns. In this case, the EELS spectra did not contain any significant intensity for the N edge, hence indicating a loss of nitrogen from the ammonium compound. Consequently, one can rationalize the in situ transformation as a combined process of crystallization and NH_3 evaporation by ballistic processes leaving H^+ for charge balance in the crystals. The release of ammonium ions as NH_3 from the structure of $(NH_4)_2In_{12}Se_{19}$ is also supported by thermal analysis data showing a weight loss of ca. 1% between 100 and 200 °C (calculated weight loss ca. 1.1%) and no further weight change up to 300 °C. (The TGA graph is noisy, and it is better to avoid showing it but we can report the weight loss.)

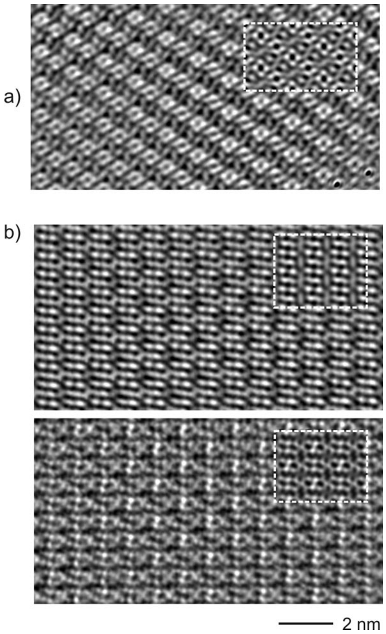

Figure 11. HRTEM micrographs of long-term irradiated $(NH_4)_2In_{12}Se_{19}$ with inserted simulations. (a) Zone axis [100] (Δf = +0 nm, t = 4.2 nm), (b) zone axis [–111] [Δf = +10 nm (top) and Δf = –35 nm (bottom), t = 7 nm].

The Pseudobinary Phase In_2Q_3

It is surprising that the pseudobinary phase In_2Q_3 (Q = S, Se, Te) with the nominal composition $In_4SSe_2Te_3$[18] shows a close structural relation to $K_2In_{12}Se_{19}$, $K_2In_{12}Se_{19-x}Te_x$, and $K_{2-y}Tl_yIn_{12}Se_{19}$. This statement holds for the Kagomé-like host structure, as well as for the inserted rods, but not for the type of disorder. The unique solid was first described in 1983 by Svensson and Albertson. According to their single-crystal analysis, In_2Q_3 is heavily disordered. Our own investigations on this compound confirm this result. Furthermore, no signs of diffuse scattering were observed in X-ray diffraction experiments. In fact, sharp superstructure reflections hkl with $-h + k + l = 3n$ and $l = 2n + 1$ consistent with category (III) instead of diffuse rings occur. The structure refinement shows that the indium atoms in the rods are ordered in terms of the structure model A (or B) of $K_2In_{12}Se_{19}$ (Figure 2, f) with a disorder type similar to $K_2In_{12}Se_{19-x}Te_x$, $K_{2-y}Tl_yIn_{12}Se_{19}$, and microsized APDs. EDX analyses performed on several crystals support the homogeneity of the sample and indicate no significant deviations from the nominal composition. HRTEM micrographs gave no signs for an aggregation of the distinct chalcogen atoms. The series of HRTEM micrographs in Figure 12 was recorded along zone axis [001].

For Δf = –60 nm the imaging conditions of the Scherzer focus are approximated. Assuming the weak-phase-object approximation, the black dots forming a Kagomé net correlate with rows of atoms forming the host structure. The perfect agreement to the inserted simulation based on the model from the XRD analysis underlines that local ordering of the chalcogen atoms is not present, but a complete

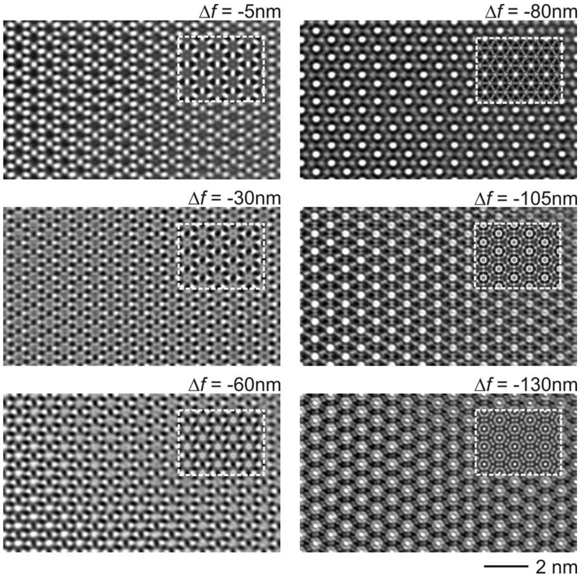

Figure 12. Experimental and simulated HRTEM micrographs (t = 7 nm) for In_2Q_3 with variable focus (see figure), zone axis [001].

averaging is observed along the zone axis. Furthermore, this is supported by images recorded under strong underfocus conditions and for other zone axis orientations.

Conclusions

Today's state-of-the-art methods for the characterization of solids include the nanoscale features, particularly those leading to deviations from long-range ordering of the structure. In this regard, the electron-microscopy imaging techniques are of paramount importance, since averaging effects dominating conventional X-ray analyses are minimized.

One drawback of electron microscopy is known from the early history of TEM development: the beam sensitivity of the samples. In the present case of $(NH_4)_2In_{12}Se_{19}$, the complex ordering of the crystals cannot be analyzed due to structural changes. However, these changes occur in a well-defined way, finally producing perfect crystals with a structure not obtained by conventional strategies. Despite the fact that such synthesis can not be extended easily to large-sample quantities, our finding demonstrates the possibility of in situ chemistry performed inside a TEM column.

Experimental Section

Synthesis and Basic Characterization of Bulk Samples: The mixed crystals of $K_2In_{12}Se_{19-x}Te_x$ and $K_{2-x}Tl_xIn_{12}Se_{19}$ as well as "$In_4SSe_2Te_3$" were prepared by heating stoichiometric mixtures of the elements in evacuated dry quartz-glass ampoules. The elements were first heated to 1000 °C for several hours and finally quenched in ice water. After homogenization under argon, the raw products were annealed at 923 K, 893 K and 873 K, respectively, for 14 d. Well-shaped single crystals of millimeter size were found in all batches. $(NH_4)_2In_{12}Se_{19}$ was prepared according to ref.[14]

Single-Crystal X-ray Investigations: Single-crystal X-ray data for $K_2In_{12}Se_{19-x}Te_x$ (**1**), $K_{2-x}Tl_xIn_{12}Se_{19}$ (**2**), and "$In_4SSe_2Te_3$" (**3**) were collected with a STOE IPDS diffractometer by using graphite-monochromatized Mo-K_α radiation. The STOE IPDS program package[19] was used for data evaluation. In particular, the programs RECEPI and SPACE were used to analyze the reciprocal space and for calculating precession images from the measured imaging plate data. Numerical absorption corrections for **1**, **2**, and **3** were made on the basis of an optimized description of the crystal (STOE X-RED,[20] X-SHAPE[21]). The trial structures were obtained by direct methods (SHELXS97[22]) and refined by using SHELXL97.[22] A summary of crystal and structure refinement data for **1**, **2**, and **3** is reported in Table 1.

$K_2In_{12}Se_{12}Te_{19-x}Te_x$ and $K_{2-x}Tl_xIn_{12}Se_{19}$: Single crystals from batches with the gross compositions "$K_2In_{12}Se_{15}Te_4$" and "$K_{1.6}Tl_{0.4}In_{12}Se_{19}$" were separated from the bulk material and mounted on the imaging-plate diffractometer. A close examination of the reciprocal spaces of both measurements shows no indication of diffuse intensities. The observed systematic extinctions are consistent with the space groups $R3$ and $R\bar{3}$. The latter, which is centrosymmetric, was chosen for each case. This choice was supported by means of the distribution of the normalized structure factors [E statistic, $N(Z)$ test]. The structure refinements converged at good R values (see Table 1) when applying Se/Te and K/Tl mixed-site occupations for all chalcogen and alkali-metal positions, respectively. Due to the mixed occupancy the displacement parameters show only in the case of the Se/Te derivative for the position Se2A/Te2A a significantly increased anisotropic vibration along the U_2 main axis of the thermal vibration ellipsoid. The thermal ellipsoid of the equivalent position in the Tl compound is also increased, but in comparison only slightly. Taking into account the residual electron density in the structure refinement of the Se/Te compound with the atomic form factor for potassium, a significant over-occupancy [*sof*(K2) = 1.38(2)] results, whereas position K1b is not fully occupied [*sof*(K1b) = 0.37(3)]. In contrast, K1a is within the threefold standard deviation fully occupied. It results in the specified composition $K_{2.08}In_{12}Se_{11.44}Te_{7.56}$. The significant over-occupancy of site K2 suggests a K^+/In^+ mixed occupancy. From the corresponding refinement results a mixed occupancy of *sof*(K^+/In^+) = 0.79(1)/0.21(1) with only marginal change in the occupation of all other sites. Whether this residual electron density can be assigned to potassium or mixed potassium/indium occupancy could not be solved conclusively. In case of the Tl derivative the atom sites A1a and A1b are mixed-occupied by potassium and thallium. Due to the refinement method the sum of the occupancy factors of these two sites is constrained to be constant (*sof* = 1). According to this a possible over- or under-occupancy at these positions as it is observed for the Se/Te compound cannot be obtained by refining the above-mentioned residual electron density using the potassium scattering factor (site K2). Contrary to the Se/Te compound, K2 is here significantly under-occupied [*sof*(K2) = 0.23(1)] and shows two maxima. The physically meaningless distance between the two maxima speaks here more for an artefact. The overall composition $K_{1.50}Tl_{0.72}In_{12}Se_{19}$ is obtained by taking into account this residual electron density with the scattering factor of potassium in the structure refinement.

High-Temperature Measurements of $(NH_4)_2In_{12}Se_{19}$: A well-shaped crystal of $(NH_4)_2In_{12}Se_{19}$ was fixed in an evacuated and sealed quartz-glass capillary and mounted on a STOE imaging-plate diffractometer equipped with a STOE high-temperature attachment at 297 K, 373 K, 423 K and 473 K by using graphite-monochromatized Mo-$K_{\alpha1}$ radiation. Starting from 297 K (room temperature) the temperature of the crystal was increased after each measurement. Between the measurements the crystal was not cooled. Further details of the crystal structure investigation are available from the Fachinformationszentrum Karlsruhe, 76344 Eggenstein-Leopoldshafen (Germany), on quoting the depository number CSD-420869 ($K_2In_{12}Se_{19-x}Te_x$), -420868 ($K_{2-x}Tl_xIn_{12}Se_{19}$), -420867 ($In_4SSe_2Te_3$), the name of the author(s), and citation of the paper.

Electron Microscopy and Chemical Analysis: HRTEM and SAED were performed with a Philips CM30ST microscope (300 kV, LaB_6 cathode, C_S = 1.15 mm). The samples were grinded and suspended in *n*-butanol. One drop of the suspension was placed on a perforated carbon/copper net which served as support of the crystallites. All images were recorded with a Gatan Multiscan CCD camera and evaluated (including Fourier filtering) with the program Digital Micrograph 3.6.1 (Gatan) or Crisp (Calidris). HRTEM micrographs (multislice formalism) were simulated with the EMS program package[23] (spread of defocus: 70 Å, illumination semiangle: 1.2 mrad). SAED (selected area electron diffraction) and PED patterns (precession angle: 3°) were calculated with the software Emaps.[24] Elemental analyses by EDX were performed in the nanoprobe and in the scanning mode of CM30ST with an Si/Li detector (Noran, Vantage System). EELS investigations were performed with a Tecnai F30 microscope operated at 300 kV with the aid of a Gatan imaging filter.

Supporting Information (see footnote on the first page of this article): Series of HRTEM micrographs for $K_2In_{12}Se_{12}Te_7$.

---

[1] B. Krebs, *Angew. Chem.* **1983**, *95*, 113–134; *Angew. Chem. Int. Ed. Engl.* **1983**, *22*, 113–134.

[2] N. Hüsing, *Angew. Chem. Int. Ed.* **2008**, *47*, 1992–1994.

[3] O. M. Yaghi, Z. Sun, D. A. Richardson, T. L. Groy, *J. Am. Chem. Soc.* **1994**, *116*, 807–808.

[4] S. Bag, P. N. Trikalitis, P. J. Chupas, G. S. Armatas, M. G. Kanatzidis, *Science* **2007**, *317*, 490–493.

[5] J. S. Sanghera, L. B. Shaw, I. D. Aggarwal, *C. R. Chim.* **2002**, *5*, 873–883.

[6] A. M. Andriesh, M. S. Iovu, S. D. Shutov, *J. Optoelectron. Adv. Mater.* **2002**, *4*, 631–647.

[7] A. L. Lacaita, D. J. Wouters, *Phys. Status Solidi* **2008**, *205*, 2281–2297.

[8] S. Ovshinsky, *Phys. Rev. Lett.* **1968**, *21*, 1450–1453.

[9] T. Mokari, S. E. Habas, M. Zhang, P. Yang, *Angew. Chem. Int. Ed.* **2008**, *47*, 5605–5608.

[10] X. Jiang, H. J. Deiseroth, C. Gu, K. Xhaxhiu, Y. Huang, J. Li, R. Che, Z. Wang, *Nanotechnology* **2008**, *19*, 205702.

[11] N. Zheng, X. Bu, H. Vu, P. Feng, *Angew. Chem. Int. Ed.* **2005**, *44*, 5299–5303.

[12] K. F. Hsu, S. Loo, F. Guo, W. Chen, J. S. Dyck, C. Uher, T. Hogan, E. K. Polychroniadis, G. Kanatzidis, *Science* **2004**, *303*, 818–821.

[13] H. Katagiri, *Thin Solid Films* **2005**, *480 –481*, 426–432.

[14] M. J. Manos, C. D. Malliakas, M. G. Kanatzidis, *Chem. Eur. J.* **2007**, *13*, 51–58.

[15] H. J. Deiseroth, S. T. Kong, H. Eckert, J. Vannahme, C. Reiner, T. Zaiss, M. Schlosser, *Angew. Chem. Int. Ed.* **2008**, *47*, 755–758.

[16] M. Schlosser, C. Reiner, H. J. Deiseroth, L. Kienle, *Eur. J. Inorg. Chem.* **2001**, 2241–2247.

[17] L. Kienle, A. Simon, *J. Solid State Chem.* **2001**, *161*, 385–395.

[18] C. Svensson, J. Albertsson, *J. Solid State Chem.* **1983**, *46*, 46–55.

[19] *IPDS Software*, Version 2.93, STOE and Cie, Darmstadt, Germany, **1999**.

[20] *X-RED 1.19*, STOE and Cie, Darmstadt, Germany, **1999**.

[21] *X-SHAPE 1.06*, STOE and Cie, Darmstadt, Germany, **1999**.

[22] G. M. Sheldrick, *SHELX-97, Program Package for the Solution and Refinement of Crystal Structures*, University of Göttingen, Göttingen, Germany, **1997**.

[23] P. A. Stadelmann, *Ultramicroscopy* **1987**, *21*, 131–146.

[24] *Empas 1.0*, AnaliTEX, Stockholm, Sweden, **2002–2007**.

Received: July 27, 2009

DOI: 10.1002/ejic.200900836

Theoretical Study on the Structural Aspects of Cu^{II} Hybrid-Spin Complexes

Tsveta Miteva,[a] Julia Romanova,[a] Anela Ivanova,[a] Alia Tadjer,*[a] and
Martin Baumgarten[b]

Keywords: Hybrid-spin molecular systems / Conformation analysis / Nitroxide radicals / Magnetic properties / Density functional calculations

Theoretical approaches to hybrid-spin systems aim at clarification of the nature of spin exchange between the metal ion and the organic radicals. This aids the molecular design of novel materials based on studies of the relevant molecular fragments. The current investigations were focused on two isomeric complexes of Cu^{II} with acetylacetonate and organic radicals (3- and 4-*N*-oxyl-tretbutylaminopyridine), whose geometry and magnetic properties were known from experimental data. A DFT approach based on the UB3LYP functional and basis sets of different size and quality were used in order to elaborate a computational protocol providing a reliable quantitative estimate of the spin–spin interaction. The computational scheme allows the elucidation of the role of various structural factors on the type and magnitude of the spin coupling, such as symmetry, spatial orientation of the radicals and type of the magnetic orbital of the metal ion. Proper symmetry assignment of the wavefunction proved to be critical for correct description of the magnetic behaviour of the complexes. The introduction of extended basis sets did not justify the computational cost, as the 6-31G* results were sufficiently accurate for the purpose of the study. Detailed analysis of the energies, the natural orbitals and the spin density distribution upon conformational changes was carried out.

Introduction

Complexes of spin-active transition metal ions with stable organic radicals are representatives of the relatively new class of hybrid-spin materials.[1,2] The latter are based on effective spin–spin interaction between the metal ion unpaired electron(s) and those of organic radical ligands, which is usually mediated by the π-conjugated system of the organic molecule. Such metal–organic complexes are deemed suitable for building blocks of molecular magnets, since they combine the ligand functionality of organic radicals with the potential for strong intermolecular exchange interaction of metal ions. The presence of several ligating sites in the organic moieties enables the formation of 3D spin networks by binding the separate complexes into crystals. The presence of the spin-bearing metal ions ensures that such magnetic materials retain their magnetic ordering at relatively high temperatures (> 10 K), unlike the purely organic molecular magnets.[1a,1c,3]

In line with this, a variety of hybrid-spin metal–organic complexes has been synthesized during the past two decades.[1a,1c,4] Copper, manganese and iron[4b–4d,4f,4g,5,6a,6b,7] have been used as the primary sources of inorganic spins, but other transition metal ions[2a,2d,4e,7c–7e,8] have been tested, too. Nitroxide-based,[2d,4c–4e,7–9] tetrathiafulvalene[4a,6] and tetracyanoquinodimethane[10] derivatives have most often been employed as organic radicals. However, other families of radicals[2a,2d,4b,4g,11] have been analyzed as well. Both the metal ions and their organic counterparts were varied in the search of an optimal pair characterized with maximum ferromagnetic or antiferromagnetic coupling between the separate radicals, which extends as far as possible from the elementary units of the crystals. It has been shown that, in order to achieve effective intermolecular spin exchange, the careful choice of crystallization conditions of the obtained complexes is essential.[12] This is due to the enhanced sensitivity of spin coupling to the structure of the material.

X-ray crystallography has served as the main tool for characterization of the structural parameters of such systems,[4b,4e–4g,6,7b–7e,10,13] while magnetic properties have been evaluated by measurements of the EPR spectra and magnetic susceptibility of the samples.[4b,4e–4g,6a,6b,7b–7e,10] A primary research goal has been to link the results from the two experiments, attempting to explain the mechanism of spin–spin interaction in the various crystals.

Theoretical modelling has always been an inseparable part of the studies of the magnetic behaviour of hybrid-spin systems, since it allows estimation of the exchange interaction within the entire complex or rationalization of its

---

[a] University of Sofia, Faculty of Chemistry,
1 James Bourchier Ave., 1164 Sofia, Bulgaria
E-mail: tadjer@chem.uni-sofia.bg
[b] Max Planck Institute for Polymer Research,
10 Ackermannweg, POB 3148, 55021 Mainz, Germany

Supporting information for this article is available on the WWW under http://dx.doi.org/10.1002/ejic.200900836.

various contributions by calculations on different model systems. Most of the computations of hybrid-spin complexes have employed the X-ray geometry of synthesized complexes to which DFT functionals with various basis sets have been applied.[4a,4d,7c,7d,14–17] Analysis of the experimental results and of the DFT calculations is often made in conjunction with model spin Hamiltonians when clarifying the magnetic properties of a specific system and comparing them to experimental data.[4c,4d,4g,7b,7d,7e,10,17,18] The most essential achievements of such analyses is the elucidation of the type of coupling between the separate spin-bearing units in the complexes and quantification of the contributions from the different fragments to the overall exchange.

In spite of the voluminous amount of tests on functionals and basis sets, there exists no unique computational scheme recommended for estimation of the magnetic properties of hybrid-spin systems. Moreover, the magnetic characteristics of specific complexes are rarely analyzed in a comprehensive or systematic way, that is, by elucidating the mechanism of spin–spin interaction on the basis of a set of computed descriptors; most often, only particular ones are discussed. In some of the studies[14c,14e,16e,19] the magnetic characteristics of the complexes are related to given geometric degrees of freedom, for instance dihedral angles or interatomic distances. However, such hypotheses are rarely substantiated by systematic variation of these parameters.

Cu^{II} complexes are often subject to molecular modelling,[17] because this metal ion possesses a single unpaired electron, which provides the simplest spin chain within an isolated complex. Iwamura and co-workers obtained two complexes from bis(hexafluoroacetylacetonato)copper(II) [Cu(hfac)$_2$] ligated with 3- and 4-(*N*-oxyl-*tert*-butylamino)-pyridines (3NOPy and 4NOPy): Cu(hfac)$_2$(3NOPy)$_2$ and Cu(hfac)$_2$(4NOPy)$_2$ with *trans*-conformations of the NOPy ligands with respect to the *hfac* plane.[20] The former features antiferromagnetic spin coupling, while in the latter the spins interact ferromagnetically. The X-ray geometry of these complexes has been studied theoretically previously by other authors[21] in an attempt to explain their magnetic behaviour. Relatively good agreement of the calculated exchange integrals (*J*) with the experimental estimates has been achieved for the ferromagnetic system, but the values for the antiferromagnetic one have been largely underestimated. The mechanism of spin–spin coupling has been discussed with respect to spin density distribution. However, the spin densities of the low-spin states have never been analyzed. Identical conclusions have been drawn from two different sets of canonical Kohn–Sham singly occupied MOs. Thus, the available theoretical information is fragmentary and somewhat ambiguous.

The goal of the present study is twofold. First, a thorough calculation of the magnetic properties of the X-ray structure of the two complexes synthesized and characterized by Iwamura and co-workers differing in topology and magnetic behaviour[20] is carried out and the spin–spin interactions within the complexes are rationalized on the basis of energy, spin density distribution and molecular orbital analysis. Second, the sensitivity of the exchange coupling within the complexes towards variation of two key dihedral angles is probed in a systematic way, which reveals additional information on the mechanism of spin exchange between the metal ion and the organic radicals.

Targets and Models

The targets of this study are two metal–organic complexes of bis(hexafluoroacetylacetonato)copper(II) [Cu(hfac)$_2$] ligated with 3- and 4-(*N*-oxyl-*tert*-butylamino)pyridines (3NOPy and 4NOPy): Cu(hfac)$_2$(3NOPy)$_2$ (META) and Cu(hfac)$_2$(4NOPy)$_2$ (PARA) in *trans*-conformations.[20] The two complexes differ in topology of the ligand-radicals: the nitroxide group (NO-) in 3NOPy is in *meta*-position with respect to the nitrogen atom of the pyridine ring (Py), whereas 4NOPy is the *para*-analogue. In order to reduce the computational cost, we use simplified models of the complexes in which the F atoms in the two equatorial *hfac* ligands are replaced by H atoms (Figure 1). The models are appropriate, because the fluorine atoms take no part in the magnetic interaction and have no noticeable influence on the structural features and the electron density distribution of the original system (Table S1). Our calculations (Table S1) for the H-substituted X-ray geometries at the SCF level compare well with the respective results for the original complexes.[21] On the other hand, the estimates of the properties of interest are based on the *difference* in total energy, which allows direct comparison between the computed results for the models and the experimental data for the real complexes.

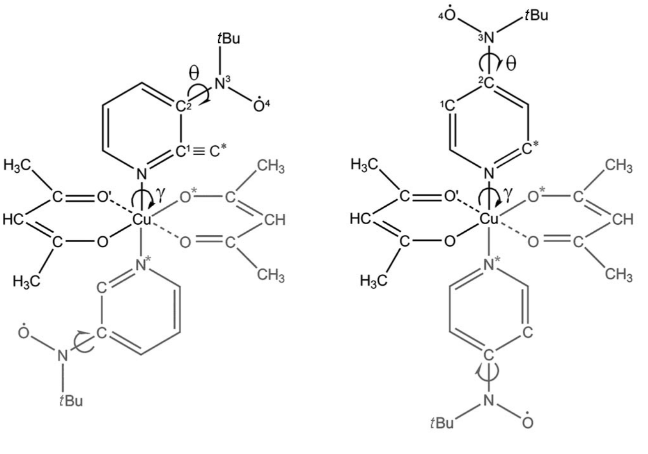

Figure 1. Schematic representation of the studied model systems: *meta*-Cu(acac)$_2$(3NOPy)$_2$ (left) and *para*-Cu(acac)$_2$(4NOPy)$_2$ (right) with labels denoting some structural parameters. Part of the hydrogen atoms is omitted for clarity.

Methods, Basis Sets, Procedures

The UB3LYP functional[22] was used throughout in the calculations; it was given preference because it describes reliably the properties of analogous systems.[21b,21c,14b,23] Quantum-mechanical simulations were carried out with three basis sets: (1) 6-31G*[24] for all atoms, (2) aug-cc-pVTZ-DK[25] for Cu (denoted DK-Cu further on) and (3) aug-cc-pVTZ-DK[25] for Cu, cc-pVTZ-DK[25] for C, N, O and double zeta (6-31G) basis for H atoms (denoted DK-Cu-N-O-C further on). The first one is considered as a basic standard for quantum chemistry and is the least demanding in terms of resources and CPU time but is expected to be unreliable for the account of the fine relativistic effects in the transition metals compounds. The second and third are more costly, but they provide a detailed physical picture and allow quantitatively correct estimates of the investigated properties. The last basis set was considered for equal-footed treatment of all non-hydrogen atoms. The comparison of the computational results with the experimental findings permits evaluation of the applicability of the small basis set for trustworthy description of molecular geometry and magnetic characteristics. The X-ray analysis of the studied complexes reveals that they belong to the $P\bar{1}$ (C_i for a single complex) symmetry point group[20] as intuitively expected from the chemical structure of the *trans*-conformers. The importance of this symmetry constraint is illustrated for the META case.

The molecular simulations comprise two objectives: (1) Checking the reproducibility of the energies and magnetic characteristics of the X-ray structures by means of SCF calculations and rationalization of the different magnetic properties of the two complexes. The three basis sets listed above were applied to the X-ray geometries of the complex in the two possible multiplicities: doublet (D) and quartet (Q). (2) Variation of the dihedral angles $\theta(^1C–^2C–^3N–^4O)$ and γ(C*–N–Cu–O*) (Figure 1) aiming at the establishment of a relationship between the structure of isomers and their magnetic characteristics. A quick scan with a step size of 45° was carried out first, and a more detailed study with step size 15° followed where appropriate.

All systems were tested for wavefunction stability and their natural orbitals (visualized at contour 0.02) and Mulliken spin density distribution were analyzed. Group spin density of the aromatic carbon atoms was obtained by summing their atomic spin density values. The energy of doublet-quartet splitting ($\Delta E_{DQ} = E_{D(BS)} - E_Q = 2J$) of the complexes was estimated and compared to the doubled experimental exchange integral.[20] In some cases, the broken symmetry (BS) solution was sought as well. All calculations were performed in vacuo with the program package Gaussian03.[26]

Results and Discussion

X-Ray Geometry

Importance of Symmetry

In compliance with experimental data, the structures under study are of C_i symmetry. For this reason, the influence of symmetry constraints on the wavefunction is taken into account. The UB3LYP/6-31G* results for the *meta*-structure are shown in Table 1.

Table 1. UB3LYP/6-31G* calculated total energy, multiplicity and doublet-quartet splitting (ΔE_{DQ}) of the X-ray structure of META with or without C_i symmetry constraint. Broken symmetry (BS) results are also presented.

META			$\Delta E_{DQ}^{exp} < -320$ K[20]
Symmetry constraint C_i			
Multiplicity	Energy /a.u.	Doublet spin configuration	ΔE_{DQ} /K
2	–3401.18234514	α-β-α	–94.8
2 BS	–3401.18234514		
4	–3401.18204526		
No symmetry constraint			
Multiplicity	Energy /a.u.	Spin configuration	ΔE_{DQ} /K
2	–3401.18149027	α-α-β	–47.3
2 BS	–3401.18149027		
4	–3401.18134035		

According to the presented data, the sign of the doublet-quartet splitting (ΔE_{DQ}) is independent of the symmetry of the wavefunction. In both cases the *meta*-isomer is characterized with an antiferromagnetic intramolecular exchange interaction.

The results show clearly the importance of symmetry constraints on the wavefunction for the interpretation of the exchange interaction. Symmetry could not influence the electronic properties of the quartet state to such an extent, as the latter allows solely α-α-α spin alignment. In the absence of any symmetry constraint, the configuration of the three spin-carrying centres R–M–R in the low-spin state is α-α-β. Such an alignment is a result of an antiferromagnetic exchange interaction of the metal centre and one of the radicals; the other radical either does not participate or is ferromagnetically coupled to the metal ion. In the case of the doublet type α-β-α, both organic spin carriers take part in the antiferromagnetic interaction. The energy of exchange coupling, expressed as energy of the doublet-quartet splitting, changes quantitatively depending on the type of doublet owing to a change in the type of spin interaction. Direct coupling between the radicals is negligible because of the large separation. Notable exchange occurs only through the pyridine rings, to which a certain amount of spin density is transferred from the spin carriers, invoking spin polarization. Regarding the systems under study, in the doublet α-α-β one of the organic radicals is not coupled to Cu^{II} (Figure S1), and the magnetic interaction involves only two spin-bearing units, while in the doublet α-β-α the coupling spans over the three radical centres, that is, the interaction is twice as strong. This is corroborated by the nature of SOMOs of the two doublets (Figure S2 and Figure 5 below).

The existence of a doublet of the type α-α-β cannot be explained from first principles, as the radicals within the complex are equivalent with respect to the centre of inversion in the absence of surrounding molecules. Moreover, as evidenced by the data in Table 1, this doublet is higher in energy than the symmetric α-β-α state, which proves that neglecting symmetry, when present, would lead to wrong conclusions about the exchange mechanism, especially in the stable doublet state.

In view of the above discussion, the characteristics of the complexes without symmetry constraints will not be considered further on. Therefore, only the α-β-α doublet is described in detail below.

Energy

The values of the doublet-quartet splitting do not differ from the experimental ones qualitatively; the sign of ΔE_{DQ} is preserved irrespective of the basis set used (Tables 2 and S2). The values of ΔE_{DQ} for the isolated complexes are of the order of 180 K for PARA and –100 K for META and seem reasonable when compared to the experimental ones for the crystal structures. Calculations with additional basis sets for all heavy atoms (Table 2, columns DK-Cu-C-O-N) do not justify the excess computational time, as the absolute value of ΔE_{DQ} remains constant or it changes slightly for identical doublet types. Consequently, it is possible to obtain qualitatively and semiquantitatively correct results for the type of the exchange interaction with the simpler (6-31G*) basis set. A definite trend for the influence of the basis set upon the magnitude of exchange coupling of META cannot be determined, as experimental data provide evidence for a strong intermolecular antiferromagnetic exchange, since the adjacent NO groups of neighbouring complexes are separated by less than 2 Å. For this reason, the experimental estimates do not correspond to pure intramolecular interaction. The value of the exchange integral for the *para*-analogues with the three basis sets (Table 2) is higher than the experimental one, which is probably due to the choice of a functional and the neglect of intermolecular interactions. Investigation of the latter is in progress.

Table 2. Doublet-quartet splitting (ΔE_{DQ}) of the X-ray structures. The values are obtained with B3LYP/6-31G*, or when an extra basis set is used for copper (DK-Cu) or for all heavy atoms (DK-Cu-N-O-C). BS denotes broken symmetry results.

META C_i Symmetry			$\Delta E_{DQ}{}^{exp} < -320$ K[20]
	6-31G*	DK-Cu	DK-Cu-N-O-C
ΔE_{DQ} /K	–94.8	–104.4	–104.1
ΔE_{BS-Q} /K	–94.8	–104.4	–52.1
PARA C_i Symmetry			$\Delta E_{DQ}{}^{exp} = 120.8$ K[20]
	6-31G*	DK-Cu	DK-Cu-N-O-C
ΔE_{DQ} /K	181.3	186.5	188.5
ΔE_{BS-Q} /K	89.8	92.3	93.5

In all cases the explicit doublet calculations yield wavefunctions of the type α-β-α. The broken symmetry estimates for the low-spin structures of META with the two smaller basis sets preserve the doublet type (α-β-α) both in terms of spin alignment and energy (Tables 2 and S2). The largest basis set yields an α-α-β BS doublet, but it is higher in energy than the regular doublet (Table S2). All broken symmetry calculations of the PARA isomer result in a change of the type of doublet to α-α-β. Furthermore, slightly lower energy corresponds to the obtained BS wavefunction (Table S2).

The results show that the magnitude of exchange interaction in the *meta* complex is smaller than that in the *para*-analogues. However, the qualitative picture should not be underestimated. It shows trends and gives an adequate description of the mechanism of exchange interaction.

Spin Density

The signs of the atomic spin densities in the *meta*-isomers do not change with any of the basis sets used, which is an indication that qualitatively the mechanism of spin exchange is insensitive to basis set extension and to inclusion of relativistic effects.

Irrespective of the basis set, the stable spin states are characterized with spin polarization, which is interrupted at the metal centre (Tables 3, 4 and Figure 2). A certain amount of spin density is delocalized from the metal ion to the closest atoms (N3 and O9) without change of sign. The presence of spin polarization in the framework of the radical is an indication of stable multiplicity but is not the only stabilizing factor.

Table 3. Mulliken atomic spin densities of META calculated with UB3LYP and different basis sets (atom numbering according to Figure 2).

Atoms	Doublet			Quartet		
	6-31G*	DK-Cu	DK-Cu-N-O-C	6-31G*	DK-Cu	DK-Cu-N-O-C
Cu	–0.753	–0.663	–0.664	0.755	0.666	0.671
O1	0.544	0.545	0.539	0.545	0.546	0.540
N2	0.397	0.395	0.394	0.398	0.396	0.395
N3	–0.065	–0.083	–0.078	0.033	0.051	0.052
C4	0.047	0.047	0.039	0.036	0.036	0.030
C5	–0.042	–0.042	–0.034	–0.033	–0.032	–0.025
C6	0.046	0.046	0.043	0.037	0.036	0.034
C7	–0.026	–0.027	–0.022	–0.016	–0.016	–0.012
C8	0.042	0.042	0.038	0.031	0.031	0.030
O9	–0.072	–0.096	–0.094	0.072	0.097	0.095
O10	0.002	0.001	0.001	–0.002	–0.001	–0.001

Table 4. Mulliken atomic spin densities of PARA calculated with UB3LYP and different basis sets (atom numbering corresponds to Figure 2).

Atoms	Doublet			Quartet		
	6-31G*	DK-Cu	DK-Cu-N-O-C	6-31G*	DK-Cu	DK-Cu-N-O-C
Cu	–0.756	–0.672	–0.673	0.756	0.663	0.669
O1	0.518	0.519	0.511	0.517	0.518	0.510
N2	0.337	0.335	0.328	0.336	0.334	0.327
N3	0.052	0.035	0.030	0.153	0.175	0.167
C4	–0.046	–0.046	–0.038	–0.055	–0.055	–0.045
C5	0.115	0.114	0.101	0.123	0.124	0.110
C6	–0.078	–0.076	–0.053	–0.085	–0.084	–0.060
C7	0.104	0.103	0.093	0.113	0.113	0.102
C8	–0.043	–0.043	–0.035	–0.053	–0.053	–0.042
O9	–0.070	–0.093	–0.090	0.071	0.093	0.090
O10	0.003	0.003	0.003	0.000	0.000	0.000

In the energetically unfavourable spin states (doublet PARA and quartet META) the qualitative picture also does not change upon basis set extension. In all cases, the spin

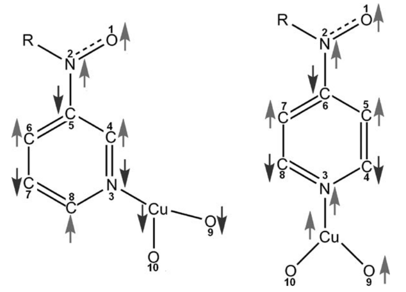

Figure 2. Spin density patterns of the energetically favourable META doublet (left) and PARA quartet (right).

polarization is overridden by a delocalization of the spin density from Cu^{2+} to the pyridine N atom, resulting in a change of the sign of its spin density compared to the free radical (Figure S1). Overall, spin delocalization prevails in the unfavourable structures and destabilizes them.

The values of the Mulliken atomic spin densities are a function of the basis set used. The addition of a DK basis set for the metal ion results in a significant change of its spin density and in the amount of spin density distributed among its nearest neighbours. The value of the spin density at the metal centre is about 0.1 lower than that obtained with the minimal basis set 6-31G*. The excess quantity is transferred to a similar extent to each pyridine N atom and proximate (acac) oxygen atom through spin delocalization. The spin densities of the rest of the pyridine ring and the nitroxide group remain relatively unaffected by variation of the basis set.

The increase in the number of atoms described by the DK basis set changes the spin shares in the radical, softening the spin density wave. However, the magnitude of spin polarization is not influenced greatly by the change of basis set.

The comparative analysis of the two isomeric structures shows that the spin localized on the NO group is close to unity in the *meta* complexes, whereas in the *para*-radicals it has a lower value (Tables 3 and 4). The difference between the degrees of spin density delocalization to the aromatic ring can be explained with the dissimilar spatial structure of the complex. The angle between the nitroxide fragment and the pyridine ring is about 39° in META, whereas in PARA the nitroxide group lies essentially in the plane of the pyridine ring (the angle is about 6°). The lower value of the dihedral angle brings about stronger spin delocalization from the nitroxide fragment to the pyridine ring within the framework of the radical in PARA.

Orbital Analysis

The magnetic behaviour of the two isomers is defined by the SOMOs of the isolated organic radicals and the possibility for overlap between these orbitals and that of the metal ion. A careful examination of the natural orbitals of the complexes shows that the metal ion contributes with its $d_{x^2-y^2}$ to the magnetic orbitals. It is directed along the Cu–N3 and Cu–O9 bonds (Figure 2). Such a type of magnetic orbital corresponds to other studies of the X-ray structure of the same complexes.[21b] The metal d orbital is the same for both META and PARA structures (Figures 3 and 4).

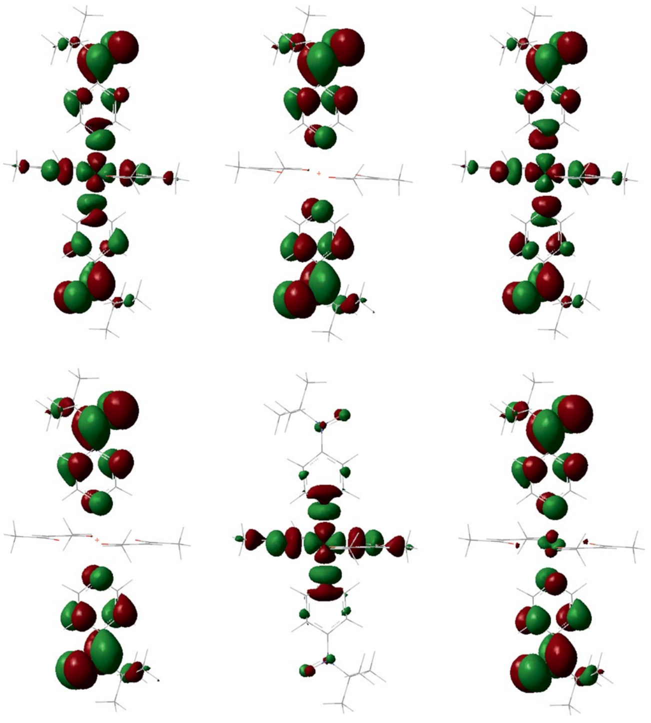

Figure 3. UB3LYP/6-31G* natural SOMOs of doublet (type α-β-α) (top) and quartet (bottom) PARA; these orbitals are qualitatively identical to the ones obtained with the larger basis sets (Figure S3).

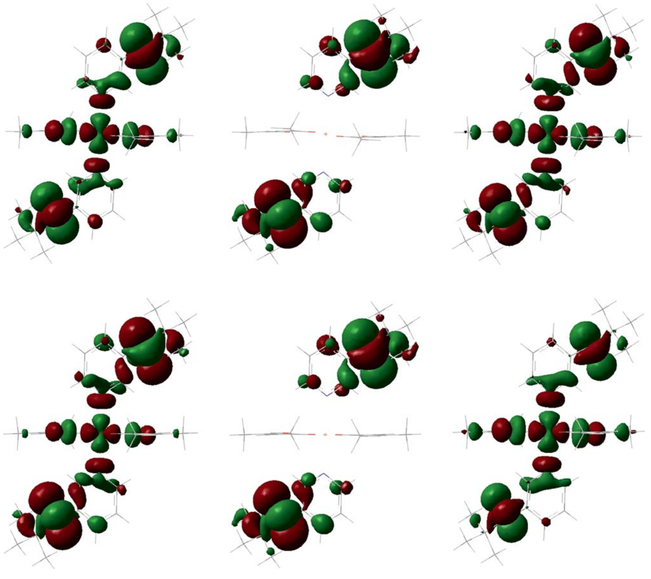

Figure 4. UB3LYP/6-31G* natural SOMOs of doublet (type α-β-α) (top) and quartet (bottom) META; these orbitals are qualitatively identical to the ones obtained with the larger basis sets (Figure S4).

The stable doublet form of the META complex possesses the three SOMOs shown in Figure 4 (top). Two of them illustrate the interaction between the radicals and the metal ion accomplished through the aromatic rings. The lone-pair electrons of the pyridine N atom are located on a sp^2 hybrid orbital directed along the axis of the Cu–N bond. The latter orbitals are responsible for the indirect exchange interaction between the copper ion and the NO fragments. The π-electron density in the two orbitals is strictly localized at the nitroxide fragments. The interaction between the aromatic ring and Cu^{2+} is carried out through the shortest possible route to the metal centre, mainly across the σ-skeleton. It is exactly the significant coefficient of the binding unit (N* in Figure 1) of the radical and its appropriate spatial orientation to $d_{x^2-y^2}$ that determine the antiferromagnetic coupling. The third half-filled molecular orbital is a linear combination of the atomic orbitals of the organic radicals. It represents the possible interaction between the spins of the radicals without the participation of the metal ion. The large distance between the unpaired electrons determines the small ferromagnetic contribution of this coupling to the total antiferromagnetic interaction. Orbital analysis of the ferromagnetic state of the *meta* complex indicates that the SOMOs do not change qualitatively compared to the doublet. However, the values of the coefficients in the corresponding linear combination of atomic orbitals (AOs) are different. The spatial form of the ligating orbital provides a favourable route for spin delocalization from the metal ion to the pyridine N* atom, which destabilizes the quartet form.

The ground state of the *para*-isomer is a quartet. The mechanism of exchange interaction can be extracted by inspection of the three SOMOs in Figure 3 (bottom). Two of these orbitals illustrate spin localization within the organic radicals; the third one represents spin localization on the metal ion and its nearest neighbours. The former MOs are of π-electronic nature and are characterized with the participation of the 2p-AO of the pyridine nitrogen atom in the linear combination. The π-electron density of PARA in the quartet spin state is distributed over the entire organic radical, and the exchange interaction is carried out through the π-conjugated system. The 2p-AO of the pyridine nitrogen atom is orthogonal to the magnetically active d-AO of the copper ion (the latter has a negligible contribution in the linear expansion). The NO fragments of the radicals participate with small coefficients in the third molecular orbital; it is localized around the coordination bonds. Two of the half-filled MOs are a linear combination of orbitals of the ligands (which participate equitably) and the metal ion in the doublet state of the complex. The nonhybrid atomic orbital of the pyridine nitrogen is at an angle to the metal orbital. This hinders antiferromagnetic exchange interaction and destabilizes the doublet state. The third singly occupied MO is composed solely of orbitals of the aminoxyl ligands.

The electron density distribution does not change significantly upon the introduction of a relativistic basis set for the proper description of the heavy atoms. By analogy with the distribution of the spin density, the electron density (Figures S3 and S4) is well delocalized in the pyridine rings (the coefficient of the metal orbital in the linear combination is smaller). The obtained singly occupied orbitals are linear combinations in which the weights of the distinct molecular fragments are equal; hence the similar magnitude of the exchange coupling with these basis sets.

Variation of the Dihedral Angle θ(C–C–N–O)

In order to test the sensitivity of spin–spin interaction to the geometry of the organic radical-ligand, models of the X-ray structure with variation of the dihedral $\theta(^1C–^2C–^3N–^4O)$ (Figure 1) by increments of 15° were considered, as the quick search at larger step size proved strong dependence between these characteristics. Single point calculations of the doublet and quartet state of each model were carried out with UB3LYP/6-31G*, as the above data showed qualitative and quantitative agreement of the results obtained with different basis sets. The trends in total energy, energy of doublet-quartet splitting, selected atomic spin densities and SOMOs as a function of the torsion were monitored.

Energy

Figure 5 represents the relative energy of META and PARA with respect to the most stable structure of the complexes at each multiplicity. For example, the lowest energy structure of doublet PARA (see Figure 6) is at $\theta = 0°$ and

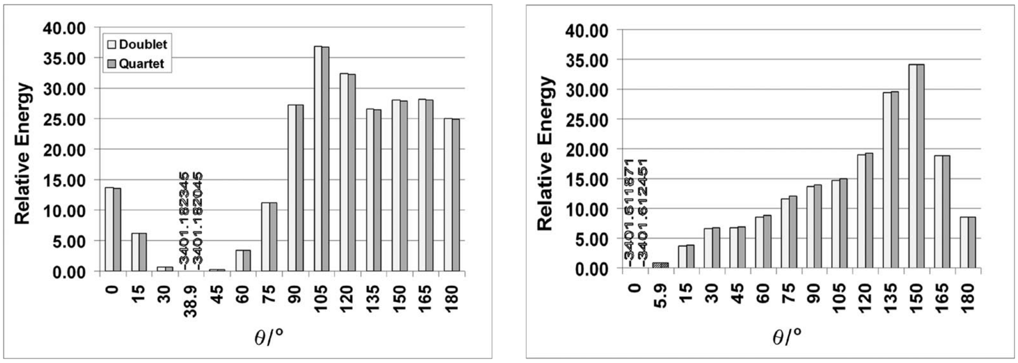

Figure 5. UB3LYP/6-31G* relative energy (kcal/mol) vs. torsion angle $\theta(^1C–^2C–^3N–^4O)$ (Figure 1) of the META (left) and the PARA (right) complex; the X-ray geometry of META has the lowest energy (shown as reference values in a.u.) within its series; patterned bars of PARA correspond to the X-ray geometry; the energies (in a.u.) of the lowest-energy PARA doublet and quartet are shown as reference values.

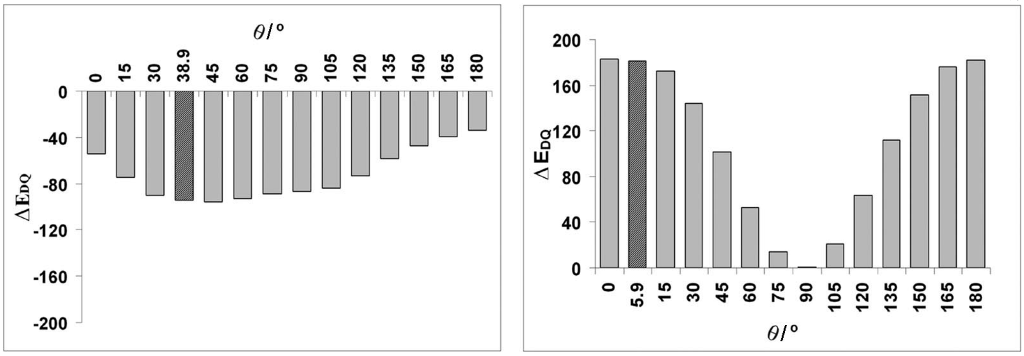

Figure 6. UB3LYP/6-31G* energy of doublet-quartet splitting, ΔE_{DQ} (K), vs. the torsion angle $\theta(^1C–^2C–^3N–^4O)$ (Figure 1) for the X-ray geometry of the *meta*- (left) and the *para* complex (right); patterned bars correspond to the experimental angle.

its energy is set as reference value for the other PARA doublets in this series. The same is done for the quartets. The lowest values for each isomer and multiplicity are presented in the respective plot. Figure 6 shows the dependence of the magnitude of doublet-quartet splitting on the torsion angle $\theta(^1C–^2C–^3N–^4O)$ (Figure 1) for the META and PARA isomers. The experimental value of the torsion angle of META is approximately 39° and that of PARA is approximately 6°.

According to the results for the relative energy (Figure 5), the most stable *meta*-conformer (with respect to variation of the dihedral angle) after the X-ray geometry is the one at 45°. In the series considered, this value of the torsion angle is closest to the experimental one, the latter assumed to be due to intermolecular interaction.[20]

Unlike the *para*-analogue (Figure 5), planarity is not of prime importance for the stabilization of the *meta* complexes. The relative energy of both the doublet and the quartet states varies synchronously with the angle.

The results for the relative energy of PARA (Figure 5) indicate that the 0°-conformer is the most favourable among all conformers (with respect to variation of the internal coordinate).

The energy of the complexes increases markedly up to 150° (Figure 5, Table S3). As the NO fragment approaches the plane of the pyridine ring at 180°, the conformers become energetically more favourable. Apparently, the two spin states exhibit a similar change in their stability as a function of the torsion angle. In general, the stable conformers are not too far in stability from the experimental ones (Figure 5, Table S3).

The performed calculations show that the magnitude of ΔE_{DQ} for META (Figure 6) varies with the angle $\theta(^1C–^2C–^3N–^4O)$ (Figure 1). Compared to the *para*-isomers (Figure 6), the dependence in this case is weaker (–33 to –96 K for META and 0.8 to 183 K for PARA). None of the *meta*-conformers possesses a zero value of doublet-quartet splitting. The largest absolute value of ΔE_{DQ}, which corresponds to the maximum strength of the exchange interaction, is obtained for the most stable conformer at 45°. The profile of the dependence is asymmetric, since the symmetry of the *meta*-radical is lower than that of its *para*-analogue. As the value of the dihedral angle beyond 45° approaches 180°, the energy difference between the two multiplets decreases, and so does the strength of the antiferromagnetic interaction. However, the variation of the angle does not lead to a change in the sign of ΔE_{DQ}.

The dependence of ΔE_{DQ} on the torsion angle $\theta(^1C–^2C–^3N–^4O)$ for the *para* complexes (Figure 6) provides evidence for the strong dependence of the magnitude of the exchange interaction on the torsion angle $\theta(^1C–^2C–^3N–^4O)$ (Figure 1). The value of ΔE_{DQ} reaches a minimum at 90° in the PARA complexes (Figure 6). The two spin states are practically degenerate at this value of θ. The energy gap between the two states diminishes with the deviation of the NO group from the plane of the aromatic ring. The profile of the dependence is symmetric with respect to 90° because of the innate symmetry of the complex. However, the change of the angle does not lead to an antiferromagnetic ground state, that is, the character of the exchange interaction is preserved.

Planar *para*-structures exhibit the strongest ferromagnetic interaction. The possibility for conjugation of the NO group with the aromatic ring favours the ferromagnetic exchange coupling. Owing to the effect of conjugation, these structures are among the most stable in terms of relative energy. The combination of these factors confirms the suitability of this complex as a building block of molecular ferromagnets.

Spin Density

Atomic spin densities (Figure 7 for META and Figure 8 for PARA) can be used to derive a relationship between the magnitude of exchange interaction and the value of the dihedral angle. However, in order to follow the modification of the spin density distribution due to complex formation, it is useful to discuss it relative to that of the isolated aminoxyl radicals cut out from the X-ray structures or optimized with UB3LYP/6-31G* (see the discussion in the Supporting Information, Figure S1).

It is worthwhile remarking that the atomic spin density at the Cu ion is identical for the respective multiplicity of the two complexes (0.756 ± 0.001 in all quartets and $–0.755 \pm 0.001$ in all doublets) at any value of θ (Figure S5). The spin density transfer from Cu^{2+} to each (acac) also depends only on the spin state, 0.075 ± 0.001 and $–0.074 \pm 0.001$ in the quartet and doublet, respectively, the

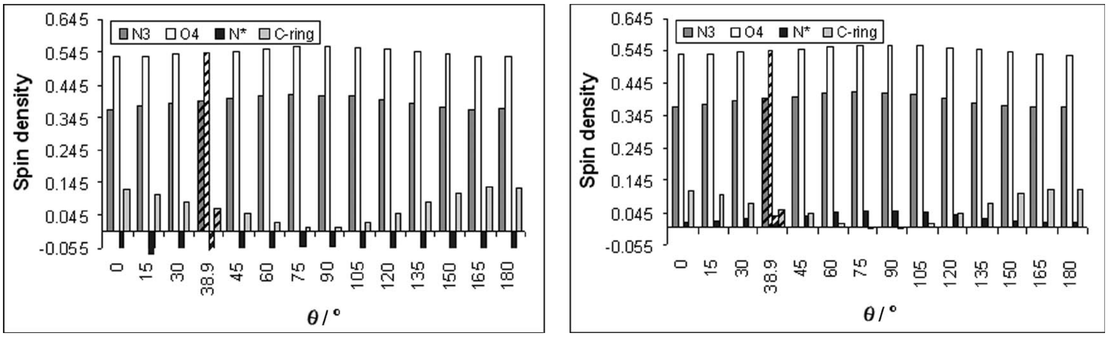

Figure 7. Dependence of the Mulliken atomic spin density distribution (NO fragments, pyridine N atoms) and group spin density of the aromatic carbon atoms in the META doublet (left) and quartet (right) on the dihedral angle θ; patterned bars correspond to the X-ray geometry (atom numbering according to Figure 1).

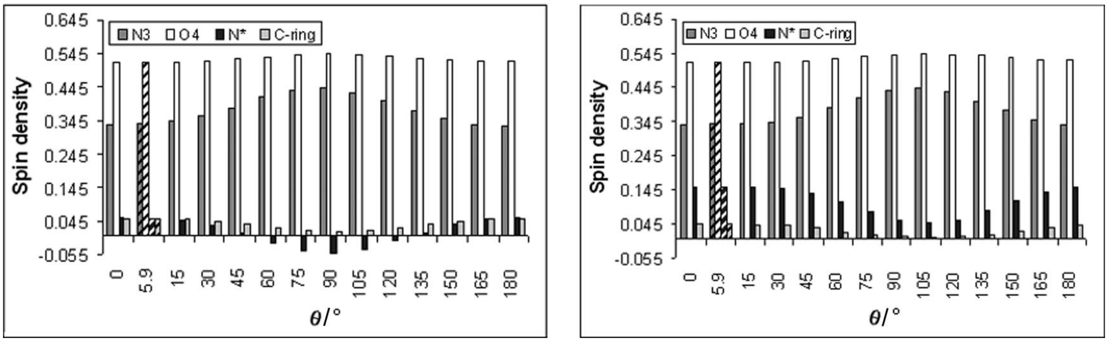

Figure 8. Dependence of the Mulliken atomic spin density distribution (NO fragments, pyridine N atoms) and group spin density of the aromatic carbon atoms in the PARA doublet (left) and quartet (right) on the dihedral angle θ; patterned bars correspond to the X-ray geometry (atom numbering according to Figure 1).

values being similar to previous findings.[21b] Obviously, the remaining fraction of the spin at Cu^{2+} is shared by the organic radicals, each of them receiving a portion of approximately ± 0.050, the sign depending on the multiplicity of the complex. This amount, summed with the atomic spin density at N* in the bare radical with X-ray geometry, yields exactly the corresponding value at N* in the respective complex at $\theta = 0°$. With the increase in θ, the spin delocalization from the NO group to the ring decreases and the group spin density of the former increases, which can be regarded as a natural effect of the increased spin localization in the absence of a proper route for spin transfer to the aromatic ring at these angles. In both spin states of the *meta* complex, this group density changes from 0.907 to 0.978 in the range 0–90°, whereas in the *para*-isomer the variation spans the values from 0.852 to 0.987, the largest quantity being at 90° in the doublet and at 105° in the quartet. In line with this increase, the spin polarization in the ring softens to the point of disappearing in the quartet of META and the doublet of PARA at 90° (in the region in which the spin density at N* even changes its sign!) or appreciably diminishes in the doublet of META and the quartet of PARA at the corresponding extrema of the NO density. Thus, at these points the spin density at N* consists practically solely of the share it received from Cu^{2+}.

The minima of the spin density at the pyridine nitrogen in META are shifted by 15° with respect to those of PARA, which results in asymmetric profiles of the total energy and ΔE_{DQ} of META. The sum of the atomic spin densities at the two nitrogen atoms (which have the same signs in the free radical) of each radical is constant in PARA, whereas in META their difference (opposite signs in the free radical) has a steady value. Since the spin densities at the Cu ion and the (acac) oxygen atoms are the same in the two complexes, this is an additional expression of the variation of spin polarization with θ. In the regions 0–45° and 120–180° of the doublet the spin polarization within the radical is preserved. In these parts of the conformational space the most pronounced delocalization of spin density from the NO group to the aromatic ring occurs at the boundary values of θ, which stabilizes the structures and enhances the spin polarization. As in the quartets, the polarization in the doublets of META becomes quite weak (and is even broken) in the range 60–105°, alongside with hindered delocalization. The spin density at the pyridine nitrogen atom has the same sign as that of the Cu ion in this range, which results in local ferromagnetic contribution to the spin–spin interaction.

The magnitude of exchange interaction in PARA correlates with the spin localized at the pyridine nitrogen: it is largest at the highest values of ΔE_{DQ}. The ferromagnetic coupling of the two NO-radicals is mediated by the pyridine nitrogen atoms and the metal ion, the latter being loaded with the same-sign spin density.

Thus, redistribution of the spin density occurs with the increase in θ: it grows at the NO groups and is depleted at the pyridine nitrogen. It is apparent from the constant sum of the spin density at the two nitrogen atoms within each radical-ligand in the entire range of θ values for both multiplicities of PARA (Figure 8) that the spin density values at the two nitrogen atoms are counter-correlated.

The high-spin state of the PARA conformers under study is characterized with the preservation of spin polarization in the framework of the organic radical. Only the spin density distribution therein is influenced by the degree of nonplanarity, as discussed above. The deviation from the ideally planar structure results in a significant change of the spin distribution in the organic radical for the doublet states of the conformers. Spin polarization within the radical is preserved in the conformations between 0–45° and 120–180°. The terminal conformers, 0° and 180°, are characterized with a marked spin transfer from the NO group to the aromatic ring. Deviation from planarity in the region 60–105° results in a reduced possibility for delocalization, and polarization in the radical is partially broken.

The difference in the degree of spin delocalization from NO and the pattern of spin polarization in the two isomers is most probably due to the nonidentical route of spin exchange in the stable multiplicities. Whereas in PARA the latter is effectuated exclusively through the π-system of the organic radicals, appreciable σ-contribution is present in META. This statement could be substantiated also by the orbital analysis (see below). All of the factors mentioned above effectively strengthen the ferromagnetic coupling in PARA and the antiferromagnetic one in META.

Orbital Analysis

It is important to emphasize that the metal orbital participating in all SOMOs is the same for all spin states and conformations (Figures 9 and 10). Its weight in the linear combination also remains invariant in one of the three SOMOs at each θ. It is identical to the orbital of the experimental structure: $d_{x^2-y^2}$ (Figures 3 and 4). This is a rightful result, as the performed conformational search does not change the direct surroundings of Cu^{2+}, nor the geometry of the ligand field.

One of the SOMOs of META is characteristic for both multiplicities of the complex. In planar structures and in those at angles 150° and 165° it comprises contributions only from the NO group and p-AOs of pyridine carbon atoms with positive spin density. With larger deviation from planarity, the share of the carbon atom farthest from NO vanishes, and the other two carbon atoms in the ring are coupled to the NO-linking carbon atom of the pyridine ring with hybrid sp^2-AOs. Cu^{2+} and its closest coordination shell do not participate. In planar geometries, the other two SOMOs look pretty much alike with contributions from NO, Cu^{2+}, the spin-bearing (acac) oxygen atoms and a bridge of σ-overlapping hybrid AOs at N* and its immediate pyridinic neighbours. In one of the two SOMOs, this bridge is extended to almost reach the NO group, thus providing a route for spin exchange through the σ-system of the pyridine rings. Upon deplanarization of the organic radical the SOMOs become more and more localized, but this σ-pathway is always preserved in the doublet META SOMOs, thus increasing the stability of the doublets and ensuring a channel for antiferromagnetic coupling. In the META quartets, no direct connection between the spin-bearing units exists, except in the structures at 30° and 135°, which destabilizes this state. Hence, the negative values of ΔE_{DQ} varying unimportantly with θ in the region 30°–105°. In the SOMO of quartets, which is a linear combination of the three spin-bearing units at 15°, 165° and 180°, and in the same orbital of the doublets at 165° and 180°, the carbon atoms contribute with pure p-AOs. This adds a partial ferromagnetic share to the spin–spin coupling, which leads to the smallest doublet-quartet splitting of these structures. Moreover, in these regions the spin polarization along the radicals is intact, which stabilizes additionally the high-spin state. The preserved spin polarization, combined with a still

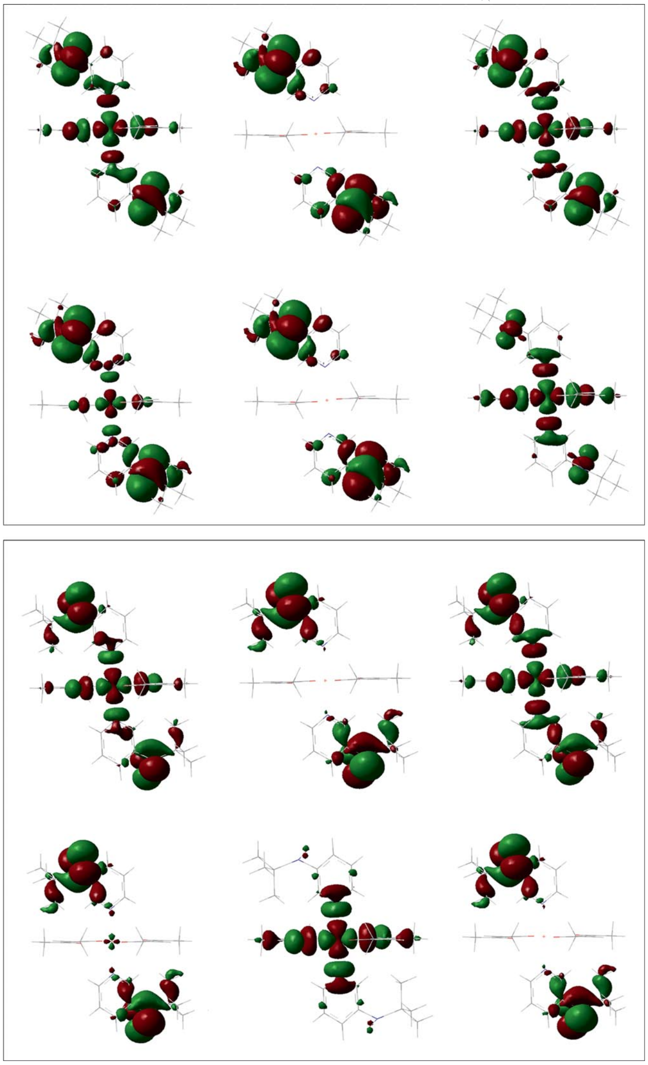

Figure 9. UB3LYP/6-31G* natural SOMOs of the META doublet (top) and quartet (bottom) at 45° (upper panel) and at 105° (lower panel); the orbitals at the remaining angles are shown in Figures S6 and S7.

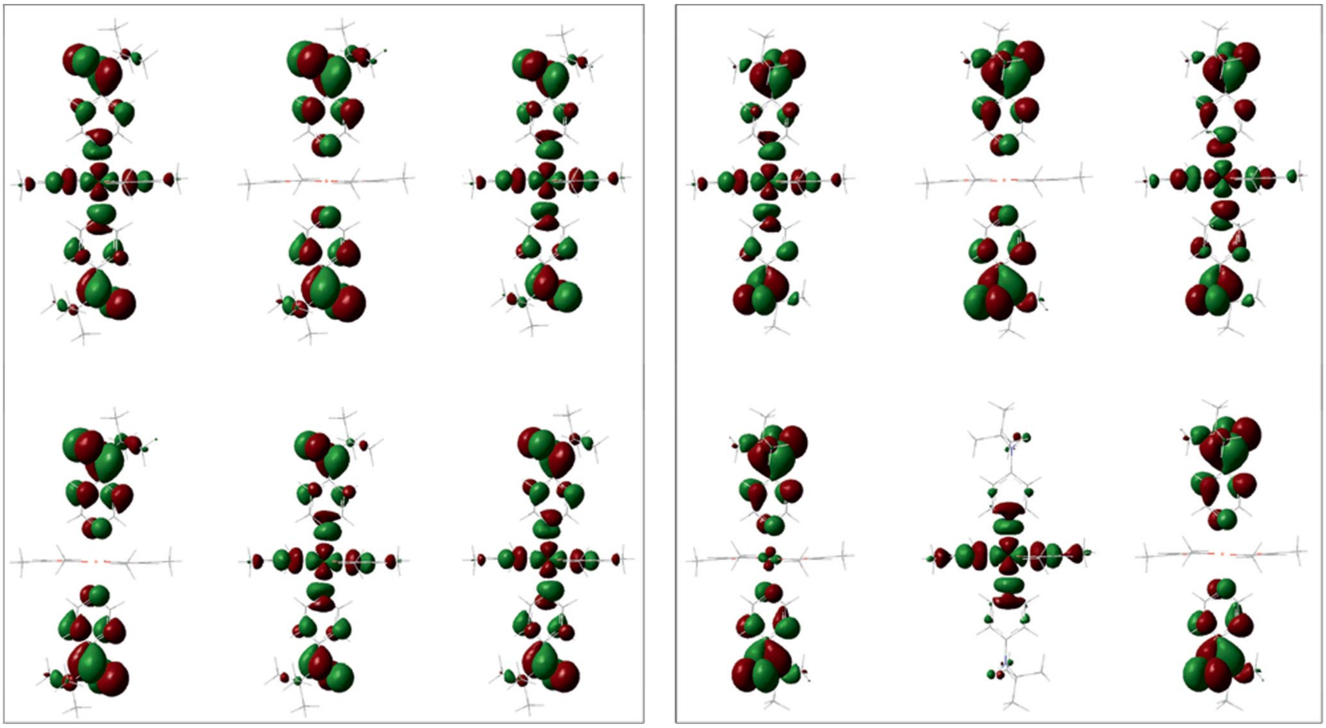

Figure 10. UB3LYP/6-31G* natural SOMOs of the META doublet (top) and quartet (bottom) at 45° (left panel) and at 105° (right panel); the orbitals at the remaining angles are shown in Figures S8 and S9.

existing σ-route for spin transfer, is probably the reason for the intermediate magnitude of ΔE_{DQ} (Figure 6) for the complexes at 15° and from 120° to 150°.

Two of the three SOMOs of the PARA doublets are equivalent, comprising identical contributions from Cu^{2+}, NO groups and the two spin-bearing O atoms of the (acac) ligands at any value of θ. The variation of that torsion angle affects the value of the coefficients and the type of AOs of the pyridine carbon atoms with positive spin density (those with negative spin density have zero coefficients) and the sp^2-AO of the ligating N*. The coefficients of all participants from the aromatic ring decrease monotonously from 0–90° and grow back in the range 90–180°. Along with that, the two contributing carbon atoms of each pyridine participate with p-AOs when θ has values close to the boundaries of the interval 0–180°; the orbitals are gradually replaced by sp^2 ones when θ approaches 90°.

The third SOMO is of different type and undergoes more pronounced changes upon variation of θ. It contains no contribution from the equatorial portion of the complex and is localized on particular centres of the organic radical. The major share belongs to the two NO groups at any θ value. The pyridine atoms loaded with positive spin density take part with a p-AO at the termini of the 0–180° range. Carbon p-AOs are replaced by hybrid ones, and the coefficients of N* p-AOs have small values or are zero in the range 60–120°. This change matches the interval in which the spin density at N* changes its sign and the spin polarization is interrupted. The latter type of SOMO is present at any value of θ in the quartet PARA structures too, and the linear combination changes in the same manner as in the doublets. The other two SOMOs of the quartets resemble those of the doublets only at specific torsions (0, 15, 75, 90, 105 and 180°), not perfectly identical even at these angles. In the intervals 30–60° and 120–165° these two SOMOs disproportionate, one of them gradually getting more localized on Cu^{2+} and its closest σ-oriented ligating atoms, the other one – on the NO groups with small participation of Cu^{2+} d-AO and the p-AO of N*. In the region 75–105° the SOMOs of the two spin states are almost indistinguishable, which explains the small values of ΔE_{DQ} (Figure 6) at these degrees of deplanarization. In all SOMOs featuring linear combinations between $Cu(acac)_2$ and the organic radicals, the N* sp^2-AO is orthogonal to $d_{x^2-y^2}$ of Cu^{II} and never delocalizes to the neighbouring centres. This guarantees the ferromagnetic character of spin exchange in the *para* complexes.

In summary, the most favourable structures of PARA from the energetic point of view are the planar ones. They are characterized with the strongest ferromagnetic interaction, as the effect of spin polarization outbalances most markedly that of spin delocalization. Any intermolecular interaction, leading to a deviation from planarity, diminishes the strength of the exchange interaction in the *para*-structures.

Variation of the Dihedral Angle γ(C-N-Cu-O)

The quick scan of the potential energy curve (Figure S10) and the changes in the spin density distribution (Figure S12) as a function of γ showed that there was no need for more detailed study of these correlations, because the changes were minor. Therefore, we restricted ourselves to the step size of 45°, illustrating the lesser importance of this torsion angle than that of the θ considered above. More detailed discussion can be found in the Supporting Information (Figures S10–S12).

In a nutshell, the variation of γ invokes effects which are an order of magnitude weaker than those resulting from the variation of θ and can be considered unimportant for the overall magnetic performance of the complexes under study.

Conclusions

The nature of spin–spin coupling in Cu^{II} complexes with two isomeric aminoxyl radicals was studied in detail. It was shown that the assignment of proper symmetry is essential for the reliability of the calculated spin states and parameters. The basis set extension proved to have weak influence on the results. The spin density distribution and the natural orbital analysis of the X-ray geometries should be studied in combination in order to rationalize the origin and magnitude of spin coupling.

Structural parameters of prime importance in the systems under study are deemed in the literature the torsion angles, rendering different alignments of the spin-loaded fragments in the complexes. The variation of the angle reflecting the coplanarity of the nitroxide group with the pyridine ring (θ) revealed extensive changes in all features considered (total energy, energy of doublet-quartet splitting, spin density distribution, content of SOMOs). The effect is more substantial for the *para*-isomer and less pronounced in the *meta*-analogue, as demonstrated by means of careful analysis of the interplay of spin polarization and spin delocalization (derived from spin density data and visualized by the modification of SOMOs upon variation of this torsion angle). On the other hand, the alteration of the axial dihedral γ resulted in immaterial modulations of the parameters of interest, demonstrating the minor importance of this structural element. All geometrical variations left the Cu^{2+} magnetically active orbital unchanged. Likewise, no switch of the ground state multiplicity occurred upon modification of the torsion angles.

We believe that the relationships between structure and magnetic properties found in this study will aid the rationalization of already synthesized Cu^{II}-based hybrid-spin systems and provide insight for the design of novel ones.

Supporting Information (see footnote on the first page of this article): UB3LYP/6-31G* computed properties of the X-ray structures of META and PARA with hydrogen and fluorine atoms (Table S1); UB3LYP total energy of the X-ray structures of META and PARA calculated with different basis sets (Table S2); UB3LYP/6-31G* total energy of META and PARA at various dihedral angles θ (Table S3); Mulliken spin densities of doublet META with and without symmetry constraints and of the isolated radicals (Figure S1); natural SOMOs of the X-ray structure of META doublet without symmetry constraints (Figure S2); SOMOs of quartet PARA (Figure S3) and doublet META (Figure S4) obtained with the two relativistic basis sets; dependence of the atomic spin densities of Cu and O9 of META and PARA on the value of θ (Figure S5); SOMOs of doublet (Figure S6) and quartet (Figure S7) META and doublet (Figure S8) and quartet (Figure S9) PARA as a function of θ; relative energy (Figure S10), doublet-quartet splitting (Figure S11), atomic spin densities (Figure S12) and SOMOs (Figures S13 and S14) of META and PARA upon variation of the dihedral angle γ.

Acknowledgments

Deutscher Akademischer Austausch Dienst (DAAD) is acknowledged for a research grant (J. R.). The research is supported by Project SU-32/2008 of the Science Fund of the University of Sofia and Grants DO-02–82/2008 and DO-02–136/2008 of the National Science Fund of Bulgaria. An equipment grant from the Alexander von Humboldt Foundation is highly appreciated.

---

[1] a) J. Veciana (Ed.), *π-Electron Magnetism: From Molecules to Magnetic Materials*, Springer, Berlin, Heidelberg, **2001**; b) P. Day, A. E. Underhill (Eds.), *Metal–Organic and Organic Molecular Magnets*, The Royal Society of Chemistry, Cambridge, **1999**; c) O. Kahn, *Molecular Magnetism*, Wiley-VCH, New York, **1993**; d) D. Gatteschi, O. Kahn, J. S. Miller, F. Palacio (Eds.), *Magnetic Molecular Materials*, Kluwer Academic Publishers, Dordrecht, **1991**.

[2] a) J. S. Miller, *Engineering of Crystalline Materials Properties* (Eds.: J. J. Novoa, D. Braga, L. Addadi), Springer, Dordrecht, **2008**; b) K. E. Vostrikova, *Coord. Chem. Rev.* **2008**, *252*, 1409–1419; c) S. J. Blundell, *Contemp. Phys.* **2007**, *48*, 275–290; d) N. Koga, S. Karasawa, *Bull. Chem. Soc. Jpn.* **2005**, *78*, 1384–1400; e) A. Caneschi, D. Gatteschi, N. Lalioti, C. Sangregorio, R. Sessoli, *J. Chem. Soc., Dalton Trans.* **2000**, 3907–3912; f) J. Veciana, H. Iwamura, *MRS Bull.* **2000**, *25*, 41–51; g) B. Pilawa, *Annalen Phys.* **1999**, *8*, 191–254; h) A. P. Alivisatos, P. F. Barbara, A. W. Castleman, J. Chang, D. A. Dixon, M. L. Klein, G. L. McLendon, J. S. Miller, M. A. Ratner, P. J. Rossky, S. I. Stupp, M. E. Thompson, *Adv. Mater.* **1998**, *10*, 1297–1336.

[3] a) J. S. Miller, M. Drillon, *Magnetism: Molecules to Materials*, Wiley, Weinheim, **2001**; b) K. Itoh, M. Kinoshita, *Molecular Magnetism – New Magnetic Materials*, Gordon and Breach, New York, **2000**.

[4] a) G. Prabusankar, Y. Molard, S. Cordier, S. Golhen, Y. Le Gal, C. Perrin, L. Ouahab, S. Kahlal, J. F. Halet, *Eur. J. Inorg. Chem.* **2009**, 2153–2161; b) N. Roques, D. Maspoch, F. Luis, A. Camon, K. Wurst, A. Datcu, C. Rovira, D. Ruiz-Molina, J. Veciana, *J. Mater. Chem.* **2008**, *18*, 98–108; c) P. M. Lahti, M. Baskett, L. M. Field, M. C. Moron, F. Palacio, A. Paduan, N. F. Oliveira, *Inorg. Chim. Acta* **2008**, *361*, 3697–3709; d) N. Mihara, Y. Teki, *Polyhedron* **2007**, *26*, 2142–2146; e) Y. Numata, K. Inoue, *J. Magn. Magn. Mater.* **2007**, *310*, 1847–1848; f) J. Y. Zhang, C. M. Liu, D. Q. Zhang, S. Gao, D. B. Zhu, *Inorg. Chim. Acta* **2007**, *360*, 3553–3559; g) D. Maspoch, D. Ruiz-Molina, K. Wurst, J. Vidal-Gancedo, C. Rovira, J. Veciana, *Dalton Trans.* **2004**, 1073–1082.

[5] a) G. Cosquer, F. Pointillart, Y. Le Gal, S. Golhen, O. Cador, L. Ouahab, *Dalton Trans.* **2009**, 3495–3502.

[6] a) E. Coronado, S. Curreli, C. Gimenez-Saiz, C. J. Gomez-Garcia, A. Alberola, *Inorg. Chem.* **2006**, *45*, 10815–10824; b) W. Lu, Y. Zhang, J. Dai, Q. Y. Zhu, G. Q. Bian, D. Q. Zhang, *Eur. J. Inorg. Chem.* **2006**, 1629–1634; c) E. Ribera, C. Rovira, J. Veciana, J. Tarres, E. Canadell, R. Rousseau, E. Molins, M. Mas, J. P. Schoeffel, J. P. Pouget, J. Morgado, R. T. Henriques, M. Almeida, *Chem. Eur. J.* **1999**, *5*, 2025–2039.

[7] a) D. Luneau, P. Rey, *Coord. Chem. Rev.* **2005**, *249*, 2591–2611; b) C. Aoki, T. Ishida, T. Nogami, *Inorg. Chem.* **2003**, *42*, 7616–7625; c) L. M. Field, P. M. Lahti, *Inorg. Chem.* **2003**, *42*, 7447–7454; d) H. Oshio, M. Yamamoto, T. Ito, H. Kawauchi, N. Koga, T. Ikoma, S. Tero-Kubota, *Inorg. Chem.* **2001**, *40*, 5518–

5525; e) C. Stroh, P. Turek, P. Rabu, R. Ziessel, *Inorg. Chem.* **2001**, *40*, 5334–5342.

[8] M. Mikuriya, D. Yoshioka, M. Handa, *Coord. Chem. Rev.* **2006**, *250*, 2194–2211.

[9] T. Sugano, S. J. Blundell, F. L. Pratt, T. Jestadt, B. W. Lovett, W. Hayes, P. Day, *Mol. Cryst. Liq. Cryst.* **1999**, *334*, 477–486.

[10] M. T. Johnson, A. M. Arif, J. S. Miller, *Eur. J. Inorg. Chem.* **2000**, 1781–1787.

[11] a) B. D. Koivisto, R. G. Hicks, *Coord. Chem. Rev.* **2005**, *249*, 2612–2630; b) N. Koga, H. Iwamura, *Mol. Cryst. Liq. Cryst.* **1997**, *305*, 415–424.

[12] a) C. Rajadurai, V. Enkelmann, V. Ikorskii, V. I. Ovcharenko, M. Baumgarten, *Inorg. Chem.* **2006**, *45*, 9664–9669; b) H. Iwamura, *Proc. Jpn. Acad. B* **2005**, *81*, 233–243; c) G. Zoppellaro, A. Ivanova, V. Enkelmann, A. Geies, M. Baumgarten, *Polyhedron* **2003**, *22*, 2099–2110.

[13] a) V. I. Ovcharenko, E. V. Gorelik, S. V. Fokin, G. V. Romanenko, V. N. Ikorskii, A. V. Krashilina, V. K. Cherkasov, G. A. Abakumov, *J. Am. Chem. Soc.* **2007**, *129*, 10512–10521.

[14] a) S. Zalis, B. Sarkar, C. Duboc, W. Kaim, *Monatsh. Chem.* **2009**, *140*, 765–773; b) Y. Miura, I. Kato, Y. Teki, *Dalton Trans.* **2006**, 961–966; c) Z. P. Ni, X. M. Ren, J. Ma, J. L. Xie, C. L. Ni, Z. D. Chen, Q. J. Meng, *J. Am. Chem. Soc.* **2005**, *127*, 14330–14338; d) W. D. Zou, Z. L. Liu, K. L. Yao, *J. Magn. Magn. Mater.* **2004**, *277*, 379–384; e) Y. Takano, Y. Kitagawa, T. Onishi, Y. Yoshioka, K. Yamaguchi, N. Koga, H. Iwamura, *J. Am. Chem. Soc.* **2001**, *123*, 450–461.

[15] a) I. Ciofini, C. A. Daul, *Coord. Chem. Rev.* **2003**, *238*, 187–209; b) K. Yamaguchi, T. Kawakami, T. Taniguchi, S. Nakano, Y. Kitagawa, H. Nagao, T. Ohsaku, R. Takeda, *Polyhedron* **2003**, *22*, 2077–2090; c) M. Deumal, J. J. Novoa, *THEOCHEM* **2000**, *506*, 287–296.

[16] a) W. D. Zou, Z. L. Liu, K. L. Yao, *J. Theor. Comput. Chem.* **2003**, *2*, 345–349; b) A. Bencini, F. Totti, C. A. Daul, K. Doclo, P. Fantucci, V. Barone, *Inorg. Chem.* **1997**, *36*, 5022–5030; c) T. Ren, *Inorg. Chim. Acta* **1995**, *229*, 195–202; d) S. Bruni, A. Caneschi, F. Cariati, C. Delfs, A. Dei, D. Gatteschi, *J. Am. Chem. Soc.* **1994**, *116*, 1388–1394; e) E. Ressouche, J. X. Boucherle, B. Gillon, P. Rey, J. Schweizer, *J. Am. Chem. Soc.* **1993**, *115*, 3610–3617.

[17] E. V. Gorelik, V. I. Ovcharenko, M. Baumgarten, *Eur. J. Inorg. Chem.* **2008**, *18*, 2837–2846.

[18] a) H. Tamekuni, Y. Teki, *Polyhedron* **2007**, *26*, 1984–1988; b) K. Herve, O. Cador, S. Golhen, K. Costuas, J. F. Halet, T. Shirahata, T. Muto, T. Imakubo, A. Miyazaki, L. Ouahab, *Chem. Mater.* **2006**, *18*, 790–797; c) C. J. Lee, H. H. Wei, G. H. Lee, Y. Wang, *Inorg. Chem. Commun.* **2000**, *3*, 690–693.

[19] F. Setifi, L. Ouahab, S. Golhen, A. Miyazaki, T. Enoki, J. Yamada, *C. R. Acad. Sci., Ser. IIc: Chim.* **2003**, *6*, 309–316.

[20] a) Y. Ishimaru, M. Kitano, H. Kumada, N. Koga, H. Iwamura, *Inorg. Chem.* **1998**, *37*, 2273–2280; b) H. Iwamura, N. Koga, *Pure Appl. Chem.* **1999**, *71*, 231–238; c) S. Karasawa, Y. Sano, T. Akita, N. Koga, T. Itoh, H. Iwamura, P. Rabu, M. Drillon, *J. Am. Chem. Soc.* **1998**, *120*, 10080–10087.

[21] a) Z. An, J. Zhang, R. Wang, N. Koga, *Polyhedron* **2007**, *26*, 2126–2128; b) E. A. A. Noh, J. Zhang, *Chem. Phys.* **2006**, *330*, 82–89; c) J. Zhang, L. Wang, R. Wang, N. Koga, *Synth. Met.* **2003**, *137*, 1355–1356.

[22] a) A. D. Becke, *Phys. Rev. A* **1988**, *38*, 3098; b) A. D. Becke, *J. Chem. Phys.* **1993**, *98*, 5648; c) C. Lee, W. Yang, R. G. Parr, *Phys. Rev. B* **1988**, *37*, 785; d) B. Miehlich, A. Savin, H. Stoll, H. Preuss, *Chem. Phys. Lett.* **1989**, *157*, 200.

[23] P. A. Papanikolaou, P. C. Christidis, A. T. Chaviara, C. A. Bolos, A. C. Tsipis, *Eur. J. Inorg. Chem.* **2006**, *10*, 2083–2095.

[24] R. Ditchfield, W. J. Hehre, J. A. Pople, *J. Chem. Phys.* **1971**, *54*, 724.

[25] a) T. H. Dunning Jr., *J. Chem. Phys.* **1989**, *90*, 1007–1023; b) N. B. Balabanov, K. A. Peterson, *J. Chem. Phys.* **2005**, *123*, 064107.

[26] M. J. Frisch, G. W. Trucks, H. B. Schlegel, G. E. Scuseria, M. A. Robb, J. R. Cheeseman, J. A. Montgomery Jr., T. Vreven, K. N. Kudin, J. C. Burant, J. M. Millam, S. S. Iyengar, J. Tomasi, V. Barone, B. Mennucci, M. Cossi, G. Scalmani, N. Rega, G. A. Petersson, H. Nakatsuji, M. Hada, M. Ehara, K. Toyota, R. Fukuda, J. Hasegawa, M. Ishida, T. Nakajima, Y. Honda, O. Kitao, H. Nakai, M. Klene, X. Li, J. E. Knox, H. P. Hratchian, J. B. Cross, C. Adamo, J. Jaramillo, R. Gomperts, R. E. Stratmann, O. Yazyev, A. J. Austin, R. Cammi, C. Pomelli, J. W. Ochterski, P. Y. Ayala, K. Morokuma, G. A. Voth, P. Salvador, J. J. Dannenberg, V. G. Zakrzewski, S. Dapprich, A. D. Daniels, M. C. Strain, O. Farkas, D. K. Malick, A. D. Rabuck, K. Raghavachari, J. B. Foresman, J. V. Ortiz, Q. Cui, A. G. Baboul, S. Clifford, J. Cioslowski, B. B. Stefanov, G. Liu, A. Liashenko, P. Piskorz, I. Komaromi, R. L. Martin, D. J. Fox, T. Keith, M. A. Al-Laham, C. Y. Peng, A. Nanayakkara, M. Challacombe, P. M. W. Gill, B. Johnson, W. Chen, M. W. Wong, C. Gonzalez, J. A. Pople, *Gaussian 03*, Gaussian, Inc., Wallingford CT, **2004**.

Received: August 24, 2009

DOI: 10.1002/ejic.200901011

Diastereoselective Protonation, Substitution and Addition Reactions at Pseudotetrahedral Rhenium Complexes

Frank Bock,[a] Frank Fischer,[a] Krzysztof Radacki,[a] and Wolfdieter A. Schenk*[a]

Dedicated to Professor Dr. R. Tacke on the occasion of his 60th birthday

Keywords: Rhenium / Chiral resolution / N,P ligands / S ligands

The chiral N,P ligand P(Me)(Ph)[8-(2-methylquinolinyl)] (**3**) was synthesized and separated into its enantiomers via diastereomeric palladium complexes. The reactions of **3** and (R_P)-**3** with [CpRe(CO)(NO)(NCMe)]BF_4 (**7**) gave the diastereomeric complexes [CpRe(CO)(NO){P(Me)(Ph)($C_{10}H_8N$)}]BF_4 [**8** and ($R_{Re},S_P/S_{Re},S_P$)-**8**], which, upon borohydride reduction, yielded the corresponding methyl complexes [CpRe(NO){P(Me)(Ph)($C_{10}H_8N$)}(CH_3)] [**9** and ($R_{Re},S_P/S_{Re},S_P$)-**9**]. Treatment of **9** with HBF_4 under carefully controlled conditions gave the diastereomerically pure chelates [CpRe(NO){P(Me)(Ph)($C_{10}H_8N$)}]BF_4 [($R_{Re},S_P/S_{Re},R_P$)-**10**, ($R_{Re},R_P/S_{Re},S_P$)-**10** and (R_{Re},S_P)-**10**]. The chelate ring was opened with NaSH to produce the hydrosulfido complexes [CpRe(NO){P(Me)(Ph)($C_{10}H_8N$)}(SH)] [($R_{Re},S_P/S_{Re},R_P$)-**11**, ($R_{Re},R_P/S_{Re},S_P$)-**11** and (R_{Re},S_P)-**11**]. Each step in this sequence proceeded with retention of configuration at rhenium. Complex **11** underwent acid-promoted condensation with aldehydes to give thioaldehyde complexes [CpRe(NO){P(Me)(Ph)($C_{10}H_8N$)}(S=CHR)]BF_4 (**12a**–**d**, R = Ph, Me, 4-C_6H_4OMe, C_6F_5). The addition of nucleophiles X^- to **12a** gave rhenium-coordinated α-chiral thiolate complexes [CpRe(NO){P(Me)(Ph)($C_{10}H_8N$)}{SC(H)(Ph)(X)}] (**13a**–**e**, X = acac, $PhCH_2S$, EtS, *t*BuS, CN) with 42–89 % *de*. The thiolate can readily be cleaved from the rhenium complex by a methylation/chelate ring-closure strategy. The stereochemistry of the entire reaction sequence was corroborated for each step by X-ray crystallography.

Introduction

The activation of prochiral unsaturated substrates by chiral, enantiomerically pure transition metal Lewis acids is a promising and often highly efficient strategy for enantioselective synthesis.[1] The chirality may be based either on the coordination geometry around the metal atom itself ("metal-based chirality") – prominent examples are the pseudotetrahedral half-sandwich complexes [CpMn(CO)(NO)(PPh_3)],[2] [CpFe(CO)(PPh_3)($COCH_3$)],[3] and [CpRe(NO)(PPh_3)(CH_3)][4] – or may be added through the use of chiral ligands ("ligand-based chirality") as exemplified by the pioneering work of Knowles,[5] Noyori,[6] and Sharpless[7] on enantioselective catalysis. The two concepts have been combined in order to study the often facile epimerization at the metal center[8–10] and hopefully overcome the problems associated with it with regard to asymmetric synthesis and catalysis.[10]

Recently, we have found a kinetically controlled, highly efficient chirality transfer between an amine-functionalized phosphane ligand and the metal center (Scheme 1).[11]

The high diastereoselectivity is rooted in the intramolecular proton transfer from the dimethylamino sidearm of the chiral phosphane ligand to rhenium, which is much faster for the *unlike* diastereomer. Thus, starting from the mixture ($R_{Re},S_P/S_{Re},S_P$)-**1** the two enantiomerically pure diastereomers (R_{Re},S_P)-**2** and (S_{Re},S_P)-**2** were obtained in 99% *ee* and 93% *de*.[11] A considerable drawback of compounds **2** is their inertness in ligand-substitution reactions. The five-membered chelate ring could be opened only with NaCN under quite forcing conditions.[12] We now report on a similar system which is reactive enough to be further elaborated.

Results

Phosphane Synthesis and Enantiomer Separation

The synthesis of the new chiral phosphane **3** by nucleophilic substitution (Scheme 2) follows well-established methods.[13,14]

Phosphane **3** is a yellow, slightly air-sensitive crystalline solid with the expected NMR spectroscopic data, e.g. a doublet at δ = 1.76 ppm for the PCH_3 group, a singlet at δ = 2.70 for the $ArylCH_3$ group, and a ^{31}P signal at δ = –33.8 ppm.

---

[a] Institut für Anorganische Chemie, Universität Würzburg, 97074 Würzburg, Germany
E-mail: wolfdieter.schenk@uni-wuerzburg.de

Supporting information for this article is available on the WWW under http://dx.doi.org/10.1002/ejic.200901011.

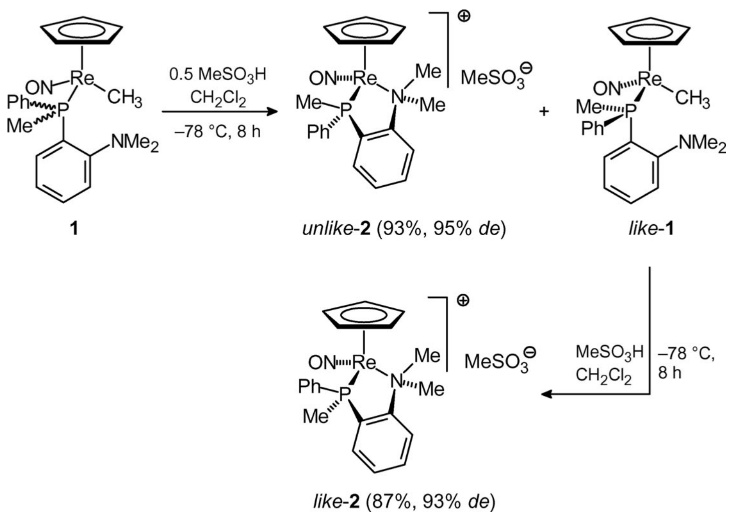

Scheme 1.

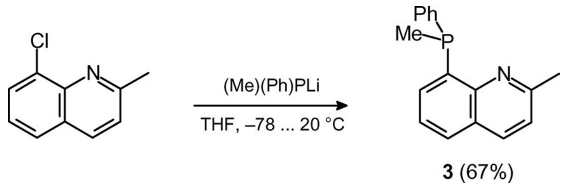

Scheme 2.

We have made several attempts to devise an enantioselective synthesis for **3**. Thus (S_P)-(Ph)(Me)(H_3B)PH[15] was deprotonated at –78 °C with butyllithium and added to 2-methyl-8-chloroquinoline, but failed to react at this temperature. Higher temperatures would have led to racemization of the borane-protected lithium phosphide reagent.[15] The reverse strategy, Br/Li exchange on 2-methyl-8-bromoquinoline[16] followed by reaction with various chlorophosphanes such as (Ph)(Me)PCl, $PhPCl_2$, or $(Et_2N)_2PCl$ never gave any tractable results.

(R_P)-**3** was finally obtained with 99% *ee* via diastereomeric palladium complexes as reported by Wild et al. for the similar 8-(methylphenylphosphanyl)quinoline.[14] Reaction of the dimeric Pd complex (S_C)-**4** with phosphane **3** followed by addition of NH_4PF_6 gave complex **5** as a mixture of diastereomers in high yield (Scheme 3).

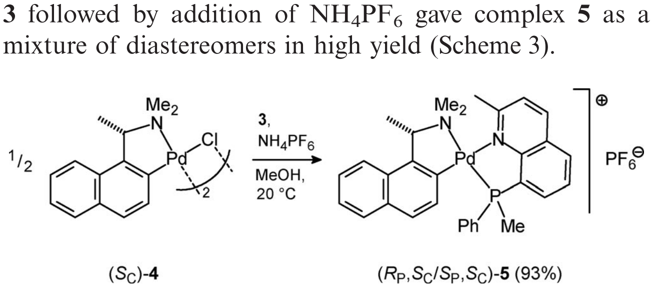

Scheme 3.

Slow crystallization of (R_P,S_C/S_P,S_C)-**5** from boiling 2-butanone gave a 54% crop of (S_P,S_C)-**5** which after recrystallization was obtained with 99% *de*. The structure of (S_P,S_C)-**5** was determined crystallographically in order to assign the configuration at phosphorus. The salt crystallized from acetone in the triclinic space group *P*1 with two independent formula units and one molecule of acetone in the unit cell. A view of one of the cations is shown in Figure 1.

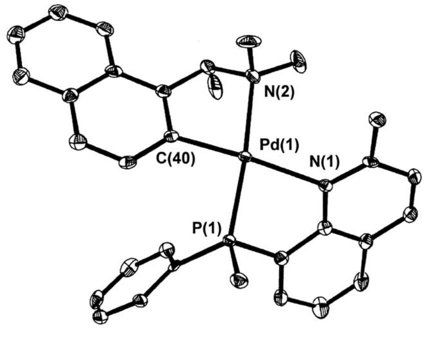

Figure 1. Structure of the cation of (S_P,S_C)-**5**, hydrogen atoms were omitted for clarity. Thermal ellipsoids drawn at 50% level. Space group *P*1; selected distances [pm] and angles [°] (standard deviations in parentheses): Pd(1)–P(1) 221.74(6), Pd(1)–N(1) 223.7(2), Pd(1)–N(2) 216.8(2), Pd(1)–C(40) 199.9(3), P(1)–Pd(1)–N(1) 80.23(5), P(1)–Pd(1)–N(2) 169.58(6), P(1)–Pd(1)–C(40) 95.33(7), N(1)–Pd(1)–N(2) 103.69(8), N(1)–Pd(1)–C(40) 174.09(9), N(2)–Pd(1)–C(40) 80.04(9).

As expected, the structure is very similar to that of the (S_P,R_C) diastereomer of the analogous complex of 8-(methylphenylphosphanyl)quinoline.[14] The two cations in the unit cell differ somewhat with regard to the geometry around the Pd atom. While the one shown in Figure 1 is almost perfectly planar, the other one is folded with a trans angle P–Pd–N of 156.2°. Inspection of the unit cell diagram shows that this is caused by packing forces within the crystal.

(R_P)-**3** was cleaved from (S_P,S_C)-**5** by treatment with ethylenediamine, and the ethylenediamine palladium complex (S_C)-**6** converted back to (*S*)-**4** by reaction with 2 M aqueous HCl (Scheme 4).

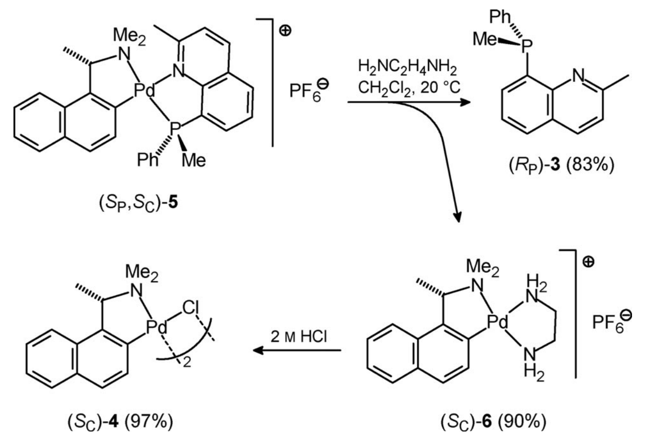

Scheme 4.

Synthesis of Diastereomeric Rhenium Complexes

The acetonitrile complex [CpRe(CO)(NO)(NCMe)]BF_4 (**7**) is a perfectly suited starting material for the synthesis of chiral half-sandwich rhenium complexes.[17–19] Fusing **7** together with a slight excess of racemic **3** under vacuum and without solvent gave a high yield of racemic **8**. Similarly, diastereomeric (R_{Re},S_P/S_{Re},S_P)-**8** was obtained from the reaction of **7** and (R_P)-**3** with > 98% *ee* (determined by ^{1}H NMR spectroscopy in the presence of Eu(tfc)$_3$). In this case the temperature should not exceed 90 °C to keep the phosphane from racemizing (Scheme 5).

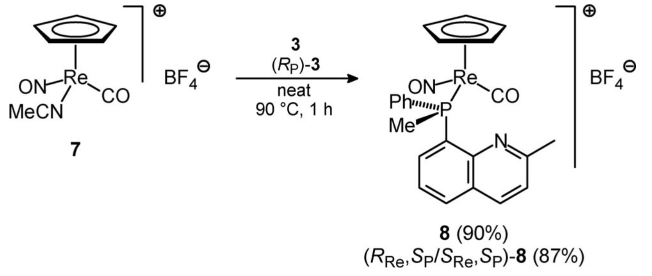

Scheme 5.

The structure of racemic **8** was determined crystallographically. The compound crystallized in the space group $P2_1/c$ with the CO and NO ligands disordered. A view of the cation is shown in Figure 2. Interatomic distances and angles are very similar to those of analogous complexes.[4,18]

Borohydride reduction of the carbonyl ligand[17] gave the methyl complexes **9** and (R_{Re},S_P/S_{Re},S_P)-**9**, respectively (Scheme 6). The success of the reaction is immediately evident from the disappearance of the CO stretching absorption in the infrared spectrum and new doublets in the ^{1}H and ^{13}C NMR spectra typical of a Re–CH_3 group.

By crystallization from toluene/pentane, **9** was partially separated into (R_{Re},R_P/S_{Re},S_P)-**9** (87% *de*) and (R_{Re},S_P/S_{Re},R_P)-**9** (72% *de*). (R_{Re},R_P/S_{Re},S_P)-**9** crystallized in the triclinic space group $P\bar{1}$, a view of the molecule is shown in Figure 3.

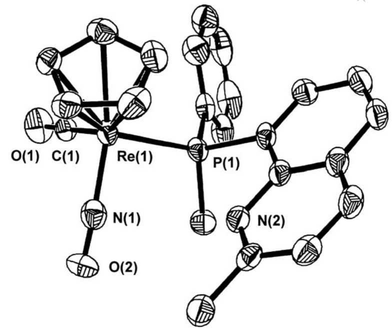

Figure 2. Structure of the cation of **8**, hydrogen atoms were omitted for clarity. Thermal ellipsoids drawn at 50% level. C(1) and N(1) are disordered and were labeled arbitrarily. Space group $P2_1/c$; selected distances [pm] and angles [°] (standard deviations in parentheses): Re(1)–P(1) 241.41(11), Re(1)–C(1) 185.6(4), Re(1)–N(1) 184.8(4), P(1)–Re(1)–C(1) 93.16(12), P(1)–Re(1)–N(1) 91.72(12), C(1)–Re(1)–N(1) 92.46(16).

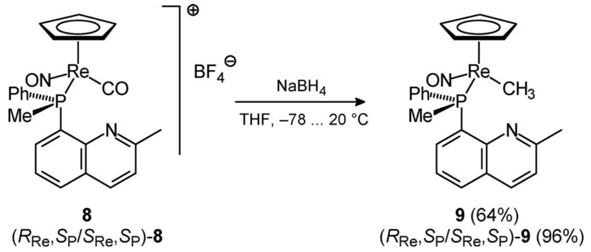

Scheme 6.

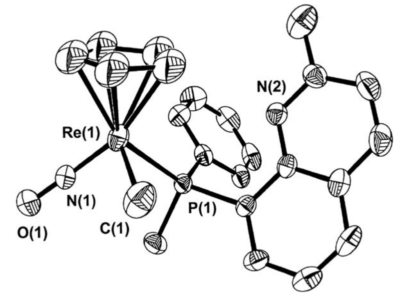

Figure 3. Structure of the compound (R_{Re},R_P/S_{Re},S_P)-**9**, hydrogen atoms were omitted for clarity. Thermal ellipsoids drawn at 50% level. Space group $P\bar{1}$; selected distances [pm] and angles [°] (standard deviations in parentheses): Re(1)–P(1) 235.12(14), Re(1)–C(1) 227.2(8), Re(1)–N(1) 174.3(5), N(1)–O(1) 121.0(7), P(1)–Re(1)–C(1) 84.1(2), P(1)–Re(1)–N(1) 92.8(2), C(1)–Re(1)–N(1) 94.0(3).

A sample of (R_{Re},S_P/S_{Re},R_P)-**9** (72% *de*) was treated at –78 °C with 0.86 equiv. HBF_4, i.e. just enough to protonate the faster reacting[11] *unlike* diastereomer. The ionic product (R_{Re},S_P/S_{Re},R_P)-**10** was crystallized by addition of diethyl ether and thus easily separated from residual (R_{Re},R_P/S_{Re},S_P)-**9** (Scheme 7).

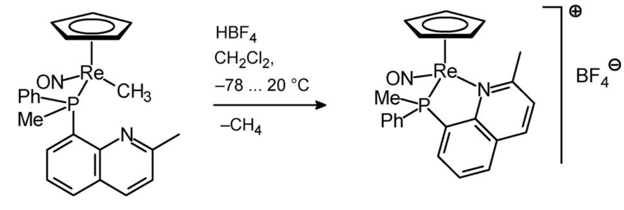

$(R_\text{Re},S_\text{P}/S_\text{Re},R_\text{P})$-**9** (72% *de*)

$(R_\text{Re},S_\text{P}/S_\text{Re},R_\text{P})$-**10** (74%, 97% *de*)

Scheme 7.

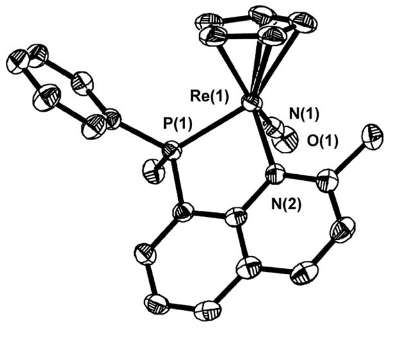

Figure 4. Structure of the cation of $(R_\text{Re},R_\text{P}/S_\text{Re},S_\text{P})$-**10**, hydrogen atoms were omitted for clarity. Thermal ellipsoids drawn at 50% level. Space group *C*2/*c*; selected distances [pm] and angles [°] (standard deviations in parentheses): Re(1)–P(1) 231.50(9), Re(1)–N(1) 176.4(3), Re(1)–N(2) 218.9(3), N(1)–O(1) 119.6(4), P(1)–Re(1)–N(1) 92.59(10), P(1)–Re(1)–N(2) 81.12(8), N(1)–Re(1)–N(2) 96.68(13).

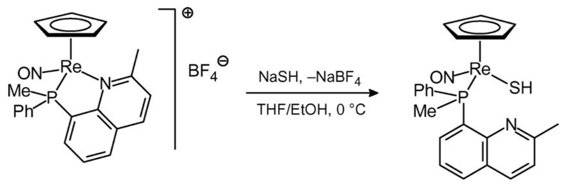

$(R_\text{Re},S_\text{P}/S_\text{Re},R_\text{P})$-**10** (97% *de*)
$(R_\text{Re},R_\text{P}/S_\text{Re},S_\text{P})$-**10** (94% *de*)
(S_Re,S_P)-**10** (92% *de*)

$(R_\text{Re},S_\text{P}/S_\text{Re},R_\text{P})$-**11** (70%, 96% *de*)
$(R_\text{Re},R_\text{P}/S_\text{Re},S_\text{P})$-**11** (92%, 94% *de*)
(S_Re,S_P)-**11** (55%, 98% *de*)

Scheme 9.

Similarly, a trace of HBF_4 was added to a sample of $(R_\text{Re},R_\text{P}/S_\text{Re},S_\text{P})$-**9** (87% *de*) to convert the residual *unlike* diastereomer into the ring-closed ionic complex which was precipitated and discarded. The supernatant was then treated with more acid yielding $(R_\text{Re},R_\text{P}/S_\text{Re},S_\text{P})$-**10** with 94% *de*. The relative configuration of both diastereomers was assigned on the basis of ^{1}H-^{1}H NOESY spectra: Both isomers gave strong crosspeaks between the Cp signal and the resonance of the CH_3 group on the quinoline ring. For $(R_\text{Re},S_\text{P}/S_\text{Re},R_\text{P})$-**10**, additional crosspeaks connected the Cp signal with the PCH_3 signal, while for $(R_\text{Re},R_\text{P}/S_\text{Re},S_\text{P})$-**10** a correlation was observed between the Cp ring and the *ortho* protons of the PC_6H_5 group. This assignment was finally corroborated by an X-ray structure determination of $(R_\text{Re},R_\text{P}/S_\text{Re},S_\text{P})$-**10** (Figure 4).

By the two-step process outlined above a sample of nonracemic $(R_\text{Re},S_\text{P}/S_\text{Re},S_\text{P})$-**9** was finally converted into (R_Re,S_P)-**10** (71% *de*) and (S_Re,S_P)-**10** (92% *de*) (Scheme 8). For the success of this reaction it is very important that the amount of acid in the first step is carefully controlled.

Ring opening with the strong, soft nucleophile SH^- proceeds smoothly and stereospecifically at 0 °C (Scheme 9).

The lower yield of enantiomerically pure (S_Re,S_P)-**11** is mainly due to its good solubility in pentane which is responsible for losses during workup. The presence of the Re–SH group reveals itself through a doublet (J = 13.5 Hz) in the ^{1}H NMR spectrum near δ = 0.2. A structure determination of the $(R_\text{Re},R_\text{P}/S_\text{Re},S_\text{P})$-diastereomer was carried out as an unambiguous proof of the relative configuration at rhenium and phosphorus (Figure 5).

Not unexpectedly, the structure is very similar to that of the methyl complex $(R_\text{Re},R_\text{P}/S_\text{Re},S_\text{P})$-**9** (Figure 3). One noteworthy difference is the large angle S(1)–Re(1)–N(1). This is a common feature of all complexes [CpRe(NO)(PR′$_3$)(SR)],

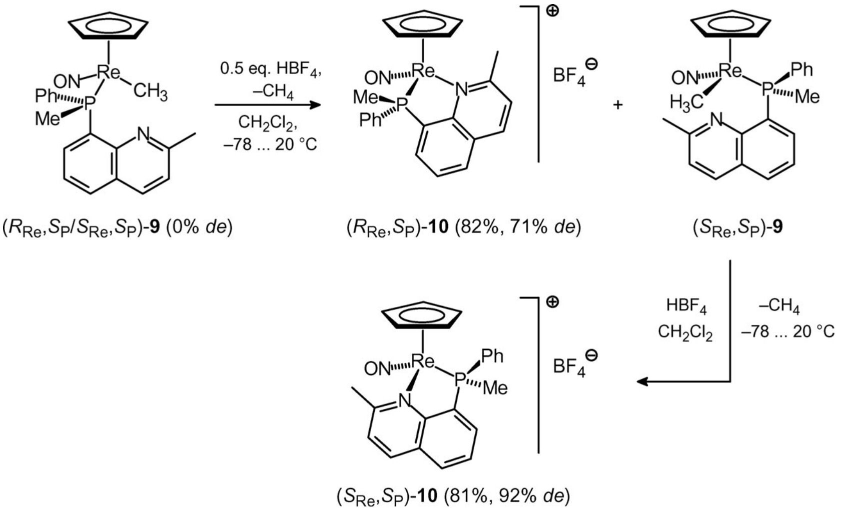

$(R_\text{Re},S_\text{P}/S_\text{Re},S_\text{P})$-**9** (0% *de*)

(R_Re,S_P)-**10** (82%, 71% *de*)

(S_Re,S_P)-**9**

(S_Re,S_P)-**10** (81%, 92% *de*)

Scheme 8.

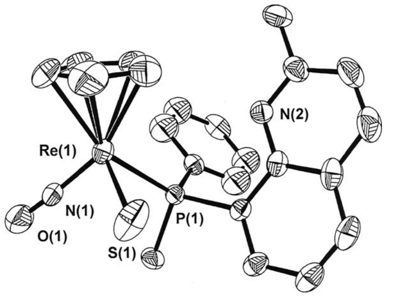

Figure 5. Structure of the compound (R_{Re},R_P/S_{Re},S_P)-**11**, hydrogen atoms were omitted for clarity. Thermal ellipsoids drawn at 50% level. Space group $P\bar{1}$; selected distances [pm] and angles [°] (standard deviations in parentheses): Re(1)–P(1) 237.11(15), Re(1)–S(1) 239.1(2), Re(1)–N(1) 179.6(6), N(1)–O(1) 115.0(8), P(1)–Re(1)–S(1) 83.76(6), P(1)–Re(1)–N(1) 91.8(2), S(1)–Re(1)–N(1) 98.5(2).

which is caused by an antibonding interaction between the strongly π-donating SR ligand and the HOMO–1 of the [CpRe(NO)(PR′$_3$)] complex fragment.[19–21]

Condensation reactions with a number of aldehydes were carried out on both diastereomers of **11**. The desired thioaldehyde complexes **12** were formed in high yields and, as expected, with retention of configuration at rhenium (Scheme 10).

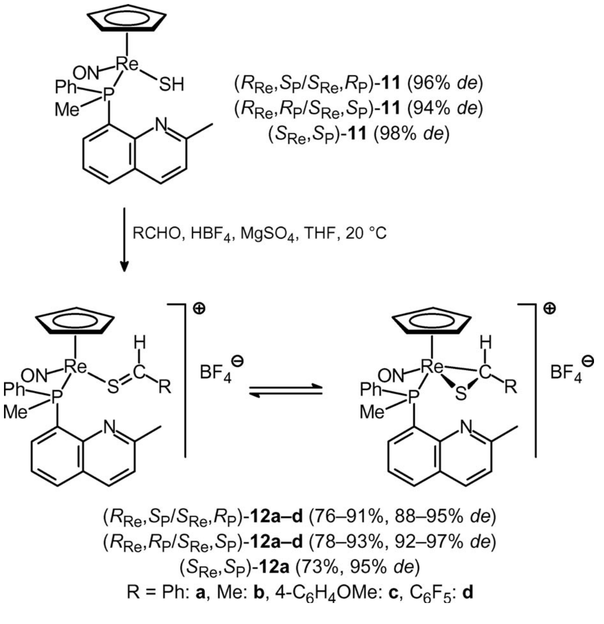

Scheme 10.

As indicated in Scheme 10, the thioaldehyde complexes **12** exist as rapidly equilibrating mixtures of η^1 and η^2 isomers. This can easily be inferred from the appearance of two well separated NO stretching vibrations in the infrared spectra. The ratio of the isomers depends on the group R and the relative configuration at rhenium and phosphorus. Thus, both diastereomers of **12b** and the like diastereomers of **12c** and **12d** are essentially pure η^2 isomers, both diastereomers of **12a** contain smaller fractions of the η^1 isomers, and the unlike diastereomers of **12c** and **12d** are roughly equimolar mixtures of both forms.

A structure determination of (R_{Re},S_P/S_{Re},R_P)-**12c** was undertaken, the major concern again being the relative configuration at rhenium and phosphorus. A view of the cation is shown in Figure 6.

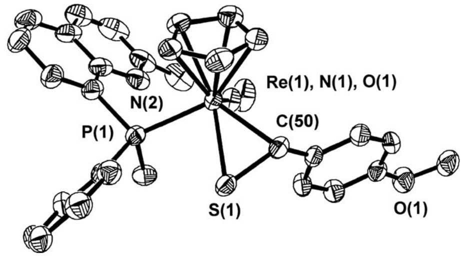

Figure 6. Structure of the cation of (R_{Re},S_P/S_{Re},R_P)-**12c**, hydrogen atoms were omitted for clarity. Thermal ellipsoids drawn at 50% level. Space group $P2(1)/n$; selected distances [pm] and angles [°] (standard deviations in parentheses): Re(1)–S(1) 239.12(14), Re(1)–C(50) 223.2(5), S(1)–C(50) 173.1(6), Re(1)–P(1) 243.22(14), Re(1)–N(1) 176.0(5), N(1)–O(1) 117.4(7), S(1)–Re(1)–C(50) 43.80(15), P(1)–Re(1)–S(1) 79.80(5), P(1)–Re(1)–C(50) 121.45(15), P(1)–Re(1)–N(1) 90.42(17).

As expected, the structure is very similar to that of [CpRe(NO)(PPh$_3$)(η^2-S=CHPh)]BF$_4$.[22] The S(1)–C(50) bond is almost parallel to the Re(1)–P(1) bond such as to maximize the interaction between the HOMO of the [CpRe(NO)(PR$_3$)]$^+$ complex fragment and the π* orbital of the thiocarbonyl group.[4] This interaction results in a lengthening of the S(1)–C(50) bond in comparison with 2,4,6-tri(*tert*-butyl)thiobenzaldehyde (160.2 pm)[23] or [CpRu(dppe)(η^1-S=CHC$_6$H$_4$OMe)]PF$_6$ (162.7 pm).[24] The aryl group is located *anti* to the Cp ligand such that the configurations at rhenium and carbon are the same.

Diastereoselective Addition of Nucleophiles

As a first test of the asymmetric induction between rhenium and the thioaldehyde ligand we chose the addition of various nucleophiles X$^-$ to both diastereomers of **12a** (Scheme 11).

The addition products were isolated in satisfactory yields. The diastereoselectivity of the addition was only moderate. A crystal of the major isomer of (R_{Re},R_P/S_{Re},S_P)-**13d** was investigated by X-ray crystallography. The compound crystallizes in the triclinic space group $P\bar{1}$ with two molecules in the unit cell which are related by a center of inversion. One of them is shown in Figure 7.

The geometry around the rhenium atom is almost identical to that of (R_{Re},R_P/S_{Re},S_P)-**11**, including the typically large angle S(1)–Re(1)–N(1). The angles at C(50) are close to tetrahedral with the relative configuration at this atom the same as at Re(1) and P(1).

The enantiomerically enriched addition product (S_{Re},S_P,S_C)-**13b** was finally chosen to explore ways to cleave the thiolate ligand from the rhenium complex. Initial experiments to achieve this by protonation with CF$_3$COOH or HBF$_4$ failed. Methylation however worked well. Monitoring the reaction by NMR spectroscopy indicated that a thioether complex was involved as an intermediate. Upon

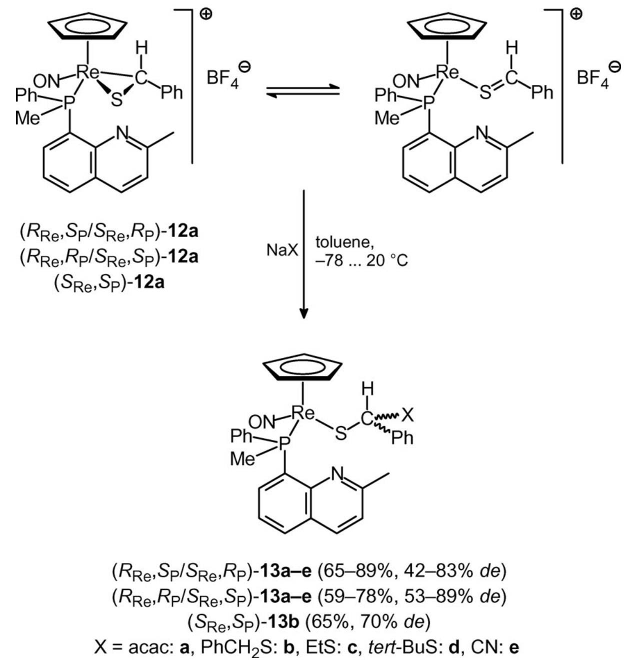

Scheme 11.

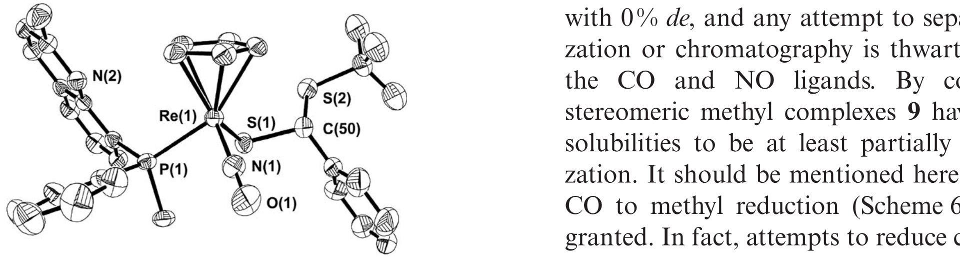

Figure 7. Structure of the compound (R_{Re},R_P,R_C/S_{Re},S_P,S_C)-**13d**, hydrogen atoms were omitted for clarity. Thermal ellipsoids drawn at 50% level. Space group $P\bar{1}$; selected distances [pm] and angles [°] (standard deviations in parentheses): Re(1)–P(1) 236.10(9), Re(1)–S(1) 238.53(9), Re(1)–N(1) 175.4(3), N(1)–O(1) 119.6(4), S(1)–C(50) 184.8(4), S(2)–C(50) 181.8(4), P(1)–Re(1)–S(1) 86.51(3), P(1)–Re(1)–N(1) 89.4(1), S(1)–Re(1)–N(1) 99.0(1), S(1)–C(50)–S(2) 104.5(2).

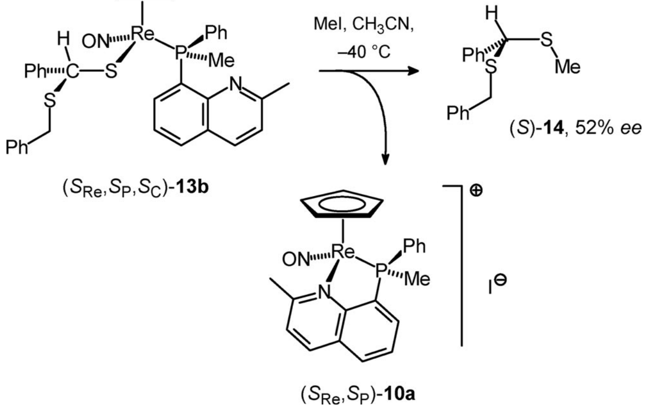

Scheme 12.

workup, however, the ring-closed complex (S_{Re},S_P)-**10a** was isolated along with the dithioacetal (S)-**14** whose enantiomeric excess was determined by chiral HPLC (Scheme 12).

Discussion

The present study was undertaken with several goals in mind: (i) to establish a broader applicability of the diastereoselective proton transfer from base-functionalized phosphane ligands to metal centers,[11] (ii) to investigate the stereochemical course of chelate ring-opening and -closing reactions, and (iii) to find out whether the presence of an additional stereogenic center might influence the diastereoselectivity of nucleophilic addition reactions to unsaturated ligands. In order to arrive at unambiguous conclusions we decided to carry the entire reaction sequence through with both diastereomers and track the stereochemical course of each step by X-ray crystallography.

Horner-type phosphanes PR^{1}R^{2}R^3 are configurationally stable at temperatures below 100 °C.[25] Thus the reactivity of the acetonitrile complex **7** is just sufficient not to jeopardize the stereochemical outcome of the substitution reaction described in Scheme 5. As expected the two spectroscopically distinguishable diastereomers of **8** are formed with 0% *de*, and any attempt to separate them by crystallization or chromatography is thwarted by the similarity of the CO and NO ligands. By contrast, the two diastereomeric methyl complexes **9** have sufficiently different solubilities to be at least partially separated by crystallization. It should be mentioned here that the success of the CO to methyl reduction (Scheme 6) cannot be taken for granted. In fact, attempts to reduce complexes analogous to **8** with the ligands P(Me)(Ph)(8-quinolinyl), P(Me)(Ph)(2-pyridyl) or P(Me)(Ph)(CH$_2$NMe$_2$) gave intractable mixtures which contained little if any of the desired methyl complexes.[12]

As we have pointed out in our previous communication,[11] the striking diastereoselectivity of the proton transfer/methane elimination reaction of Scheme 6 and 7 rests on a number of well-established facts: (i) The basicity of electron-rich transition metal complexes is similar to or even exceeds that of organic nitrogen bases;[26] (ii) the rate of proton transfer to the metal ("kinetic basicity") is, however, smaller by several orders of magnitude;[27,28] (iii) acid induced methyl cleavage involves metal protonation at a site cis to CH$_3$ followed by reductive elimination.[29,30] As a result, a metal complex bearing an amine function on the side arm of one of the ligands will first be protonated at nitrogen followed by intramolecular H$^+$ transfer to the metal.[31] This situation is graphically illustrated in Scheme 13.

Here, K(N) and K(M) represent the (roughly similar) basicities of the nitrogen and metal centers, respectively, and the various k_x(N) and k_x(M) are the corresponding rate constants of proton transfer to nitrogen or metal, with $k_x(N) >> k_x(M)$. In the absence of a basic solvent a substoichiometric amount of acid HA will be rapidly and completely consumed by the formation of the N-protonated spe-

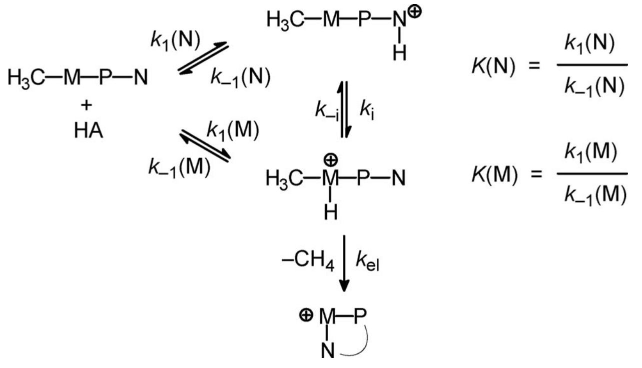

Scheme 13.

cies. In a dilute solution, the entropy-favored *intramolecular* proton transfer (k_i step) will be much faster than the *intermolecular* reprotonation of the conjugate base A^- followed by direct metal protonation. As the reductive elimination of methane from rhenium is rapid even at low temperatures[30,31] (i.e. $k_{el} >> k_{-i}$) it follows that the intramolecular proton transfer from nitrogen to rhenium is the rate-determining step. A clue as to how this step could bring about a high diastereoselectivity comes from an inspection of the structure of the cation of (R_{Re},R_P/S_{Re},S_P)-**10** (Figure 4). In this slower formed diastereomer the phenyl group at phosphorus eclipses the cyclopentadienyl ligand on rhenium, whereas in the rapidly formed (R_{Re},S_P/S_{Re},R_P)-diastereomer the phenyl group eclipses the svelte NO ligand (see also the structure determinations of both diastereomers of **2**[11]). Because the geometry of the transition state of the proton transfer from N to Re approaches that of the final product, it seems safe to assume that this repulsive interaction is responsible for slowing down the proton transfer within the (R_{Re},R_P/S_{Re},S_P) diastereomer (Scheme 14).

The opening of the chelate ring by the attacking nucleophile SH^- proceeds with retention of configuration at the rhenium center (Scheme 9). It is tempting to ascribe this outcome to the configurational stability of the pyramidal Lewis acid intermediate $[CpRe(NO)(PR_3)]^+$.[9] However, it has already been pointed out by Gladysz et al. that substitution reactions of half-sandwich rhenium complexes $[CpRe(NO)(PPh_3)(L^1)]^+$ proceed by an associative mechanism with a bent-nitrosyl intermediate $[CpRe(NO)(PPh_3)(L^1)(L^2)]^+$. The observed retention of configuration was tentatively explained as the result of steric repulsions which cause the entering ligand L^2 to attack from a direction *anti* to the bulky PPh_3 ligand.[32] For the case presented here this explanation is not quite satisfying. Inspection of a space-filling model of the cation of (R_{Re},R_P/S_{Re},S_P)-**10** shows that for such a mechanism both possible sites of attack are similarly shielded. Furthermore, for the opposite diastereomer (R_{Re},S_P/S_{Re},R_P)-**10**, where the Ph and Me groups at phosphorus have exchanged positions, the interstice between NO and phosphorus is even more protected. Thus, if the selectivity were mainly determined by steric interactions we would have to expect (i) a generally lower diastereoselectivity, and (ii) that both diastereomers of **10** would ring-open with significantly different selectivities, which is clearly not the case. We are left to conclude that the origin of the high stereoselectivity of the substitution at rhenium is still an open question.

The synthesis of the thioaldehyde complexes **12a–d** by acid-promoted condensation of the Re–SH complex **11** with aldehydes is straightforward and also more reliable than the alternative H^--abstraction from the corresponding benzylthiolate complexes.[33,34] In addition, it is also more convenient as it is based on a common rhenium complex as starting material. **12a–d** exist in solution as mixtures of η^1(S)

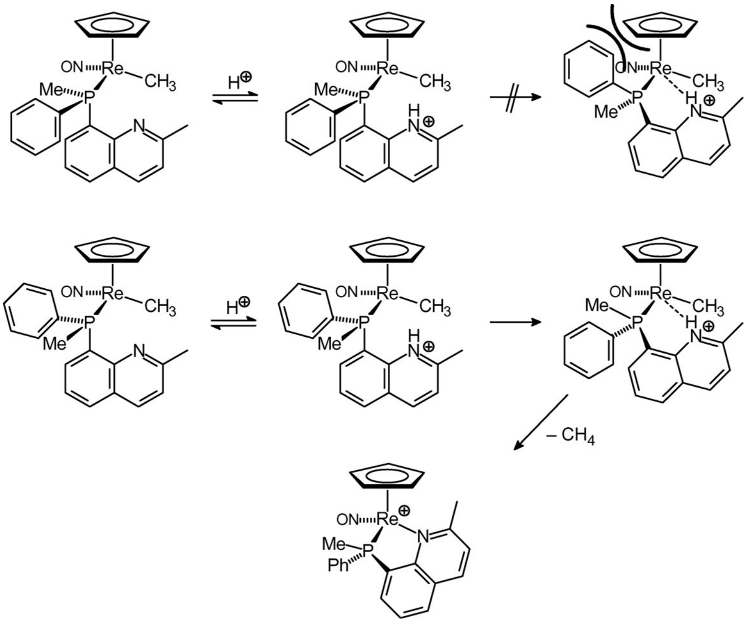

Scheme 14. For the sake of clarity, only species with (R_{Re})-configuration are shown.

and η^2(S=C) bonded isomers. This is a quite common phenomenon and has been observed not only for rhenium complexes of thioaldehydes[33,34] but also for similar complexes of aldehydes, ketones and imines.[35–37] Such a situation is detrimental with regard to the stereoselectivity of addition to the coordinated π ligand, as there are three competing pathways: backside attack at the η^2(S=C) isomer and attack on both enantiofaces of the η^1(S)-bonded thioaldehyde (see Scheme 11). Gladysz et al. have pointed out that both pathways may favor, if to different extents, the same diastereomer of the addition products.[35,38] With diastereoselectivities up to 89% this hope was at least partially fulfilled. From the fact that the diastereoselectivity of the addition to carbon is similar for both diastereomers of **12a** we conclude that the configuration at phosphorus is only of minor importance for the outcome of the reaction.

As a guide for further development we briefly explored ways to remove the newly formed ligand from rhenium. Methylation transforms the anionic ligand into a neutral one, which, like in many other cases,[39–42] is only weakly bound. The thioacetal ligand is then given off under mild conditions while the chelate ring is closed with high stereoselectivity. The two products are easily separated on the basis of their different solubilities (Scheme 12), allowing also the rhenium chelate to be isolated and recycled.

Experimental Section

General: All experiments were carried out in Schlenk tubes under nitrogen using suitably purified solvents. IR: Bruker IFS 25. ^{1}H NMR: Bruker AMX 400, Bruker Avance 500, Jeol JNM-LA 300, δ values relative to TMS. ^{13}C NMR: Bruker AMX 400, Bruker Avance 500, Jeol JNM-LA 300, δ values relative to TMS, assignments were routinely checked by DEPT procedures. In some cases the ^{13}C NMR signals of quaternary carbon atoms were too weak to be detected. ^{31}P NMR: Bruker AMX 400, Bruker Avance 500, Jeol JNM-LA 300, δ values relative to 85% H_3PO_4. Elemental analyses: Analytical Laboratory of the Institut für Anorganische Chemie. BF_4^- salts occasionally give low carbon values due to trace formation of fluorocarbon compounds which escape detection. Spectroscopic and analytical data are listed as Supporting Information HPLC: Daicel Chiralcel OD-H column (4.6 × 250 mm), Jasco pump, gradient unit and multi-wavelength detector. X-ray structures: Bruker SMART APEX CCD. The following starting materials were obtained as described in the literature: [CpRe(CO)(NO)(NCMe)]BF_4 (**7**),[17] NaSH,[43] PH(Me)(Ph),[44] [(S_C)-**4**].[14] Acetylacetone and the thiols were converted into their sodium salts by adding a stoichiometric amount of sodium metal to solutions in ethanol, followed by evaporation to dryness. All other reagents were used as purchased.

P(Me)(Ph)[8-(2-methylquinolinyl)] (3): A solution of 2.5 M *tert*-butyllithium in hexane (8.5 mL, 13.6 mmol) was added to a solution of PH(Me)(Ph) (1.45 g, 12.4 mmol) in THF (15 mL). The resulting red solution was added at –78 °C to a solution of 2-methyl-8-chloroquinoline (2.97 g, 16.7 mmol) in THF (10 mL). After stirring for 1.5 h at –78 °C and 2 h at 20 °C water (40 mL) was added. The resulting slurry was extracted with CH_2Cl_2 (4 × 20 mL) and the combined organic phases dried with $MgSO_4$. The solvent was removed under vacuum and the brownish-yellow residue recrystallized from methanol at –30 °C; yield 2.18 g (67%) light yellow crystals.

(S_P,S_C)-[Pd($Me_2NC_{12}H_{10}$)(P(Me)(Ph)($C_{10}H_8N$))]PF_6 [(S_P,S_C)-5]: Compound **3** (7.93 g, 30.0 mmol) was added at 20 °C to a suspension of (S_C)-**4** (10.2 g, 14.9 mmol) in methanol (120 mL). After stirring for 1.5 h at this temperature, some colorless precipitate had formed which was removed by filtration through a 0.45-μ membrane filter. A solution of NH_4PF_6 (9.80 g, 60.0 mmol) in water (20 mL) was added to the filtrate whereupon the product began to crystallize. More water (250 mL) was added with stirring, the voluminous precipitate was filtered off, washed with water, water/methanol (1:1), and finally with diethyl ether, and dried under vacuum; yield 19.8 g (93%) colorless crystalline powder. This material was dissolved in a just sufficient amount of boiling 2-butanone and the solution allowed to slowly cool to ambient temperature. The precipitate was collected and recrystallized from 2-butanone; yield 5.7 g (54%) yellow crystals.

(R_P)-P(Me)(Ph)[8-(2-methylquinolinyl)] [(R_P)-3]: Ethylenediamine (1.35 g, 22.4 mmol) and diethyl ether (100 mL) were added to a solution of [(S_P,S_C)-**5**] (3.20 g, 4.48 mmol) in dichloromethane (90 mL). The mixture was stirred for 1 h at 20 °C, the colorless precipitate filtered off, washed with diethyl ether, and dried. This material was identified spectroscopically (^{1}H, ^{31}P NMR) as (S_C)-**6**,[14] yield 2.10 g (90%). The filtrate was taken to dryness and the residue taken up in diethyl ether (60 mL) and water (20 mL). The ether phase was collected, the aqueous phase extracted with diethyl ether (2 × 20 mL), and the combined organic phases dried with $MgSO_4$. Evaporation gave a colorless solid; yield 0.95 g (83%), spectroscopically (^{1}H, ^{31}P NMR) identical with racemic **3**. ^{1}H NMR in the presence of the chiral shift reagent (–)-1-(9-anthryl)-2,2,2-trifluoroethanol gave an *ee* of 99%.

(S_C)-[(PdCl($Me_2NC_{12}H_{10}$))$_2$] [(S_C)-4]: 2 N aqueous HCl (30 mL, 60 mmol) was added to a suspension of (S_C)-**6** (7.60 g, 14.7 mmol) in methanol (180 mL). After 10 min a yellow solid had formed which was filtered off, washed with methanol, and dried under vacuum; yield 4.87 g (97%), spectroscopically (^{1}H NMR) identified as (S_C)-**4**.[14]

[CpRe(CO)(NO){P(Me)(Ph)($C_{10}H_8N$)}]BF_4 (8): [CpRe(CO)(NO)(NCMe)]BF_4 (**7**) (0.60 g, 1.37 mmol) and **3** (0.52 g, 1.96 mmol) were fused together for 4 h at 90 °C under vacuum. After cooling to 20 °C the mixture was taken up in THF (9 mL) and stirred until a yellow solid had formed. This was filtered off, washed with diethyl ether, and dried; yield 0.81 g (90%), yellow crystalline solid; m.p. 167 °C.

(R_{Re},S_P/S_{Re},S_P)-[CpRe(CO)(NO){P(Me)(Ph)($C_{10}H_8N$)}]BF_4 [(R_{Re},S_P/S_{Re},S_P)-8]: This compound was obtained as described above from **7** (1.90 g, 4.34 mmol) and (R_P)-**3** (1.30 g, 4.90 mmol); yield 2.50 g (87%), spectroscopically identical with **8**. ^{1}H NMR in the presence of the chiral shift reagent tris[(trifluoromethyl-hydroxymethylene)-(–)-camphorato]europium gave an *ee* of 98%.

[CpRe(NO){P(Me)(Ph)($C_{10}H_8N$)}(CH_3)] (9): $NaBH_4$ (0.14 g, 3.75 mmol) was added to a suspension of carbonyl complex **8** (0.71 g, 1.07 mmol) in THF (5 mL). The mixture was stirred for 3 h at 20 °C and the solvents evaporated to dryness. The residue was dissolved in toluene (15 mL) and filtered through a layer of celite. The filtrate was concentrated to 8 mL and stored at –30 °C whereupon brick-red crystals of (R_{Re},R_P/S_{Re},S_P)-**9** formed. The supernatant was syringed off and the crystals washed with pentane and dried; yield 0.26 g (85%) red crystalline solid, 87% *de* (^{1}H NMR).

The supernatant was concentrated to 4 mL and pentane (15 mL) added to precipitate the orange-colored (R_{Re},S_P/S_{Re},R_P)-**9**; yield 0.13 g (43%), orange crystalline solid, 72% *de* (^{1}H NMR).

$(R_{Re},S_P/S_{Re},S_P)$-[CpRe(NO){P(Me)(Ph)($C_{10}H_8N$)}(CH_3)] [$(R_{Re},S_P/S_{Re},S_P)$-9]: $NaBH_4$ (0.39 g, 10.3 mmol) was added at –78 °C to a suspension of $(R_{Re},S_P/S_{Re},S_P)$-**8** (1.95 g, 2.95 mmol) in THF (40 mL). The mixture was stirred and warmed to 20 °C over a period of 4 h. The solvent was removed under vacuum and the residue dissolved in toluene (25 mL) and filtered through a layer of celite. The filtrate was taken to dryness leaving a red solid; yield 1.60 g (96%), spectroscopically identical with **9**. This material was used in the next step without further purification.

$(R_{Re},S_P/S_{Re},R_P)$-[CpRe(NO){P(Me)(Ph)($C_{10}H_8N$)}]BF_4 [$(R_{Re},S_P/S_{Re},R_P)$-10]: A solution of 54% HBF_4 in diethyl ether (26 µL, 0.19 mmol) was added to a solution of $(R_{Re},S_P/S_{Re},R_P)$-**9** (127 mg, 0.23 mmol, 72% *de*) in dichloromethane (5 mL) at –78 °C . The mixture was warmed to 20 °C and diethyl ether (15 mL) added. A precipitate formed which was collected by filtration, washed with pentane, and dried under vacuum; yield 105 mg (74%), orange crystalline solid, 97% *de* (^{1}H NMR); m.p. 83 °C.

$(R_{Re},R_P/S_{Re},S_P)$-[CpRe(NO){P(Me)(Ph)($C_{10}H_8N$)}]BF_4 [$(R_{Re},R_P/S_{Re},S_P)$-10]: A solution of 54% HBF_4 in diethyl ether (8 µL, 0.06 mmol) was added to a solution of $(R_{Re},R_P/S_{Re},S_P)$-**9** (255 mg, 0.454 mmol, 87% *de*) in dichloromethane (10 mL) at –78 °C . The mixture was warmed to 20 °C and diethyl ether (20 mL) added. An orange precipitate of $(R_{Re},S_P/S_{Re},R_P)$-**10** formed which was filtered off and discarded. The filtrate was evaporated to dryness and the residue treated with 54% HBF_4 (55 µL, 0.40 mmol) and worked up as described above for $(R_{Re},S_P/S_{Re},R_P)$-**10**; yield 195 mg (68%), orange crystalline solid, 94% *de* (^{1}H NMR); m.p. 194 °C.

(R_{Re},S_P)-[CpRe(NO){P(Me)(Ph)($C_{10}H_8N$)}]BF_4 [(R_{Re},S_P)-10]: A solution of 54% HBF_4 in diethyl ether (195 µL, 1.42 mmol) was added to a solution of $(R_{Re},S_P/S_{Re},S_P)$-**9** (1.60 g, 2.84 mmol) in dichloromethane (25 mL) at –78 °C The mixture was warmed to 20 °C, concentrated to 12 mL, and diethyl ether (40 mL) added. A dark orange precipitate formed which was collected by filtration, washed with diethyl ether and pentane, and dried under vacuum; yield 0.77 g (82%), brownish-red crystalline powder, 71% *de* (^{1}H NMR). The product is spectroscopically identical with $(R_{Re},S_P/S_{Re},R_P)$-**10**.

(S_{Re},S_P)-[CpRe(NO){P(Me)(Ph)($C_{10}H_8N$)}]BF_4 [(S_{Re},S_P)-10]: The filtrate of the previous step was evaporated to dryness, redissolved in dichloromethane, treated with HBF_4 (240 µL, 1.76 mmol) and worked up as described above; yield 0.76 g (81%), red crystalline powder, 92% *de* (^{1}H NMR). The product is spectroscopically identical with $(R_{Re},R_P/S_{Re},S_P)$-**10**.

$(R_{Re},S_P/S_{Re},R_P)$-[CpRe(NO){P(Me)(Ph)($C_{10}H_8N$)}(SH)] [$(R_{Re},S_P/S_{Re},R_P)$-11]: NaSH (60 mg, 1.06 mmol) was added at 0 °C to a suspension of $(R_{Re},S_P/S_{Re},R_P)$-**10** (0.50 g, 0.79 mmol) in THF (15 mL) and ethanol (1 mL). The mixture was warmed to 20 °C, stirred for 2 h, and the solvents evaporated to dryness. The residue was dissolved in benzene, filtered through Celite, and the filtrate evaporated to 2 mL. Addition of pentane (20 mL) induced the product to crystallize, which was filtered off, washed with pentane, and dried; yield 0.32 g (70%), brown powder, 96% *de* (^{1}H NMR); m.p. 92 °C.

$(R_{Re},R_P/S_{Re},S_P)$-[CpRe(NO){P(Me)(Ph)($C_{10}H_8N$)}(SH)] [$(R_{Re},R_P/S_{Re},S_P)$-11]: This compound was prepared as above from $(R_{Re},R_P/S_{Re},S_P)$-**10**; yield 0.45 g (92%), ochre powder, 94% *de* (^{1}H NMR); m.p. 60 °C.

(S_{Re},S_P)-[CpRe(NO){P(Me)(Ph)($C_{10}H_8N$)}(SH)] [(S_{Re},S_P)-11]: This compound was prepared as above from (S_{Re},S_P)-**10** (0.76 g, 1.20 mmol) and NaSH (0.14 g, 2.40 mmol); yield 0.38 g (55%), yellow powder, 98% *de* (^{1}H NMR). The product is spectroscopically identical with $(R_{Re},R_P/S_{Re},S_P)$-**11**.

$(R_{Re},S_P/S_{Re},R_P)$-[CpRe(NO){P(Me)(Ph)($C_{10}H_8N$)}(S=CHPh)]BF_4 [$(R_{Re},S_P/S_{Re},R_P)$-12a]: $(R_{Re},S_P/S_{Re},R_P)$-**11** (1.21 g, 2.09 mmol), benzaldehyde (2.22 g, 20.9 mmol), $MgSO_4$ (0.50 g, 4.16 mmol), THF (10 mL) and 54% HBF_4 in diethyl ether (0.61 mL, 4.66 mmol) were combined and stirred for 10 min at 20 °C. Basic alumina (0.50 g) was added to absorb excess acid, the solids were filtered off and rinsed with acetone (2 × 5 mL) and the combined filtrate taken to dryness. The residue was recrystallized from THF (2 mL)/diethyl ether (20 mL); yield 1.48 g (91%), yellow powder, 95% *de* (^{1}H NMR); m.p. 197 °C.

$(R_{Re},R_P/S_{Re},S_P)$-[CpRe(NO){P(Me)(Ph)($C_{10}H_8N$)}(S=CHPh)]BF_4 [$(R_{Re},R_P/S_{Re},S_P)$-12a]: This compound was prepared as above from $(R_{Re},R_P/S_{Re},S_P)$-**11** (1.69 g, 2.91 mmol), benzaldehyde (3.10 g, 29.2 mmol), $MgSO_4$ (0.70 g, 5.82 mmol) and 54% HBF_4 (0.85 mL, 6.50 mmol); yield 1.81 g (82%), yellow powder, 92% *de* (^{1}H NMR); m.p. 207 °C.

(S_{Re},S_P)-[CpRe(NO){P(Me)(Ph)($C_{10}H_8N$)}(S=CHPh)]BF_4 [(S_{Re},S_P)-12a]: This compound was prepared as above from (S_{Re},S_P)-**11** (0.38 g, 0.65 mmol), benzaldehyde (0.69 g, 6.50 mmol), $MgSO_4$ (0.15 g, 1.25 mmol) and 54% HBF_4 (0.19 mL, 2.40 mmol); yield 0.36 g (73%), yellow powder, 95% *de* (^{1}H NMR). The product is spectroscopically identical with $(R_{Re},R_P/S_{Re},S_P)$-**12a**.

[CpRe(NO){P(Me)(Ph)($C_{10}H_8N$)}(S=CHR)]BF_4 (12b–d): Common protocol: The respective diastereomer of **11** (120 mg, 0.207 mmol), aldehyde (2.00 mmol), $MgSO_4$ (80 mg, 0.66 mmol), THF (5 mL) and 54% HBF_4 in diethyl ether (70 µL, 0.51 mmol) were combined and stirred for 10 min at 20 °C. Basic alumina (100 mg) was added to absorb excess acid. The supernatant was syringed off, the solution was filtered through a nylon syringe filter (0.45 µ) and the filtrate taken to dryness. The residue was recrystallized from THF (1 mL)/diethyl ether (10 mL).

$(R_{Re},S_P/S_{Re},R_P)$-[CpRe(NO){P(Me)(Ph)($C_{10}H_8N$)}(S=CHMe)]BF_4 [$(R_{Re},S_P/S_{Re},R_P)$-12b]: Yield 109 mg (76%), ochre powder, 95% *de* (^{1}H NMR); m.p. 195 °C.

$(R_{Re},R_P/S_{Re},S_P)$-[CpRe(NO){P(Me)(Ph)($C_{10}H_8N$)}(S=CHMe)]BF_4 [$(R_{Re},R_P/S_{Re},S_P)$-12b]: Yield 112 mg (78%), yellow powder, 96% *de* (^{1}H NMR); m.p. 185 °C.

$(R_{Re},S_P/S_{Re},R_P)$-[CpRe(NO){P(Me)(Ph)($C_{10}H_8N$)}(S=CHC_6H_4OMe)]BF_4 [$(R_{Re},S_P/S_{Re},R_P)$-12c]: Yield 128 mg (79%), yellow powder, 88% *de* (^{1}H NMR); m.p. 103 °C.

$(R_{Re},R_P/S_{Re},S_P)$-[CpRe(NO){P(Me)(Ph)($C_{10}H_8N$)}(S=CHC_6H_4-OMe)]BF_4 [$(R_{Re},R_P/S_{Re},S_P)$-12c]: Yield 132 mg (81%), yellow powder, 96% *de* (^{1}H NMR); m.p. 195 °C.

$(R_{Re},S_P/S_{Re},R_P)$-[CpRe(NO){P(Me)(Ph)($C_{10}H_8N$)}(S=CHC_6F_5)]BF_4 [$(R_{Re},S_P/S_{Re},R_P)$-12d]: Yield 157 mg (86%), yellow powder, 94% *de* (^{1}H NMR); m.p. 132 °C.

$(R_{Re},R_P/S_{Re},S_P)$-[CpRe(NO){P(Me)(Ph)($C_{10}H_8N$)}(S=CHC_6F_5)]BF_4 [$(R_{Re},R_P/S_{Re},S_P)$-12d]: Yield 163 mg (86%), yellow powder, 97% *de* (^{1}H NMR); m.p. 116 °C.

[CpRe(NO){P(Me)(Ph)($C_{10}H_8N$)}{SC(H)(Ph)(X)}] (13a–e): Common protocol: The respective sodium salt NaX was added at –78 °C to a suspension of **$(R_{Re},S_P/S_{Re},R_P)$-12a** or **$(R_{Re},R_P/S_{Re},S_P)$-12a** (150 mg, 0.20 mmol) in toluene (2 mL). The mixture was stirred for 12 h and allowed to slowly reach room temperature. A solid was removed by syringe filtration (0.2 µ), the filter was rinsed with toluene (3 mL) and the clear solution concentrated under vacuum to 1 mL. Pentane (10 mL) was slowly added at –78 °C which caused the product to crystallize. The supernatant was syringed off and the residue washed with pentane (3 × 3 mL) and dried.

(R_{Re},S_P/S_{Re},R_P)-[CpRe(NO){P(Me)(Ph)($C_{10}H_8N$)}{SC(H)(Ph)(acac)}] [(R_{Re},S_P/S_{Re},R_P)-13a]: Yield 118 mg (77%), yellow powder, 70% *de* (^{1}H NMR); m.p. 167 °C.

(R_{Re},R_P/S_{Re},S_P)-[CpRe(NO){P(Me)(Ph)($C_{10}H_8N$)}{SC(H)(Ph)(acac)}] [(R_{Re},R_P/S_{Re},S_P)-13a]: Yield 90 mg (59%), yellow powder, 53% *de* (^{1}H NMR); m.p. 165 °C.

Table 1. Details of the structure determinations of compounds **5**, **8**, **9**, **10**, **11**, **12c** and **13d**.

	5·0.5acetone	**8**	**9**	**10**·$CHCl_3$
Empirical formula	$C_{32.5}H_{35}F_6N_2O_{0.5}P_2Pd$	$C_{23}H_{21}BF_4N_2O_2PRe$	$C_{23}H_{24}N_2OPRe$	$C_{23}H_{22}BCl_3F_4N_2OPRe$
Formula mass	743.97	661.40	561.61	752.76
Crystal color/habit	yellow prism	yellow plate	red block	orange block
Crystal system	triclinic	monoclinic	triclinic	monoclinic
Space group	$P1$	$P2_1/c$	$P\bar{1}$	$C2/c$
a [Å]	11.6022(4)	8.891(2)	9.277(3)	23.0316(16)
b [Å]	12.0416(5)	24.452(5)	10.025(3)	14.2414(10)
c [Å]	13.3622(5)	10.651(2)	13.613(4)	18.9208(13)
α [°]	83.283(2)	90	70.323(6)	90
β [°]	66.151(1)	94.910(4)	85.212(6)	120.593(1)
γ [°]	70.367(2)	90	80.924(6)	90
V [Å^3]	1607.77(11)	2307.1(9)	1176.6(6)	5342.2(6)
Θ [°]	1.67–26.03	2.09–26.11	2.18–26.14	1.76–26.09
h	–14 to 14	–10 to 10	–11 to 11	–28 to 28
k	–14 to 14	–30 to 30	–12 to 12	–17 to 17
l	–15 to 16	–13 to 13	–16 to 16	–23 to 23
Z	2	4	2	8
μ(Mo-K_α) [mm^{-1}]	0.739	5.393	5.246	4.958
Crystal size [mm]	0.54 × 0.36 × 0.19	0.15 × 0.10 × 0.03	0.23 × 0.19 × 0.16	0.24 × 0.11 × 0.10
$D_{calcd.}$ [g cm^{-1}]	1.537	1.904	1.585	1.872
T [K]	100(2)	173(2)	173(2)	173(2)
Reflections collected	43516	26041	16410	37589
Independent reflections	11804	4567	4666	5292
Parameter	793	329	226	327
R_1 [$I > 2\sigma(I)$]	0.0218	0.0282	0.0362	0.0255
R_1 (overall)	0.0226	0.0316	0.0373	0.0287
R_2 [$I > 2\sigma(I)$]	0.0478	0.0661	0.0894	0.0582
R_2 (overall)	0.0482	0.0676	0.0902	0.0599
Absolute structure parameter	–0.012(9)			
Diff. peak/hole [e Å^{-3}]	0.318/–0.514	1.811/–0.459	4.023/–1.677	1.331/–0.972
CCDC	749532	749533	749534	749535

	11·0.5C_6H_6	**12c**·0.5OEt_2	**13d**
Empirical formula	$C_{25}H_{25}N_2OPReS$	$C_{32}H_{34}BF_4N_2O_{2.5}PReS$	$C_{33}H_{36}N_2OPReS_2$
Formula mass	618.70	822.69	757.93
Crystal color/habit	orange plate	yellow block	brown plate
Crystal system	triclinic	monoclinic	triclinic
Space group	$P\bar{1}$	$P2_1/n$	$P\bar{1}$
a [Å]	9.280(3)	11.9197(3)	9.5885(15)
b [Å]	10.248(4)	14.3281(3)	12.839(2)
c [Å]	13.668(5)	19.0098(4)	14.116(2)
α [°]	68.784(6)	90	74.461(2)
β [°]	86.103(7)	100.465(1)	72.009(2)
γ [°]	80.555(6)	90	87.221(2)
V [Å^3]	1195.2(7)	3192.62(12)	1591.4(4)
Θ [°]	2.16–28.36	1.79–26.08	1.95–26.02
h	–12 to 12	–14 to 14	–11 to 11
k	–13 to 13	–17 to 17	–15 to 15
l	–18 to 18	–23 to 23	–17 to 17
Z	2	4	2
μ(Mo-K_α) [mm^{-1}]	5.257	3.980	4.028
Crystal size [mm]	0.23 × 0.20 × 0.08	0.39 × 0.17 × 0.16	0.31 × 0.24 × 0.16
$D_{calcd.}$ [g cm^{-1}]	1.719	1.712	1.582
T [K]	173(2)	173(2)	173(2)
Reflections collected	32134	50639	32718
Independent reflections	5946	6283	6264
Parameter	246	378	354
R_1 [$I > 2\sigma(I)$]	0.0430	0.0397	0.0249
R_1 (overall)	0.0463	0.0417	0.0267
R_2 [$I > 2\sigma(I)$]	0.1084	0.1083	0.0637
R_2 (overall)	0.1106	0.1099	0.0647
Absolute structure parameter			
Diff. peak/hole [e Å^{-3}]	3.793/–3.178	3.757/–2.203	1.786/–1.029
CCDC	749536	749537	749538

(R_{Re},S_P/S_{Re},R_P)-[CpRe(NO){P(Me)(Ph)($C_{10}H_8N$)}{SC(H)(Ph)(SCH_2Ph)}] [(R_{Re},S_P/S_{Re},R_P)-13b]: Yield 115 mg (73%), ochre powder, 65% *de* (^{1}H NMR); m.p. 122 °C.

(R_{Re},R_P/S_{Re},S_P)-[CpRe(NO){P(Me)(Ph)($C_{10}H_8N$)}{SC(H)(Ph)(SCH_2Ph)}] [(R_{Re},R_P/S_{Re},S_P)-13b]: Yield 123 mg (78%), ochre powder, 89% *de* (^{1}H NMR); m.p. 121 °C.

(S_{Re},S_P,S_C)-[CpRe(NO){P(Me)(Ph)($C_{10}H_8N$)}{SC(H)(Ph)(SCH_2Ph)}] [(S_{Re},S_P,S_C)-13b]: Yield 103 mg (65%), yellow powder, 70% *de* (^{1}H NMR). The product is spectroscopically (^{1}H, ^{31}P NMR) identical with (R_{Re},R_P/S_{Re},S_P)-**13b**.

(R_{Re},S_P/S_{Re},R_P)-[CpRe(NO){P(Me)(Ph)($C_{10}H_8N$)}{SC(H)(Ph)(SEt)}] [(R_{Re},S_P/S_{Re},R_P)-13c]: Yield 95 mg (65%), ochre powder, 60% *de* (^{1}H NMR); m.p. 166 °C.

(R_{Re},R_P/S_{Re},S_P)-[CpRe(NO){P(Me)(Ph)($C_{10}H_8N$)}{SC(H)(Ph)(SEt)}] [(R_{Re},R_P/S_{Re},S_P)-13c]: Yield 90 mg (62%), ochre powder, 79% *de* (^{1}H NMR); m.p. 40 °C.

(R_{Re},S_P/S_{Re},R_P)-[CpRe(NO){P(Me)(Ph)($C_{10}H_8N$)}{SC(H)(Ph)(S*t*Bu)}] [(R_{Re},S_P/S_{Re},R_P)-13d]: Yield 108 mg (71%), ochre powder, 42% *de* (^{1}H NMR); m.p. 52 °C.

(R_{Re},R_P/S_{Re},S_P)-[CpRe(NO){P(Me)(Ph)($C_{10}H_8N$)}{SC(H)(Ph)(S*t*Bu)}] [(R_{Re},R_P/S_{Re},S_P)-13d]: Yield 114 mg (75%), ochre powder, 46% *de* (^{1}H NMR); m.p. 87 °C.

(R_{Re},S_P/S_{Re},R_P)-[CpRe(NO){P(Me)(Ph)($C_{10}H_8N$)}{SC(H)(Ph)(CN)}] [(R_{Re},S_P/S_{Re},R_P)-13e]: Yield 137 mg (94%), yellow crystalline solid, 83% *de* (^{1}H NMR); m.p. 199 °C.

(R_{Re},R_P/S_{Re},S_P)-[CpRe(NO){P(Me)(Ph)($C_{10}H_8N$)}{SC(H)(Ph)(CN)}] [(R_{Re},R_P/S_{Re},S_P)-13e]: Yield 102 mg (70%), ochre crystalline solid, 79% *de* (^{1}H NMR); m.p. 49 °C.

(*S*)-$PhCH_2SC(H)(Ph)(SMe)$ [(*S*)-14]: Methyl iodide (16 µL, 0.26 mmol) was added at –40 °C to a solution of (S_{Re},S_P,S_C)-**13b** (200 mg, 0.25 mmol) in acetonitrile (12 mL). The mixture was warmed to room temperature overnight. The solution was concentrated to 2 mL and extracted with pentane (4 × 10 mL). The acetonitrile fraction was evaporated to dryness, the residue recrystallized from dichloromethane (2 mL)/diethyl ether (5 mL), washed with diethyl ether, and dried; yield 120 mg (65%), orange crystalline solid, identified by NMR as (S_{Re},S_P)-**10a**, the iodide analog of (S_{Re},S_P)-**10**, 69% *de*. The combined pentane fractions were evaporated to dryness and the residue chromatographed over silica with hexane/ethyl acetate, 20:1 as eluent; yield 24 mg (37%), colorless oil, spectroscopically identical with an authentic racemic sample.[45] HPLC over a chiral column (Daicel Chiralcel OD-H) with hexane/2-propanol, 98:2 as eluent gave an *ee* of 52%.

X-ray Structure Determinations: Single crystals were bonded to a glass fiber with frozen perfluorinated polyether oil in each case. A Bruker Smart Apex CCD instrument was used for data collection (graphite monochromator, Mo-K_α radiation, λ = 0.71073 Å). The structures were solved using Patterson methods and refined with full-matrix least-squares against F^2 (SHELXS-97).[46] Hydrogen atoms were included in their calculated positions and refined using a riding model. The details of the measurement are summarized in Table 1. CCDC numbers given in Table 1 contain the supplementary crystallographic data for this paper. These data can be obtained free of charge from The Cambridge Crystallographic Data Centre via www.ccdc.cam.ac.uk/data_request/cif.

Supporting Information (see also footnote on the first page of this article): Spectroscopic and analytical data of the new compounds.

---

[1] *Handbook of Lewis Acids – Application in Organic Synthesis* (Ed.: H. Yamamoto), Wiley-VCH, Weinheim, **2000**.
[2] H. Brunner, *Angew. Chem.* **1969**, *81*, 395–396; *Angew. Chem. Int. Ed. Engl.* **1969**, *8*, 382.
[3] S. G. Davies, *Aldrichimica Acta* **1990**, *23*, 31–37.
[4] J. A. Gladysz, B. J. Boone, *Angew. Chem.* **1997**, *109*, 566–602; *Angew. Chem. Int. Ed. Engl.* **1997**, *36*, 550–583.
[5] W. S. Knowles, *Angew. Chem.* **2002**, *114*, 2096–2107; *Angew. Chem. Int. Ed.* **2002**, *41*, 1998–2007, and references therein.
[6] R. Noyori, *Angew. Chem.* **2002**, *114*, 2108–2123; *Angew. Chem. Int. Ed.* **2002**, *41*, 2008–2022, and references therein.
[7] K. B. Sharpless, *Angew. Chem.* **2002**, *114*, 2126–2135; *Angew. Chem. Int. Ed.* **2002**, *41*, 2024–2032, and references therein.
[8] H. Brunner, T. Zwack, *Organometallics* **2000**, *19*, 2423–2426.
[9] T. R. Ward, O. Schafer, C. Daul, P. Hofmann, *Organometallics* **1997**, *16*, 3207–3215.
[10] V. Alezra, G. Bernardinelli, C. Corminboeuf, U. Frey, E. P. Kündig, A. E. Merbach, C. M. Saudan, F. Viton, J. Weber, *J. Am. Chem. Soc.* **2004**, *126*, 4843–4853, and references therein.
[11] F. Bock, F. Fischer, W. A. Schenk, *J. Am. Chem. Soc.* **2006**, *128*, 68–69.
[12] F. Bock, Dissertation, University of Würzburg, **2007**.
[13] K. Issleib, M. Haftendorn, *Z. Anorg. Allg. Chem.* **1970**, *376*, 79–86.
[14] D. G. Allen, G. M. McLaughlin, G. B. Robertson, W. L. Steffen, G. Salem, S. B. Wild, *Inorg. Chem.* **1982**, *21*, 1007–1014.
[15] B. Wolfe, T. Livinghouse, *J. Org. Chem.* **2001**, *66*, 1514–1516.
[16] D. Sirbu, G. Consiglio, S. Gischig, *J. Organomet. Chem.* **2006**, *691*, 1143–1150.
[17] F. Agbossou, E. J. O'Connor, C. M. Garner, N. Q. Méndez, J. M. Fernández, A. T. Patton, J. A. Ramsden, J. A. Gladysz, *Inorg. Synth.* **1992**, *29*, 211–225.
[18] S. Dilsky, W. A. Schenk, *Eur. J. Inorg. Chem.* **2004**, 4859–4870.
[19] N. Burzlaff, M. Hagel, W. A. Schenk, *Z. Naturforsch., Teil B* **1998**, *53*, 893–899.
[20] N. Burzlaff, W. A. Schenk, *Eur. J. Inorg. Chem.* **1998**, 2055–2061.
[21] M. A. Cranswick, N. E. Gruhn, O. Oorhles-Steele, K. R. Ruddick, N. Burzlaff, W. A. Schenk, D. L. Lichtenberger, *Inorg. Chim. Acta* **2008**, *361*, 1122–1133.
[22] W. A. Schenk, N. Burzlaff, H. Burzlaff, *Z. Naturforsch., Teil B* **1994**, *49*, 1633–1639.
[23] A. Ishii, T. Ishida, N. Kumon, N. Fukuda, H. Oyama, N. Inamoto, F. Iwasaki, R. Okazaki, *Bull. Chem. Soc. Jpn.* **1996**, *69*, 709–717.
[24] W. A. Schenk, T. Stur, E. Dombrowski, *Inorg. Chem.* **1992**, *31*, 723–724.
[25] L. Horner, *Pure Appl. Chem.* **1980**, *52*, 843–858.
[26] H. Werner, *Angew. Chem.* **1983**, *95*, 932–954; *Angew. Chem. Int. Ed. Engl.* **1983**, *22*, 927–949.
[27] R. F. Jordan, J. Norton, *J. Am. Chem. Soc.* **1982**, *104*, 1255–1263.
[28] C. Creutz, N. Sutin, *J. Am. Chem. Soc.* **1988**, *110*, 2418–2427.
[29] J. H. Merrifield, J. M. Fernandez, W. E. Buhro, J. A. Gladysz, *Inorg. Chem.* **1984**, *23*, 4022–4029.
[30] J. M. Fernandez, J. A. Gladysz, *Organometallics* **1989**, *8*, 207–219.
[31] M. A. Esteruelas, A. M. López, E. Oñate, E. Royo, *Inorg. Chem.* **2005**, *44*, 4094–4103.
[32] M. A. Dewey, Y. Zhou, Y. Liu, J. A. Gladysz, *Organometallics* **1993**, *12*, 3924–3932.
[33] N. Burzlaff, W. A. Schenk, *Eur. J. Inorg. Chem.* **1999**, 1435–1443.
[34] S. Dilsky, W. A. Schenk, *Z. Naturforsch., Teil B* **2004**, *59*, 1093–1102.
[35] D. M. Dalton, C. M. Garner, J. M. Fernández, J. A. Gladysz, *J. Org. Chem.* **1991**, *56*, 6823–6829.
[36] N. Q. Mendez, J. W. Seyler, A. M. Arif, J. A. Gladysz, *J. Am. Chem. Soc.* **1993**, *115*, 2323–2334.
[37] G. A. Stark, J. A. Gladysz, *Inorg. Chem.* **1996**, *35*, 5509–5513.
[38] D. M. Dalton, J. M. Fernández, K. Emerson, R. D. Larsen, A. M. Arif, J. A. Gladysz, *J. Am. Chem. Soc.* **1990**, *112*, 9198–9212.
[39] W. A. Schenk, J. Bezler, *Eur. J. Inorg. Chem.* **1998**, 605–611.
[40] W. A. Schenk, J. Kümmel, I. Reuther, N. Burzlaff, A. Wuzik, O. Schupp, G. Bringmann, *Eur. J. Inorg. Chem.* **1999**, 1745–1756.

[41] W. A. Schenk, J. Bezler, N. Burzlaff, M. Hagel, B. Steinmetz, *Eur. J. Inorg. Chem.* **2000**, 287–297.
[42] W. A. Schenk, N. Kuhnert, *Z. Naturforsch., Teil B* **2000**, *55*, 527–535.
[43] F. Fehér, in: *Handbuch der Präparativen Anorganischen Chemie* (Ed.: G. Brauer), Enke, Stuttgart, **1960**, pp. 325–326.
[44] W. Wolfsberger, *Chem.-Ztg.* **1986**, *112*, 450–452.
[45] K.-H. Geiß, D. Seebach, B. Seuring, *Chem. Ber.* **1977**, *110*, 1833–1851.
[46] G. M. Sheldrick, *Acta Crystallogr., Sect. A* **2008**, *64*, 112–122.

Received: October 16, 2009

DOI: 10.1002/ejic.200900900

Reactions of Unsaturated Nickel–Molybdenum and –Tungsten Complexes with Primary Amines: Chemoselective N-Coordination to Nickel To Give the First Structurally Characterised Primary Amine–Organonickel Complexes

Carmen Cuncillos Carmona,[a] Sarah Clapham,[b] Mathieu Gonidec,[a] Vincent Ritleng,[a] Pierre Braunstein,[b] Richard Welter,[c] and Michael J. Chetcuti*[a]

Keywords: Nickel / Amines / Hydrogen bonding / Heterodimetallic compounds / Group 6 metals

The reactions of selected primary amines with the unsaturated heterodimetallic complex [(η-C$_5$Me$_5$)Ni(μ-CO)Mo(CO)$_2$(η-C$_5$H$_5$)](*Ni*$\overset{\cdots}{-}$*Mo*) (**1a**) were investigated. Primary amines react with this heterodimetallic complex to form unstable adducts, which are in equilibrium with the free amine and complex **1a** in solution. Complex **1b**, the nickel–tungsten analogue of **1a**, reacts similarly with benzylamine. The position of the equilibrium shifts in favour of the adducts at low temperature, and crystals of the allylamine and benzylamine complexes [(η-C$_5$Me$_5$)(RNH$_2$)Ni–Mo(CO)$_3$(η-C$_5$H$_5$)], (**2a**, R = C$_3$H$_5$; **4a**, R = PhCH$_2$) could be isolated. Their structures were established by single-crystal X-ray diffraction studies. The primary amines in complexes **2a** and **4a** are each coordinated, by means of their respective nitrogen atoms, to the nickel atom and thus provide the first structurally characterised examples of primary amine organometallic nickel complexes. The bonding of the amine to the heterodimetallic centre is in contrast to what has been observed with phosphorus-containing 2-electron donor ligands, in which the phosphane ligand is coordinated to the group 6 metal atom. A measure of the Ni–N bond dissociation enthalpy for the (benzylamine)nickel–tungsten complex **4b** was obtained from a VT ^{1}H NMR spectroscopic study and was found to be –149 ± 10 kJ mol^{-1}. *N*-Bonded hydrogen atoms in both **2a** and **4a** exhibit intermolecular hydrogen-bonding interactions in the solid state with carbonyl oxygen atoms of adjacent molecules. These molecules exist as loosely bound dimers in the solid state. Complex **2a** (C$_{21}$H$_{27}$MoNNiO$_3$) crystallises in the monoclinic space group $P2_1/n$ with a = 10.1922(2), b = 11.1538(3), c = 18.8053(4) Å, β = 90.777(2)° and Z = 4. Complex **4a** (C$_{25}$H$_{29}$MoNNiO$_3$) also crystallises in the monoclinic space group $P2_1/n$ with a = 12.0840(4), b = 10.9490(4), c = 17.4930(6) Å, β = 90.396(3)° and Z = 4.

Introduction

The complex [(η-C$_5$Me$_5$)Ni$\overset{\cdots}{-}$Mo(CO)$_3$(η-C$_5$H$_5$)] (**1a**) is both heterodimetallic and unsaturated. It can also be formulated as [(η-C$_5$Me$_5$)Ni(μ-CO)Mo(CO)$_2$(η-C$_5$H$_5$)](*Ni=Mo*) (**1a**) and can be considered to contain a formal Ni=Mo double bond.[1] Despite the rich chemistry exhibited by **1a**,[2,3] some of its simple coordination chemistry has still not yet been fully investigated. Complex **1a**, according to the HSAB concept introduced by Pearson more than 40 years ago,[4] contains a "harder" metallic element (Mo) bonded to a "softer" metal (Ni). Simple two-electron donor ligands such as di- and trialkylphosphanes add reversibly to this complex and to its Ni–W analogue **1b**.[5] Structural data have so far been restricted to the allyldiphenylphosphane adduct of **1a**[6] and show that the group 15 donor ligand is indeed bonded to the molybdenum atom. Spectroscopic data on Ni–W analogues of **1a** with other phosphane ligands, notably the magnitude of the ^{183}W-^{31}P coupling, indicate that two-electron donor phosphorus ligands such as PMe$_3$ and PMe$_2$Ph, coordinate to the group 6 metal atom (Scheme 1).[5] Reactions of **1a** and related Ni–W analogues with potentially bridging ligands (CO, *t*BuNC, CH$_2$, SO$_2$) afford complexes in which the ligand is either bridging (CH$_2$, SO$_2$)[5,7,8] or else undergoes rapid bridge/terminal exchange (CO, *t*BuNC, Scheme 1).[5,7] For the *t*BuNC adduct NiW(CO)$_3$(*t*BuNC)(η-C$_5$H$_5$)(η-C$_5$Me$_5$) resonances for isomers with bridging or with terminal *t*BuNC groups were observed in the IR spectrum.[5] Never having previously observed terminal ligand coordination to the nickel atom, we believed that amine adducts of **1a** would also contain Mo–N bonds.

In view of the above summary, the research discussed below had two goals. A primary goal was the structural characterisation of an adduct of **1a** coordinated to an N-donor ligand by means of a simple two-electron bond in

---

[a] Laboratoire de Chimie Organométallique Appliquée, UMR 7509 CNRS, Ecole Européenne de Chimie, Polymères et Matériaux, Université de Strasbourg,
25 rue Becquerel, 67087 Strasbourg, France
Fax: +33-3-68552639
E-mail: chetcuti@chimie.u-strasbg.fr
[b] Laboratoire de Chimie de Coordination, UMR 7177 CNRS, Institut de Chimie, Université de Strasbourg,
4 rue Blaise Pascal, 67070 Strasbourg, France
[c] Laboratoire DECOMET, UMR 7177 CNRS, Institut de Chimie, Université de Strasbourg,
4 rue Blaise Pascal, 67070 Strasbourg, France

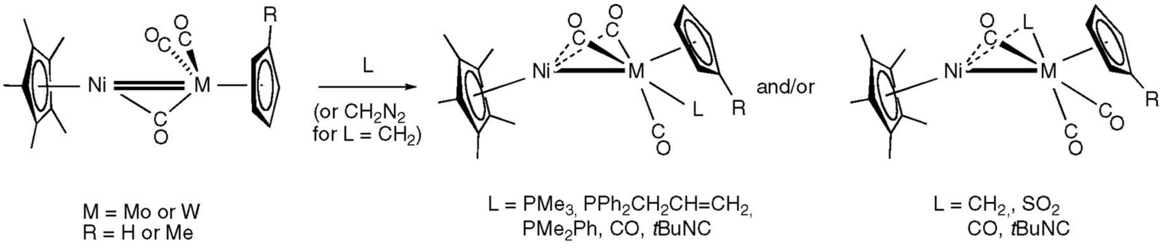

Scheme 1. Reactions of complexes **1a**, **1b** and of related [(η-C_5Me_5)Ni=W(CO)$_3$(η^5-C_5H_4Me)] species with two-electron donor ligands.[5–8]

order to establish whether there is coordination of the amine to the group 6 metal atom or to the nickel atom. Secondly, we believed that the reaction of **1a** with an N-donor ligand containing a pendant olefin functionality might, following initial N-coordination, lead to alkene coordination and/or activation. Allylamine, a sterically undemanding N-donor ligand was the initial target ligand for this study, since both goals were potentially achievable with this ligand. N-coordination of the allylamine to the nickel atom was indeed observed but without activation of the olefinic bond of the coordinated allylamine. Subsequently, the reactions of other primary amines with complexes **1a** and **1b** were investigated to see whether amine coordination to the nickel atom was in fact a general phenomenon.

Results and Discussion

Reactions of 1a and 1b with Primary Amines

When excess allylamine was added to a solution of **1a** in thf, the deep green-blue colour characteristic of **1a** in solution gave way to a purplish colour. The green-blue colour of **1a** reappeared when this solution was concentrated under reduced pressure. The ^{1}H NMR spectrum of an equimolar solution of **1a** and allylamine showed very broad resonances characteristic of a paramagnetic complex. Solutions of **1a** are paramagnetic and green-blue in colour,[1] so these observations suggest that coordination of the allylamine ligand to **1a** to give the new species **2a** is reversible. The mixture of the amine and **1a** showed broad poorly resolved peaks even at –25 °C which could not be readily assigned. Furthermore, mixtures of **1a** and allylamine decompose in solution and lead to the appearance of new uncharacterised signals in the ^{1}H NMR spectrum. Despite repeated attempts, it proved to be impossible to further characterise the reaction products spectroscopically, though an IR spectrum of a solution of **1a** and allylamine in diethyl ether could be obtained. The spectrum displays two strong ν(CO) peaks at 1879 and 1780 cm^{-1} (Table 1), indicating the presence of terminal and semi-bridging CO ligands. These results are consistent with the initial equilibrium reaction shown in Scheme 2.

Table 1. IR ν(CO) data for the complexes [(η-C_5Me_5)(RNH_2)Ni–M(CO)$_3$(η-C_5H_5)] (**2a**, **3a**, **4a** and **4b**). Data were obtained on solid samples except for **2a** (Et_2O solution).

Compound	ν(CO)$_{term.}$	ν(CO)$_{semi–bridg.}$
2a (R = CH_2=CHCH$_2$, M = Mo)	1879 (s)	1780 (s, br)
3a (R = *n*Pr, M = Mo)	1881 (s)	1737 (s, br.)
4a (R = PhCH$_2$, M = Mo)	1866 (s)	1739 (sh), 1741 (s, br.)
4b (R = PhCH$_2$, M = W)	1861 (s)	1733 (s, br)

An X-ray diffraction study was carried out on a single crystal of **2a**. The study (vide infra) established complex **2a** as [(η-C_5Me_5)($C_3H_5NH_2$)Ni–Mo(CO)$_3$(η-C_5H_5)], in which the allylamine is N-coordinated to the nickel atom (Figure 1). The molecule contains three molybdenum-bound CO ligands, two of which are semi-bridging to the nickel atom. Complex **2a** is unstable and decomposes, even in the solid state at room temperature under an inert gas. Elemental analysis could not be obtained.

Other primary amines also react reversibly with complex **1a**. When **1a** and *n*PrNH$_2$ are mixed, the colour of the resultant solution is also temperature- and concentration-de-

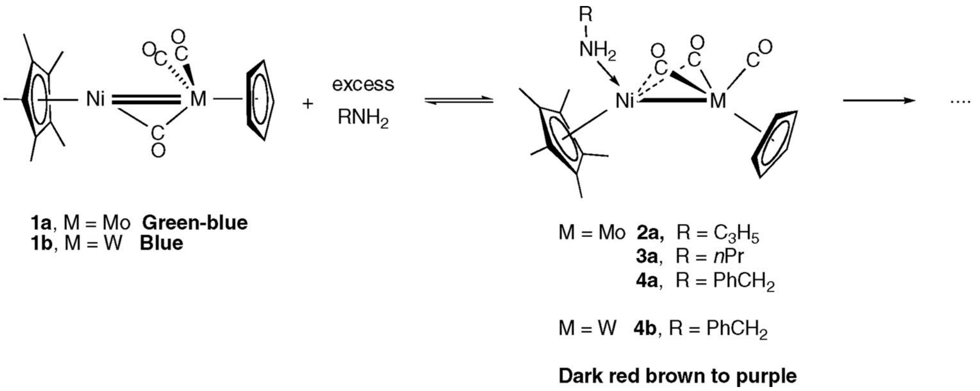

Scheme 2. Equilibria reactions of complexes **1** with some primary amines.

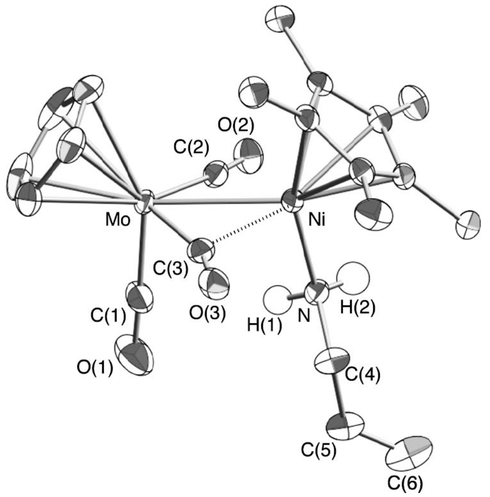

Figure 1. ORTEP plot of [(η-C_5Me_5)(CH_2=$CHCH_2NH_2$)Ni(μ-CO)Mo$(CO)_2$(η-C_5H_5)](*Ni–Mo*) (**2a**). Ellipsoids are shown at the 50% probability level. The only hydrogen atoms shown (as white spheres) are those bound to the nitrogen atom.

pendent. An orange solid **3a** could be precipitated from dark red concentrated solutions of **1a** and propylamine. The solid-state IR spectra of **3a** showed two small ν(NH) peaks and strong ν(CO) peaks. One ν(CO) peak appears in the terminal region of the IR spectrum (1881 cm^{-1}) and another peak (with a shoulder) is apparent in the bridging or semi-bridging CO region at 1737 cm^{-1}.[9] Such CO vibrations are comparable with the IR spectrum of **2a** which displays similar terminal and semi-bridging ν(CO) stretches (Table 1). Complex **3a** decomposes even in the solid state at room temperature. ^{1}H NMR spectroscopy at room temp. shows that solutions of **3a** lose amine to afford **1a** and free *n*PrNH_2 (i.e. only free *n*PrNH_2 was observed since **1a** is paramagnetic). When excess *n*PrNH_2 is present, amine, η-C_5H_5 and η-C_5Me_5 resonances can be observed. However the amine peaks lose all fine structure and are observed as broad featureless singlets. These results, when coupled with those of the allylamine reaction, are in line with the equilibrium depicted in Scheme 2.

A similar reaction of **1a** with the less volatile benzylamine afforded the somewhat more stable adduct [(η-C_5Me_5)($PhCH_2NH_2$)Ni–Mo$(CO)_3$(η-C_5H_5)] (**4a**), which was crystallised from the reaction mixture. An X-ray diffraction study on crystals of **4a** confirmed that the benzylamine coordinates to the nickel atom (Figure 2). The complex (vide infra for a discussion of the structure) has the same geometry as is found in complex **2a**, with a nickel-bound benzylamine ligand and two semi-bridging CO ligands. The related nickel–tungsten derivative [(η-C_5Me_5)($PhCH_2NH_2$)Ni–W$(CO)_3$(η-C_5H_5)] (**4b**) could also be harvested from the reaction of the Ni–W complex **1b** with benzylamine. Complexes **4a** and **4b** exhibited very similar solid-state IR spectra which mirror that of complex **3a**. They also appear to be the most stable of all the amine complexes in the solid state, perhaps because of the lower volatility of free benzylamine. The solution NMR spectra of complexes **4** are comparable and indicate that these complexes are also more stable than the allyl- and *n*-propylamine analogues in solution.

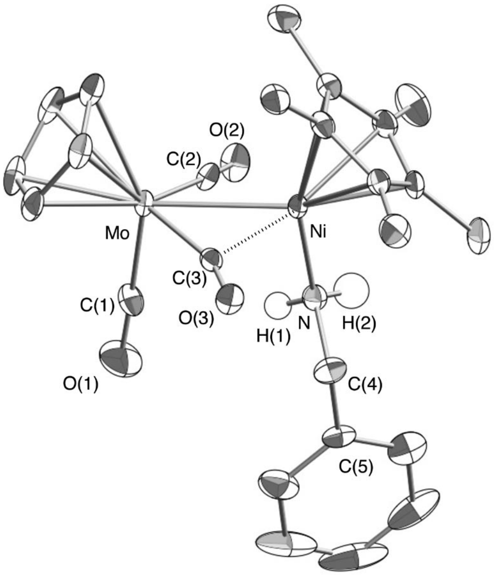

Figure 2. ORTEP plot of [(η-C_5Me_5)($PhCH_2NH_2$)Ni(μ-CO)-Mo$(CO)_2$(η-C_5H_5)](*Ni–Mo*) (**4a**). Ellipsoids are shown at the 50% probability level. The only hydrogen atoms shown (as white spheres) are those bound to the nitrogen atom.

Complexation Study of 1b with Benzylamine by VT ^{1}H NMR Spectroscopy

The equilibrium reaction between complex **1b** and benzylamine was investigated quantitatively by VT ^{1}H NMR spectroscopy. This reaction was selected since the benzylamine adducts appear to be the most stable ones. In addition, theoretical studies suggest that, in general, third-row transition metals form stronger bonds than second-row metals.[10] ^{1}H NMR spectra of an equimolar solution of **1b** and benzylamine in [D_8]thf were obtained over the +60 to –60 °C temperature range. The NMR analysis showed that at a 23 mM concentration at 20 °C, the solution consisted of only 5% **4b** (the rest of the equilibrium mixture being **1b** and free benzylamine). However, chilling this sample to –25 °C led to quantitative complexation of the amine to **1b**. In addition to the singlets corresponding to the η-C_5H_5 and η-C_5Me_5 ligands, Ph and CH_2 multiplets and the amine NH_2 proton signals were now also visible, with the latter signals at chemical shifts different from reported values for benzylamine. The enthalpy of the addition reaction (ΔH°_{rxn}) of the amine to **1b** was found to be -149 ± 10 kJ mol^{-1}.

Many factors (solvation, steric interactions, geometrical changes on coordination) may impact on ΔH_{rxn} but, nevertheless, a major contributor to this numerical value is the formation of the Ni–N bond. Measurements of nickel–ligand bond strengths have been obtained from ion cyclotron resonance (ICR) spectroscopy, and these results are thus all from the gas-phase with no solvation effects. In one study, the experimental $\Delta H°_{rxn}$ values (and the calculated values in parentheses) of the gas-phase reaction of (η-C_5H_5)Ni^+ with either NH_3 or $MeNH_2$ were found to be –234 (–233) and –222 (–221) kJ mol^{-1}, respectively.[11] Competition studies between two bases towards (η-C_5H_5)Ni^+ cations allowed the establishment of an absolute value of –219 ± 21 kJ mol^{-1} for the (η-C_5H_5)Ni^+–NH_3 reaction.[12] Later, theoretical calculations on (η-C_5H_5)- and (η-C_5Me_5)Ni ligand systems gave results consistent with these gas-phase experimental results.[13] The value we report here for the Ni–N bond enthalpy provides a measure of this value in solution and is ca. 25 % smaller (in absolute value) than the results obtained in the gas phase.

Structural Data for Complexes 2a and 4a

Ellipsoidal plots of the structures of [(η-C_5Me_5)(RNH_2)-Ni–Mo(CO)$_3$(η-C_5H_5)] (R = C_3H_5, **2a**; $PhCH_2$, **4a**) are shown in Figures 1 and 2, respectively. The two structures are comparable and are depicted in the same orientation to emphasise their similarity. Lists of key bond lengths and angles are collected in Table 2.

Table 2. Key geometrical parameters of complexes **2a** and **4a**, with ESDs in parentheses.[a]

Atom distances [Å] and angles [°]	**2a**	**4a**
Mo–Ni	2.7322(5)	2.7200(7)
Mo–C(1)	1.925(4)	1.919(6)
Mo–C(2)	1.963(3)	1.978(5)
Mo–C(3)	1.965(3)	1.977(5)
Ni–N	1.976(3)	1.988(4)
Ni···C(2)	2.348(3)	2.337(5)
Ni···C(3)	2.141(3)	2.136(5)
Mo–C(η-C_5H_5, mean)	2.360	2.370
Mo–(η-C_5H_5)$_{centroid}$	2.036	2.045
Ni–C(η-C_5Me_5, mean)	2.157	2.154
Ni–(η-C_5Me_5)$_{centroid}$	1.783	1.779
H(2)···O(2′)[b]	2.372	2.441
H(1)···O(1′)	2.818	2.937
H(3)···O(3′)	2.958	2.850
Mo–C(1)–O(1)	178.1(3)	177.8(5)
Mo–C(2)–O(2)	169.0(3)	169.5(4)
Mo–C(3)–O(3)	159.8(3)	159.2(4)
Ni–Mo–C(1)	97.35(11)	96.69(16)
Ni–Mo–C(2)	57.25(9)	57.08(14)
Ni–Mo–C(3)	51.12(9)	51.15(14)
Mo–Ni–N	97.64(9)	98.70(15)
C(1)–Mo–Ni–N	6.2(2)	8.9(2)
(η-C_5H_5)$_{centroid}$–Mo–Ni–(η-C_5Me_5)$_{centroid}$	13.5	14.1
N–H(2)···O(2′)[b]	159	161
N–H(1)···O(1′)	150	144

[a] The same labelling scheme is used for **2a** and **4a**. [b] Intermolecular interactions.

The two complexes exhibit very similar geometries in the solid state and, in addition, equivalent intermolecular interactions are seen in both structures. Both complexes contain (η-C_5Me_5)Ni groups bonded to Mo(CO)$_3$(η-C_5H_5) moieties. Both amines are κ^1-coordinated to the nickel atom solely by the nitrogen atom: there are no olefinic or benzylic interactions with the dimetal centre. Three CO ligands are bound to the molybdenum atom, and two of them interact with the nickel atom in a semi-bridging fashion. The nickel interactions with C(3)–O(3) are significant and are manifested by the nonlinear Mo–C(3)–O(3) angles of just under 160° and short Ni···C(3) distances of around 2.14 Å for both complexes. Nickel interactions with carbonyl group C(2)–O(2) are also present in both molecules but are less significant and are therefore not represented in the figures. The Ni–Mo bond lengths of 2.7321(5) and 2.7200(7) Å are in the upper range of known Ni–Mo single-bond lengths but, nevertheless, remain consistent with Ni–Mo single-bond lengths.[6a,6b]

Both molecules are almost bisected by a noncrystallographically imposed mirror plane that contains the Ni–Mo bond, the two dienyl ring centroids, the terminal CO ligand C(1)–O(1) and the Ni–N bond. Thus, in each structure, the Ni–N bond almost eclipses the terminal Mo–C(1) bond [N–Ni–Mo–C(1) 6.2 and 8.9° for **2a** and **4a**, respectively]. However, the hydrogen atoms on the nitrogen atom and the allyl or benzyl groups do not lie in this pseudo plane – their skewed orientation allows fairly strong *inter*molecular hydrogen bonds and weaker *intra*molecular N–H···O interactions to take place in both molecules. These interactions are somewhat more pronounced in complex **2a**. One of the N–H hydrogen atoms interacts with the CO group oxygen atom of a neighbouring molecule, and this is manifested in relatively short *inter*molecular N–H···O distances [H(2)···O(2′) 2.372 Å for **2a**; 2.441 Å for **4a**] and an N–H(2)···O(2′) angle of 159° (**2a**) and 161° (**4a**). The other amine N–H bonds exhibit weaker *intra*molecular interactions with the oxygen atoms of the other Mo–CO ligands. Key portions of the two molecules showing the primary intermolecular interactions are depicted in Figure 3.

In contrast to other structurally characterised complexes with a Cp†Ni–MCp† skeleton (M = Mo or W; Cp† = η-C_5H_5, η-C_5H_4Me or η-C_5Me_5) with two bridging/semi-bridging CO ligands, the η-C_5H_5 and η-C_5Me_5 ligands are in a *cis* conformation in both complexes [the (η-C_5Me_5)$_{cent.}$–Ni–Mo–(η-C_5H_5)$_{cent}$ torsion angles are 13.5° and 14.1° for **2a** and **4a**, respectively]. This *cisoid* conformation allows pairs of molecules of both complexes to approach each other closely, and it is this geometry that allows the intermolecular H-bonding interactions to take place.

The C–C bonds of the η-C_5Me_5 ligand are not all the same. In both structures, "allyl-ene"-type distortions of this ligand can be observed (see Figure 4). Such distortions have been seen occasionally in other η-C_5H_5 and η-C_5Me_5 structures of nickel and have been explained by a significant energy difference between the "in-plane" and "out-of-plane" (η-C_5H_5)M fragment orbitals in (η-C_5H_5)ML_2 systems.[14–16] The "ene" carbon atoms and the central atom of the "allyl" portion of the η-C_5Me_5 ligand in complexes **2a** and **4a** both exhibit longer Ni–C distances than what is seen for the other two η-C_5Me_5 ring carbon atoms. No such

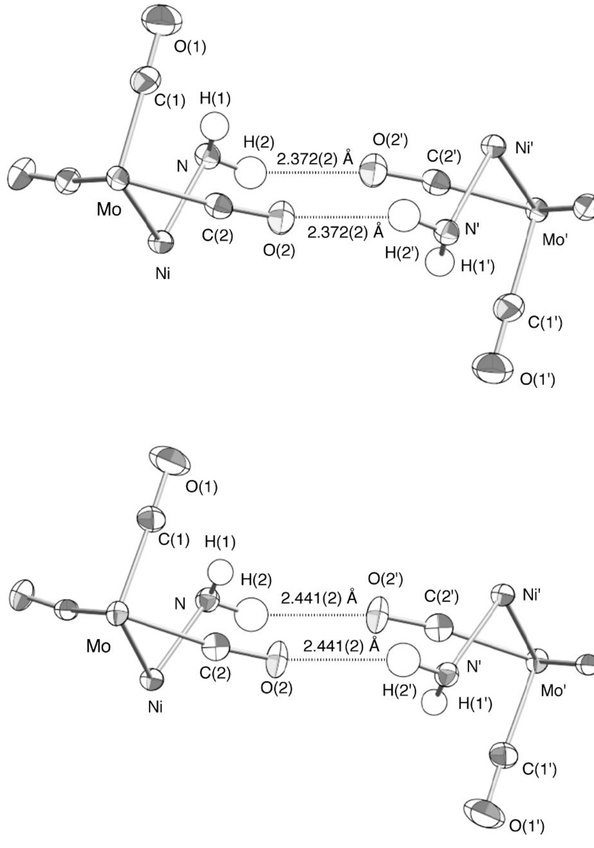

Figure 3. H-bonded interactions between pairs of nitrogen-bound H atoms and O atoms of a carbonyl group of a neighbouring molecule in the relevant portions of **2a** (top) and **4a** (bottom). Each pair of molecular fragments is shown in the same orientation. Intramolecular H(1)···O(1′) and H(1)···O(3′) distances are longer: 2.818 and 2.958 Å, respectively, for **2a**, and 2.937 and 2.850 Å, respectively, for **4a**.

distortions are seen in the molybdenum-bound C_5H_5 ligands: in this case, the five C–C bonds are statistically identical.

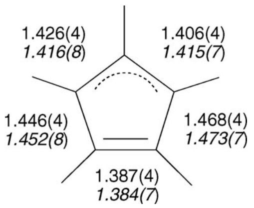

Figure 4. "Allyl-ene" distortions in the η-C_5Me_5 ligands of **2a** and **4a**. Distances are in Å with ESDs in parentheses. Those of **4a** are italicised.

There are, to the best of our knowledge, no examples of structurally characterised primary amine organometallic complexes of nickel. A theoretical study predicts an average Ni–N distance of 1.968 Å in $[(\eta\text{-}C_5H_5)Ni\text{–}(NH_nMe_{3-n})]^+$ (n = 0–3) cations.[13] This value is close to the $(\eta\text{-}C_5Me_5)Ni$–N distances of 1.976(3) Å and 1.988(4) Å found in **2a** and **4a**, respectively. We are aware of only two reports of structurally characterised organometallic species with Ni–NH bonds. Thus, the Ni–N distances in **2a** and **4a** are comparable but slightly shorter than the Ni–N distances of 1.995(3) and 2.002(3) Å found in the complex $[Ni(Et_2NH)_2\{\eta^3\text{-}C_3H_4(2\text{-}CONEt_2)\}]$, and to 1.984(5) Å in the related complex $[Ni(Et_2NH)I\{\eta^3\text{-}C_3H_4(2\text{-}CH_2CHMeC(O)NEt_2)\}]$.[17] In the three structurally characterised μ-amido complexes $[(\eta\text{-}C_5Me_4Et)Ni(\mu\text{-}NHR)_2Ni(\eta\text{-}C_5Me_4Et)]$ (R = *p*-tolyl, 2,6-xylyl, *t*Bu), the Ni–N distances are 1.951(3) and 1.950(3) Å (R = *p*-tolyl), 1.957(5) and 1.962(6) Å (R = 2,6-xylyl), and 1.944(2) and 1.942(2) Å (R = *t*Bu).[16] These values are slightly smaller than the distances of 1.976(3) and 1.988(4) Å observed in **2a** and **4a**, respectively. An older crystallographic study of the triangular paramagnetic cluster $[Ni_3(\eta\text{-}C_5H_5)_3(\mu_3\text{-}NBu)]$ revealed average Ni–N distances of 1.96(2) Å.[18] Nickel–amine coordination complexes exhibit longer Ni–N bonds. Thus, for example, nickel(II) complexes with cyclotriazane ligands and coordinated *n*-propylamine groups exhibit Ni–N(nPrNH$_2$) distances of 2.049(7) and 2.059(7) Å. The cyclotriazane Ni–N distances are 0.15–0.20 Å longer.[19] The observed values for Ni–N distances in complexes **2a** and **4a** are quite comparable to the Ni–N$_{\text{amine}}$ distances given here.

Complex **1a** has been shown to activate methyl acrylate in a unique manner. Reaction with this olefin afforded a methyl acrylate "dimer" ligand that is allylically bound to a molybdenum atom. The new ligand was obtained from the coupling of two methyl acrylate units, and a μ$_3$-alkylidyne cluster was also formed in the reaction.[20] An interaction with, and an activation of the C=C bond in allylamine by **1a**, was conceivable. However, the solid-state structure of **2a** reveals that the olefinic group does not interact with any of the metal atoms present.

Conclusions

Reactions of simple two-electron donor ligands with the unsaturated complexes **1** are complicated. Coordination to the group 6 or to the group 10 metal atom is possible. For most two-electron donor ligands, the donors coordinate to the group 6 metal atom. Spectroscopic evidence indicates that even the N-donor ligand pyridine coordinates to the group 6 metal atom.[5] In addition, we have previously reported that the reaction of $[(\eta\text{-}C_5H_5)Ni(PMe_3)Cl]$ with $[W(CO)_3(\eta\text{-}C_5H_4Me)]^-$ results in an unusual PMe_3 migration reaction to give $[(\eta\text{-}C_5H_5)Ni(\mu\text{-}CO)_2W(CO)\text{-}(PMe_3)(\eta\text{-}C_5H_4Me)]$ with a now tungsten-bound PMe_3 group.[5] This again suggests a greater thermodynamic stability for complexes in which the ligand is bound to a group 6 metal atom.

Nevertheless, the research reported here demonstrates for the first time that primary amine ligands do coordinate to the nickel atom in the dimetallic complexes **1**. Complexes **2a** and **4a** are the first structurally characterised primary amine organometallic complexes of nickel. In addition to the nickel-bound amine ligands, the diffraction studies also show that **2a** and **4a** exist as loosely bound H-bonded dimers in the solid state.

All the complexes reported here are isolable in the solid state but lose amine and are significantly dissociated to the unsaturated heterodimetallic species and the free amine in solution at ambient temperature. The extreme oxygen sensitivity of all these complexes in solution results partly from the presence of the highly air-sensitive unsaturated complex **1a** or **1b** that is present in equilibrium with the free ligand. Further slow reaction with the amine also subsequently takes place, but despite repeated attempts, we have been unable to isolate any other products. A simple isomerisation to a group 6 metal atom bound primary amine dimetallic complex is unlikely. A variable-temperature NMR study of the reaction between the nickel–tungsten analogue of **1a** and benzylamine allowed some thermodynamic parameters of this equilibrium to be evaluated and compared with the results of ICR gas-phase studies.

Experimental Section

General: All reactions were carried out under dry argon by using standard Schlenk techniques. Solvents were distilled from appropriate drying agents under argon prior to use. Solution ^{1}H NMR spectra were recorded with FT Bruker Ultra Shield 300 and FT Bruker-Spectrospin 400 spectrometers operating at 300.13 or 400.14 MHz, at room temperature unless otherwise stated. The chemical shifts are referenced to the residual deuterated solvent peaks. Chemical shifts (δ) are expressed in ppm. The ^{1}H NMR variable-temperature experiment with complex **4b** was recorded at 400.14 MHz in [D$_8$]-thf from –60 to +60 °C. The IR spectrum of **2a** was recorded with a Perkin–Elmer 1600 FTIR spectrometer by using KBr pellets. The ATR-IR spectra of **3a**, **4a** and **4b** were recorded with a Perkin–Elmer Spectrum One spectrometer. Vibrational frequencies are expressed in cm^{-1}. Commercial amines were used as received but were degassed by means of three freeze-pump-thaw cycles and stored under argon. Complexes **1** were prepared according to published procedures.[1,2]

Reaction of [(η-C$_5$Me$_5$)Ni(μ-CO)Mo(CO)$_2$(η-C$_5$H$_5$)]($Ni\overset{\cdots}{-}Mo$) (1a) with Allylamine. Synthesis of [(η-C$_5$Me$_5$)(CH$_2$=CHCH$_2$NH$_2$)Ni–Mo(CO)$_3$(η-C$_5$H$_5$)](*Ni–Mo*) (2a): Allylamine (0.4 mL, 5.32 mmol) was added dropwise to a solution of freshly prepared **1a** (308 mg, 0.70 mmol) in thf (15 mL). An immediate colour change from blue-green to burgundy was observed. The solution was stirred at ambient temperature for 30 min, and then the solvent volume was reduced to a minimum in vacuo. Slow diffusion of degassed pentane, containing a drop of allylamine, into this thf solution at –20 °C afforded dark green crystals of **2a** (38 mg, 0.077 mmol, 11 %).

Reaction of [(η-C$_5$Me$_5$)Ni(μ-CO)Mo(CO)$_2$(η-C$_5$H$_5$)]($Ni\overset{\cdots}{-}Mo$) (1a) with *n*-Propylamine. Synthesis of [(η-C$_5$Me$_5$)(*n*PrNH$_2$)Ni–Mo(CO)$_3$(η-C$_5$H$_5$)](*Ni–Mo*) (3a): *n*-Propylamine (0.8 mL, 0.95 mmol) was added dropwise to a solution of freshly prepared **1a** (415 mg, 0.95 mmol) in pentane (7 mL). An immediate colour change from blue-green to dark red ensued. The solution was stirred at ambient temperature overnight, during which time an orange solid deposited. The solvent was then removed and the solid washed with cold pentane (2× 2 mL) to give the thermally unstable complex **3a** (432 mg, 0.86 mmol, 90 %). IR [ν(NH), ATR]: $\tilde{\nu}$ = 3319 (w), 3270 (w) cm^{-1}. ^{1}H NMR (3-fold molar excess of *n*PrNH$_2$, CDCl$_3$, 300.13 MHz): δ = 4.65 (C$_5$*H*$_5$), 2.26 (br., C*H*$_2$N), 1.78 (C$_5$Me$_5$), 0.98 (br., C*H*$_2$Me), 0.58 (br., *Me*) ppm. The N*H*$_2$ signals were not observed.

Reaction of [(η-C$_5$Me$_5$)Ni(μ-CO)Mo(CO)$_2$(η-C$_5$H$_5$)]($Ni\overset{\cdots}{-}Mo$) (1a) with Benzylamine. Synthesis of [(η-C$_5$Me$_5$)(PhCH$_2$NH$_2$)Ni–Mo(CO)$_3$(η-C$_5$H$_5$)](*Ni–Mo*) (4a): Benzylamine (0.14 mL, 0.76 mmol) was added dropwise to a green-blue solution of freshly prepared **1a** (333 mg, 0.76 mmol) in pentane (7 mL). An immediate colour change from blue-green to brown was observed. After 5 min, precipitation of a purple crystalline solid was observed. The solution was removed by syringe and the solid was washed with pentane (2× 2 mL) and dried in vacuo to give air-sensitive **4a** (248 mg, 0.45 mmol, 59 %). IR [ν(NH), ATR]: $\tilde{\nu}$ = 3310 (w), 3261 (w) cm^{-1}. ^{1}H NMR (CDCl$_3$, 300.13 MHz): δ = 7.59 and 7.20 (m, 5 H, Ph), 5.19 (5 H, C$_5$*H*$_5$), 1.82 (15 H, C$_5$Me$_5$) ppm. The C*H*$_2$ and N*H*$_2$ resonances were not observed.

Reaction of [(η-C$_5$Me$_5$)Ni(μ-CO)W(CO)$_2$(η-C$_5$H$_5$)]($Ni\overset{\cdots}{-}W$) (1b) with Benzylamine. Synthesis of [(η-C$_5$Me$_5$)(PhCH$_2$NH$_2$)Ni–W(CO)$_3$(η-C$_5$H$_5$)](*Ni–W*) (4b): Benzylamine (1.0 mL, 9.1 mmol) was added dropwise to solid **1b** (180 mg, 0.34 mmol) under agron in a Schlenk tube. The solution became red-violet in colour. After 10 min, a thf/pentane (1:8) mixture was added (9 mL), and precipitation of a red-violet solid ensued. (Precipitation is difficult as the complex is very soluble in both thf and benzylamine, and while the complex is sparingly soluble in pentane, this liquid is immiscible with benzylamine.) The solid was washed with pentane (3× 5 mL) and dried rapidly in vacuo to give air-sensitive **4b** (65 mg, 0.103 mmol, 30 %). IR [ν(NH), ATR]: $\tilde{\nu}$ = 3307 (w), 3257 (w) cm^{-1}. ^{1}H NMR ([D$_8$]thf, 400 MHz, –20 °C): δ = 7.23–7.12 (m, 5 H, Ph), 5.39 (5 H, C$_5$H$_5$), 3.27 and 3.25 (m, 2 H, *CH*$_2$), 1.50 (15 H, C$_5$Me$_5$), 1.28 (s, 2 H, N*H*$_2$) ppm.

Determination of the Enthalpy of the Reaction of [(η-C$_5$Me$_5$)Ni(μ-CO)W(CO)$_2$(η-C$_5$H$_5$)]($Ni\overset{\cdots}{-}W$) (1b) with Benzylamine: A sample of **4b** (5.0 mg, 0.0092 mmol) was dissolved in [D$_8$]thf (400 µL) to give a solution of 23 mmol L^{-1}. The VT ^{1}H NMR spectrum was recorded between –65 and +60 °C. The concentrations of free and coordinated amine were determined by signal integration of the free and coordinated amine protons, and the equilibrium constant *K* for the reaction could thus be obtained at various temperatures. By using the thermodynamic relationship $\Delta G^\circ = \Delta H^\circ - T\Delta S^\circ = -RT(\ln K)$, values of ΔH and ΔS can be obtained from a plot of $\ln K$ vs. T.

Crystallographic Data Collection and Structure Determinations: Single crystals of **2a** and **4a** suitable for X-ray diffraction studies were obtained from slow diffusion of a pentane/allylamine solution into a thf solution (**2a**) or of pentane into a thf solution (**4a**), both at –25 °C. Data for all compounds were collected at 173(2) K with a Nonius Kappa-CCD area detector diffractometer with graphite-monochromated Mo-K_α radiation (λ = 0.71073 Å). A summary of crystal data, data-collection parameters and structure refinements for the two molecules is given in Table 3. Diffraction data for cell parameters were determined from reflections taken from one set of ten frames (1.0° steps in ϕ angle), each at 20 s exposure. Data were processed with HKL2000.[21] All structures were solved by direct methods with SHELXS-97 and refined against F^2 for all reflections by using SHELXL-97 software.[22] Multiscan absorption corrections (MULscanABS in PLATON)[23] were applied for **2a** and **4a**. All non-hydrogen atoms were refined with anisotropic displacement parameters. All hydrogen atoms (except those of the NH$_2$ group in both structures) were generated according to stereochemistry and refined as fixed contributors by using a riding model in SHELXL97.[22] CCDC-742150 (for **2a**) and -742151 (for **4a**) contain the supplementary crystallographic data for this paper. These data can be obtained free of charge from The Cambridge Crystallographic Data Centre via www.ccdc.cam.ac.uk/data_request/cif.

Table 3. Crystal, data-collection and refinement parameters for the complexes [(η-C_5Me_5)(RNH_2)Ni–Mo$(CO)_3$(η-C_5H_5)] (**2a**, R = CH_2=$CHCH_2$; **4a**, R = $PhCH_2$).

	2a	**4b**
Empirical formula	$C_{21}H_{27}MoNNiO_3$	$C_{25}H_{29}MoNNiO_3$
Formula mass	496.09	546.14
Space group	$P2_1/n$ (no. 14)	$P2_1/n$ (no. 14)
a [Å]	10.1922(2)	12.0840(4)
b [Å]	11.1538(3)	10.9490(4)
c [Å]	18.8053(4)	17.4930(6)
β [°]	90.777(2)	90.396(3)
V [Å^3]	2137.62(8)	2314.40(14)
Z	4	4
T [K]	173(2)	173(2)
λ [Å]	0.71073	0.71073
$D_{\text{calcd.}}$ [g cm^{-3}]	1.541	1.567
μ [cm^{-1}]	1.487	1.381
$R(F_o^2)$	0.0738	0.0867
$R_w(F_o^2)$	0.1157	0.1601

Acknowledgments

Financial support from the Centre National de la Recherche Scientifique (CNRS), the Ministère de la Recherche et de l'Enseignement Supérieur, the University of Strasbourg (former Université Louis Pasteur), and the Région Alsace is gratefully acknowledged. C. C. C. and S. C. gratefully acknowledge funding from the Erasmus European exchange program.

---

[1] M. J. Chetcuti, B. E. Grant, P. E. Fanwick, M. J. Geselbracht, A. M. Stacy, *Organometallics* **1990**, *9*, 1343.

[2] E. Brenner, M. J. Chetcuti, *Commun. Inorg. Chem.* **2006**, *27*, 145.

[3] V. Ritleng, M. J. Chetcuti, *Chem. Rev.* **2007**, *107*, 797.

[4] R. G. Pearson, *J. Am. Chem. Soc.* **1963**, *85*, 3533.

[5] M. J. Chetcuti, K. J. Deck, P. E. Fanwick, J. C. Gordon, B. E. Grant, *Organometallics* **1992**, *11*, 2128.

[6] a) N. M. Boag, P. Braunstein, M. J. Chetcuti, S. Clapham, R. Welter, *Organometallics* **2008**, *27*, 1758 and cited references; b) P. Braunstein, M. J. Chetcuti, R. Welter, *C. R. Acad. Sci. IIc* **2002**, *5*, 67.

[7] M. J. Chetcuti, B. E. Grant, P. E. Fanwick, *Organometallics* **1990**, *9*, 1345.

[8] A. F. Bartlone, M. J. Chetcuti, R. Navarro III, M. Shang, *Inorg. Chem.* **1995**, *34*, 980.

[9] (η-C_5Me_5)Ni complexes are highly electron-rich, and the increased back-bonding caused by the high electron density often shifts the observed ν(CO) frequencies in such species by 50–100 cm^{-1} lower than expected.

[10] T. Ziegler, *Can. J. Chem.* **1995**, *73*, 743.

[11] R. S. Drago, D. C. Ferris, N. Wong, *J. Am. Chem. Soc.* **1990**, *112*, 8953.

[12] R. R. Corderman, J. L. Beauchamp, *J. Am. Chem. Soc.* **1976**, *98*, 3998.

[13] L. Throckmorton, D. S. Marynick, *J. Phys. Chem.* **1988**, *92*, 645.

[14] M. E. Smith, R. A. Andersen, *J. Am. Chem. Soc.* **1998**, *120*, 11119.

[15] A. E. Smith, *Inorg. Chem.* **1974**, *13*, 165.

[16] P. L. Holland, R. A. Andersen, R. G. Bergman, *J. Am. Chem. Soc.* **1996**, *118*, 1092.

[17] H. Hoberg, G. Heger, C. Krüger, Y. H. Ysay, *J. Organomet. Chem.* **1988**, *348*, 261.

[18] N. Kamijyo, T. Watanabe, *Bull. Chem. Soc. Jpn.* **1974**, *47*, 373.

[19] P. B. Hitchcock, T. H. Lee, G. J. Leigh, *Inorg. Chim. Acta* **2003**, *355*, 168.

[20] P. Braunstein, M. J. Chetcuti, R. Welter, *Chem. Commun.* **2001**, 2508.

[21] Z. Otwinowski, M. Minor, *Methods Enzymol.* **1977**, *276*, 397.

[22] G. M. Sheldrick, *Acta Crystallogr., Sect. A* **2008**, *64*, 112.

[23] A. L. Spek, *J. Appl. Crystallogr.* **2003**, *36*, 7.

Received: September 10, 2009

DOI: 10.1002/ejic.200900940

1-D-Tin(II) Phenylchalcogenolato Complexes $^{1}_{\infty}[Sn(EPh)_2]$ (E = S, Se, Te) – Synthesis, Structures, Quantum Chemical Studies and Thermal Behaviour

Andreas Eichhöfer,*[a] Ji-Jun Jiang,[a,b] Heino Sommer,[c] Florian Weigend,[a] Olaf Fuhr,[a] Dieter Fenske,[a,c] Cheng-Yong Su,[b] and Gernot Buth[d]

Keywords: Tin / Chalcogens / Complexes / X-ray diffraction / TGA / Density functional calculations

A series of three 1-D-tin(II) phenylchalcogenolato complexes $^{1}_{\infty}[Sn(EPh)_2]$ (E = S, Se, Te) were synthesized in yields > 80 % by reaction of $SnCl_2$ with two equivalents of $PhESiMe_3$ in organic solvents. In the crystal the molecules form two different types of one-dimensional chains. In $^{1}_{\infty}[Sn(SPh)_2]$ the tin atoms are distorted trigonal pyramidal coordinated by sulfur atoms (two bonds within a monomer and one longer bond between neighbored monomers), while in $^{1}_{\infty}[Sn(EPh)_2]$ (E = Se, Te) the tin atoms show contacts to two neighbored monomers leading to a fourfold coordination of the tin atoms by either selenium or tellurium atoms. The bond situation is discussed on the basis of density functional calculations. Thermal treatment mostly leads to the formation of the corresponding phase pure tin(II) chalcogenides however sublimation plays an increasing role ongoing from the tellurolato to the thiolato complex especially for the use of vacuum conditions. The investigation of the volatile cleavage products reveals the occurence of more complex reactions in the gas phase than the formal stoichiometric cleavage of EPh_2 (E = S, Se, Te) with formation of SnE.

Introduction

Metal chalcogenolato complexes have attracted interest due to their rich structural chemistry,[1–3] their potential use as precursors for M/Se materials[4,5] and their relevance as models for active sites of chalcogen containing metalloproteins.[6,7]

Tin(IV)chalcogenolato complexes like $Sn(SPh)_4$,[8] $Sn(SePh)_4$[9,10] and $Sn(Se\text{-}2\text{-}NC_5H_4)_4$[11] as well as related tin(II) compounds like $[Sn\{ESi(SiMe_3)_3\}_2]_2$ (E = S, Se, Te)[12] and $[Sn(2\text{-}SeNC_5H_4)_2]_2$[11] have been studied in view of their use as precursor compounds for MOCVD of SnE and SnE_2 (E = S, Se) while the corresponding tin(II) compounds also attracted interest due to the synthesis of "carbene analogues" and the realisation of low coordination modes. Synthetic procedures for compounds with the general formula $Sn(ER)_2$ (E = S, Se, Te; R = organic group) are especially for thiolato complexes well established. With respect to the compounds under investigation $Sn(SPh)_2$[13–16] as well as $Sn(SePh)_2$[17] have been synthesized before while no report could be found for the tellurium analogue. However the structures of only a few compounds of this type are reported including monomeric $[Sn(S\text{-}2,4,6\text{-}tC_4H_9C_6H_2)_2]$,[18] dimeric $[Sn\{TeSi(SiMe_3)_3\}_2]_2$[12] and $[Sn(2\text{-}SeNC_5H_4)_2]_2$,[11] trimeric $[Sn(S\text{-}2,6\text{-}(iC_3H_7)_2C_6H_3)_2]_3$ as well as polymeric $^{1}_{\infty}[Sn(StC_4H_9)_2]$[19] and $^{1}_{\infty}[Sn(SnC_4H_9)_2]$.[20] The build up of the structures is mostly determined by the stereochemical effect of the "inert" electron pair and the interplay of the steric demand of the organic ligands vs. the tendency of tin(II) to realize higher coordination modes than two together with a minor influence of the kind of chalcogen element.

Reported here are the synthesis of three 1-D-Tin(II) phenylchalcogenolato complexes $^{1}_{\infty}[Sn(EPh)_2]$ (E = S, Se, Te) by reaction of $SnCl_2$ with two equivalents of $PhESiMe_3$ in organic solvents along with their structural characterization and an investigation of their thermal behaviour.

Results and Discussion

Synthesis and Structure

The tin(II) chalcogenolato complexes $^{1}_{\infty}[Sn(SPh)_2]$ (**1**), $^{1}_{\infty}[Sn(SePh)_2]$ (**2**) and $^{1}_{\infty}[Sn(TePh)_2]$ (**3**) were prepared by reaction of anhydrous $SnCl_2$ with two equivalents of $PhESiMe_3$ (E = S, Se, Te) in dme for **1** and **2** or thf for **3** in accordance to Scheme 1.

---

[a] Institut für Nanotechnologie, Forschungszentrum Karlsruhe,
Postfach 3640, 76021 Karlsruhe, Germany
Fax: +49-7247-82-6368
E-mail: eichhoefer@int.fzk.de
[b] MOE Laboratory of Bioinorganic and Synthetic Chemistry and State Key Laboratory of Optoelectronic Materials and Technologies, School of Chemistry and Chemical Engineering, Sun Yat-Sen University,
Guangzhou 510275, P. R. China
[c] Institut für Anorganische Chemie der Universität,
Engesserstrasse, Geb. 30.45, 76128 Karlsruhe, Germany
[d] Institut für Synchrotronstrahlung (ISS), Forschungszentrum Karlsruhe GmbH,
Postfach 3640, 76021 Karlsruhe, Germany

Supporting information for this article is available on the WWW under http://dx.doi.org/10.1002/ejic.200900940.

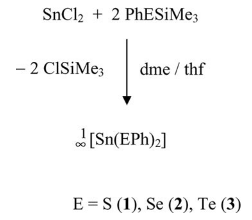

Scheme 1.

1 crystallizes in the orthorhombic space group *Pca*2_1 (Table 3). In the crystal structure the $Sn(SPh)_2$ units of **1** are μ_2-bridged in one dimension by one of the phenylthiolato ligands (S(2)) to form infinite chains along *a* (Figure 1) while the other SPh^- group coordinates the tin atom as a terminal ligand. Two of the three Sn–S distances Sn(1)–S(1) [251.8(2) pm] and Sn(1)–S(2) [257.7(2) pm] are distinctly smaller than the contact between Sn(1) and S(2)′ with 273.1(2) pm. Although these shorter distances are slightly longer than the Sn–S bond [243.5(1) pm] found in monomeric $[Sn(S\text{-}2,4,6\text{-}tC_4H_9C_6H_2)_2]$[18] one can therefore better describe the structure as consisting of monomeric $Sn(SPh)_2$ units which are linked by two additional weaker sulfur to tin donor-acceptor bonds to form the polymeric chains (see chapter Quantum Chemical Considerations). This leads in summary to a distorted trigonal pyramidal coordination around the tin atom [S–Sn(1)–S angles: S(1)–Sn(1)–S(2) 77.16(6), S(1)–Sn(1)–S(2)′ 92.68(6), S(2)–Sn(1)–S(2)′ 87.58(5)°]. The polymeric structure thus differs from those found for ${}^{1}_{\infty}[Sn(StC_4H_9)_2]$[19] and ${}^{1}_{\infty}[Sn(SnC_4H_9)_2]$[20] where the tin atoms were found to be fourfold coordinated by the thiolato ligands. A similar trigonal pyramidal coordination was observed for two of the tin atoms in trimeric $[Sn(S\text{-}2,6\text{-}(iC_3H_7)_2C_6H_3)_2]_3$.[18]

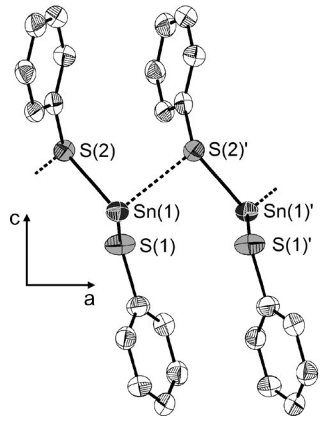

Figure 1. Section of the crystal structure of ${}^{1}_{\infty}[Sn(SPh)_2]$ (**1**) viewed down *b* (50% ellipsoids, H atoms omitted for clarity). Symmetry transformation for generation of equivalent atoms: ′ *x* + 1/2, –*y* + 2, z. Selected bond length [pm]: Sn(1)–S(1) 251.8(2), Sn(1)–S(2) 257.7(2), Sn(1)–S(2)′ 273.1(2). Selected bond angles (°): S(1)–Sn(1)–S(2) 77.16(6), S(1)–Sn(1)–S(2)′ 92.68(6), S(2)–Sn(1)–S(2)′ 87.58(5), Sn(1)–S(2)′–Sn(1)′ 97.03(5).

2 crystallises in the monoclinic space group *P*2_1/*n* with two formula units in the asymmetric unit (Table 3). In contrast to **1** the $Sn(SePh)_2$ units of **2** are in the solid state μ_2-bridged in one dimension by both phenylselenolato ligands [Se(1), Se(2) and Se(3), Se(4)] to form infinite chains along *b* (Figure 2). Two of the Sn–Se distances [Sn(1)–Se(1): 266.87(8), Sn(1)–Se(2): 267.57(7), Sn(2)–Se(3): 268.32(7), Sn(2)–Se(4): 267.37(8) pm] are distinctly smaller than the "secondary" Sn–Se contacts [Sn(1)–Se(3) 291.45(7), Sn(2)–Se(2) 298.02(7), Sn(1)′–Se(4) 321.80(7), Sn(2)–Se(1)′ 310.73(7) pm]. The shorter Sn–Se distances are similar to those found in $AsPh_4[Sn(SePh)_3]$ (264.9–267.0 pm)[21] and $[Yb(C_4H_8O)_6][Sn(SePh)_3]_2$ (262.9–268.5).[22] Therefore the crystal structure of **2** consists of $Sn(SePh)_2$ units [Se–Sn–Se angles: Se(1)–Sn(1)–Se(2) 88.15(3), Se(4)–Sn(2)–Se(3) 82.37(3)] which are linked by four additional weaker selenium to tin donor-acceptor bonds in order to form one dimensional chains. The polymeric structure is thus comparable to those found for ${}^{1}_{\infty}[Sn(StC_4H_9)_2]$[19] and ${}^{1}_{\infty}[Sn(SnC_4H_9)_2]$.[20]

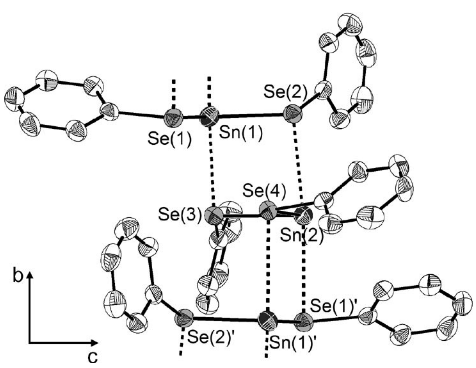

Figure 2. Section of the crystal structure of ${}^{1}_{\infty}[Sn(SePh)_2]$ (**2**) viewed down *a* (50% ellipsoids, H atoms omitted for clarity). Symmetry transformation for generation of equivalent atoms: ′ –*x* + 1/2, *y* – 1/2, –*z* + 1/2. Selected bond length [pm]: Sn(1)–Se(1) 266.87(8), Sn(1)–Se(2) 267.57(7), Sn(2)–Se(3) 268.32(7), Sn(2)–Se(4) 267.37(8), Sn(1)···Se(3) 291.45(7), Sn(2)···Se(2) 298.02(7), Sn(1)′···Se(4) 321.8(1), Sn(2)···Se(1)′ 310.7(1). Selected bond angles (°): Se(1)–Sn(1)–Se(2) 88.15(3), Se(1)–Sn(1)–Se(3) 83.85(1), Se(2)–Sn(1)–Se(3) 86.37(1), Se(4)–Sn(2)–Se(3) 82.37(3), Se(4)–Sn(2)–Se(2) 83.00(1), Se(3)–Sn(2)–Se(2) 84.92(1), Sn(1)–Se(2)–Sn(2) 92.88(1), Sn(2)–Se(3)–Sn(1) 94.21(1).

3 crystallises also in the monoclinic space group *P*2_1/*n* with two formula units in the asymmetric unit (Table 3). Similar to **2** the $Sn(TePh)_2$ units of **3** are in the crystal μ_2-bridged in one dimension by both of the phenyltellurolato ligands [Te(1), Te(2) and Te(3), Te(4)] to form infinite chains along *b* (Figure 3). Different bond lengths and angles as well as different orientations of the phenyl rings lead to another crystal packing for the $Sn(TePh)_2$ units in **3** in comparison to **2** expressed by different lattice constants. However the bonding situation is similar to **2** with $SnTePh_2$ units [Sn(1)–Te(2) 287.2(1), Sn(1)–Te(1) 289.5(1), Sn(2)–Te(4) 287.9(1), Sn(2)–Te(3) 288.4(1) pm]; [Te(2)–Sn(1)–Te(1) 87.28(3), Te(4)–Sn(2)–Te(3) 91.31(3)] which are linked by weaker tellurium to tin donor acceptor bonds [Sn(1)–Te(4) 327.4(1), Sn(2)–Te(1) 312.8(1), Sn(1)–Te(3) 316.8(1), Sn(2)′–Te(2) 334.5(1) pm] to form the one dimensional chains. Two different Sn–Te bond length [280.0(1) and

295.6(1) pm] were also found in dimeric [Sn{TeSi(SiMe$_3$)$_3$}$_2$]$_2$[12] where the tin atoms adopt a distorted trigonal pyramidal coordination in the crystal.

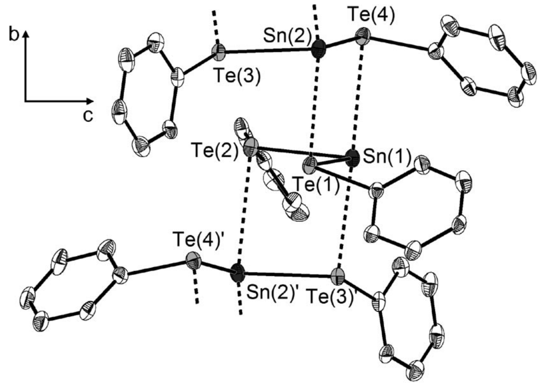

Figure 3. Section of the crystal structure of $^{1}_{\infty}$[Sn(TePh)$_2$] (**3**) viewed down *a* (50% ellipsoids, H atoms omitted for clarity). Symmetry transformations for generation of equivalent atoms: ′ –*x* + 3/2, *y* – 1/2, –*z* + 1/2. Selected bond length [pm]: Sn(1)–Te(2) 287.2(1), Sn(1)–Te(1) 289.5(1), Sn(2)–Te(4) 287.9(1), Sn(2)–Te(3) 288.4(1), Sn(1)···Te(4) 327.4(1), Sn(2)···Te(1) 312.8(1), Sn(1)···Te(3)′ 316.8(1), Sn(2)′···Te(2) 334.5(1). Selected bond angles (°): Te(2)–Sn(1)–Te(1) 87.28(3), Te(2)–Sn(1)–Te(3) 91.12(1), Te(1)–Sn(1)–Te(3) 78.06(1) Te(4)–Sn(2)–Te(3) 91.31(3), Te(4)–Sn(2)–Te(1) 89.20(2), Te(3)–Sn(2)–Te(1) 80.36(1), Sn(1)–Te(1)–Sn(2) 93.69(1), Sn(2)′–Te(3)–Sn(1) 92.28(1).

A comparison of the measured and calculated X-ray powder diffraction patterns for **1**, **2** and **3** reveal their crystalline purity with respect to the formation of other crystalline compounds (Figure S1). Slightly increasing differences in the position of the peaks with increasing detection angle arise from the temperature difference of the detection of the single crystal data and the powder patterns.

Optical Properties

Dried crystalline powders of **1**, **2** and **3** appear light-yellow, yellow and golden-yellow, respectively. The UV/Vis spectra in the solid state display a small shift in the absorption onset on going from **1** (440 nm) to **2** (470 nm) and a significant red shift for **3** (690 nm) (Figure 4). All spectra show only weakly pronounced features.

Upon going from **1** to **3** the solubility decreases significantly presumably due to the change in the structures as well as a stronger bonding of the large and soft base tellurolato ligands to the large and soft acid tin atoms compared to the thiolato and selenolato ligands. While **1** is well soluble in thf similar amounts of **2** need mixtures of more strongly coordinating solvents like CH$_3$CN and dmf. Although **3** shows some solubility in thf or CH$_3$CN it is only well soluble in dmso. However all solutions of **3** show upon standing decomposition indicated by the formation of black precipitates of SnTe as already observed for ether solutions of the related silylated compound [Sn{TeSi(SiMe$_3$)$_3$}$_2$]$_2$ by addition of Lewis bases like CH$_3$CN.[4]

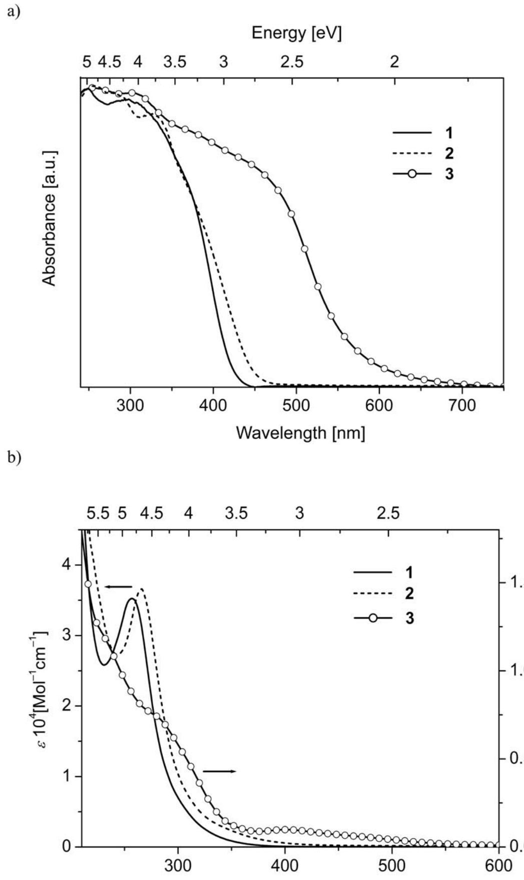

Figure 4. UV/Vis spectra of $^{1}_{\infty}$[Sn(SPh)$_2$] (**1**), $^{1}_{\infty}$[Sn(SePh)$_2$] (**2**) and $^{1}_{\infty}$[Sn(TePh)$_2$] (**3**) a) in solid state (powder in mineral oil between quartz plates) and b) in thf.

UV/Vis spectra in thf display two nearly similar curves for **1** and **2** with maxima at 257 nm and 265 nm respectively most probably dominated by strong π-π* transitions of the chalcogenolato ligands (Figure 8). **3** although not completely soluble and slowly decomposing shows an onset of a weak and broad absorption already at 560 nm which might be assigned to ligand to metal charge transfer transitions followed by two shoulders at 280 nm and 232 nm. Calculation of the electronic triplet excitation spectrum of the mononuclear compounds Sn(EPh)$_2$ (E = S, Se, Te) with time-dependent density functional theory (for technical details see next section) reveals that the lowest excitations show a similar energetic shift from the sulfur to the tellurium species as observed in the measurements. However the strong red-shift which was especially observed in the solid state spectra of **3** compared to that of **2** is not reproduced in the calculations; calculated lowest excitations are at 1.8 eV(Te), 2.2 eV (Se) and 2.4 eV (S), see Figure S2 of the supplementary material. This discrepancy is not too surprising, as intermolecular interactions in the one-dimensional chains are not considered in the calculations. The lowest excitation mainly is a transition from the HOMO, located at the chalcogen atoms, to the LUMO, located mainly at the Sn atom (Figure 5). Similar is true for the two excitations following in energy, so the lowest excitations are *p-p* ligand to metal charge transfer transitions.

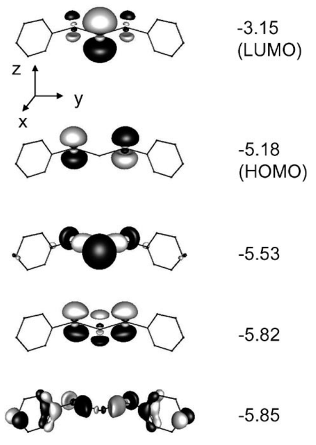

Figure 5. Molecular frontier orbitals of monomeric $Sn(TeC_6H_5)_2$. Contours are drawn at 0.05 a.u., orbital energies (right) are given in eV.

Quantum Chemical Considerations

The bond situation within a monomeric $Sn(EPh)_2$ (E = S, Se, Te) unit may be described by two-electron-two-centre E–Sn and E–C bonds. The remaining electrons form two lone pairs at each of the chalcogen atoms and one at the tin atom. For a better understanding and in order to rationalize the polymerization, density functional calculations (program system TURBOMOLE,[23] BP-86 functional,[24,25] def2-SV(P) bases[26] plus RI-J auxiliary bases,[27] effective core potentials for tin and tellurium[28,29]) were carried out. The frontier molecular orbitals for the monomer in C_{2v} symmetry with E = Te are shown in Figure 5; the shape is very similar for E = S, Se. The highest occupied molecular orbital (HOMO) is the antisymmetric combination of the *p*-orbitals of the tellurium atoms perpendicular to the molecular plane, p_z(Te). The HOMO-2 mainly consists of their symmetric combination plus small contributions from p_z(Sn). HOMO-1 and HOMO-3 are in the molecular plane; HOMO-1 consists of p_x(Sn) plus s(Sn) together with symmetry-matching combinations of p_x(Te) and p_y(Te); HOMO-3 involves p_y(Sn) and similar combinations from the tellurium atoms. The ratio of atomic contributions to the MOs and even their energetic sequence depend on spatial extension and energy difference of *s*- and *p*-orbitals of E (for E = Se HOMO-3 and HOMO-2 are interchanged, for E = S additionally HOMO-1 and HOMO). The lowest unoccupied orbital (LUMO) is the p_z(Sn) plus small contributions of p_z(Te). Agreement with the simple description given in the beginning of this section can be achieved by the consideration of localized molecular orbitals (LMOs); this is also helpful for understanding the mechanism of polymerization. LMOs are linear combinations of the occupied canonical MOs (CMOs), i.e. those resulting Hartree–Fock or DFT calculations (Figure 5); LMOs are obtained from CMOs by unitary transformation with the requirement that they have to be localized at as few as possible atoms (Pipek-Mezey localization[30]). In this way one loses the information of orbital energies, but gains objects that are suited for intuitive interpretation (bonds, lone pairs). We note that this transformation is not unique, i.e. different localization procedures will lead to slightly different LMOs. In Figure 6 (left hand side) we show the relevant LMOs located at tellurium and tin for the monomer: the Te–Sn and the Te–C bond (LMO1, LMO2), *s*-type lone pairs at tin and tellurium (LMO3, LMO4) and a *p*-type lone-pair at tellurium (LMO5). For the bonds also the contributions from the bond partners (from a Mulliken population analysis[31]) are shown. As expected, the Te–Sn-bond is significantly polarized towards the tellurium atom, the C–Te bond is slightly polarized towards the carbon atom.

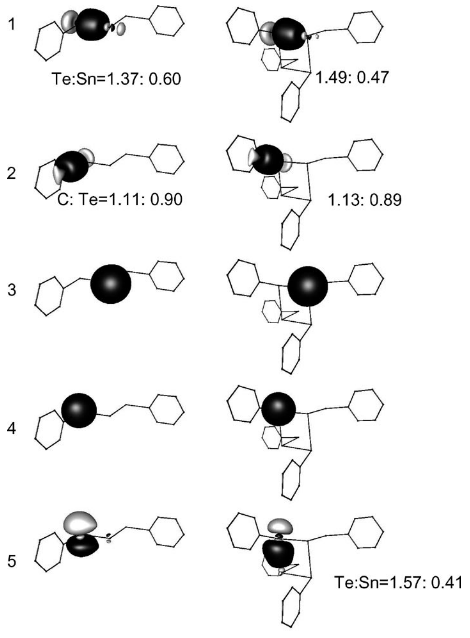

Figure 6. Selected localized molecular orbitals (Pipek-Mezey localization) of $Sn(TeC_6H_5)_2$ (left) and $[Sn(TeC_6H_5)_2]_2$ (right). Contours are drawn at 0.05 a.u. The numbers indicating the contributions from bond partners are calculated by a Mulliken population analysis.

Formation of polymers is studied for E = Te in detail, differences for E = S are given in the end. Polymerization is driven mainly by electron transfer from the p_z orbitals from the E atoms (electron donor, Lewis base) of one monomer to the empty p_z orbitals of the Sn atom (electron acceptor, Lewis acid) of a second monomer. This can be seen from the changes of some of the LMOs from the monomer to the dimer, right hand side of Figure 6. One observes significant electron transfer to the empty p_z orbital (LMO5) of the tin atom of the second monomer; the contribution of this atom to this LMO amounts to 0.41 electrons (from a Mulliken population analysis for this LMO). Further the polar character of the intramolecular Sn–Te-bond (LMO1) is enhanced; it is very similar to that of the intermolecular Sn–Te bond. In the same way electrons are transferred from p_z(Te) of the second unit to p_z(Sn) of the first unit. For each dimer the two remaining p_z(Te), which are not involved in this bond, are used to bind to the next dimer by the same mechanism. This on the other hand means that in each dimer the tin atoms act as acceptors for electrons from *two* further tellurium atoms (additional to that of the monomer).

For E = Se matters are very similar, but for E = S each tin atom is connected only to one further sulfur atom. This may have steric reasons, but also the lower energy of the *p*(S) orbitals compared to the *p*(Te) might be considered. This will lead to less pronounced electron transfer from sulfur to tin and thus to a preference for accepting electrons from only one additional sulfur atom. For clarity we finally note that the d-orbitals of Sn do not play a role in these considerations. This is confirmed by values for their occupation from natural population analyses (NPA),[32] which in all cases amount to less than 0.01 electrons.

Thermal Behaviour

Upon heating **1** starts to melt around 198 °C to give a brownish-yellow liquid and decomposes around 280 °C while **2** and **3** start to visibly decompose with formation of black powders already at 180 °C and 108 °C, respectively. In order to investigate the thermal properties of **1**–**3** in more detail we first performed thermogravimetric analysis under helium gas flow and under vacuum conditions. In addition thermolysis experiments were then carried out in Schlenk tubes to further investigate the cleavage products.

Thermogravimetric analyses under helium gas flow display clearly one step mass losses for **2** and **3** while **1** displays a minor gradual mass loss starting around 125 °C before the main decomposition step which occurs between 265 °C and 348 °C (Figure 7a, Table 1). The selenolato complex **2** decomposes between 200 °C and 310 °C while **3** is, as already indicated by its instability in solution, much more unstable than **1** and **2** and decomposes between 126 °C and 206 °C. The X-ray powder patterns of the residues reveal the formation of pure binary SnE (E = S, Se, Te) phases[33–35] (Figure S3) comparable with the pyrolysis products of the $\mathrm{Sn^{VI}}$ precursor molecules $(\mathrm{Ph_3Sn})_2\mathrm{E}$ (E = S, Se, Te) which start to decompose around 330 °C.[36] Carbon and hydrogen contents were found to be less than 1%. While the experimental total mass loss for **3** is in good agreement with the calculated value for the formal cleavage of one equivalent of $\mathrm{TePh_2}$ from $\mathrm{Sn(TePh)_2}$ to yield SnTe according to Scheme 2, it differs for **1** and **2** (see Table 1).

Thermogravimetric analyses in vacuo in principle also display one step mass losses for **1**–**3** with two weak shoulders indicated for **3** (Figure 7b). Again, the tellurolate complex **3** decomposes much earlier, already between 50 °C and 145 °C, than **1** and **2**. The X-ray powder patterns of the residues of **2** and **3** indicate formation of pure orthorhombic SnSe and SnTe, respectively (C, H < 1%). Now for all compounds the experimental mass change is not in line with the calculated one according to Scheme 2 and Table 1.

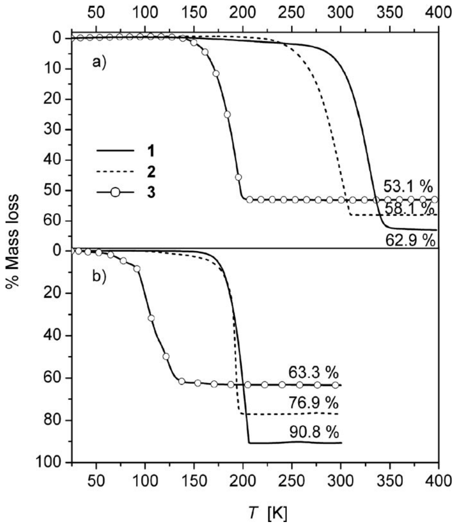

Figure 7. Thermogravimetric analysis of $^{1}_{\infty}[\mathrm{Sn(SPh)_2}]$ (**1**), $^{1}_{\infty}[\mathrm{Sn(SePh)_2}]$ (**2**) and $^{1}_{\infty}[\mathrm{Sn(TePh)_2}]$ (**3**) under a) He gas flow and b) in vacuo (see also Table 1).

Table 1. Experimental and theoretical mass loss (due to Scheme 2) for the thermal gravimetric analyses (Figure 7) of $^{1}_{\infty}[\mathrm{Sn(SPh)_2}]$ (**1**), $^{1}_{\infty}[\mathrm{Sn(SePh)_2}]$ (**2**) and $^{1}_{\infty}[\mathrm{Sn(TePh)_2}]$ (**3**).

Compound	Experimental mass loss [%]		Theoretical mass loss [%]
	He gas flow	vacuum	
1	62.4	90.8	55.3
2	58.1	76.9	54.1
3	53.1	63.3	53.4

$$\mathrm{Sn(EPh)_2} \xrightarrow{\Delta} \mathrm{SnE} + \mathrm{EPh_2} \quad (\mathrm{E} = \mathrm{S, Se, Te})$$

Scheme 2.

While for **3** the difference is about 10% for the thermal treatment of **2** the experimental mass loss of even more differs from its theoretical value compared to the TGA under helium atmosphere. For **1** the residue is only 9.2% in mass of the precursor complex and is characterised by powder XRD to be solely elemental tin suggesting not only sublimation but also a different thermal reaction than observed under atmospheric pressure.

In order to further investigate the cleavage products, thermolysis experiments were carried out in preparative scale (ca. 200 mg) under $\mathrm{N_2}$ atmosphere (up to 350 °C) and in vacuo (up to 300 °C) in Schlenk tubes located inside a tube furnace (for details see experimental part and Table 2).

The cleavage products of the thermolysis of **1** under $\mathrm{N_2}$ atmosphere could by careful condensation be almost completely separated in a yellow crystalline powder and a pale yellow liquid. However apart from the identification of the liquid main product $\mathrm{SPh_2}$ by NMR[37,38] it was not possible to clearly identify the other compounds (see experimental section). In contrast, for the thermolysis of **1** under vacuum conditions only the formation of a light yellow solid precipitate on the walls of the glass tube outside the furnace is observed which is identified by powder XRD to consist

Table 2. Thermolysis data of $^{1}_{\infty}[Sn(SPh)_2]$ (**1**), $^{1}_{\infty}[Sn(SePh)_2]$ (**2**) and $^{1}_{\infty}[Sn(TePh)_2]$ (**3**).

Compound	Final temperature [°C]	Residue[a]	Residual mass [%] (th.)[b]	Identified cleavage products[c]	Visible mp/decomp. [°C]
Thermolysis under N_2					
1	350	SnS	36.7 (44.7)	$S(Ph)_2$	198/280
2	350	SnSe	41.0 (45.9)	$Se(Ph)_2$	–/180
3	350	SnTe	46.0 (46.6)	$Te(Ph)_2$	–/108
Thermolysis under vacuum (2×10^{-6} mbar)					
1	300	Sn	8.2 (–)	$Sn(SPh)_2$, $Sn(SPh)_4$	198/–
2	300	SnSe	21.9 (45.9)		–/180
3	300	SnTe	36.0 (46.6)		–/110

[a] Identified by powder-XRD (C, H < 1%). [b] Calculated mass% of the residue due to the formal cleavage of one equivalent of $E(Ph)_2$ (E = S, Se, Te) (Scheme 2) with the exception of the vacuum thermolysis of $Sn(SPh)_2$ where 100% sublimation was assumed. [c] Identified by ^{1}H-, ^{13}C-NMR or powder XRD.

mainly of **1** (Figure 8). However the sublimation is accompanied by a partial decomposition reaction of **1** to give a 8.2% (TGA: 9.2%) mass percent residue of elemental tin and in the sublimate appropriate amounts of the oxidation product $Sn(SPh)_4$ as proven by the corresponding powder diffraction patterns[39,8] (26% decomposition product).

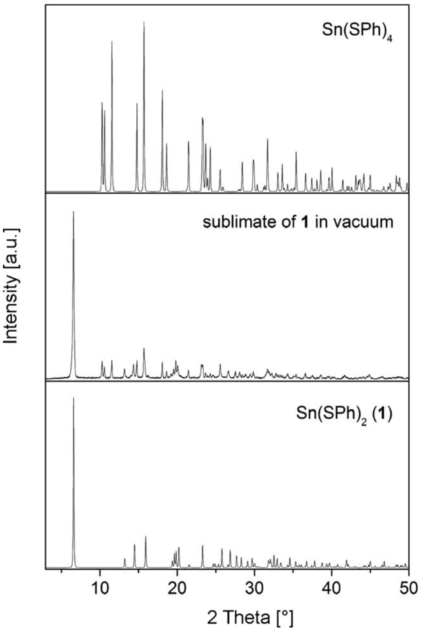

Figure 8. Powder XRD pattern of the cleavage products of the thermolysis of $^{1}_{\infty}[Sn(SPh)_2]$ (**1**) under vacuum (2×10^{-6} mbar) compared with the calculated one of $Sn(SPh)_4$[8] and **1**.

The yellow cleavage product of the thermal treatment of **2** under nitrogen clearly display in the ^{1}H- and ^{13}C-NMR spectra peaks of the main product $SePh_2$[40,41] together with not yet identifiable additional peaks. Thermolysis of **2** under vacuum resulted also in the formation of a yellow liquid which condenses outside the furnace but in addition a black metallic mirror is formed on the walls of the glass tube inside the furnace. Due to the ^{1}H and ^{13}C NMR spectra the liquid cleavage products contain several not identifiable compounds while the black precipitate on the glass walls was characterized to be orthorhombic SnSe like the residue in the quartz boat. In line with the mass loss this suggests that **2** distinctly sublimes under the conditions of the experiment but decomposes at the hot walls of the tube before being able to leave the hot reaction zone.

Decomposition of **3** under N_2 atmosphere yields an orange oil as the cleavage product which was identified by ^{1}H- and ^{13}C-NMR to consist of $TePh_2$[42,43] with small amounts of unidentifiable side products. This is in agreement with the proposed reaction mechanism according to Scheme 2 and the results of the investigations of the thermolysis of $[Sn\{TeSi(SiMe_3)_3\}_2]_2$ which was reported to decompose cleanly at 250 °C to yield SnTe and $Te\{Si(SiMe_3)_3\}_2$.[12] In contrast ^{1}H and ^{13}C NMR spectra of the cleavage products from the thermolysis experiment of **3** under vacuum in a Schlenk tube (a red powder and a yellow liquid) show several signals for aromatic C and H atoms and do not clearly reveal the formation of $TePh_2$ which again indicates a more complex decomposition reaction then expected according to Scheme 2.

These findings are partially in agreement with observations on the thermal reactions of $[Sn\{ESi(SiMe_3)_3\}_2]_2$ (E = S, Se) where the cleavage products were contaminated with unidentifiable $SiMe_3$-containing species. However for these compounds the formed binary chalcogenides SnE (E = S, Se) also proved to be extremely rich in elemental tin which was in our case only observed for the vacuum thermolysis of **1**.[12]

Conclusions

Reaction of $SnCl_2$ with two equivalents of $PhESiMe_3$ (E = S, Se, Te) yielded the 1-D-tin(II) phenylchalcogenolato complexes $^{1}_{\infty}[Sn(EPh)_2]$ in high yields. The closely related 1D chain structure of the selenolato and tellurolato complex in the solid state differ from the thiolato analogue with respect to the coordination modes of the tin atoms which is found to be larger in the case of the heavier chalcogen elements. DFT calculations reveal that the structures should be described as consisting of monomeric "$Sn(EPh)_2$" units which are linked by additional weaker chalcogen to tin donor acceptor bonds to form polymeric chains. With respect to the optical and thermal behaviour $^{1}_{\infty}[Sn(TePh)_2]$ shows a significant red shift of the absorption onset and a distinctly reduced thermal stability compared to the other two homologues. While thermal treatment of the tellurolate complex leads under comparable mild conditions (200 °C, N_2) to the almost stoichiometric formation of SnTe and $TePh_2$ the other reactions are ongoing from the tellurolato to the thiolato complex and by the use of vacuum conditions increasingly dominated by sublimation. In addition investigations of the volatile reaction products suggest more complex reactions in the gas phase than the formal stoichiometric cleavage of EPh_2 (E = S, Se, Te) with formation of SnE. However the investigations suggest that more easily sublimable compounds $[Sn(ER)_2]$ (E = S, Se; R = alkyl group) could have a potential for the use as single source precursor compounds for the synthesis of SnE in CVD processes.

Experimental Section

Synthesis: Standard Schlenk techniques were employed throughout the syntheses using a double manifold vacuum line (10^{-3} mbar) with high purity nitrogen (99.99990%). The solvents thf (tetrahydofuran), dme (1,2-dimethoxyethan) and ethyl ether were dried with sodium-benzophenone, and distilled under nitrogen. $PhSSiMe_3$ and $SnCl_2$ were purchased from Aldrich. $PhSeSiMe_3$[44] and $PhTeSiMe_3$[45] were prepared according to literature procedures.

$[Sn(SPh)_2]$ (1): $SnCl_2$ [0.162 g (0.85 mmol)] is dissolved in 10 mL of dme to give a clear solution. Upon addition of $PhSSiMe_3$ [0.34 mL (1.79 mmol)] tiny yellow needles soon start to crystallize from the solution. Filtration and washing with ethyl ether after two days resulted in 0.20 g of **1**. Evaporation of the pure filtrate to dryness, redissolution of the solid residue in 10mL of thf and layering with ethyl ether yielded further 0.03g of **1** to give a total yield of 81%. **1** is soluble in thf, slightly soluble in dme and not soluble in ethyl ether. $C_{12}H_{10}S_2Sn$ (337.01): calcd. C 42.8, H 3.0, S 19.0; found C 42.8, H 3.0, S 19.5. M.p. 198 °C. IR (KBr): $\tilde{\nu}$ = 3053 (m, sh), 3049 (m), 3010 (w), 1938 (w, br), 1859 (w, br), 1796 (w, br), 1732 (w, br), 1572 (m), 1472 (m), 1460 (m, sh), 1433 (s), 1384 (s), 1328 (w), 1298 (m), 1263 (m), 1181 (w), 1158 (w, br), 1081 (m), 1066 (m), 1021 (m), 895 (w), 835 (w), 732 (vs), 687 (vs), 475 (s) cm^{-1}. UV/Vis (thf) $\lambda_{max} = 257$ nm; $\varepsilon = 3.4 \times 10^4$ l mol^{-1} cm^{-1}. ^1H NMR [300 MHz, $(CD_3)_2SO$]: δ = 7.29 (t, 1 H, *para*-C*H*), 7.38 (t, 2 H, *meta*-C*H*) , 7.52 (d, 2 H, *ortho*-C*H*) ppm. $^{13}C\{^1H\}$ NMR [75 MHz, $(CD_3)_2SO$]: δ = 127.6 (s, *para*-CH), 128.0 (s, *ortho*-CH), 129.9 (s, *meta*-CH), 136.2 (s, *C*SSn) ppm. ESI-TOF-MS: m/z_{exp} 109.01, rel. int. 100, (m/z_{calc} 109.01 $SC_6H_5^-$); m/z_{exp} 446.94, rel. int. 100 [m/z_{calc} 446.94 $Sn(SC_6H_5)^{3-}$].

$[Sn(SePh)_2]$ (2): $SnCl_2$ [0.154 g (0.81 mmol)] is dissolved in 25 mL of thf to give a clear solution. Upon addition of $PhSeSiMe_3$ [0.34 mL (1.79 mmol)] the mixture immediately turns yellow and a voluminous precipitate forms. Standing overnight yields thin yellow needles of **2** which are filtered and washed with dme to give a total yield of 86% (0.30 g). **2** is sparingly soluble in thf and well soluble in dmf and dmso. $C_{12}H_{10}Se_2Sn$ (430.81): calcd. C 33.5, H 2.3; found C 34.2, H 2.6. IR (KBr): $\tilde{\nu}$ = 3052 (m), 3015 (w), 2980 (w), 1936 (w, br), 1865 (w, br), 1793 (w, br), 1732 (vw, br), 1631 (w), 1570 (s), 1470 (s), 1432 (m), 1384 (s), 1323 (m), 1296 (m), 1264 (w), 1178 (w), 1158 (w, br), 1097 (vw, br), 1066 (m), 1017 (m), 997 (w), 894 (w), 840 (w), 726 (vs), 686 (vs), 666 (s), 460 (s) cm^{-1}. UV/Vis (thf) λ_{max} = 266 nm; $\varepsilon = 3.6 \times 10^4$ l mol^{-1} cm^{-1}. ^1H NMR [300 MHz, $(CD_3)_2SO$]: δ = 7.32 (m, 3 H, *meta*-C*H*, *para*-C*H*), 7.62 (d, 2 H, *ortho*-C*H*) ppm. $^{13}C\{^1H\}$ NMR [75 MHz, $(CD_3)_2SO$]: δ = 128.3 (s, *para*-CH), 130 (s, *meta*-CH), 130.5 (s, *C*SeSn), 131.3 (s, *ortho*-CH) ppm. ESI-TOF-MS: m/z_{exp} 156.96, rel. int. 100, (m/z_{calc} 156.96 $SeC_6H_5^-$); m/z_{exp} 586.78, rel. int. 100 [m/z_{calc} 586.77 $Sn(SeC_6H_5)^{3-}$].

$[Sn(TePh)_2]$ (3): To a solution of $SnCl_2$ [0.38 g (1.983 mmol)] in 160 mL of thf $PhTeSiMe_3$ [0.96 mL (4.17 mmol)] is added at –70 °C. Soon the reaction solution turns orange and a voluminous precipitate forms. The reaction solution is warmed up to 4 °C overnight without stirring and then kept at this temperature in a refrigerator. Tiny yellow needles of **3** form in a deep dark yellow solution which are filtered cool and quickly washed with a 1:1 mixture of thf/dme (cooled to –5 °C) to give a total yield of 82% (0.862 g). **3** is slightly soluble in thf and well soluble in dmso. However all solutions show upon standing decomposition with formation of SnTe. $C_{12}H_{10}SnTe_2$ (528.09): calcd. C 27.3, H 1.9; found C 27.2, H 2.0. IR (KBr): $\tilde{\nu}$ = 3035 (m), 3025 (w), 2973 (w), 1940 (w, br), 1865 (w, br), 1800 (vw, br), 1566 (s), 1498 (vw), 1467 (s), 1428 (m), 1384 (s), 1322 (m), 1294 (m), 1262 (w), 1173 (w), 1157 (w), 1059 (vw, br), 1013 (m), 996 (w), 900 (w), 836 (w), 802 (w), 727 (vs), 689 (vs), 649 (m), 450 (s) cm^{-1}. UV/Vis (thf) λ_{max} = 402 nm (br); $\varepsilon = 0.0988 \times 10^4$ l mol^{-1} cm^{-1}, λ = 278 nm (sh); $\varepsilon = 0.7888 \times 10^4$ l mol^{-1} cm^{-1}, λ_{max} = 233 nm (sh); $\varepsilon = 1.172 \times 10^4$ l mol^{-1} cm^{-1}. ^1H NMR [300 MHz, $(CD_3)_2SO$]: δ = 7.0 (t, 2 H, *meta*-C*H*), 7.11 (1 H, *para*-C*H*), 7.68 (d, 2 H, *ortho*-C*H*) ppm. $^{13}C\{^1H\}$ NMR [75 MHz, $(CD_3)_2SO$]: δ = 114 (s, *C*TeSn), 125.7 (s, *para*-CH), 129 (s, *meta*-CH), 139.3 (s, *ortho*-CH) ppm. ESI-TOF-MS: m/z_{exp} 206.95, rel. int. 100, (m/z_{calc} 206.95 $TeC_6H_5^-$); m/z_{exp} 324.85, rel. int. 25, (m/z_{calc} 324.85 $TeSnC_6H_5^-$); m/z_{exp} 734.74, rel. int. 50 [m/z_{calc} 734.74 $Sn(TeC_6H_5)^{3-}$].

Thermolysis: Thermolysis experiments were carried out using a Linn High Term FRHT-70/500/1100 programmable tube furnace, 70 cm long and 4 cm in diameter equipped with a ca. 50 × 3 cm borosilicate Schlenk tube. For experiments under vacuum the tube was directly connected with a cool trap to a turbo molecular pump setup from Edwards (vacuum 10^{-6} mbar) while for thermolysis under nitrogen the tube with the cool trap were connected via a Viton tubing to a mercury bubbler of a Schlenk line. The samples to be pyrolysed were placed in either quartz or porcelain boats in the center of the furnace (ca. 200 mg). For all samples the oven was programmed to ramp at a rate of 2 °C/min to 350 °C under a static pressure of N_2 and to 300 °C under vacuum (2×10^{-6} mbar) and hold at this temperature for 1h before allowing the oven to cool to room temperature. The solid residues in the porcelain or quartz boats were weighed and characterized by powder X-ray analyses while the volatile cleavage products which deposit in the part of the tube outside the furnace and in the cool trap were collected with thf (liquid products) for NMR and ESI-TOF analysis or investigated by powder XRD in the case of solids.

Details of the Thermolysis of 1: The cleavage products of **1** could by careful condensation be almost completely separated in a yellow powder and a pale yellow liquid. The liquid contains beside the main product SPh_2[46,47] other products with aromatic C and H atoms which could not be identified by NMR spectroscopy. The XRD powder pattern of the yellow powder reveals the existence of crystalline material however it does not match that of **1**. ESI-TOF mass spectra of solutions of this powder in thf show SPh^- ions (m/z_{calc} 109.01, m/z_{exp} 108.99, rel. int. 44) but do not display the characteristic fragment $[Sn(SPh)_3]^-$ (m/z_{calc} 446.94, m/z_{exp} 446.94) which was found as the major component beside SPh^- in solutions of 1. Instead other fragments which contain tin atoms and a higher S:C/H ratio were found like $SnS_3C_6H_7^-$ (m/z_{calc} 294.87, m/z_{exp} 294.84 rel. int. 11), $SnS_3C_{12}H_9^-$ (m/z_{calc} 368.89, m/z_{exp} 368.88 rel. int. 100), $SnS_5C_{18}H_{13}$ (m/z_{calc} 508.86, m/z_{exp} 508.86 rel. int. 40) and $SnS_6C_{24}H_{17}$ (m/z_{calc} 616.87, m/z_{exp} 616.86 rel. int. 4). Suggestions for the structures of these fragments are difficult to make because no other S, C, H containing ligands could be identified in the mass spectra.

Crystallography: Crystals suitable for single-crystal X-ray diffraction were taken directly from the reaction solution of the compound and then selected in perfluoroalkylether oil. Single-crystal X-ray diffraction data of **1** and **2** were collected using graphite-monochromatised Mo-K_α radiation (λ = 0.71073 Å) on a STOE IPDS II (Imaging Plate Diffraction System). Single-crystal X-ray diffraction data of **3** were collected using synchrotron radiation (λ = 0.80 Å) on a STOE IPDS II (Imaging Plate Diffraction System) at the ANKA synchrotron source in Karlsruhe. Raw intensity data were collected and treated with the STOE X-Area software Version 1.39. Data for all compounds were corrected for Lorentz and polarisation effects. Based on a crystal description numerical absorption corrections were applied for **1** and **3** (Table 3).[48] The structures were solved with the direct methods program SHELXS of the SHELXTL PC suite programs,[49] and were refined with the use of the full-matrix least-squares program SHELXL. Molecular diagrams were prepared using Diamond.[50]

Table 3. Crystallographic data for $^{1}_{\infty}[\mathrm{Sn(SPh)_2}]$ (**1**), $^{1}_{\infty}[\mathrm{Sn(SePh)_2}]$ (**2**) and $^{1}_{\infty}[\mathrm{Sn(TePh)_2}]$ (**3**).

	1	**2**	**3**
fw [g/mol]	337.01	430.81	528.09
Crystal system	orthorhombic	monoclinic	monoclinic
Space group	$Pca2_1$	$P2_1/n$	$P2_1/n$
Cell			
a [Å]	7.141(1)	11.708(2)	12.389(3)
b [Å]	6.110(1)	11.893(2)	11.833(2)
c [Å]	26.740(5)	18.427(4)	18.504(4)
β [°]		93.32(3)	101.89(3)
V [Å^3]	1166.8(4)	2561.3(9)	2654.5(9)
Z	4	8	8
T [K]	190	150	130
λ [Å]	MoK_α	MoK_α	0.8000
d_c [g cm^{-3}]	1.919	2.234	2.643
$\mu(\lambda)$ [mm]$^{-1}$	2.509	7.644	8.651
$F(000)$	656	1600	1888
$2\theta_{\max}$ [°]	49	52	56
Measured reflns.	3512	17192	12661
Unique reflns.	1851	4805	4379
R_{int}	0.0516	0.0350	0.0535
Reflns. with $I > 2\sigma(I)$	1755	4172	3930
Refined params.	137	351	351
$R1[I > 2\sigma(I)]$[a]	0.0373	0.0242	0.0272
$wR2$(all data)[b]	0.0996	0.0565	0.0688
Abs. struct. param.	0.55		

[a] $R_1 = \Sigma||F_o| - |F_c||/\Sigma|F_o|$. [b] $wR_2 = \{\Sigma[w(F_o^2 - F_c^2)^2]/\Sigma[w(F_o^2)^2]\}^{1/2}$.

All Sn, S, Se, Te, and C atoms were refined with anisotropic displacement parameters whilst H atoms were located in the difference fourier map and freely refined for **2** and **3** and calculated in fixed positions for **1**.

CCDC-724254(**1**), –724255(**2**) and –724256(**3**) contain the supplementary crystallographic data for this paper. These data can be obtained free of charge from The Cambridge Crystallographic Data Centre via www.ccdc.cam.ac.uk/data_request/cif.

X-ray powder diffraction patterns (XRD) for $^{1}_{\infty}[\mathrm{Sn(SPh)_2}]$ (**1**), $^{1}_{\infty}[\mathrm{Sn(SePh)_2}]$ (**2**) and $^{1}_{\infty}[\mathrm{Sn(TePh)_2}]$ (**3**) were measured on a STOE STADI P diffractometer (Cu-$K_{\alpha 1}$ radiation, Germanium monochromator, Debye–Scherrer geometry) in sealed glass capillaries which agree with the theoretical powder diffraction patterns which were calculated on the basis of the atom coordinates obtained from single-crystal X-ray analysis by using the program package STOE WinXPOW.[51]

Physical Measurements: C, H, S elemental analyses were performed on an "Elementar vario Micro cube" instrument.

UV/Vis absorption spectra of **1**–**3** in solution were measured on a Varian Cary 500 spectrophotometer in quartz cuvettes. Solid state absorption spectra were measured as micron sized crystalline powders between quartz plates with a Labsphere integrating sphere.

^{1}H-NMR and ^{13}C-NMR spectra were recorded on a Bruker DPX Avance 300.

IR spectra were measured on a Perkin–Elmer Spectrum GX as KBr pellets in a region from 4000 to 350 cm^{-1}.

Thermogravimetric analyses were run in Al_2O_3 crucibles on a thermobalance STA 409 from Netzsch in vacuo (7×10^{-6} mbar) or with a dynamic helium gas flow (25 mL/ min) at a heating rate of 2 °C/min. The crucibles were filled (20–35 mg) inside an argon glove box, transferred in Schlenk tubes and mounted under a stream of argon to the balance. However trace contamination of oxygen indicated by the formation of SnO and SnO_2 could not be totally avoided in this way in all cases. Caution should be taken with respect to the toxic and bad smelling volatile products formed in the thermolysis.

Mass spectra were taken on a Time of Flight (TOF) mass spectrometer (Bruker Daltonics, MicroTOF-QII) equipped with an electrospray ion source (off axis sprayer). The solutions were sprayed at typical flow rates of about 180 µL/h and nebulized using dry nitrogen. The desolvation glass capillary was heated to 180 °C. For all ion signals observed the charge state was immediately evident from their isotopomere splitting and assignment to an ionic species was unequivocally confirmed by comparison to the computed isotopic distribution. All *m*/*z* values given in the text correspond to the most abundant peak of the respective distributions.

Acknowledgments

This work was supported by the National Science Foundation of China (Grant 20525310, 20773167) the Deutsche Forschungsgemeinschaft (center for functional nanostructures CFN) and the Research Center of Karlsruhe. The authors are grateful to E. Tröster and N. Metz for their valuable assistance in the practical work.

---

[1] I. Dance, K. Fisher, *Prog. Inorg. Chem.* **1994**, *41*, 637–803.
[2] S. Dehnen, A. Eichhöfer, D. Fenske, *Eur. J. Inorg. Chem.* **2002**, 279–317.
[3] M. W. DeGroot, J. F. Corrigan, *Comprehensive Coordination Chemistry II*; M. Fujita, A. Powell, C. Creutz (Eds.); Pergamon: Oxford, U. K., **2004**; Vol. 7, pp. 57–123.
[4] J. Arnold, *Prog. Inorg. Chem.* **1995**, *43*, 353–417.
[5] M. Bochmann, *Chem. Vap. Deposition* **1996**, *2*, 85–96.
[6] B. Krebs, G. Henkel, *Angew. Chem.* **1991**, *103*, 785–804; *Angew. Chem. Int. Ed. Engl.* **1991**, *30*, 769–788.
[7] B. Krebs, G. Henkel, *Chem. Rev.* **2004**, *104*, 801–824.
[8] G. Barone, T. G. Hibbert, M. F. Mahon, K. C. Molloy, L. S. Price, I. P. Parkin, A. M. E. Hardy, M. N. Field, *J. Mater. Chem.* **2001**, *11*, 464–468.
[9] D. H. R. Barton, H. Dadoun, *New J. Chem.* **1982**, *6*, 53–57.
[10] S. Schlecht, M. Budde, L. Kienle, *Inorg. Chem.* **2002**, *41*, 6001–6005.
[11] Y. Cheng, T. J. Emge, J. G. Brennan, *Inorg. Chem.* **1996**, *35*, 342–346.
[12] A. L. Seligson, J. Arnold, *J. Am. Chem. Soc.* **1993**, *115*, 8214–8220.

[13] D. E. Fenton, R. R. Gould, P. G. Harrison, T. B. Harvey, G. M. Omletanski, K. C.-T. Sze, J. J. Zuckerman, *Inorg. Chim. Acta* **1970**, *4*, 235–243.
[14] P. G. Harrison, S. R. Stobart, *Inorg. Chim. Acta* **1973**, *7*, 306–310.
[15] M. E. Peach, *J. Inorg. Nucl. Chem.* **1979**, *41*, 1390–1392.
[16] J. L. Hencher, M. Khan, F. F. Said, R. Sieler, D. G. Tuck, *Inorg. Chem.* **1982**, *21*, 2787–2791.
[17] J. J. Arsenault, P. A. W. Dean, *Can. J. Chem.* **1983**, *61*, 1516–1523.
[18] P. B. Hitchcock, M. F. Lappert, B. J. Samways, E. L. Weinberg, *J. Chem. Soc., Chem. Commun.* **1983**, 1492–1494.
[19] M. Veith, P. Hobein, R. Rösler, *Z. Naturforsch., Teil B* **1989**, *44*, 1067–1081.
[20] N. N. Zemlyanskii, I. V. Borisova, M. G. Kuznetsova, E. N. Khrustalev, M. Yu. Antipin, Yu. A. Ustynyuk, E. E. Lunin, C. Eaborn, M. S. Hill, J. D. Smith, *Russ. J. Org. Chem.* **2003**, *39*, 491–500.
[21] P. A. W. Dean, J. J. Vittal, N. C. Payne, *Can. J. Chem.* **1985**, *63*, 394–400.
[22] J. Lee, T. J. Emge, J. Brennan, *Inorg. Chem.* **1997**, *36*, 5064–5068.
[23] TURBOMOLE V6.0, TURBOMOLE GmbH Karlsruhe, **2009**, http://www.turbomole.de. TURBOMOLE is a development of University of Karlsruhe and Forschungszentrum Karlsruhe, **1989–2007**, TURBOMOLE GmbH since **2007**.
[24] A. D. Becke, *J. Chem. Phys.* **1993**, *98*, 5648–5652.
[25] J. P. Perdew, *Phys. Rev. B* **1986**, *33*, 8822–8824.
[26] F. Weigend, R. Ahlrichs, *Phys. Chem. Chem. Phys.* **2005**, *7*, 3297–3305.
[27] F. Weigend, *Phys. Chem. Chem. Phys.* **2006**, *8*, 1057–1065.
[28] B. Metz, H. Stoll, M. Dolg, *J. Chem. Phys.* **2000**, *113*, 2563–2569.
[29] K. A. Peterson, D. Figgen, E. Goll, H. Stoll, M. Dolg, *J. Chem. Phys.* **2003**, *119*, 11113–11123.
[30] J. Pipek, P. G. Mezey, *J. Chem. Phys.* **1989**, *90*, 4916–4926.
[31] R. Mulliken, *J. Chem. Phys.* **1955**, *23*, 1833–1840.
[32] J. P. Foster, F. Weinhold, *J. Am. Chem. Soc.* **1980**, *102*, 7211–7218.
[33] P. S. DelBucchia, J. C. Jumas, M. Maurin, *Acta Crystallogr., Sect. B* **1981**, *37*, 1903–1905.
[34] K. Adouby, C. Perez-Vicente, J. C. Jumas, *Z. Kristallogr.* **1998**, *213*, 343–349.
[35] T. S. Yeoh, S. G. Teoh, H. K. Fun, *J. Phys. Soc. Jpn.* **1988**, *57*, 3820–3823.
[36] M. Scheer, G. McCarthy, D. Seidler, P. Boudjouk, *Chem. Mater.* **1994**, *6*,2108–2112.
[37] S. Perumal, R. Chandrasekaran, V. Vijayabaskar, D. A. Wilson, *Magn. Reson. Chem.* **1995**, *33*, 779–790.
[38] S.-K. Chung, K. Sasamoto, *J. Org. Chem.* **1981**, *46*, 4590–4592.
[39] H. E. Swanson, E. Tatge, Natl. Bur. Stand. (U. S.), Circ. 539, I (**1953**), 24–27.
[40] M. R. Dettig, M. D. Seidler, *J. Org. Chem.* **1982**, *47*, 1354–1356.
[41] D. J. Gulliver, E. G. Hope, W. Levason, *J. Chem. Soc., Perkin Trans. 2* **1984**, *3*, 429–434.
[42] Th. Arnauld, D. H. R. Barton, J. F. Normant, *J. Org. Chem.* **1999**, *64*, 3722–3725.
[43] R. K. Chadha, J. M. Miller, *J. Chem. Soc., Dalton Trans.* **1982**, 117–120.
[44] N. Miyoshi, H. Ishii, K. Kondo, S. Mui, N. Sonoda, *Synthesis* **1979**, 301–304.
[45] J. E. Drake, R. T. Hemmings, *Inorg. Chem.* **1980**, *19*, 1879–1883.
[46] S. Perumal, R. Chandrasekaran, V. Vijayabaskar, D. A. Wilson, *Magn. Reson. Chem.* **1995**, *33*, 779–790.
[47] S.-K. Chung, K. Sasamoto, *J. Org. Chem.* **1981**, *46*, 4590–4592.
[48] *X-RED32 1.01*, Data Reduction Program, Stoe & Cie GmbH, Darmstadt, Germany, **2001**.
[49] G. M. Sheldrick, *SHELXTL PC version 5.1*, An Integrated System for Solving, Refining, and Displaying Crystal Structures from Diffraction Data, Bruker Analytical X-ray Systems, Karlsruhe, **2000**.
[50] *Diamond Version 2.1d*, K. Brandenburg, Crystal Impact GbR, **1996–2000**.
[51] *STOE*, *WinXPOW*, STOE & Cie GmbH, Darmstadt, **2000**.

Received: September 21, 2009

DOI: 10.1002/ejic.200900681

Low-Temperature Synthesis, Magnetic and Microwave Electromagnetic Properties of Substoichiometric Spinel Cobalt Ferrite Octahedra

Xi'an Fan,[a] **Jianguo Guan,***[a] **Xiaofen Cao,**[a] **Wei Wang,**[a] **and Fangzhi Mou**[a]

Keywords: Cobalt / Ferrites / Coprecipitation / Oxidation / Octahedral morphology / Magnetic properties / Microwave electromagnetic properties

Substoichiometric spinel cobalt ferrite octahedra were prepared by using a versatile coprecipitation/air oxidation method in a low-temperature aqueous system without any surfactants and directing agents. The microstructure, magnetic and microwave electromagnetic properties of the resultant products as functions of the nominal molar ratio $[Co^{2+}]/[Fe^{2+}]$ were investigated. The results show that the $[Co^{2+}]/[Fe^{2+}]$ ratio has a strong influence on the kinetic reaction rate of the coprecipitation/oxidation reaction of Co^{2+} and Fe^{2+} and consequently determines the chemical composition, crystal structure and morphology of the resultant products. Substoichiometric spinel cobalt ferrite octahedra of about 150 nm were available at a $[Co^{2+}]/[Fe^{2+}]$ ratio of 1:4, due to the control over the nucleation and selective crystallographic direction growth. Too high $[Co^{2+}]/[Fe^{2+}]$ values significantly accelerate the kinetic rate of copercipiation/oxidation reaction, which results in irregular $Co_xFe_{3-x}O_4$ nanoparticles and a decreasing level of Co^{2+} incorporation in the crystal lattice. The inverse spinel $Co_{0.59}Fe_{2.41}O_4$ octahedra have the largest saturation magnetization, coercivity, complex permittivity and permeability among all the resultant products. This phenomenon, together with the strong resonance behavior of the imaginary permittivity and imaginary permeability for $Co_{0.59}Fe_{2.41}O_4$ octahedra at frequency above 16 GHz, is explained in terms of a correlation with the chemical composition, the Co^{2+} distribution over tetrahedral and octahedral sites and the incorporation level of Co^{2+} into the ferrite lattice.

Introduction

Spinel ferrite ($M_xFe_{3-x}O_4$) is an important class of iron oxide materials, which can be regarded as the products of cation substitution of magnetite ($Fe^{2+}Fe^{3+}{}_2O_4$). Magnetite is a soft ferromagnet with an inverse spinel cubic structure, in which one-third of the tetrahedral (A) sites are occupied by Fe^{3+} ions, and the remaining Fe ions (mixed-valent Fe ions with an average charge of +2.5 per formula unit) are located at the octahedral (B) sites.[1] Many cations M^{2+}, such as Mn^{2+}, Zn^{2+}, Cd^{2+}, Co^{2+}, Ni^{2+} etc., can replace Fe^{2+} in $Fe^{2+}Fe^{3+}{}_2O_4$, thus forming ferromagnetic ferrites with a similar spinel structure.[2–9] These cation distribution determines the structural, electrical and magnetic properties for a particular ferrite system.[10,11]

Cobalt ferrites, as high-density magnetic recording media, microwave devices, magnetic fluids, medical diagnostics, drug delivery and electromagnetic wave absorption materials, are widely investigated because of their high Curie temperature, large magnetocrystalline anisotropy, moderate magnetization, chemical stability and corrosion resistivity.[12–15] The properties of cobalt ferrites depend strongly upon the preparation approach, the doped cobalt content, the cation distribution over the A and B sites, the particle size and morphology. Up to now, various preparation methods, such as coprecipitation/post high-temperature annealing process,[16,17] sol–gel pyrolysis,[18] solid-state reactions,[19] mechanical alloying,[20] hydrothermal methods,[21] reverse micelle processes,[22] high-temperature solution-phase reactions,[23] combustion methods[24] etc., have been developed to synthesize spinel cobalt ferrites. Among these synthetic methods, most of them show unavoidable disadvantages of complicated multi-steps, harsh synthesis conditions (e.g. high temperature, high pressure and time consumption), and irregularity of the particle shape, though the hydrothermal method has been reported to have a good shape controllability of the as-obtained stoichiometric cobalt ferrite particles in the presence of surfactants or directing agents.[25,26] To the best of our knowledge, there is by far no report about a one-pot synthesis of spinel cobalt ferrites with highly crystalline and regular morphology at low-temperature and normal pressure.

The low-temperature aqueous-phase method is known to be advantageous because of its mild and environmentally friendly synthesis conditions for mass production of high-quality products. Successful syntheses of some particular

---

[a] State Key Laboratory of Advanced Technology for Materials Synthesis and Processing, Wuhan University of Technology, 122 Luoshi Road, Wuhan 430070, People's Republic of China
Fax: +86-27-87879468
E-mail: guanjg@whut.edu.cn

Supporting information for this article is available on the WWW under http://dx.doi.org/10.1002/ejic.200900681.

nanostructures including nanowires,[27] nanorods,[28] nanotubes[29] etc., have been accomplished by accurately controlling such experimental conditions as pH value, temperature, pressure and reaction time.[30] In the present work, we demonstrate a simple and convenient coprecipitation/air oxidation method that allows for the facile and large-scale synthesis of spinel cobalt ferrites with octahedral morphology in a low-temperature aqueous system without any surfactants or directing agents. The effects of the nominal molar ratio $[Co^{2+}]/[Fe^{2+}]$ on the crystal structures, morphologies, and static magnetic and microwave electromagnetic properties of the resultant products were investigated. The as-obtained substoichiometric cobalt ferrite octahedra have a saturation magnetization of 74.53 emu/g, a coercivity of 867 Oe and a remnant magnetism of 33.65 emu/g, and exhibit a strong resonance behavior of the imaginary permittivity and imaginary permeability above 16 GHz. The results provided here will inspire more versatile access to low-cost and large-scale syntheses of spinel $M_xFe_{3-x}O_4$ (where M is a divalent ion, $0 \leq x \leq 1$) octahedra and more extensive application exploration of ferrites with octahedral morphology in magnetic recording media, microwave devices, and as a high-temperature, anticorrosive and low-cost microwave absorber.

Results and Discussion

Figure 1 shows XRD patterns of the resultant products obtained at different nominal molar ratios of $[Co^{2+}]/[Fe^{2+}]$. Clearly, all the XRD diffraction peaks for the sample without Co^{2+} (Figure 1a) can be well indexed to a pure orthorhombic α-FeOOH phase [space group *Pbnm* (62), JCPDS 29-0713]. With increasing $[Co^{2+}]/[Fe^{2+}]$ ratio, the diffraction peaks corresponding to α-FeOOH were gradually replaced by those corresponding to face-centered cubic (*fcc*) substoichiometric cobalt ferrites [$Co_xFe_{3-x}O_4$, $0 \leq x \leq 1$, space group *Fd*3*m* (227), JCPDS 22-1086], which suggests the transformation of the resultant products from the orthorhombic phase of α-FeOOH into the *fcc* phase of $Co_xFe_{3-x}O_4$. In this protocol, the following relevant chemical reactions can be summarized as Equations (1), (2), (3) and (4).

$$Co^{2+} + 2\,OH \rightarrow Co(OH)_2 \quad (1)$$

$$Fe^{2+} + 2\,OH \rightarrow Fe(OH)_2 \quad (2)$$

$$4\,Fe(OH)_2 + O_2 \rightarrow 4\,FeOOH + 2\,H_2O \quad (3)$$

$$(12\text{–}4x)\,Fe(OH)_2 + 4x\,Co(OH)_2 + (3 - x)\,O_2 \rightarrow 4\,Co_xFe_{3-x}O_4 + (10 + 2x)\,H_2O + (4 - 4x)\,OH^- \quad (4)$$

Without the incorporation of Co^{2+}, lemon yellow goethite (α-FeOOH) is easily obtained according to Equations (2) and (3) due to its low energy for nucleation in an alkaline solution and an air oxidation atmosphere. However, the co-precipitation and oxidation reactions shown in Equations (1) and (4) will also take place and yield cobalt ferrites when Co^{2+} is present. Consequently, products with both α-FeOOH and $Co_xFe_{3-x}O_4$ are formed. Obviously, the oxidation reactions in Equations (3) and (4) show a somewhat kinetically competitive relationship, and an increasing Co^{2+} content favors Equation (4). As $Co_xFe_{3-x}O_4$ with spinel cubic structure has a lower solubility than α-FeOOH,[31] $Co_xFe_{3-x}O_4$ is more easily available than α-FeOOH when sufficient Co^{2+} is introduced into the system. Therefore, $Co_xFe_{3-x}O_4$ is thermodynamically more stable than α-FeOOH even though the reaction rate of Equation (3) is higher than that of Equation (4). As a result, the $Co_xFe_{3-x}O_4$/α-FeOOH ratio in the resultant products increases with increasing $[Co^{2+}]/[Fe^{2+}]$ ratio. When $[Co^{2+}]/[Fe^{2+}] = 1:9$, the obtained products still show some weak diffraction peaks of α-FeOOH in their XRD patterns (Figure 1c), suggesting that the Co^{2+} content is too low to cause a complete phase transformation from orthorhombic α-FeOOH to face-centered cubic cobalt ferrites. When $[Co^{2+}]/[Fe^{2+}] = 1:4$, there are no diffraction peaks of α-FeOOH, but only those of pure cobalt ferrites in the XRD pattern (Figure 1d). The sharp XRD peaks indicate that the resultant product is of high crystallinity. The samples obtained at $[Co^{2+}]/[Fe^{2+}] = 3:7$ show weak and broad diffraction peaks, indicating a poor crystallinity and a fine grain size. As the doped Co^{2+} content deviates from the ideal stoichiometric composition of $CoFe_2O_4$, Co^{2+} only partially replaces Fe^{2+} and forms $Co_xFe_{3-x}O_4$ ($0 \leq x \leq 1$).

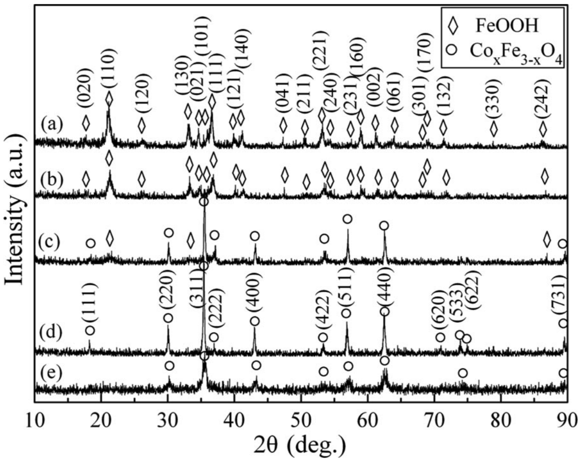

Figure 1. XRD patterns of the products obtained at different $[Co^{2+}]/[Fe^{2+}]$ ratios: (a) 0, (b) 1:19, (c) 1:9, (d) 1:4, (e) 3:7.

Figure 2 shows infrared spectra of the products obtained at different $[Co^{2+}]/[Fe^{2+}]$ ratios. For the samples obtained at $[Co^{2+}]/[Fe^{2+}] = 0$ or 1:19, the infrared spectra (Figure 2a and b) have the typical features of α-FeOOH. A very strong band at 3131 cm^{-1} is due to the presence of –OH stretching modes. Two typical bands at 899 and 797 cm^{-1} can be ascribed to Fe–O–H bending vibrations. The infrared band recorded at 631 cm^{-1} is attributed to Fe–O stretching vibrations.[32] When the $[Co^{2+}]/[Fe^{2+}]$ ratio is increased to 1:9 (Figure 2c), weak features of α-FeOOH are still observed. However, the –OH stretching mode at 3131 cm^{-1} completely disappears, and the Fe–O–H bending vibrations at 899 and 797 cm^{-1} also become very weak. The shift of the Fe–O stretching vibration from 631 to 588 cm^{-1} suggests that the new phase cobalt ferrite is formed by replacement of Fe^{2+} by Co^{2+}, which enters the lattice of the resultant products. This is consistent with the XRD results mentioned above. For the samples obtained at $[Co^{2+}]/[Fe^{2+}]$ = 1:4 or 3:7 (Figure 2d and e), the complete disappearance of the –OH stretching and the Fe–O–H bending vibration modes, together with the presence of only the Fe(Co)–O stretching vibration mode at 588 cm^{-1}, indicates the typical infrared band features of cobalt ferrite $Co_xFe_{3-x}O_4$.

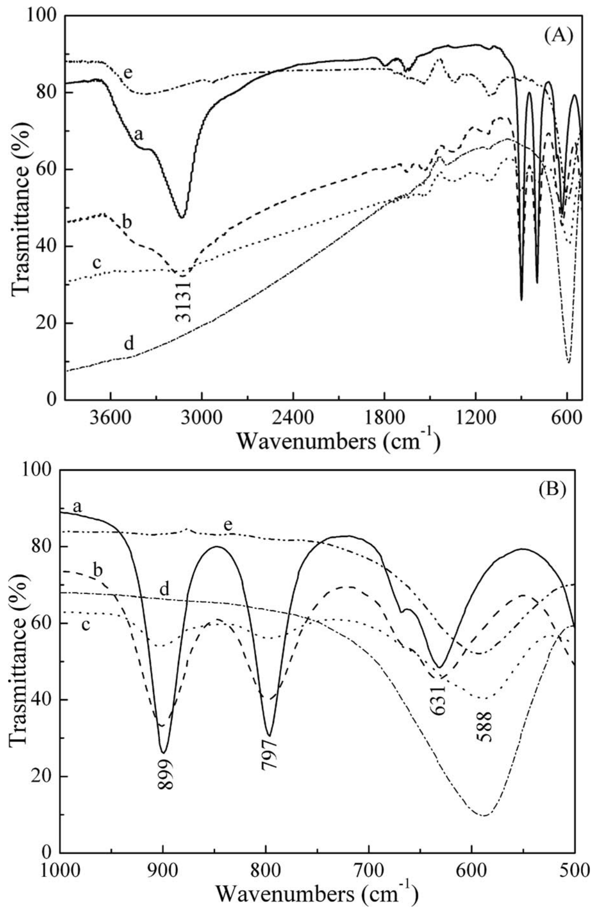

Figure 2. Infrared spectra (A) and partial enlarged spectra (B) of the products obtained at different $[Co^{2+}]/[Fe^{2+}]$ ratios: (a) 0, (b) 1:19, (c) 1:9, (d) 1:4, (e) 3:7.

Raman spectroscopy and XPS pattern are known to be sensitive and powerful techniques to identify the distribution of cobalt ions between octahedral and tetrahedral sites in the ferrite nanocrystals.[33] To further confirm that the Co^{2+} has replaced Fe^{2+}, resulting in the formation of substoichiometric cobalt ferrites, we have measured Raman spectra of the products obtained at different $[Co^{2+}]/[Fe^{2+}]$ ratios (Figure 3) and XPS patterns of the cobalt ferrite obtained at $[Co^{2+}]/[Fe^{2+}]$ = 1:4 (Figures 4 and S1). For the products obtained at $[Co^{2+}]/[Fe^{2+}] < 1:19$, the Raman spectra showed the presence of α-FeOOH. Compared to the samples without Co^{2+}, the decreasing vibrating peaks for the samples obtained at $[Co^{2+}]/[Fe^{2+}]$ = 1:19 may be attributed to the presence of trace cobalt ferrites, which interferes with the growth of α-FeOOH crystals. For the samples obtained at $[Co^{2+}]/[Fe^{2+}]$ = 1:9, the three first-order Raman-active modes ($A_{1g} + E_g + F_{2g}$) are observed, suggesting that the cubic spinel phase of $Co_xFe_{3-x}O_4$ is dominant in the samples. The modes above 600 cm^{-1} of the cubic spinels mostly correspond to the motion of oxygen in tetrahedral AO_4 groups.[33–35] Therefore, the mode at 670 cm^{-1} can be reasonably considered as A_{1g}-symmetric. The other low-frequency modes below 600 cm^{-1}, such as 293 cm^{-1} (E_g) and 471 cm^{-1} (F_{2g}) represent the characteristics of the octahedral sites (BO_6). The Raman mode at 396 cm^{-1} suggests the existence of an impurity (α-FeOOH), which is also proved by XRD and the FTIR spectrum. When the $[Co^{2+}]/[Fe^{2+}]$ ratio is increased to 1:4, the three first-order vibration modes at 293, 471 and 670 cm^{-1} exhibit a broad and intense characteristic. When $[Co^{2+}]/[Fe^{2+}]$ = 3:7, the vibration modes present broader characteristics.

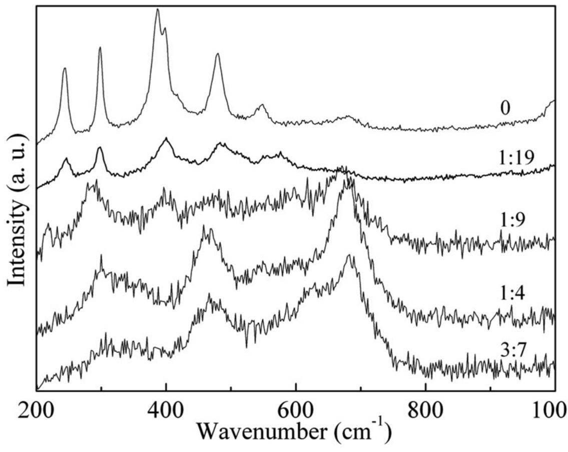

Figure 3. Raman spectra of the products obtained at different $[Co^{2+}]/[Fe^{2+}]$ ratios.

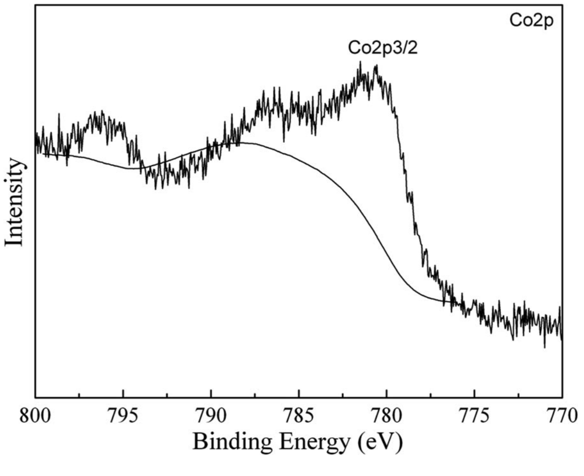

Figure 4. Co2p XPS pattern of the cobalt ferrite obtained at $[Co^{2+}]/[Fe^{2+}]$ = 1:4.

When comparing the peak-intensity ratios at 471 and 670 cm^{-1} (I_{471}/I_{670}), the samples obtained at $[Co^{2+}]/[Fe^{2+}]$ = 1:4 show the strongest peak-intensity ratio among all the samples. This indicates that Co^{2+} in the samples obtained at $[Co^{2+}]/[Fe^{2+}] = 1:4$ mainly occupies the octahedral sites, and an inverse spinel cubic phase is formed in this case, as the vibration mode at 471 cm^{-1} is solely due to Co^{2+} at octahedral sites, whereas that at 670 cm^{-1} may be contributed by both the magnetite and cobalt ferrite phases in the particles.[33] The relative broad and weak vibration modes in the samples obtained at $[Co^{2+}]/[Fe^{2+}] = 3:7$ may be ascribed to the disorder of Co and Fe cations occurring in the tetrahedral and octahedral sites.

Figure 4 shows a Co2p XPS pattern of the cobalt ferrite obtained at $[Co^{2+}]/[Fe^{2+}] = 1:4$. Obviously, Co2p3/2 exhibits an asymmetric XPS spectrum with a peak at 781.3 eV and an intense characteristic satellite peak at 786.6 eV. This suggests that the Co^{2+} cations occupy the octahedral sites in the cobalt ferrite spinel lattice.

The typical energy-dispersive spectra (EDS) and element-composition analyses are presented in Figure 5 and Table 1, respectively. It can be seen that the actual molar ratio of element Co/Fe is very close to the nominal molar ratio. This suggests that all the metal ions including Co^{2+} and Fe^{2+} are completely transformed into either $Co_xFe_{3-x}O_4$ or α-FeOOH. From the above results of XRD, FTIR and Raman spectra, it is concluded that the samples obtained at $[Co^{2+}]/[Fe^{2+}] = 1:4$ and 3:7 are pure cobalt ferrites. Therefore, according to the element composition analysis, the chemical formulae of these two samples can be written as $Co_{0.59}Fe_{2.41}O_4$ and $Co_{0.92}Fe_{2.08}O_4$, respectively.

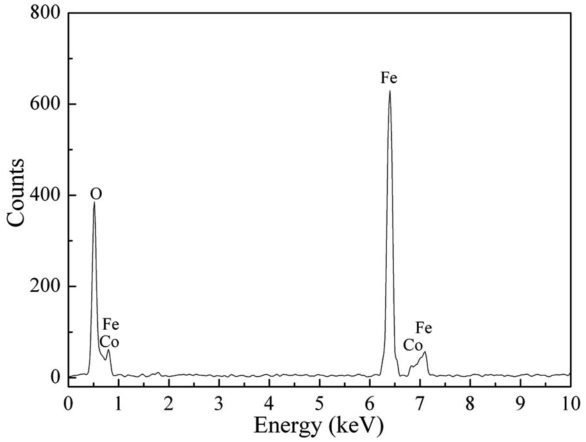

Figure 5. Typical EDS spectrum of the products obtained at $[Co^{2+}]/[Fe^{2+}] = 1:4$.

The morphological evolution of the as-prepared products with the $[Co^{2+}]/[Fe^{2+}]$ ratio is shown in Figure 6. When no Co^{2+} is incorporated, the as-prepared samples are mainly composed of nanorods with a relatively smooth surface characteristic, ca. 50 nm in diameter and about 0.4–0.6 μm in length (Figure 6a). The dispersibility of nanorods is very bad, and some nanorods aggregate into bunches composed of 2–6 nanorods. This may be ascribed to the –OH polar groups at the surface of α-FeOOH.

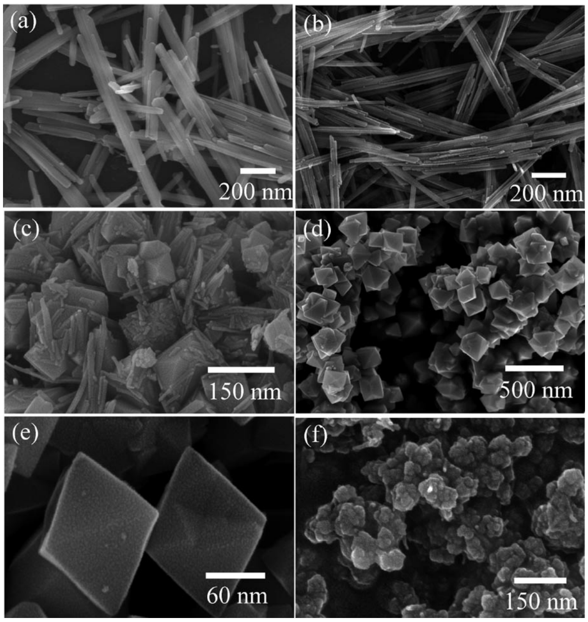

Figure 6. SEM images of the products obtained at different $[Co^{2+}]/[Fe^{2+}]$ ratios: (a) 0, (b) 1:19, (c) 1:9, (d, e) 1:4, (f) 3:7.

When small quantities of Co^{2+} ions, for example $[Co^{2+}]/[Fe^{2+}] = 1:19$, are introduced into the reaction system, the resultant materials are still composed of nanorods (Figure 6b). Compared with the samples without Co^{2+}, the dispersibility of the nanorods obtained at $[Co^{2+}]/[Fe^{2+}] = 1:19$ becomes worse, and there exist more aggregates composed of more than ten nanorods. Besides the effect of the –OH polar groups of α-FeOOH, the worse dispersibility is possibly ascribed to the magnetic-moment effect resulting from a new magnetic cobalt ferrite phase. Figure 6c shows that in the samples obtained at $[Co^{2+}]/[Fe^{2+}] = 1:9$, a large amount of octahedra ($Co_xFe_{3-x}O_4$) is present, with some small immethodical nanorods (α-FeOOH) adhered on their surfaces. The α-FeOOH nanorods are broken into pieces and have a decreasing axis length. It suggests that the incorporation of a few Co^{2+} ions initiates the occurrence of Equation (4) and causes the reaction in Equation (3) to move to the left side, resulting in slight dissolution of α-

Table 1. Element composition of the products obtained at different $[Co^{2+}]/[Fe^{2+}]$ ratios.

$[Co^{2+}]/[Fe^{2+}]$	Fe [mol-%]	Co [mol-%]	O [mol-%]	Actual molar ratio Co/Fe
0	–	–	–	0
1:19	21.0	1.2	77.8	1:17.5
1:9	27.2	3.1	69.7	1:8.8
1:4	25.9	6.4	67.7	1:4.1
3:7	22.0	9.7	68.3	1:2.3

FeOOH nanoparticles. When the [Co^{2+}]/[Fe^{2+}] ratio is further increased, $Co_xFe_{3-x}O_4$ gradually grows with slowly diminishing α-FeOOH.

Figure 6d and e show that samples obtained at [Co^{2+}]/[Fe^{2+}] = 1:4 are almost octahedra with a size of about 150 nm, and no nanorods are observable. This indicates that a substoichiometric inverse spinel $Co_{0.59}Fe_{2.41}O_4$ with an octahedral morphology has been available for the first time in the absence of any surfactants or directing agents. To the best of our knowledge, previous octahedral MFe_2O_4 (M = Mn, Fe, Ni and Co) was obtained only by using hydrothermal routes and under the assistance of directing agents.[25] It is generally accepted that the crystal-structure anisotropy and the relative growth rate between different directions are identified to be the main factors determining the shape of crystals. According to the surface free-energy minimization principle, a single-crystal particle has to be enclosed by crystallographic facets with lowest surface energy. This usually produces a specific shape. For face-centered cubic $Co_{0.59}Fe_{2.41}O_4$ crystals (TEM and SAED analysis shown in Figure S2), the increasing sequence of surface energy is confirmed as $\gamma\{111\} < \gamma\{100\} < \gamma\{110\}$.[36] The growth rate along the low-index plane (100) is faster than that along the high-index plane (111). Therefore, the (100) plane will be gradually eliminated, and an octahedron enclosed by a (111) plane is finally formed. Similar structure models are also described in the literatures.[37,38]

We noticed that fine irregular nanoparticles or nanoparticle aggregates are obtained at [Co^{2+}]/[Fe^{2+}] = 3:7 (Figure 6f). When the [Co^{2+}]/[Fe^{2+}] ratio is increased to 3:7, a vast nucleation of $Co_xFe_{3-x}O_4$ will simultaneously take place at the expense of crystal growth, resulting in a significant decrease of the grain size. It is reasonable to conclude that the Co^{2+} concentration not only affects the thermodynamically competitive relationship between Equations (3) and (4), but also influences the reaction rate of Equation (4), consequently determining the nucleation and growth process of $Co_xFe_{3-x}O_4$. The morphology evolution of the resultant products from octahedra to irregular nanoparticles upon increasing the [Co^{2+}]/[Fe^{2+}] ratio from 1:9 to 3:7 may be reasonably explained as long as one realizes that an increase of [Co^{2+}] accelerates the reaction rate of Equation (4), which results in a less selective crystallographic growth direction. This result is in good agreement with XRD and Raman spectra results, and it suggests that the Co^{2+} concentration in this protocol not only affects the kinetics of the formation of $Co_xFe_{3-x}O_4$ but also determines the anisotropy growth of $Co_xFe_{3-x}O_4$. A relative low Co^{2+} concentration favors the growth along selective crystallographic directions (in this case, thermodynamically dominated), whereas a relative high Co^{2+} concentration leads to a rapid rate of nucleation and growth, as a result of a significant increase of the reaction rate of co-precipitation/air oxidation and a vast replacement of Co^{2+} by Fe^{2+}, apt to cause lattice distortion (in this case, kinetically dominated).

Figure 7 shows the hysteresis loops of the products obtained at different [Co^{2+}]/[Fe^{2+}] ratios, and correlative magnetic properties are also presented in Table 2. It can be seen that the saturation magnetization (M_s) firstly increases from 0.43 to 74.53 emu/g with increasing [Co^{2+}]/[Fe^{2+}] ratio from 0 to 1:4, then decreases abruptly to 51.69 emu/g when [Co^{2+}]/[Fe^{2+}] = 3:7. The coercivity (H_c), remnant magnetism (M_r) and square ratio (S) also present a similar variation trend. When [Co^{2+}]/[Fe^{2+}] = 0, the M_s, H_c and M_r values are very low as a result of the only non-magnetic α-FeOOH phase in the specimens. When the [Co^{2+}]/[Fe^{2+}] ratio increases, the content of ferromagnetic cobalt ferrites in the as-prepared samples increases, whereaas the amount of Co^{2+} at the B sites in the substoichiometric cobalt ferrite samples also increases, thus significantly enhancing the magnetocrystalline anisotropy and coercivity by L-S coupling. Consequently, the magnetic properties including M_s, M_r and H_c are expected to increase.

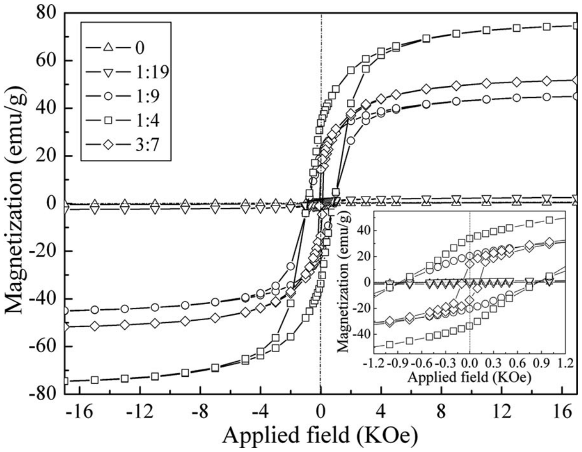

Figure 7. Hysteresis loops of the products obtained at different [Co^{2+}]/[Fe^{2+}] ratios.

Table 2. Magnetic properties of the products obtained at different [Co^{2+}]/[Fe^{2+}] ratios.

[Co^{2+}]/[Fe^{2+}]	H_c [Oe]	M_s [emu/g]	M_r [emu/g]	S
0	64.47	0.43	0.16	0.04
1:19	514.44	2.48	0.76	0.31
1:9	846.66	44.99	20.30	0.45
1:4	867.23	74.53	33.65	0.45
3:7	105.96	51.69	13.61	0.26

It is worth noting that pure cobalt ferrites are available when the [Co^{2+}]/[Fe^{2+}] ratio increases to 1:4 or more; however, the as-prepared $Co_{0.92}Fe_{2.08}O_4$ specimens (obtained at [Co^{2+}]/[Fe^{2+}] = 3:7) show not only smaller M_s and M_r but also much lower H_c values than the as-prepared samples $Co_{0.59}Fe_{2.41}O_4$ (obtained at [Co^{2+}]/[Fe^{2+}] = 1:4). As we know, the as-prepared substoichiometric cobalt ferrites $Co_xFe_{3-x}O_4$ show a partially inverse spinel structure with a formula unit of $(Co^{II}_yFe^{III}_{1-y})^A[Co^{II}_{x-y}Fe^{II}_{1-x}Fe^{III}_{1+y}]^BO_4$, where y denotes the amount of Co^{2+} cations in tetrahedral (A) sites. According to the single-ion anisotropy model, the orbital magnetism of the Co^{2+} cations in the B sites of the spinel dominantly contributes to the magnetocrystalline anisotropy and coercivity by L-S coupling, since they have high-spin ligand fields and possess 7 3d electrons with 3 of them unpaired. Generally, when Co^{2+} ions replace Fe^{2+} ions and are incorporated into the *fcc* crystal lattice, they prefer to occupy B sites rather than A sites as the former can hold 2 times more metal ions than the latter. Therefore, for substoichiometric cobalt ferrite $Co_xFe_{3-x}O_4$, the coercivity will increase with x if the doped Co^{2+} cations occupy B sites. However, if annealing or synthesis conditions are varied, the Co^{2+} cations in the B sites may migrate to the A sites, or when the content of Co^{2+} occupying B sites further increases, the subsequent Co^{2+} ions are forced to occupy A sites. Both of these cases will cause the Fe^{3+} ions to transfer from B sites to A sites. As a result, the magnetocrystalline anisotropy and coercivity will decrease as the tetrahedral sites have less anisotropic environment (tetrahedral symmetry).

As shown in Table 2, H_c of the as-prepared $Co_{0.92}Fe_{2.08}O_4$ specimens is much smaller than that of $Co_{0.59}Fe_{2.41}O_4$. This suggests that the Co^{2+} ions doped in $Co_{0.92}Fe_{2.08}O_4$ specimens either mainly occupy the tetrahedral sites rather than the octahedral sites, or do not incorporate well into crystal lattices. This is in accordance with the Raman spectrum, which indicates a relative weak intensity ratio between the vibration modes at 471 and 670 cm^{-1} (I_{471}/I_{670}). Due to superexchange interaction, the magnetic moment of ions in A sites of $Co_xFe_{3-x}O_4$ is antiparallel to that in octahedral (B) sites. The total net magnetic moment M is defined as $M = M_B - M_A$, where M_A and M_B are the magnetic moments in the A and B sites, respectively.[39] As the magnetic moments of Fe^{3+} (5 μ_B) and Fe^{2+} (4 μ_B) both are larger than that of Co^{2+} (3 μ_B), the total net magnetic moment M of the ferrites will possibly increase with x if the possibility for Co^{2+} to occupy A sites is one-third more than that to occupy B sites. But from Table 2, M_s of the as-prepared $Co_{0.92}Fe_{2.08}O_4$ specimens is smaller than that of $Co_{0.59}Fe_{2.41}O_4$. This suggests that the Co^{2+} ions doped in $Co_{0.92}Fe_{2.08}O_4$ specimens do not well incorporate into crystal lattices, consistent with the above XRD (Figure 1 indicates its poor crystallinity) and kinetic analysis of Equation (4). Additionally, the small M_s values of the as-prepared $Co_{0.92}Fe_{2.08}O_4$ specimens may also be associated with the small particle size and large specific surface areas with "dead" magnetic zone.

Figure S3 displays microwave electromagnetic parameters vs. frequency for the composites containing 50 wt.-% resultant products dispersed in paraffin matrix. It can be seen that in the entire frequency range of 2–18 GHz, all four microwave electromagnetic parameters including complex permittivity ($\varepsilon' - j\varepsilon''$) and complex permeability ($\mu' - j\mu''$) firstly show a maximum value at $[Co^{2+}]/[Fe^{2+}] = 1:4$, then decrease abruptly with further increasing $[Co^{2+}]/[Fe^{2+}]$ ratio. Obviously, the increasing complex permittivity and permeability with the $[Co^{2+}]/[Fe^{2+}]$ ratio are ascribed to the increasing content of cobalt ferrites in the resultant specimens, as cobalt ferrites show a higher polarization and a larger magnetization than α-FeOOH. The obvious decrease of the complex permittivity at $[Co^{2+}]/[Fe^{2+}] = 3:7$ may be interpreted in terms of a correlation between the increasing occupancy of Co^{2+} at B sites (though as mentioned before, the incorporation level is poor) and the decreasing Fe^{2+} content at B sites, as a decreasing Fe^{2+} content at B sites will decrease the polarizability of cobalt ferrites through electron hopping between adjacent Fe^{2+} and Fe^{3+} pairs in octahedral sites.[40,41]

For the octahedral $Co_{0.59}Fe_{2.41}O_4$ obtained at $[Co^{2+}]/[Fe^{2+}] = 1:4$, both ε'' and μ'' abruptly increase above 16 GHz. This indicates a strong resonance behavior resulting from the small-size effect, the surface-shape effect, the specific chemical composition and the spin-wave excitation effect.[42,43] It is believed that the strong natural resonance leads to a strong electromagnetic loss ability and enhances the electromagnetic wave absorption of the spinel substoichiometric cobalt ferrites with octahedral morphology.

Conclusions

We demonstrated a simple coprecipitation/air oxidation approach to prepare substoichiometric spinel cobalt ferrite octahedra of about 150 nm by controlling the nucleation and the selective crystallographic direction growth through a simple optimization of $[Co^{2+}]$. The role of $[Co^{2+}]$ is elucidated to control the kinetic reaction rate of the coprecipitation/air oxidation reaction of Co^{2+} and Fe^{2+}. As this method is carried out in a low-temperature (45 °C) aqueous system containing dimetallic cations and especially does not need any surfactants or directing agents, it can be easily extended to a large-scale synthesis of spinel $M_xFe_2O_4$ (where M is a divalent ion, $0 \le x \le 1$) octahedra. The as-synthesized inverse spinel octahedral $Co_{0.59}Fe_{2.41}O_4$ has a saturation magnetization of 74.53 emu/g, coercivity of 867 Oe and remnant magnetism of 33.65 emu/g, and exhibits a strong resonance behavior of the imaginary permittivity and imaginary permeability above 16 GHz. Thus, they have potential applications in magnetic recording media, microwave devices, and as a high-temperature, anticorrosive and low-cost microwave absorber.

Experimental Section

All chemicals used in this paper were of analytical grade without further purification. The resultant products were obtained in a low-temperature aqueous system by a coprecipitation/air oxidation method. In a typical procedure, The mixed solution containing different contents of $CoCl_2$ and $FeSO_4$ (100 mL, 0.72 mol/L) (the nominal molar ratios $[Co^{2+}]/[Fe^{2+}]$ were confined as 0, 1:19, 1:9, 1:4 and 3:7) was quickly poured into NaOH solution (400 mL, 4.38 mol/L) at 45 °C under vigorous stirring for 30 min. Subsequently, compressed air was introduced into the mixtures at a speed of 5 L/min. After 7 h, the solution was allowed to cool to room temperature. The resultant products of precipitated powders were separated by centrifugation, washed with deionized water and absolute ethanol for several times, and dried under vacuum at 60 °C for 24 h. X-ray diffraction (XRD) patterns were recorded with a

D/MAX-RB diffractometer by using Cu-K_α radiation (λ = 1.5418 Å). Infrared spectra were recorded with a NICOLET 60-SXB FTIR spectrophotometer. Raman scattering measurements were performed by using a Renishaw Laser Confocal Raman Microscope. The Raman spectra at room temperature were recorded with a spectrometer equipped with a charge-coupled device (CCD) detector. The 514 nm line of an argon ion laser was used to excite the samples. For the avoidance of local laser damage that could easily occur under the microscope, a laser power not exceeding an approximate level of 2 mW was used. The morphologies of the as-prepared samples were observed with a Hitachi S-4800 field emission scanning electron microscope (FE-SEM). The element compositions were characterized with a Horbia EX-250 X-ray energy-dispersive spectrometer (EDS) associated with FE-SEM. Transmission electron microscopy (TEM) images and the corresponding selected-area electron diffraction (SAED) patterns were captured with a JEM-100CXΠ instrument at an acceleration voltage of 150 kV. X-ray photoelectron spectroscopy (XPS) measurements were carried out with a VG Multilab 20000 spectrometer using a monochromated Al-K_α X-ray radiation. The hysteresis loops were recorded with a Model 4HF vibrating sample magnetometer (VSM) at room temperature. The complex dielectric permittivity ($\varepsilon = \varepsilon' - j\varepsilon''$) and magnetic permeability ($\mu = \mu' - j\mu''$) were obtained by measuring the S_{11} and S_{21} parameters using a network analyzer (Agilent Technologies, N5230) by coaxial reflection/transmission technique in a frequency range of 2–18 GHz. The samples were prepared by randomly dispersing the magnetic particles into a paraffin matrix with a mass content of 50 wt.-% and pressing into coaxial rings with an outer diameter of 7 mm, an inner diameter of 3 mm and a thickness of 3–3.5 mm for electromagnetic wave measurements.

Supporting Information (see footnote on the first page of this article): XPS patterns, typical TEM and SAED images of the cobalt ferrite obtained at [Co^{2+}]/[Fe^{2+}] = 1:4; frequency dependence of the electromagnetic parameters of paraffin composites containing 50 wt.-% products obtained at different [Co^{2+}]/[Fe^{2+}] ratios.

Acknowledgments

This work was supported by the National Fundamental Research Project (D1420061057), the New Century Excellent Talents from the Ministry of Education (No. NCET-05-0660), the National High-Technology Research and Development Program of China (No. 2006AA03A209), and the Chinese Postdoctoral Science Fund (20070420169, 200902459).

---

[1] L. Horng, G. Chern, M. C. Chen, P. C. Kang, D. S. Lee, *J. Magn. Magn. Mater.* **2004**, *270*, 389–396.
[2] C. S. Kim, Y. S. Yi, K. T. Park, H. Namgung, J. G. Lee, *J. Appl. Phys.* **1999**, *85*, 5223–5225.
[3] N. Z. Bao, L. M. Shen, P. Padhan, A. Gupta, *Appl. Phys. Lett.* **2008**, *92*, 173101.
[4] C. N. Chinnasamy, B. Jeyadevan, K. Shinoda, K. Tohji, D. J. Djayaprawira, M. Takahashi, R. J. Joseyphus, A. Narayanasamy, *Appl. Phys. Lett.* **2003**, *83*, 2862–2864.
[5] K. Parekh, R. V. Upadhyay, L. Belova, K. V. Rao, *Nanotechnology* **2006**, *17*, 5970–5975.
[6] H. Shokrollahi, K. Janghorban, *Mater. Sci. Eng. B* **2007**, *141*, 91–107.
[7] A. M. M. Farea, S. Kumar, K. M. Batoo, A. Y. Alimuddin, *Physica B* **2008**, *403*, 684–701.
[8] B. Jeyadevan, C. N. Chinnasamy, K. Shinoda, K. Tohji, H. Oka, *J. Appl. Phys.* **2003**, *93*, 8450–8452.
[9] X. Jia, D. R. Chen, X. L. Jiao, T. He, H. Y. Wang, W. Jiang, *J. Phys. Chem. C* **2008**, *112*, 911–917.
[10] G. Salazar-Alvarez, R. T. Olsson, J. Sort, W. A. A. Macedo, J. D. Ardisson, M. D. Baró, U. W. Gedde, J. Nogués, *Chem. Mater.* **2007**, *19*, 4957–4963.
[11] E. E. Sileo, L. G. Rodenas, C. O. Paiva-Santos, P. W. Stephens, P. J. Morando, M. A. Blesa, *J. Solid State Chem.* **2006**, *179*, 2237–2244.
[12] G. Vaidyanathan, S. Sendhilnathan, *Physica B* **2008**, *403*, 2157–2167.
[13] R. C. Che, C. Y. Zhi, C. Y. Liang, X. G. Zhou, *Appl. Phys. Lett.* **2006**, *88*, 033105.
[14] W. Y. Fu, S. K. Liu, W. H. Fan, H. B. Yang, X. F. Pang, J. Xu, G. T. Zou, *J. Magn. Magn. Mater.* **2007**, *316*, 54–58.
[15] E. Manova, B. Kunev, D. Paneva, I. Mitov, L. Petrov, C. Estournès, C. D'Orléans, J. L. Rehspringer, M. Kurmoo, *Chem. Mater.* **2004**, *16*, 5689–5696.
[16] M. Veverka, P. Veverka, O. Kaman, A. Lančok, K. Závěta, E. Pollert, K. Knížek, J. Boháček, M. Beneš, P. Kašpar, E. Duguet, S. Vasseur, *Nanotechnology* **2007**, *18*, 345704.
[17] V. L. Mathe, R. B. Kamble, *Mater. Res. Bull.* **2008**, *43*, 2160–2165.
[18] M. E. Mata-Zamora, H. Montiel, G. Alvarez, J. F. Barrón, H. Arriola, J. M. Saniger, R. Valenzuela, *J. Magn. Magn. Mater.* **2008**, *320*, e139–e142.
[19] C. S. Kim, S. W. Lee, S. I. Park, J. Y. Park, Y. J. Oh, *J. Appl. Phys.* **1996**, *79*, 5428–5430.
[20] J. Ding, X. Y. Liu, J. Wang, Y. Shi, *Mater. Lett.* **2000**, *44*, 19–22.
[21] C. Q. Hu, Z. H. Gao, X. R. Yang, *J. Magn. Magn. Mater.* **2008**, *320*, L70–L73.
[22] V. L. Calero-DdelC, C. Rinaldi, *J. Magn. Magn. Mater.* **2007**, *314*, 60–67.
[23] S. H. Sun, H. Zeng, D. B. Robinson, S. Raoux, P. M. Rice, S. X. Wang, G. X. Li, *J. Am. Chem. Soc.* **2004**, *126*, 273–279.
[24] A. F. Júnior, E. C. O. Lima, M. A. Novak, P. R. Wells, *J. Magn. Magn. Mater.* **2007**, *308*, 198–202.
[25] X. M. Liu, S. Y. Fu, L. P. Zhu, *J. Solid State Chem.* **2007**, *180*, 461–466.
[26] D. E. Zhang, X. J. Zhang, X. M. Ni, J. M. Song, H. G. Zheng, *J. Magn. Magn. Mater.* **2006**, *305*, 68–70.
[27] J. Wang, Q. W. Chen, C. Zeng, B. Y. Hou, *Adv. Mater.* **2004**, *16*, 137–140.
[28] X. B. Cao, L. Gu, *Nanotechnology* **2005**, *16*, 180–185.
[29] C. J. Jia, L. D. Sun, Z. G. Yan, L. P. You, F. Luo, X. D. Han, Y. C. Pang, Z. Zhang, C. H. Yan, *Angew. Chem. Int. Ed.* **2005**, *44*, 4328–4333.
[30] G. X. Tong, J. G. Guan, Z. D. Xiao, F. Z. Mou, W. Wang, G. Q. Yan, *Chem. Mater.* **2008**, *20*, 3535–3539.
[31] R. T. Olsson, G. Salazar-Alvarez, M. S. Hedenqvist, U. W. Gedde, F. Lindberg, S. J. Savage, *Chem. Mater.* **2005**, *17*, 5109–5118.
[32] S. Krehula, S. Popović, S. Musić, *Mater. Lett.* **2002**, *54*, 108–113.
[33] G. Shemer, E. Tirosh, T. Livneh, G. Markovich, *J. Phys. Chem. C* **2007**, *111*, 14334–14338.
[34] F. Nakagomi, S. W. Silva, V. K. Garg, A. C. Oliveira, P. C. Morais, A. F. Júnior, E. C. D. Lima, *J. Appl. Phys.* **2007**, *101*, 09M514.
[35] Z. W. Wang, D. Schiferl, Y. S. Zhao, H. S. C. O'Neill, *J. Phys. Chem. Solids* **2003**, *64*, 2517–2523.
[36] L. Zhang, R. He, H. C. Gu, *Mater. Res. Bull.* **2006**, *41*, 260–267.
[37] R. Swaminathan, M. A. Willard, M. E. McHenry, *Acta Mater.* **2006**, *54*, 807–816.
[38] L. J. Zhao, H. J. Zhang, Y. Xing, S. Y. Song, S. Y. Yu, W. D. Shi, X. M. Guo, J. H. Yang, Y. Q. Lei, F. Cao, *Chem. Mater.* **2008**, *20*, 198–204.

[39] Y. Li, Q. Q. Fang, Y. M. Liu, Q. R. Lv, P. Yin, *J. Magn. Magn. Mater.* **2007**, *313*, 57–61.
[40] E. E. Sileo, L. G. Rodenas, C. O. Paiva-Santos, P. W. Stephens, P. J. Morando, M. A. Blesa, *J. Solid State Chem.* **2006**, *179*, 2237–2244.
[41] M. A. Blesa, A. J. G. Maroto, P. J. Morando, *J. Chem. Soc. Faraday Trans.* **1986**, *82*, 2345–2352.
[42] R. C. Chen, L. M. Peng, X. F. Duan, Q. Chen, X. L. Liang, *Adv. Mater.* **2004**, *16*, 401–405.
[43] C. C. Lee, D. H. Chen, *Appl. Phys. Lett.* **2007**, *90*, 193102.

Received: July 20, 2009

DOI: 10.1002/ejic.200900776

Cluster-Based Cu^{II}–Azide Polymers: Synthesis, Structure, Magnetic Properties, and Effect of Polyamines on Crystal Structures

Chong-Bin Tian,[a,b] Zhi-Hua Li,[a] Jian-Di Lin,[a,b] Shu-Ting Wu,[c] Shao-Wu Du,*[a] and Ping Lin*[a]

Dedicated to Professor Xin-Tao Wu on the occasion of his 70th birthday

Keywords: Copper / Polynuclear compounds / Magnetic properties / Solid-state structures / Amines

Three new cluster-based Cu^{II}–azide coordination polymers, $[Cu_8(N_3)_{16}(222\text{-tet})_2]_n$ (**1**), $[Cu_{10}(N_3)_{20}(dien)_2]_n$ (**2**), and $[Cu_{12}(N_3)_{24}(Me_5dien)_2]_n$ (**3**) as well as a 1D polymer $[Cu_2(N_3)_4(dien)]_n$ (**4**) were prepared by hydrothermal reactions of Cu^{II} ions with NaN_3 in the presence of various polyamines. Single-crystal X-ray diffraction studies reveal that **1** has a 1D chain structure based on an octanuclear cluster unit $\{Cu_8(N_3)_{16}(222\text{-tet})_2\}$. Complexes **2** and **3** are 3D polymers and in both cases the azido anions display five different bridging modes (μ-1,1, μ-1,3, μ-1,1,1, μ-1,1,3,μ-1,1,1,3). Compound **4** is a 1D chain that represents the first example of a Cu^{II}–azide compound that contains *cis*-EE, double EO, and terminally bonded azido ligands. The magnetic susceptibility data, measured from 2 to 300 K, showed ferromagnetic couplings in **1**, **2**, and **4** and antiferromagnetic interaction in **3**. The magnetic data of **1** and **4** were fitted with rough models, giving the exchange coupling constants $J = 4.19\ cm^{-1}$ for **1** and $J = 25.31\ cm^{-1}$ for **4**.

Introduction

The investigation of magnetic properties of materials based on molecular entities has been one of the fascinating subjects that have received much attention during the past decades.[1–6] In this field, the polynuclear metal clusters or coordination polymers that have paramagnetic centers are of great interest, as they not only provide ideal systems for understanding the nature of magnetic interactions but also have potential applications in information storage and quantum computation in the future.[7–9] In order to understand the interaction between the transition metals, major work has been done using an azido anion as a bridging ligand[5,6,10] because of its diversity of coordination modes with transition metals (Scheme 1). In general, the modes observed for the azido linker are a monatomic bridge (end-on coordination mode, EO) and a biatomic bridge (end-to-end, EE). The first bridging mode (EO) can mediate antiferromagnetic or ferromagnetic coupling, which depends on the M–N–M angle. When the angle is smaller than 108°, it propagates ferromagnetic; otherwise, it is antiferromagnetic.[11–15] A more recent study based on theoretical calculations suggests a smaller critical angle (≈104°).[16–18] The second bridging mode (EE) usually gives rise to antiferromagnetic coupling and only in a few cases does ferromagnetic coupling occur through this pathway.[19,20]

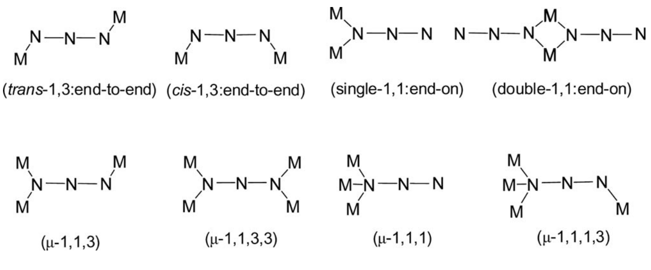

Scheme 1. Different bridging modes of azides.

On the other hand, in order to study the magnetostructural correction of the Cu^{II}–azide complexes, several co-ligands, especially those with multiple N donors, were introduced to this system.[21–34] Previous studies indicated that the incorporation of polyamines into the Cu^{II}–azide complexes may bring about some interesting structures with different magnetic properties. For example, the discrete complexes $[Cu_3(N_3)_6(dien)_2]$[27] and $[Cu_2(N_3)_2(Me_5dien)_2](ClO_4)_2$[28] both displayed antiferromagnetic exchange be-

---

[a] State Key Laboratory of Structure Chemistry, Fujian Institute of Research on the Structure of Matter, Chinese of Academy of Sciences,
Fujian, Fuzhou 350002, P. R. China
Fax: +86-591-83709847
+86-591-83709470
E-mail: swdu@fjirsm.ac.cn
pinglin@fjirsm.ac.cn
[b] Graduate University of Chinese Academy of Science,
Beijing 100039, P. R. China
[c] College of Chemistry and Chemical Engineering, Fuzhou University,
Fujian 350002, P. R. China

Supporting information for this article is available on the WWW under http://dx.doi.org/10.1002/ejic.200900776.

tween the Cu^{II} ions through the double EO and the double EE azido bridges, respectively, whereas the 2D polymers $[Cu_4(N_3)_8(en)_4]_n$[33] and $[Cu_3\{(R)\text{-phea}\}_2(N_3)_6]_n$[34] (phea = phenylethylamine) showed ferromagnetic interactions among the Cu^{II} ions through the EO azido bridges. It has been found from the literature that most of the Cu^{II}–azide complexes with polyamines were synthesized by solution methods;[27–38] those prepared by hydrothermal reactions are sparse probably due to the potential explosive character of azides. Furthermore, it is anticipated that the nature of the polyamines may have a strong influence on the bridging mode of the azido ligands and the structures of the resulting metal–azide products. This inspired us to investigate the reactions of Cu^{II} ions with NaN_3 in the presence of various polyamines under hydrothermal conditions. Our initial attempt afforded four new azido copper(II) compounds: $[Cu_8(N_3)_{16}(222\text{-tet})_2]_n$ (**1**), $[Cu_{10}(N_3)_{20}(dien)_2]_n$ (**2**), $[Cu_{12}(N_3)_{24}(Me_5dien)_2]_n$ (**3**), and $[Cu_2(N_3)_4(dien)]_n$ (**4**) (222-tet = triethyleneteramine, dien = diethylenetriamine, Me_5-dien = pentamethyldiethylenetriamine). Structure determinations reveal that **1** has a 1D chain structure with an octanuclear cluster repeating unit $\{Cu_8(N_3)_{16}(222\text{-tet})_2\}$ and a very small Cu–N–Cu angle (98.98°) for the single EO mode; this is unusual because only one example has been reported to date where such a bond angle is smaller than 100°.[33] Both **2** and **3** are 3D frameworks, which represent the first examples of an azide-containing metal coordination polymer where five different azido bridges (μ-1,1, μ-1,3, μ-1,1,1, μ-1,1,3, μ-1,1,1,3) coexist in a molecular structure. Because the high denticity of the polyamines greatly reduces the available coordination sites of the metal ions, which thus prevents the formation of high-dimensional frameworks, most of the Cu^{II}–azide complexes with polyamines reported to date are simple discreet molecules or polymers with low dimensionalities; those with high-dimensional networks are extremely rare. In fact, only four 3D polymers $[Cu_5(N_3)_{10}(en)_2]_n$,[33] $[Cu_6(N_3)_{12}(en)_4]_n$,[33] $[Cu_6(N_3)_{12}(N\text{-Eten})]_n$[39] (*N*-Eten = *N*-ethylethylenediamine) and $\{[Cu_9(N_3)_{18}(1,2\text{-pn})]\cdot H_2O\}_n$[39] (1,2-pn = 1,2-diaminopropane) have been reported recently for this system. Compound **4** is a 1D chain that is the first example of a Cu^{II}–azide compound that contains *cis*-EE, double EO, and terminally bonded azido ligands. The crystallographic structures of **1**–**4**, together with their magnetic behavior are described below.

Results and Discussion

Synthesis

Compound **1** was obtained in moderate yield by the reaction of $Cu(NO_3)_2\cdot 3H_2O$ with NaN_3 (2 equiv.) and 222-tet (0.5 equiv.) in the presence of triethyl orthoformate in water under hydrothermal conditions. Similar reactions with dien and Me_5dien gave **2** and **3** also in moderate yields. Compound **4** was obtained in a similar way to that of **2** except a mixture of MeOH and water (4:1) was used as the solvent. Without triethyl orthoformate, no products were isolated from these reactions. Although the role of triethyl orthoformate is not clear, it is reasonable to assume that the hydrolysis of triethyl orthoformate takes place during the reaction to form acetic acid, which controls the pH value of the solution by consuming some of the polyamine ligands. The formation of **2** and **3** indicates that even a small change in the substituent on the polyamines may cause structural differences in their corresponding Cu^{II}–azide complexes.

The IR spectra of **1**–**4** display characteristic absorption peaks in the range 2031–2089 cm^{-1} for the azido ligands. Multiple peaks in all the four cases are due to the presence of multiple bridging modes of the azide. In addition, peaks in the range 2891–3413 cm^{-1} are attributed to ν(N–H) of the polyamines.

Crystal Structure of $[Cu_8(N_3)_{16}(222\text{-tet})_2]_n$ (1)

Compound **1** is a 1D chain based on an octanuclear cluster repeating units $\{Cu_8(N_3)_{16}(222\text{-tet})_2\}$. Its asymmetric unit consists of four crystallographically independent Cu^{II} ions, one triethyleneteramine ligand, and eight nonequivalent azido anions. A perspective view of the octanuclear cluster is shown in Figure 1a, and selected bond lengths and angles are given in Table 1. The four copper atoms are in a square-pyramidal geometry but in different coordination environments. The Cu1 atom is surrounded by four 222-tet N atoms in the basal plane and an azido N atom in the apical position, whereas Cu2, Cu3, and Cu4 have similar coordination environments and each is ligated by five azido N atoms. The axial bond lengths of Cu1–N5, Cu2–N23B, Cu3–N8A, and Cu4–N11B are 2.310(6), 2.494(8), 2.415(6), and 2.660(8) Å, respectively, which are significantly longer than those for their corresponding equatorial Cu–N bonds [$Cu1–N_{222\text{–tet}}$ 1.995(6)–2.019(5) Å and $Cu–N_{azide}$ 1.923(6)–2.036(5) Å], indicating the presence of a strong Jahn–Teller effect. With the method of Addison et al.,[40] the geometrical parameter τ values are 0.24, 0.06, 0.22, and 0.12 for the Cu1, Cu2, Cu3, and Cu4 centers, respectively. The Cu1 atom is deviated by 0.1197 Å from the mean square plan towards the axial nitrogen atom (0.0356 Å for Cu2, 0.1632 Å for Cu3, and 0.1721 Å for Cu4). In the asymmetric unit, the Cu2, Cu3, and Cu4 atoms are linked through two double EO azido bridges to form a trimeric unit, in which the dihedral angles are 5.4° for the basal planes of the Cu2 and Cu3 centers and 5.0° for those of the Cu3 and Cu4 centers. The Cu2 atom is connected to a {Cu(222-tet)} fragment through an EE azido bridge (Cu1–N5–N6–N7···Cu2) so that the Cu1, Cu2, Cu3, and Cu4 atoms are arranged in a linear configuration. Two such linear structures are connected by two bridging azido anions to form an octanuclear cluster $\{Cu_8(N_3)_{16}(222\text{-tet})_2\}$. As illustrated in Figure 1b, the neighboring cluster units are linked by two basal-apical EO and two μ-1,1,1 azido bridges, generating an interesting neutral azide–copper molecular tape, with alternately fused parallel six-membered and four-membered copper rings (Figure S1, Supporting Information). Within each cluster unit, the Cu···Cu distances across the double EO azido bridge are 3.112(8) and 3.092(1) Å, whereas those through the single EO azido bridge and across the single

EE azido bridge are 3.357(3) and 5.514(0) Å, respectively. The value of Cu···Cu separation between the nearest cluster units is 3.410(7) Å.

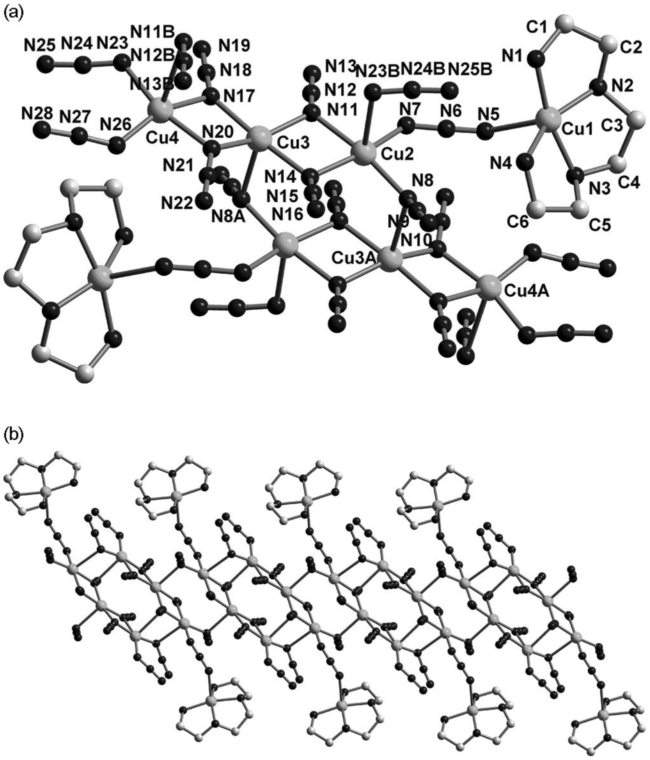

Figure 1. (a) View of the main unit and the coordination environment of Cu^{II} in **1**; (b) view of the 1D chain structure of **1**. Symmetry code A: –*x*, 1 –*y*, –z; B: 1 – *x*, 1 –*y*, 1 – *z*.

Table 1. Selected bond lengths/Å and angles/° for **1**.[a]

Cu1–N1	1.995(6)	Cu1–N2	2.002(5)
Cu1–N3	2.013(6)	Cu1–N4	2.019(5)
Cu2–N7	1.976(5)	Cu2–N8	1.962(6)
Cu2–N11	2.032(5)	Cu2–N14	2.023(5)
Cu3–N11	1.991(5)	Cu3–N14	1.995(5)
Cu3–N17	1.993(5)	Cu3–N20	1.975(5)
Cu4–N17	2.007(5)	Cu4–N20	2.011(5)
Cu4–N23	1.952(6)	Cu4–N26	1.923(6)
N1–Cu1–N2	85.4(2)	N1–Cu1–N3	167.5(2)
N1–Cu1–N4	100.6(2)	N2–Cu1–N3	84.1(2)
N2–Cu1–N4	153.1(2)	N3–Cu1–N4	85.9(2)
N7–Cu2–N8	93.1(2)	N7–Cu2–N14	168.1(2)
N7–Cu2–N11	91.7(2)	N8–Cu2–N14	96.8(2)
N8–Cu2–N11	171.5(2)	N11–Cu2–N14	77.7(2)
N11–Cu3–N14	79.3(2)	N11–Cu3–N20	162.4(2)
N11–Cu3–N17	98.8(2)	N14–Cu3–N20	101.5(2)
N14–Cu3–N17	175.4(2)	N17–Cu3–N20	78.9(2)
N17–Cu4–N20	77.7(2)	N17–Cu4–N26	159.1(3)
N17–Cu4–N23	91.3(2)	N20–Cu4–N26	91.1(2)
N20–Cu4–N23	166.5(2)	N23–Cu4–N26	101.7(2)
Cu2–N8–Cu3A	99.6(2)		

[a] Symmetry code A: –*x*, 1 –*y*, –*z*.

Accept for the two terminal azido anions that are attached to the Cu4 atom, the others can be divided into four types in terms of their bridging modes: double EO fashion within the trimeric Cu^{II} unit, *cis*-EE fashion as those connecting Cu1 and Cu2 atoms, single EO fashion between two trimeric Cu^{II} units, and μ-1,1,1 between the adjacent octanuclear cluster units. Generally, when an EE azide links two metal centers, it usually adopts a *trans* coordination fashion. The *cis*-EE bridging mode as in **1** is rare. The only two known examples are $[Cu_4(N_3)_8(en)_4]_n$[33] and [Cu$_3$(6-hydroxynicotinate)$_4$(N$_3$)$_2$(H$_2$O)$_3$],[41] in which a *cis*-type of EE coordination is observed. Besides, an azido anion with a single EO mode is not commonly encountered, because when it bridges two metals in an EO fashion, it is always accompanied with a second azide or other bridging moieties.[16,42–49] It has been found that the single EO mode usually results in large M–N–M angle separations (≥120°) in comparison with that through the double EO fashion. However, in **1**, the Cu2–N8–Cu3A angle associated with the single EO mode is 99.68°, which is close to that of the shortest M–N–M bond angle (98.98°) for a single EO azido bridge observed in $[Cu_4(N_3)_8(en)_4]_n$.[33]

Crystal Structure of $[Cu_{10}(N_3)_{20}(dien)_2]_n$ *(2)*

The crystallographic asymmetric unit of **2** is shown in Figure 2a, and selected bond lengths and angles are given in Table 2. It consists of 5 Cu^{II} ions, 1 diethylenetriamine ligand, and 10 azido anions for its charge balance. In the asymmetric unit of **2**, the Cu2, Cu3, Cu4, and Cu5 are in a linear structure with each pair of adjacent Cu atoms being connected by two azido bridges. A Cu/dien fragment is attached to Cu2 through a single EO azido bridge (Cu1–N12–Cu2). The copper···copper distances across the double azido bridges (Cu2···Cu3, Cu3···Cu4, and Cu4···Cu5) and through the single EO azido bridge (Cu1···Cu2) are 3.339(8), 3.096(4), 3.250(2), and 3.656(3) Å, respectively.

The Cu1 atom has a square-pyramidal coordination sphere with a dien acting as a tridentate ligand and two azido groups occupying the axial and equatorial positions, respectively. The Cu2 and Cu3 atoms each has a distorted elongated octahedral coordination geometry and is surrounded by four azido nitrogen atoms in the equatorial position and two weakly bonded azido nitrogen atoms in the axial position (Cu2–N7B 2.576 Å and Cu2–N9C 2.507 Å; Cu3–N7 2.603 Å and Cu3–N24D 2.613 Å). The Cu4 and Cu5 atoms adopting a square-pyramidal coordination sphere are also bound to only azido ligands. The Cu–N$_{dien}$ distances [1.969(4)–2.005(4) Å] are consistent with those for other amine–copper complexes. As in **1**, the Jahn–Teller distortion of the Cu^{II} ions causes a remarkable elongation of the axial Cu–N$_{azide}$ distances [2.383(5)–2.612(7) Å] compared to those of the basal Cu–N$_{azide}$ bonds [1.952(4)–2.044(3) Å]. The Cu–N–Cu bond angles at the double EO azido bridges between Cu2/Cu3, Cu3/Cu4, and Cu4/Cu5 range from 91.681(2) to 112.76(2)°, whereas those at the single EO between Cu1/Cu2 is 129.21(18)°. The latter is obviously larger than the corresponding value found for **1**. The dihedral angles between the basal plans of Cu1 and Cu2, Cu2 and Cu3, Cu3 and Cu4, as well as Cu4 and Cu5 are 71.9, 78.9, 5.3, and 74.4°, respectively.

The basic building blocks of this compound can be regarded as $\{Cu(dien)(N_3)_2\}$ and $\{Cu_8(N_3)_{16}\}$ units, which are linked into a 3D network with the aid of several types

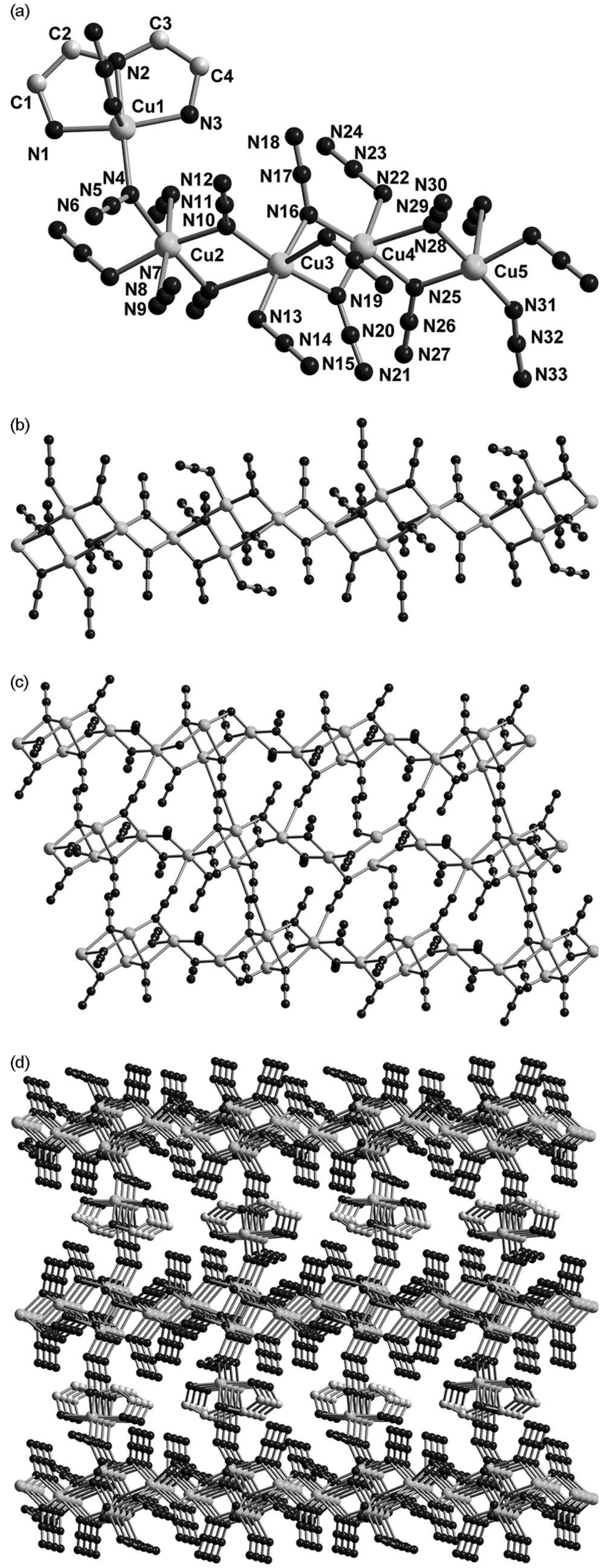

Figure 2. (a) The asymmetric unit and the coordination environment of Cu^{II} in **2**; (b) view of the 1D chain in **2**; (c) view of the 2D sheet in **2**; (d) view of the 3D structure of **2**. Symmetry code A: 0.5 – *x*, 0.5 + *y*, 0.5 – *z*; B: 1 – *x*, –*y*, 1 – *z*; C: –*x*, –*y*, – 1 – *z*; D: 1 + *x*, *y*, *z*; E: –*x*, –*y*, –*z*.

Table 2. Selected bond lengths/Å and angles/° for **2**.[a]

Cu1–N3	1.969(4)	Cu1–N1	2.005(4)
Cu1–N2	2.005(5)	Cu1–N4	2.027(3)
Cu2–N10	2.016(3)	Cu2–N7	2.017(3)
Cu2–N4	2.021(3)	Cu2–N13B	2.025(3)
Cu3–N19	1.977(3)	Cu3–N10	1.995(3)
Cu3–N16	2.004(4)	Cu3–N13	2.021(3)
Cu4–N16	1.989(3)	Cu4–N25	1.996(3)
Cu4–N19	2.005(4)	Cu4–N22	2.028(3)
Cu4–N28	2.409(3)	Cu5–N25	2.001(3)
Cu5–N28	2.011(3)	Cu5–N31	1.952(4)
N1–Cu1–N2	83.89(18)	N1–Cu1–N3	164.5(2)
N1–Cu1–N4	97.10(15)	N2–Cu1–N3	83.68(19)
N2–Cu1–N4	177.6(3)	N3–Cu1–N4	94.97(16)
N4–Cu2–N10	92.78(13)	N4–Cu2–N7	174.08(14)
N10–Cu2–N7	84.85(13)	N4–Cu2–N13	91.19(13)
N10–Cu2–N13^B	166.91(14)	N7–Cu2–N13^B	92.66(14)
N10–Cu3–N16	91.97(14)	N16–Cu3–N19	78.21(15)
N19–Cu3–N13	97.22(14)	N10–Cu3–N13	92.63(14)
N16–Cu4–N22	95.84(14)	N22–Cu4–N25	92.98(14)
N25–Cu4–N19	93.19(14)	N19–Cu4–N16	77.91(15)
N25–Cu5–N28	82.95(13)	N25–Cu5–N31	96.18(16)
N28–Cu5–N31	178.52(19)	Cu1–N4–Cu2	129.21(18)
Cu3–N19–Cu4	102.06(16)	Cu3–N16–Cu4	101.68(16)

[a] Symmetry code B: 2 – *x*, –*y*, 2 – *z*.

of bridging azido groups. As illustrated in Figure 2b, the $\{Cu_8(N_3)_{16}\}$ unit is composed of two nearly identical Cu^{II} tetramers and each can be considered as two incomplete cubane-like $\{Cu_3(N_3)_4\}$ moieties being fused together through sharing a $\{Cu_2(N_3)_2\}$ dimeric unit. These tetramers are linked through two EO azido bridges (Cu3–N16···Cu4 and Cu3–N19···Cu4), resulting in an infinite chain structure that consists of sequentially connected azido-bridged four-membered copper rings. These chains are further linked into sheets through μ-1,1,1,3 (N7–N8–N9) and μ-1,1,3 (N22–N23–N24) azido groups (Figure 2c). The whole $\{Cu(N_3)_2(dien)\}$ unit, serving as a bridge, links neighboring sheets through a single EO (Cu1–N4–Cu2) and a single EE azido anion (Cu1–N33–N32–N31–Cu5) to form a complicated 3D framework (Figure 2d). This 3D structure closely resembles that of $[Cu_5(N_3)_{10}(en)_2]$.[33] The main difference between them is that in $[Cu_5(N_3)_{10}(en)_2]$ the 2D sheets are linked by $\{Cu(N_3)_2(en)_2\}$ units through *trans*-1,3 azido bridges, whereas in **2**, the corresponding sheets are connected by $\{Cu(N_3)_2(dien)\}$ through *cis*-1,3 azido bridges on one side and single EO azido bridges on the other side. Compound **2** is the first example of an azido-containing metal coordination polymer where five different azido bridges (μ-1,1, μ-1,3, μ-1,1,1, μ-1,1,3, and μ-1,1,1,3) coexist despite the fact that the compound $[Cu_5(N_3)_{10}(en)_2]$[33] has four different bridging modes of the azide in its structure.

Crystal Structure of $[Cu_{12}(N_3)_{24}(Me_5dien)_2]_n$ *(3)*

X-ray analysis reveals that **3** has a complicated 3D polymeric structure similar to that of **2**. Its asymmetric unit is shown in Figure 3a, and the main bond lengths and angles are given in Table 3. The core structure contains 6 crystallographically independent Cu^{II} ions, 1 pentamethyldiethylenetriamine ligand, and 12 nonequivalent azido anions for its charge balance. The Cu1 atom is pentacoordinate by

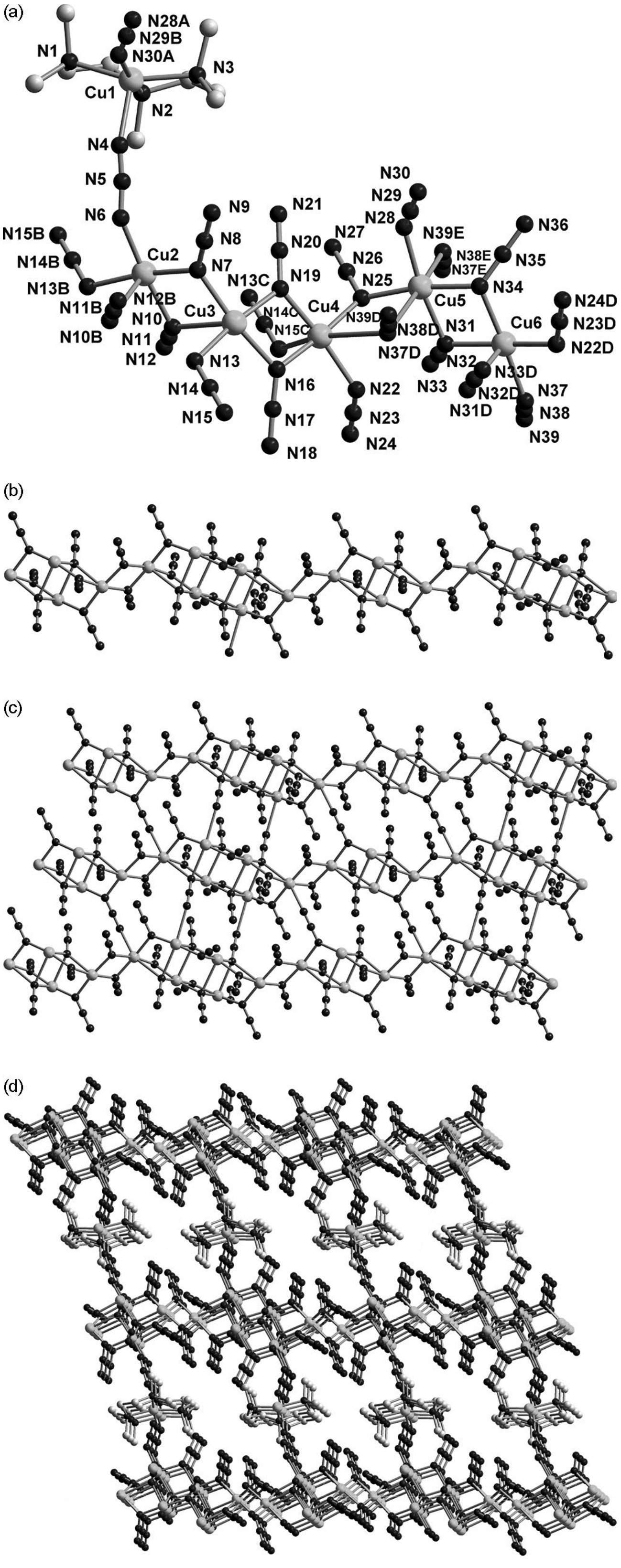

Figure 3. (a) The asymmetric unit and the coordination environment of Cu^{II} in **3**: (b) view of the 1D chain in **3**; (c) view of the 2D layer in **3**; (d) view of the 3D structure of **3**. Symmetry code A: 2 – *x*, 1 –*y*, –z; B: 2 –*x*, –*y*, –*z*; C: –1 + *x*, *y*, *z*; D: 1 –*x*, –*y*, –1 – *z*; E: –*x*, –*y*, –1 – *z*.

three N atoms of the Me$_5$dien, one N atom of azide, and one N atom of the other bridging azido group. The rest of the Cu atoms are connected one by one through a double azido bridge to form a linear configuration. Unlike **2**, the Cu/Me$_5$dien fragment is attached to the linear Cu chain through an EE azido bridge with a Cu1–N$_3$–Cu2 torsion angle of 6.884°. The coordination polyhedron around Cu1, Cu2, Cu3, and Cu6 can be described as an axially elongated square planar pyramid, whereas that of Cu4 and Cu5 can be regarded as an axially elongated octahedron. The values of τ are 0.21, 0.10, 0.03, 0.10, 0.03, and 0.09 for Cu1, Cu2, Cu3, Cu4, Cu5, and Cu6, respectively. The dihedral angles are 140.1° for the Cu1 and Cu2 centers, 103.3° for the Cu2 and Cu3 centers, 178.2° for the Cu3 and Cu4 centers, 116.1° for the Cu4 and Cu5 centers, and 22.9° for the Cu5 and Cu6 centers. Except for the Cu/Me$_5$dien unit where there is no obvious lengthening of the apical Cu–N bond length, the axial Cu–N$_{azide}$ bond lengths for the other Cu atoms exhibit large elongation [2.473(6) to 2.672(5) Å] compared to those of the basal Cu–N$_{azide}$ bond lengths [1.958(7) to 2.036(6) Å] and can be considered as semicoordinated Cu–N bonds. A similar situation also happens for **1** and **2** and can be attributed to the Jahn–Teller effect. The Cu···Cu distances of the adjacent Cu atoms within the linear Cu^{II}–azide structure range from 3.097(3) to 3.440(3) Å, whereas the distance between Cu1 and Cu2 is 5.963(7) Å.

Table 3. Selected bond lengths/Å and angles/° for **3**.[a]

Cu1–N1	2.066(8)	Cu1–N2	2.035(7)
Cu1–N3	2.037(8)	Cu1–N4	2.170(9)
Cu2–N6	1.958(7)	Cu2–N7	2.012(6)
Cu2–N10	1.999(6)	Cu2–N13B	2.027(6)
Cu3–N16	1.991(6)	Cu3–N7	1.994(6)
Cu3–N19	2.020(6)	Cu3–N13	2.034(6)
Cu4–N19	1.981(6)	Cu4–N16	2.002(6)
Cu4–N22	2.005(6)	Cu4–N25	2.026(6)
Cu5–N28	1.988(7)	Cu5–N25	2.002(6)
Cu5–N34	2.004(6)	Cu5–N31	2.036(6)
Cu6–N37	1.998(6)	Cu6–N31	2.018(6)
Cu6–N22D	1.980(6)	Cu6–N34	2.020(6)
N1–Cu1–N2	85.2(3)	N2–Cu1–N3	87.1(4)
N3–Cu1–N30A	94.3(4)	N1–Cu1–N30A	89.4(3)
N6–Cu2–N7	93.4(3)	N7–Cu2–N10	84.1(3)
N7–Cu3–N19	92.7(3)	N19–Cu3–N16	78.0(3)
N16–Cu3–N13	96.5(2)	N13–Cu3–N7	92.8(2)
N19–Cu4–N25	96.9(2)	N25–Cu4–N22	92.9(2)
N22–Cu4–N16	91.5(2)	N16–Cu4–N19	78.6(3)
N25–Cu5–N28	92.5(3)	N28–Cu5–N34	95.5(3)
N34–Cu5–N31	79.2(2)	N31–Cu5–N25	93.3(2)
N31–Cu6–N37	96.9(3)	N31–Cu6–N34	79.2(2)
Cu2–N7–Cu13	109.3(3)	Cu3–N19–Cu4	101.5(3)
Cu5–N34–Cu6	101.2(3)	Cu5–N31–Cu6	100.2(3)

[a] Symmetry code A: 2 –*x*, 1 –*y*, –*z*; B: 2 –*x*, –*y*, –*z*; D: 1 –*x*, –*y*, –1 –*z*.

In comparison with **2**, the basic repeating unit of **3** is a decanuclear cluster {[Cu$_4$(N$_3$)$_6$]($\mu_{1,1}$N$_3$)$_2$[Cu$_6$(N$_3$)$_{11}$]} (Figure S2, Supporting Information), which comprises a tetrameric {Cu$_4$(N$_3$)$_6$} unit as observed in **2** and a hexameric {Cu$_6$(N$_3$)$_{11}$} unit, being linked by several double EE azido bridges. The latter can be viewed as three face-sharing incomplete cubane-like {Cu$_3$(N$_3$)$_5$} units. These tetramers and hexamers are alternately connected by a double EO azido bridge, generating an infinite chain (Figure 3b), where the arrangement of the Cu atoms can be considered as serially connected four-membered and six-membered copper rings. These Cu^{II}–azide chains are cross-linked through μ-1,1,1,3 (N37–N38–N39) and μ-1,1,3 (N13–N14–N15) azido bridges, yielding a 2D layer (Figure 3c). The resulting sheet-like structures are connected by $\{Cu(N_3)_2(Me_5dien)\}$ units through *cis*-1,3 azido linkers to form a complicated 3D framework (Figure 3d). Like **2**, the coexistence of up to five bridging modes for the azide is observed in **3**. Although the complexes based on Cu_4 or Cu_6 secondary building blocks have been reported as in $[Cu_4(OH)_2(SIPA)_2(bipy)_2\cdot 2H_2O]_n$[50] ($H_3SIPA$ = 5-sulfoisophthalic acid, bipy = 4,4′-bipyridine) and $\{[Cu_6I_6(2\text{-}C_5H_5NH)_6]_n\cdot 2nCH_3CN\}$,[51] those with Cu_4 + Cu_6 as a basic unit have not been reported.

Except for the difference in the basic building blocks, another structural difference between **2** and **3** is the way the {Cu(polyamine)}fragments attach to the polymer backbone. In **2**, they connect the 2D layers into a 3D framework with one μ-1,1 and one μ-1,3 azido ligand, whereas in **3** it is with two μ-1,3 azido ligands. Because the hydrothermal reactions are carried out in sealed vessels under certain conditions, it is difficult to study the formation mechanism for the products, and the role of each reagent cannot be fully understood. However, we believe that the hindrance from the methyl groups of Me_5dien may be responsible for these differences.

Although the 3D frameworks of **2** and **3** are similar, they are of different topological nets. Topologically, in **2**, the azido ligands and the bridging $\{Cu(dien)(N_3)_2\}$ fragments can be regarded as spacers and the basic repeating unit $\{Cu_8(N_3)_{16}\}$ can be treated as two eight-connected nodes, in which the Cu2, Cu3, Cu2A, and Cu3A are defined as L1 and Cu4, Cu5, Cu4A, and Cu5A as L2 (Figure S3, Supporting Information). The Schläfli symbol for this net is $(3^6 4^{18} 5^3 6)(3^6 4^{18} 5^3 6)$ with the vertex symbol for both L1 and L2 nodes being $3\cdot3\cdot3\cdot3\cdot3\cdot3\cdot4\cdot4\cdot4\cdot4\cdot4\cdot4\cdot4\cdot4\cdot4\cdot4\cdot4\cdot4\cdot4\cdot4\cdot4\cdot4\cdot4\cdot4\cdot5_2\cdot5_2\cdot5_2\cdot6_6$. Similarly, the basic repeating unit of **3** acts as two nodes, where the Cu2, Cu3, Cu2A, and Cu3A are defined as L1 (six-connected nodes) and Cu4, Cu5, Cu6, Cu4A, Cu5A, and Cu6A as L2 (eight-connected nodes) to generate a (6,8)-connected 3D network (L1/L2). Its Schläfli symbol is $(3^2 4^{10} 5^2 6)(3^4 4^{12} 5^8 6^4)$ and the vertex symbols are $3\cdot3\cdot4\cdot4\cdot4\cdot4\cdot4\cdot4\cdot4\cdot4\cdot4\cdot4\cdot5_2\cdot5_2\cdot6_6$ for the L1 node and $3\cdot3\cdot3\cdot3\cdot4\cdot4\cdot4\cdot4\cdot4\cdot4\cdot4\cdot4\cdot4\cdot4\cdot4\cdot4\cdot5\cdot5\cdot5\cdot5\cdot5_4\cdot5_4\cdot5_4\cdot5_4\cdot6_2\cdot6_4\cdot6_4\cdot6_4$ for the L2 node (Figure S4, Supporting Information).

Crystal Structure of $[Cu_2(N_3)_4(dien)]_n$ (4)

The structure determination of **4** reveals that its asymmetric unit consists of half a dinuclear $[Cu_2(N_3)_6]^{2-}$ anion and one $[Cu(N_3)dien]^+$ cation. A perspective view of the asymmetric unit with an atomic numbering scheme is given in Figure 4a, and selected bond lengths and angles are given in Table 4. The coordination environment of Cu1 can be better described as distorted square pyramidal, with the apical position occupied by one azido N atom [Cu–N6A 2.499(7) Å] and the basal sites are filled by three N atoms from a dien [Cu–N 1.995(4)–2.020(4) Å] and one N atom of the other azide [Cu1–N4 2.000(4) Å]. The adjacent $[Cu(N_3)dien]^+$ cations are linked by a *cis*-EE azido bridge to form a 1D cationic chain (Figure 4b, top). The Cu2 atom is in a square-planar geometry surrounded by four azido groups, whereas Cu3 is in a distorted octahedral geometry, coordinated by six azido N atoms [$Cu–N_{basal}$ 2.009(4)–2.031(3) Å; $Cu–N_{axial}$ 2.541(1) Å]. The values of τ are 0.2 for Cu1, but 0 for both Cu2 and Cu3. The Cu2 and Cu3 atoms are connected by two EO azido bridges to form a dimer, which then extends into an anionic chain (Figure 4b, bottom). The Cu···Cu distance within each dimeric unit is 3.266 Å, and the Cu–N–Cu angles associated with the EO azido bridges are 91.88 and 107.31°, respectively. The structure of **4** is similar to, but different from, that of $\{[Pr_4N]_2[Cu_3(N_3)_8]\}_n$,[52] where the anionic chains are separated by $[Pr_4N]^+$ cations.

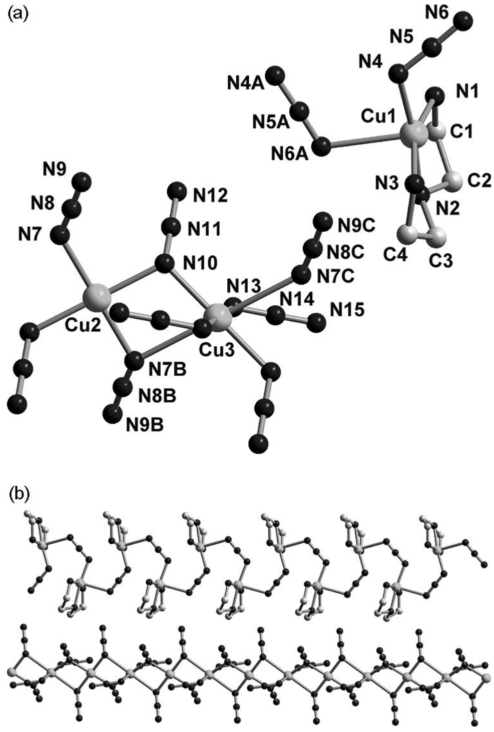

Figure 4. (a) The asymmetric unit and the coordination environment of Cu^{II} in **4**; (b) view of the 1D chain of **4**. Symmetry code A: 0.5 – *x*, 0.5 + *y*, 0.5 – *z*; B: – 1 –*x*, 4 –*y*, –*z*; C: *x*, –1 + *y*, *z*.

Table 4. Selected bond lengths/Å and angles/° for **4**.[a]

Cu1–N1	2.020(4)	Cu1–N2	2.011(3)
Cu1–N3	1.994(4)	Cu2–N7	1.970(4)
Cu2–N10	2.025(3)	Cu3–N10	2.031(3)
Cu3–N13	2.009(4)	Cu1–Cu2	7.421(3)
Cu1–Cu3	8.620(5)		
N1–Cu1–N2	83.59(17)	N2–Cu1–N3	84.39(15)
N3–Cu1–N4	97.53(17)	N4–Cu1–N1	96.38(17)
N7–Cu2–N10	93.25(15)	N10–Cu3–N13	90.21(15)
N10–Cu3–N7B	72.70(17)	Cu2–N10–Cu3	107.31(16)
Cu2–N7B–Cu3	91.93(19)		

[a] Symmetry code B: – 1 – *x*, 4 – *y*, –*z*.

Magnetic Properties

Complex 1

The temperature dependence of the χ_m and χ_mT product for **1** per Cu_8^{2+} are shown in Figure 5. The plot of χ_m vs. T indicates that the value of χ_m slowly increases from 0.01 cm^3 mol^{-1} at 300 K with a decrease in the temperature to a value of 0.25 cm^3 mol^{-1} at 3 K, and then rapidly decreases to 0.24 cm^3 mol^{-1} upon cooling to 2 K. The value of χ_mT at 300 K is 3.08 cm^3 mol^{-1} K, which is close to the expected value for eight uncoupled Cu^{2+} ions (χ_mT = 3 cm^3 mol^{-1} K for eight spin S = 1/2 ions with g = 2). The χ_mT value gradually increases upon decreasing the temperature from room temperature to 140 K and reaches a maximum of 3.17 cm^3 mol^{-1} K. Further cooling decreases the χ_mT value to 0.48 cm^3 mol^{-1} at 2 K. This magnetic behavior suggests ferromagnetic coupling and is further supported by the unsaturated magnetization of 4.12 Nμ_B under 8 T magnetic field (Figure S5, Supporting Information). According to the structure, the slight increase in the value of χ_mT from room temperature down to 140 K is caused by ferromagnetic interaction within the cluster $\{Cu_8(N_3)_{16}$-(222-tet)$_2\}$, where the Cu–$(N_3)_2$–Cu and Cu–(N_3)–Cu angles (99.6–101.7°) are in the range for a ferromagnetic interaction. The sharp decrease in the value of χ_mT down to 2 K is presumably caused by zero-field splitting (ZFS) effects and/or the intercluster antiferromagnetic interaction at low temperature. Taking into consideration the 1D structure of **1**, there is no appropriate model for such a system that could be used. However, **1** can be treated as a linear trimeric model of Cu^{II} and one isolated [Cu(222-tet)]$^{2+}$ ion. The spin Hamiltonian of the trimeric model can be written as $H = -2J(S_1S_2 + S_2S_3)$. The magnetic susceptibility is given by Equations (1) and (2).

$$x_{octa} = \frac{Ng^2\beta^2}{4K(T-\theta)}\frac{10\exp(J/K_BT)+\exp(-2J/K_BT)+1}{2\exp(J/K_BT)+\exp(-2J/K_BT)+1} + 2x_{Cu} \qquad (1)$$

$$x = \frac{x_{octa}}{1-\left(2zj'/Ng^2\beta^2\right)x_{octa}} \qquad (2)$$

With this approximate model, the best-fitting parameter gives g = 2.05, J = 4.19 cm^{-1}, θ = 0.22 cm^{-1}, zj' = –1.83 cm^{-1}, and $R = 2\times10^{-5}$, in which θ represents the interaction of linear Cu_3 trimer (Cu2···Cu3···Cu4) and zj' stands for the magnetic coupling between the adjacent octanuclear cluster units. The fitting results confirm ferromagnetic coupling in the trimer, weak ferromagnetic coupling between the adjacent trimers, and antiferromagnetic interaction between the adjacent octanuclear cluster units.

Complex 2

The temperature dependence of the χ_m and χ_mT product for **2** per Cu_5^{2+} is shown in Figure 6. The plot of χ_m vs. T indicates that the value of χ_m slowly increases from 0.01 cm^3 mol^{-1} at 300 K with a decrease in the temperature to a value of 1.114 cm^3 mol^{-1} at 12 K and then rapidly decreases to 1.073 cm^3 mol^{-1} at 5 K, which further increases to 1.077 cm^3 mol^{-1} upon cooling to 2 K. The value of χ_mT at 300 K is 2.39 cm^3 mol^{-1} K, which is larger than the expected value for five uncoupled Cu^{2+} ions (χ_mT = 1.875 cm^3 mol^{-1} K for five spin S = 1/2 ions with g = 2). Upon cooling, the value of χ_mT continuously increases to reach a value of 13.14 cm^3 mol^{-1} K at 12 K and then decreases to 2.16 cm^3 mol^{-1} K at 2 K, suggesting the occurrence of ferromagnetic interaction in **2**, which can be further confirmed by the nearly saturated magnetization of 3.48 Nμ_B under 8 T (Figure 7). Furthermore, as shown in the inset of Figure 7, the hysteresis loop was observed at 2 K with a remnant magnetization (M_r) of 0.277 Nβ and a coercive field (H_c) of 600 Oe. Between 100 and 300 K, χ_m

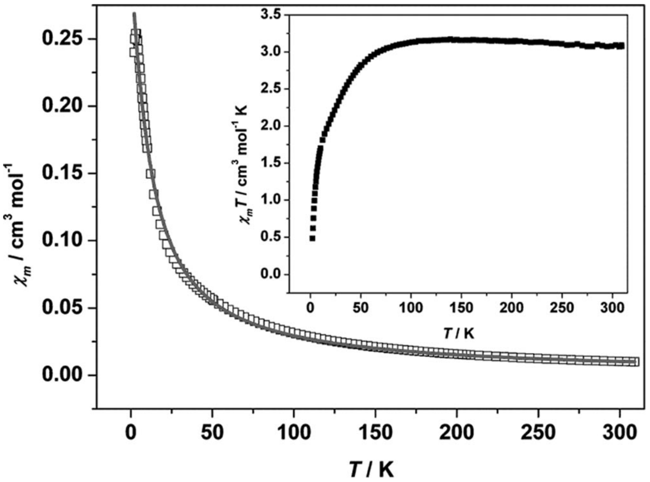

Figure 5. Plots of χ_m vs. T and χ_mT vs. T (inset) of **1** in the 2–300 K temperature range. The solid line indicates the fitting by using a theoretical model (see text).

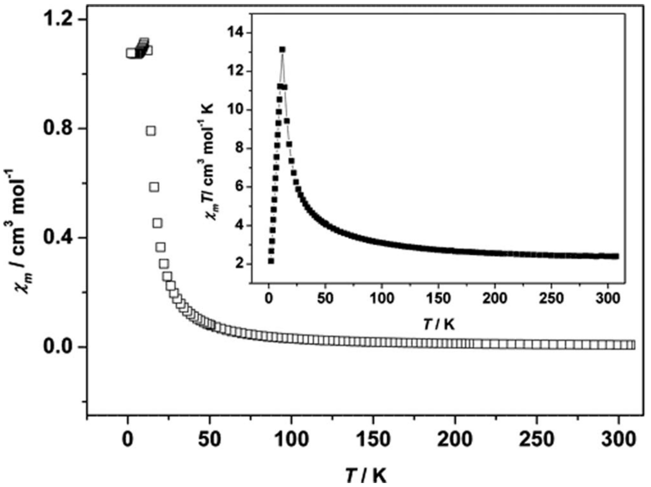

Figure 6. Plots of χ_m vs. T and χ_mT vs. T (inset) of **2** in the 2–300 K temperature range. The solid line is a guide for the eye.

follows the Curie–Weiss law, with $C = 2.15\ \mathrm{cm^3\,mol^{-1}\,K}$ and $\theta = 32.10$ K. From a structural point of view, both ferromagnetic and antiferromagnetic interactions exist in **2**, where the Cu–N–Cu angles are in the range for these two types of interactions (101.7–129.2°). The continuous increase in the value of $\chi_\mathrm{m}T$ from room temperature down to 12 K is caused by ferromagnetic interaction within the 1D rail-road chain, where the ferromagnetic interaction dominates over the antiferromagnetic interaction. Below 12 K, the reverse order is followed, which may be caused by the interchain antiferromagnetic interaction through μ-1,1,1,3 and μ-1,1,3 EE azido bridges and/or intersheet antiferromagnetic interaction through $\{Cu(dien)(N_3)_2\}$ and/or ZFS effects. We tried to fit the magnetic susceptibility data by using a $\{Cu_8(N_3)_{16}\}$ model, and to our disappointment, we did not find any appropriate formulas for this model.

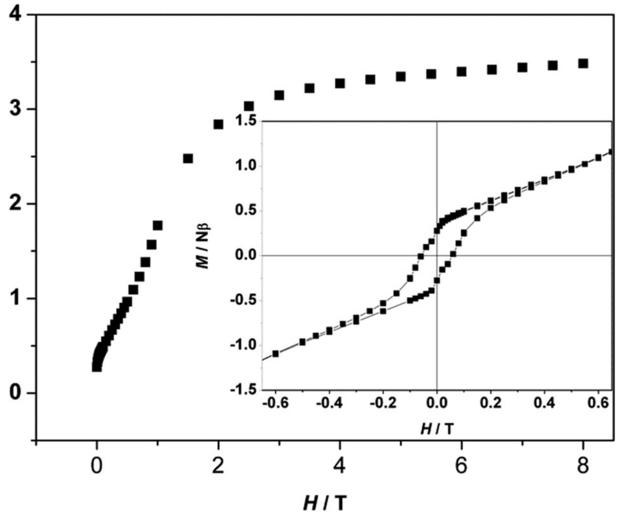

Figure 7. Field dependence of the magnetization (M) up to H = 8 T of **2**. The inset shows the hysteresis loop in the ±0.65 T range at T = 2 K. The solid line is a guide for the eye.

Complex 3

The temperature dependence of the magnetic susceptibility of **3** per Cu_6^{2+} is shown as $\chi_\mathrm{m}T$ vs. T and χ_m vs. T plots in Figure 8. Upon cooling, the χ_m product slowly increases from a value of $0.01\ \mathrm{cm^3\,mol^{-1}}$ at 300 K to a value of $0.52\ \mathrm{cm^3\,mol^{-1}}$ at 2 K. The value of the $\chi_\mathrm{m}T$ product ($3.14\ \mathrm{cm^3\,mol^{-1}\,K}$) at room temperature is slightly larger than that expected for six isolated Cu^{2+} ions ($\chi_\mathrm{m}T = 2.25\ \mathrm{cm^3\,mol^{-1}\,K}$ for six spin $S = 1/2$ ions with $g = 2$). The $\chi_\mathrm{m}T$ value decreases monotonically upon decreasing the temperature and reaches a minimum of $1.04\ \mathrm{cm^3\,mol^{-1}\,K}$ at 2 K. This feature indicates an antiferromagnetic interaction in **3**. The antiferromagnetic coupling is further confirmed by a negative Weiss constant $\theta = -10.82$ K by using the data within the 30–300 K temperature range, according to the Curie–Weiss law. Taking into account the structural date of **3**, this magnetic behavior may be attributed to the antiferromagnetic interaction in the 1D infinite chain (in which the antiferromagnetic interaction dominates compared to the ferromagnetic interaction) and/or intersheet antiferromagnetic interaction through $\{Cu(N_3)_2(Me_5dien)\}$.

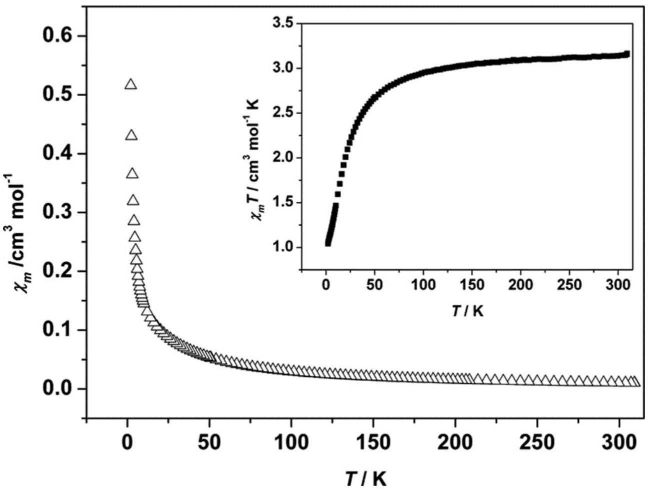

Figure 8. Plots of χ_m vs. T and $\chi_\mathrm{m}T$ vs. T (inset) of **3** in the 2–300 K temperature range.

Complex 4

The temperature dependence of the χ_m and $\chi_\mathrm{m}T$ product for **4** per Cu_2^{2+} is shown in Figure 9. At 300 K, the $\chi_\mathrm{m}T$ value is $0.67\ \mathrm{cm^3\,mol^{-1}\,K}$, which is lower than that expected for two uncoupled Cu^{2+} ions ($\chi_\mathrm{m}T = 0.75\ \mathrm{cm^3\,mol^{-1}\,K}$ for two spin $S = 1/2$ ions with $g = 2$). Upon cooling, the value of $\chi_\mathrm{m}T$ increases gradually and up to a maximum of $1.10\ \mathrm{cm^3\,mol^{-1}\,K}$ at 10 K, and then decrease to $0.27\ \mathrm{cm^3\,mol^{-1}\,K}$ at 2 K This magnetic behavior suggests the occurrence of ferromagnetic coupling in the anionic chain through double EO azido ligands. The ferromagnetic behavior can also be confirmed by the magnetization vs. field plot at T = 2 K (Figure S6, Supporting Information): at low field the magnetization increases steeply with the magnetic field, whereas at high field it increases slowly and

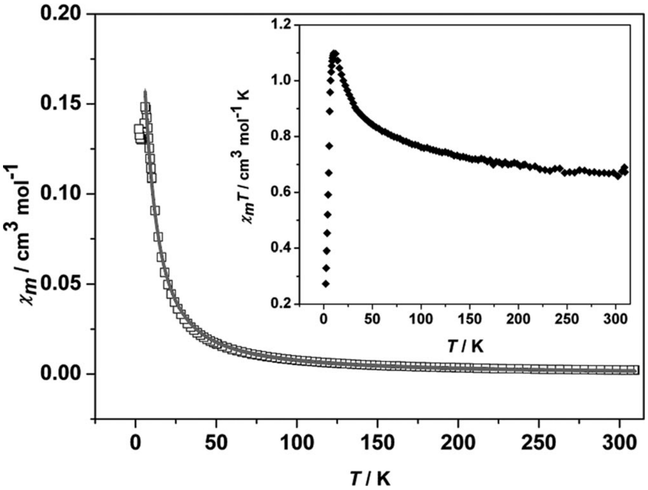

Figure 9. Plots of χ_m vs. T and $\chi_\mathrm{m}T$ vs. T (inset) of complex **4** in the temperature range 2–300 K. The solid line indicates the fitting by using a theoretical model (see text).

finally reaches an unsaturated magnetization value of 1.32 Nμ_B at 8 T. According to the structure, the coordination environment of the Cu1 atom indicates that the nitrogen at one end of the azide interacts with the magnetic orbital $d_{x^2-y^2}$, whereas that at the other end interacts with the nonmagnetic orbital d_{z^2}, which makes the magnetic coupling smaller.[53–55] On the other hand, the double EO azido bridge (in the anionic chain) always mediates a medium or a strong ferromagnetic exchange[33,56–58] for small Cu–N–Cu bond angles (≤104°). Therefore, the magnetic coupling in the anionic chain dominates and that in the cationic chain can be ignored.

On the basis of the aforementioned state and the structural data, complex **4** can be roughly described as a 1D uniform chain[59] and mononuclear $[Cu(N_3)dien]^+$ cation, where J and zj' stand for the exchange integrals within the anionic chain and between the anionic chains, respectively [Equations (3), (4), and (5)].

$$x_{chain} = \frac{Ng^2\beta^2}{4KT}[\frac{N}{D}]^{2/3} \tag{3}$$

$$x = x_{chain} + x_{cu} \tag{4}$$

$$x_m = \frac{x}{1-(2zj'/Ng^2\beta^2)x} \tag{5}$$

with $N = 1.0 + 5.7979916y + 16.902653y^2 + 29.376885y^3 + 29.832959y^4 + 14.036918y^5$

$D = 1.0 + 2.7979916y + 7.0086780y^2 + 8.6538644y^3 + 4.5743114y^4$

$y = J/2KT$

With this rough model, the magnetic susceptibility of **4** above 6 K was simulated by Equations (4) and (5), giving the best fit with $J = 25.31\ cm^{-1}$, $zj' = -1.82\ cm^{-1}$, and $R = 3.45 \times 10^{-6}$ when fixing $g = 2.0$.

Conclusions

In summary, we have synthesized four new Cu^{II}–azide polymers with different structures and cluster repeating units by changing the polyamines used under hydrothermal conditions. Complex **1** features an octanuclear cluster $\{Cu_8(N_3)_{16}(222\text{-tet})_2\}$, in which a small Cu–N–Cu bond angle (99.68°) for the single EO azido bridge is observed. Complexes **2** and **3** both have a complicated 3D structure that contains up to five different azido bridging modes. The arrangement of the Cu^{II} atoms in **1**, **2**, and **3** can be regarded as alternately fused, parallel, six-membered and four-membered copper rings; sequentially connected four-membered copper rings; and serially connected four-membered and six-membered copper rings, respectively. Complex **4** is the first example of a 1D chain for the metal–azide system that contains *cis*-EE, double EO, and terminally bonded azido ligands. The magnetic data show that **1**, **2**, and **4** are all ferromagnets, whereas **3** is an antiferromagnetic material. The magnetic data for **1** and **4** were fitted reasonably well by using rough theoretical models. The results reveal ferromagnetic couplings within the octanuclear unit and antiferromagnetic interaction between the neighboring octanuclear units for **1**, as well as ferromagnetic couplings within the anionic chain and antiferromagnetic couplings between the adjacent anionic chains for **4**. Our present work demonstrates wider possibilities for the design of new magnetic material using metal–azide clusters as framework builders by hydrothermal methods. Further investigation on the preparation of metal–azide cluster-based magnetic materials by using other metal ions and polyamines is in progress.

Experimental Section

Materials: All the materials were purchased from commercial sources and used without further purification.

Physical Measurements: Variable-temperature magnetic susceptibility and field-dependence magnetization of polycrystalline samples of **1**, **2**, **3**, and **4** were performed with a Quantum Design PPMS-9T magnetometer. We collected the susceptibility data by using an applied magnetic field of 5 kOe in the temperature range of 2–300 K. Diamagnetic corrections of the constituent atoms were estimated from Pascal's tables.[1]

WARNING ! Metal–azide complexes have the potential to be explosive. Therefore, only a small amount of material should be prepared, and it should be handled with great caution.

Crystal Structure Analyses: Suitable single crystals of the compounds were carefully selected and glued to thin glass fibers with epoxy resin. Intensity data were collected at room temperature with a Rigaku Mercury CCD area-detector diffractometer with a graphite monochromator by utilizing Mo-K_α radiation (λ = 0.71073 Å). The structures were solved by direct methods[60] and refined on F^2 by full-matrix least-squares by using the SHELXL-97 program package.[61] All non-hydrogen atoms were refined anisotropically. The hydrogen atoms bonded to carbon were generated geometrically (C–H 0.97 or 0.93 Å) and U(H) values set as 1.2 times Ueq(C). In **2**, the unique C3 atom is disordered over two positions and was refined as two atoms of half occupancy, viz. C3 and C3′′′ The crystallographic data for **1**–**4** are listed in Table 5. CCDC-740383 (for **1**), -740384 (for **2**), -740385 (for **3**), and -740382 (for **4**) contain the supplementary crystallographic data for this paper. These data can be obtained free of charge from The Cambridge Crystallographic Data Centre via www.ccdc.cam.ac.uk/data_request/cif.

Complex 1: Hydrothermal treatment of a mixture of $Cu(NO_3)_2 \cdot 3H_2O$ (1.0 mmol, 0.241 g), NaN_3 (2.0 mmol, 0.130 g), 222-tet (0.5 mmol, 0.1 mL), triethyl orthoformate (2.0 mmol, 0.3 mL), and H_2O (10 mL) was kept in a Teflon-lined autoclave at 95 °C for 1 d. After slow cooling to room temperature, black needle-like crystals were obtained. Yield: 0.112 g (61% based on Cu). $Cu_8N_{56}C_{12}H_{36}$ (1473.28): calcd. C 9.78, H 2.46, N 53.24; found C 9.98, H 2.37, N 53.83. IR (KBr pellet): $\tilde{\nu} = \nu(N_3^-)$ stretching 2085 (vs), 2060 (s), 2037(s); ν(N–H) stretching 3434 (m), 3343 (m), 3250 (m), 3152 (m), 2973(m) cm^{-1}.

Complex 2: The complex was prepared by a procedure similar to that described for **1**, except that dien was used instead of 222-tet.

Table 5. Crystallographic data for complexes **1**–**4**.

	1	**2**	**3**	**4**
Empirical formula	$Cu_8N_{56}C_{12}H_{36}$	$Cu_{10}N_{66}C_8H_{26}$	$Cu_{12}N_{78}C_{18}H_{46}$	$Cu_2N_{15}C_4H_{13}$
Fw	1473.28	1682.23	2117.67	398.35
Crystal system	monoclinic	monoclinic	triclinic	monoclinic
Space group	$P2_1/c$	$P2_1/n$	$P\bar{1}$	$P2_1/n$
a / Å	8.825(4)	6.6879(3)	7.001(10)	10.394(5)
b / Å	14.483(7)	23.0595(10)	14.70(2)	6.533(3)
c / Å	19.248(9)	16.1437(9)	18.88(3)	20.462(9)
α / °	90.00	90.00	109.219(18)	90.00
β / °	102.138(8)	94.314(4)	94.790(4)	96.708(7)
γ / °	90.00	90.00	103.210(19)	90.00
V / Å^3	2405.0(19)	2482.6(2)	1759(4)	1380.0(10)
Z	2	2	1	4
$D_{calcd.}$ / g cm^{-3}	2.034	2.251	1.999	1.917
μ / mm^{-1}	3.551	4.285	3.633	3.104
$F(000)$	1464	1652	1048	800
Parameters	343	389	487	194
R_1[a], wR_2[b] [$I > 2\sigma(I)$]	0.0658/0.0879	0.0448/0.1068	0.0645/0.1325	0.0519/0.1128
R_1[a], wR_2[b] [all data]	0.1271/0.1069	0.0568/0.1159	0.1087/0.1620	0.0577/0.1177
Good-of-fit on F^2	0.998	1.068	1.017	1.039

[a] $R_1 = \Sigma||F_o| - |F_c||/\Sigma|F_o|$. [b] $wR_2 = [\Sigma w(F_o^2 - F_c^2)^2/\Sigma w(F_o^2)^2]^{0.5}$.

Black diamond-like crystals were obtained. Yield: 0.159 g (63% based on Cu). $Cu_{10}N_{66}C_8H_{26}$ (1682.23): calcd. C 5.71, H 1.57, N 54.95; found C 5.85, H 1.54, N 55.39. IR (KBr pellet): $\tilde{\nu} = \nu(N_3^-)$ stretching 2075 (vs); ν(N–H) stretching 3413(s), 3236(m) cm^{-1}.

Complex 3: The complex was prepared by a procedure similar to that described for **1**, except that Me_5dien was used instead of 222-tet. Complex **3** was isolated as black needle-like crystals. Yield: 0.205 g (58% based on Cu). $Cu_{12}N_{78}C_{18}H_{46}$ (2117.67): calcd. C 10.21, H 2.19, N 51.59; found C 10.69, H 2.21, N 51.78. IR (KBr pellet): $\tilde{\nu} = \nu(N_3^-)$ stretching 2088 (vs), 2057 (s); ν(N–H) stretching 3413 (s), 2930 (m) cm^{-1}.

Complex 4: The complex was obtained as black needle-like crystals by a procedure similar to that described for **1** by using MeOH/H_2O (4:1, 10 mL) as the solvent. Yield: 0.142 g (48% based on Cu). $Cu_2N_{15}C_4H_{13}$ (398.35): calcd. C 12.06, H 3.29, N 52.74; found C 12.02, H 3.32, N 53.05. IR (KBr pellet): $\tilde{\nu} = \nu(N_3^-)$ stretching 2065 (vs), 2031 (vs); ν(N–H) stretching 3412 (s), 3287 (m), 3235 (m), 3200 (m), 2959 (m) cm^{-1}.

Supporting Information (see footnote on the first page of this article): Six additional figures are available including the molecular tape of **1**, the basic repeating unit of **3**, perspective view of the topology of **2** and **3**, and the magnetization vs. field curves of **1** and **4**.

Acknowledgments

This work was financially supported by grants from the State Key Laboratory of Structural Chemistry, Fujian Institute of Research on the Structure of Matter, Chinese Academy of Sciences (CAS, SZD08002-2), National Basic Research Program of China (973 Program, 2007CB815306), National Natural Science Foundation of China (20733003 and 20673117), Young Scientist's Foundation of Fujian Province (2006F3163), and Knowledge Innovation Program of the Chinese Academy of Sciences.

---

[1] O. Kahn, *Molecular magnetism,* VCH, Weinheim, **1993**, pp. 2–4 and pp. 9–51.
[2] J. A. Real, A. B. Gaspar, M. C. Muñoz, *Dalton Trans.* **2005**, 2062–2079.
[3] N. Hoshion, A. M. Ako, A. K. Powell, H. Oshio, *Inorg. Chem.* **2009**, *48*, 3396–3407.
[4] T. C. Stamatatos, G. Christou, *Inorg. Chem.* **2009**, *48*, 3308–3322.
[5] X. Y. Wang, Z. M. Wang, S. Gao, *Chem. Commun.* **2008**, 281–294.
[6] Y. F. Zeng, X. Hu, F. C. Liu, X. H. Bu, *Chem. Sov. Rev.* **2009**, *38*, 469–480.
[7] M. N. Leuenberge, D. Loss, *Nature* **2001**, *410*, 789–793.
[8] W. Wernsdorfer, N. Aliaga-Acalde, D. N. Hendrickson, G. Christou, *Nature* **2002**, *416*, 406–409.
[9] S. Hill, R. S. Edwards, N. Aliaga-Alcade, G. Christou, *Science* **2003**, *302*, 1015–1018.
[10] Microreview: E. Escuer, G. Aromi, *Eur. J. Inorg. Chem.* **2006**, *23*, 4721–4736.
[11] S. Sikorav, I. Bkouche-Waksman, O. Kahn, *Inorg. Chem.* **1984**, *23*, 490–495.
[12] O. Kahn, T. Mallah, J. Gouteron, S. Jeannin, Y. Jeannin, *J. Chem. Soc., Dalton Trans.* **1989**, 1117–1126.
[13] R. Cortés, M. K. Urtiaga, L. Lezama, J. R. Larramendi, M. I. Arriortua, T. Rojo, *J. Chem. Soc., Dalton Trans.* **1993**, 3685–3694.
[14] S. S. Tandon, L. K. Thompson, M. E. Manuel, J. N. Bridson, *Inorg. Chem.* **1994**, *33*, 5555–5570.
[15] L. K. Thompson, S. S. Tandon, M. E. Manuel, *Inorg. Chem.* **1995**, *34*, 2356–2366.
[16] M. A. Aebersold, B. Gillon, O. Plantevin, L. Pardi, O. Kahn, P. Bergeral, I. von Seggern, F. Tuczek, L. Öhrström, A. Grand, E. Lelièvre-Berna, *J. Am. Chem. Soc.* **1998**, *120*, 5238–5245.
[17] E. Ruiz, J. Cano, S. Alvarez, P. Alemany, *J. Am. Chem. Soc.* **1998**, *120*, 11122–11129.
[18] C. Adamo, V. Barone, A. Bencini, F. Totti, I. Ciofini, *Inorg. Chem.* **1999**, *38*, 1996–2004.
[19] J. Ribas, *Coord. Chem. Rev.* **1999**, *193–195*, 1027–1068 and references cited therein.
[20] P. S. Mukherjee, T. K. Maji, G. Mostafa, T. Mallah, N. Ray Chaudhuri, *Inorg. Chem.* **2000**, *39*, 5147–5150.
[21] X. H. Bu, M. Du, Z. L. Shang, L. Zhang, Q. H. Zhao, R. H. Zhang, M. Shionoya, *Eur. J. Inorg. Chem.* **2001**, *6*, 1551–1558.
[22] N. K. Karan, S. Mitra, T. Matsushita, V. Gramlich, G. Rosair, *Inorg. Chim. Acta* **2002**, *332*, 87–91.
[23] P. Manikandan, R. Muthukumaran, K. R. Justin Thomas, B. Varghese, G. V. R. Chandramouli, P. T. Manoharan, *Inorg. Chem.* **2001**, *40*, 2378–2389.

[24] B. Graham, M. T. W. Hearn, P. C. Junk, C. M. Kepert, F. E. Mabbs, B. Moubaraki, K. S. Murray, L. Spiccia, *Inorg. Chem.* **2001**, *40*, 1536–1543.

[25] T. H. Lu, S. C. Lin, H. Aneetha, K. Panneerselvam, C. S. Chung, *J. Chem. Soc., Dalton Trans.* **1999**, 3385–3391.

[26] O. Kahn, S. Sikorav, J. Gouteron, S. Jeannin, Y. Jeannin, *Inorg. Chem.* **1983**, *22*, 2877–2883.

[27] J. Luo, X. G. Zhou, S. Gao, L. H. Weng, Z. H. Shao, C. M. Zhang, Y. R. Li, J. Zhang, R. F. Cai, *Polyhedron* **2004**, *23*, 1243–1248.

[28] E. Escuer, M. Font-Bardía, E. Peñalba, X. Solans, R. Vicente, *Inorg. Chim. Acta* **2000**, *298*, 195–201.

[29] S. Triki, C. J. Gómez-García, E. Ruiz, J. Sala-Pala, *Inorg. Chem.* **2005**, *44*, 5501–5508.

[30] S. S. Massoud, F. A. Mautner, *Inorg. Chim. Acta* **2005**, *358*, 3334–3340.

[31] L. C. Li, D. Z. Liao, Z. H. Jiang, J. M. Mouesca, P. Rey, *Inorg. Chem.* **2006**, *45*, 7665–7670.

[32] S. S. Tandon, S. D. Bunge, D. Motry, J. S. Costa, G. Aromí, J. Reedijk, L. K. Thompson, *Inorg. Chem.* **2009**, *48*, 4873–4881.

[33] K. C. Mondal, P. S. Mukherjee, *Inorg. Chem.* **2008**, *47*, 4215–4225.

[34] Z. G. Gu, Y. Song, J. L. Zuo, X. Z. You, *Inorg. Chem.* **2007**, *46*, 9522–9524.

[35] J. Comarmond, P. Plumere, J. M. Lehn, Y. Agnus, R. Louis, R. Weiss, O. Kahn, I. Morgesten-badarau, *J. Am. Chem. Soc.* **1982**, *104*, 6330–6340.

[36] L. Banci, A. Bencini, D. Gatteschi, *Inorg. Chem.* **1984**, *23*, 2138–2141.

[37] P. Manikandan, R. Muthumaran, K. R. Justin Thomas, B. Varghese, G. V. R. Chandramouli, P. T. Manoharan, *Inorg. Chem.* **2001**, *40*, 2378–2389.

[38] A. Escuer, M. Font-Bardía, S. S. Massoud, F. A. Mautner, E. Peñalba, X. Solans, R. Vicente, *New J. Chem.* **2004**, *28*, 681–686.

[39] Z. G. Gu, J. L. Zuo, X. Z. You, *Dalton Trans.* **2007**, 4067–4072.

[40] W. Addison, T. N. Rao, J. Reedijk, J. Van Rijin, G. C. Verschoor, *J. Chem. Soc., Dalton Trans.* **1984**, 1349–1356.

[41] Y. F. Zeng, J. P. Zhao, B. W. Hu, X. Hu, F. C. Liu, J. Ribas, J. R. Arino, X. H. Bu, *Chem. Eur. J.* **2007**, *13*, 9924–9930.

[42] S. S. Tandon, L. K. Thompson, D. O. Miller, *J. Chem. Soc., Chem. Commun.* **1995**, 1907–1908.

[43] F. A. Mautner, S. Hanna, R. Cortés, L. Lezema, M. Gotzone, T. Rojo, *Inorg. Chem.* **1999**, *38*, 4647–4652.

[44] S. S. Tandon, L. K. Thompson, M. E. Manuel, J. N. Bridson, *Inorg. Chem.* **1994**, *33*, 5555–5570.

[45] A. Escuer, R. Vicente, J. M. S. Ribas, M. S. El Fallah, X. Solans, *Inorg. Chem.* **1993**, *32*, 1033–1035.

[46] J. Ribas, M. Monfort, C. Diaz, C. Bastos, X. Solans, *Inorg. Chem.* **1994**, *33*, 484–489.

[47] A. Escuer, R. Vicente, J. Ribas, M. S. El Fallah, X. Solans, M. Font Bardía, *Inorg. Chem.* **1994**, *33*, 1842–1847.

[48] R. Vicente, A. Escuer, J. Ribas, M. S. El Fallah, X. Solans, M. Font Bardía, *Inorg. Chem.* **1995**, *34*, 1278–1281.

[49] J. Ribas, M. Monfort, B. K. Ghosh, R. Cortés, X. Solans, M. Font-Bardía, *Inorg. Chem.* **1996**, *35*, 864–868.

[50] D. F. Sun, R. Cao, Y. Q. Sun, W. H. Bi, D. Q. Yuan, Q. Shi, X. Li, *Chem. Commun.* **2003**, 1528–1529.

[51] T. S. Lobana, R. Sharma, R. Sharma, S. Mehra, A. Castineiras, P. Turner, *Inorg. Chem.* **2005**, *44*, 1914–1921.

[52] S. Saha, S. Koner, J. P. Tuchagues, A. K. Boudalis, K. I. Okamoto, S. Banerjee, D. Mal, *Inorg. Chem.* **2005**, *44*, 6379–6385.

[53] S. Dalai, P. S. Mukherjee, T. Mallah, M. G. B. Drew, N. R. Chaudhuri, *Inorg. Chem. Commun.* **2002**, *5*, 472–474.

[54] T. K. Maji, P. S. Mukherjee, S. Koner, G. Mostafa, J. P. Tuchagues, N. R. Chaudhuri, *Inorg. Chim. Acta* **2001**, *314*, 111–116.

[55] H. R. He, C. F. Wang, Y. Song, J. L. Zuo, X. Z. You, *Inorg. Chem.* **2005**, *44*, 9039–9045.

[56] I. von Seggern, F. Tuczek, W. Bensch, *Inorg. Chem.* **1995**, *34*, 5530–5547.

[57] G. A. van Albada, M. T. Lakin, N. Veldman, A. L. Spek, J. Reedijk, *Inorg. Chem.* **1995**, *34*, 4910–4917.

[58] A. Escuer, M. A. S. Goher, F. A. Mautner, R. Vicente, *Inorg. Chem.* **2000**, *39*, 2107–2112.

[59] G. A. Baker, G. S. Rushbrooke, H. E. Gilbert, *Phys. Rev. A* **1964**, *135*, A1272–A1277.

[60] G. M. Sheldrick, *SHELXS-97 Program for X-ray Crystal Structure Solution*, University of Göttingen, Germany, **1997**.

[61] G. M. Sheldrick, *SHELXL-97 Program for X-ray Crystal Structure Refinement*, University of Göttingen, Germany, **1997**.

Received: August 7, 2009

DOI: 10.1002/ejic.200900890

Mononuclear Platinum(II) Complexes of a Bis(bidentate) Ligand Based on 1,3,4-Oxadiazole and Their Reactions with Copper(I) Salts

Marc-Etienne Moret[a] **and Peter Chen***[a]

Keywords: Platinum / Copper / N ligands / Metal–metal interactions / Bridging ligands

Reaction of the bis(bidentate) ligand 2,5-bis[2-(dimethylamino)phenyl]-1,3,4-oxadiazole (oxanMe) with the precursors *trans*-[$PtMeCl(SMe_2)_2$] and [$(PhCN)_2PtCl_2$] afforded the mononuclear complexes [(oxanMe)Pt(Me)Cl] and [(oxanMe)$PtCl_2$], respectively. [(oxanMe)$PtMe_2$] was observed in equilibrium with oxanMe, [$Pt_2Me_4(\mu\text{-}SMe_2)_2$], and [$PtMe_2(SMe_2)_2$], but could not be isolated. Reaction of [(oxanMe)$PtCl_2$] with silver acetate gave access to [(oxanMe)$Pt(OAc)_2$] in excellent yield. The latter was treated with [$Cu(NCMe)_4$]BArF, resulting in a disproportionation reaction that afforded the novel trimetallic complex {[(oxanMe)$Pt(OOCCH_3)_2]_2$Cu}$\{BArF\}_2$. This complex features a linear Pt^{II}–Cu^{II}–Pt^{II} chain consisting of two Pt→Cu dative bonds supported by two bridging acetate ligands each.

Introduction

Complexes of platinum(II) with chelating, N-donor ligands have attracted a lot of interest in the last decade due to their use as precursors for C–H bond activation of unreactive substrates.[1–10] In particular, complexes incorporating a methyl ligand are useful because the transient Pt^{IV} hydrides formed by oxidative addition of a C–H bond can then reductively eliminate methane, which drives the reaction to completion.[11–23] Some Pt^{II} carboxylate complexes have also been shown to be active benzene deuteration catalysts.[5,24,25] In search for novel reactivity related to C–H bond activation, we recently became interested in polynuclear complexes incorporating platinum and copper centers in close proximity.[26,27]

Incarvito et al. recently introduced a class of N-donor, dinucleating ligands based on a 1,3,4-oxadiazole bridging unit and showed that these could be used to form dinuclear compounds.[28,29] The simplest member and common precursor of this family is the ligand oxanH (**1**; Scheme 1). In this contribution, we present the synthesis of its tetramethylated derivative, oxanMe (**2**), and explore the coordination chemistry of **2** with common Pt^{II} precursors, showing that it preferentially forms mononuclear Pt^{II} complexes. Reaction of these complexes with [$Cu(NCMe)_4$]$^+$ salts does not allow the isolation of the desired heterobimetallic complexes, but in one case a novel trimetallic complex exhibiting an acetate-supported Pt^{II}–Cu^{II}–Pt^{II} chain can be isolated and characterized by single crystal X-ray diffraction (XRD).

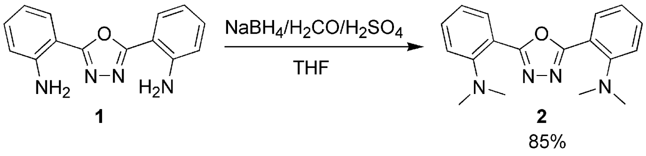

Scheme 1. Synthesis of oxanMe (**2**).

Results and Discussion

Ligand **2** was synthesized in 85% yield by tetramethylation of **1** by using the method of Giumanini et al.[30] for the selective dimethylation of anilines (Scheme 1). This procedure relies on the condensation of the aniline functionality with formaldehyde to form transient iminium cations that are subsequently hydrogenated by $NaBH_4$.

The reaction of ligand **2** with the precursor [$Pt_2Me_4(\mu\text{-}SMe_2)_2$] proceeded over a few minutes to form new complex **3** [Scheme 2, reaction (I)]. However, this reaction did not run to completion, but reached equilibrium at ca 35% conversion (based on the amount of **2**). The ^1H NMR spectrum of **3** exhibits eight aromatic signals, two signals corresponding to NMe_2 moieties and two different Pt–Me signals, in accord with the formulation of **3** as the mononuclear complex [(oxanMe)$PtMe_2$]. Furthermore, the fact that one of the NMe_2 moieties in **3** is coordinated to the platinum center is evident from the appearance of platinum satellites ($^3J_{H,Pt}$ = 14.0 Hz) around the corresponding methyl hydrogen signal.

Several attempts were made to shift the equilibrium by selective crystallization or removal of dimethyl sulfide under low pressure, but isolation of **3** remained elusive, partly due to the moderate stability of [$Pt_2Me_4(\mu\text{-}SMe_2)_2$] in solution. In a related experiment, the reaction was performed in the presence of CuBr, with the hope that SMe_2 would be

---

[a] Laboratorium für Organische Chemie, Eidgenössische Technische Hochschule (ETH) Zürich,
8093 Zürich, Switzerland
Fax: +41-44 632 15 92
E-mail: peter.chen@org.chem.ethz.ch

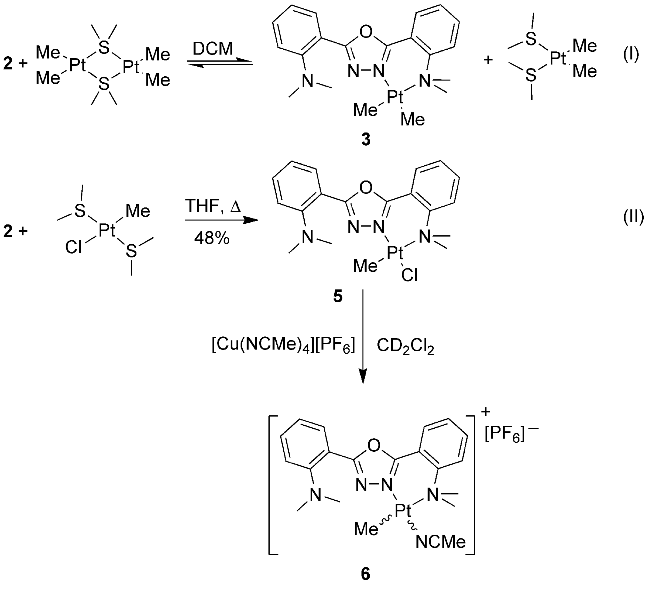

Scheme 2. Reactions of **2** with methylplatinum(II) precursors.

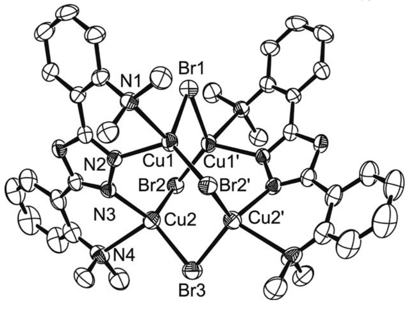

Figure 1. ORTEP representation of **4**. Ellipsoids are drawn at 50% probability. Four CH_2Cl_2 molecules are omitted for clarity. Selected distances [Å], angles [°], and torsion angles [°]: Cu1–N1 2.434(4), Cu1–N2 2.024(4), Cu1–Br1 2.4120(9), Cu1–Br2′ 2.3650(8), Cu2–N3 1.994(4), Cu2–N4 2.434(5), Cu2–Br2 2.4345(9), Cu2–Br3 2.3656(9), N1–Cu1–N2 80.79(15), N1–Cu1–Br1 97.57(11), N1–Cu1–Br2′ 101.17(11), N2–Cu1–Br1 107.10(13), N2–Cu1–Br2′ 118.98(13), Br1–Cu1–Br2′ 132.26(3), N3–Cu2–N4 81.35(16), N3–Cu2–Br2 106.96(13), N3–Cu2–Br3 134.39(13), N4–Cu2–Br2 102.33(13), N4–Cu2–Br3 103.28(13), Br2–Cu2–Br3 115.87(3), Cu1–Br1–Cu1′ 79.79(4), Cu1–Br2′–Cu2′ 90.63(3), Cu2–Br3–Cu2′ 86.42(4), Cu1–N2–N3–Cu2 1.7(5).

withdrawn from the solution by formation of the poorly soluble solid $CuBr{\cdot}SMe_2$. However, CuBr was solubilized by interaction with **2** and only the complex [(oxanMe)$_2$-Cu_4Br_4] (**4**) could be isolated from the reaction mixture.

XRD analysis of **4** (Figure 1) revealed a C_2-symmetrical $(CuBr)_4$ cycle stabilized by N,N chelation of all four copper(I) centers. Each metal has a distorted tetrahedral environment, with large Br–Cu–Br angles [132.26(3) and 115.87(3)°] and acute N–Cu–N bite angles [80.79(15) and 81.35(15)°]. The Cu–N bonds involving the oxadiazole unit are remarkably shorter than those involving the NMe_2 moiety [2.024(4) and 1.994(4) Å vs. 2.434(4) and 2.434(5) Å], indicating that the former are stronger donors, even though the oxadiazole ring acts as a bridge between two metals. The rare $(CuBr)_4$ cycle found in **4** is similar to that reported by Filinchuk et al.[31] in the complex {[1-(fur-2-yl)-2-azapenta-1,4-diene]$_2Cu_4Br_4$}.

A methylplatinum(II) complex of **2** was obtained by reaction with the more robust precursor [$(SMe_2)_2$Pt(Me)Cl], which yielded complex **5** in 48% yield [Scheme 2, reaction (II)] as a single stereoisomer that was identified by XRD (Figure 2). In the crystal structure of **5**, the platinum(II) center experiences only a slightly distorted square planar environment, the bite angle of oxanMe [85.1(2)°] being close to the ideal 90°. The Pt1–N1 bond is markedly longer than Pt1–N2 [2.256(7) vs. 1.990(5) Å], which is due both to the weaker σ-donor character of N1 and to the stronger *trans*-influence of the methyl ligand as compared to chloride.

Reaction of **5** with [Cu(NCMe)$_4$][PF_6] did not result in the formation of a dinuclear complex. In contrast, the chloride ligand was abstracted by precipitation of CuCl, resulting in the formation of cationic complex **6** (Scheme 2), which was identified by ^{1}H NMR spectroscopy and mass spectrometry (ESI). Isolation of **6** was not attempted.

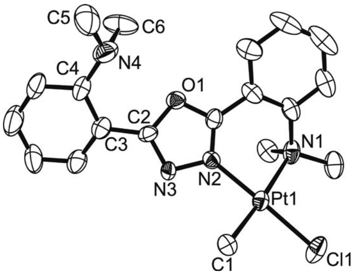

Figure 2. ORTEP representation of **5**. Ellipsoids are drawn at 50% probability. Selected distances [Å], angles [°], and torsion angles [°]: Pt1–C1 2.039(8), Pt1–Cl2 2.2830(19), Pt1–N1 2.256(7), Pt1–N2 1.990(5), C1–Pt1–Cl2 88.4(2), C1–Pt1–N2 90.8(3), Cl1–Pt1–N1 95.69(16), N1–Pt1–N2 85.1(2), Pt1–N2–N3 125.9(4), N3–C2–C3–C4 155.4(7), C3–C4–N4–C5 –147.3(8), C3–C4–N4–C6 92.1(9).

Platinum(II) diacetate complex **9** was accessed in two steps from ligand **2**. First, dichlorido complex **7** was obtained by heating **2** at reflux with [$(PhCN)_2PtCl_2$] in THF for 68 h, during which time **7** (83%) precipitated in analytical purity (Scheme 3). Upon storage of the liquid phase for several days, a byproduct crystallized as pale-yellow needles, which were identified as bi-oxanMe complex **8**. Complex **7** was then treated with silver acetate to yield diacetato complex **9** in excellent yield (Scheme 3). Complexes **7**, **8**, and **9** were subjected to XRD analysis.

Two different polymorphic structures **A** and **B** (Figure 3) were obtained by recrystallization of **7** from acetonitrile and dichloromethane/diethyl ether, respectively. The molecular units in **A** and **B** differ mainly by a rotation around the C4–C5 bond, with N3–C4–C5–C6 dihedral angles of 153(8) and –12.6(10)°, respectively. In both cases, the geometry around the platinum atom is square planar, with bite angles of 86.5(2) and 86.20(18)°. Despite the fact that both nitrogen atoms are located *trans* to a chloride ligand, the Pt1–N1 bond is considerably longer than Pt1–N2 [**A**: 2.142(5) vs.

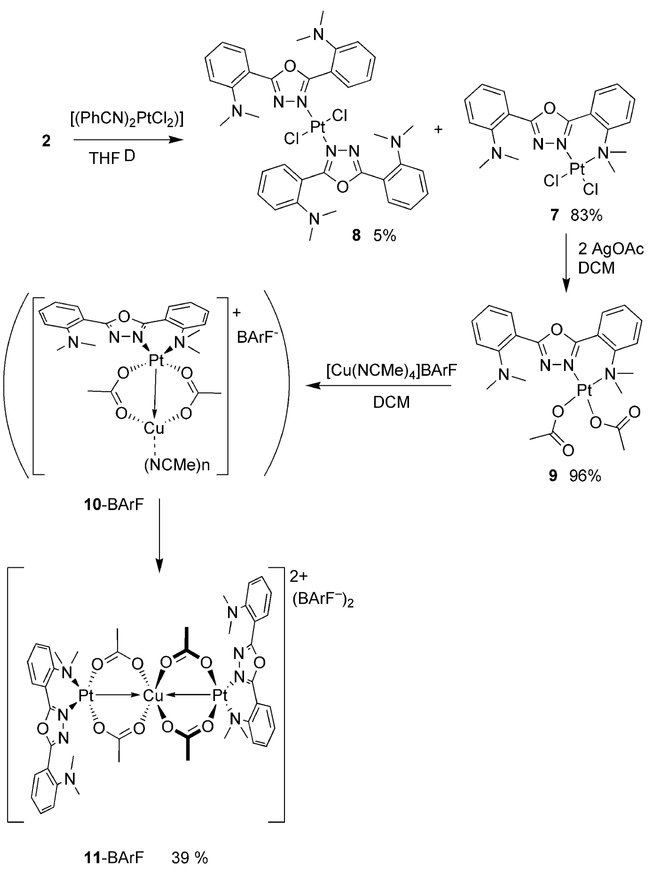

Scheme 3. Synthesis of [(oxanMe)Pt(OAc)$_2$] (**9**) and its reaction with [Cu(NCMe)$_4$]BArF {BArF = tetrakis[3,5-bis(trifluoromethyl)phenyl]borate}.

2.005(5) Å; **B**: 2.135(5) vs. 2.003(4) Å]. This indicates that the Pt–N1 interaction is weaker than Pt–N2, in accord with the observation that both oxanMe units are coordinated through N2 in the 2:1 byproduct **8** (Figure 4).

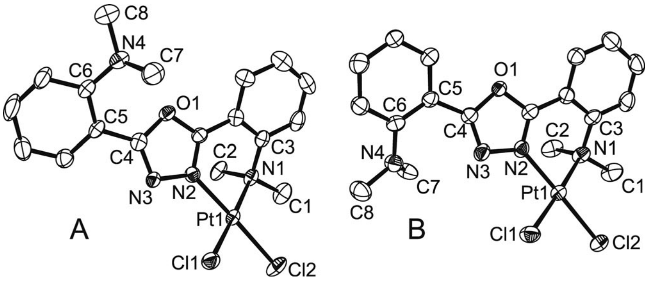

Figure 3. ORTEP representations of the two different structures found for **7**. Ellipsoids are drawn at 50% probability. Selected distances [Å], angles [°], and torsion angles [°]: For structure **A**: Pt1–Cl1 2.2929(15), Pt1–Cl2 2.2838(15), Pt1–N1 2.142(5), Pt1–N2 2.005(5), Cl1–Pt1–Cl2 87.96(6), Cl1–Pt1–N2 90.53(15), Cl2–Pt1–N1 95.06(14), N1–Pt1–N2 86.5(2), Pt1–N2–N3 128.0(4), N3–C4–C5–C6 153.8(6), C5–C6–N4–C7 125.4(8), C5–C6–N4–C8 –56.6(9); for structure **B**: Pt1–Cl1 2.2905(15), Pt1–Cl2 2.2904(13), Pt1–N1 2.135(5), Pt1–N2 2.003(4), Cl1–Pt1–Cl2 88.20(5), Cl1–Pt1–N2 90.46(14), Cl2–Pt1–N1 95.15(13), N1–Pt1–N2 86.20(18), Pt1–N2–N3 127.0(4), N3–C4–C5–C6 –12.6(10), C5–C6–N4–C7 164.6(6), C5–C6–N4–C8 –47.2(8).

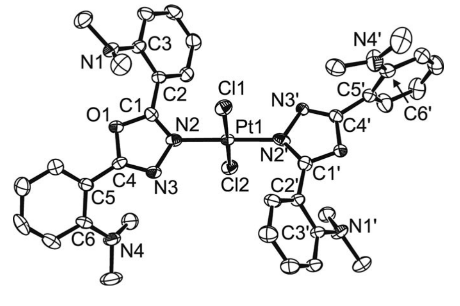

Figure 4. ORTEP representation of **8**. Ellipsoids are drawn at 50% probability. Selected distances [Å], angles [°], and torsion angles [°] (values for the right-most oxanMe ligand in square brackets): Pt1–Cl1 2.2982(18), Pt1–Cl2 2.2915(18), Pt1–N2 1.971(6) [1.974(6)], Cl1–Pt1–N2 90.02(17) [88.89(18)], Cl2–Pt1–N2 88.44(17) [92.69(18)], Pt1–N2–N3 120.5(4) [121.2(4)], Cl1–Pt1–N2–N3 –102.9(5) [–84.3(5)], N2–C1–C2–C3 –138.8(8) [132.8(8)], N3–C4–C5–C6 –36.3(12) [95.9(10)].

The XRD structure of **8** exhibits a square-planar geometry around $\mathrm{Pt^{II}}$. The two oxanMe units are bound to platinum through the oxadiazole units, which are approximately perpendicular to the coordination plane, with Cl1–Pt1–N2–N3 and Cl1–Pt1–N2′–N3′ dihedral angles of –102.9(5) and –84.3(5)°, respectively. The N-donor ligands are in a *trans* position, which is likely due to steric repulsion between them.

The unit cell of **9** contains two crystallographically independent molecules (Figure 5) that differ by the conformation of the exocyclic C–C bond [N3–C3–C4–C5 dihedral angles of 157.9(6) and –5.1(10)°, respectively]. In both molecules, the acetate ligands are bound in a *syn* fashion, that is, the Pt1–O1–C1–O3 [–3.4(8), 15.8(8)°] and Pt1–O2–C2–O4 [6.2(9), –5.9(8)°] dihedral angles have values close to 0, and their uncoordinated oxygen atoms are on opposite sides of the coordination plane.

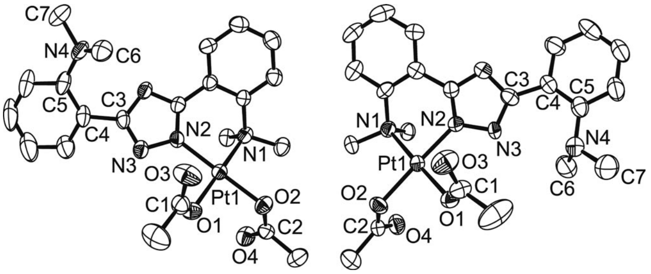

Figure 5. ORTEP representations of the two crystallographically different molecules found in the unit cell of **9**. Ellipsoids are drawn at 50% probability. For clarity, one molecule of diethyl ether present in the unit cell is omitted. Selected distances [Å], angles [°], and torsion angles [°] for the molecule plotted on the left [right]: Pt1–O1 2.004(4) [2.021(4)], Pt1–O2 2.028(4) [2.026(4)], Pt1–N1 2.097(5) [2.114(5)], Pt1–N2 1.980(4) [1.969(4)], O1–C1 1.267(7) [1.274(8)], C1–O3 1.220(7) [1.232(7)], O2–C2 1.274(7) [1.287(7)], C2–O4 1.222(6) [1.224(7)], O1–Pt1–O2 85.98(16) [85.80(16)], O1–Pt1–N2 92.33(18) [91.01(17)], O2–Pt1–N1 94.63(17) [95.63(17)], N1–Pt1–N2 87.35(18) [87.68(18)], Pt1–O1–C1 119.1(4) [118.1(4)], Pt1–O2–C2 118.4(3) [120.7(3)], Pt1–O1–C1–O3 –3.4(8) [15.8(8)], Pt1–O2–C2–O4 6.2(9) [–5.9(8)], N3–C3–C4–C5 157.9(6) [–5.1(10)], C4–C5–N4–C6 –53.0(9) [69.0(7)], C4–C5–N4–C7 167.3(6) [–161.6(6)].

The interaction of **9** with copper(I) was studied by ESI-MS analysis of a dichloromethane solution containing equimolar amounts of **9** and [Cu(NCMe)$_4$]BArF (BArF = tetrakis[3,5-bis(trifluoromethyl)phenyl]borate). The obtained spectrum features one main peak at *m*/*z* = 685, which is assigned to the 1:1 complex [(oxanMe)Pt(OAc)$_2$Cu]$^+$ (**10$^+$**) on the basis of its isotope pattern (Figure 6). Upon collision-induced dissociation (CID), it loses either acetic acid or a molecule of copper(I) acetate, in accord with its assignment.

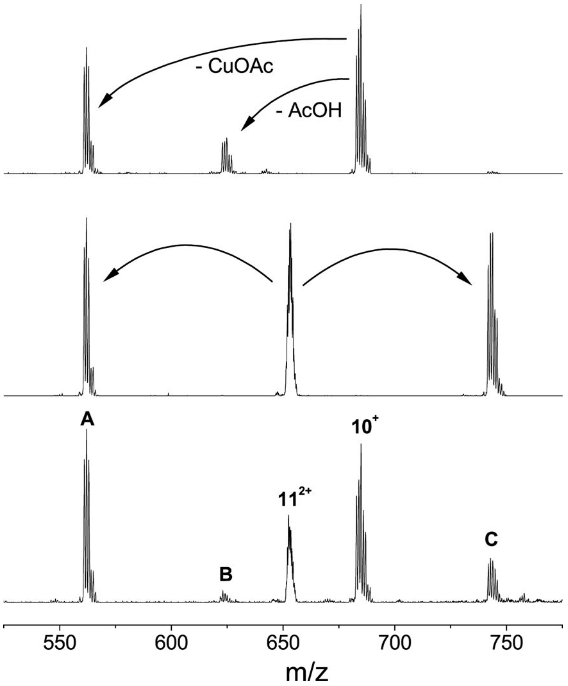

Figure 6. Bottom: ESI mass spectrum of a solution of **9** and [Cu(NCMe)$_4$]BArF 1 d after preparation, showing cations **10$^+$** and **11^{2+}** together with their fragmentation products. Middle: CID spectrum of **11^{2+}**. Top: CID spectrum of **10$^+$**. Peak assignment: **A**: [(oxanMe)Pt(OAc)]$^+$; **B**: **10$^+$** – AcOH; **C**: [(oxanMe)PtCu(OAc)$_3$]$^+$.

Because mass spectrometry provides no structural information, the structure of **10$^+$** was investigated by density functional theory (DFT) calculations at the BP86/6-31+G(d);Pt,Cu:SDD level, which we have previously shown to yield reliable geometries and energies for related Pt–Cu mixed complexes.[27] We optimized the geometries of the two most plausible structures (Figure 7): **10A$^+$**, in which the Cu^I center is chelated by the free nitrogen atoms of the oxanMe ligand and a bridging acetate, and **10B$^+$**, which features a dative Pt→Cu bond supported by two acetate bridges, resulting in a slightly distorted T-shaped tricoordinate environment around the Cu^I center. The Pt→Cu bond in **10B$^+$** (2.731 Å) is markedly longer than that found in the related complex {[(NN)PtMe$_2$]Cu(OTf)} [2.399 Å, NN = 2,3-bis(2,6-dichlorophenylimino)butane],[27] which is likely caused by the fact that acetate ligands are weaker σ-donors than methyl groups, resulting in reduced Lewis basicity of the platinum center. Structure **10B$^+$** was found to be more stable than **10A$^+$** by 10.6 kcal/mol and is thus the preferred structure of **10$^+$** in the gas phase.

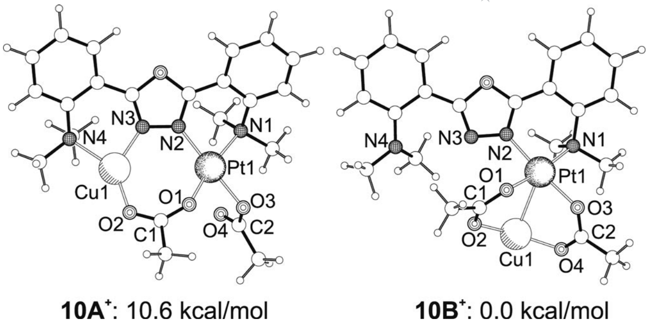

Figure 7. Calculated structures and relative energies for cation **10$^+$**. Selected distances [Å], angles [°], and torsion angles [°] for **10A$^+$**: Pt1–N1 2.145, Pt1–N2 2.018, Pt1–O1 2.082, Pt1–O3 2.083, Pt1–Cu1 3.743, Cu1–N3 1.958, Cu1–N4 2.146, Cu1–O2 1.877, N1–Pt1–N2 84.8, N3–Cu1–N4 88.2, N2–Pt1–O1 101.6, O1–Pt1–O3 78.8, Pt1–O1–C1 142.4, Cu1–O2–C1 125.9, Pt1–O3–C2 115.3, Pt1–N2–N3–Cu1 22.5; for **10B$^+$**: Pt1–N1 2.159, Pt1–N2 2.004, Pt1–O1 2.079, Pt1–O3 2.079, Pt1–Cu1 2.731, Cu1–O2 1.885, Cu1–O4 1.886, N1–Pt1–N2 86.6, N2–Pt1–O1 87.1, N1–Pt–O3 92.7, O1–Pt1–O3 93.0, O2–Cu–O4 156.3, Pt1–O1–C1 122.0, Pt1–O2–C2 124.2, Cu1–O2–C1 112.2, Cu1–O4–C2 113.6, Pt1–O1–C1–O2 19.6, Pt1–O3–C2–O4 –5.8, Cu1–O2–C1–O1 22.3, Cu1–O4–C2–O3 28.0.

A more detailed understanding of the reasons underlying the lower stability of **10A$^+$** – which may appear surprising at first sight – is given by a close inspection of its geometry. The square-planar environment of the Pt^{II} center is distorted, with N2–Pt1–O1 and O1–Pt1–O2 angles of 101.6 and 78.8°, respectively, and the Pt1–O1–C1 angle of 142.4° is wider than the ideal value of ca. 120°. Furthermore, the Pt1–N2–N3–Cu1 dihedral angle (22.5°) is large, indicating suboptimal coordination of the oxadiazole bridge to the metals. Thus, structure **10A$^+$** is highly strained, indicating that ligand **2** is presumably not suited for preparing dinuclear complexes incorporating planar 1,3-bridging ligands and a square-planar metal center.

The interaction of **9** with copper(I) was also studied in solution by ^{1}H NMR spectroscopy. Upon addition of one equivalent of [Cu(NCMe)$_4$]BArF to a solution of **9** in CD$_2$Cl$_2$, the resonances corresponding to the acetate ligands undergo a slight downfield shift from δ = 1.94 and 2.00 ppm to δ = 2.06 and 2.11 ppm, but the signal of the uncoordinated NMe$_2$ moiety is not affected. Thus, we infer that a, presumably acetonitrile solvated, salt of **10B$^+$** (**10**-BArF) exists in solution (Scheme 3).

Attempts to isolate **10$^+$** with a range of counterions (PF$_6^-$, ClO$_4^-$, BArF$^-$) failed due to its instability in solution. When a solution of **10**-BArF was stored for several hours at room temperature, a black precipitate (presumably Cu^0) forms. The concomitant appearance of a few very broad resonances in the ^{1}H NMR spectrum indicates the formation of a paramagnetic Cu^{II} species by disproportionation of Cu^I. ESI-MS analysis (Figure 6) shows the appearance of a new peak at *m*/*z* = 653, which is identified as the Cu^{II} complex [(oxanMe)$_2$Pt$_2$(OAc)$_4$Cu]$^{2+}$ (**11^{2+}**) on the basis of its isotope pattern. Upon CID, dication **11^{2+}** cleanly fragments into two monocations of formula [(oxanMe)Pt(OAc)]$^+$ and [(oxanMe)Pt(OAc)$_3$Cu]$^+$, confirming its assignment.

In contrast to **10**$^+$, dication **11**$^{2+}$ could be isolated and crystallized as its BArF$^-$ salt. The XRD crystal structure of **11**-BArF (Figure 8) shows that **11**$^{2+}$ has a centrosymmetrical structure in which the central Cu^{II} atom is encapsulated by two [(oxanMe)Pt(OAc)$_2$] units, forming a linear Pt^{II}–Cu^{II}–Pt^{II} chain. The copper center experiences an apically distorted octahedral environment with four short Cu–O bonds [1.942(3) and 1.960(3) Å] in the equatorial plane and two Pt→Cu dative bonds (Pt–Cu 2.7506 Å) in apical positions. There is precedence for Pt^{II}→Cu^{II} dative bonds supported by 1,3-bridging nucleobases,[32–34] including a similar Pt^{II}–Cu^{II}–Pt^{II} chain with 1-methyluracilate and 1-methylcytosine as bridging ligands.[35] Additionally, compounds exhibiting acetate-supported Pt–Hg bonds are known.[36] However, to the best of our knowledge, the carboxylate-bridged Pt^{II}–Cu^{II}–Pt^{II} motif found in **11**-BArF is unprecedented.

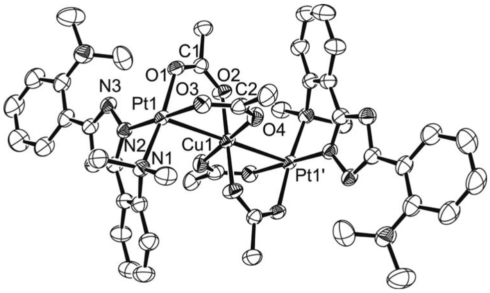

Figure 8. ORTEP representation of the centrosymmetric dication of **11**-BArF. Ellipsoids are drawn at 50% probability. For clarity, the two BArF counterions and a disordered diethyl ether molecule are omitted. Selected distances [Å] and angles [°]: Pt1–N1 2.087(4), Pt1–N2 1.975(4), Pt1–O1 2.007(3), Pt1–O3 2.019(3), Pt1–Cu1 2.7506(5), Cu1–O2 1.942(3), Cu1–O4 1.960(3), C1–O1 1.271(5), C1–O2 1.258(5), C2–O3 1.272(6), C2–O4 1.245(5), N1–Pt1–N3 87.65(14), N1–Pt1–O3 92.95(14), N2–Pt1–O1 91.26(13), O1–Pt1–O2 88.13(13), Pt1–O1–C1 125.1(3), Pt1–O3–C2 123.7(3), O2–Cu1–O4 91.38(14), O2–Cu1–O4′ 88.63(14), Cu1–O2–C1 123.4(3), Cu1–O4–C2 124.9(3).

Conclusions

The novel ligand oxanMe (**2**) was synthesized by methylation of the known oxan (**1**). The oxanMe ligand can be used to synthesize mononuclear complexes with common platinum(II) fragments, but it acts as a bis(bidentate) ligand in the tetranuclear copper(I) complex [(oxanMe)$_2$Cu$_4$Br$_4$] (**4**). The tendency of **2** to form mononuclear species is presumably due to the fact that coordination of a metal inductively removes electron density from the – already electron-poor – oxadiazole ring, making it weakly coordinating toward the second metal. In the reaction of diacetato complex **4** with [Cu(NCMe)$_4$]BArF, we observed the unexpected formation of a trinuclear complex that exhibits a Pt^{II}–Cu^{II}–Pt^{II} chain consisting of two Pt^{II}→Cu^{II} dative bonds supported by two acetate bridges each. Although no stable heterobinuclear complexes were obtained, the empty pocket of the mononuclear complexes could in principle be used to stabilize bimetallic intermediates in a catalytic cycle. This concept is currently investigated in our group.

Experimental Section

General: Solvents were obtained commercially in p.a. quality and used as received. For reactions involving metal complexes, solvents were distilled under an atmosphere of nitrogen over sodium (hexane, toluene), Na/K alloy (diethyl ether), potassium (tetrahydrofuran), or CaH$_2$ (acetonitrile, dichloromethane). All chemical manipulations involving metal complexes were performed under an inert atmosphere by using standard Schlenk and glove box techniques unless otherwise stated. ^{1}H and ^{13}C NMR spectra were recorded with Varian Gemini 300 and Varian Mercury 300 instruments. ^{1}H and ^{13}C chemical shifts are reported in ppm relative to tetramethylsilane, using residual solvent proton and ^{13}C resonances as internal references. Apparent singlets, doublets, and triplets are indicated by "s", "d", and "t", respectively. Elemental analyses were carried out by the Mikrolabor of the Laboratorium für Organische Chemie of ETH Zürich. Melting points are uncorrected and were measured in unsealed capillaries. Organolithium reagents were titrated by using the procedure of Watson and Eastham.[37] OxanH[28] (**1**), [Pt$_2$(CH$_3$)$_4$(μ-Me$_2$S)$_2$],[38] [(Me$_2$S)$_2$Pt(Me)Cl],[38] (PhCN)$_2$PtCl$_2$,[39] Na[BArF],[40] and [Cu(NCMe)$_4$][ClO$_4$],[41] were prepared according to literature procedures. All other chemicals were obtained commercially and used as received.

2,5-Bis[2-(dimethylamino)phenyl]-1,3,4-oxadiazole (oxanMe, 2): A suspension of NaBH$_4$ (2.2 g, 58 mmol) and **1** (1.01 g, 4 mmol) in THF (50 mL) was added over 30 min to a cooled mixture of formaldehyde (37% in water, 4 mL, 53 mmol), H$_2$SO$_4$ (3 M, 6.7 mL, 1 mmol), and THF (20 mL), resulting in a yellow suspension. Water (30 mL) was added, resulting in phase separation, followed by sodium carbonate until the pH of the water phase was distinctly basic. The organic phase was decanted, the water phase extracted with DCM (40 + 2 × 20 mL). The combined organic extract was washed with brine (30 mL), dried with MgSO$_4$, and concentrated under reduced pressure to yield a yellow solid. This residue was purified by column chromatography (110 g of silica, 1:3 ethyl acetate/petroleum ether containing 3% triethylamine) to yield a slightly yellow solid (1.04 g, 85%). M.p. 112–115 °C. ^{1}H NMR (300 MHz, [D$_6$]DMSO): δ = 7.74 (dd, $^3J_{H,H}$ = 7.7 Hz, $^5J_{H,H}$ = 1.7 Hz, 2 H, ArH^6), 7.50 (ddd, $^3J_{H,H}$ = 8.4 Hz, $^3J_{H,H}$ = 7.3 Hz, $^5J_{H,H}$ = 1.7 Hz, 2 H, ArH^4), 7.18 (dd, $^3J_{H,H}$ = 8.4 Hz, $^5J_{H,H}$ = 0.9 Hz, 2 H, ArH^3), 7.06 ("t"d, $^3J_{H,H}$ = 7.5 Hz, $^5J_{H,H}$ = 1.1 Hz, 2 H, ArH^5), 2.70 [s, 12 H, N(CH$_3$)$_2$] ppm. ^{13}C{^{1}H} NMR (75 MHz, [D$_6$]DMSO): δ = 164.2, 152.2, 132.3, 131.3, 120.4, 118.2, 114.9 (7 C_{Ar}), 43.3 (CH$_3$) ppm. C$_{18}$H$_{20}$N$_4$O (308.38): calcd. C 70.11, H 6.54, N 18.17; found C 69.85, H 6.63, N 18.24.

Reaction of 2 with [Pt$_2$Me$_4$(μ-SMe$_2$)$_2$]: CD$_2$Cl$_2$ (0.7 mL) was added to a mixture of **2** (6.1 mg, 20 μmol) and [Pt$_2$Me$_4$(μ-SMe$_2$)$_2$] (5.7 mg, 10 μmol), resulting in a yellow solution that was left standing for 30 min. ^{1}H NMR analysis showed that the mixture contained **2** (45%), **3** (24%), [Pt$_2$Me$_4$(μ-SMe$_2$)$_2$] (12%), and [PtMe$_2$(SMe$_2$)$_2$] (19%), indicating a conversion rate of 35% based on the amount of **2**. Further standing at room temperature did not result in higher conversion, but slow decomposition was observed instead, leading to an intractable mixture of products over several hours. ^{1}H NMR (300 MHz, CD$_2$Cl$_2$): Only the signals of novel complex **3** are reported. The signals marked with * suffer from partial overlap with signals of **2**. δ = 7.93 (dd, $^3J_{H,H}$ = 7.6 Hz, $^5J_{H,H}$ = 1.7 Hz, 1 H, ArH^6), 7.92 (dd, $^3J_{H,H}$ = 7.9 Hz, $^5J_{H,H}$ = 1.7 Hz, 1 H, ArH^6), 7.64 (ddd, $^3J_{H,H}$ = 8.6 Hz, $^3J_{H,H}$ = 7.3 Hz, $^5J_{H,H}$ = 1.7 Hz, 1 H, ArH^4), 7.51* (ddd, $^3J_{H,H}$ = 8.5 Hz, $^3J_{H,H}$ = 7.1 Hz, $^5J_{H,H}$ = 1.7 Hz, 1 H, ArH^4), 7.41* (dd, $^3J_{H,H}$ hidden, $^5J_{H,H}$ = 0.7 Hz, 1 H, ArH^3), 7.35 ("t"d, $^3J_{H,H}$ = 7.6 Hz, $^5J_{H,H}$ = 0.9 Hz, 1 H, ArH^5), 7.18 (dd, $^3J_{H,H}$ = 8.3 Hz, $^5J_{H,H}$ = 0.7 Hz, 1 H, ArH^3), 7.07* ("t"d, $^3J_{H,H}$ = 7.6 Hz, $^5J_{H,H}$ = 1.1 Hz, 1 H, ArH^5), 3.08 [s, $^3J_{H,Pt}$ = 14.0 Hz, 3 H, PtN(CH_3)$_2$], 2.85 [s, 3 H, N(CH_3)$_2$], 0.85 (s, $^2J_{H,Pt}$ = 94.6 Hz, 3 H, PtCH_3), 0.56 (s, $^2J_{H,Pt}$ = 85.5 Hz, 3 H, PtCH_3).

[(oxanMe)$_2$Cu$_4$Br$_4$] (4): CuBr (29 mg, 0.2 mmol) was added to a mixture of **2** (62 mg, 0.2 mmol) and [Pt$_2$(CH$_3$)$_4$(μ-Me$_2$S)$_2$] (58 mg, 0.1 mmol) in DCM (3 mL), and the solution was stirred for 0.5 h, during which time a small quantity of yellow needles formed. The orange solution was concentrated to ca. 1 mL and diethyl ether (4 mL) was added slowly while stirring. Filtration, washing of the solid with diethyl ether (3 × 1 mL), and drying in vacuo yielded the product as a yellow powder. ^{1}H NMR (300 MHz, CD$_2$Cl$_2$): δ = 8.00 (dd, $^3J_{H,H}$ = 7.9 Hz, $^5J_{H,H}$ = 1.6 Hz, 2 H, ArH^6), 7.60 (ddd, $^3J_{H,H}$ = 8.4 Hz, $^3J_{H,H}$ = 7.3 Hz, $^5J_{H,H}$ = 1.7 Hz, 2 H, ArH^4), 7.37 (dd, $^3J_{H,H}$ = 8.4 Hz, $^5J_{H,H}$ = 0.9 Hz, 2 H, ArH^3), 7.25 (ddd, $^3J_{H,H}$ = 7.9 Hz, $^3J_{H,H}$ = 7.4 Hz, $^5J_{H,H}$ = 1.1 Hz, 2 H, ArH^5), 2.88 (s, 12 H, CH_3) ppm. No ^{13}C NMR could be obtained due to poor solubility in DCM. $C_{36}H_{40}Br_4Cu_4N_8O_2$ (1190.56): calcd. C 36.32, H 3.39, N 9.41; found C 36.43, H 3.61, N 9.28. Crystals suitable for XRD analysis were obtained by vapor diffusion of diethyl ether into a dichloromethane solution of **4** at 4 °C.

[(oxanMe)Pt(Me)Cl] (5): This reaction was performed without protection from air. OxanMe (165 mg, 0.53 mmol) and *trans*-[PtMeCl(SMe$_2$)$_2$] were dissolved in THF (5 mL). The flask was placed in an 85 °C oil bath and boiled to almost dryness (ca. 10 min) The oily residue was dissolved again in THF (5 mL), and this cycle was repeated 15 times. The brown residue was dissolved in DCM (1 mL), treated with activated charcoal and filtered. Diethyl ether (ca. 2 mL) was added until persistent turbidity of the solution. After cooling at 4 °C for 1 h, an oily, brown precipitate was removed from the orange solution by decantation. The solvent was evaporated in vacuo, and the residue was dissolved in a minimal amount of DCM. Diethyl ether (ca. 3 mL) was added until persistent turbidity of the solution. The latter was stored at –20 °C overnight, during which time the product crystallized. Decantation of the solvent, washing with diethyl ether (3 × 1 mL) and drying in vacuo yielded the product as orange nodules (140 mg, 48 %). An analytically pure sample was obtained by recrystallization from DCM/octane. ^{1}H NMR (300 MHz, CDCl$_3$): δ = 7.92 (dd, $^3J_{H,H}$ = 7.7 Hz, $^5J_{H,H}$ = 1.6 Hz, 2 H, ArH^6), 7.91 (dd, $^3J_{H,H}$ = 7.9 Hz, $^5J_{H,H}$ = 1.7 Hz, 2 H, ArH^6), 7.68 (ddd, $^3J_{H,H}$ = 8.5 Hz, $^3J_{H,H}$ = 7.4 Hz, $^5J_{H,H}$ = 1.7 Hz, 1 H, ArH^4), 7.54–7.46 (m, 2 H, Ar$H^{4,5}$), 7.38 ("t"d, $^3J_{H,H}$ = 7.6 Hz, $^5J_{H,H}$ = 1.0 Hz, 1 H, ArH^5), 7.16 (dd, $^3J_{H,H}$ = 8.4 Hz, $^5J_{H,H}$ = 0.9 Hz, 1 H, ArH^3), 7.06 (ddd, $^3J_{H,H}$ = 7.9 Hz, $^3J_{H,H}$ = 7.3 Hz, $^5J_{H,H}$ = 1.1 Hz, 1 H, ArH^5), 3.15 [br. s, $^3J_{H,Pt}$ not resolved, 6 H, PtN(CH_3)$_2$], 2.87 [s, 6 H, N(CH_3)$_2$], 1.38 (s, $^2J_{H,Pt}$ = 83.5 Hz, 3 H, PtCH_3) ppm. ^{13}C{^{1}H} NMR (75 MHz, CDCl$_3$): δ = 163.8, 158.9, 153.2, 151.2, 133.8, 133.5, 131.3, 129.4, 126.5, 120.7, 119.8, 118.7, 116.8, 112.7 (14 C^{Ar}), 51.0 [PtN(CH$_3$)$_2$], 44.3 [N(CH$_3$)$_2$], –22.7 (PtCH$_3$), no $J_{C,Pt}$ observed ppm. $C_{19}H_{23}ClN_4OPt$ (553.95): calcd. C 41.20, H 4.18, N 10.11; found C 40.96, H 4.38, N 10.04. Crystals suitable for XRD analysis were obtained by dissolving **5** in a minimal amount of DCM, adding ten volumes of diethyl ether and letting the suspension stand for 3 d.

Reaction of 5 with [Cu(NCMe)$_4$][PF$_6$]: CD$_2$Cl$_2$ (0.7 mL) was added to **5** (11 mg, 20 μmol) and [Cu(NCMe)$_4$][PF$_6$] (7 mg, 19 μmol). After 30 min, the yellow suspension was filtered into an NMR tube and subjected to ^{1}H NMR and ESI-MS analysis, which showed that [(oxanMe)PtMe(NCMe)][PF$_6$] (**6**) was cleanly formed. ^{1}H NMR (300 MHz, CD$_2$Cl$_2$): δ = 8.01 (dd, $^3J_{H,H}$ = 7.7 Hz, $^5J_{H,H}$ = 1.6 Hz, 1 H, ArH^6), 7.95 (dd, $^3J_{H,H}$ = 7.9 Hz, $^5J_{H,H}$ = 1.7 Hz, 1 H, ArH^6), 7.82 ("t"d, $^3J_{H,H}$ = 7.7 Hz, $^5J_{H,H}$ = 1.5 Hz, 1 H, ArH^4), 7.65 (d, $^3J_{H,H}$ = 8.4 Hz, 1 H, ArH^3), 7.58 ("t"d, $^3J_{H,H}$ = 7.8 Hz, $^5J_{H,H}$ = 1.6 Hz, 1 H, ArH^4), 7.54 ("t", $^3J_{H,H}$ = 7.6 Hz, 1 H, ArH^5), 7.24 (d, $^3J_{H,H}$ = 8.0 Hz, 1 H, ArH^3), 7.12 ("t", $^3J_{H,H}$ = 7.6 Hz, 1 H, ArH^5), 3.20 [br. s, $^3J_{H,Pt}$ not resolved, 6 H, PtN(CH_3)$_2$], 2.87 [s, 6 H, N(CH_3)$_2$], 2.56 (s, $^3J_{H,Pt}$ = 12.9 Hz, 3 H, CH_3CNPt), 1.20 (s, $^3J_{H,Pt}$ = 80.1 Hz, 3 H, PtCH_3) ppm. MS (ESI+, DCM): *m*/*z* = 559 [M]$^+$.

[(oxanMe)PtCl$_2$] (7): A mixture of oxanMe (594 mg, 1.94 mmol) and [(PhCN)$_2$PtCl$_2$] (915 mg, 1.94 mmol) in THF (20 mL) was heated at reflux for 68 h. After cooling to room temperature, the precipitate was collected by filtration, washed with THF (3 × 3 mL), and dried in vacuo to afford 924 mg (1.62 mmol, 83 %) of a yellow powder. ^{1}H NMR (300 MHz, CD$_2$Cl$_2$): δ = 8.04 (dd, $^3J_{H,H}$ = 7.6 Hz, $^5J_{H,H}$ = 1.7 Hz, 1 H, ArH^6), 7.95 (dd, $^3J_{H,H}$ = 7.9 Hz, $^5J_{H,H}$ = 1.7 Hz, 1 H, ArH^6), 7.77 (ddd, $^3J_{H,H}$ = 8.7 Hz, $^3J_{H,H}$ = 7.4 Hz, $^5J_{H,H}$ = 1.7 Hz, 1 H, ArH^4), 7.62–7.50 (m, 3 H, Ar$H^{3,4,5}$), 7.20 (dd, $^3J_{H,H}$ = 8.5 Hz, $^5J_{H,H}$ = 0.7 Hz, 1 H, ArH^3), 7.08 (ddd, $^3J_{H,H}$ = 7.9 Hz, $^3J_{H,H}$ = 7.3 Hz, $^5J_{H,H}$ = 1.0 Hz 1 H, ArH^5), 3.29 [s, $^3J_{H,Pt}$ = 26.5 Hz (br. Pt satellites), 6 H, PtN(CH_3)$_2$] 2.90 [s, 6 H, N(CH_3)$_2$] ppm. ^{13}C{^{1}H} NMR (75 MHz, CD$_2$Cl$_2$): δ = 165.1, 158.2, 153.8, 150.4, 135.3, 134.1, 131.7, 130.4, 128.5, 120.7, 119.5, 118.9, 116.5, 112.0 (14 C_{Ar}), 55.9 [PtN(CH$_3$)$_2$], 44.3 [N(CH$_3$)$_2$] ppm. MS (ESI+, MeCN, AgOTf): *m*/*z* = 580 [M – Cl$^-$ + MeCN]$^+$. MS–MS (+580): *m*/*z* = 543 [580 – HCl], 739 [580 – MeCN], 502 [580 – MeCN – HCl]. $C_{18}H_{20}Cl_2N_4OPt$ (574.37): calcd. C 37.64, H 3.51, N 9.75; found C 37.31, H 3.55, N 9.37. Crystals suitable for XRD analysis were grown by slow concentration of a solution of **7** in MeCN (polymorph **A**) or by vapor diffusion of diethyl ether into a solution of **7** in dichloromethane (polymorph **B**).

***trans*-[(oxanMe)$_2$PtCl$_2$] (8):** After collection of **7** by filtration from the reaction described above, the filtrate was stored at room temperature for 3 d, during which time **8** crystallized as thin, pale-yellow needles containing 2 equiv. of THF (52 mg, ca. 5 %). A solvent free sample was obtained by crystallization from MeCN. ^{1}H NMR (300 MHz, CD$_2$Cl$_2$): δ = 8.75 (dd, $^3J_{H,H}$ = 7.8 Hz, $^5J_{H,H}$ = 1.6 Hz, 1 H, ArH^6), 7.84 (dd, $^3J_{H,H}$ = 8.0 Hz, $^5J_{H,H}$ = 1.5 Hz, 1 H, ArH^6), 7.54 (ddd, $^3J_{H,H}$ = 8.5 Hz, $^3J_{H,H}$ = 7.3 Hz, $^5J_{H,H}$ = 1.7 Hz, 1 H, ArH^4), 7.50 (ddd, $^3J_{H,H}$ = 8.4 Hz, $^3J_{H,H}$ = 7.3 Hz, $^5J_{H,H}$ = 1.7 Hz, 1 H, ArH^4), 7.19 (dd, $^3J_{H,H}$ = 8.4 Hz, $^5J_{H,H}$ = 0.9 Hz, 1 H, ArH^3), 7.09–6.95 (m, 3 H, Ar$H^{3,5,5}$), 2.86 [s, 6 H, N(CH_3)$_2$], 2.81 [s, 6 H, N(CH_3)$_2$] ppm. ^{13}C{^{1}H} NMR (75 MHz, CD$_2$Cl$_2$): δ = 165.6, 164.9, 154.1, 153.4, 134.2, 133.9, 133.8, 131.8, 121.2, 119.8, 119.3, 117.5, 114.0, 111.9 (14 C_{Ar}), 44.6, 43.5 [2 N(CH$_3$)$_2$] ppm. MS (ESI+, DCM): *m*/*z* = 883 (weak) [M + H]$^+$, +847 [M – Cl$^-$]$^+$. MS–MS (+883): *m*/*z* = 847 [883 – HCl]. MS–MS (+847): *m*/*z* = 810 [847 – HCl]. $C_{36}H_{40}Cl_2N_8O_2Pt$ (882.75): calcd. C 48.98, H 4.57, N 12.69; found C 48.69, H 4.75, N 12.52. Crystals suitable for XRD analysis were obtained by crystallization from hot MeCN.

[(oxanMe)Pt(OOCCH$_3$)$_2$] (9): A mixture of **7** (350 mg, 0.61 mmol) and silver acetate (204 mg, 1.22 mmol) in DCM (20 mL) was stirred for 20 h in the dark. Filtration and washing of the precipitate with DCM (2 × 2 mL) yielded a brown solution, from which the solvent was removed in vacuo to yield the product as a light-brown powder (366 mg, 96 %). An analytically pure sample was obtained by slow crystallization from DCM/Et$_2$O. ^{1}H NMR (300 MHz, CD$_2$Cl$_2$): δ = 8.08 (dd, $^3J_{H,H}$ = 7.7 Hz, $^5J_{H,H}$ = 1.7 Hz, 1 H, ArH^6), 7.90 (dd, $^3J_{H,H}$ = 7.9 Hz, $^5J_{H,H}$ = 1.7 Hz, 1 H, ArH^6), 7.77 (ddd, $^3J_{H,H}$ = 8.6 Hz, $^3J_{H,H}$ = 7.4 Hz, $^5J_{H,H}$ = 1.7 Hz, 1 H, ArH^4), 7.66 (dd, $^3J_{H,H}$ = 8.5 Hz, $^5J_{H,H}$ = 0.9 Hz, 1 H, ArH^3), 7.58 ("t"d, $^3J_{H,H}$ = 7.6 Hz, $^5J_{H,H}$ = 1.1 Hz, 1 H, ArH^5), 7.53 (ddd, $^3J_{H,H}$ = 8.5 Hz, $^3J_{H,H}$ = 7.3 Hz, $^5J_{H,H}$ = 1.7 Hz, 1 H, ArH^4), 7.20 (dd, $^3J_{H,H}$ = 8.4 Hz, $^5J_{H,H}$ = 0.9 Hz, ArH^3), 7.07 (ddd, $^3J_{H,H}$ = 8.2 Hz, $^3J_{H,H}$ = 7.4 Hz, $^5J_{H,H}$ = 1.1 Hz, 1 H, ArH^5), 3.27 [s (br., $^3J_{H,Pt}$ not resolved, 6 H, PtN(CH_3)$_2$], 2.85 [s, 6 H, N(CH_3)$_2$], 2.00 (s, 3 H, CH_3COO), 1.94 (s, 3 H, CH_3COO) ppm. ^{13}C{^{1}H} NMR (75 MHz, CD_2Cl_2): δ = 177.4, 177.3 [2 *C*(=O)O], 164.4, 156.7, 153.8, 149.9, 135.1, 134.0, 131.5, 130.0, 128.9, 120.9, 120.0, 119.1, 116.2, 112.6 (14 C_{Ar}), 55.5 [PtN(CH_3)$_2$], 44.3 [N(CH_3)$_2$], 23.5, 22.5 (2 H_3CCOO) ppm. MS (ESI+, DCM): m/z = 562 [M – MeCOO$^-$]$^+$, 870 [M + oxanMe – MeCOO$^-$]$^+$, 1183 [2M – MeCOO$^-$]$^+$. MS–MS (+562): m/z = 502 [562 – MeCOOH]. MS–MS (+870): m/z = 562 [870 – oxanMe]. MS–MS (+1183): m/z = 562 {1183 – [(oxanMe)Pt(OOCMe)$_2$]}. $C_{22}H_{26}N_4O_5Pt$ (621.55): calcd. C 42.51, H 4.22, N 9.01; found C 42.22, H 4.26, N 8.90. Crystals suitable for XRD analysis were obtained by vapor diffusion of diethyl ether into a dichloromethane solution of **9** at 4 °C.

{[(oxanMe)Pt(OOCCH$_3$)$_2$]$_2$Cu}{BArF}$_2$ (11-BArF): A mixture of [Cu(NCMe)$_4$]ClO$_4$ (83 mg, 0.25 mmol) and NaBArF (150 mg, 0.17 mmol) in diethyl ether (10 mL) was stirred for 35 min and filtered. The filtrate, containing [Cu(NCMe)$_4$]BArF,[42] was freed from solvent in vacuo and dissolved in DCM (3 mL). A solution of **9** (95 mg, 0.15 mmol) in DCM (7 mL) was slowly added, and the mixture was stirred for 1.5 h. The solvent was evaporated, and the solid residue was extracted with diethyl ether (5 + 2 mL). The solvent was evaporated, and the residue taken up in diethyl ether (5 mL) and freed from solvent in vacuo. The solid residue was then dissolved in DCM (8 mL), a dark solid (presumably Cu^0) was filtered off, and hexane was added until persistent turbidity. The mixture was cooled to –20 °C for 2 h, and the formed dark oil was removed by decantation. Further concentration, filtration, and drying in vacuo yielded the product as a mustard-yellow powder (90 mg, 0.03 mmol, 39% based on **9**). An analytically pure sample, containing one equivalent of solvent, was obtained by crystallization from diethyl ether. MS (ESI+, DCM): m/z = 653 [M]$^{2+}$, 562 [(oxanMe)Pt(OOCMe)]$^+$, 744 [(oxanMe)Pt(OOCMe)$_3$Cu]$^+$. MS–MS (+653): m/z = 562 [(oxanMe)Pt(OOCMe)]$^+$, 744 [(oxanMe)Pt(OOCMe)$_3$Cu]$^+$. MS (ESI–, DCM): m/z = –863 [BArF]$^-$. $C_{108}H_{76}B_2CuF_{48}N_8O_{10}Pt_2\cdot C_4H_{10}O$ (3107.19): calcd. C 43.29, H 2.79, N 3.61; found C 43.28, H 2.77, N 3.65. Crystals suitable for XRD analysis were obtained from diethyl ether.

Reaction of 9 with [Cu(NCMe)$_4$]BArF: Compound **9** (17 µmol) was added to a freshly prepared solution of [Cu(NCMe)$_4$]BArF (17 µmol) in CD_2Cl_2 (0.7 mL), and the resulting solution was subjected to ^{1}H NMR analysis. ^{1}H NMR (300 MHz, CD_2Cl_2): δ = 8.15 (dd, $^3J_{H,H}$ = 7.7 Hz, $^5J_{H,H}$ = 1.6 Hz, 1 H, ArH^6), 7.93 (dd, $^3J_{H,H}$ = 7.9 Hz, $^5J_{H,H}$ = 1.6 Hz, 1 H, ArH^6), 7.90–7.50 (m, 4 H, Ar$H^{3,4,4,5}$), 7.72 (br. s, 8 H, BAr$H^{2,6}$), 7.56 (br. s, 4 H, BArH^4), 7.25 (d, $^3J_{H,H}$ = 8.5 Hz, ArH^3), 7.07 ("t"d, $^3J_{H,H}$ = 7.6 Hz, $^5J_{H,H}$ = 1.1 Hz, 1 H, ArH^5), 3.25 [br. s, $^3J_{H,Pt}$ not resolved, 6 H, PtN(CH_3)$_2$], 2.85 [s, 6 H, N(CH_3)$_2$], 2.11 (s, 3 H, CH_3COO), 2.06 (s, 3 H, CH_3COO), 1.97 (s, 12 H, NCCH_3) ppm.

Computational Methods: All DFT calculations were performed using Gaussian 03.[43] Geometry optimizations were performed using the BP86 functional. The SDD basis set and effective core potential were used for transition metals, along with a 6-31+G(d) basis set on all other atoms. A frequency calculation was performed on all converged geometries to verify that they were minima.

Crystallographic Data: Relevant details about the structure refinements are given in Tables 1 and 2, and selected geometrical parameters are included in the captions of the corresponding figures. Data collection was performed with a Bruker-Nonius Kappa-CCD (graphite monochromator, Mo-K_α). The structures were solved by direct methods[44] and refined by full-matrix least-squares analysis[45] including an isotropic extinction correction. All non H-atoms were refined anisotropically (H-atoms isotropically, whereby H-positions are based on stereochemical considerations). CCDC-729779 (for **7A**), -729780 (for **7B**), -729781 (for **9**), -729782 (for **8**), -729783

Table 1. Crystallographic data for compounds **4**, **5**, **7**, and **8**.

	4	**5**	**7A**	**7B**	**8**
Formula	$C_{40}H_{48}N_8O_2Cl_8Cu_4Br_4$	$C_{19}H_{23}N_4OClPt$	$C_{18}H_{20}N_4OCl_2Pt$	$C_{18}H_{20}N_4OCl_2Pt$	$C_{36}H_{40}N_8O_2Cl_2Pt$
Fw	1526.23	553.95	574.37	574.37	882.75
Cryst. syst.	monoclinic	orthorhombic	orthorhombic	monoclinic	monoclinic
Space group	*C*2/*c*	$P2_12_12_1$	$P2_12_12_1$	*C*2/*c*	*C*2/*c*
a [Å]	16.5611(9)	8.7523(2)	8.5356(2)	21.5110(6)	36.0153(6)
b [Å]	21.9832(10)	13.4873(3)	13.4192(3)	15.3857(4)	9.1396(2)
c [Å]	15.6790(8)	16.9174(4)	16.9765(4)	14.5491(4)	27.6811(7)
α [°]	90	90	90	90	90
β [°]	98.699(2)	90	90	125.751(1)	128.548(1)
γ [°]	90	90	90	90	90
V [Å^3]	5642.5(5)	1997.01(8)	1944.50(8)	3907.84(18)	7126.1(3)
Z	4	4	4	8	8
$D_{calcd.}$ [g/cm^3]	1.797	1.842	1.962	1.953	1.646
F(000)	2992	1072	1104	2208	3520
μ [1/mm]	4.739	7.175	7.506	7.469	4.133
Temp. [K]	180	220	220	220	173
Wavelength [Å]	0.7107	0.7107	0.7107	0.7107	0.7107
Measd. rflns.	11426	4534	4442	8702	13793
Unique rflns.	6370	2591	4442	4471	8076
Data/restr./param.	6370/0/295	2591/0/241	4442/0/251	4471/0/264	8076/0/451
R(F) [$I > 2\sigma(I)$]	0.0547	0.0374	0.0327	0.0384	0.0553
$wR(F^2)$ [$I > 2\sigma(I)$]	0.1443	0.0991	0.0772	0.0952	0.1209
GOF	1.002	1.048	1.016	1.014	1.102

(for **4**), -729784 (for **5**), and -729785 (for **11**-BArF) contain the supplementary crystallographic data for this paper. These data can be obtained free of charge from The Cambridge Crystallographic Data Centre via www.ccdc.cam.ac.uk/data_request/cif.

Table 2. Crystallographic data for compounds **9** and **11**-BArF.

	9	**11**-BArF
Formula	$C_{48}H_{62}N_8O_{11}Pt_2$	$C_{116}H_{76}N_8O_{12}B_2F_{48}CuPt_2$
Fw	1317.24	3161.19
Cryst. syst.	triclinic	triclinic
Space group	$P\bar{1}$	$P\bar{1}$
a [Å]	12.9129(13)	13.1020(12)
b [Å]	14.1881(13)	13.1469(12)
c [Å]	15.3750(14)	19.773(2)
α [°]	107.069(12)	100.909(11)
β [°]	107.261(12)	102.815(12)
γ [°]	90.020(11)	97.414(10)
V [Å^3]	2559.7(5)	3208.6(6)
Z	2	1
$D_{\text{calcd.}}$ [g/cm^3]	1.709	1.636
$F(000)$	1300	1551
μ [1/mm]	5.525	2.468
Temp. [K]	220	200
Wavelength [Å]	0.7107	0.7107
Measd. rflns.	20890	24503
Unique rflns.	11758	14608
Data/restr./param.	11758/0/636	14608/0/829
$R(F)$ [$I > 2\sigma(I)$]	0.0468	0.0446
$wR(F^2)$ [$I > 2\sigma(I)$]	0.1111	0.1152
GOF	1.045	1.007

Acknowledgments

The authors acknowledge support from the Swiss National Foundation. We thank Mr. P. Seiler for the X-ray structure determinations.

---

[1] M. Lersch, M. Tilset, *Chem. Rev.* **2005**, *105*, 2471–2526.

[2] J. L. Garnett, R. J. Hodges, *J. Am. Chem. Soc.* **1967**, *89*, 4546–4547.

[3] J. P. Perdew, K. Burke, Y. Wang, *Phys. Rev. B* **1996**, *54*, 16533.

[4] S. Reinartz, P. S. White, M. Brookhart, J. L. Templeton, *J. Am. Chem. Soc.* **2001**, *123*, 12724–12725.

[5] K. J. H. Young, S. K. Meier, J. M. Gonzales, J. Oxgaard, W. A. Goddard III, R. A. Periana, *Organometallics* **2006**, *25*, 4734–4737.

[6] R. A. Periana, D. J. Taube, S. Gamble, H. Taube, T. Satoh, H. Fujii, *Science* **1998**, *280*, 560–564.

[7] H. C. Lo, A. Haskel, M. Kapon, E. Keinan, *J. Am. Chem. Soc.* **2002**, *124*, 3226–3228.

[8] D. D. Wick, K. I. Goldberg, *J. Am. Chem. Soc.* **1997**, *119*, 10235–10236.

[9] U. Fekl, K. I. Goldberg, *J. Am. Chem. Soc.* **2002**, *124*, 6804–6805.

[10] T. J. Williams, A. J. M. Caffyn, N. Hazari, P. F. Oblad, J. A. Labinger, J. E. Bercaw, *J. Am. Chem. Soc.* **2008**, *130*, 2418–2419.

[11] L. Johannsson, O. B. Ryan, M. Tilset, *J. Am. Chem. Soc.* **1999**, *121*, 1974–1975.

[12] S. M. Kloek, K. I. Goldberg, *J. Am. Chem. Soc.* **2007**, *129*, 3460–3461.

[13] B. Butschke, M. Schlangen, D. Schröder, H. Schwarz, *Helv. Chim. Acta* **2008**, *91*, 1902–1914.

[14] E. Khaskin, P. Y. Zavalij, A. N. Vedernikov, *J. Am. Chem. Soc.* **2006**, *128*, 13054–13055.

[15] C. M. Thomas, J. C. Peters, *Organometallics* **2005**, *24*, 5858–5867.

[16] H. A. Zhong, J. A. Labinger, J. E. Bercaw, *J. Am. Chem. Soc.* **2002**, *124*, 1378–1399.

[17] G. S. Chen, J. A. Labinger, J. E. Bercaw, *Proc. Natl. Acad. Sci. USA* **2007**, *104*, 6915–6920.

[18] C. N. Iverson, C. A. G. Carter, R. T. Baker, J. D. Scollard, J. A. Labinger, J. E. Bercaw, *J. Am. Chem. Soc.* **2003**, *125*, 12674–12675.

[19] D. Karshtedt, J. L. McBee, A. T. Bell, T. D. Tilley, *Organometallics* **2006**, *25*, 1801–1811.

[20] D. Song, W. L. Jia, S. Wang, *Organometallics* **2004**, *23*, 1194–1196.

[21] L. A. Hammad, G. Gerdes, P. Chen, *Organometallics* **2005**, *24*, 1907–1913.

[22] M.-E. Moret, P. Chen, *Organometallics* **2007**, *26*, 1523–1530.

[23] F. Zhang, C. W. Kirby, D. W. Hairsine, M. C. Jennings, R. J. Puddephatt, *J. Am. Chem. Soc.* **2005**, *127*, 14196–14197.

[24] G. Gerdes, P. Chen, *Organometallics* **2004**, *23*, 3031–3036.

[25] V. R. Ziatdinov, J. Oxgaard, O. A. Mironov, K. J. H. Young, W. A. Goddard III, R. A. Periana, *J. Am. Chem. Soc.* **2006**, *128*, 7404–7405.

[26] M.-E. Moret, P. Chen, *Organometallics* **2008**, *27*, 4903–4916.

[27] M.-E. Moret, P. Chen, *J. Am. Chem. Soc.* **2009**, *131*, 5675–5690.

[28] C. Incarvito, A. L. Rheingold, C. J. Qin, A. L. Gavrilova, B. Bosnich, *Inorg. Chem.* **2001**, *40*, 1386–1390.

[29] C. Incarvito, A. L. Rheingold, A. L. Gavrilova, C. Jin Quin, B. Bosnich, *Inorg. Chem.* **2001**, *40*, 4101–4108.

[30] A. G. Giumanini, G. Chiavari, M. M. Musiani, P. Rossi, *Synthesis* **1980**, *9*, 743–746.

[31] Y. E. Filinchuk, M. G. Myskiv, V. N. Davydov, *J. Struct. Chem.* **2000**, *41*, 851–857.

[32] D. Neugebauer, B. Lippert, *J. Am. Chem. Soc.* **1982**, *104*, 6596–6601.

[33] G. Fusch, E. C. Fusch, A. Erxleben, J. Hüttermann, H.-J. Scholl, B. Lippert, *Inorg. Chim. Acta* **1996**, *252*, 167–178.

[34] J. A. R. Navarro, E. Freisinger, B. Lippert, *Eur. J. Inorg. Chem.* **2000**, 147–151.

[35] B. Lippert, U. Thewalt, H. Schöllhorn, D. M. L. Goodgame, R. W. Rollins, *Inorg. Chem.* **1984**, *23*, 2807–2813.

[36] A. F. M. van der Ploeg, G. van Koten, K. Vrieze, A. L. Spek, A. J. M. Duisenberg, *J. Chem. Soc., Chem. Commun.* **1980**, 469–471.

[37] S. C. Watson, J. F. Eastham, *J. Organomet. Chem.* **1967**, *9*, 165–168.

[38] G. S. Hill, M. J. Irwin, C. J. Levy, L. M. Rendina, R. J. Puddephatt, *Inorg. Synth.* **1998**, *32*, 149–152.

[39] G. K. Anderson, M. Lin, *Inorg. Synth.* **1990**, *28*, 60–63.

[40] N. A. Yakelis, R. G. Bergman, *Organometallics* **2005**, *24*, 3579–3581.

[41] H.-C. Liang, K. D. Karlin, R. Dyson, S. Kaderli, B. Jung, A. D. Zuberbühler, *Inorg. Chem.* **2000**, *39*, 5884–5894.

[42] M.-A. Kopf, Y.-M. Neuhold, A. D. Zuberbühler, K. D. Karlin, *Inorg. Chem.* **1999**, *38*, 3093–3102.

[43] M. J. Frisch, G. W. Trucks, H. B. Schlegel, G. E. Scuseria, M. A. Robb, J. R. Cheeseman, J. A. Montgomery Jr., T. Vreven, K. N. Kudin, J. C. Burant, J. M. Millam, S. S. Iyengar, J. Tomasi, V. Barone, B. Mennucci, M. Cossi, G. Scalmani, N. Rega, G. A. Petersson, H. Nakatsuji, M. Hada, M. Ehara, K. Toyota, R. Fukuda, J. Hasegawa, M. Ishida, T. Nakajima, Y. Honda, O. Kitao, H. Nakai, M. Klene, X. Li, J. E. Knox, H. P. Hratchian, J. B. Cross, V. Bakken, C. Adamo, J. Jaramillo, R. Gomperts, R. E. Stratmann, O. Yazyev, A. J. Austin, R. Cammi, C. Pomelli, J. W. Ochterski, P. Y. Ayala, K. Morokuma, G. A. Voth, P. Salvador, J. J. Dannenberg, V. G. Zakrzewski, S. Dapprich, A. D. Daniels, M. C. Strain, O. Farkas, D. K. Malick, A. D. Rabuck, K. Raghavachari, J. B. Foresman, J. V. Ortiz, Q. Cui, A. G. Baboul, S. Clifford, J. Cioslowski, B. B. Stefanov, G. Liu, A. Liashenko, P. Piskorz, I. Komaromi, R. L.

Martin, D. J. Fox, T. Keith, M. A. Al-Laham, C. Y. Peng, A. Nanayakkara, M. Challacombe, P. M. W. Gill, B. Johnson, W. Chen, M. W. Wong, C. Gonzalez, J. A. Pople, *Gaussian 03*, Revision D.01, Gaussian, Inc., Wallingford, CT, **2004**.

[44] A. Altomare, M. Burla, M. Camalli, G. Cascarano, C. Giacovazzo, A. Guagliardi, A. Moliterni, G. Polidori, R. J. Spagna, *Appl. Crystallogr.* **1999**, *32*, 115–119.

[45] G. M. Sheldrick, *SHELXL-97 Program for the Refinement of Crystal Structures*, University of Göttingen, Germany, **1997**.

Received: September 8, 2009

DOI: 10.1002/ejic.200900958

Synthesis, Structure, and Catalytic Activity of Bimetallic Pt^{II}–Ir^{III} Complexes Bridged by Cyclooctane-1,2-dithiolato Ligands

Norio Nakata,[a] Masahiro Sakashita,[a] Chizuru Komatsubara,[a] and Akihiko Ishii*[a]

Keywords: Heterometallic complexes / Platinum / Iridium / S ligands / Hydrosilylation

Cationic Pt^{II}–Ir^{III} heterobimetallic complexes bridged by cyclooctane-1,2-dithiolato ligands $[(PPh_3)_2Pt(\mu^2\text{-SRS})IrCl(\eta^5\text{-Cp}^*)][SbF_6]$ [R = *cis*-C_8H_{14} (**5**), *trans*-C_8H_{14} (**6**), Cp* = C_5Me_5] were synthesized by reaction of (cyclooctane-1,2-dithiolato)-Pt^{II} complexes $[Pt(SRS)(PPh_3)_2]$ [R = *cis*-C_8H_{14} (**3**), *trans*-C_8H_{14} (**4**)] with $[IrCl(\mu\text{-Cl})(\eta^5\text{-Cp}^*)]_2$ in thf in the presence of $AgSbF_6$. The structures of complexes **5** and **6** were fully characterized by their NMR spectroscopic data. Moreover, X-ray crystallographic analysis of **5** revealed that the PtS_2Ir core exhibits a hinged arrangement, in which the *cis*-cyclooctane-1,2-dithiolate acts as a bridging ligand between the platinum and iridium metals. Complexes **5** and **6** served as a catalyst in the hydrosilylation of terminal alkynes R′CCH (R′ = Ph, Bu, CO_2Me) with tertiary hydrosilanes such as Et_3SiH and Ph_3SiH to afford selectively β-(Z)-vinylsilanes **8** in high yields.

Introduction

Heterobimetallic complexes involving sulfur ligands are of current interest because of their relevance in applications as catalyst precursors in homogeneous catalytic processes and as starting materials for clusters preparation.[1] While many examples of heterobimetallic complexes with thiolato bridging ligands (RS–) have been reported so far,[2] dithiolato-bridged (–SRS–) heterobimetallic complexes have been investigated for several cases of the early–late and late–late types.[3,4] Among them, a number of complexes containing group 8 and group 10 metals bridged by the dithiolato ligands have been described recently. Claver et al. described the synthesis and X-ray determination of the first examples of heterobimetallic Pt^{II}–Rh^I and Pd^{II}–Rh^I complexes (**A**) with a bridging 1,2-ethanedithiolato ligand.[5] They have also found that these bimetallic complexes served as catalyst precursors for the hydroformylation of styrene.[6] In addition, half-sandwich heterobimetallic Pt^{II}–Rh^{III} and Pt^{II}–Ir^{III} complexes (**B**) containing a 1,2-ethanedithiolato ligand have also been prepared by Masdeu-Bultó and coworkers.[7] Recently, Woollins et al. reported the synthesis and characterization of heterobimetallic Pt^{II}–Rh^I, Pt^{II}–Rh^{III}, and Pt^{II}–Ir^{III} complexes (**C**, **D**) containing a bridging naphthalene-1,8-dithiolato ligand.[8] However, X-ray structural analysis and the reactivity of heterobimetallic dithiolato-bridged Pt–Ir complexes has not been reported.

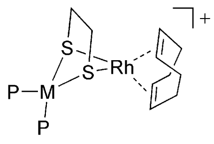

A

M = Pt, Pd

P–P = $(PPh_3)_2$, dppb, dppp

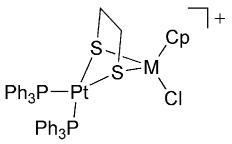

B

M = Rh, Ir

Cp = C_5H_5

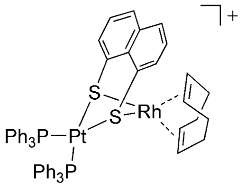

C

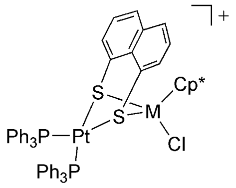

D

M = Rh, Ir

Meanwhile, the coordination chemistry of cycloalkane-1,2-dithiolato ligands is quite rare relative to that of complexes containing other bidentate dithiolato ligands such as benzene-1,2-dithiolate or ethane-1,2-dithiolate. Recently, we reported the preparation of novel *cis*- and *trans*-cyclooctane-1,2-dithiols.[9] In addition, we developed a large-scale synthetic method for *trans*-cyclooctane-1,2-dithiol.[10,11] In this paper, we present the synthesis and characterization of (cyclooctane-1,2-dithiolato)platinum complexes *cis*-$[Pt(SRS)(PPh_3)_2]$ [R = *cis*-C_8H_{14}, *trans*-C_8H_{14}] and cationic Pt^{II}–Ir^{III} heterobimetallic complexes bridged by cyclooctane-1,2-dithiolato ligands $[(PPh_3)_2Pt(\mu^2\text{-SRS})IrCl(\eta^5\text{-Cp}^*)][SbF_6]$ [R = *cis*-C_8H_{14}, *trans*-C_8H_{14}, Cp* = C_5Me_5]. We also describe the stereoselective hydrosilylation of terminal alkynes catalyzed by these Pt^{II}–Ir^{III} heterobimetallic complexes.

---

[a] Department of Chemistry, Graduate School of Science and Engineering, Saitama University
Shimo-okubo, Sakura-ku, Saitama, 338-8570, Japan
Fax: +81-48-858-3700
E-mail: ishiiaki@chem.saitama-u.ac.jp

Results and Discussion

Synthesis and Structure of (Cyclooctane-1,2-dithiolato)Pt^{II} Complexes

First, we prepared (cyclooctane-1,2-dithiolato)Pt^{II} complexes *cis*-[Pt(SRS)(PPh$_3$)$_2$] [R = *cis*-C$_8$H$_{14}$ (**3**), *trans*-C$_8$H$_{14}$ (**4**)] as the starting materials. Thus, treatment of *cis*- or *trans*-cyclooctane-1,2-dithiol (**1**, **2**) with [PtCl$_2$(Ph$_3$P)$_2$] in the presence of an acid scavenger such as Et$_3$N in CH$_2$Cl$_2$ at 0 °C formed efficiently the corresponding complexes **3** and **4**, which were purified by washing with Et$_2$O, in 90 and 84% yield, respectively (Scheme 1).

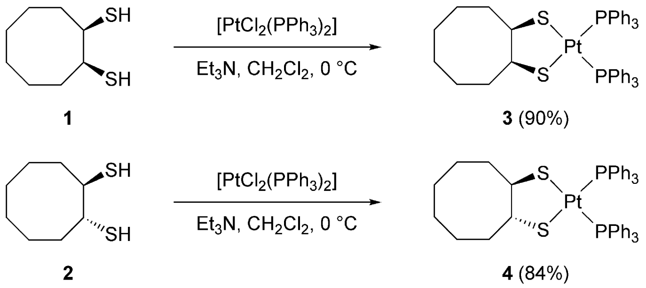

Scheme 1. Synthesis of (cyclooctane-1,2-dithiolato)Pt^{II} complexes **3** and **4**.

The molecular structures of **3** and **4** were fully determined by NMR spectroscopy and X-ray crystallography. In the ^{1}H NMR spectra, the equivalent methine protons in the cyclooctane ring of **3** (δ = 3.38–3.52 ppm) and **4** (δ = 2.89–2.90 ppm) are shifted upfield from those of starting materials **1** (δ = 3.40–3.46 ppm) and **2** (δ = 3.09–3.11 ppm). The ^{31}P{^{1}H} NMR spectra of **3** and **4** showed single resonances with ^{195}Pt satellites at δ = 21.6 ppm ($^1J_{Pt,P}$ = 2863 Hz) and δ = 21.4 ppm ($^1J_{Pt,P}$ = 2847 Hz), respectively. These coupling constant values are quite similar to those of aliphatic *cis*-(dithiolato)Pt^{II} complexes, [Pt(S$_2$C$_7$H$_8$)(PPh$_3$)$_2$] (C$_7$H$_8$ = 5,6-cyclohepta-1,3-dienyl) ($^1J_{Pt,P}$ = 2847 Hz)[12] and [Pt(SCH$_2$–1-Ad)$_2$(PPh$_3$)$_2$] (1-Ad = 1-adamantyl) ($^1J_{Pt,P}$ = 2827 Hz).[13] The crystal structures of complexes **3** and **4** are shown in Figures 1 and 2 and selected bond lengths and angles are summarized in Table 1. X-ray structural analyses revealed that the platinum centers of **3** and **4** have distorted square-planar environments, and the dithiolato ligands chelate to the platinum metals, forming twisted five-membered rings. The cyclooctane rings in **3** and **4** adopt boat–boat and crown conformations, respectively. The P1–Pt1–P2 angles of **3** and **4** are in the range of 96.73(3)–97.34(3)° and somewhat deviated from the ideal 90°. A similar deviation, attributed to steric repulsion between two PPh$_3$ ligands, was observed in previously investigated platinum(II) complexes, [Pt(S$_2$C$_7$H$_8$)(PPh$_3$)$_2$] [98.50(11)°],[12] [Pt(2,2′-S$_2$-biphen)-(PPh$_3$)$_2$] [97.21(12)°],[14] [Pt(SC$_6$F$_4$H)(PPh$_3$)$_2$][96.54(4)°],[15] and [Pt(SC$_6$F$_5$)(PPh$_3$)$_2$] [96.31(7)°].[15] The S1–Pt1–S2 angles [**3**: 86.63(10)°; **4**: 87.39(3)°] are close to those in the ideal square-planar geometry. The Pt–S bond lengths [**3**: 2.3136(9), 2.309(5) Å; **4**: 2.3025(10), 2.3185(10) Å] lie in a narrow range and are similar to those in cyclic dithiolato ligands in platinum complexes, [Pt(S$_2$C$_7$H$_8$)(PPh$_3$)$_2$] [2.308(4), 2.339(4) Å],[12] [Pt(2,2′-S$_2$-biphen)(PPh$_3$)$_2$] [2.330(10), 2.368(10) Å],[14] and [Pt(1,8-S$_2$-nap)(PMe$_3$)$_2$]

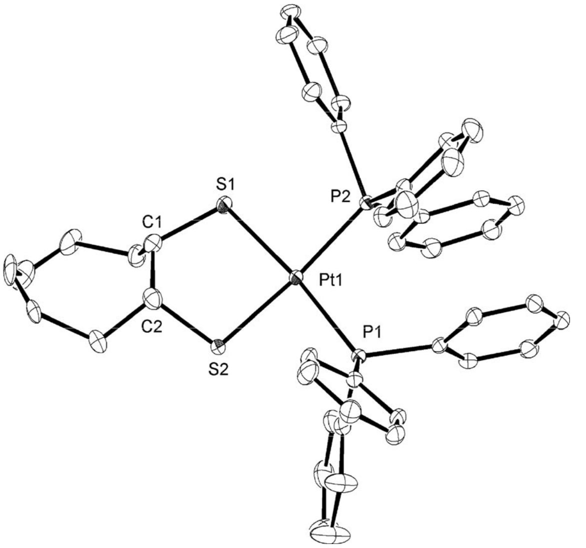

Figure 1. ORTEP drawing of (*cis*-cyclooctane-1,2-dithiolato)Pt^{II} complex **3** with 30% thermal ellipsoids. A solvated CH$_2$Cl$_2$ molecule and hydrogen atoms are omitted for clarity.

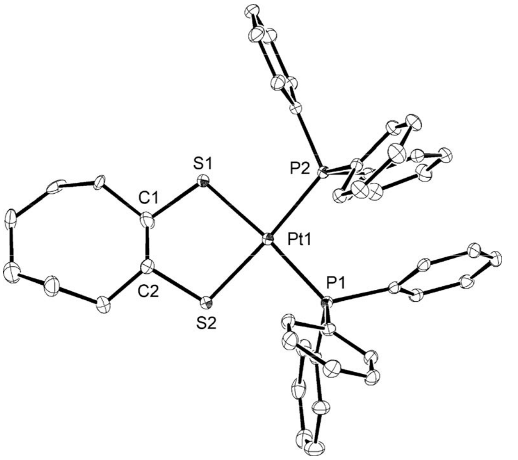

Figure 2. ORTEP drawing of (*trans*-cyclooctane-1,2-dithiolato)Pt^{II} complex **4** with 30% thermal ellipsoids. A solvated CH$_2$Cl$_2$ molecule and hydrogen atoms are omitted for clarity.

Table 1. Selected bond lengths [Å] and bond angles [°] of complexes **3** and **4**.

	3	4
Pt1–S1	2.3136(9)	2.3025(10)
Pt1–S2	2.309(5)	2.3185(10)
Pt1–P1	2.2826(9)	2.2888(10)
Pt1–P2	2.2750(9)	2.2748(10)
S1–C1	1.810(6)	1.831(5)
S2–C2	1.810(8)	1.824(4)
C1–C2	1.521(9)	1.492(7)
S1–Pt1–S2	86.63(10)	87.39(3)
P1–Pt1–P2	97.34(3)	96.73(3)
S1–Pt1–P2	88.66(3)	88.36(3)
S2–Pt1–P1	87.34(10)	87.51(3)
S1–Pt1–P1	173.93(3)	174.86(3)
S2–Pt1–P2	174.90(9)	175.73(3)

[2.320(1), 2.326(1) Å].[4b,16] The Pt–P bond lengths [**3**: 2.2826(9), 2.2750(9) Å; **4**: 2.2888(10), 2.2748(10) Å] are also comparable to the corresponding bonds in [$Pt(S_2C_7H_8)(PPh_3)_2$] [2.275(3), 2.296(3) Å][12] and [Pt(2,2′-S_2-biphen)$(PPh_3)_2$] [2.283(6), 2.295(9) Å].[14]

Synthesis and Structures of Cationic Pt^{II}–Ir^{III} Bimetallic Complexes Bridged by Cyclooctane-1,2-dithiolato Ligands

The synthetic approach for heterobimetallic complexes comprising group 8 (Rh, Ir) and group 10 (Pd, Pt) metals has been shown as the direct reaction of mononuclear dithiolato Pd^{II} or Pt^{II} complexes with cationic Rh^{I} or Ir^{I} complexes.[5–8] In our investigation, we modified this synthetic approach and examined the metal-exchange reactions of cationic dithiolato Pt^{II}–Ag^{I} complexes with the dimeric Ir^{III} complex [$IrCl(\mu\text{-}Cl)(\eta^5\text{-}Cp^*)]_2$. Thus, complexes **3** and **4** were allowed to react with $AgSbF_6$ (2 equiv.) in thf at room temperature, followed by treatment with [$IrCl(\mu\text{-}Cl)(\eta^5\text{-}Cp^*)]_2$ to give efficiently the corresponding cationic Pt^{II}–Ir^{III} heterobimetallic complexes [$(PPh_3)_2Pt(\mu^2\text{-}SRS)IrCl(\eta^5\text{-}Cp^*)$][$SbF_6$] [R = *cis*-$C_8H_{14}$ (**5**, 71%), *trans*-C_8H_{14} (**6**, 61%)] as orange crystals (Scheme 2).

The molecular structures of **5** and **6** were determined by ^1H, $^{13}C\{^1H\}$, and $^{31}P\{^1H\}$ NMR spectroscopy and X-ray crystallographic analysis for **5**. The ^1H NMR spectra of **5** and **6** showed one singlet due to the Cp* moiety (**5**: δ = 1.68 ppm; **6**: δ = 1.66 ppm) and a multiplet due to the methine protons in the bridging dithiolato ligand (**5**: δ = 3.00–3.14 ppm; **6**: δ = 2.82–3.05 ppm). The $^{31}P\{^1H\}$ NMR spectrum of **5** displayed one singlet with ^{195}Pt satellites at δ = 14.5 ppm ($^1J_{Pt,P}$ = 3188 Hz). By contrast, the $^{31}P\{^1H\}$ NMR spectrum of **6** exhibited two nonequivalent doublet signals at δ = 11.6 and 14.4 ppm with similar $^{195}Pt,^{31}P$ coupling constants: 3240 and 3269 Hz. These $^{195}Pt,^{31}P$ coupling constant values are slightly larger than those of starting complexes **3** and **4**, which indicates that the Pt–P bonds became stronger as a result of the weakening of the Pt–S bonds due to the bridging coordination of the Ir^{III} metal. An ORTEP drawing of complex **5** is depicted in Figure 3 and selected bond lengths and angles are given in Table 2. The crystal structure of *trans*-derivative **6** was also revealed by X-ray diffraction; however, we do not discuss it because of insufficient refinement. The central IrS_2Pt fragment of **5** exhibits a hinged arrangement, which has 125.2° of the respective angle between the two neighboring coordination planes. This angle (125.2°) is greater than those of the related Pt^{II}–Rh^{III} bimetallic complexes, [$(PPh_3)_2Pt(\mu\text{-}SCH_2CH_2S)RhCl(\eta^5\text{-}C_5H_5)$][$BF_4$] (124.6°)[5] and [$(PPh_3)_2Pt(\mu\text{-}SCH_2CH_2S)Rh(cod)$][$ClO_4$] (111.27°),[7] probably due to the steric influence between the cyclooctane ring and the Cp* ligand on the iridium center. The iridium center of **5** adopts a distorted tetrahedral geometry with the centroid of Cp* ring, the chlorido, and the 1,2-dithiolato sulfur

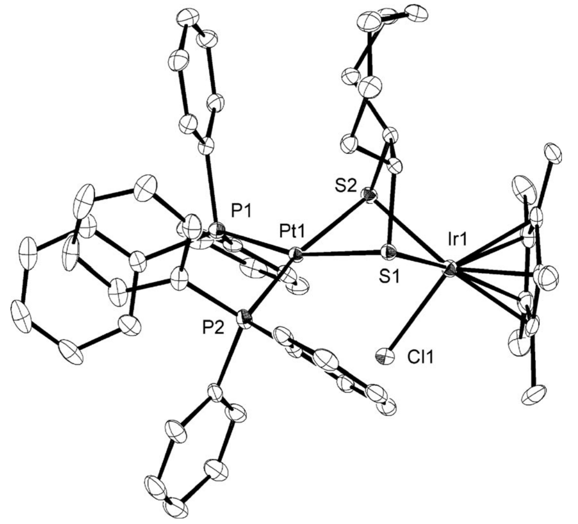

Figure 3. ORTEP drawing of cationic Pt^{II}–Ir^{III} heterobimetallic complex **5** with 30% thermal ellipsoids. Two solvated thf molecules, the [SbF_6] counteranion, and hydrogen atoms are omitted for clarity.

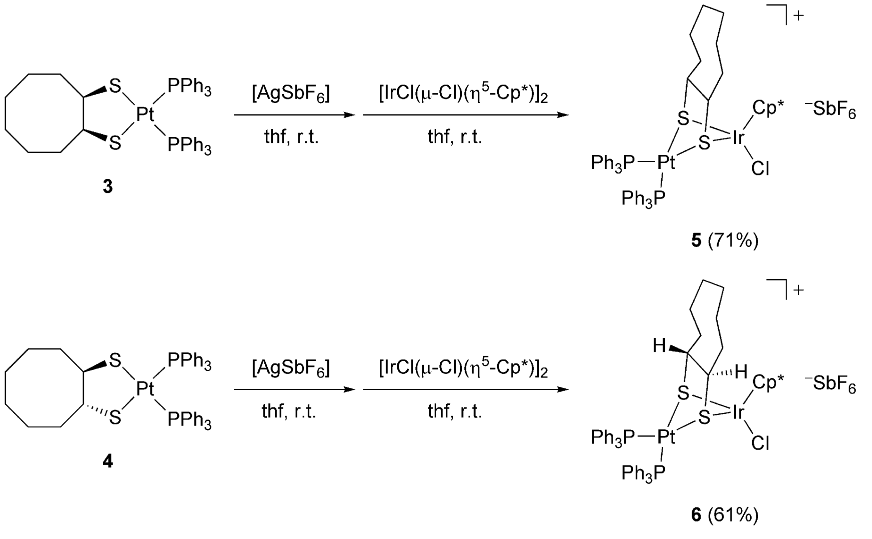

Scheme 2. Synthesis of cationic Pt^{II}–Ir^{III} heterobimetallic complexes **5** and **6**.

atoms as the apexes. The platinum center of **5** also has a distorted square-planar environment (sum of the bond angles around platinum atom: 360.41°). The cyclooctane ring of **5** takes a twist chair–chair conformation. The Pt–S bond lengths [2.3669(13), 2.3832(12) Å] are slightly shorter than those of starting complex **3** [2.309(5), 2.3136(9) Å] and relatively similar to those observed in a half-sandwich heterobimetallic Pt–Rh dithiolato-bridged complex $[(PPh_3)_2Pt(\mu\text{-}SCH_2CH_2S)RhCl(\eta^5\text{-}C_5H_5)][BF_4]$ [2.376(3), 2.387(3) Å].[7] The Ir–S bond lengths [2.3638(13), 2.4081(13) Å] are in reasonable agreement with those in half-sandwich type Ir–thiolato complexes, $[Ir(Cl)_2(2\text{-}SPyH)(\eta^5\text{-}Cp^*)]$ [2.357(9) Å][17] and $[IrCl(\eta^5\text{-}Cp^*)(\eta^2\text{-}2\text{-}Ph_2PC_6H_4S)]$ [2.380(2) Å].[18] The Pt–P bond lengths [2.2892(13), 2.2800(13) Å] are close to those in complex **3** [2.283(6), 2.295(9) Å] and $[(PPh_3)_2Pt(\mu\text{-}SCH_2CH_2S)RhCl(\eta^5\text{-}C_5H_5)][BF_4]$ [2.282(2), 2.302(2) Å].[7]

Table 2. Selected bond lengths [Å] and bond angles [°] of complex **5**.

Ir1–S1	2.3638(13)	Pt1–P2	2.2800(13)
Ir1–S2	2.4081(13)	S1–C1	1.849(5)
Ir1–Cl1	2.4075(13)	S2–C2	1.845(6)
Pt1–S1	2.3669(13)	C1–C2	1.562(7)
Pt1–S2	2.3822(12)	S1–Ir1–S2	73.28(4)
Pt1–P1	2.2892(13)		
S1–Ir1–Cl1	89.71(4)	S2–Pt1–P1	92.29 (4)
S2–Ir1–Cl1	91.05(4)	S1–Pt1–P1	163.75(4)
S1–Pt1–S2	73.68(4)	S2–Pt1–P2	158.02(5)
P1–Pt1–P2	99.50(5)	Ir1–S1–Pt1	91.44(5)
S1–Pt1–P2	94.94(4)	Ir1–S2–Pt1	89.96(4)

Catalytic Activities of Cationic Pt^{II}–Ir^{III} Bimetallic Complexes

Transition-metal-catalyzed hydrosilylation of alkynes is still the most simple and straightforward method for the preparation of vinylsilanes, which are very useful precursors in organic synthesis.[19] The hydrosilylation of alkynes generally produces three regioisomers, that is, α, β-(*E*), and β-(*Z*) isomers. As reported, Rh-[20] and Ir-catalyzed[21] hydrosilylation of alkynes leads to the formation of β-(*E*) adducts as the major product. To shed light on the catalytic activities of the cationic Pt^{II}–Ir^{III} heterobimetallic complexes bridged by cyclooctane-1,2-dithiolato ligands, we examined the Ir-catalyzed hydrosilylation of terminal alkynes **7** by using 1 mol-% of catalysts **5** and **6** under thf-reflux conditions for 3 h. The results are summarized in Table 3. In all cases, β-(*Z*)-vinylsilanes **8** were obtained in good yields with high selectivity. The catalytic activity of *cis*-derivative **5** is slightly higher than that of *trans*-derivative **6**. The reactions of phenylacetylene with Et_3SiH or Ph_3SiH were complete within 30 min even at room temperature (Table 3, Entries 2, 6, 10, and 14) to give **8** in high yields. Methyl propiolate also underwent a similar reaction to give the corresponding β-(*Z*) adducts in moderate yields (Table 3, Entries 4, 8, 12, and 16). While the presence of an electron-withdrawing substituent such as a methoxycarbonyl group reduced the yield of the adducts, it did not affect the β-(*Z*) selectivity of the reaction. Although the reactions of terminal alkynes **7** with Et_3SiH afforded β-(*Z*) adducts **8** together with a small amount of β-(*E*) isomers **9** (Table 3, Entries 1–4, and 9–12), this result was explained by the subsequent isomerization of kinetic β-(*Z*) product **8** under the conditions. On the other hand, the reactions with Ph_3SiH efficiently produced only β-(*Z*) vinylsilanes **8** without the formation of β-(*Z*) **9** or α isomers **10** (Table 3, Entries 5–8, and 13–16). This tendency was also observed in the hydrosilylation of terminal alkynes by using $[RhCl(\mu\text{-}Cl)(\eta^5\text{-}Cp^*)]_2$[20] and $[IrCl(\mu\text{-}Cl)(\eta^5\text{-}Cp^*)]_2$.[21a]

Table 3. Catalytic hydrosilylation of terminal alkynes with Ir–Pt bimetallic complexes **5** and **6**.

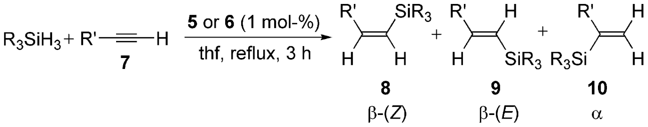

Entry	Cat.	Silane	Alkyne **7** (R′)	Ratio[b] **8**/**9**/**10**	Yield [%][c]
1	**5**	Et_3SiH	Ph	94:6:0	91
2[a]	**5**	Et_3SiH	Ph	96:4:0	97
3	**5**	Et_3SiH	Bu	84:16:0	82
4	**5**	Et_3SiH	CO_2Me	74:26:0	67
5	**5**	Ph_3SiH	Ph	100:0:0	91
6[a]	**5**	Ph_3SiH	Ph	100:0:0	96
7	**5**	Ph_3SiH	Bu	100:0:0	78
8	**5**	Ph_3SiH	CO_2Me	100:0:0	53
9	**6**	Et_3SiH	Ph	94:6:0	90
10[a]	**6**	Et_3SiH	Ph	96:4:0	91
11	**6**	Et_3SiH	Bu	87:13:0	78
12	**6**	Et_3SiH	CO_2Me	76:24:0	72
13	**6**	Ph_3SiH	Ph	100:0:0	84
14[a]	**6**	Ph_3SiH	Ph	100:0:0	80
15	**6**	Ph_3SiH	Bu	100:0:0	71
16	**6**	Ph_3SiH	CO_2Me	100:0:0	55

[a] Reactions were performed at room temperature for 30 min. [b] The ratio of stereoisomers was determined by ^1H NMR spectroscopy. [c] Isolated yields of mixtures of vinylsilanes after column chromatography. All the vinylsilanes exhibited spectroscopic data that was in agreement with the assigned structures.

A possible catalytic cycle for the hydrosilylation of alkynes catalyzed by **5** is illustrated in Scheme 3. The first step involves the oxidative addition of the iridium center of complex **5** to the Si–H bond of tertiary silanes, yielding the cationic six-coordinate Ir^V species **11**. Then, by the so-called modified Chalk–Harrod mechanism,[22] insertion of terminal alkynes **7** into the Ir–Si bond of **11** occurs through the coordination of alkynes **7** to the iridium center (**12**) to produce cationic vinyl–Ir^V complexes **13** or **15**. On the basis of the present *Z* selectivity of vinylsilanes obtained, the cationic vinyl–Ir^V complex undergoing reductive elimination in the final step should be (*E*)-vinyl–Ir^V species **15**. Intermediate **15** can be formed by the isomerization of initially formed (*Z*)-vinyl–Ir^V species **13** through η^2-vinyl intermediate **14** as proposed by Crabtree[23] or by the direct reaction of **11** and **7** as proposed by Leong.[21a] The driving force for the former path is the riddance of steric repulsion between the (*Z*)-vinyl moiety and the other ligands in **13**.

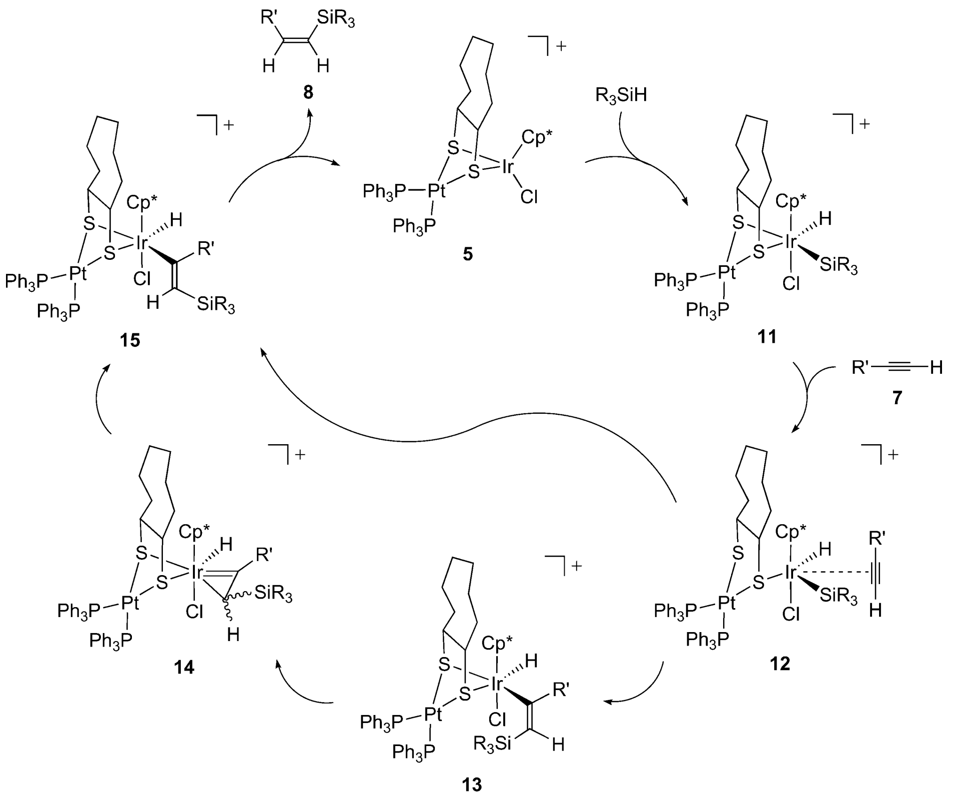

Scheme 3. A possible catalytic cycle for the hydrosilylation of terminal alkynes catalyzed by **5**.

To explore the oxidative addition step in the mechanistic pathway shown in Scheme 3, we examined the reaction of **5** with an equimolar amount of Ph_3SiH at room temperature in thf. The ^1H NMR spectrum of the reaction mixture exhibited the characteristic broad signals at $\delta = -13.2$ and -13.1 ppm, which were assignable to the hydrido ligands of six-coordinate Ir^V species **11** and its stereoisomer. These chemical shifts are comparable to that of reported Ir^V complex $[IrCl(H)_2(SiPh_3)(\eta^5\text{-}Cp^*)]$ ($\delta = -11.6$ ppm).[21a,24]

Conclusions

We have reported the systematic synthesis of (cyclooctane-1,2-dithiolato)platinum complexes *cis*-$[Pt(SRS)(PPh_3)_2]$ [R = *cis*-C_8H_{14} (**3**), *trans*-C_8H_{14} (**4**)] and cationic platinum–iridium heterobimetallic complexes bridged by cyclooctane-1,2-dithiolato ligands $[(PPh_3)_2Pt(\mu^2\text{-}SRS)IrCl(\eta^5\text{-}Cp^*)][SbF_6]$ [R = *cis*-C_8H_{14} (**5**), *trans*-C_8H_{14} (**6**)]. The molecular structures of complexes **3**, **4**, and **5** were revealed by their spectroscopic data and by X-ray crystallography. We also found that the hydrosilylation of terminal alkynes was catalyzed by platinum–iridium heterobimetallic complexes **5** and **6** to afford selectively β-(*Z*) vinylsilanes **8** in good yields. Further investigations on the preparations and catalytic activities of the novel Pt–Rh and Pt–Ir heterobimetallic complexes bridged by cyclooctane-1,2-dithiolato ligands are underway.

Experimental Section

General: All experiments were performed under an argon atmosphere unless otherwise noted. Solvents were dried by standard methods and freshly distilled prior to use. ^1H, ^{13}C, and ^{31}P NMR spectra were recorded with Bruker DPX-400 or DRX-400 (400, 100.7, and 162 MHz, respectively) spectrometers with the use of $CDCl_3$ as the solvent at room temperature. Elemental analyses were carried out at the Molecular Analysis and Life Science Center of Saitama University. High-resolution mass spectrometry (HRMS) data were recorded by using a Hitachi-Hitec NanoFrontier eLD. All melting points were determined with a Mel-Temp capillary tube apparatus and are uncorrected.

(Cyclooctane-*cis*-1,2-dithiolato)bis(triphenylphosphane)platinum (3): A mixture of $[PtCl_2(PPh_3)_2]$ (608.2 mg, 0.769 mmol) and *cis*-cyclooctane-1,2-dithiol (**1**) (134.8 mg, 0.764 mmol) in CH_2Cl_2 (10 mL) was stirred at 0 °C for 5 min and then Et_3N (0.3 mL, 2.166 mmol) was added. The mixture was stirred at 0 °C for 2.5 h. After quenching with dilute HCl and extraction with CH_2Cl_2, the organic layer was dried with anhydrous Na_2SO_4. After removal of the solvent in vacuo, the residual pale-yellow solid was purified by washing with Et_2O (ca. 10 mL) to give analytically pure $[Pt(cis\text{-}S_2C_8H_{14})(PPh_3)_2]$ (**3**; 616.2 mg, 90%) as pale-yellow crystals. M.p. 239–240 °C (decomp.). ^1H NMR (400 MHz, $CDCl_3$): $\delta = 1.40$–1.65 (m, 8 H), 1.77–1.82 (m, 2 H), 2.10–2.17 (m, 2 H), 3.38–3.52 (m, 2 H), 7.11–7.15 (m, 12 H), 7.23–7.26 (m, 6 H), 7.42–7.47 (m, 12 H) ppm. ^{13}C NMR (100.6 MHz, $CDCl_3$): $\delta = 26.6$ (CH_2), 28.7 (CH_2), 32.5 (CH_2), 54.8 (CH), 127.8 (t, $^2J_{P,C} = 5.7$ Hz), 130.0 (s), 134.9 (t, $^3J_{P,C} = 5.1$ Hz) ppm. ^{31}P NMR (162 MHz, $CDCl_3$): $\delta = 21.6$ (s, $^1J_{Pt,P} = 2863$ Hz) ppm. $C_{43}H_{38}P_2PtS_2$ (875.93): calcd. C 55.21, H 4.74; found C 55.08, H 4.68.

(Cyclooctane-*trans*-1,2-dithiolato)bis(triphenylphosphane)platinum (4): A mixture of [PtCl$_2$(PPh$_3$)$_2$] (457.6 mg, 0.578 mmol) and *trans*-cyclooctane-1,2-dithiol (**2**; 101.9 mg, 0.578 mmol) in CH$_2$Cl$_2$ (10 mL) was stirred at 0 °C for 5 min and then Et$_3$N (0.3 mL, 2.166 mmol) was added. The mixture was stirred at 0 °C for 2.5 h. After quenching with dilute HCl and extraction with CH$_2$Cl$_2$, the organic layer was dried with anhydrous Na$_2$SO$_4$. After removal of the solvent in vacuo, the residual pale-yellow solid was purified by washing with Et$_2$O (ca. 10 mL) to give analytically pure [Pt(*trans*-S$_2$C$_8$H$_{14}$)(PPh$_3$)$_2$] (**4**; 431.5 mg, 84%) as pale-yellow crystals. M.p. 277–279 °C (decomp.). ^{1}H NMR (400 MHz, CDCl$_3$): δ = 1.37–1.64 (m, 8 H), 1.71–1.79 (m, 2 H), 1.98–2.05 (m, 2 H), 2.89–2.90 (m, 2 H), 7.11–7.14 (m, 12 H), 7.23–7.26 (m, 6 H), 7.43–7.47 (m, 12 H) ppm. ^{13}C NMR (100.6 MHz, CDCl$_3$): δ = 26.1 (CH$_2$), 26.4 (CH$_2$), 33.8 (CH$_2$), 56.0 (CH), 127.4 (t, $^2J_{\mathrm{P,C}}$ = 5.9 Hz), 129.9 (s), 134.9 (t, $^3J_{\mathrm{P,C}}$ = 5.1 Hz) ppm. ^{31}P NMR (162 MHz, CDCl$_3$): δ = 21.4 (s, $^1J_{\mathrm{Pt,P}}$ = 2847 Hz) ppm. C$_{43}$H$_{38}$P$_2$PtS$_2$ (875.93): calcd. C 55.21, H 4.74; found C 55.38, H 4.62.

[(PPh$_3$)$_2$Pt(μ-*S*,*S*-*cis*-C$_8$H$_{14}$)IrCl(η^5-C$_5$Me$_5$)][SbF$_6$] (5): A solution of AgSbF$_6$ (21.1 mg, 0.064 mmol) in thf (5 mL) was added to a suspension of **3** (50.9 mg, 0.057 mmol) in thf (7 mL). The mixture was stirred at room temperature for 10 min, and then a solution of [IrCl(μ-Cl)(η^5-Cp*)]$_2$ (23.1 mg, 0.029 mmol) in thf (7 mL) was added. The color of the solution changed to yellow from colorless. The silver chloride salts formed were removed by filtration through a pad of Celite and rinsed with hexane. After removal of the solvent in vacuo, the residual yellow solid was purified by washing with hexane (ca. 5 × 3 mL) to give analytically pure complex **5** (61.4 mg, 71%) as yellow crystals. M.p. 198–200 °C (decomp.). ^{1}H NMR (400 MHz, CDCl$_3$): δ = 1.09–1.56 (m, 12 H), 1.68 (s, 15 H), 3.00–3.14 (m, 2 H), 7.24–7.28 (m, 12 H), 7.32–7.42 (m, 18 H) ppm. ^{13}C NMR (100.6 MHz, CDCl$_3$): δ = 8.7 (CH$_3$), 25.4 (CH$_2$), 30.8 (CH$_2$), 32.4 (CH$_2$), 64.5 (CH), 90.5 (C), 128.4 (t, $^2J_{\mathrm{P,C}}$ = 6.0 Hz), 129.3 (d, $^1J_{\mathrm{P,C}}$ = 59.4 Hz), 131.2 (s), 134.4 (t, $^3J_{\mathrm{P,C}}$ = 5.0 Hz) ppm. ^{31}P NMR (162 MHz, CDCl$_3$): δ = 14.5 (s, $^1J_{\mathrm{Pt,P}}$ = 3188 Hz) ppm. HRMS: calcd. for C$_{54}$H$_{59}$ClIrP$_2$PtS$_2$ [M – SbF$_6$]$^+$ 1257.2494; found 1257.2489.

[(PPh$_3$)$_2$Pt(μ-*S*,*S*-*trans*-C$_8$H$_{14}$)IrCl(η^5-C$_5$Me$_5$)][SbF$_6$] (6): A solution of AgSbF$_6$ (52.2 mg, 0.152 mmol) in thf (5 mL) was added to a suspension of **4** (136.6 mg, 0.152 mmol) in thf (5 mL). The mixture was stirred at room temperature for 10 min and then a solution of [IrCl(μ-Cl)(η^5-Cp*)]$_2$ (60.5 mg, 0.076 mmol) in thf (5 mL) was added. The color of the solution changed to yellow from colorless. The silver chloride salts formed were removed by filtration through a pad of Celite and rinsed with hexane. After removal of the solvent in vacuo, the residual yellow solid was purified by washing with hexane (ca. 5 × 3 mL) to give analytically pure complex **6** (141.4 mg, 61%) as yellow crystals. M.p. 200–201 °C (decomp.). ^{1}H NMR (400 MHz, CDCl$_3$): δ = 1.06–1.39 (m, 8 H), 1.66 (m, 15 H), 1.82–1.86 (m, 2 H), 1.97–1.99 (m, 2 H), 2.82–3.05 (m, 2 H), 7.21–7.34 (m, 18 H), 7.38–7.47 (m, 12 H) ppm. ^{13}C NMR (100.6 MHz, CDCl$_3$): δ = 9.5 (CH$_3$), 23.9 (CH$_2$), 24.3 (CH$_2$), 25.7 (CH$_2$), 26.2 (CH$_2$), 35.6 (CH$_2$), 38.8 (CH$_2$), 62.6 (CH), 23.8 (CH), 90.9 (C), 128.4 (d, $^2J_{\mathrm{P,C}}$ = 11.1 Hz), 128.5 (d, $^1J_{\mathrm{P,C}}$ = 57.4 Hz), 129.3 (d, $^1J_{\mathrm{P,C}}$ = 59.4 Hz), 131.0 (d, $^4J_{\mathrm{P,C}}$ = 1.0 Hz), 131.1 (d, $^4J_{\mathrm{P,C}}$ = 1.0 Hz), 133.7 (d, $^3J_{\mathrm{P,C}}$ = 11.1 Hz), 134.1 (d, $^3J_{\mathrm{P,C}}$ = 10.1 Hz) ppm. ^{31}P NMR (162 MHz, CDCl$_3$): δ = 11.6 (d, $^2J_{\mathrm{P,P}}$ = 16.2 Hz, $^1J_{\mathrm{Pt,P}}$ = 3240 Hz), 14.4 (d, $^2J_{\mathrm{P,P}}$ = 16.2 Hz, $^1J_{\mathrm{Pt,P}}$ = 3269 Hz) ppm. HRMS: calcd. for C$_{54}$H$_{59}$ClIrP$_2$PtS$_2$ [M – SbF$_6$]$^+$ 1257.2494; found 1257.2489.

General Protocol for the Catalytic Hydrosilylation of Terminal Alkynes: The hydrosilylation of terminal alkynes with Et$_3$SiH or Ph$_3$SiH was performed by using 1 mol-% of Pt–Ir complexes **5** and **6** in thf. The mixture was stirred under reflux for 3 h, and the solvent was removed under reduced pressure. The residue was purified by silica-gel column chromatography (hexane/CH$_2$Cl$_2$, 4:1). The relative proportion of products was determined by careful integration of the ^{1}H NMR spectrum. The assignments for the β-(*Z*), and β-(*E*)-vinylsilanes were based upon spectroscopic comparison with literature.[21a,25]

X-ray Crystallographic Studies: Pale-yellow single crystals of **3** and **4** were grown by the slow evaporation of saturated CH$_2$Cl$_2$ and hexane solutions, respectively, and yellow single crystals of **5** were grown by the slow evaporation of its saturated thf and hexane solu-

Table 4. Crystallographic data and details of refinement for **3**, **4**, and **5**.

	3	4	5
Formula	C$_{45}$H$_{46}$Cl$_2$P$_2$PtS$_2$	C$_{45}$H$_{46}$Cl$_2$P$_2$PtS$_2$	C$_{62}$H$_{75}$ClF$_6$IrO$_2$P$_2$PtS$_2$Sb
Formula weight	978.87	978.87	1636.77
Color	pale yellow	pale yellow	yellow
Crystal size [mm]	0.36 × 0.23 × 0.21	0.42 × 0.40 × 0.32	0.24 × 0.20 × 0.11
Temperature [K]	103	103	103
Crystal system	triclinic	triclinic	orthorhombic
Space group	$P\bar{1}$	$P\bar{1}$	*Pbca*
a [Å]	11.3697(4)	11.3832(10)	16.7715(8)
b [Å]	14.8444(6)	14.7997(14)	21.4419(10)
c [Å]	14.8930(6)	14.8307(14)	34.3421(17)
α [°]	60.6520(10)	61.780(2)	90
β [°]	68.6770(10)	69.821(2)	90
γ [°]	86.1650(10)	73.570(2)	90
V [Å^3]	2021.73(14)	2044.6(3)	12349.9(10)
Z	2	2	8
$D_{\mathrm{calcd.}}$ [g cm^{-3}]	1.608	1.590	1.761
No. of unique data	8769	7579	11478
No. of parameters	579	497	708
No. of restraints	29	0	0
R_1 [$I > 2\sigma(I)$]	0.0313	0.0295	0.0333
wR_2 (all data)	0.0823	0.0756	0.0820
GOF	1.019	1.034	1.031

tion in a Schlenk tube. The intensity data were collected at 103 K for **3**–**5** with a Bruker AXS SMART diffractometer by employing graphite-monochromated Mo-K_α radiation (λ = 0.71073 Å). The determination of crystal class and unit-cell parameters was carried out by the SMART program package. The raw frame data were processed by using SAINT and SADABS to yield the reflection data file.[26] The structures were solved by direct methods and refined by full-matrix least-squares procedures on F^2 for all reflections (SHELX-97).[27] The hydrogen atoms were placed at the calculated positions and were included in the structure calculation without further refinement of the parameters. Crystal data, data collection, and processing parameters for complexes **3**–**5** are summarized in Table 4. CCDC-743418 (for **3**), -743419 (for **4**), and -743420 (for **5**) contain the supplementary crystallographic data for this paper. These data can be obtained free of charge from The Cambridge Crystallographic Data Centre via www.ccdc.cam.ac.uk/data_request/cif.

Acknowledgments

This work was supported by the Ministry of Education, Science, Sports, and Culture of Japan through a Grant-in-Aid for Scientific Research (Nos. 18750026, 19027014, and 20036013).

---

[1] For general reviews, see: a) P. Braunstein, J. Rose in *Comprehensive Organometallic Chemistry II* (Eds.: G. Wilkinson, F. G. A. Stone, E. W. Abel), Pergamon, Oxford, **1995**, vol. 10, p. 351; b) R. D. Adams, M. J. Chetcuti in *Comprehensive Organometallic Chemistry II* (Eds.: G. Wilkinson, F. G. A. Stone, E. W. Abel), Pergamon, Oxford, **1995**, vol. 10, p. 1, p. 23; c) for the chemistry of heteronuclear clusters and multimetallic catalysts, see: R. D. Adams, W. A. Herrmann, *Polyhedron* **1988**, *7*, 2251–2253; d) N. Wheatley, P. Kalck, *Chem. Rev.* **1999**, *99*, 3379–3403.

[2] a) D. W. Stephan, *Coord. Chem. Rev.* **1989**, *95*, 41–107; b) M. D. Janssen, D. M. Grove, G. Van Koten, *Prog. Inorg. Chem.* **1997**, *46*, 97–149; c) M. Y. Darensbourg, M. Pala, S. A. Houliston, K. P. Kidwell, D. Spencer, S. S. Chojnacki, J. H. Reibenspies, *Inorg. Chem.* **1992**, *31*, 1487–1493; d) V. W.-W. Yam, K. M.-C. Wong, K.-K. Cheung, *Organometallics* **1997**, *16*, 1729–1734; e) R. Rousseau, D. W. Stephan, *Organometallics* **1991**, *10*, 3399–3403.

[3] T. T. Nadasdi, D. W. Stephan, *Inorg. Chem.* **1994**, *33*, 1532–1538 and references cited therein.

[4] a) J. Vicente, M. T. Chicote, S. Huertas, D. Bautista, P. G. Jones, A. K. Fischer, *Inorg. Chem.* **2001**, *40*, 2051–2057; b) J. Vicente, M. T. Chicote, S. Huertas, P. G. Jones, A. K. Fischer, *Inorg. Chem.* **2001**, *40*, 6193–6200; c) J. Forniés-Cámer, A. M. Masdeu-Bultó, C. Claver, *Inorg. Chem. Commun.* **2002**, *5*, 351–354; d) R. Y. C. Shin, J. J. Vittal, Z.-Y. Zhou, L. L. Koh, L. Y. Goh, *Inorg. Chim. Acta* **2003**, *352*, 220–228; e) S. M. Aucott, H. L. Milton, S. D. Robertson, A. M. Z. Slawin, J. D. Woollins, *Dalton Trans.* **2004**, 3347–3352; f) R. Y. C. Shin, G. K. Tan, L. L. Koh, L. Y. Goh, R. D. Webster, *Organometallics* **2004**, *23*, 6108–6115; g) Y.-D. Chen, L.-Y. Zhang, L.-X. Shi, Z.-N. Chen, *Inorg. Chem.* **2004**, *43*, 7493–7501; h) R. Y. C. Shin, M. E. Teo, G. K. Tan, L. L. Koh, J. J. Vittal, L. Y. Goh, K. S. Murray, B. Moubaraki, X.-Y. Zhou, *Organometallics* **2005**, *24*, 4265–6273; i) S. Takemoto, D. Shimadzu, K. Kamikawa, H. Matsuzaka, R. Nomura, *Organometallics* **2006**, *25*, 982–988; j) J. Vicente, P. González-Herrero, M. Pérez-Cadenas, P. G. Jones, D. Bautista, *Inorg. Chem.* **2007**, *46*, 4718–4732; k) R. Y. C. Shin, V. W. L. Ng, L. L. Koh, G. K. Tan, L. Y. Goh, R. D. Webster, *Organometallics* **2007**, *26*, 4555–4561; l) S. D. Robertson, A. M. Z. Slawin, J. D. Woollins, *Eur. J. Inorg. Chem.* **2007**, 247–253; m) J. L. Hess, H. L. Conder, K. N. Green, M. Y. Daresbourg, *Inorg. Chem.* **2008**, *47*, 2056–2063; n) J. Vicente, P. González-Herrero, Y. García-Sánchez, D. Bautista, *Inorg. Chem.* **2008**, *47*, 10662–10673.

[5] J. Forniés-Cámer, A. M. Masdeu-Bultó, C. Claver, C. J. Cardin, *Inorg. Chem.* **1998**, *37*, 2626–2632.

[6] J. Forniés-Cámer, A. M. Masdeu-Bultó, C. Claver, C. Tejel, M. A. Ciriano, C. J. Cardin, *Organometallics* **2002**, *21*, 2609–2618.

[7] J. Forniés-Cámer, C. Claver, A. M. Masdeu-Bultó, C. J. Cardin, *J. Organomet. Chem.* **2002**, *662*, 188–191.

[8] S. M. Aucott, D. Duerden, Y. Li, A. M. Z. Slawin, J. D. Woollins, *Chem. Eur. J.* **2006**, *12*, 5495–5504.

[9] A. Ishii, M. Suzuki, T. Sone, N. Nakata, *Phosphorus Sulfur Silicon Relat. Elem.* **2009**, *184*, 1184–1205.

[10] A. Ishii, A. Ono, N. Nakata, *J. Sulfur Chem.* **2009**, *30*, 236–244.

[11] For a recent application of *trans*-cyclooctane-1,2-dithiol, see: A. Ishii, T. Toda, N. Nakata, T. Matsuo, *J. Am. Chem. Soc.* **2009**, *131*, 13566–13567.

[12] A. Ishii, S. Kashiura, Y. Hayashi, W. Weigand, *Chem. Eur. J.* **2007**, *13*, 4326–4333.

[13] N. Nakata, S. Yamamoto, W. Hashima, A. Ishii, *Chem. Lett.* **2009**, *38*, 400–401.

[14] S. M. Aucott, P. Kilian, S. D. Robertson, A. M. Z. Slawin, J. D. Woollins, *Chem. Eur. J.* **2006**, *12*, 895–902.

[15] F. Estudiante-Negrete, R. Redón, S. Hernández-Ortega, R. A. Toscano, D. Morales-Morales, *Inorg. Chim. Acta* **2007**, *360*, 1651–1660.

[16] S. M. Aucott, H. L. Milton, S. D. Robertson, A. M. Z. Slawin, G. D. Walker, J. D. Woollins, *Chem. Eur. J.* **2004**, *10*, 1666–1676.

[17] Y.-F. Han, Y.-B. Huang, Y.-J. Lin, G.-X. Jin, *Organometallics* **2008**, *27*, 961–966.

[18] M. Gorol, H. W. Roesky, M. Noltemeyer, H.-G. Schmidt, *Eur. J. Inorg. Chem.* **2005**, 4840–4844.

[19] B. Marciniec in *Comprehensive Handbook on Hydrosilylation*, Pergamon, Oxford, **1992**, p. 130.

[20] J. W. Faller, D. G. D'Alliessi, *Organometallics* **2002**, *21*, 1743–1746.

[21] For recent examples of highly β-(*Z*)-selective, Ir-catalyzed hydrosilylations, see: a) V. S. Sridevi, W. Y. Fan, W. K. Leong, *Organometallics* **2007**, *26*, 1157–1160; b) Y. Miyake, E. Isomura, M. Iyoda, *Chem. Lett.* **2006**, *35*, 836–837; c) M. Viciano, E. Mas-Marza, M. Sanau, E. Peris, *Organometallics* **2006**, *25*, 3063–3069; d) E. Mas-Marza, M. Sanau, E. Peris, *Organometallics* **2006**, *25*, 3713–3720; e) E. Mas-Marza, M. Sanau, E. Peris, *Inorg. Chem.* **2005**, *44*, 9961–9967.

[22] a) J. F. Harrod, A. J. Chalk, I. Wender, P. Pino in *Organic Synthesis via Metal Carbonyls*, Wiley, New York, **1977**, vol. 2, p. 673; b) M. A. Schroeder, M. S. Wrighton, *J. Organomet. Chem.* **1977**, *128*, 345–358.

[23] R. H. Crabtree, *New J. Chem.* **2003**, *27*, 771–772.

[24] M.-J. Fernandez, P. M. Maitlis, *J. Chem. Soc., Dalton Trans.* **1984**, 2063–2066.

[25] a) E. Lukevics, R. Ya. Sturkovich, O. A. Pudova, *J. Organomet. Chem.* **1985**, *292*, 151–158; b) E. Lukevics, V. V. Dirnens, Y. S. Goldberg, E. E. Liepinsh, *J. Organomet. Chem.* **1986**, *316*, 249–254.

[26] G. M. Sheldrick, *SADABS: Program for Empirical Absorption Correction of Area Detector Data*, University of Göttingen, Göttingen, Germany, **1996**.

[27] G. M. Sheldrick, *SHELXTL 5.10 for Windows NT: Structure Determination Software Programs*, Bruker Analytical X-ray Systems, Inc., Madison, WI, **1997**.

Received: September 25, 2009

DOI: 10.1002/ejic.200900962

Frameworks by Solvent-Free Synthesis of Rare Earth Chlorides with Molten 1,3-Benzodinitrile and Tailoring of the Particle Size: ${}^{3}_{\infty}[\mathrm{LnCl_3}\{1,3\text{-}\mathrm{C_6H_4(CN)_2}\}]$, Ln = Y, Dy, Ho, Er, Yb

Christoph J. Höller[a] and Klaus Müller-Buschbaum*[a]

Keywords: Lanthanides / 1,3-Benzodinitrile / Framework structures / Nanoparticles / Solvent-free synthesis / Metal–organic frameworks

The solvent-free melt reactions of anhydrous rare earth trichlorides with molten 1,3-benzodinitrile [1,3-$C_6H_4(CN)_2$, $C_8H_4N_2$] result in isophthalonitrile frameworks of the rare earth elements. The particle size of the products can be varied from the millimeter to the nanometer scale (down to 50–400 nm) depending on the synthesis conditions. Thus, these network structures are among the very few coordination polymers that can be synthesized as nanoparticles. A constitution of 1:1 concerning $LnCl_3$/1,3-$C_6H_4(CN)_2$ is found for Y (**1**), Dy (**2**), Ho (**3**), Er (**4**), and Yb (**5**) in isotypic ${}^{3}_{\infty}[\mathrm{LnCl_3}\{1,3\text{-}\mathrm{C_6H_4(CN)_2}\}]$. The ligand 1,3-$C_6H_4(CN)_2$ functions both as chemical scissors and replaces chloride linkages by degrading the rare earth chloride structures, and subsequently forms new 3D-framework structures. They consist of strands of chlorido-coordinated lanthanide atoms, which are linked in two dimensions by 1,3-$C_6H_4(CN)_2$ molecules. Compounds **1**–**5** were obtained as single crystals from the melt reaction, and their crystal structures were determined by single-crystal X-ray analysis. They can also be obtained as nanocrystalline materials from a ball mill treatment, identified by electron microscopy (REM) and EDX analysis.

Introduction

The synthesis of nanoparticles within the field of coordination polymers, framework or MOF chemistry is a real challenge with few results known.[1,2] Nonetheless, particle size is important as it can directly influence the properties of a compound. Thus, it is interesting to investigate the possibility to tailor the properties of coordination polymers and frameworks by a rational synthesis of different particle sizes down to the nanoscale by the use of different reaction conditions and treatments. In the domain of coordination polymer, framework and MOF chemistry including rare earth compounds, nearly all treatments and reactions are carried out in solution and either give crystalline or microcrystalline products.[3–8] This chemistry therefore strongly depends on the solvents used. In contrast, solvent-free syntheses by high-temperature reactions, e.g. in the melt of a ligand, can also be utilized. This treatment is especially useful for the highly oxophilic rare earth elements,[9–11] if cocoordination of solvents is to be avoided, as shown for organic amides of the rare earth elements.[12–17] For solvent-free syntheses, a strong tendency towards coordination polymers can be observed, depending on the coordinative ability of the ligand resulting in 1D,[18–23] or 2D and 3D linked framework and MOF structures.[24–30] This also proves a formidable synthesis strategy for nitrile-containing coordination polymers[31–33] including 1,4-benzodinitrile frameworks[34] that were obtained from reactions of anhydrous Ln chlorides with melts of 1,4-benzodinitrile. For the 1,3-isomer, the isophthalonitrile, so far only one 1D coordination polymer was reported,[35] and no framework structures. We can now present a series of 3D linked framework structures of the rare earth elements including the group 3 metal yttrium (**1**–**5**) with the 1,3-benzodinitrile ligand from syntheses in the melt of this ligand. The dimensionality of the coordination polymer/framework can be related to the temperature of the melt reaction. These reactions lead to crystalline as well as microcrystalline materials. If treatment in a ball mill[36] is carried out, particle sizes down to 50–400 nm become available.

Results and Discussion

In order to synthesize and characterize nanoparticles of rare earth chloride 1,3-benzodinitrile frameworks, a four-step approach is utilized. In the first step, the solvent-free

---

[a] Department of Chemistry and Biochemistry, Ludwig-Maximilians-Universität München,
Butenandtstraße 5-13 (D), 81377 München, Germany
Fax: +49-89-2180-77851
E-mail: kmbch@uni-muenchen.de

Supporting information for this article is available on the WWW under http://dx.doi.org/10.1002/ejic.200900962.

ampoule reactions of rare earth chlorides (dysprosium, holmium, erbium, yttrium and ytterbium) with isophthalonitrile were carried out in the melt of the nitrile. These reactions result in the formation of linear coordination polymers of the formula ${}^{1}_{\infty}[Ln_2Cl_6\{1,3\text{-}C_6H_4(CN)_2\}_3]$ as reported for holmium [Equation (1)].[35]

$$2\ LnCl_3 + 3\ 1,3\text{-}C_6H_4(CN)_2 \rightarrow {}^{1}_{\infty}[Ln_2Cl_6\{1,3\text{-}C_6H_4(CN)_2\}_3] \qquad (1)$$

At higher temperatures above 255 °C, a condensation reaction by release of 1 equiv. of isophthalonitrile occurs. The coordination sites on the rare earth ions that were occupied by the released $1,3\text{-}C_6H_4(CN)_2$ ligands are replaced by remaining $1,3\text{-}C_6H_4(CN)_2$ ligands coordinating at the back side of the metal centres. This yields the 3D-framework structures **1**–**5** [Equation (2)].

$${}^{1}_{\infty}[Ln_2Cl_6\{C_6H_4(CN)_2\}_3] \xrightarrow{\Delta T} 2\ {}^{3}_{\infty}[LnCl_3\{C_6H_4(CN)_2\}] + C_6H_4(CN)_2 \uparrow \qquad (2)$$

Originally, this melt reaction is fast and yields microcrystalline products of micrometer particle size. Therefore, it can also be carried out and observed by using a thermal analyser (see Figure 1, top).

Appropriate annealing, heating rates and reaction temperatures help growing crystals of suitable sizes to perform single-crystal X-ray analyses of **1**–**5**. This step is essential to characterize the products. A formation of nanoscale particles is not observed.

As step three of our approach we successfully used a ball-mill treatment of the products of the previously described reaction steps to obtain smaller particles. Depending on the milling time, particles as small as 50–400 nm are available. Figure 2 displays electron-microscopy images of ${}^{3}_{\infty}[ErCl_3\{1,3\text{-}C_6H_4(CN)_2\}]$ (**4**) on millimeter, micrometer and nanometer scales.

For our approach it is thereby shown that a treatment of rare earth chlorides with $1,3\text{-}C_6H_4(CN)_2$ in a ball mill is possible and has also been carried out. It can be assumed that the milling produces enough energy to carry out the reactions described in Equations (1) and (2). In case of **4**, however, we only found an amorphous product, but no evidence that a crystalline product was formed. It has to be underlined though, that it might be impossible to directly structurally characterize the nanoscale material because of the half-widths of the powder reflections in the nanoregion, the low symmetry of the products, and the low scattering values of the ligand atoms.[39] See the Supporting Information for additional REM investigations on the series of isotypic compounds (**1** and **5**). TEM investigations reveal that the compounds decompose and evaporate due to the high energy of the electron beam of a TEM.[b]

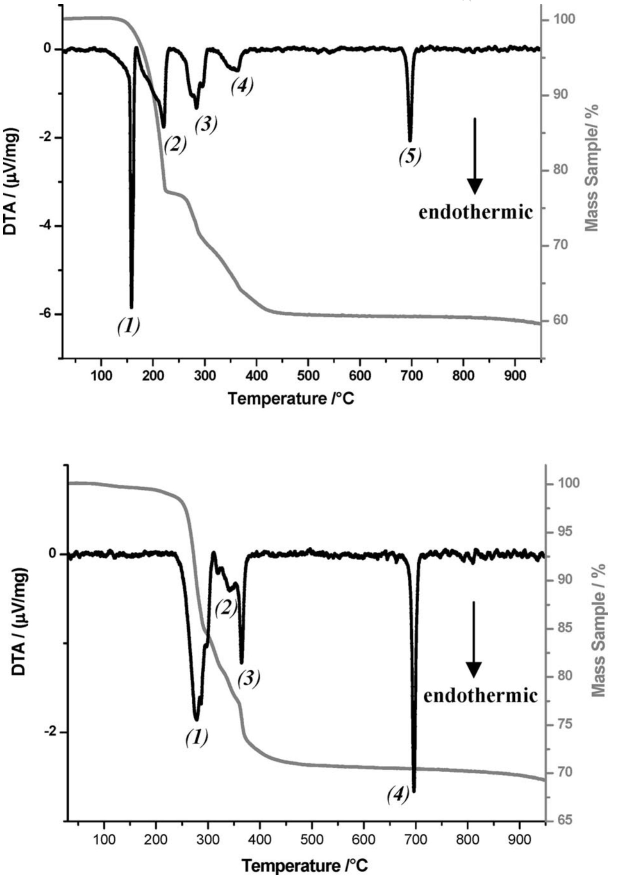

Figure 1. Simultaneous DTA/TG of the reaction of $HoCl_3$ with $1,3\text{-}C_6H_4(CN)_2$ [top: (1) melting point of $1,3\text{-}C_6H_4(CN)_2$ (163–165 °C),[37] (2) boiling point of excess $1,3\text{-}C_6H_4(CN)_2$ (239 °C),[37] (3)–(5) decomposition of the network (260–330 °C), (6) melting point of $HoCl_3$ (690 °C)[38]] and DTA/TG of the pure product ${}^{3}_{\infty}[HoCl_3(1,3\text{-}C_6H_4(CN)_2)]$ (**3**) [bottom: (1)–(3) decomposition of the network under release of $1,3\text{-}C_6H_4(CN)_2$ to $HoCl_3$ (260–330 °C), (4) melting point of $HoCl_3$ (690 °C)[38]].

Therefore, step four of our approach is necessary for understanding, i.e. comparison of the structure and other analyses of **1**–**5** of the different synthetic approaches (including powder patterns, IR, microanalysis, DTA/TG). For reactions leading to the formation of 3D frameworks ${}^{3}_{\infty}[LnCl_3\{1,3\text{-}C_6H_4(CN)_2\}]$ (**1**–**5**), the reaction path is essential for the particle size of the products. To achieve particles of nanometer size from the melt syntheses, the products of the melt reactions of **1**–**5** can be used for a subsequent ball mill treatment. The available particle sizes of the milling process vary between 2 µm and 50 nm. Prolonged milling times for both the products of the initial reactions and for the products of the milling process do not lead to smaller nanoparticles, but another reaction step. It can be assumed by the results of thermal analysis and microanalysis that this is combined to further release of 1,3-benzodinitrile and thus a change in the constitution of the product. It has not yet been possible to characterize these products because of the problems described in step three of our approach. The powder patterns are different from ${}^{3}_{\infty}[LnCl_3\{1,3\text{-}C_6H_4(CN)_2\}]$ (**1**–**5**) (see Supporting Information). Therefore, a ball mill treatment is difficult to control if further reaction and decomposition steps are possible. It can be assumed that it is a synthesis strategy that cannot be generally utilized to obtain nanoparticles of all soft materials like coordination polymers.

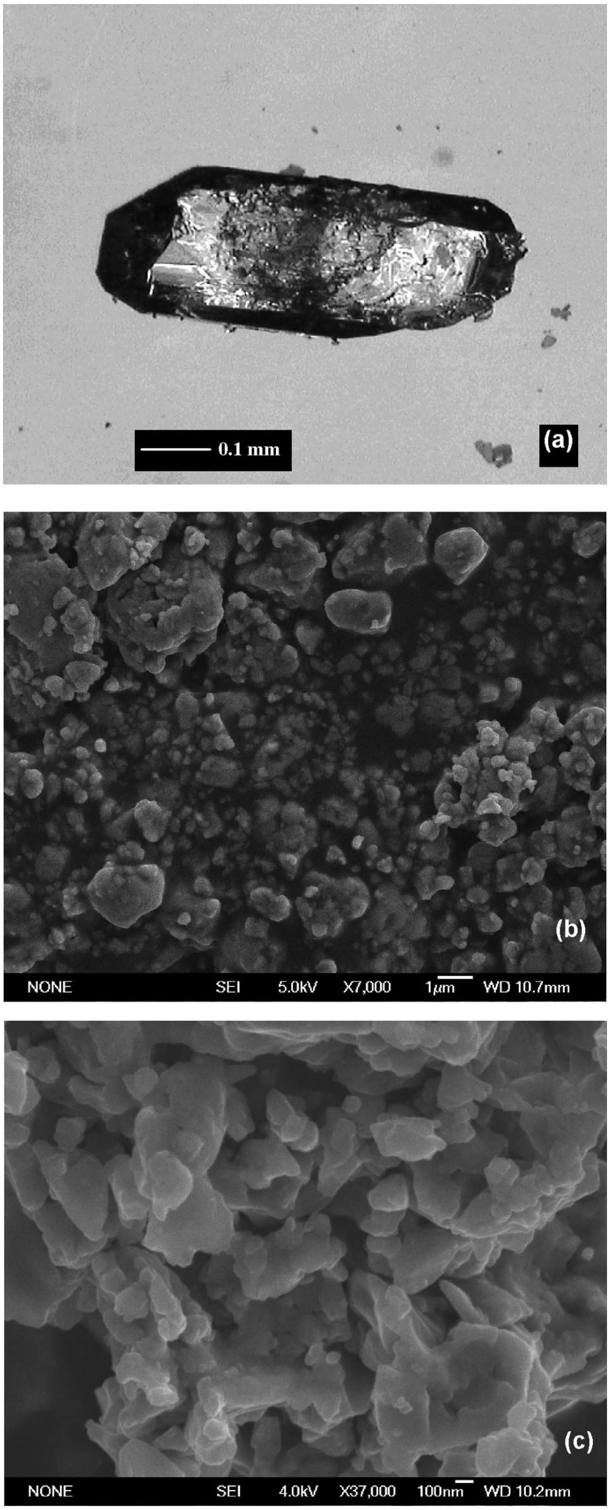

Figure 2. Electron-microscopy images of crystalline particles of $^{3}_{\infty}[\mathrm{ErCl_3}\{1,3\text{-}\mathrm{C_6H_4(CN)_2}\}]$ (**4**) on millimeter (a) micrometer (b), and nanometer scale (c) after melt synthesis, milling for 10 min, and milling for 45 min, respectively. The scale and dimension bars correspond to 0.1 mm for (a), 1 µm for (b) and 100 nm for (c).

Sample Characterization

For sample characterization, the bulk samples of **1**–**5** were purified by evaporating excess 1,3-$C_6H_4(CN)_2$ at 140 °C. FIR, MIR and Raman spectra show a series of bands that cannot be identified with the reagents used, but represent the typical bands for Ln–N stretching modes in the products [far-IR: Y (**1**): 268, 229, 196 cm^{-1}; Dy (**2**): 271, 229, 195 cm^{-1}; Ho (**3**): 275, 228, 203 cm^{-1}; Er (**4**): 275, 224, 191 cm^{-1}; Yb (**5**): 264, 225, 193 cm^{-1}]. The observed vibrations are in the region of known Ln–N vibrations. For comparison, Ln nitrile complexes with 1,4-$C_6H_4(CN)_2$ in $^{3}_{\infty}[\mathrm{LnCl_3}\{1,4\text{-}\mathrm{C_6H_4(CN)_2}\}]$ (Ln = Sm, Gd, Tb) and $^{3}_{\infty}[\mathrm{YCl_3}\{1,4\text{-}\mathrm{C_6H_4(CN)_2}\}_2]$[34] exhibit Ln–N vibrations in the region 270–180 cm^{-1}. Between 570 and 480 cm^{-1} [far- and mid-IR: Y (**1**): 595, 502 cm^{-1}; Dy (**2**): 592, 504 cm^{-1}; Ho (**3**): 589, 510 cm^{-1}; Er (**4**): 566, 515 cm^{-1}; Yb (**5**): 552, 492 cm^{-1}] asymmetric Ln–Cl vibrations can be identified.[41,42] The strong bands between 2230 and 2300 cm^{-1} represent the $\nu(C\equiv N)$ of the nitrile groups [mid-IR: Y (**1**): 2268 cm^{-1}; Dy (**2**): 2267 cm^{-1}; Ho (**3**): 2263 cm^{-1}; Er (**4**): 2261 cm^{-1}; Yb(**5**): 2267 cm^{-1}].

For the analysis of the particle sizes of the thermal reactions and ball-mill treatments, electron microscopy was used (REM/TEM).[b] The thermal properties as well as the progress of the reaction leading to **3** were studied by simultaneous DTA/TG in a continuous He flow of 50 mL/min in a temperature range of room temperature to 1000 °C with a constant heating rate of 10 °C/min. Powder patterns of the frameworks **1**–**5** were simulated based on the single-crystal X-ray data and compared to diffractograms of powder samples of the products of the different treatments. The diffractograms only show **1**–**5** as the main phases. Their crystallographic data is shown in Table 1.

Structure Description

The crystal structure of $^{3}_{\infty}[\mathrm{LnCl_3}\{1,3\text{-}\mathrm{C_6H_4(CN)_2}\}]$ consists of a three-dimensional framework. The use of 1,3-benzodinitrile as chemical scissors permits degradation of the $LnCl_3$ structure down to Ln–Cl chains, whereby the ligand is inserted in the dimensionally reduced structure, building up a three-dimensional coordination network (see Figure 3 and Supporting Information).

The two crystallographically independent Ln atoms exhibit different coordination numbers (c.n.); Ln1 is surrounded by two terminal and three bridging Cl atoms as well as three additional N atoms from connecting 1,3-benzodinitriles. This results in a twofold capped trigonal prism and a c.n. of 7+1. For Ln2, a reduced c.n. of 6 can be found, which is attained by two terminal, three bridging Cl atoms and only one N atom from a 1,3-benzodinitrile, leading to a slightly distorted octahedron (see Figure 4).

The Ln–N distances in $^{3}_{\infty}[\mathrm{LnCl_3}\{1,3\text{-}\mathrm{C_6H_4(CN)_2}\}]$ [Y–N (**1**): 2.446(4)–2.523(4) Å; Dy–N (**2**): 2.459(6)–2.530(6) Å; Ho–N (**3**): 2.451(5)–2.513(5) Å; Er–N (**4**): 2.440(4)–2.500(4) Å; Yb–N (**5**): 2.402(5)–2.463(5) Å] match the known Ln–N distances of nitrile ligands like in $^{1}_{\infty}[\mathrm{HoCl_3}\{1,3\text{-}\mathrm{C_6H_4(CN)_2}\}_2]$[35] (Ho–N: 2.42–2.49 Å). In comparison with mononitrile complexes such as $[\mathrm{Y}\{(\mathrm{Me_3Si})_2\mathrm{N}\}_3(\mathrm{PhCN})_2]$, which has Y–N(nitrile) distances of 2.47–2.49 Å,

Table 1. Crystallographic data for $^{3}_{\infty}$[LnCl$_3${1,3-C$_6$H$_4$(CN)$_2$}]; Ln = Y (**1**), Dy (**2**), Ho (**3**), Er (**4**), Yb (**5**). Deviations are given in parentheses.

	1	**2**	**3**	**4**	**5**
Empirical formula	$C_8H_4Cl_3N_2Y$	$C_8H_4Cl_3DyN_2$	$C_8H_4Cl_3HoN_2$	$C_8H_4Cl_3ErN_2$	$C_8H_4Cl_3N_2Yb$
Formula mass	323.39	396.98	398.91	401,74	407.56
Crystal system	monoclinic	monoclinic	monoclinic	monoclinic	monoclinic
Space group	$P2_1/c$	$P2_1/c$	$P2_1/c$	$P2_1/c$	$P2_1/c$
a [Å]	19.224(4)	19.180(2)	19.204(4)	19.205(2)	19.117(2)
b [Å]	11.054(2)	11.094(1)	11.005(2)	10.994(1)	10.866(1)
c [Å]	11.277(2)	11.249(1)	11.240(2)	11.260(1)	11.270(2)
β [°]	106.95(3)	106.66(1)	106.93(3)	106.83(1)°	107.25(2)°
V [Å^3]	2292.3(3)	2293.0(3)	2272.6(8)	2275.6(3)	2235.7(3)
Z	8	8	8	8	8
$d_{\mathrm{calcd.}}$ [g cm^{-1}]	1.874	2.300	2.332	2.345	2.421
μ [cm^{-1}]	57.47	71.76	76.27	80.39	90.42
T [K]	170	170	170	170	170
Data range [°]	$4.30 \leq 2\theta \leq 59.26$	$4.28 \leq 2\theta \leq 54.54$	$5.30 \leq 2\theta \leq 60.61$	$4.32 \leq 2\theta \leq 54.60$	$5.32 \leq 2\theta \leq 60.82$
X-ray radiation	Mo-K_α, λ = 71.073 Å	Mo-K_α, λ = 71.073 Å	Mo-K_α, λ = 71.073 Å	Mo-K_α, λ = 71.073 Å	Mo-K_α, λ = 71.073 Å
No. of unique reflections	6413	5090	6772	5027	6303
No. of parameters	285	285	285	285	285
R_1[a] for n reflections [$F_o > 4\sigma(F_o)$]	0.040	0.039	0.030	0.023	0.034
n	4396	4318	4630	4132	5097
R_1 (all)	0.068	0.040	0.030	0.031	0.041
wR_2[b] (all)	0.098	0.085	0.062	0.054	0.089
Electron density [e/pm^3 10^6]	+0.8/–1.1	+0.9/–2.3	+0.9/–2.0	+0.8/–1.6	+1.9/–1.8

[a] $R_1 = \Sigma[|F_o| - |F_c|]/\Sigma|F_o|$. [b] $wR_2 = \Sigma w(F_o^2 - F_c^2)^2/[\Sigma w(F_o^4)]^{1/2}$.[40]

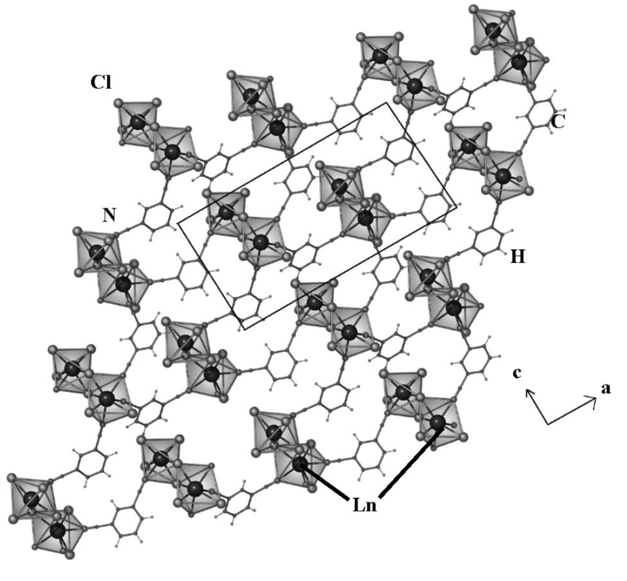

Figure 3. Crystal structure of $^{3}_{\infty}$[LnCl$_3${1,3-C$_6$H$_4$(CN)$_2$}]; Ln = Y, Dy, Ho, Er, Yb.

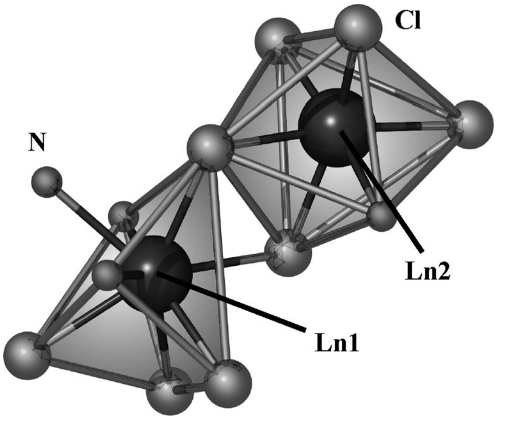

Figure 4. Twofold capped trigonal-prismatic coordination around Ln1 and slightly distorted octahedral coordination around Ln2 in $^{3}_{\infty}$[LnCl$_3${1,3-C$_6$H$_4$(CN)$_2$}].

a good correlation can be found, too.[43] The Ln–Cl distances of **1**–**5** (see Table 2) correspond to the expected values for the trivalent state of the lanthanides[44] (Y–Cl: 2.58–2.69 Å; Dy–Cl: 2.59–2.61 Å; Ho–Cl: 2.57–2.59 Å; Er–Cl: 2.56–2.58 Å; Yb–Cl 2.54–2.56 Å). A comparison of the Ln–Cl distances in **1** [Y–Cl: 2.625(2)–2.792(2)] with those in $^{3}_{\infty}$[Y$_2$Cl$_6${1,4-C$_6$H$_4$(CN)$_2$}] (Y–Cl: 2.68–2.75 Å) shows conformity for μ_2-bridging Cl atoms. The large Ln1–Cl3 distance [Y1–Cl3: 3.254(2) Å; Dy1–Cl3: 3.212(2) Å; Ho1–Cl3: 3.238(2) Å; Er1–Cl3: 3.271(2) Å; Yb1–Cl3: 3.308(2) Å] leads to an overall 7+1 coordination around Ln1.

Due to the different c.n. of the two Ln atoms (Ln1 = 7+1, Ln2 = 6) the topology of $^{3}_{\infty}$[LnCl$_3${1,3-C$_6$H$_4$(CN)$_2$}] cannot be described by a three-dimensional network consisting of two perpendicular two-dimensional nets. Still two two-dimensional nets can be assembled that each have a (4,4) topology and that are connected by a 59° angle. The (4,4) topology includes that coplanar pairs of Cl atoms (μ^2-connecting to Ln atoms) are counted as one bridge only. The 1,3-C$_6$H$_4$(CN)$_2$ ligands are responsible for the other bridges. Accordingly, the overall topology for the three-dimensional network can be identified as (4,5) (see Figure 5).

Nevertheless, this is a simplified topological consideration. To fully describe the absolute connectivity of the Ln atoms, coplanar pairs of Cl atoms should be counted twice as "double-bridges"[45] of Cl atoms. Thus, the connectivity

Table 2. Selected distances [Å] and angles [°] between atoms of $^{3}_{\infty}$[LnCl$_3${1,3-C$_6$H$_4$(CN)$_2$}]; Ln = Y (**1**), Dy (**2**), Ho (**3**), Er (**4**) and Yb (**5**). Deviations are given in parentheses.

Atom distances	**1**	**2**	**3**	**4**	**5**
Ln1–N1	2.466(4)	2.475(6)	2.453(5)	2.432(4)	2.423(5)
Ln1–N2	2.523(4)	2.530(6)	2.513(5)	2.500(4)	2.463(5)
Ln1–N3	2.446(4)	2.459(6)	2.451(5)	2.440(4)	2.402(5)
Ln1–Cl1	2.560(2)	2.560(2)	2.556(2)	2.545(2)	2.516(2)
Ln1–Cl2	2.792(2)	2.795(2)	2.781(2)	2.780(2)	2.756(2)
Ln1–Cl3	2.720(2)	2.744(2)	2.712(2)	2.677(2)	2.665(2)
Ln1–Cl4[a]	2.690(2)	2.700(2)	2.681(2)	2.692(2)	2.655(2)
Ln1–Cl3[a]	3.254(2)	3.212(2)	3.238(2)	3.271(2)	3.308(2)
Ln2–N4	2.481(4)	2.492(7)	2.475(5)	2.463(4)	2.415(5)
Ln2–Cl2	2.625(2)	2.632(2)	2.618(2)	2.605(2)	2.589(2)
Ln2–Cl3	2.687(2)	2.696(2)	2.678(2)	2.632(2)	2.632(2)
Ln2–Cl4	2.644(2)	2.651(2)	2.637(2)	2.632(2)	2.616(2)
Ln2–Cl5	2.520(2)	2.523(2)	2.512(2)	2.503(2)	2.481(2)
Ln2–Cl6	2.548(2)	2.551(2)	2.542(2)	2.525(2)	2.503(2)
Angles					
N1–Ln1–N3	139.5(2)	142.7(2)	139.5(2)	140.0(2)	140.3(2)
Cl2–Ln1–Cl3	76.2(1)	76.1(1)	76.4(1)	76.4(2)	76.6(4)
Ln1–N1–C1	173.4(3)	173.5(6)	173.1(3)	172.0(4)	172.7(5)
Cl2–Ln2–Cl4	155.9(1)	155.6(1)	156.2(1)	156.2(3)	157.0(4)
N4–Ln2–Cl5	87.7(1)	87.4(1)	87.6(1)	87.5(2)	87.7(2)
N4–Ln2–Cl6	173.9(1)	174.0(1)	174.5(1)	174.5(2)	175.0(2)
Cl4–Ln2–Cl5	95.8(1)	95.7(1)	95.8(1)	95.8(2)	95.7(1)

[a] Symmetry operation: x, $1/2 - x$, $1/2 + z$.

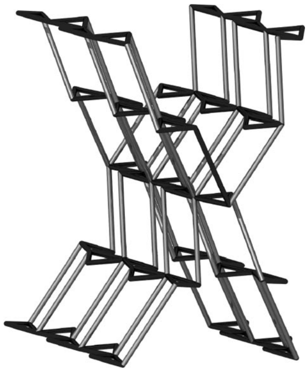

Figure 5. Depiction of the connectivity and topology of the (4,5) or (4,9) framework $^{3}_{\infty}$[LnCl$_3${1,3-C$_6$H$_4$(CN)$_2$}]; Ln = Er (**1**) to Yb (**5**). For a description as (4,5), each line represents one ligand bridge. For a description as (4,9) the dark lines represent "double-bridges" and represent the complete connectivity description of the topology.

for the three-dimensional network is also increasing. The overall lattice symbol then is (4,9) of two 2D nets that each have a connectivity of (4,6). A comparison with the literature shows that this topology has not been described before.

Conclusions

The three-dimensional frameworks **1**–**5** are the first 3D networks of lanthanides together with the isophthalonitrile ligand and exhibit a previously unreported network topology. They can be synthesised with different particle sizes tailored from the millimeter to nanometer scale depending on the reaction path and conditions. Thermal reactions always yield at least microcrystalline or lager particles. Ball-mill treatment can provide particle sizes down to 50 nm. Hence, our solvent-free synthesis strategy can be extended to and combined with other principal reaction types and developed to the previously rarely populated field of nanoscale coordination polymers.

Experimental Section

Synthesis: All manipulations were carried out under inert atmospheric conditions by using glove-box, Schlenk, DURAN™-ampoule as well as vacuum-line techniques. Heating furnaces with Al$_2$O$_3$ tubes together with EUROTHERM 2416 control elements were used for the ampoule experiments. For **1**–**4** the trichlorides LnCl$_3$ (Ln = Y, Dy, Ho, Er) were prepared according to the well-known ammonium halide route[46] by using the oxides Ln$_2$O$_3$ (ChemPur, 99.9%), HCl solution (10 mol/L, reagent grade) and ammonium chloride (Fluka, 99.5%), and purified by decomposition of the trivalent ammonium chlorides under vacuum and subsequent sublimation of the products. YbCl$_3$ (Alfa Aesar, 99.99%) was used as purchased. All products are air- and moisture-sensitive.

$^{3}_{\infty}$[YCl$_3${1,3-C$_6$H$_4$(CN)$_2$}] (1): YCl$_3$ (0.5 mmol, 97.63 mg) and 1,3-benzodinitrile [1,3-C$_6$H$_4$(CN)$_2$; 1.5 mmol, 192 mg] were sealed in an evacuated Duran glass ampoule and heated to 150 °C in 6.5 h and to 170 °C in another 20 h. This temperature was maintained for 48 h. The reaction mixture was then cooled to 155 °C over 50 h, to 145 °C in 10 h and to room temperature within 24 h. The reaction resulted in highly reflecting transparent colourless crystals of the product next to the excess ligand and some YCl$_3$. Yield: 134 mg (83%). C$_8$H$_4$Cl$_3$N$_2$Y (323.39): calcd. C 24.96, N 7.27, H 1.05; found C 25.09, N 7.23, H 0.96. MIR (KBr): $\tilde{\nu}$ = 3075 (w), 2268 (s), 2234 (s), 1600 (m), 1577 (m), 1480 (s), 1423 (s), 1334 (w), 1338 (w), 1185 (w), 1148 (m), 1104 (w), 906 (s), 800 (s), 676 (s), 501 (s) cm^{-1}. FIR (PE): $\tilde{\nu}$ = 502 (m), 461 (m), 383 (m), 268 (w), 196 (w), 144 (m), 65 (m) cm^{-1}. Raman: $\tilde{\nu}$ = 3079 (m), 2275 (vs), 1600 (m), 1576 (m), 1243 (m), 1002 (m), 704 (w), 144 (w) cm^{-1}. To obtain paricles of 50–400 nm, 25mg of **1** was treated with a ball mill. Samples of **1** were investigated with REM after 10–45 min milling time (ν = 60 Hz).

$^{3}_{\infty}$[DyCl$_3${1,3-C$_6$H$_4$(CN)$_2$}] (2): DyCl$_3$ (0.5 mmol, 134 mg) and 1,3-benzodinitrile [1,3-C$_6$H$_4$(CN)$_2$; 1.5 mmol, 192 mg] were sealed in an evacuated Duran glass ampoule and treated as described for **1**. The reaction resulted in highly reflecting transparent colourless crystals of **2**. Yield: 177 mg (89%). C$_8$H$_4$Cl$_3$DyN$_2$ (396.98): calcd. C 24.52, N 7.15, H 1.03; found C 24.39, N 7.13, H 1.87. MIR (KBr): $\tilde{\nu}$ = 3069 (m), 2267 (s), 2236 (s), 1618 (vs), 1528 (w), 1477 (m), 1421 (m), 1262 (w), 1239 (w), 1178 (w), 1149 (w), 1098 (w), 905 (w), 804 (s), 676 (s), 592 (w), 504 (m) cm^{-1}. FIR (PE): $\tilde{\nu}$ = 510 (m), 355 (w), 195 (w) cm^{-1}. Raman: $\tilde{\nu}$ = 3071 (w), 2272 (s), 1241 (w), 1001 (s), 247 (w) cm^{-1}.

$^{3}_{\infty}$[HoCl$_3${1,3-C$_6$H$_4$(CN)$_2$}] (3): HoCl$_3$ (0.5 mmol, 136 mg) and 1,3-benzodinitrile [1,3-C$_6$H$_4$(CN)$_2$; 1.5 mmol, 192 mg] were sealed in an evacuated Duran glass ampoule and treated as described for **1**. The reaction formed a bulk of highly reflecting transparent orange crystals of the product, excess ligand and a small amount of $^{3}_{\infty}$[Ho$_2$Cl$_6${1,3-C$_6$H$_4$(CN)$_2$}][35] observed by powder diffraction. Yield: 156 mg (78%). C$_8$H$_4$Cl$_3$HoN$_2$ (398.91): calcd. C 24.42, N 7.12, H 1.02; found C 24.62, N 7.06, H 1.08. MIR (KBr): $\tilde{\nu}$ = 3068 (w), 2263 (s), 2235 (s), 1633 (m), 1598 (msh), 1477 (m), 1421 (m), 1276 (w), 1178 (w), 1149 (w), 1099 (m), 1009 (w), 904 (s), 806 (s), 677 (s), 510 (s) cm^{-1}. FIR (PE): $\tilde{\nu}$ = 589 (w), 511 (w), 482 (w), 461 (w), 386 (w), 275 (w), 228 (w), 203 (w) cm^{-1}. Raman: $\tilde{\nu}$ = 3072 (w), 2263 (s), 2237 (s), 1598 (m), 1576 (w), 1240 (m), 1001 (w), 700 (w), 158 cm^{-1}.

$^{3}_{\infty}$[ErCl$_3${1,3-C$_6$H$_4$(CN)$_2$}] (4): ErCl$_3$ (0.5 mmol, 137 mg) and 1,3-benzodinitrile [1,3-C$_6$H$_4$(CN)$_2$; 1.5 mmol, 192 mg] were sealed in an evacuated Duran glass ampoule and also treated as described for **1**. In good yield, highly reflecting transparent light orange crystals of **4** resulted from the reaction. Yield: 171 mg (85%). $C_8H_4Cl_3ErN_2$ (401.74): calcd. C 18.52, N 5.40, H 0.78; found C 18.35, N 5.37, H 0.79. MIR (KBr): $\tilde{\nu}$ = 3091 (s), 2261 (s), 1630 (ssh), 1619 (s), 1525 (m), 1496 (m), 1402 (s), 1284 (s), 1225 (w), 1202 (w), 1017 (m), 849 (s), 831 (ssh), 665 (m) cm^{-1}. FIR (PE): $\tilde{\nu}$ = 566 (vs), 550 (m), 540 (msh), 275 (ssh), 224 (s), 191 (msh), 170 (s), 125 (w) cm^{-1}. To obtain paricles of 50–400 nm, 25 mg of **4** was treated with a ball mill. Samples of **4** were investigated with REM after 10 and 45 min milling time. Instead of the thermal synthesis a direct ball-mill treatment of the reagents was carried out. ErCl$_3$ (0.25 mmol, 68 mg) and 1,3-benzodinitrile [1,3-C$_6$H$_4$(CN)$_2$; 0.75 mmol, 96 mg] were treated in a ball mill for 10/30/60 min (ν = 60 Hz) leading to an amorphous product next to excess ErCl$_3$.

$^{3}_{\infty}$[YbCl$_3${1,3-C$_6$H$_4$(CN)$_2$}] (5): YbCl$_3$ (0.5 mmol, 140 mg) and 1,3-benzodinitrile [1,3-C$_6$H$_4$(CN)$_2$; 1.5 mmol, 192 mg] were sealed in an evacuated Duran glass ampoule and also treated as described for **1**; this afforded highly reflecting transparent orange crystals of **5**. Yield: 190 mg (93%). $C_8H_4Cl_3N_2Yb$ (407.52): calcd. C 49.98, N 8.33, H 2.99; found C 50.21, N 8.29, H 2.82. MIR (KBr): $\tilde{\nu}$ = 3358 (m), 3109 (w), 3035 (w), 2267 (vs), 1595 (m), 1487 (m), 1446 (s), 1293 (w), 1201 (w), 1176 (m), 1164 (w), 1094 (w), 1068 (w), 1028 (w), 999 (w), 761 (vs), 683 (s), 552 (s), 492 (m) cm^{-1}. FIR (PE): $\tilde{\nu}$ = 566 (m), 528 (w), 380 (w), 235 (m), 203 (w), 163 (w) cm^{-1}. To obtain paricles of 50–400 nm, 25 mg of **5** was treated with a ball mill. Samples of **5** were investigated with REM after 10 and 45 min milling time. Instead of the thermal synthesis, a direct ball-mill treatment of the reagents was carried out. YbCl$_3$ (0.25 mmol, 70 mg) and 1,3-benzodinitrile [1,3-C$_6$H$_4$(CN)$_2$; 0.75 mmol, 96 mg] were treated in a ball mill for 10/30/60 min (ν = 60 Hz) leading to an amorphous colourless product next to excess YbCl$_3$.

X-ray Diffraction: Suitable single crystals of $^{3}_{\infty}$[LnCl$_3${1,3-C$_6$H$_4$(CN)$_2$}] [Ln = Y (**1**), Dy (**2**), Ho (**3**), Er (**4**), Yb (**5**)] were selected for single-crystal X-ray investigations under glove-box conditions and sealed in glass capillaries. Data collection for **1**, **2** and **4** was carried out with a STOE IPDS-II diffractometer at 170 K (Mo-K_α radiation, λ = 0.7107 Å). Data collection for compounds **3** and **5** was carried out with a STOE IPDS-I diffractometer at 170 K (Mo-K_α radiation, λ = 0.7107 Å). The structures of **1**–**5** were determined by using direct methods.[47] All non-H atoms were refined anisotropically by least-squares techniques.[40] The hydrogen positions were completely retrieved from the differential Fourier map and refined isotropically.[40] The compounds $^{3}_{\infty}$[LnCl$_3${1,3-C$_6$H$_4$(CN)$_2$}] with Ln = Y, Dy, Ho, Er, Yb are isotypic and crystallize in the monoclinic space group $P2_1/c$. Integrity of symmetry and extinction were checked.[48] Numerical absorption corrections were applied to compounds **1**, **3**, **4** and **5**.[49] For **3**, **4**, and **5** the shape of the crystals was determined on the diffractometer, and the resulting *h*,*k*,*l* reflections and orientation matrices were used for the absorption correction. For **1** the crystal shape was refined from an appearance adjusted to the shape of the crystal but without predefined orientation.[50] Crystallographic data are summarized in Table 1. CCDC-748171 (**1**), -748167 (**2**), -748169 (**3**), -748168 (**4**), -748170 (**5**) contain the supplementary crystallographic data for this paper. These data can be obtained free of charge from The Cambridge Crystallographic Data Centre via www.ccdc.cam.ac.uk/data_request/cif.

Microanalysis: EDX spectra of selected crystals were obtained with a JSM 6500F scanning electron microscope (JEOL) equipped with an EDX detector 7418 (Oxford Instruments).

Vibrational Spectroscopy: IR spectra were recorded with a BRUKER FTIR-IS66V-S spectrometer, Raman spectra with a BRUKER FRA 106-S spectrometer. KBr pellets for mid-IR and PE pellets for far-IR investigations were used under vacuum.

Thermal Analysis: For thermal analysis and powder diffraction the products were purified by evaporating excess 1,3-C$_6$H$_4$(CN)$_2$ at 140 °C. The thermal decomposition of $^{3}_{\infty}$[LnCl$_3${1,3-C$_6$H$_4$(CN)$_2$}] was studied by simultaneous DTA/TG (TG-DTA92 Setaram) on the holmium-containing network **3** as an example; 15.1 mg of **3** was heated from 20 to 1000 °C in a constant He flow of 50 mL/min with a heating rate of 10 °C/min.

Ball-Mill Treatment: To obtain particles of 50–400 nm size, treatments and reactions were carried out with a ball mill (Specamill Specac; ν = 60 Hz).

Supporting Information (see footnote on the first page of this article): Additional information on the structural details for $^{3}_{\infty}$[LnCl$_3$-(1,3-C$_6$H$_4$(CN)$_2$)], including powder patterns, as well as electron microscopy images of different particle sizes of $^{3}_{\infty}$[YbCl$_3${1,3-C$_6$H$_4$(CN)$_2$}] and $^{3}_{\infty}$[YCl$_3${1,3-C$_6$H$_4$(CN)$_2$}].

Acknowledgments

We gratefully acknowledge the Deutsche Forschungsgemeinschaft for funding this work within the project "3D-Raumnetze komplexer Selten-Erd-Amide, ein Weg zu neuartigen MOFs", the Wilhelm-Klemm foundation, the Dr.-Otto-Röhm-Gedächtnis foundation as well as Prof. Dr. W. Schnick and the LMU München for their kind support. We also thank Dr. M. Döblinger for his continued attempts to investigate the crystalline and amorphous products presented here under TEM conditions (however, the products proved only stable under REM conditions), C. Minke for REM investigations and T. Miller for the single-crystal data collection.

---

[1] M. Oh, C. A. Mirkin, *Nature* **2005**, *438*, 651–654.
[2] S. Vaucher, J. Fielden, M. Li, E. Dujardin, *Nano Lett.* **2002**, *2*, 225–229.
[3] S. I. Vagin, A. K. Ott, B. Rieger, *Chem. Ing. Tech.* **2007**, *79*, 767–780.
[4] Z. Chen, B. Zhao, Y. Zhang, W. Shi, P. Cheng, *Cryst. Growth Des.* **2008**, *8*, 2291–2298.
[5] L. Han, S. Zhang, Y. Wang, X. Yan, X. Lu, *Inorg. Chem.* **2009**, *48*, 786–788.
[6] S. Noro, S. Kitagawa, T. Akutagawa, T. Nakamura, *Prog. Polym. Sci.* **2009**, *34*, 240–279.
[7] R. Robson, *Dalton Trans.* **2008**, *38*, 5113–5131.
[8] O. A. Efremova, Y. V. Mironov, V. E. Fedorov, *Eur. J. Inorg. Chem.* **2006**, *13*, 2533–2549.
[9] K. Mueller-Buschbaum, *Z. Anorg. Allg. Chem.* **2005**, *631*, 811–828.
[10] F. Gandara, A. de Andres, B. Gomez-Lor, E. Gutierrez-Puebla, M. Iglesias, M. A. Monge, D. M. Proserpio, N. Snejko, *Cryst. Growth Des.* **2008**, *8*, 378–380.
[11] X.-P. Yang, R. A. Jones, J. H. Rivers, R. Pen-Jen Lai, *Dalton Trans.* **2007**, 3936–3942.
[12] A. J. D. Barnes, T. J. Prior, M. G. Francesconi, *Chem. Commun.* **2007**, 4638–4640.
[13] A. Zurawski, E. Wirnhier, K. Müller-Buschbaum, *Eur. J. Inorg. Chem.* **2009**, 2482–2486.

[14] K. Müller-Buschbaum, C. C. Quitmann, *Inorg. Chem.* **2003**, *42*, 2742–2750.
[15] K. Müller-Buschbaum, C. C. Quitmann, *Inorg. Chem.* **2006**, *45*, 2678–2687.
[16] C. C. Quitmann, K. Müller-Buschbaum, *Z. Anorg. Allg. Chem.* **2005**, *631*, 2651–2654.
[17] K. Müller-Buschbaum, Y. Mokaddem, *Z. Anorg. Allg. Chem.* **2007**, *633*, 521–523.
[18] K. Müller-Buschbaum, C. C. Quitmann, *Z. Anorg. Allg. Chem.* **2003**, *629*, 1610–1616.
[19] K. Müller-Buschbaum, C. C. Quitmann, *Eur. J. Inorg. Chem.* **2004**, 4330–4337.
[20] K. Müller-Buschbaum, Y. Mokaddem, *Eur. J. Inorg. Chem.* **2006**, 2000–2010.
[21] C. C. Quitmann, K. Müller-Buschbaum, *Z. Naturforsch., Teil B* **2004**, *59*, 562–566.
[22] C. C. Quitmann, K. Müller-Buschbaum, *Z. Anorg. Allg. Chem.* **2005**, *631*, 1191–1198.
[23] C. C. Quitmann, V. Bezugly, F. R. Wagner, K. Müller-Buschbaum, *Z. Anorg. Allg. Chem.* **2006**, *632*, 1173–1186.
[24] K. Müller-Buschbaum, Y. Mokaddem, C. J. Höller, *Z. Anorg. Allg. Chem.* **2008**, *634*, 2973–2977.
[25] K. Müller-Buschbaum, *Z. Naturforsch., Teil B* **2006**, *61*, 792–798.
[26] K. Müller-Buschbaum, Y. Mokaddem, *Chem. Commun.* **2006**, 2060–2062.
[27] K. Müller-Buschbaum, S. G. Torres, P. Larsen, C. Wickleder, *Chem. Mater.* **2007**, *19*, 655–659.
[28] K. Müller-Buschbaum, Y. Mokaddem, F. Schappacher, R. Pöttgen, *Angew. Chem.* **2007**, *119*, 4463–4465; *Angew. Chem. Int. Ed.* **2007**, *46*, 4385–4387.
[29] K. Müller-Buschbaum, Y. Mokaddem, *Solid State Sci.* **2008**, *10*, 416–420.
[30] K. Müller-Buschbaum, Y. Mokaddem, *Z. Anorg. Allg. Chem.* **2008**, *634*, 2360–2366.
[31] L. Carlucci, G. Ciani, D. W. v. Gudenberg, D. M. Proserpio, *New J. Chem.* **1999**, *23*, 397–402.
[32] T. Niu, J. Lu, G. Grisci, A. Jacobson, *Polyhedron* **1998**, *17*, 4079–4089.
[33] M. Munakata, G. L. Ning, T. Kurado-Sowa, M. Maekawa, Y. Suenaga, T. Horino, *Inorg. Chem.* **1998**, *37*, 5651–5656.
[34] C. J. Höller, K. Müller-Buschbaum, *Inorg. Chem.* **2008**, *47*, 10141–10149.
[35] C. J. Höller, K. Müller-Buschbaum, *Z. Anorg. Allg. Chem.* **2007**, *633*, 2614–2618.
[36] S. C. Chanda, A. Manna, V. Vijayan, P. K. Nayak, M. Ashok, H. N. Acharya, *Mater. Lett.* **2007**, *61*, 5059–5062.
[37] J. A. Campbell, *Synthesis* **2007**, *20*, 3179–3184.
[38] G. Jantsch, *Z. Anorg. Allg. Chem.* **1932**, *207*, 353–367.
[39] N. Pinna, *Prog. Colloid Polym. Sci.* **2005**, *130*, 29–32.
[40] G. M. Sheldrick, *SHELXL-97, Program for the refinement of Crystal Structures*, Göttingen, **1997**.
[41] K. Nakamoto, *Infrared and Raman Spectra of Inorganic and Coordination Compounds*, 3rd ed., Wiley-VCH, Weinheim, **1978**.
[42] J. Weidlein, U. Müller, K. Dehnicke, *Schwingungsfrequenzen II, Nebengruppenelemente*, Georg Thieme Verlag, Stuttgart, **1986**.
[43] M. Westerhausen, M. Hartmann, A. Pfitzner, W. Schwarz, *Z. Anorg. Allg. Chem.* **1995**, *621*, 837–850.
[44] R. D. Shannon, *Acta Crystallogr., Sect. A* **1976**, *32*, 751–767.
[45] D.-L. Long, A. J. Blake, N. R. Champness, C. Wilson, M. Schröder, *Angew. Chem. Int. Ed.* **2001**, *40*, 2444–2447; *Angew. Chem.* **2001**, *113*, 2510–2513.
[46] G. Meyer, *Inorg. Synth.* **1989**, *25*, 146–150.
[47] G. M. Sheldrick, *SHELXS-97, Program for the resolution of Crystal Structures*, Göttingen, **1997**.
[48] A. L. Spek, *PLATON-2000, A Multipurpose Crystallographic Tool*, Utrecht, **2000**.
[49] STOE Software Package, V.1.16, *X-RED*, *Program for the numerical absorption correction*, Darmstadt, **2001**.
[50] STOE Software Package, V.1.16, *X-Shape*, *Program for the crystal appearance*, Darmstadt, **2001**.

Received: September 28, 2009

DOI: 10.1002/ejic.200900784

A Distorted Trigonal Antiprismatic Cationic Silicon Complex with Ureato Ligands: Syntheses, Crystal Structures and Solid State ^{29}Si NMR Properties

Dana Schöne,[a] Daniela Gerlach,[a] Conny Wiltzsch,[a] Erica Brendler,[b] Thomas Heine,[c]
Edwin Kroke,*[a] and Jörg Wagler*[a]

Dedicated to Prof. Gerhard Roewer on the occasion of his 70th birthday

Keywords: Silicon / Chelates / Density-functional calculations / Hypercoordination

Insertion of phenyl isocyanate into the Si–N bond of *N*-(trimethylsilyl)diethylamine yields the *N′*-silylated *N*,*N*-diethyl-*N′*-phenylurea **1**, which undergoes transsilylation with $SiCl_4$ to yield the C_3-symmetric cationic hexacoordinate silicon complex **3s⁺** [tris-κ-*O*,*N′*-(*N*,*N*-diethyl-*N′*-phenylureato)siliconium] as chloride salt, which was characterized crystallographically. The cationic complex **3s⁺** exhibits a distorted trigonal antiprismatic coordination sphere about the silicon atom with *fac* arrangement of the three N-atoms (and the three O-atoms) relative to one another. This C_3-symmetric complex undergoes isomerization into its asymmetric isomer **3a⁺** (*mer* arrangement of NNN or OOO relative to one another) in $CDCl_3$ solution. Hence, two ^{29}Si NMR signals appear and four sets of signals emerge in the ^{1}H and ^{13}C NMR spectra. Despite its pronounced axial symmetry, the ^{29}Si NMR shielding tensor of the cation **3s⁺** in its chloride salt exhibits an unusually small span (less than 20 ppm), which was analyzed CP/MAS NMR spectroscopically and by computational methods.

Introduction

Among the class of hypercoordinate silicon complexes[1] those with a hexacoordinate silicon atom[2] were found to exhibit more or less distorted octahedral coordination spheres. Deviation from the ideal octahedral geometry is mainly caused by different substituents X (thus resulting in different Si–X bond lengths) and steric strain, either caused by intramolecular sources such as chelate effects or by intermolecular interactions in the crystal packing. The most obvious sign for distortion of an octahedron is the deviation of the axial angles from 180°. As shown in Scheme 1 for selected examples of bis- and tris-chelate hexacoordinate silicon complexes[3] the presence of small chelate rings results in pronounced distortion.

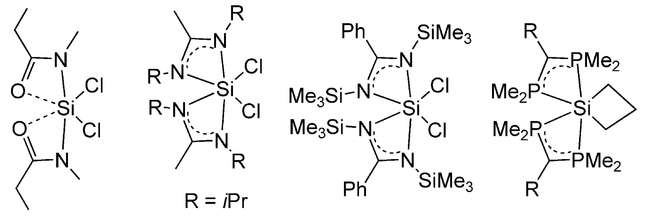

I	II	III	IV
NSiN: 158.9	NSiN: 163.0	NSiN: 169.4	PSiP: 155.2
OSiCl: 165.5	NSiCl: 164.0	NSiCl: 164.3	PSiC: 166.3
OSiCl: 164.9	NSiCl: 164.7	NSiCl: 164.3	PSiC: 166.3

Scheme 1. Examples for "distorted octahedral" Si complexes. The three axial angles are given below the respective drawing. For **II** only data for one of the two crystallographically independent molecules are given here as representative example (for **IV**: R = $PhMe_2Si$).

The presence of different substituents in the octahedral coordination sphere of silicon was already shown to occasionally provoke a pronounced span of the ^{29}Si chemical shift anisotropy (CSA) tensor.[2c,4] The transition to a more axial system, i.e., pentacoordinate silicon complexes with a trigonal bipyramidal Si-coordination sphere, causes an even wider span.[5] To the best of our knowledge, the ^{29}Si NMR spectroscopic role of axial deformation of the octahedron with respect to the threefold axis, also creating a molecular system with a unique axis, has not been elucidated yet. Our recent investigations on silylated urea derivatives provided

---

[a] Institut für Anorganische Chemie, Technische Universität Bergakademie Freiberg,
09596 Freiberg, Germany
Fax: +49-3731-39-4058
E-mail: edwin.kroke@chemie.tu-freiberg.de
joerg.wagler@chemie.tu-freiberg.de
[b] Institut für Analytische Chemie, Technische Universität Bergakademie Freiberg,
09596 Freiberg, Germany
[c] School of Engineering and Science, Theoretical Physics – Theoretical Materials Science, Jacobs University Bremen,
28759 Bremen, Germany

Supporting information for this article is available on the WWW under http://dx.doi.org/10.1002/ejic.200900784.

access to a cationic hexacoordinate siliconium complex comprising three four-membered chelate rings, resulting in a pronounced C_3-symmetric deformation of the coordination sphere from octahedral towards distorted antiprismatic. Thus, this interesting complex was subjected to X-ray diffractional, ^{29}Si NMR spectroscopic and computational analyses.

Results and Discussion

Phenyl isocyanate reacts with *N*-(trimethylsilyl)diethylamine under formal insertion into the Si–N bond, thus providing convenient access to the *N′*-trimethylsilylated *N*,*N*-diethyl-*N′*-phenylurea **1**, whereas excess of phenyl isocyanate would lead to the formation of **2** as a by-product (Scheme 2). Synthesis of **1** in hexane, however, provides a product of sufficient purity for further reactions since **1** is obtained as a hexane-soluble colorless oil, whereas compound **2**, even though formed as a minor by-product, precipitates from hexane to yield white crystalline needles suitable for X-ray diffraction analysis (Figure 1).

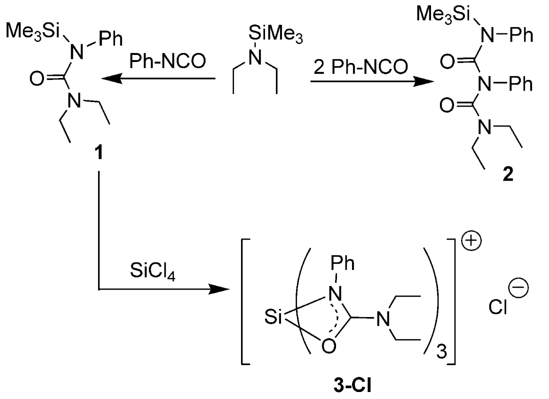

Scheme 2. Synthesis of the silylated urea derivative **1** and the hexacoordinate silicon compound **3-Cl** thereof (representation of one canonical form).

Deliberate synthesis of **2** by treating *N*-(trimethylsilyl)diethylamine with two equivalents of phenyl isocyanate proved a convenient route to generate this interesting ligand precursor in reasonable yield. In the present work, however, we want to focus on **1** as a chelating ligand precursor.

As shown in previous reports, trimethylsilylated (*O*,*N*)-chelators proved useful as starting materials in the syntheses of hypercoordinate silicon chelate complexes since the by-product of the reactions, Me_3SiCl, is volatile and may be easily removed from the product.[1a,1b] So far, a number of carboxylic acid derivatives such as carboxylates,[6] amides[3a] and amidinates[3b,3c] has been studied as ligands capable of setting up coordination spheres with coordination number 5 or 6 about a silicon atom. Whereas the former were occasionally found to act as bidentate chelators, urea moieties, although reported in the context of silicon coordination chemistry, served the role of a monodentate donor or were bidentately bound to the Si-atom in a κ(O,C)-mode.[7]

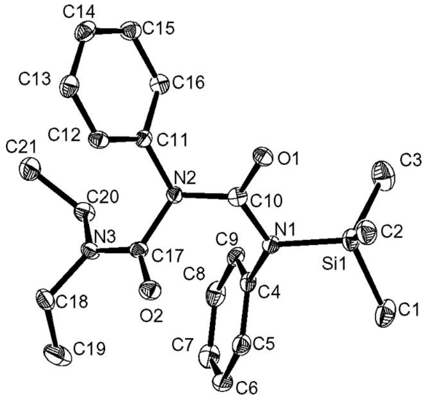

Figure 1. ORTEP drawing of **2** in the crystal (ellipsoids at the 50% probability level, hydrogen atoms omitted for clarity). Selected bond lengths [Å] and dihedral angles [°]: Si1–N1 1.783(2), O1–C10 1.225(2), O2–C17 1.222(2), N1–C10 1.374(3), N2–C10 1.401(2), N2–C17 1.437(3), N3–C17 1.354(2), Si1–N1–C10–N2 177.3(1), N1–C10–N2–C17 41.9(3), C10–N2–C17–N3 149.0(2), N2–C17–N3–C18 169.2(2).

Hence, we probed the chelator qualities of compound **1** in a reaction with silicon tetrachloride (Scheme 2, bottom). The reaction proceeds towards the cationic tris-chelate $\mathbf{3}^+$ (which was found to exist in two diastereomeric forms in solution, i.e., the enantiomers of the asymmetric $\mathbf{3a}^+$ and the C_3-symmetric $\mathbf{3s}^+$ cations) in a clean manner. In the ^{29}Si solid state NMR spectrum only one signal was detected at δ = –165.9 ppm. Attempts to synthesize the bis-chelate complex **4** by adjusting the molar ratio **1**/$SiCl_4$ to 2:1 failed: The co-existence of $\mathbf{3}^+$ and unreacted $SiCl_4$ was proven ^{29}Si NMR spectroscopically. Apparently, the mono- and di-substituted silanes $LSiCl_3$ and L_2SiCl_2, respectively, (L = *N*,*N*-diethyl-*N′*-phenylureate) exhibit enhanced reactivity relative to $SiCl_4$, thus furnishing $\mathbf{3}^+$ as the final substitution product. In order to explore an alternative route towards compound **4** phenyl isocyanate was treated with bis(diethylamino)dichlorosilane. Again, complex $\mathbf{3}^+$ was formed, thus hinting at ligand scrambling which should have given rise to the formation of $\mathbf{3}^+$ from intermediately formed **4** (not detected; Scheme 3).

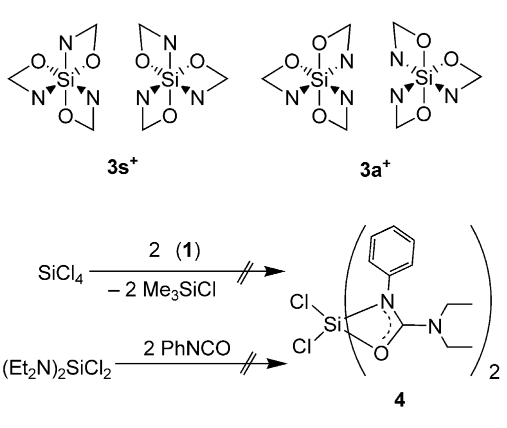

Scheme 3. Top: schematic representation of the two pairs of diastereomers of the cation $\mathbf{3}^+$ found in chloroform solution ($\mathbf{3s}^+$ = *fac*, $\mathbf{3a}^+$ = *mer*). Bottom: attempts to synthesize **4**, leading also to **3-Cl**.

In addition to not delivering the desired product **4**, this alternative route resulted in the formation of a byproduct, namely trimerized phenyl isocyanate, which crystallizes with **3s-Cl** as **3s-Cl·THF·(PhNCO)$_3$** (**structure A**) (Figure 2). From the same reaction further crystals were obtained which consist of **3s-Cl** only (**structure B**) (Figure 3). The presence of more than one hexacoordinate silicon compound in the solid obtained was furthermore indicated by ^{29}Si CP/MAS NMR spectra, which produced a peak at δ = –165.9 ppm (as for the former product) and a less intense one at δ = –164.1 ppm (with a shoulder). Except the special features caused by the additional components in the crystal structure [interaction between chloride and (PhNCO)$_3$ with a separation of 3.028(1) Å between Cl$^-$ and the centroid of the triazine system, as well as a THF molecule located on a threefold axis with its O-atom pointing towards the Si-atom of **3s$^+$** from a distance of 5.522(3) Å] the features of the cation **3s$^+$** are very similar in both solids (see Figure caption 3). Thus, only the molecular structure of **3s-Cl** will be discussed. As indicated in the canonical formula in Scheme 2, bottom, and by the bond lengths C7–N1 and C7–N2, the diethylamino substituent donates electron density towards the ligand donor sites, thus enhancing the double bond character of bond C7–N2, whereas bonds C7–O1 and C7–N1 represent single bonds strengthened by π-conjugation. This additional donor action of N2 can be considered source of the structural differences between the ureato ligand in **3s$^+$** and the carbamido ligand in the complex Scheme 1 **I**,[3a] which exhibits shorter C–O and C–N bonds (1.299, 1.308 and 1.300, 1.303 Å, respectively). In a related study, Kost et al. have shown that the transition from hydrazinimides to semicarbazones is also accompanied by reinforcement of the ligand donor capabilities by the additional R$_2$N group,[8] and the same was shown to apply to pyridine ligands upon substitution with a 4-dimethylamino group.[4a] Hence, the ureato ligand in **3s$^+$** is setting up Si–N and Si–O bonds of similar length, whereas in the carbamide complex **A** in Scheme 1 the Si–O bonds (1.885, 1.886 Å) are longer than the Si–N bonds (1.830, 1.835 Å), again accounting for the carbamide character of the ligand utilized by Yang and Verkade. In addition to the axial angles being much smaller than 180°, the coordination sphere about the silicon atom in **3s$^+$** deviates from octahedral by two distinct features: These are (i) the significantly reduced rotation of the two opposite triangular faces NNN and OOO by only 40.7(1)°, which corresponds to a 32.2% rotation towards trigonal prismatic, and (ii), the noticeably low ratio [IPD/AEL$_{(complex)}$] = 0.666 (IPD = inter-planar distance, AEL = average edge length of the triangles, [IPD/AEL$_{(octahedron)}$] = 0.816), thus confirming 18.4% compression of the octahedron along the ideal threefold axis. Thus, one cannot consider this coordination geometry as slightly distorted octahedral any longer, whereas distorted trigonal antiprismatic would hold for any rotation angle between 30 and 60° regardless the degree of compression or stretching of the two parallel triangular faces along the threefold axis.

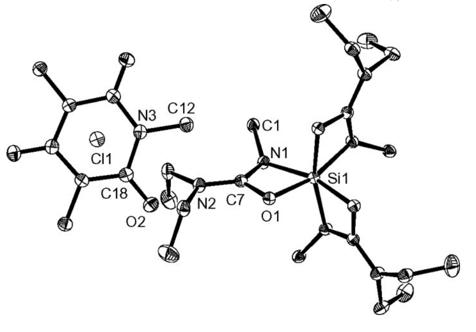

Figure 2. ORTEP drawing of **3s$^+$** and the **(PhNCO)$_3$·Cl$^-$** counterion in the crystal structure of **3s-Cl·THF·(PhNCO)$_3$** (**structure A**) (view along the crystallographic *c*-axis, 30% probability ellipsoids, hydrogen atoms, THF molecule and phenyl groups omitted, selected atoms of asymmetric unit labeled). Atoms Si1 and Cl1 are located on threefold axes.

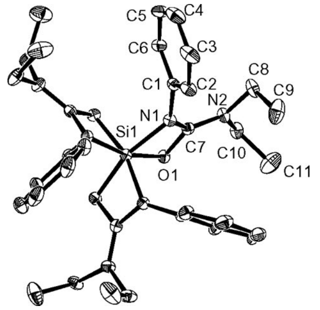

Figure 3. ORTEP drawing of **3s$^+$** in the crystal structure of **3s-Cl** (**structure B**) (30% probability ellipsoids, hydrogen atoms omitted, atoms of asymmetric unit labeled). Selected bond lengths [Å] and angles [°] of **3s$^+$** in **3s-Cl**: Si1–O1 1.810(2), Si1–N1 1.833(2), O1–C7 1.323(3), N1–C7 1.344(3), N2–C7 1.318(3), O1–Si1–N1 71.8(1), C7–N2–C8 121.7(2), C7–N2–C10 119.9(2), C8–N2–C10 118.2(2); corresponding parameters of **3s$^+$** in **3s-Cl·THF·(PhNCO)$_3$**: Si1–O1 1.800(1), Si1–N1 1.840(2), O1–C7 1.315(2), N1–C7 1.346(2), N2–C7 1.315(2), O1–Si1–N1 71.9(1), C7–N2–C8 121.3(2), C7–N2–C10 119.4(2), C8–N2–C10 119.0(1).

Although the axial angles N–Si–O* [162.8(1)°] are in the same range as the inter-chelate axial angles of the compounds depicted in Scheme 1 (in **3s-Cl** position O* is generated from O1 by operation $2 - y$, $1 + x - y$, z), the three identical chelates create a particularly high symmetry of this tris-chelate complex. The pronounced C_3-symmetric distortion of the Si-coordination sphere in **3s$^+$**, which should result in pronounced axiality of the ^{29}Si NMR CSA tensor, tempted us to analyze this property experimentally and computationally. Since the product obtained from the reaction of phenyl isocyanate with bis(diethylamino)dichlorosilane was contaminated with by-products, the compound obtained from the reaction of **1** with SiCl$_4$ was used for ^{29}Si CP/MAS NMR analysis of the CSA tensor. The ^{29}Si CP/MAS NMR spectrum of **3s-Cl**, depicted in Figure 4, reveals a very narrow span of the chemical shift anisotropy. Although the axiality of the CSA tensor can be discerned from the principal component δ_{22} being closer to δ_{33} than to δ_{11}, this result was not expected.

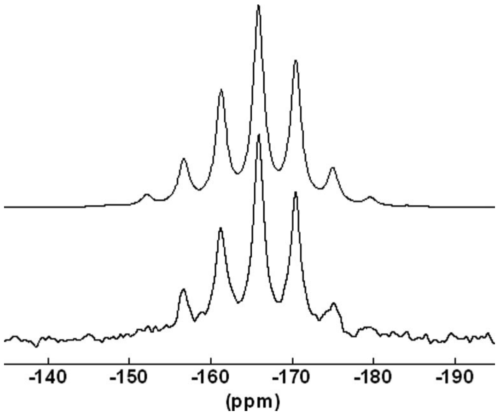

Figure 4. Bottom: ^{29}Si CP/MAS NMR spectrum of **3s-Cl** (ν_{spin} = 364 Hz). Top: overlay of the simulated spectrum using the CSA tensor data from the entry "exp." in Table 1.

We analyzed the CSA tensor by means of quantum chemistry, approximating the solid-state structure by the formally positively charged cation **3s$^+$** at the frozen low-temperature XRD **structure B**. The CSA tensor, computed at various DFT and HF levels, confirms the narrow span (Table 1). The skew, which must be –1 in this axial molecular system according to the system's C_3 symmetry (two degenerate principal axes in the molecular and crystal environment of threefold symmetry), was not reproduced as such by the experimental methods applied. HF and DFT approaches with larger basis sets (i.e. calculations 4 and 5) converge to similar results, which indicates that theory can describe the model compound rather well, as both methods contain quite different approximations. In conclusion, all methods applied proved suitable to describe the narrow span of the CSA tensor, which is located in the cation as follows: Component (11) points along the threefold axis, whereas components (22) and (33) are degenerate in the plane orthogonal to the threefold axis.

Table 1. ^{29}Si NMR CSA tensor of **3s$^+$** determined experimentally and computationally for **structure B**. The principal components δ_{11}, δ_{22} and δ_{33} as well as the span Ω and skew κ are given according to the Herzfeld–Berger notation.[9]

Entry[a]	δ_{iso}	δ_{11}	δ_{22}	δ_{33}	Ω	κ
exp.	–165.9	–154.7	–167.1	–175.8	21.1	–0.17
calc1	–176.2	–168.1	–180.3	–180.3	12.2	–1.00
calc2	–170.1	–162.2	–174.1	–174.1	11.9	–1.00
calc3	–165.2	–155.3	–170.2	–170.2	14.9	–1.00
calc4	–173.3	–163.4	–178.3	–178.3	14.9	–1.00
calc5	–171.9	–164.4	–175.7	–175.7	11.3	–1.00

[a] Exp.: determined from the MAS spectrum at ν_{spin} = 364 Hz, calc1: DFT-IGLO-III (PBE), calc2: B3LYP/6-311G(d,p), calc3: HF/6-311G(d,p), calc4: HF/6-311G(2d,p), calc5: GIAO-PBE/TZ2P (Slater basis).[10]

Analysis of the contributions to the overall shielding with DFT-IGLO (using Pipek–Mezey localizition) confirmed similar influence of the oxygen and nitrogen donor atoms, as shown in Table 2. Whereas one dominating lone pair contribution was analyzed for the N-atoms (e.g., N –47.9), the oxygen atoms were found to exhibit two distinct lone pair contributions (e.g., O –14.9 and –25.3), the sum of which, however, is close to the N-atom influence. Due to the C_3 symmetry of the cation, the influences of all O-atoms (the same holds for the N-atoms) in direction (11) is equal, whereas the degenerate character of (22) and (33) is reflected in the permutational influence of the O- and N-atoms in these directions.

Table 2. Selected individual contributions to the ^{29}Si shielding tensor of **3s$^+$**, determined using DFT-IGLO-III (Pipek–Mezey localization).

Atom[a]	σ_{iso}	σ_{11}	σ_{22}	σ_{33}
O	–14.9	–14.8	–4.3	–25.7
O	–25.3	–22.4	–12.7	–40.6
O*	–15.0	–14.8	–18.5	–11.8
O*	–25.2	–22.5	–43.4	–9.9
O**	–14.9	–14.8	–22.4	–7.6
O**	–25.3	–22.6	–23.8	–29.5
N	–47.9	–51.6	–52.6	–39.4
N*	–48.0	–51.7	–14.0	–78.4
N**	–48.0	–51.5	–71.9	–20.5

[a] The asterisked atoms represent symmetry equivalents in the crystal system.

So far, no satisfactory explanation was found for the skew of the CSA tensor deviating from –1 in the experiment. Thermal motion of the molecules in the crystal at elevated temperatures was considered to violate the perfect C_3 symmetry, hence influencing the shape of the CSA tensor. In order to probe this hypothesis, the collection of an X-ray diffraction data set at elevated temperatures was planned, and a tiny single-crystalline needle (from the sample which was used for CSA tensor analysis) was chosen for data collection. Unit cell determination at 250 K revealed trigonal cell parameters, but different from those of compound **3s-Cl**, the structure of which was determined at 150 K (a = 20.109, c = 14.518 Å for the former, a = 12.028, c = 14.354 Å for the latter). Upon cooling to 150 K and further to 100 K no phase transition (at least by means of striking changes in the unit cell parameters) was observed. Structure solution revealed a further trigonal modification of **3s-Cl** (**structure C**, space group $P3$), but with six crystallographically independent Si-environments. The molecular shapes of the six individual cations **3s$^+$** are similar to those in **structure B** (space group $P31c$), thus rendering further discussion of bond lengths and angles superfluous. **Structure C** (at 100 K) exhibits an average molecular volume of 847 Å^3 per unit **3s-Cl**. In sharp contrast, the spatial demand of **3s-Cl** in **structure B** (at 150 K) is much greater with 899 Å^3. This notable difference, which does not only originate from the different temperatures of X-ray data collection, gives rise to the assumption that the more closely packed **structure C** should be the more stable one (rendering the crystal of **structure B** a discovery by chance). Indeed, repeated crystal picking and unit cell determination of crystals obtained from the reaction of bis(diethylamino)dichlorosilane and phenyl isocyanate (upon storage of the reaction mixture for 3 weeks) revealed that, in addition to **3s-Cl·THF·(PhNCO)$_3$ (structure A)**, crystals of **3s-Cl (structure C)** were present in the solid product.

Despite similar Si–N and Si–O bond lengths, the trigonal-antiprismatic distortion of the six individual Si-coordination spheres in **structure C** varies slightly (with the distortion towards trigonal-prismatic ranging from 32.3 to 36.3%, the compression along the threefold axis ranging from 15.7 to 16.9%). Characteristic parameters of the Si-coordination polyhedra in **structure C** are summarized in Table 3.

Table 3. Geometric parameters of the Si-coordination spheres of the six individual cations 1–6 in the crystal **structure C** of **3s-Cl**. [edge lengths N···N′ and O···O′, the average edge length (AEL) thereof and NNN-OOO inter-planar distance (IPD) of the trigonal-antiprisms in Å, dihedral angle of the O- and N-donor atom of one chelate about the C_3-axis (tors.(O–C_3–N)) in °].

Cation	1	2	3	4	5	6
d(N···N′)[a]	2.795	2.795	2.801	2.800	2.807	2.779
d(O···O′)[a]	2.642	2.626	2.621	2.634	2.611	2.641
tors. (O–C_3–N)[b]	40.04	39.97	38.94	40.62	38.20	40.01
% trig. prism.	33.3	33.4	35.1	32.3	36.3	33.3
AEL	2.7185	2.7105	2.711	2.717	2.709	2.710
IPD	1.853	1.852	1.865	1.843	1.863	1.858
IPD/AEL	0.682	0.683	0.688	0.678	0.688	0.686
% compression	16.4	16.3	15.7	16.9	15.7	15.9

[a] Standard deviation: 0.004. [b] Standard deviation: 0.15.

These six slightly different coordination spheres might give rise to six CSA tensors of slightly different span, the superposition of which would provide an explanation for the ^{29}Si solid state NMR spectrum observed in the experiment (Figure 4). In order to get an idea of the variability of the span of the CSA tensor among these six cations their solid-state structures were, upon optimization of the H-positions, employed for CSA tensor calculation on the HF/6-311G(d,p) level. The results, listed in Table 4, indeed offer an explanation for seemingly lower axiality of the CSA tensor observed in the experiment. Although the isotropic chemical shift was predicted to be very similar for the six independent ^{29}Si nuclei, the CSA tensors of cations 3 and 5 (which exhibit pronounced distortion of the coordination sphere towards trigonal prismatic) can be expected to show a larger span than the other four cations. Upon removal of the computational error on the value of δ_{iso} (i.e., upon setting δ_{iso} = –165.9 ppm for each of the six CSA tensors in Table 4), the superposition of the six individual spectra created therefrom (each of the six individual Si nuclei contributing with 16.7%) indeed produces a picture which reflects the experimental data very well (Figure 5). Although a plausible explanation was found, additional effects of molecular thermal motion at room temperature might also contribute to the overall shape of the experimental ^{29}Si CP/MAS NMR spectrum of **3s-Cl** (**structure C**).

Table 4. ^{29}Si NMR CSA tensor of **3s$^+$** for the six independent cations of **structure C**, determined computationally using HF/6-311G(d,p). The principal components δ_{11}, δ_{22} and δ_{33} as well as the span Ω are given according to the Herzfeld–Berger notation.[9]

Cation	1	2	3	4	5	6
δ_{iso}	–162.1	–163.3	–162.8	–162.9	–162.7	–164.7
δ_{11}	–152.4	–153.1	–150.9	–154.2	–148.8	–154.2
δ_{22}	–166.7	–168.3	–168.8	–166.9	–169.7	–169.9
δ_{33}	–167.2	–168.3	–168.8	–166.9	–169.7	–169.9
Ω	14.8	15.2	17.9	12.8	20.9	15.7

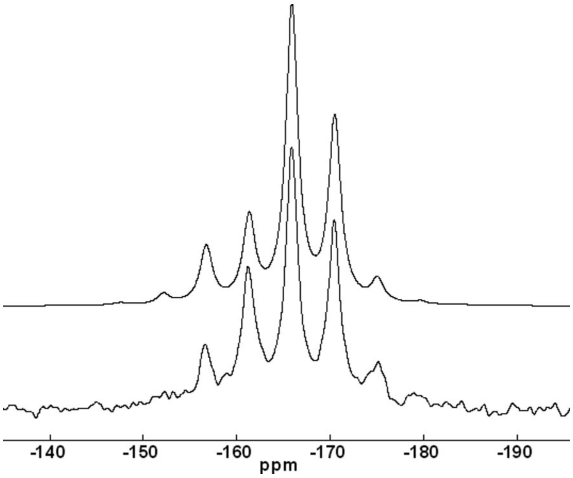

Figure 5. Bottom: ^{29}Si CP/MAS NMR spectrum of **3s-Cl** (ν_{spin} = 364 Hz). Top: simulated spectrum using the weighted CSA tensor data (16.7% contribution of each tensor) from Table 4 (upon setting δ_{iso} = –165.9 ppm for each of the six CSA tensors).

Conclusions

The insertion of phenyl isocyanate into the Si–N bond of a trimethylsilylamine was shown to provide convenient access to an interesting class of chelating ureato systems, the coordination behavior of which will be addressed in further studies. A first example of a hexacoordinate silicon complex synthesized therefrom already revealed some special features of these ligands in exhibiting donor qualities different from those of related carbamide systems (**I**, Scheme 1): the electron releasing diethylamino substituent supports strong coordination of both the N- and O-donor site. This pronounced stabilizing effect of the (O,N) chelate is considered to facilitate the formation of the herein presented silicon tris-chelate **3$^+$** (in sharp contrast to the bis-chelates **I**, **II** and **III** in Scheme 1). The special coordination geometry of this silicon complex, i.e., distorted trigonal antiprismatic, was found to give rise to a very narrow ^{29}Si NMR shielding tensor. The pronounced axiality of the Si-coordination sphere (C_3 symmetry) was expected to generate a ^{29}Si solid state NMR spectrum also exhibiting pronounced axiality. Instead, a less axial CSA tensor was found in the experiment, hinting at effects like disturbances of the ideal C_3 symmetry in the crystal lattice at ambient temperatures and at the superposition of various axial CSA tensors of different span. Whereas the symmetry-disturbing influence of molecular thermal motion at room temperature can always be considered a source of error, repeated single crystal structure analyses proved the latter hypothesis true and ^{29}Si solid state NMR spectroscopy a valuable tool complementing X-ray diffraction analyses.

Experimental Section

Synthesis of *N*,*N*-Diethyl-*N′*-(trimethylsilyl)-*N′*-phenylurea (1): To a solution of *N*-(trimethylsilyl)diethylamine (10.8 g, 74.4 mmol) in hexane (50 mL), which was stirred in a 15 °C water bath, phenyl isocyanate (9.32 g, 78.3 mmol) was added dropwise within a few minutes and stirring was continued for 3 h. Within this time some white crystalline precipitate formed (1.38 g, 3.6 mmol, 4.8% of **2**, as identified later), which was filtered off. Upon removal of the volatiles from the filtrate under reduced pressure product **1** remains in the flask as a viscous yellowish oil. NMR spectroscopy indicated sufficient purity for further reactions. (Yield: 18.6 g, 70.5 mmol, 95%). NMR spectra of **1** exhibit broadened signals originating from configurational exchange processes at the urea moiety. ^{1}H NMR (400.13 MHz, $CDCl_3$, 22 °C): δ = 0.2 [br. s, 9 H, $Si(CH_3)_3$], 0.84 (br. s, 6 H, NCH_2CH_3), 3.11 (br. s, 4 H, CH_2), 6.9–7.3 (3m, 4 H, 2 H, 4 H, Ph) ppm. ^{13}C NMR (100.62 MHz, $CDCl_3$, 22 °C): δ = –0.1 [-$Si(CH_3)_3$], 12.2 (NCH_2CH_3), 41.5 (CH_2), 124.2, 127.0, 128.4, 143.4 (Ph), 162.5 (C=O) ppm. ^{29}Si NMR (79.5 MHz, $CDCl_3$, 22 °C): δ = 8.5 ppm (br.).

This compound is very sensitive towards hydrolysis. Although stored in a sealed Schlenk flask, some crystals of the *N*,*N*-diethyl-*N′*-phenylurea, obviously liberated by traces of moisture, formed upon storage of the remaining product for some weeks. The solid-state structure of *N*,*N*-diethyl-*N′*-phenylurea was confirmed X-ray crystallographically. CCDC-743688, crystal dimensions 0.40 × 0.12 × 0.04 mm, $C_{11}H_{16}N_2O$, M_r = 192.26, T = 90(2) K, orthorhombic, space group *Pbcn*, a = 15.1284(8), b = 8.8584(4), c = 16.3355(8) Å, V = 2189.18(19) Å^3, Z = 8, $\rho_{calcd.}$ = 1.167 Mg m^{-3}, μ(Mo-K_α) = 0.076 mm^{-1}, F(000) = 832, $2\theta_{max}$ = 52.0°, 16958 collected reflections, 2139 unique reflections (R_{int} = 0.0654), 132 parameters, S = 1.004, R_1 = 0.0391 [$I > 2\sigma(I)$], wR_2(all data) = 0.0951, max./min. residual electron density +0.188/–0.225 e Å^{-3}.

Synthesis of Compound 2: To a solution of *N*-(trimethylsilyl)diethylamine (3.79 g, 26.1 mmol) in hexane (50 mL), which was stirred in a 15 °C water bath, phenyl isocyanate (6.21 g, 52.2 mmol) was added dropwise within a few minutes and stirring was continued for further 15 min. Within this time precipitation of **2** commenced. The mixture was stored at room temperature overnight, whereupon the solid product was filtered off, washed with hexane (20 mL) and dried in vacuo; yield 7.96 g, 20.8 mmol, 79.7%; m.p. 112 °C. $C_{21}H_{29}N_3O_2Si$ (383.56): calcd. C 65.76, H 7.62, N 10.96; found C 66.19, H 7.26, N 10.99. ^{1}H NMR (400.13 MHz, $CDCl_3$, 22 °C): δ = 0.21 [s, 9 H, $Si(CH_3)_3$], 0.54 (br. s, 6 H, NCH_2CH_3), 2.72 (br. s, 4 H, CH_2), 6.9–7.3 (3m, 4 H, 2 H, 4 H, Ph) ppm. ^{13}C NMR (100.62 MHz, $CDCl_3$, 22 °C): δ = –0.1 [-$Si(CH_3)_3$], 11.7 (NCH_2CH_3), 41.3 (CH_2), 125.8, 126.0, 126.1, 128.3, 129.0, 129.6, 140.6, 141.1 (Ph), 156.3, 161.3 (C=O) ppm. ^{29}Si NMR (79.5 MHz, $CDCl_3$, 22 °C): δ = 12.4 ppm. X-ray structure analysis of **2**. CCDC-743689, crystal dimensions 0.30 × 0.10 × 0.03 mm, $C_{21}H_{29}N_3O_2Si$, M_r = 383.56, T = 100(2) K, monoclinic, space group $P2_1/c$, a = 17.3226(7), b = 6.3823(2), c = 20.2088(7) Å, β = 111.396(2)°, V = 2080.26(13) Å^3, Z = 4, $\rho_{calcd.}$ = 1.225 Mg m^{-3}, μ(Mo-K_α) = 0.133 mm^{-1}, F(000) = 824, $2\theta_{max}$ = 50.0°, 13391 collected reflections, 3668 unique reflections (R_{int} = 0.0563), 249 parameters, S = 0.963, R_1 = 0.0426 [$I > 2\sigma(I)$], wR_2(all data) = 0.0925, max./min. residual electron density +0.263/–0.265 e Å^{-3}.

Synthesis of Tris-κ-*O*,*N′*-(*N*,*N*-diethyl-*N′*-phenylureato)siliconium Chloride (3-Cl): To a solution of **1** (17.8 g, 67.4 mmol) in chloroform (30 mL), which was stirred in a 15 °C water bath, $SiCl_4$ (3.82 g, 22.5 mmol) was added dropwise within a few minutes and stirring was continued for further 2 h. The color of the solution slowly changed from colorless via yellow to brownish-red. The volatiles were removed under reduced pressure and the remaining viscous oil was dissolved in THF (50 mL), whereupon crystallization of **3s-Cl** commenced overnight. After 24 h the solid was filtered off, washed with THF (3 × 5 mL) and dried in a vacuum. (Yield: 3.33 g, 5.23 mmol, 23%). This compound decomposes without melting when heated up to 300 °C in a sealed capillary. $C_{33}H_{45}ClN_6O_3Si$ (637.29): calcd. C 62.20, H 7.12, N 13.19; found C 61.85, H 7.11, N 12.99. The NMR spectra of a solution of **3-Cl** in $CDCl_3$ exhibit sets of signals corresponding to a mixture of the isomeric cations **3s⁺** and **3a⁺** in solution. The ^{1}H NMR spectrum exhibits various superimposed triplets in the range 0.6–1.4 ppm originating from the ethyl-CH_3 groups and quartets in the range 2.8–3.6 ppm for the CH_2 groups. Even less informative is the part of the aromatic proton signals. The ^{13}C NMR spectroscopic data, however, clearly show the presence of 3 small signals of equal intensity for **3a⁺** and, in the same chemical shift range, one intense signal for **3s⁺** in distinct parts of the spectrum, whereas the chemical shift range of the phenyl-*o*,*m*,*p*-carbon atoms is characterized by various superimposed signals (125.0, 125.7, 126.3, 126.6, 127.0, 127.8, 128.4, 129.2, 129.4, 129.7 ppm). For clarity reasons selected ^{13}C NMR spectroscopic data are presented in Table 5.

Table 5. ^{13}C NMR spectroscopic data of **3-Cl** (chemical shift δ in ppm) in $CDCl_3$ solution at 22 °C.

δ for **3s⁺**	δ for **3a⁺**	Moiety
12.8, 13.7	12.6, 12.9 (2 ×), 13.1, 13.4, 14.0	CH_3
41.4, 44.1	41.3, 41.6, 42.1, 43.5, 44.1 (2 ×)	CH_2
137.7	137.1, 137.5, 138.2	Ph-*ipso*
160.2	159.6, 159.7, 160.8	C=O

^{29}Si NMR (79.5 MHz, $CDCl_3$, 22 °C): δ = –168.2, –169.7 ppm, similar intensity. ^{29}Si NMR (79.5 MHz, solid state, CP, ν_{spin} = 4 kHz): δ_{iso} = –165.9 ppm.

X-ray Crystal Structure Analysis of 3s-Cl (structure C): CCDC-743692, crystal dimensions 0.38 × 0.12 × 0.08 mm, $C_{33}H_{45}ClN_6O_3Si$, M_r = 637.29, T = 100(2) K, trigonal, space group *P*3, a = b = 20.1088(3), c = 14.5184(5) Å, V = 5084.2(2) Å^3, Z = 6, $\rho_{calcd.}$ = 1.249 Mg m^{-3}, μ(Mo-K_α) = 0.190 mm^{-1}, F(000) = 2040, $2\theta_{max}$ = 50.0°, 33245 collected reflections, 10598 unique reflections (R_{int} = 0.0665), 793 parameters, S = 0.993, Flack parameter –0.03(5), R_1 = 0.0493 [$I > 2\sigma(I)$], wR_2(all data) = 0.0966, max./min. residual electron density +0.448/–0.302 e Å^{-3}.

In an alternative attempt, **3s-Cl** was obtained from the reaction of bis(diethylamino)dichlorosilane with phenyl isocyanate: To a solution of bis(diethylamino)dichlorosilane (2.50 g, 10.3 mmol) in THF (20 mL) phenyl isocyanate (2.45 g, 20.6 mmol) was added dropwise. From the clear solution white crystals formed within one day upon storage at room temperature. The supernatant was decanted and the crystals were briefly dried in vacuo. Yield: 1.13 g. This product, however, consisted of various crystalline compounds as recognized by ^{29}Si solid state NMR spectroscopy (CP/MAS, ν_{spin} = 4 kHz), signals at δ_{iso} = –165.9, –164.1 ppm), two of which were identified crystallographically as **3s-Cl·THF·(PhNCO)$_3$ (structure A)** and **3s-Cl (structure B)**.

X-ray Crystal Structure Analysis of 3s-Cl·THF·(PhNCO)$_3$ (structure A): CCDC-743690, crystal dimensions 0.35 × 0.30 × 0.25 mm, $C_{58}H_{68}ClN_9O_7Si$, M_r = 1066.75, T = 150(2) K, trigonal, space group *R*3*c*, a = b = 11.8203(1), c = 70.3118(14) Å, V = 8507.8(2) Å^3, Z = 6, $\rho_{calcd.}$ = 1.249 Mg m^{-3}, μ(Mo-K_α) = 0.148 mm^{-1}, F(000) = 3396, $2\theta_{max}$ = 52.0°, 21647 collected reflections, 3623 unique reflections (R_{int} = 0.0293), 237 parameters, S = 1.067, Flack parameter 0.03(7), R_1 = 0.0322 [$I > 2\sigma(I)$], wR_2(all data) = 0.0784, max./min. residual electron density +0.288/–0.238 e Å^{-3}.

X-ray Crystal Structure Analysis of 3s-Cl (structure B): CCDC-743691, crystal dimensions 0.45 × 0.30 × 0.25 mm, $C_{33}H_{45}ClN_6O_3Si$, M_r = 637.29, T = 150(2) K, trigonal, space group $P31c$, $a = b$ = 12.0280(6), c = 14.3543(14) Å, V = 1798.5(2) Å^3, Z = 2, $\rho_{\text{calcd.}}$ = 1.177 Mg m^{-3}, μ(Mo-K_α) = 0.179 mm^{-1}, F(000) = 680, $2\theta_{\max}$ = 50.0°, 6127 collected reflections, 2109 unique reflections (R_{int} = 0.0402), 135 parameters, S = 1.023, Flack parameter 0.00(10), R_1 = 0.0371 [$I > 2\sigma(I)$], wR_2(all data) = 0.0852, max./min. residual electron density +0.167/–0.180 e Å^{-3}.

Supporting Information (see also the footnote on the first page of this article): Color representations of the six independent cations **3s⁺** of **structure C** of **3s-Cl**.

Acknowledgments

TU Bergakademie Freiberg and the Deutsche Forschungsgemeinschaft (DFG) are acknowledged for financial support of this work.

---

[1] Selected reviews on hypercoordinate silicon chemistry: a) D. Kost, I. Kalikhman, *Acc. Chem. Res.* **2009**, *42*, 303–314; b) D. Kost, I. Kalikhman, *Adv. Organomet. Chem.* **2004**, *50*, 1–106; c) R. Tacke, M. Pülm, B. Wagner, *Adv. Organomet. Chem.* **1999**, *44*, 221–273; d) C. Chuit, R. J. P. Corriu, C. Reye, J. C. Young, *Chem. Rev.* **1993**, *93*, 1371–1448; e) R. J. P. Corriu, C. Guerin, J. J. E. Moreau, in: *Chem. Org. Silicon Compd.* (Eds: S. Patai, Z. Rappoport), Wiley, Chichester, **1989**, vol. 1, pp. 305–370; f) R. J. P. Corriu, J. C. Young, in: *Chem. Org. Silicon Compd.* (Eds: S. Patai, Z. Rappoport), Wiley, Chichester, **1989**, vol. 2, pp. 1241–1288.

[2] For recent publications on hexacoordinate silicon complexes see for example: a) A. Kämpfe, E. Kroke, J. Wagler, *Eur. J. Inorg. Chem.* **2009**, 1027–1035; b) K. Lippe, D. Gerlach, E. Kroke, J. Wagler, *Organometallics* **2009**, *28*, 621–629; c) G. W. Fester, J. Wagler, E. Brendler, U. Böhme, D. Gerlach, E. Kroke, *J. Am. Chem. Soc.* **2009**, *131*, 6855–6864; d) S. Metz, C. Burschka, R. Tacke, *Chem. Asian J.* **2009**, *4*, 581–586; e) S. Metz, C. Burschka, R. Tacke, *Organometallics* **2009**, *28*, 2311–2317; f) G. González-García, E. Álvarez, Á. Marcos-Fernández, J. A. Gutiérrez, *Inorg. Chem.* **2009**, *48*, 4231–4238; g) I. Kalikhman, E. Kertsnus-Banchik, B. Gostevskii, N. Kocher, D. Stalke, D. Kost, *Organometallics* **2009**, *28*, 512–516; h) S. Yakubovich, B. Gostevskii, I. Kalikhman, D. Kost, *Organometallics* **2009**, *28*, 4126–4132.

[3] a) J. Yang, J. G. Verkade, *J. Organomet. Chem.* **2002**, *651*, 15; b) H. H. Karsch, P. A. Schlüter, M. Reisky, *Eur. J. Inorg. Chem.* **1998**, 433–436; c) C.-W. So, H. W. Roesky, P. M. Gurubasawaraj, R. B. Oswald, M. T. Gamer, P. G. Jones, S. Blaurock, *J. Am. Chem. Soc.* **2007**, *129*, 12049–12054; d) H. H. Karsch, R. Richter, E. Witt, *J. Organomet. Chem.* **1996**, *521*, 185.

[4] a) G. W. Fester, J. Wagler, E. Brendler, U. Böhme, G. Roewer, E. Kroke, *Chem. Eur. J.* **2008**, *14*, 3164–3176; b) J. Wagler, U. Böhme, E. Brendler, S. Blaurock, G. Roewer, *Z. Anorg. Allg. Chem.* **2005**, *631*, 2907–2913.

[5] a) D. Gerlach, E. Brendler, T. Heine, J. Wagler, *Organometallics* **2007**, *26*, 234–240; b) R. Bertermann, A. Biller, M. Kaupp, M. Penka, O. Seiler, R. Tacke, *Organometallics* **2003**, *22*, 4104–4110.

[6] a) B. Theis, C. Burschka, R. Tacke, *Chem. Eur. J.* **2008**, *14*, 4618–4639; b) O. Seiler, C. Burschka, T. Fenske, T. Troegel, R. Tacke, *Inorg. Chem.* **2007**, *46*, 5419–5424; c) N. Kano, N. Nakagawa, Y. Shinozaki, T. Kawashima, Y. Sato, Y. Naruse, S. Inagaki, *Organometallics* **2005**, *24*, 2823–2826; d) J. Wagler, U. Böhme, E. Brendler, B. Thomas, S. Goutal, H. Mayr, B. Kempf, G. Ya. Remennikov, G. Roewer, *Inorg. Chim. Acta* **2005**, *358*, 4270–4286.

[7] a) J. Wagler, A. F. Hill, *Organometallics* **2008**, *27*, 6579–6586; b) J. Wagler, A. F. Hill, *Organometallics* **2007**, *26*, 3630–3632; c) A. R. Bassindale, S. J. Glynn, P. G. Taylor, N. Auner, B. Herrschaft, *J. Organomet. Chem.* **2001**, *619*, 132–140.

[8] I. Kalikhman, B. Gostevskii, M. Botoshansky, M. Kaftory, C. A. Tessier, M. J. Panzner, W. J. Youngs, D. Kost, *Organometallics* **2006**, *25*, 1252–1258.

[9] a) J. Herzfeld, A. E. Berger, *J. Chem. Phys.* **1980**, *73*, 6021; b) J. Mason, *Solid State Nucl. Magn. Reson.* **1993**, *2*, 285.

[10] a) *Calculation of NMR and EPR parameters: Theory and Applications* (Eds.: M. Kaupp, M. Bühl, V. G. Malkin), Wiley-VCH, **2004**; b) A. M. Köster, P. Calaminici, M. E. Casida, R. Flores-Moreno, G. Geudtner, A. Goursot, T. Heine, A. Ipatov, F. Janetzko, J. M. del Campo, S. Patchkovskii, J. Ulises Reveles, D. R. Salahub, A. Vela, *deMon2k* developers, **2006**; c) M. J. Frisch, G. W. Trucks, H. B. Schlegel, G. E. Scuseria, M. A. Robb, J. R. Cheeseman, J. A. Montgomery, Jr., T. Vreven, K. N. Kudin, J. C. Burant, J. M. Millam, S. S. Iyengar, J. Tomasi, V. Barone, B. Mennucci, M. Cossi, G. Scalmani, N. Rega, G. A. Petersson, H. Nakatsuji, M. Hada, M. Ehara, K. Toyota, R. Fukuda, J. Hasegawa, M. Ishida, T. Nakajima, Y. Honda, O. Kitao, H. Nakai, M. Klene, X. Li, J. E. Knox, H. P. Hratchian, J. B. Cross, V. Bakken, C. Adamo, J. Jaramillo, R. Gomperts, R. E. Stratmann, O. Yazyev, A. J. Austin, R. Cammi, C. Pomelli, J. W. Ochterski, P. Y. Ayala, K. Morokuma, G. A. Voth, P. Salvador, J. J. Dannenberg, V. G. Zakrzewski, S. Dapprich, A. D. Daniels, M. C. Strain, O. Farkas, D. K. Malick, A. D. Rabuck, K. Raghavachari, J. B. Foresman, J. V. Ortiz, Q. Cui, A. G. Baboul, S. Clifford, J. Cioslowski, B. B. Stefanov, G. Liu, A. Liashenko, P. Piskorz, I. Komaromi, R. L. Martin, D. J. Fox, T. Keith, M. A. Al-Laham, C. Y. Peng, A. Nanayakkara, M. Challacombe, P. M. W. Gill, B. Johnson, W. Chen, M. W. Wong, C. Gonzalez, J. A. Pople, *Gaussian 03*, Revision C.02, Gaussian, Inc., Wallingford, CT, **2004**; d) G. te Velde, F. M. Bickelhaupt, E. J. Baerends, C. Fonseca Guerra, S. J. A. van Gisbergen, J. G. Snijders, T. Ziegler, *J. Comput. Chem.* **2001**, *22*, 931; e) ADF 2008.01, *ADF User's Guide*, http://www.scm.com, SCM, Theoretical Chemistry, Vrije Universiteit, Amsterdam.

Received: August 12, 2009

DOI: 10.1002/ejic.200900806

The Tricarbonyliron Chalcogenolates $[(OC)_3Fe(\mu\text{-}ESi\mathit{t}Bu_3)]_2$ (E = S, Se, Te)

Theresa Kückmann,[a] Frauke Schödel,[a] Inge Sänger,[a] Michael Bolte,[a]
Matthias Wagner,[a] and Hans-Wolfram Lerner*[a]

Keywords: Sulfur / Selenium / Iron / Supersilyl chalcogenolates / [FeFe]-Hydrogenase

The tricarbonyliron thiolate and selenolate $[(OC)_3Fe(\mu\text{-}ESi\mathit{t}Bu_3)]_2$ (E = S, Se) were synthesized photochemically from the reaction of 2 equiv. of pentacarbonyliron with the dichalcogenides $\mathit{t}Bu_3Si–E_2–Si\mathit{t}Bu_3$ (E = S, Se). X-ray-quality crystals of the tricarbonyliron thiolate $[(OC)_3Fe(\mu\text{-}SSi\mathit{t}Bu_3)]_2$ (monoclinic, $P2_1/n$) and selenolate $[(OC)_3Fe(\mu\text{-}SeSi\mathit{t}Bu_3)]_2$ (monoclinic, $P2_1/n$) were grown from benzene. The cyclic voltammograms of $[(OC)_3Fe(\mu\text{-}ESi\mathit{t}Bu_3)]_2$ (E = S, Se, Te) resemble each other. Electrochemical reduction at potential below –2.2 V or reduction of $[(OC)_3Fe(\mu\text{-}ESi\mathit{t}Bu_3)]_2$ (E = S, Se, Te) with Na or K led to degradation of the complex core with the formation of the chalcogenolates $[ESi\mathit{t}Bu_3]^-$ (E = S, Se, Te). The dichalcogenides $\mathit{t}Bu_3Si–E_2–Si\mathit{t}Bu_3$ (E = Se, Te) are accessible by the reaction of $Na[ESi\mathit{t}Bu_3]$ with oxygen. However, the disulfide $\mathit{t}Bu_3Si–S_2–Si\mathit{t}Bu_3$ (monoclinic, $P2_1/c$) which is used in the synthesis of tricarbonyliron thiolates $[(OC)_3Fe(\mu\text{-}ESi\mathit{t}Bu_3)]_2$ as starting material, was prepared from S_2Cl_2 and $Na[Si\mathit{t}Bu_3]$. Depending on the solvent used for crystallization, the sodium supersilyl chalcogenolates $Na[ESi\mathit{t}Bu_3]$ (E = S, Se) form dimeric or tetrameric structures in the solid state. Single crystals of the dimeric thiolate $[Na(thf)_2SSi\mathit{t}Bu_3]_2$ (monoclinic, $P2_1/c$) were obtained from thf at –25 °C whereas crystals suitable for X-ray diffraction of tetrameric chalcogenolates $[Na(thf)ESi\mathit{t}Bu_3]_4$ (E = S, Se) were grown from hexane at –25 °C.

Introduction

In transition metal complexes, the electronic nature of the ligands often plays a decisive role in determining the electronic situation at the metal center. Chalcogen-based ligands offer a variety of possible binding modes, with chalcogenide E^{2-}, dichalcogenide E_2^{2-} and chalcogenolate RE^- being common.[1] In addition, chalcogenides and chalcogenolates as well as isoelectronic phosphanediides[2] are often found bridging two or more metal ions. Normally, transition metal complexes possess $6e^-$ thiolate ligands in a μ^3-binding mode. Recently however, we have shown that the anion of the mixed-valence Mn(I/II) complex $Na(thf)_6[(OC)_3Mn(\mu\text{-}SSi\mathit{t}Bu_3)_3MnSSi\mathit{t}Bu_3]$ contains a terminal thiolate ligand with a linear Mn–S–Si unit. The prerequisite for six-electron donation (2 σ- and 4 π-electrons) comparable with Cp^- is thus fulfilled.[3]

The flexibility of chalcogenides and chalcogenolates is also manifested in a number of biological systems, most notably iron–sulfur clusters such as the $[Fe(Cys)_4]^{2-}$ active site in rubredoxin, the $[Fe_2S_2(Cys)_4]^{4-}$ and $[Fe_4S_4(Cys)_4]^{4-}$ sites in ferrodoxins, Fe_3S_4-proteins as $[Fe_3S_4(Cys)_3]^{5-}$, mononitrogenase component I $[Fe_8S_7(Cys)_6]^{4-}$, and prismane proteins $[Fe_6S_6(L)_6]^{n-}$ (L = ligand, Cys = thiolate coordination from cysteinate). It is interesting to note that the active site of [FeFe]-hydrogenases resembles $[(OC)_3Fe(\mu\text{-}SR)]_2$ derivatives, which consist of a butterfly Fe_2S_2 cluster core.[4]

Chalcogen-based systems are potentially redox-active. This redox activity can be exploited in the synthesis of transition metal complexes, making oxidative addition of dichalcogenides RE_2R to low-oxidation-state metal centers a viable route to new coordination compounds.[5] When the advantages of bulky silyl groups and chalcogenolates are combined, intriguing systems can be studied. In a preliminary study we have shown that the complex $[(OC)_3Fe(\mu\text{-}TeSi\mathit{t}Bu_3)]_2$ is available by irradiation with a domestic fluorescent lamp of a 2:1 benzene solution of $Fe(CO)_5$ in the presence of ditelluride $\mathit{t}Bu_3Si–Te_2–Si\mathit{t}Bu_3$.[6]

In this paper, the synthesis of $[(OC)_3Fe(\mu\text{-}ESi\mathit{t}Bu_3)]_2$ (E = S, Se) by irradiation of $[Fe(CO)_5]$ in the presence of dichalcogenides $\mathit{t}Bu_3Si–E_2–Si\mathit{t}Bu_3$ (E = S, Se, Te) is described. The results of electrochemical investigation of $[(OC)_3Fe(\mu\text{-}ESi\mathit{t}Bu_3)]_2$ (E = S, Se, Te) are noted. In addition we report here the crystal structures of $[(OC)_3Fe(\mu\text{-}ESi\mathit{t}Bu_3)]_2$ (E = S, Se), the disulfide $\mathit{t}Bu_3Si–S_2–Si\mathit{t}Bu_3$, the dimeric sodium thiolate $[Na(thf)_2(SSi\mathit{t}Bu_3)]_2$, and the tetrameric sodium chalcogenolates $[Na(thf)(ESi\mathit{t}Bu_3)]_4$ (E = S, Se).

Results and Discussion

Synthesis of the Supersilylated Chalcogenolates $NaESi\mathit{t}Bu_3$ and Dichalcogenides $\mathit{t}Bu_3Si–E_2–Si\mathit{t}Bu_3$ (E = S, Se)

As we noted previously,[6] due to the lower electronegativity of the higher chalcogens (S, Se, Te), it is not practical

---

[a] Institut für Anorganische Chemie, Goethe-Universität Frankfurt am Main,
Max-von-Laue-Straße 7, 60438 Frankfurt am Main, Germany
Fax: +49-69-79829260
E-mail: lerner@chemie.uni-frankfurt.de

to prepare silyl thiolates, selenolates, and tellurolates by the same routes as applied for silanolates[7,8] (siloxides). When elemental chalcogens (S, Se and Te) are treated with a slight excess of sodium silanides $\mathrm{NaSiR}t\mathrm{Bu}_2$[9,10] in thf, the silyl chalcogenolates $\mathrm{Na[ESiR}t\mathrm{Bu}_2]$ (R = *t*Bu, Ph; E = S, Se, Te) are formed cleanly.[6] The reactions with sulfur are faster than with selenium and tellurium, but in all cases conversion is complete after stirring overnight. Concentration of a thf solution of $\mathrm{Na[SSi}t\mathrm{Bu}_3]$ leads to the deposition of colorless crystals of the sodium thiolate $[\mathrm{Na(thf)_2SSi}t\mathrm{Bu}_3]_2$. If, however, the chalcogenolates $[\mathrm{Na(thf)_2ESi}t\mathrm{Bu}_3]_2$ (E = S, Se) are not recrystallized from thf, but from a non-coordinating solvent as hexane, crystals displaying a tetrameric, monosolvated structure $[\mathrm{Na(thf)ESi}t\mathrm{Bu}_3]_4$ (E = S, Se) can also be isolated for these chalcogenolates.

The dichalcogenides $t\mathrm{Bu_3Si{-}E_2{-}Si}t\mathrm{Bu}_3$ (E = Se, Te) are accessible by reaction of the sodium chalcogenolates $\mathrm{Na[ESi}t\mathrm{Bu}_3]$ with oxygen. The disulfide $t\mathrm{Bu_3Si{-}S_2{-}Si}t\mathrm{Bu}_3$, however, can be prepared by another route, which is independent of the oxidation of thiolate. When a solution of the sodium silanide $\mathrm{Na[Si}t\mathrm{Bu}_3]$[9] in thf is treated with $\mathrm{S_2Cl_2}$, disulfide $t\mathrm{Bu_3Si{-}S_2{-}Si}t\mathrm{Bu}_3$ is formed rapidly and in good yield.

Syntheses of the Complexes $[(\mathrm{OC})_3\mathrm{Fe}(\mu\text{-}\mathrm{ESi}t\mathrm{Bu}_3)]_2$ [E = S (1), Se (2), Te (3)]

Oxidative addition of disilyl dichalcogenides to transition metal centers was investigated as a suitable route. In the literature, this method has been successfully applied to the synthesis of transition metal chalcogenolate complexes.[5,6] In this study $[\mathrm{Fe(CO)_5}]$ was chosen for oxidative addition studies since it is easily activated photochemically, and since its iron center is in a low oxidation state. When a 2:1 benzene solution of $[\mathrm{Fe(CO)_5}]$ and ditelluride $t\mathrm{Bu_3Si{-}Te_2{-}Si}t\mathrm{Bu}_3$ is irradiated with a domestic fluorescent lamp, the deep blue color of $t\mathrm{Bu_3Si{-}Te_2{-}Si}t\mathrm{Bu}_3$ turns to deep red over the course of 8 h.[6] If the same procedure is followed using diselenide $t\mathrm{Bu_3Si{-}Se_2{-}Si}t\mathrm{Bu}_3$ and $[\mathrm{Fe(CO)_5}]$ the end result is the homologous complex **2** with bridging selenolates ligands, but the reaction takes two weeks rather than 8 h for completion. The reaction of the colorless disulfide $t\mathrm{Bu_3Si{-}S_2{-}Si}t\mathrm{Bu}_3$ with $[\mathrm{Fe(CO)_5}]$ to obtain deep red **1** is not complete even after six months. Thereby the thiolate complex **1** was synthesized in 75% yield (Scheme 1). Irradiation with a more powerful lamp does speed up the rate of reaction, but the reaction is not as specific, and significant amounts of by-product are obtained.

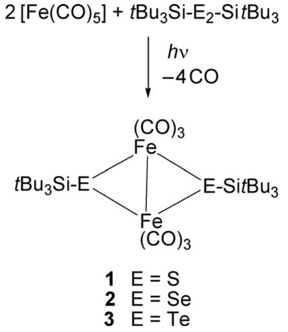

Scheme 1.

Obviously, the reactivity of the dichalcogenides differs significantly. Based on this evidence, the rate-determining step in these reactions is probably not the conversion of $[\mathrm{Fe(CO)_5}]$, but appears to involve the activation of the chalcogen–chalcogen bond. This conclusion is consistent with theoretical studies of the addition of $\mathrm{R{-}E_2{-}R}$ (E = S, Se, Te) to $\mathrm{Pd^0}$ and $\mathrm{Pt^0}$ species.[11] It was demonstrated that the energetic barrier to oxidative addition is smallest for ditellurides and largest for disulfides, all else being equal. This can be attributed to the weaker Te–Te bond compared to the S–S bond. Conversely, formation of $\mathrm{M(SR)_2}$ (M = Pd, Pt) was found to be more exothermic than formation of $\mathrm{M(TeR)_2}$. For both activation barrier and exothermicity, the selenium species were found to lie between corresponding sulfur and tellurium compounds.

When considering the carbonyl IR stretching frequencies of the complexes **1**, **2**, and **3**, it is immediately apparent that the bands observed for the tellurolate complex **3** are shifted to lower wavenumbers compared to the thiolate and selenolate species **1** and **2**, which display similar spectra (Table 1). Apparently, the tellurolate is the strongest donor in this series. The carbonyl stretching frequencies reported in the literature for complexes of the type $[(\mathrm{OC})_3\mathrm{Fe}(\mu\text{-}\mathrm{ER})]_2$ also seem to follow this trend, but no homologous series has been published, so comparisons are hard to draw.[12–15]

Table 1. Carbonyl IR stretching frequencies [cm^{-1}] for **1**, **2**, and **3**.

1	2	3
2068	2066	2048
2035	2028	2016
1999	–	–
1989	1982	1977

The cyclic voltammograms of **1**, **2**, and **3** resemble each other. The electrochemical parameters of the redox events exhibited by **1**, **2**, and **3** are summarized in Table 2. The cyclic voltammograms of **1**, **2**, and **3** display two reduction processes. However, in all cases the processes are not chemically reversible, as shown in Figure 1. Electrochemical reduction at potential below –2.2 V of **3** led to degradation of the complex core with the formation of the tellurolate $[\mathrm{TeSi}t\mathrm{Bu}_3]^-$ and a black precipitate of elemental iron. This is confirmed by the results of chemical reduction of **1**, **2**,

Table 2. Formal electrode potentials (given in V, vs. $\mathrm{Cp_2Fe/Cp_2Fe^+}$) for the redox processes of **1**, **2**, and **3** in thf solutions.

	1. red	1. ox	2. red	2. ox
1	–1.63	–0.86	–2.09	–1.87
2	–1.69	–0.93	–1.99	–1.85
3	–1.74	–0.86	–2.01	–1.87

and **3** with Na and K. Thereby obtained chalcogenolates [ESi*t*Bu$_3$]$^-$ (E = S, Se, Te) were monitored by NMR spectroscopy.

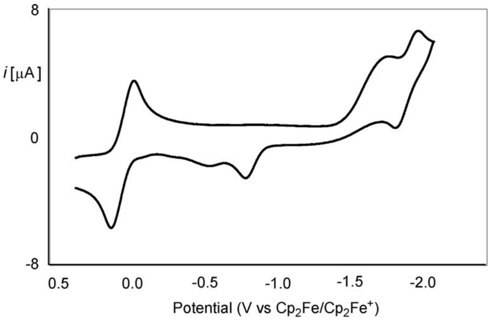

Figure 1. Cyclic voltammogram of the tricarbonyliron tellurolate complex **3** in 0.1 M *n*Bu$_4$NPF$_6$ thf solution, scan rate: 100 mV/s.

Structure of the Sodium Chalcogenolates [Na(thf)$_2$(SSi*t*Bu$_3$)]$_2$ and [Na(thf)(SSi*t*Bu$_3$)]$_4$ (E = S, Se)

Figures 2 and 3 represent the molecular structures of the sodium thiolates [Na(thf)$_2$SSi*t*Bu$_3$]$_2$ (monoclinic, $P2_1/c$) and [Na(thf)SSi*t*Bu$_3$]$_4$ (monoclinic, $P2_1$), respectively; the selected bond lengths and angles are listed in the corresponding captions.

The sodium chalcogenolates [Na(thf)SSi*t*Bu$_3$]$_4$ and [Na(thf)SeSi*t*Bu$_3$]$_4$[16] are isostructural. Unlike [NaOSi*t*Bu$_3$]$_4$[7] and [NaOSiPh*t*Bu$_2$]$_4$,[7] which were crystallized from heptane and are unsupported by external donor, each sodium atom in [Na(thf)SSi*t*Bu$_3$]$_4$ and [Na(thf)SeSi*t*Bu$_3$]$_4$ is bound to one molecule of thf. The heterocubane structure of the chalcogenolates [Na(thf)SSi*t*Bu$_3$]$_4$ and [Na(thf)SeSi*t*Bu$_3$]$_4$ is much closer to a regular cube than that of the homologous siloxide [NaOSi*t*Bu$_3$]$_4$,[7] but the structure of [Na(thf)SSi*t*Bu$_3$]$_4$ has a somewhat less regular cubane core than [Na(thf)SSiPh*t*Bu$_2$]$_4$,[6] with average Na–S–Na angles of 83.8(1)° and average S–Na–S angles of 95.8(1)°. The Na–S distances are longer than in [Na(thf)$_2$SSi*t*Bu$_3$]$_2$, at an average of 2.816(3) Å, which is probably due to the steric overloading in this compound. The Si–C distances vary only little and are in the expected range.[17]

X-ray-quality crystals of the sodium thiolate [Na(thf)$_2$SSi*t*Bu$_3$]$_2$ were obtained from thf. A planar four-membered S$_2$Na$_2$ ring builds the core of this structure (Figure 2). This motif has also been observed in the solid-state structures of [Na(thf)$_2$ESi*t*Bu$_3$]$_2$ (E = Se, Te) and [Na(thf)$_2$SeSiPh*t*Bu$_2$]$_2$.[6] Only half of the dimer is found in the asymmetric unit; it is related to its second half via a twofold rotational axis. The Na–S–Na angles [85.22(8)°] are larger and the S–Na–S angles [94.78(8)°] are smaller than in tetrameric [Na(thf)SSi*t*Bu$_3$]$_4$, but the Na–S distances, 2.738(3) and 2.747(3) Å are in the same range for both compounds. The coordination spheres around the sodium atoms in [Na(thf)$_2$SSi*t*Bu$_3$]$_2$ are distorted. The small S–Na–S and O(thf)–Na–O(thf) angles [the latter is 88.7(2)°] are compensated for by larger S–Na–O(thf) angles, which range between 101.52(14)° and 137.20(19)°. All other structural parameters are in the same range as for [Na(thf)SSi*t*Bu$_3$]$_4$.

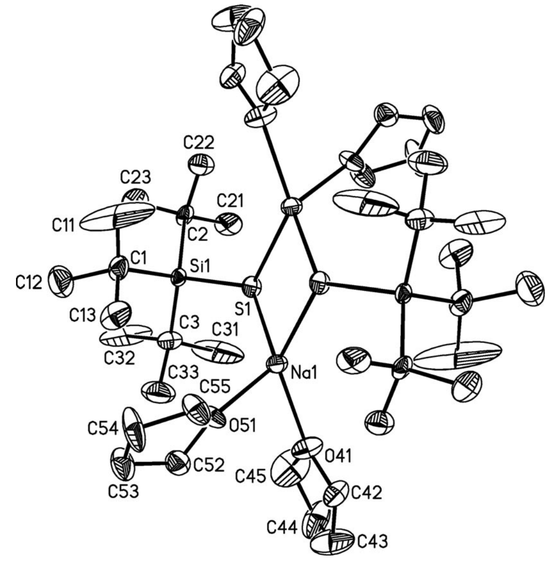

Figure 2. Plot of [Na(thf)$_2$SSi*t*Bu$_3$]$_2$ showing the atomic numbering scheme. The displacement ellipsoids are drawn at the 50% probability level. H atoms have been omitted for clarity. Selected bond lengths [Å] and angles [°]: Na(1)–O(51) 2.298(5), Na(1)–O(41) 2.354(5), Na(1)–S(1) 2.738(3), Na(1)–S(1)#1 2.747(3), Na(1)–Na(1)#1 3.713(5), S(1)–Si(1) 2.086(2), S(1)–Na(1)#1 2.747(3), Na(1A)–O(41A) 2.312(5), Na(1A)–O(51A) 2.362(5), Na(1A)–S(1A) 2.727(3), Na(1A)–S(1A)#2 2.755(3), Na(1A)–Na(1A)#2 3.722(5), S(1A)–Si(1A) 2.094(2), S(1A)–Na(1A)#2 2.755(3), O(51)–Na(1)–O(41) 88.99(19), O(51)–Na(1)–S(1) 127.29(17), O(41)–Na(1)–S(1) 111.53(16), O(51)–Na(1)–S(1)#1 101.52(14), O(41)–Na(1)–S(1)#1 137.20(19), S(1)–Na(1)–S(1)#1 94.78(8), O(51)–Na(1)–Na(1)#1 126.47(15), O(41)–Na(1)–Na(1)#1 144.43(18), Si(1)–S(1)–Na(1) 127.24(11), Si(1)–S(1)–Na(1)#1 121.61(10), Na(1)–S(1)–Na(1)#1 85.22(8), O(41A)–Na(1A)–S(1A) 127.93(18), O(51A)–Na(1A)–S(1A) 112.17(17), O(41A)–Na(1A)–S(1A)#2 101.80(15), O(51A)–Na(1A)–S(1A)#2 136.34(18), S(1A)–Na(1A)–S(1A)#2 94.48(9), O(41A)–Na(1A)–Na(1A)#2 127.00(16), O(51A)–Na(1A)–Na(1A)#2 144.29(18), Si(1A)–S(1A)–Na(1A) 126.48(11), Si(1A)–S(1A)–Na(1A)#2 121.70(11), Na(1A)–S(1A)–Na(1A)#2 85.52(9). Symmetry transformations used to generate equivalent atoms: #1 – x, –y + 1, –z #2 –x + 1, –y, –z + 1.

Structure of the Disulfide *t*Bu$_3$Si–S$_2$–Si*t*Bu$_3$

X-ray-quality crystals of the disulfide *t*Bu$_3$Si–S$_2$–Si*t*Bu$_3$ were grown from a hexane solution at ambient temperature. Selected bond lengths and angles for *t*Bu$_3$Si–S$_2$–Si*t*Bu$_3$ are found in the caption of Figure 4. The disulfide *t*Bu$_3$Si–S$_2$–Si*t*Bu$_3$ crystallizes in the monoclinic space group $P2_1/n$ with one half molecule in the asymmetric unit, which is related to its second half via a crystallographic inversion center in the middle of the S–S bond (Figure 4). The molecular structures of the dichalcogenides *t*Bu$_3$Si–E$_2$–Si*t*Bu$_3$ (E = S, Se, Te) are all quite similar. In *t*Bu$_3$Si–S$_2$–Si*t*Bu$_3$, the Si–S–S–Si chain is exactly *s-trans.* The corresponding torsional angle of 180° is mandated by the crystallographic inversion centers. The disulfide *t*Bu$_3$Si–S$_2$–Si*t*Bu$_3$ displays Si–S–S

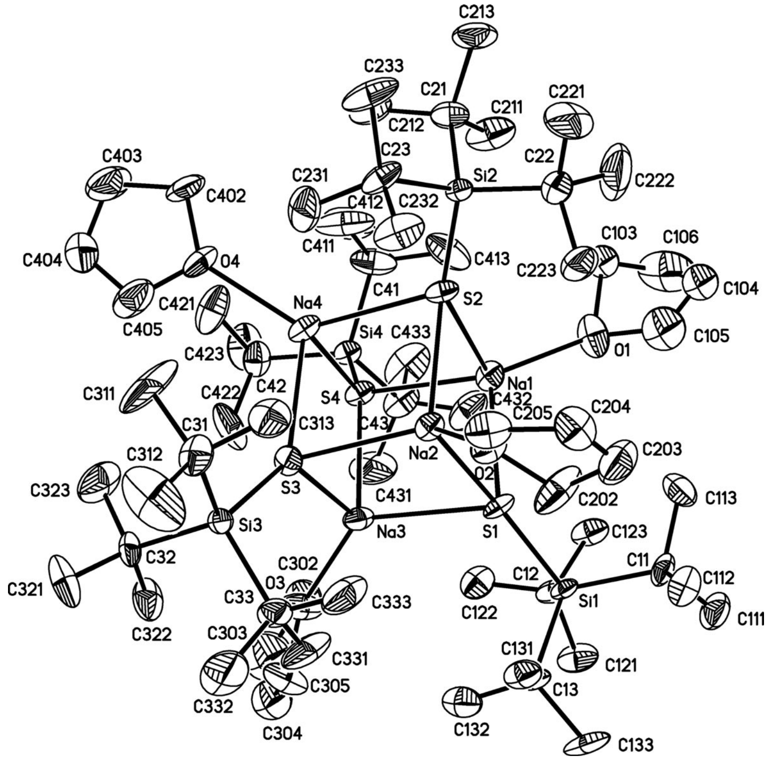

Figure 3. Plot of $[Na(thf)SSi\mathit{t}Bu_3]_4$ showing the atom numbering scheme. The displacement ellipsoids are drawn at the 50% probability level. H atoms have been omitted for clarity. Selected bond lengths [Å] and angles [°]: Na(1)–O(1) 2.330(6), Na(1)–S(4) 2.800(3), Na(1)–S(1) 2.806(3), Na(1)–S(2) 2.812(3), Na(2)–O(2) 2.280(5), Na(2)–S(3) 2.770(3), Na(2)–S(2) 2.783(3), Na(2)–S(1) 2.860(3), Na(2)–C(202) 3.063(9), Na(2)–Na(4) 3.717(3), Na(2)–Na(3) 3.737(4), Na(3)–O(3) 2.336(6), Na(3)–S(3) 2.782(3), Na(3)–S(1) 2.834(3), Na(3)–S(4) 2.859(3), Na(3)–Na(4) 3.824(3), Na(4)–O(4) 2.350(5), Na(4)–S(4) 2.795(3), Na(4)–S(2) 2.842(3), Na(4)–S(3) 2.851(3), S(1)–Si(1) 2.1130(18), S(2)–Si(2) 2.101(2), S(3)–Si(3) 2.115(2), S(4)–Si(4) 2.102(2), S(4)–Na(1)–S(1) 97.77(10), S(4)–Na(1)–S(2) 94.06(9), S(1)–Na(1)–S(2) 97.04(9), S(4)–Na(1)–Na(2) 93.15(9), S(3)–Na(2)–S(2) 98.77(9), S(3)–Na(2)–S(1) 96.02(9), S(2)–Na(2)–S(1) 96.45(8), S(3)–Na(3)–S(1) 96.32(9), O(3)–Na(3)–S(4) 113.3(2), S(3)–Na(3)–S(4) 94.50(8), S(1)–Na(3)–S(4) 95.78(9), S(4)–Na(4)–S(2) 93.51(9), S(4)–Na(4)–S(3) 94.41(8), S(2)–Na(4)–S(3) 95.54(9), Si(1)–S(1)–Na(1) 123.58(9), Si(1)–S(1)–Na(3) 113.24(9), Na(1)–S(1)–Na(3) 83.21(9), Si(1)–S(1)–Na(2) 150.23(9), Na(1)–S(1)–Na(2) 82.11(7), Na(3)–S(1)–Na(2) 82.02(8), Si(2)–S(2)–Na(2) 122.74(9), Si(2)–S(2)–Na(1) 143.57(11), Na(2)–S(2)–Na(1) 83.39(8), Si(2)–S(2)–Na(4) 120.20(9), Na(2)–S(2)–Na(4) 82.70(9), Na(1)–S(2)–Na(4) 85.18(9), Si(3)–S(3)–Na(2) 114.62(9), Si(3)–S(3)–Na(3) 125.18(10), Na(2)–S(3)–Na(3) 84.59(8), Si(3)–S(3)–Na(4) 144.39(10), Na(2)–S(3)–Na(4) 82.77(8), Na(3)–S(3)–Na(4) 85.49(8), Si(4)–S(4)–Na(4) 121.90(9), Si(4)–S(4)–Na(1) 116.78(10), Na(4)–S(4)–Na(1) 86.29(9), Na(4)–S(4)–Na(3) 85.11(8), Na(1)–S(4)–Na(3) 82.88(8).

angles smaller than 109°. The S–S bond in $\mathit{t}Bu_3Si{-}S_2{-}Si\mathit{t}Bu_3$ (2.106 Å) is somewhat longer than typical bond lengths for aryl and alkyl-substituted disulfides RS–SR (mean S–S distance for aryl disulfides: 2.050 Å; mean for alkyl disulfides: 2.024 Å).[18]

Structure of the Tricarbonyliron Thiolate and Selenolate 1 and 2

X-ray-quality crystals of the tricarbonyliron chalcogenolato complexes **1** and **2** were grown from benzene solutions at ambient temperature. Both carbonyl chalcogenolato complexes **1** and **2** (see Figures 5 and 6) crystallize in the monoclinic space group $P2_1/n$. The unit cell contains two formula units. The dinuclear complexes **1**, **2**, and **3** all adopt a butterfly-type structure in which each of the iron atoms is coordinated by three carbonyl ligands and two bridging chalcogenolates. The distorted octahedral coordination spheres are completed by an iron–iron bond. Selected bond lengths and angles for all three compounds are given in Table 3 and in the corresponding Figure captions.

The "butterfly" structural motif observed in **1**, **2**, and **3** is also found in other carbonyliron chalcogenolates although no other similar complex with a silyl chalcogenolate has yet been reported. The iron–iron distances reported in the literature for thiolate complexes of the type $[(CO)_3Fe(SR)]_2$[18] are in the same range as for **1**. The Fe–S distances, however, are somewhat shorter [average 2.54 Å vs. 2.607(2) Å]. This disparity can be attributed to the differences between the silyl substituents in **1** and the alkyl substituents in the literature complexes.[12–15] These general trends also hold true for selenolate and tellurolate derivatives, with similar Fe–Fe distances in the silyl and alkyl species, but with longer Fe–E bonds for the silyl chalcogenolates **2** and **3**. The exception is the thiolate complex bearing the bulky 2,4,6-triisopropylthiophenolate ligand, which displays a short Fe–Fe distance [2.466(2) Å] and Fe–S bonds [2.311(2)–2.321(2) Å] of roughly the same length as in **1**.[15]

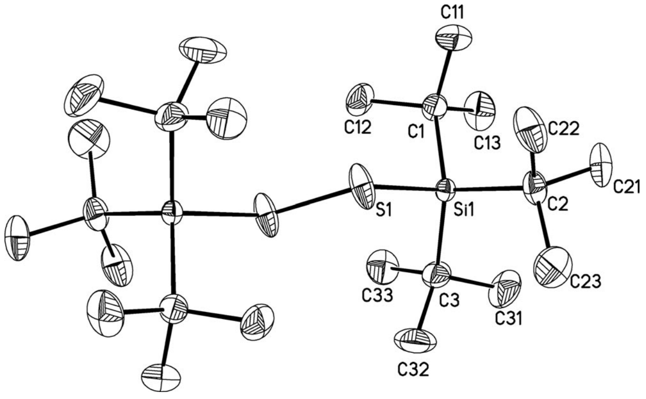

Figure 4. Plot of $tBu_3Si–S_2–SitBu_3$ showing the atom numbering scheme. The displacement ellipsoids are drawn at the 50% probability level. H atoms have been omitted for clarity. Selected bond lengths [Å] and angles [°]: Si(1)–C(3) 1.936(2), Si(1)–C(1) 1.938(2), Si(1)–C(2) 1.9453(19), Si(1)–S(1) 2.1781(8), S(1)–S(1)#1 2.1060(11), C(3)–Si(1)–C(1) 113.44(10), C(3)–Si(1)–C(2) 113.03(9), C(1)–Si(1)–C(2) 112.64(9), C(3)–Si(1)–S(1) 110.69(8), C(1)–Si(1)–S(1) 107.73(6), C(2)–Si(1)–S(1) 98.14(7), S(1)#1-S(1)–Si(1) 105.14(4). Symmetry transformations used to generate equivalent atoms: #1 $–x + 1, –y + 1, –z + 1$.

Conclusions

In summary, it has been shown that the tricarbonyliron thiolate and selenolate, **1** and **2**, can be cleanly prepared photochemically from the reaction of 2 equiv. of iron pentacarbonyl $[Fe(CO)_5]$ with the dichalcogenides $tBu_3Si–E_2–SitBu_3$ (E = S, Se). X-ray-quality crystals of the tricarbonyliron thiolate **1** and selenolate **2** were grown from benzene. The cyclic voltammograms of **1**, **2**, and **3** resemble each other and feature two redox processes. However, electrochemical reduction at potential below –2.2 V or chemical reduction with Na or K of **1**, **2**, and **3** led to the formation of the corresponding chalcogenolates $[ESitBu_3]^–$ (E = S, Se, Te). The dichalcogenides $tBu_3Si–E_2–SitBu_3$ (E = Se, Te), which are used in the synthesis of carbonyliron chalcogenolates **2** and **3** as starting material, are generally accessible by the reaction of $Na[ESitBu_3]$ with oxygen. However, the disulfide $tBu_3Si–S_2–SitBu_3$ can be prepared by another route from S_2Cl_2 and the sodium silanide $Na[SitBu_3]$. Depending on the solvent used for crystallization the sodium supersilyl chalcogenolates $Na[ESitBu_3]$ (E = S, Se) form dimeric or tetrameric structures in the solid state. Single crystals of the dimeric thiolate $[Na(thf)_2SSitBu_3]_2$ were obtained from thf at –25 °C whereas crystals suitable for X-ray diffraction of tetrameric chalcogenolates $[Na(thf)ESitBu_3]_4$ (E = S, Se) were grown from hexane at –25 °C (Table 4).

Experimental Section

General Remarks: All experiments were carried out under dry nitrogen or argon with strict exclusion of air and moisture using standard Schlenk techniques. $Na[SitBu_3]$,[19] $Na[SSitBu_3]$ (E = S, Se),[6] $tBu_3Si–E_2–SitBu_3$ (E = S, Se, Te)[6] and $[(OC)_3Fe(\mu\text{-}TeSitBu_3)]_2$[6] were prepared according to literature procedures. All other starting materials were purchased from commercial sources and used without further purification. The solvents (benzene, toluene, tetrahydrofuran) were distilled from sodium/benzophenone prior to use. C_6D_6 was dried with molecular sieves and stored under dry nitrogen.

The NMR spectra were recorded on a Bruker AM 250, a Bruker DPX 250, a Bruker Avance 300, and a Bruker Avance 400 spectrometer. The ^{29}Si NMR spectra were recorded using the INEPT

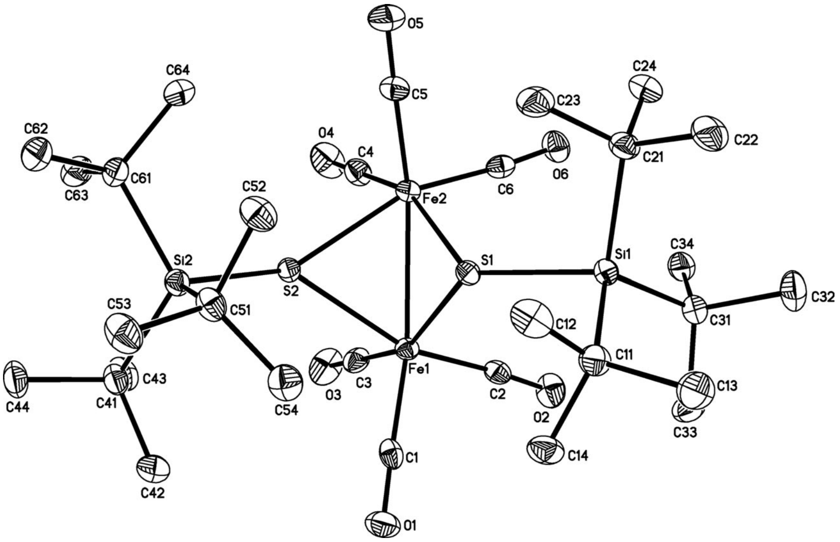

Figure 5. Plot of **1** showing the atom numbering scheme. The displacement ellipsoids are drawn at the 50% probability level. H atoms have been omitted for clarity. Selected bond lengths [Å] and angles [°]: Fe(2)–S(1) 2.3031(13), Fe(1)–S(1) 2.3176(12), Fe(1)–S(2) 2.3165(12), Fe(2)–S(2) 2.3220(12), Fe(1)–C(2) 1.765(5), Fe(1)–C(3) 1.780(5), Fe(1)–C(1) 1.812(5), Fe(2)–C(6) 1.765(5), Fe(2)–C(4) 1.782(6), Fe(2)–C(5) 1.792(4), C(1)–O(1) 1.153(5), C(2)–O(2) 1.164(5), C(3)–O(3) 1.155(6), C(4)–O(4) 1.154(6), C(5)–O(5) 1.164(5), C(6)–O(6) 1.166(5), Si(1)–S(1)–Fe(2) 131.50(6), Si(1)–S(1)–Fe(1) 133.53(6), Si(2)–S(2)–Fe(1) 133.57(7), Si(2)–S(2)–Fe(2) 140.23(6), C(2)–Fe(1)–C(3) 87.7(2), C(2)–Fe(1)–C(1) 95.8(2), C(3)–Fe(1)–C(1) 99.2(2), C(2)–Fe(1)–Fe(2) 104.00(14), C(3)–Fe(1)–Fe(2) 99.83(15), C(1)–Fe(1)–Fe(2) 152.93(14), C(6)–Fe(2)–C(4) 88.6(2), C(6)–Fe(2)–C(5) 95.1(2), C(4)–Fe(2)–C(5) 98.9(2), C(6)–Fe(2)–Fe(1) 103.91(14), C(4)–Fe(2)–Fe(1) 100.46(15), C(5)–Fe(2)–Fe(1) 153.07(16).

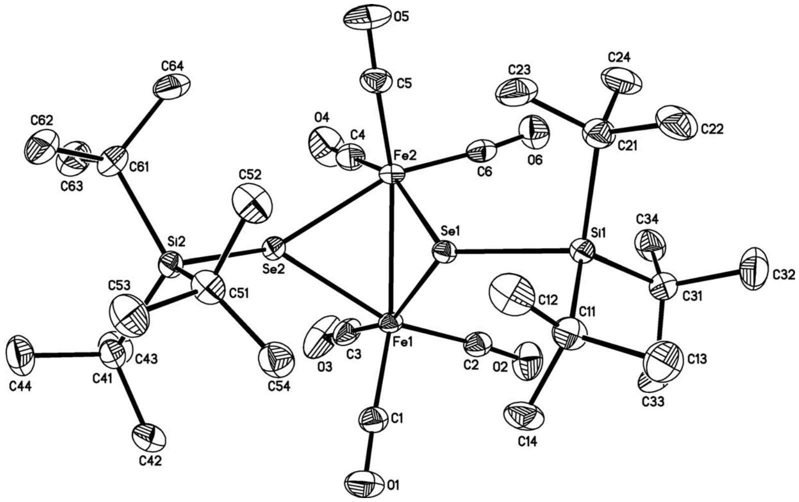

Figure 6. Plot of **2** showing the atom numbering scheme. The displacement ellipsoids are drawn at the 50% probability level. H atoms have been omitted for clarity. Selected bond lengths [Å] and angles [°]: Fe(2)–Se(1) 2.4026(6), Se(1)–Fe(1)–Se(1) 2.4175(7), Fe(1)–Se(2) 2.4301(6), Fe(2)–Se(2) 2.4340(7), Fe(1)–C(2) 1.780(4), Fe(1)–C(3) 1.791(5), Fe(1)–C(1) 1.810(4), Fe(2)–C(6) 1.781(4), Fe(2)–C(5) 1.792(4), Fe(2)–C(4) 1.799(5), C(1)–O(1) 1.146(5), C(2)–O(2) 1.141(5), C(3)–O(3) 1.131(5), C(4)–O(4) 1.137(5), C(5)–O(5) 1.154(5), C(6)–O(6) 1.144(5), Si(1)–Se(1)–Fe(1) 131.11(3), Si(2)–Se(2)–Fe(1) 128.83(3), Si(2)–Se(2)–Fe(2) 136.27(4), C(2)–Fe(1)–C(3) 88.5(2), C(2)–Fe(1)–C(1) 96.08(18), C(3)–Fe(1)–C(1) 99.9(2), C(2)–Fe(1)–Fe(2) 103.90(13), C(3)–Fe(1)–Fe(2) 99.41(13), C(1)–Fe(1)–Fe(2) 152.45(14), C(6)–Fe(2)–C(5) 96.19(18), C(6)–Fe(2)–C(4) 88.93(19), C(5)–Fe(2)–C(4) 100.68(19), C(6)–Fe(2)–Fe(1) 103.78(12), C(5)–Fe(2)–Fe(1) 151.49(13), C(4)–Fe(2)–Fe(1) 99.84(14).

Table 3. Selected bond lengths [Å] and angles [°] for **1** (E = S), **2** (E = Se), and **3** (E = Te).

	1	**2**	**3**[6]
Fe–Fe	2.5432(8)	2.5786(7)	2.645(2)
Fe–E	2.303(2)	2.4026(6)	2.584(2)
	2.318(2)	2.4175(7)	2.619(2)
	2.317(2)	2.4301(6)	
	2.322(2)	2.4340(7)	
Fe–C (avg)	1.783(6)	1.792(5)	1.784(9)
E–Si	2.231(2)	2.382(2)	2.622(2)
	2.210(2)	2.372(2)	
Fe–E–Fe	66.79(4)	64.68(2)	61.11(4)
	66.50(4)	64.03(2)	
E–Fe–E	82.55(4)	83.63(2)	77.04(3)
	82.74(5)	83.86(2)	
C–Fe–E	156.6(2)	97.8(2)	144.9(3)
	83.2(2)	156.8(2)	112.9(3)
	106.9(2)	101.6(2)	90.8(3)
	98.0(2)	157.6(2)	93.0(2)
	156.2(2)	82.2(2)	167.9(3)
	103.1(2)	105.6(2)	99.1(2)
	96.8(2)	96.0(2)	
	157.3(2)	100.3(2)	
	102.5(2)	157.8(2)	
	157.0(2)	158.4(2)	
	83.8(2)	105.1(2)	
	107.5(2)	83.7(2)	
C–Fe–Fe	104.0(2)	103.9(2)	151.5(2)
	99.8(2)	99.4(2)	114.7(3)
	152.9(2)	152.5(2)	87.7(3)
	103.9(2)	103.8(2)	
	100.5(2)	151.5(2)	
	153.1(2)	99.8(2)	

pulse sequence with empirically optimized parameters for polarization transfer from the *t*Bu substituents.

Electrochemical Procedure: Cyclic voltammograms were recorded in thf solutions with 0.1 M nBu_4NPF_6 (Fluka, electrochemical grade) as supporting electrolytes with an EG & G Princeton Applied Research M 263 A potentiostat, using a Ag/AgCl reference electrode, a Pt working electrode and a Pt wire counter electrode. Ferrocene was added as an internal reference. Prior to each experiment, the electrochemical cell was degassed for at least 10 min by using nitrogen and a blanket of nitrogen was maintained throughout. The GC working electrode was prepared by successive polishing with 1.0 and 0.3 micron diamond pastes.

Crystallization of the Sodium Thiolate $[Na(thf)_2SSitBu_3]_2$: The sodium thiolate $Na[SSitBu_3]$ (8.40 mmol) which was obtained by a literature procedure,[6] was dissolved in 10 mL of thf. Slow evaporation of the solvent yielded the product $[Na(thf)_2SSitBu_3]_2$ as crystalline colorless needles at –25 °C.

Crystallization of the Sodium Chalcogenolates $[Na(thf)ESitBu_3]_4$ (E = S, Se): The sodium chalcogenolates $Na[SSitBu_3]$ (E = S, Se) were synthesized by a literature procedure.[6] After removing the volatiles in vacuo, the residues were extracted with hexane (10 mL). X-ray-quality crystals of chalcogenolates $[Na(thf)ESitBu_3]_4$ (E = S, Se) were obtained at –25 °C.

Crystallization of the Disulfide $tBu_3Si–S_2–SitBu_3$: The disulfide $tBu_3Si–S_2–SitBu_3$ was synthesized by a literature procedure.[6] After removing the volatiles in vacuo, the residue was extracted with pentane (5 mL) and filtered through diatomaceous earth on a frit. The disulfide was obtained in 70% yield as colorless needles by slow evaporation of a cooled pentane solution. Selected data for $tBu_3Si–S_2–SitBu_3$: ^1H NMR (C_6D_6, internal TMS): δ = 1.31 (s, 27 H, *t*Bu) ppm. $^{13}C\{^1H\}$NMR (C_6D_6, internal TMS): δ = 26.0 (*C*Me$_3$), δ 30.8 (C*Me*$_3$) ppm. $^{29}Si\{^1H\}$NMR (C_6D_6, external TMS): δ = 26.0 ($SitBu_3$) ppm. $C_{24}H_{54}S_2Si_2$ (463.0): calcd. C 62.26, H 11.76; found C 61.99, H 11.66.

Synthesis of the Tricarbonyliron Thiolate 1: Disulfide $tBu_3Si–S_2–SitBu_3$ (12 mg, 0.025 mmol) and $[Fe(CO)_5]$ (6.6 µL, 9.8 mg, 0.05 mmol) were combined in C_6D_6 in an NMR tube, which was then flame-sealed. The colorless solution was irradiated with a fluorescent light bulb for 8 months. After 5 months and again after 6

Table 4. Crystallographic data and further details of the structure determination of **1**, **2**, tBu$_3$Si–S$_2$–SitBu$_3$, [Na(thf)$_2$(SSitBu$_3$]$_2$, and [Na(thf)(SSitBu$_3$]$_4$.

	1	**2**	tBu$_3$Si–S$_2$–SitBu$_3$	[Na(thf)$_2$SSitBu$_3$]$_2$	[Na(thf)SSitBu$_3$]$_4$
Empirical formula	$C_{30}H_{54}Fe_2O_6S_2Si_2$	$C_{30}H_{54}Fe_2O_6Se_2Si_2$	$C_{24}H_{54}S_2Si_2$	$C_{40}H_{86}Na_2O_2S_2Si_2$	$C_{64}H_{140}Na_4O_4S_4Si_4$
Formula weight	742.73	836.53	462.97	797.37	1306.32
Crystal system	monoclinic	monoclinic	monoclinic	monoclinic	monoclinic
Space group	$P2_1/n$	$P2_1/n$	$P2_1/n$	$P2_1/c$	$P2_1$
a [Å]	8.9399(6)	8.9357(5)	8.6760(12)	18.9536(18)	13.3756(6)
b [Å]	27.2788(14)	27.8681(19)	13.9235(16)	15.6396(10)	15.3886(4)
c [Å]	15.4510(9)	15.3592(8)	12.3224(15)	18.9675(19)	19.9654(8)
α [deg]	90	90	90	90	90
β [deg]	90.427(5)	91.034(4)	90.171(10)	118.517(7)	90.623(3)
γ [deg]	90	90	90	90	90
Volume [Å^3], Z	3767.9(4), 4	3824.1(4), 4	1488.5(3), 2	4940.3(8), 4	4109.3(3), 2
Density (calcd.) [Mg/m^3]	1.309	1.453	1.033	1.072	1.056
Abs coeff μ(Mo-K_α) [mm^{-1}]	0.981	2.761	0.268	0.207	0.233
F(000)	1576	1720	516	1760	1440
Crystal size [mm^3]	$0.23 \times 0.09 \times 0.04$	$0.21 \times 0.12 \times 0.09$	$0.37 \times 0.13 \times 0.12$	$0.52 \times 0.48 \times 0.47$	$0.24 \times 0.22 \times 0.21$
θ-range [deg]	2.40–26.03	2.39–25.44	3.62–25.64	3.47–25.73	2.25–25.49
Index ranges	$-10 \le h \le 11$, $-33 \le k \le 33$, $-19 \le l \le 18$	$-10 \le h \le 10$, $-33 \le k \le 33$, $-18 \le l \le 17$	$-10 \le h \le 9$, $-16 \le k \le 12$, $-14 \le l \le 14$	$-23 \le h \le 21$, $-17 \le k \le 18$, $-22 \le l \le 23$	$-16 \le h \le 16$, $-18 \le k \le 18$, $-24 \le l \le 24$
Reflections collected	64413	22777	7069	33368	81742
Independent reflections	7337	7031	2767	9409	15095
R(int)	0.0896	0.0815	0.0485	0.1505	0.0727
Absorption correction	semi-empirical from equivalents	semi-empirical from equivalents	semi-empirical from equivalents	semi-empirical from equivalents	semi-empirical from equivalents
$T_{\min}$, $T_{\max}$	0.8059, 0.9618	0.5948, 0.7892	0.9074, 0.9686	0.8999, 0.9089	0.9462, 0.9527
Data / restraints / parameters	7337 / 0 / 379	7031 / 0 / 379	2767 / 0 / 128	9409 / 6 / 452	15095 / 1 / 718
Goodness of fit on F^2	1.101	0.922	1.041	1.026	1.051
Final R indices [$I > 2\sigma(I)$], $R1$, $wR2$	0.0591, 0.0960	0.0378, 0.0681	0.0365, 0.0945	0.0772, 0.2117	0.0640, 0.1636
R indices (all data), $R1$, $wR2$	0.1054, 0.1052	0.0667, 0.0742	0.0394, 0.0959	0.1242, 0.2512	0.0727, 0.1755
Largest difference peak/hole [e·Å^{-3}]	0.380/–1.005	0.417/–0.685	0.327/–0.372	0.786/–0.542	0.468/–0.401

months, the NMR tube was cracked and the solution transferred to a new NMR tube and again flame-sealed. Over the course of the reaction, an accompanying color change to deep red was observed. Conversion is ca. 75% as determined by NMR spectroscopy. Slow evaporation of the solvent yields the product as blood-red needles. Due to the liberation of CO during the reaction of [Fe(CO)$_5$] with tBu$_3$Si–S$_2$–SitBu$_3$, a small scale preparation of **1** is favorable. Therefore, small scale experiments were repeated for several times to obtain **1** in larger amounts. Selected data for **1**: ^{1}H NMR (C$_6$D$_6$, internal TMS): δ = 1.19 (s, 27 H, tBu) ppm. ^{13}C{^{1}H}NMR (C$_6$D$_6$, internal TMS): δ = 25.6 (CMe$_3$), 31.3 (CMe_3), δ = 209.4 (CO) ppm. ^{29}Si{^{1}H}NMR (C$_6$D$_6$, external TMS): δ = 39.7 (SitBu$_3$) ppm. IR (hexane): $\tilde{\nu}$ = 2068 [m, ν(CO)], 2035 [s, ν(CO)], 1999 [m, ν(CO)], 1989 [s, ν(CO)] cm^{-1}. $C_{30}H_{54}Fe_2O_6S_2Si_2$ (742.74): calcd. C 48.51, H 7.33; found C 49.03, H 7.80.

Synthesis of the Tricarbonyliron Selenolate 2: Diselenide tBu$_3$Si–Se$_2$–SitBu$_3$ (20 mg, 0.036 mmol) and [Fe(CO)$_5$] (14 mg, 0.072 mmol) are combined in C$_6$D$_6$ in an NMR tube, which is then flame-sealed. The orange solution is irradiated with a fluorescent light bulb for 14 d. An accompanying color change to deep red is observed. Conversion is quantitative as determined by NMR spectroscopy. Slow evaporation of the solvent yields the product as blood red needles. Due to the liberation of CO during the reaction of [Fe(CO)$_5$] with tBu$_3$Si–Se$_2$–SitBu$_3$, a small scale preparation of **2** is favorable. Therefore, small scale experiments were repeated for several times to obtain **2** in larger amounts. Selected data for **2**: ^{1}H NMR (C$_6$D$_6$, internal TMS): δ = 1.20 (s, 27 H, tBu) ppm. ^{13}C{^{1}H}NMR (C$_6$D$_6$, internal TMS): δ = 26.1 (CMe$_3$), 31.3 (CMe_3) ppm. ^{29}Si{^{1}H}NMR (C$_6$D$_6$, external TMS): δ = 45.5 (SitBu$_3$) ppm. ^{77}Se{^{1}H}NMR (C$_6$D$_6$, external SeO$_2$): δ = –165 ppm. IR (hexane): $\tilde{\nu}$ = 2066 [m, ν(CO)], 2028 [s, ν(CO)], 1982 [s, ν(CO)] cm^{-1}. $C_{30}H_{54}Fe_2O_6Se_2Si_2$ (836.53): calcd. C 43.07, H 6.51; found C 43.79, H 6.84.

Reaction of the Tricarbonyliron Chalcogenolates 1, 2, and 3 with Sodium or Potassium: Carbonyl chalcogenolate complex [**1**: 24 mg, 0.032 mmol (Na), **1**: 14 mg, 0.019 mmol (K), **2**: 18 mg, 0.022 mmol (Na), **2**: 15 mg, 0.018 mmol (K), **3**: 32 mg, 0.034 mmol (Na), **3**: 30 mg, 0.032 mmol (K)] was added to sodium [102 mg, 4.43 mmol (**1**), 107 mg, 4.65 mmol (**2**), 120 mg, 5.22 mmol (**3**)] or potassium [95 mg, 2.43 mmol (**1**), 86 mg, 2.20 mmol (**2**), 104 mg, 2.66 mmol (**3**)] in 5 mL of thf. The mixture was stirred for 3 d at ambient temperature. After filtering and removing the volatiles in vacuo, the products were identified by NMR spectroscopy. Selected data for Na[SSitBu$_3$]: ^{1}H NMR (C$_6$D$_6$, internal TMS): δ = 1.35 (s, 27 H, tBu) ppm. ^{13}C{^{1}H}NMR (C$_6$D$_6$, internal TMS): δ = 24.4 (CMe$_3$), 31.7 (CMe_3) ppm. ^{29}Si{^{1}H}NMR (C$_6$D$_6$, external TMS): δ = 25.6 (SitBu$_3$) ppm. Selected data for Na[SeSitBu$_3$]: ^{1}H NMR (C$_6$D$_6$, internal TMS): δ = 1.41 (s, 27 H tBu) ppm. ^{13}C{^{1}H}NMR (C$_6$D$_6$, internal TMS): δ = 24.4 (CMe$_3$), 31.8 (CMe_3) ppm. ^{29}Si{^{1}H}NMR (C$_6$D$_6$, external TMS): δ = 25.6 (SitBu$_3$) ppm. Selected data for Na[TeSitBu$_3$]: ^{1}H NMR (C$_6$D$_6$, internal TMS): δ = 1.46 (s, 27 H, tBu) ppm. ^{13}C{^{1}H}NMR (C$_6$D$_6$, internal TMS): δ = 24.0 (CMe$_3$), 32.2 (CMe_3) ppm. ^{29}Si{^{1}H}NMR (C$_6$D$_6$, external TMS): δ = 38.0 (SitBu$_3$) ppm. Selected data for K[SSitBu$_3$]: ^{1}H NMR ([D$_8$]thf, internal TMS): δ = 1.14 (s, 27, H tBu) ppm. ^{13}C{^{1}H}NMR ([D$_8$]thf, internal TMS): δ = 24.3 (CMe$_3$), 32.1 (CMe_3) ppm. ^{29}Si{^{1}H}NMR ([D$_8$]thf, external TMS): δ = 22.0 (SitBu$_3$) ppm. Selected data for K[SeSitBu$_3$]: ^{1}H NMR ([D$_8$]thf, internal TMS): δ = 1.15 (s, 27 H, *t*Bu) ppm. $^{13}C\{^1H\}$NMR ([D$_8$]thf, internal TMS): δ = 24.2 (*C*Me$_3$), 32.2 (C*Me*$_3$) ppm. $^{29}Si\{^1H\}$NMR ([D$_8$]thf, external TMS): δ = 21.8 (Si*t*Bu$_3$) ppm. Selected data for K[TeSi*t*Bu$_3$]: ^1H NMR ([D$_8$]thf internal TMS): δ = 1.17 (s, 27 H, *t*Bu) ppm. $^{13}C\{^1H\}$NMR ([D$_8$]thf, internal TMS): δ = 24.4 (*C*Me$_3$), 33.2 (C*Me*$_3$) ppm. $^{29}Si\{^1H\}$NMR ([D$_8$]thf, external TMS): δ = 31.8 (Si*t*Bu$_3$) ppm.

Electrochemical Reduction of the Tricarbonyliron Tellurolate 3: Carbonyl tellurolato complex **3** (22 mg, 1.11 mmol) was combined to a solution of [NBu$_4$][PF$_6$] (2134 mg, 5.5 mmol) in 55 mL of thf. The carbonyl tellurolato complex **3** was electrolized quantitatively at potential below –2.2 V. After removing all volatiles in vacuo, dissolving in benzene and filtering, the tellurolate was identified by NMR spectroscopy. Selected data for [NBu$_4$][TeSi*t*Bu$_3$]: ^1H NMR (C_6D_6, internal TMS): δ = 0.86 (m, 12 H, CH$_3$), 1.28 (m, 16 H, CH$_2$), 2.89 (m, 8 H, *t*Bu), 1.25 (s, 27 H, *t*Bu) ppm. $^{29}Si\{^1H\}$NMR (C_6D_6, external TMS): δ = 33.6 (Si*t*Bu$_3$) ppm.

X-ray Crystallographic Study: Data collection: Stoe-IPDS-II diffractometer, graphite monochromated Mo-K_α radiation; T = 173 K. Empirical absorption correction using MULABS, structure solution by direct methods, structure refinement by full-matrix least-squares on F^2 with SHELXL-97.[20] Hydrogen atoms were placed on ideal positions and refined with fixed isotropic displacement parameters using a riding model.

CCDC-740691 (for **1**), -740690 (for **2**), -740687 (for *t*Bu$_3$Si–S$_2$–Si*t*Bu$_3$), -740688 (for [Na(thf)$_2$(SSi*t*Bu$_3$)]$_2$), and -740689 (for [Na(thf)(SSi*t*Bu$_3$]$_4$) contain the supplementary crystallographic data (excluding structure factors) for this paper. These data can be obtained free of charge from The Cambridge Crystallographic Data Centre via www.ccdc.cam.ac.uk/data_request/cif.

Acknowledgments

We are grateful to the University of Frankfurt for financial funding and the Chemetall GmbH for a gift of *tert*-butyllithium.

---

[1] P. J. Bonasia, J. Arnold, *Inorg. Chem.* **1992**, *31*, 2508; P. T. Wolczanski, *Chem. Commun.* **2009**, 740.

[2] A. Lorbach, A. Nadj, S. Tüllmann, F. Dornhaus, F. Schödel, I. Sänger, G. Margraf, J. W. Bats, M. Bolte, M. C. Holthausen, M. Wagner, H.-W. Lerner, *Inorg. Chem.* **2009**, *48*, 1005; H.-W. Lerner, G. Margraf, J. W. Bats, M. Wagner, *Chem. Commun.* **2005**, 4545; H.-W. Lerner, M. Wagner, M. Bolte, *Chem. Commun.* **2003**, 990.

[3] T. I. Kückmann, F. Schödel, I. Sänger, M. Bolte, M. Wagner, H.-W. Lerner, *Organometallics* **2008**, *27*, 3272.

[4] J. J. R. Fraústo da Silva, R. J. P. Williams, *The Biological Chemistry of the Elements*, Clarendon Press, Oxford, **1991**; D. Voet, J. G. Voet, *Biochemistry*, John Wiley & Sons, New York, **1995**; Y. Nicolet, A. L. de Lacey, X. Vernède, V. M. Fernandez, E. C. Hatchikian, J. C. Fontecilla-Camps, *J. Am. Chem. Soc.* **2001**, *123*, 1596; Y. Nicolet, B. J. Lemon, J. C. Fontecilla-Camps, J. W. Peters, *Trends Biochem. Sci.* **2000**, *25*, 138; Y. Nicolet, C. Piras, P. Legrand, C. E. Hatchikian, J. C. Fontecilla-Camps, *Structure* **1999**, *7*, 13.

[5] J. M. Gonzales, D. G. Musaev, K. Morokuma, *Organometallics* **2005**, *24*, 4908; V. G. Albano, M. Monari, I. Orabona, A. Panunzi, F. Ruffo, *J. Am. Chem. Soc.* **2001**, *123*, 4352; W. F. Liaw, M. H. Chiang, C. J. Liu, P. J. Harn, L. K. Liu, *Inorg. Chem.* **1993**, *32*, 1536.

[6] T. I. Kückmann, M. Hermsen, M. Bolte, M. Wagner, H.-W. Lerner, *Inorg. Chem.* **2005**, *44*, 3449.

[7] H.-W. Lerner, S. Scholz, M. Bolte, *Organometallics* **2002**, *21*, 3827.

[8] B. Kern, H. Vitze, M. Bolte, M. Wagner, H.-W. Lerner, *Z. Anorg. Allg. Chem.* **2008**, *631*, 1830.

[9] H.-W. Lerner, *Coord. Chem. Rev.* **2005**, *249*, 781.

[10] H.-W. Lerner, S. Scholz, M. Bolte, M. Wagner, *Z. Anorg. Allg. Chem.* **2004**, *630*, 443; H.-W. Lerner, S. Scholz, M. Bolte, *Z. Anorg. Allg. Chem.* **2001**, *627*, 1638.

[11] J. M. Gonzales, D. G. Musaev, K. Morokuma, *Organometallics* **2005**, *24*, 4908.

[12] M. M. Shieh, P.-F. Chen, Y.-C. Tsai, M.-H. Shieh, S.-M. Peng, G.-H. Lee, *Inorg. Chem.* **1995**, *34*, 2251.

[13] R. E. Bachman, K. H. Witmire, *Organometallics* **1993**, *12*, 1988.

[14] P. Mathur, R. Trivedi, M. Hossain, S. S. Tavale, V. G. Puranik, *J. Organomet. Chem.* **1995**, *491*, 291; S. Jäger, P. G. Jones, J. Laube, C. Thöne, *Z. Anorg. Allg. Chem.* **1999**, *625*, 352; S. Jeannin, Y. Jeannin, F. Robert, C. Rosenberger, *J. Organomet. Chem.* **1993**, *448*, 151; M. T. Ashby, *Inorg. Chem.* **1995**, *34*, 5429.

[15] E. Delgado, E. Hernández, N. Mansilla, F. Zamora, L. A. Martínez-Cruz, *Inorg. Chim. Acta* **1999**, *284*, 14–19.

[16] Crystal data for [Na(thf)(SeSi*t*Bu$_3$)]$_4$: orthorhombic space group *Pmn*2$_1$. Cell dimension: a = 20.0769(18) Å, b = 13.2918(14) Å, c = 15.6171(20) Å, α, β, γ = 90°, V = 4167.54(78) Å^3. Selected bond lengths: Se–Si(average) 2.210 Å, Na–Se(average) 2.891 Å. The crystal was a small not very well diffracting needle. Due to this fact the R_{int} value is relatively high and only a small part of the reflections can be regarded as observed.

[17] N. Wiberg, K. Amelunxen, H.-W. Lerner, H. Nöth, A. Appel, J. Knizek, K. Polborn, *Z. Anorg. Allg. Chem.* **1997**, *623*, 1861.

[18] Cambridge Structural Database (CSD, version 5.29 with three updates, January **2008**; Allen, **2002**). F. H. Allen, *Acta Crystallogr., Sect. B* **2002**, *58*, 380.

[19] N. Wiberg, K. Amelunxen, H.-W. Lerner, H. Schuster, H. Nöth, I. Krossing, M. Schmidt-Amelunxen, T. Seifert, *J. Organomet. Chem.* **1997**, *542*, 1.

[20] G. M. Sheldrick, *Acta Crystallogr., Sect. A* **2008**, *64*, 112.

Received: August 18, 2009

DOI: 10.1002/ejic.200900830

Simple and Efficient Aqueous Process for Nanostructured Fibrous TiO_2 Regulated by Linear Polyethyleneimine Aggregates

Pei-Xin Zhu[a] and Ren-Hua Jin*[a,b]

Keywords: Biomimetic synthesis / Titanium oxide / Photocatalysts / Nanostructures

In this paper, we report a simple and smart biomimetic process for constructing TiO_2 nanofibers in aqueous system and its derivatives with Pt nanoparticles uniformly embedded inside. It was found that regularly structured TiO_2-LPEI hybrids with fibrous networks could be easily produced when linear polyethyleneimine (LPEI) aggregates were used as a regulator in the hydrolytic condensation of water-soluble titanium bislactates (TiLact). In the XRD patterns of the as-prepared TiO_2-LPEI hybrids, a strong peak appeared at a low diffraction angle of about 4°, which indicated the formation of regularly layered domains consisting of TiO_2 and LPEI residues in the fibrous hybrids. TEM observations showed that in the as-prepared TiO_2-LPEI hybrids very tiny crystallites less than 3 nm in size were closely packed to each other, whereas the crystalline domains increased to 10 nm after the hybrids were calcined at 500 °C. Raman spectroscopy measurement confirmed the existence of anatase phase in the as-prepared hybrids. Simply mixing the TiO_2-LPEI hybrids with an aqueous solution of $PtCl_4^{2-}$ spontaneously resulted in the formation of Pt nanoparticles embedded in the TiO_2-LPEI fibers. TEM images revealed that the Pt nanoparticles homogeneously distributed in the TiO_2-LPEI hybrids without any damage to their fibrous morphologies. A typical photocatalysis evaluation revealed that under visible-light irradiation the Pt-embedded TiO_2 fibers exhibited two times higher activity in the photodecomposition of methylene blue than that of the pure TiO_2 fibers.

Introduction

In the recent years, the so-called biomimetic processes for constructing metal oxide materials in aqueous media have received great attention due to their cost-effective and environmental benign aspects.[1,2] The bioorganic matrices in biological systems such as in diatoms and sponges have a key role in the nanoscale control over the formation of hierarchical structure and multiple morphologies of biosilica.[3,4] This insight has inspired the scientists to explore a novel process for well-structured inorganic materials in aqueous solutions with the help of organic molecules and polymers.[5,6] Titanium oxides, as one of the most useful semiconductors, have been applied in a wide area due to their many promising properties.[7–11] Therefore, in recent decades intense efforts have been devoted to the preparation of TiO_2, especially so-called precisely structured nano-TiO_2 materials.[12] Although many methods have been reported for the preparation of TiO_2, such as hydrothermal methods,[13–15] electrospinning,[16–18] templated sol–gel methods (anodic aluminum membrane, organic gel as template),[19–21] and so on, the practical applications were extremely limited because most of these processes suffered from many problems, such as long reaction times, low productive ability, expensive apparatus, and so on. Hence, developing a novel process is important to overcome the mentioned-above problems. Some interesting attempts have been done to explore a biomimetic process for nanostructured TiO_2 through a controllable sol–gel process. Supramolecular assembly from organics can be used as a versatile template because of their controllable morphologies from nanofibers, nanorods, and nanoribbons. For example, cyclohexanediamine-type organogelators form helical nanofibers, leading to the construction of helical nanotubes of SiO_2, TiO_2, and Ta_2O_5.[22,23] Poly(L-lysine) was also stated as a useful template for biomimetic synthesis of TiO_2 particles.[24] The deposition of TiO_2 from water-soluble titanium complexes [aqueous solution of titanium bis(ammonium lactate)] by use of polyallylamines and peptides as catalytic templates appeared more exciting,[25,26] where the polymers were capable of promoting effectively the hydrolysis of water-soluble titanium complexes. However, it was normally difficult to construct TiO_2 materials with definite morphologies and characteristic functions by this process.

In our recent papers, we reported that self-organized crystalline aggregates of linear poly(ethyleneimine) (LPEI) in water can be successfully used in directing the formation

---

[a] Synthetic Chemistry Laboratory, Kawamura Institute of Chemical Research,
631 Sakado, Sakura, Chiba 285-0078, Japan
Fax: +81-43-498-2202
E-mail: jin@kicr.or.jp
[b] JST-CREST
631 Sakado, Sakura, Chiba 285-0078, Japan

Supporting information for this article is available on the WWW under http://dx.doi.org/10.1002/ejic.200900830.

of hierarchical SiO_2-LPEI hybrids via the hydrolytic condensation of alkoxysilanes.[27] In addition, the remaining internal LPEI in the hybrids was confirmed to be highly active for the in situ reduction of $PtCl_4^{2-}$, resulting in Pt-cored lines.[28,29] As an expansion of this process, we attempted to prepare well-shaped fibrous networks of TiO_2-LPEI hybrids in an aqueous solution by using LPEI aggregates as a regulator in the present work. It was found that the as-prepared fibrous hybrids consisted of anatase nanocrystallites and LPEI, and these hybrids had a regularly layered structure. Subsequently, Pt nanoparticles were easily converted into TiO_2-LPEI hybrids by simply mixing them with metal anionic ($PtCl_4^{2-}$), which was found to be homogenously distributed in the TiO_2 fibers. Pt-loaded TiO_2 showed that visible light was responsible for the photocatalytic decolorization of dyes.

Results and Discussion

Water-soluble titanium bislactate (Scheme 1, TiLact), used as a titanium oxide source in the present study, is acidic with a pH value around 3.0 in aqueous solution. The diluted TiLact solution appears to have strong chemical stability, which can stand long time (more than two weeks) without any hydrolysis even in basic medium with high pH value (≈12) after adjusted with 28 wt.-% ammonia solution. As we reported in the serials of our recent papers,[27] LPEI possessing only the secondary amine in its backbone can self-organized into crystalline aggregates, which is capable of directing various nanostructured silica via hydrolytic condensation of tetramethyloxysilane (TMOS) or tetraethoxysilane (TEOS). Similar to the silicification of alkoxysilane on LPEI aggregates, the LPEI aggregates also strongly catalyzed the hydrolytic condensation of water-soluble TiLact. For example, simply mixing 2 mL of LPEI aggregates (2 wt.-%) with 4 mL of TiLact solution (20 wt.-%) resulted in white precipitates. However, it was found that the obtained precipitates were irregular agglomerates in their morphologies. This was strongly different to the silica deposition, in which the morphologies of crystalline LPEI aggregates were precisely duplicated and transformed into silica-LPEI hybrids with a shell of silica and a core of LPEI. It was convinced that the crystalline LPEI aggregates with definite morphologies played two roles in the deposition of silica: scaffold and catalyst for the hydrolytic condensation of alkoxysilanes. In this silicification, the interactions (coordination, hydrogen-bonding etc.) between the surface of crystalline LPEI aggregates and silanol oligomers derived from TMOS keep the initial morphologies of the LPEI aggregates and did not suffer any damage to their shapes. However, this was different in the TiLact system. As we mentioned above, the aqueous solution of TiLact is acidic with a pH value near 3. The crystalline aggregates of LPEI are easily protonated in the acidic medium and cannot maintain their initial morphologies due to partial dissolution of the aggregates. Therefore, we firstly investigated the effects on TiO_2 deposition from the pH value of the TiLact solutions. The optimized reaction temperature was fixed at 50 °C. Figure 1 presents the SEM images of TiO_2-LPEI precipitates obtained from a mixture of 2 mL of LPEI (1 wt.-%) and 4 mL of TiLact (5 wt.-%) solution at different pH values. When the pH value of the TiLact solutions was lower than 6, uncontrolled agglomerates with irregular shapes were observed. After the pH was adjusted up to 7, fibrous structures with very rough shapes began to form. The size of fibers tended to become smaller with increasing pH values of the TiLact solution. When the pH was fixed at 9, numerous fine belt-like fibers (less than 100 nm in width) were produced. In the Raman spectra (Figure 2a) of the TiO_2 precipitates obtained at pH values lower than 8, four strong peaks were recorded at 197, 448, 545, and 630 cm^{-1}. These peaks were very similar to the vibrating bands of the crystalline anatase TiO_2[30] despite of significant peak shifts at 448, 545, and 630 cm^{-1} compared to the peaks (397, 514, and 639 cm^{-1}) of typical anatase TiO_2 (Figure 2b). LPEI molecules should be responsible for the shift peaks, which were hybridized with TiO_2 (to be discussed below) to affect the vibrations of Ti–O bonding of anatase TiO_2. It is clear that crystalline TiO_2 existed in the as-prepared TiO_2-LPEI fibers even without thermal treatment. We also found that the Raman peaks of the TiO_2-LPEI obtained at pH ≥ 9 were comparatively smaller and weaker, indicating that the crystallization of TiO_2 was seriously restrained when the pH of the TiLact solution was raised up to 9, although this condition was favorable for the fibrous morphology of TiO_2-LPEI. These results were also strongly supported by TEM observations. Figure 3 shows the HRTEM images of two samples obtained by mixing 1 wt.-% LPEI and 5 wt.-% TiLact solutions adjusted at pH = 7 and 9, respectively. It is clearly observable that the TiO_2-LPEI hybrids produced at pH = 7 were belt-like fibers (>500 nm in width) in which very tiny crystalline domains (about 3 nm) were packed closely to each other, whereas the TiO_2-LPEI hybrids obtained at pH = 9 appeared amorphous and only a few crystal domains (<2 nm) were observed.

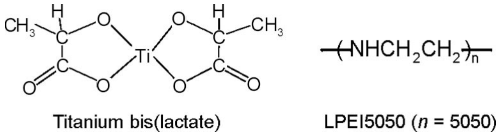

Scheme 1. Schematic representation of TiLact and LPEI5050.

The concentrations of the reactants also affected the morphologies of the TiO_2-LPEI precipitates. Figure 4 shows the SEM images of TiO_2-LPEI hybrids prepared with 4 mL of TiLact (pH = 7, 10 wt.-%) and 2 mL of LPEI aggregates with different concentrations. It is evident that the low concentrations of LPEI were obviously favorable for the formation of well-shaped fibers. When the LPEI concentration was higher than 2 wt.-%, agglomerates and fused fibers began to form. The XRD patterns (Figure 6) of all the samples showed a diffraction peak at a similar angle (2*θ* around 4°) despite the different intensities. The intensities of this peak became stronger with increasing

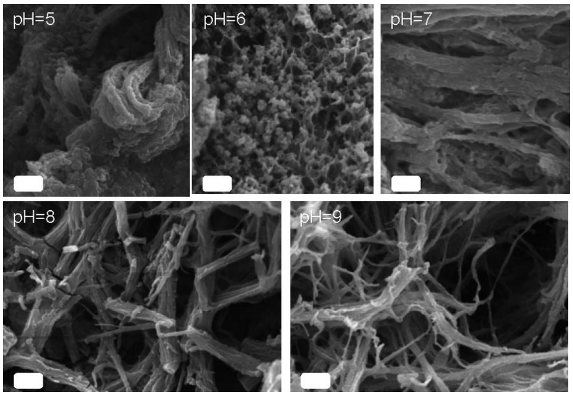

Figure 1. Effects of pH on the morphologies of TiO_2-LPEI hybrids obtained with 5 wt.-% TiLact and 1 wt.-% LPEI; scale bar: 1 µm.

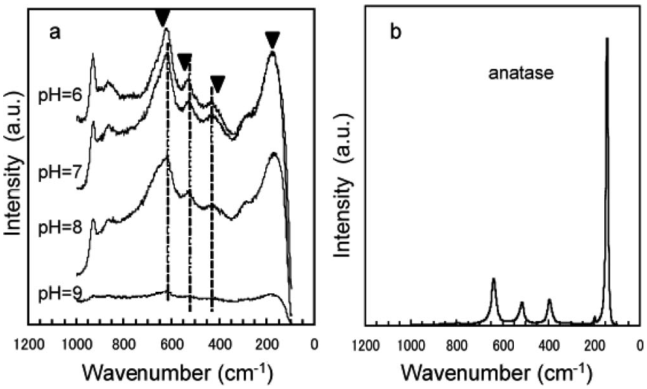

Figure 2. Raman spectra of TiO_2-LPEI hybrids obtained with 1 wt.-% LPEI and 5 wt.-% TiLact at different pH values (a) and commercially available anatase powder (b).

concentrations of LPEI and the strongest XRD peak was recorded for the sample prepared at 5 wt.-% LPEI. However, such an obvious diffraction peak was not detected in crystalline LPEI[31] or in TiO_2. Furthermore, the peak at small angle area disappeared completely when LPEI components were removed by calcinating the TiO_2-LPEI hybrids at 500 °C (see Figure 5). These features, before and after calcination, unambiguously indicate that a regularly organized structure exists in the hybrids of TiO_2-LPEI. We suggest here that the regularly organized structure may be a layered form with an interval of <2 nm between TiO_2 and LPEI. Therefore, it is noticeable that the relatively high LPEI concentrations were favorable for the formation of well-constructed TiO_2-LPEI composites with layered structures. In contrast, the pH values and the concentrations of TiLact solutions did not give the obvious effects on the layered structures of TiO_2-LPEI hybrids (Figure S1, Supporting Information) although they indeed influenced the morphologies of the resultant hybrids as stated above (Figure S2, Supporting Information). The well-organized LPEI (i.e., aging via longer aggregation time at room temperature) is also beneficial for the formation of well-shaped fibers (Figure S3, Supporting Information).

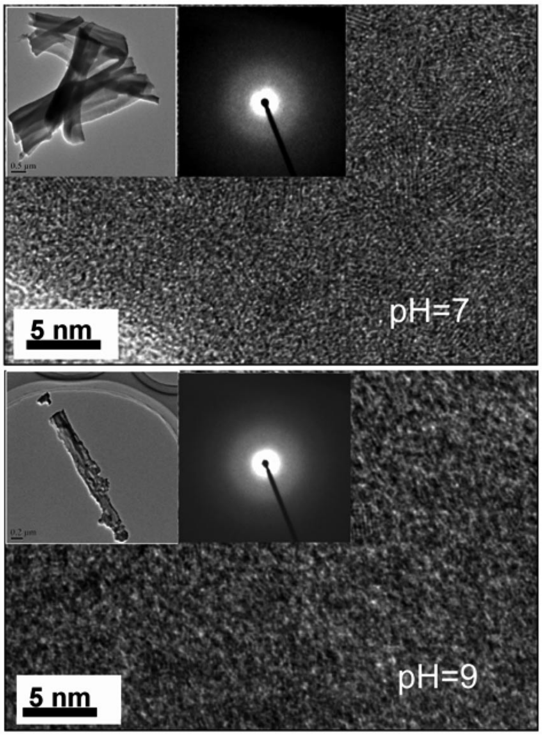

Figure 3. HRTEM images of as-prepared TiO_2-LPEI hybrids obtained with 1 wt.-% LPEI and 5 wt.-% TiLact at pH = 7 and 9. Inset: low magnification images of the hybrids.

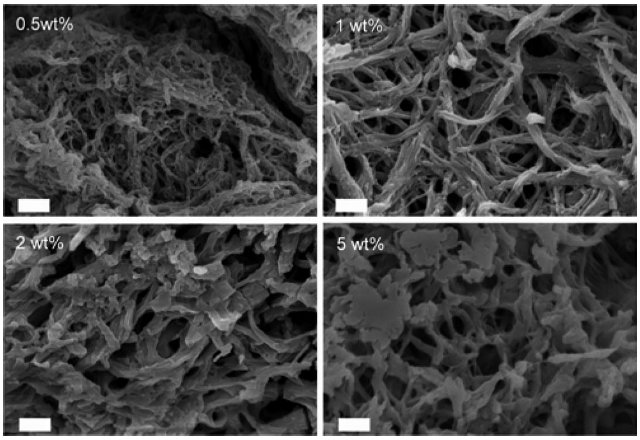

Figure 4. SEM images: effects of LPEI concentrations on the morphologies of TiO_2-LPEI hybrids obtained with 10 wt.-% TiLact at pH = 7; scale bar; 1 µm.

We further compared the thermal decomposition behaviors of various TiO_2-LPEI samples with TG-DTA analysis (Figure 6). Pure TiLact showed two exothermic peaks at 266 and 485 °C, and LPEI alone also had two thermal decomposition peaks at 306 and 532 °C. The high peak at 532 °C would be attributed to some intermediates transformed from LPEI during the thermolysis process. For the TiO_2-LPEI hybrids, three exothermic peaks were recorded. The first peak (at low temperature) was at around 232 °C, the second peak ranged from 280 to 330 °C and was greatly dependent on the LPEI concentrations, and the third peak was at 520 °C. This suggested that two phases of LPEI existed in the TiO_2-LPEI hybrids. One is the interface phase

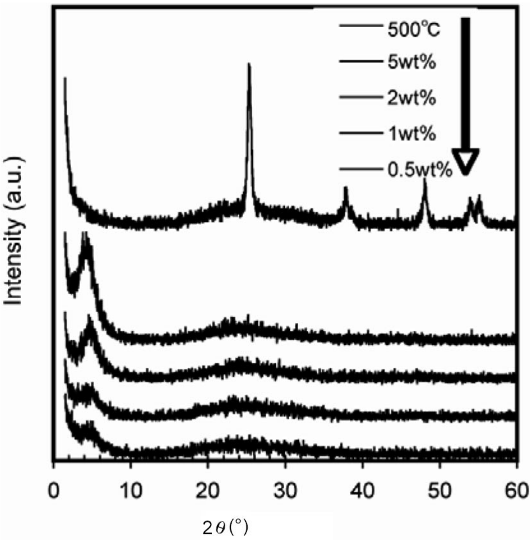

Figure 5. XRD patterns of TiO_2-LPEI hybrids obtained with 10 wt.-% TiLact (pH = 7) and different LPEI concentrations. The top line is after calcination (2 wt.-% sample) at 500 °C.

in which LPEI closely adhered on the surface of TiO_2 crystallites. This phase of matters may decompose at a relatively low temperature, corresponding to the first exothermic peak. The other one is as an isolated phase in which LPEI may not directly interact with TiO_2. This isolated residue can decompose at a relatively high temperature, probably matching the second peak. As mentioned above, the increase in the LPEI concentrations actually enhanced the layered structure. Therefore, this effect probably caused the shift of the second exothermic peaks towards higher temperature. The thermal gravimetric results in Figure 6b showed a slight increase in weight loss from 38.8 to 46.8 wt.-% (adsorbed water excluded) with an increase in the LPEI concentrations. In contrast, we also found that both the concentrations of LPEI and TiLact influenced the yields of TiO_2-LPEI precipitates. From the plots of the yields of the TiO_2-LPEI hybrids against the concentrations of TiLact (Figure 7a) and LPEI (Figure 7b), we can observe that a maximum point of the yields appeared in both plot a (LPEI was fixed at 0.5 wt.-%) and plot b (TiLact solutions at 10 wt.-%). It is worth noticing that the weight ratios of TiLact to LPEI at the maximum point in Figure 7a,b showed the same value of 20:1. By converting the weight ratios into molar ratios, we found that the maximum yield of TiO_2-LPEI precipitates was available when the molar ratio of TiLact/EI (ethyleneimine) was fixed approximately at 1:2.5. Obviously, the excess TiLact resulted in a decrease in the conversion due to the lack of LPEI (Figure 7a). However, the higher concentration of LPEI also did not lead to an increase in TiLact conversion (Figure 7b). This should be related to LPEI crystallization behaviors. When LPEI concentrations increase, the relatively larger LPEI crystalline bundles will form in the aqueous system, which is not favorable for the increase in the amine (–NH–) quantity located on the bundles surface. This means that the apparent concentrations of –NH– decreased even when the LPEI concentration increased and thus the conversion of TiLact into TiO_2 decreased.

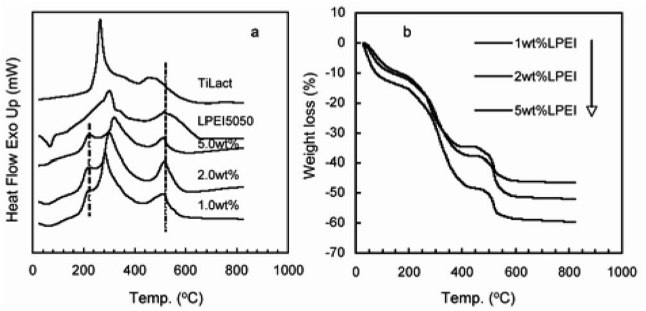

Figure 6. TG-DTA profiles of TiO_2-LPEI hybrids obtained with 10 wt.-% TiLact (pH = 7) and different LPEI concentrations.

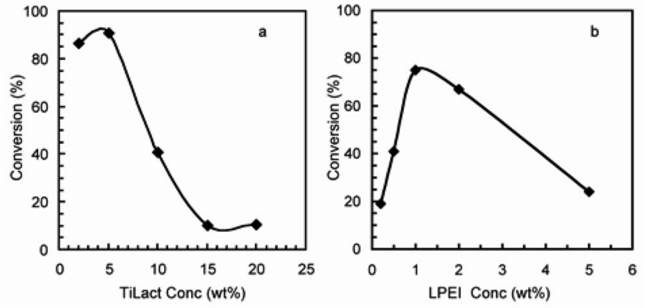

Figure 7. Plots of the yields of TiO_2-LPEI against TiLact concentrations (a) at 0.5 wt.-% LPEI and (b) at 10 wt.-% TiLact.

In order to understand the other factors involved in morphological control, we also investigated organic solvent effects on the formation of TiO_2-LPEI hybrids. Water-soluble solvents such as EtOH, acetone, and THF were added to the 5 wt.-% aqueous solution of TiLact (pH = 7) and then mixed with 2 wt.-% LPEI. The mixture was stirred in a water bath temperature of 50 °C for 1 h. As shown in Figure S4a,b (Supporting Information), the precipitates that formed in the presence of EtOH or acetone with an appropriate amount had film-like morphologies. In the case of excessive solvents, the films tended to become particulates. Particulate formation was more easily observed in the system containing THF (Figure S4c, Supporting Information). The XRD patterns of both the as-prepared films and particulates showed the same diffraction peak with 2θ near 4° (Figure S5, Supporting Information), which was similar to that of the fibrous hybrids. This suggests that the morphology of the hybrids can be altered by changing the reaction media, but the formation of a layered structure in TiO_2-LPEI hybrids is not dependent on their morphologies and the employed reaction media.

In our previous reports,[28] we reported that the as-prepared silica fibers have LPEI core-axial structures and removing the axial LPEI core by calcination led to the formation of hollow silica fibers. However, in the present case of titania system, we could not observe any hollow structures even after sintering the as-prepared TiO_2-LPEI hybrids at

500 °C. Different from the silica fibers, the sintered TiO_2 fibers appeared to have thin belt-like shapes with a homogeneous thicknesses without hollow structures (Figure 8), in which the crystalline TiO_2 domains became larger to nearly 10 nm from initial 3 nm. This suggests that the mechanism of silica fiber formation via silicification on the surface of fibrous LPEI aggregates is obviously inappropriate for the TiO_2 deposition system. Although the detail about the formation of fibrous TiO_2-LPEI hybrids is not clear yet, the following assumption may be reasonably acceptable. The hydrolysis of TiLact that is catalyzed by surface –NH– of LPEI aggregates gives the byproduct of lactic acid, which would induce the protonation of –NH– on LPEI and thus causes the dissociation of LPEI aggregates. Both hydrolysis and dissociation take place simultaneously. Consequently, all the chemical residues such as LPEI, protonated LPEI, and hydrolyzed TiOH and lactic acid interact with each other to form an intermediate structure, which finally produces regularly layered structures of TiO_2-LPEI hybrids.

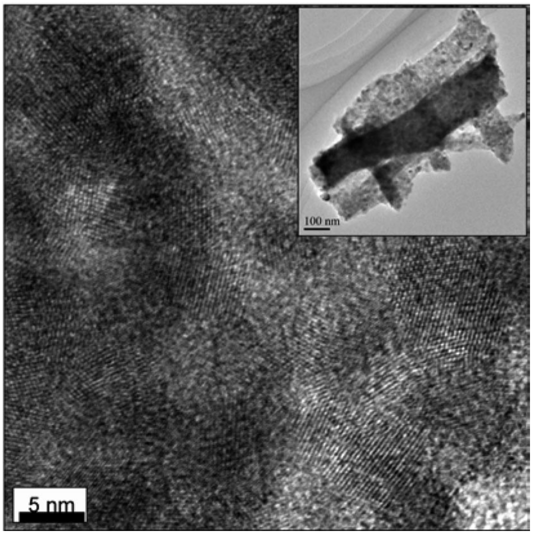

Figure 8. TEM images of TiO_2 fibers after sintering at 500 °C (1 wt.-% LPEI, 5 wt.-% TiLact, pH = 7). Inset: low magnification image.

As an amine polymer, LPEI can be also used as a reductant to reduce noble metal ions with high electrode potentials such as silver ions, $PtCl_4^{2-}$, and $AuCl_4^-$ into metallic nanoparticles.[28,29,32] For example, silver porous frameworks were successfully prepared by using LPEI hydrogel as a soft sacrificial template.[29] The anionic complexes with $(MCl_n)^{m-}$ are able to enter the core-structured SiO_2-LPEI fibers and are reduced spontaneously in situ into metallic nanoparticles. In this sense, LPEI residues in the TiO_2-LPEI hybrids should be certainly capable of reducing metal ions. We mixed 10 mL of 0.01 M Na_2PtCl_4 solutions with 0.5 g of the dried TiO_2-LPEI hybrids at room temperature. The color of the originally white powders immediately became grey due to the formation of Pt nanoparticles on the white powders. In the HRTEM images (Figure 9), we found that the fibrous morphologies remained undestroyed even with the formation of metallic nanoparticles inside. The newly formed nanoparticles were about 3 nm in diameter and homogeneously distributed in the hybrid fibers. Energy dispersive spectroscopy (EDS, data not shown here) and electron diffraction patterns also revealed the formation of Pt nanoparticles. As is well known, TiO_2 with embedded Pt nanoparticles responds to visible-light photocatalysis.[33] As a preliminary examination, we subjected the samples of Pt-embedded TiO_2 to photocatalytic tests. For this purpose, we calcined the TiO_2-LPEI before and after loading Pt nanoparticles at 600 °C and obtained LPEI free f-TiO_2 and f-TiO_2-Pt. In f-TiO_2-Pt, the XRD patterns (Figure 10) showed the main phase of anatase TiO_2 with a small amount of rutile phase after sintered at 600 °C for 6 h. In addition, two small peaks were recorded at $2\theta \approx 29.8$ and 46.2°, assigned to metallic platinum (JCPDS No. 4–802). X-ray fluorescence analysis confirmed 1.8 wt.-% of Pt existing in the f-TiO_2-Pt. UV/Vis diffuse reflection spectroscopy disclosed that f-TiO_2-Pt had stronger optical absorption in the visible range (400–666 nm) in contrast to f-

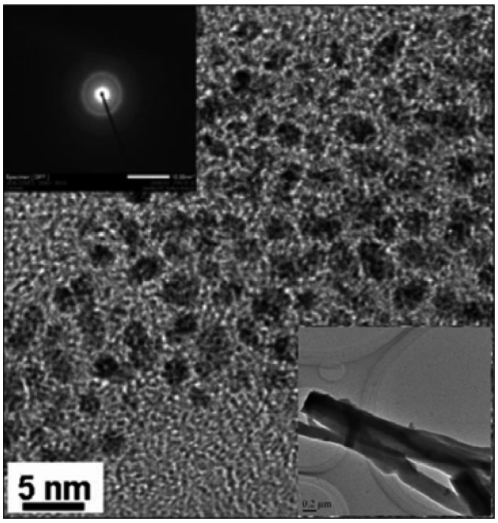

Figure 9. TEM images of TiO_2-LPEI fibers embedded with Pt nanoparticles. Inset: right bottom, low magnification images; left top, electronic diffraction pattern.

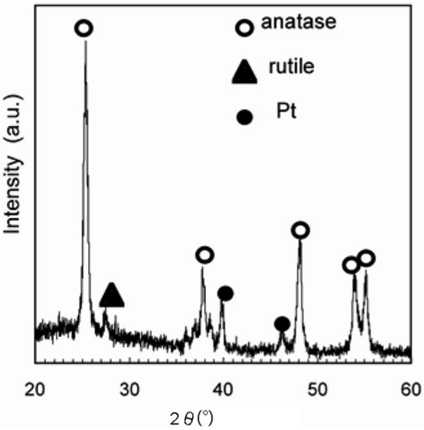

Figure 10. XRD pattern of f-TiO_2-Pt after sintered at 600 °C.

TiO_2 (<400 nm; Figure 11). The dye methylene blue (MB) was adsorbed to the point of saturation on f-TiO_2, f-TiO_2-Pt, and the anatase powders (commercially available anatase TiO_2) by soaking the powders in a MB aqueous solution (δ = 20 ppm) for 12 h. After washing and drying, the MB-adsorbed powders were cast into the dense films on glass slides. All procedures were performed in a dark room to avoid the unexpected photodecompositions. The initial intensity of the absorbance at 664 nm (before irradiation) was automatically designated as 0. After that, the decreases in the absorbance were recorded under visible- or UV-light irradiation. As seen in Figure 12, under visible-light irradiation, the photocatalytic discoloration rate for f-TiO_2-Pt was two times higher than that of f-TiO_2 and commercially available anatase, whereas the photocatalytic activities of f-TiO_2 and commercial anatase were much higher than that of f-TiO_2-Pt under UV irradiation. Generally, Pt nanoparticles in the Pt/TiO_2 system are thought to be able to trap effectively the photoexcited electron in the conduction band of TiO_2 and largely restrain the recombination of holes and electron. In the meanwhile, the presence of Pt nanoparticles probably give rise to the formation of a new energy level with low potentials in the band gap of TiO_2,[34] consequently leading to an enhancement in the response to visible-light photocatalytic activity. In the present study, however, despite the positive effects from Pt nanoparticles in TiO_2 fibers, some unconstructive influence should not be ignored with the formation of Pt nanoparticles such as the newly formed defects at the interfaces and in the matrix of the Pt-TiO_2 fibers in contrast with pure TiO_2, which are probably responsible for the decrease in the photocatalytic activity under UV-light irradiation. Accordingly, these results indicate that f-TiO_2-Pt is a desirable candidate for visible-light responsive photocatalysis for the photodegradation of organic pollutions.

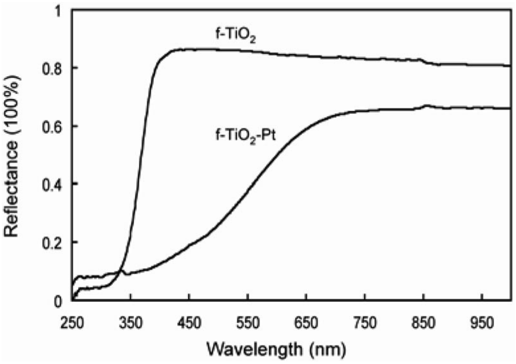

Figure 11. Diffuse reflection UV/Vis spectra of f-TiO_2 and f-TiO_2-Pt.

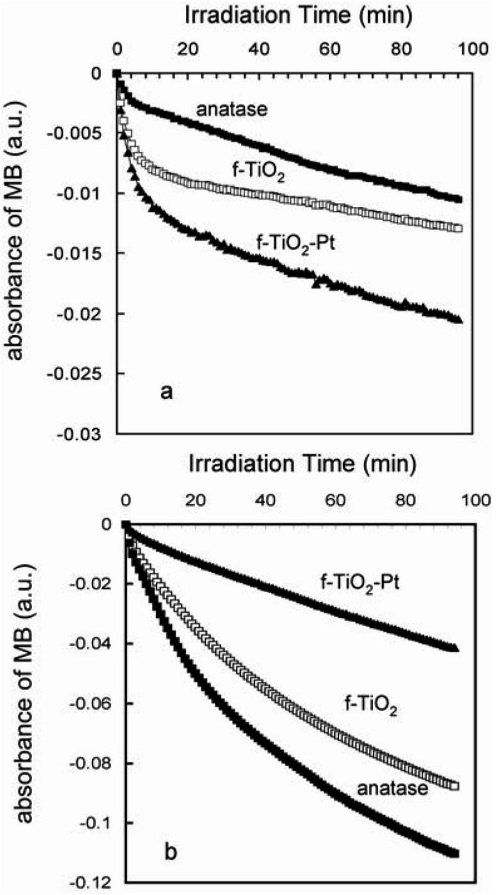

Figure 12. Photocatalytic activity of f-TiO_2, f-TiO_2-Pt, and anatase under visible (a) and UV (b) light irradiation.

Conclusions

We reported a simple biomimetic process for constructing fibrous TiO_2 networks by using linear polyethyleneimine aggregates and water-soluble TiLact. Many factors such as pH and the concentrations of LPEI and TiLact gave the effects on the morphologies and structures. The as-prepared fibrous TiO_2-LPEI hybrids had the regularly layered structures, which were composed of LPEI and TiO_2 nanocrystallites derived from the hydrolytic condensation of TiLact with LPEI aggregates. The TiO_2-LPEI hybrids were capable of loading metallic nanoparticles on their structures via spontaneously reducing metal ions on the hybrids. The Pt-nanoparticle-embedded fibrous TiO_2 showed visible-light-responsive photocatalytic activity in the decomposition of MB. We expect that the biomimetic process established in this work is favorable in constructing well-controlled nanostructured TiO_2 and the resultant TiO_2 can be simply transformed into functional materials.

Experimental Section

Synthesis of TiO_2-LPEI Hybrids: As we previously reported,[27] LPEI (average molecular weight about 20000) was prepared via the hydrolysis of the poly(2-ethyl-2-oxazoline) precursor (MW of 500000, Polyscience) in the presence of an excess amount of 5 M HCl. LPEI powders obtained were dissolved in hot distilled water at 80 °C by the concentrations of 1–5 wt.-%. After cooling slowly down to room temperature, LPEI aggregates were formed in the vessel. In contrast, water-soluble titanium bislactates (commercial name of TC310, Matsumoto Chemical Co. Japan, abbreviated as TiLact below) were concentrated by evaporation at 60 °C for 6 h.

Then, it was dissolved into distilled water again at various concentrations by 1–20 wt.-% and buffered at a range of pH 5–9 with ammonia solution (28%, Wako chemical Co. Japan). LPEI aggregates (2 mL) were mixed with TiLact solutions (4 mL) by stirring at 50 °C. After 1 h of reaction, the precipitates were thoroughly washed with distilled water, centrifuged, and dried under vacuum at 50 °C for 12 h. This procedure yielded TiO_2-LPEI hybrids.

Pt Nanoparticle Formation on TiO_2-LPEI Hybrids: The as-prepared TiO_2-LPEI fibers (0.5 g) were mixed with sodium tetrachloroplatinate(II) solutions (0.01 M, 10 mL) and stirred slowly at room temperature for 30 min. Then the fibers were washed with water (3×) and finally dried under vacuum at 50 °C for 12 h.

Characterization: The morphologies of the TiO_2-LPEI hybrids were visualized with scanning electron microscopy (Kyence, VE7800, Japan). High-resolution transmission electron microscopy (HRTEM) images were obtained with a JEM-2200FS (JEOL, Japan) transmission electron microscope. X-ray diffraction (XRD, Rigaku-Denki RX-7 diffractometer, Japan) with Cu/K_α radiation ($\lambda = 1.54$ Å) was employed to confirm the crystalline states of the hybrids. Thermal decomposition behaviors of the hybrids were verified with thermogravimetry/differential thermal analysis (TG/DTA; TG-DTA 6300, SII Nano technology Inc., Japan). UV/Vis diffuse reflection spectra were recorded with UV/Vis spectroscopy (UV3500, Hitachi Co. Japan). Raman spectroscopy was used to confirm the formation of crystalline TiO_2 (anatase or rutile). Photocatalytic activities were evaluated under visible-light irradiation of a fluorescent lamp (0.01 $\mathrm{mW\,cm^{-2}}$) and violet irradiation of UV lamp (0.2 $\mathrm{mW\,cm^{-2}}$, main wavelength 368 nm) with a simple photocatalysis evaluation apparatus (PCC-2, Ulvac Riko Co., Japan) by detecting the changes in the optical absorbance (at 664 nm) of methylene blue (MB) adsorbed on the dry powders of TiO_2 fibers (MB was adsorbed by mixing powders of TiO_2 fibers with an excess amount of 20 ppm aqueous solution of MB for 12 h). A commercially available anatase powder (Kanto chemical Co. Inc, Japan) was also used for photocatalysis evaluation as a comparison.

Supporting Information (see footnote on the first page of this article): XRD patterns of TiO_2-LPEI hybrids prepared at various pH values and various TiLact concentrations; effects of LPEI and TiLact concentrations on the morphologies of TiO_2-LPEI hybrids; effects of LPEI self-organization times on the morphologies of TiO_2-LPEI hybrids; various SEM images; XRD patterns of TiO_2-LPEI hybrid prepared in TiLact solutions with various solvents.

Acknowledgments

This research was partly supported by the Core Research for Evolutional Science and Technology (CREST) and the Japan Science and Technology Corporation (JST).

---

[1] S. Mann, *Biomimetic Materials Chemistry*, VCH Publishers, New York, **1996**.

[2] J. L. Sumerel, W. Yang, D. Kisailus, J. C. Weaver, J. H. Choi, D. E. Morse, *Chem. Mater.* **2003**, *15*, 4804.

[3] N. Kroeger, R. Deutzmann, M. Sumper, *Science* **1999**, *286*, 1129.

[4] S. S. Shankar, A. B. Ankamwar, A. Singh, A. Ahmad, M. Sastry, *Nat. Mater.* **2004**, *3*, 482.

[5] G. Pohnert, *Angew. Chem. Int. Ed.* **2002**, *41*, 3167.

[6] a) M. M. Tomczak, D. D. Glawe, L. F. Drummy, C. G. Lawrence, M. O. Stone, C. C. Perry, D. J. Pochan, T. J. Deming, R. R. Naik, *J. Am. Chem. Soc.* **2005**, *127*, 12577.

[7] A. Fujishima, K. Honda, *Nature* **1972**, *238*, 37.

[8] a) A. Hagfeldt, M. Gratzel, *Chem. Rev.* **1995**, *95*, 49; b) M. Gratzel, *Nature* **2001**, *414*, 338.

[9] A. L. Linsebigler, G. Lu, J. T. Yates Jr., *Chem. Rev.* **1995**, *95*,735.

[10] A. Fujishima, X. Zhang, A. T. Donald, *Surf. Sci. Rep.* **2008**, *63*, 2008.

[11] a) C. Burda, X. Chen, R. Narayanan, M. A. El-Sayed, *Chem. Rev.* **2005**, *105*, 1025; b) A. P. Alivisatos, *J. Phys. Chem.* **1996**, *100*, 13226; c) A. P. Alivisatos, *Science* **1996**, *271*, 933.

[12] X. Chen, S. Samuel, *Chem. Rev.* **2007**, *107*, 2891.

[13] a) T. Kasuga, M. Hiramatsu, A. Hoson, T. Sekino, K. Niihara, *Langmuir* **1998**, *14*, 3160; b) T. Kasuga, M. Hiramatsu, A. Hoson, T. Sekino, K. Niihara, *Adv. Mater.* **1999**, *11*, 1307.

[14] a) Q. Zhang, L. Gao, *Langmuir* **2003**, *19*, 967; b) X. Feng, J. Zhai, L. Jiang, *Angew. Chem. Int. Ed.* **2005**, *44*, 5115; c) Q. Huang, L. Gao, *Chem. Lett.* **2003**, *32*, 638.

[15] a) M. Andersson, L. Oesterlund, S. Ljungstroem, A. Palmqvist, *J. Phys. Chem. B* **2002**, *106*, 10674; b) S. Y. Chae, M. K. Park, S. K. Lee, T. Y. Kim, S. K. Kim, W. I. Lee, *Chem. Mater.* **2003**, *15*, 3326.

[16] J. Yuh, L. Perez, W. M. Sigmund, J. C. Nino, *Physica E: Low-Dimensional Systems and Nanostructures* **2007**, *37*, 254.

[17] P. Viswanathamurthi, N. Bhattarai, C. K. Kim, H. Y. Kim, D. R. Lee, *Inorg. Chem. Commun.* **2004**, *7*, 679.

[18] M. Y. Song, D. K. Kim, K. J. Ihn, S. M. Jo, D. Y. Kim, *Nanotechnology* **2004**, *15*, 1861.

[19] L. Miao, S. Tanemura, S. Toh, K. Kaneko, M. Tanemura, *Appl. Surf. Sci.* **2004**, *238*, 175.

[20] M. S. Sander, M. J. Cote, W. Gu, B. M. Kile, C. P. Tripp, *Adv. Mater.* **2004**, *16*, 2052.

[21] a) M. Suzuki, Y. Nakajima, T. Sato, H. Shirai, K. Hanabusa, *Chem. Commun.* **2006**, 377; b) Y. Ono, K. Nakashima, M. Sano, Y. Kanekiyo, K. Inoue, J. Hojo, S. Shinkai, *Chem. Commun.* **1998**, 1477; c) M. Suzuki, M. Kimura, H. Shirai, K. Hanabusa, *J. Am. Chem. Soc.* **2002**, *124*, 6550.

[22] Y. Yang, M. Suzuki, M. Kimura, H. Shirai, K. Hanabusa, *Chem. Commun.* **2004**, 1332.

[23] a) M. Llusar, C. Sanchez, *Chem. Mater.* **2008**, *20*, 782; b) T. Shimuzu, M. Masuda, H. Minamikawa, *Chem. Rev.* **2005**, *105*, 1401.

[24] L. Sarah, D. W. Wright, *Chem. Mater.* **2006**, *18*, 3108.

[25] a) K. Tomita, V. Petrykin, M. Kobayashi, M. Shiro, M. Yoshimura, M. Kakihana, *Angew. Chem. Int. Ed.* **2006**, *45*, 2378; b) H. MoÈckel, M. Giersig, F. Willig, *J. Mater. Chem.* **1999**, *9*, 3051.

[26] E. C. Kathryn, N. O. Andrea, M. A. Schoonen, A. M. Valentine, *Chem. Mater.* **2006**, *18*, 4592.

[27] a) J.-J. Yuan, R.-H. Jin, *Adv. Mater.* **2005**, *17*, 885; b) J.-J. Yuan, R.-H. Jin, *Langmuir* **2005**, *21*, 3136; c) R.-H. Jin, J.-J. Yuan, *Chem. Commun.* **2005**, 1399; d) R.-H. Jin, J.-J. Yuan, *Macromol. Chem. Phys.* **2005**, *206*, 2160.

[28] J.-J. Yuan, P.-X. Zhu, N. Fukazawa, R.-H. Jin, *Adv. Funct. Mater.* **2006**, *16*, 2205.

[29] R.-H. Jin, J.-J. Yuan, *J. Mater. Chem.* **2005**, *15*, 4513.

[30] a) U. Balachandran, N. G. Eror, *J. Solid State Chem.* **1982**, *42*, 276; b) H. C. Choi, Y. M. Jung, S. B. Kim, *Vib. Spectrosc.* **2005**, *37*, 33.

[31] T. Hashida, K. Tashiro, S. Aoshima, Y. Inaki, *Macromolecules* **2002**, *35*, 4330.

[32] a) C.-C. Chen, P.-L. Kuo, *J. Colloid Interface Sci.* **2006**, *293*, 101–107; b) C. Tian, B. Mao, E. Wang, Z. Kang, Y. Song, C. Wang, S. Li, *J. Phys. Chem. C* **2007**, *111*, 3651.

[33] A. L. Linsebigler, G. Lu, J. T. Yates Jr., *Chem. Rev.* **1995**, *95*, 735.

[34] T. Sasaki, N. Koshizaki, J.-W. Yoon, K. M. Beck, *J. Photochem. Photobiol.: A Chem.* **2001**, *145*, 11.

Received: August 22, 2009

DOI: 10.1002/ejic.200900905

“Naked” $[Mn_3O]^{7+}$ Triangles: The Effect of Auxiliary Ligands on Magnetic Exchange

Efi Manolopoulou,[a] Constantinos C. Stoumpos,[a,b] Milosz Siczek,[c] Tadeusz Lis,[c]
Euan K. Brechin,[d] and Constantinos J. Milios*[a]

Keywords: Manganese / Oximes / Magnetic properties / Ligand effects

The reaction between $Mn(ClO_4)_2{\cdot}6H_2O$, Et-saoH_2 (Et-saoH_2 = 2-hydroxypropiophenone oxime), NEt_4OH and $[Ni(pao)_2(py)_2]$ (paoH = 2-pyridylaldoxime) in MeOH forms the complex $[Mn^{III}_3O(Et\text{-}sao)_3(HCO_2)(MeOH)_5]$ (**1**) in good yields. The reaction of $MnCl_2{\cdot}4H_2O$, Me-saoH_2 (Me-saoH_2 = 2-hydroxyphenylethanone oxime), NEt_4OH and DL-valine in MeOH gives the complex $[Mn^{III}_3O(Me\text{-}sao)_3(MeOH)_5]Cl$ (**2**) in moderate yields. In both complexes the building block consists of a triangular $\{Mn^{III}_3O(R\text{-}sao)_3\}$ unit (R = Et, Me for **1** and **2**, respectively). In the case of **2**, the $[Mn_3]$ unit can be considered "naked" as there is no capping ligand present, whereas in the case of **1** a formate ion is terminally bonded to one metal centre. DC magnetic susceptibility measurements for **1** and **2** reveal the presence of both ferromagnetic and antiferromagnetic intramolecular interactions, depending on the Mn–N–O–Mn torsion angles within each cluster, leading to a ground state $S = 2$ for both complexes. Rationalization of this result is attempted by structural comparison of previously reported triangular $[Mn_3]$ oximate complexes on the basis of "flat" and "twisted" torsion angles and the effect of the auxiliary ligands.

Introduction

The interest in synthesizing polymetallic Mn complexes was given a major boost when it was discovered that the $[Mn_{12}O_{12}(O_2CMe)_{16}(H_2O)_4]$ complex[1] could retain its magnetization below a certain temperature and display superparamagnetic-like properties evident by the appearance of hysteresis loops in the magnetization versus field plots.[2] The origin of this phenomenon was found to be the large spin ground state of the molecule, *S*, coupled with a significant negative zero-field splitting (ZFS) parameter, *D*, giving rise to an energy barrier for the reversal of the magnetization. Molecules that exhibit such behaviour have been called single-molecule magnets (SMMs) and since their discovery much effort has been directed towards the preparation of molecules incorporating a large number of metal ions (particularly Mn) aiming to isolate compounds that possess large *S* and *D* values. Throughout this research activity several complexes were prepared, leading not only to new types of SMMs, but also to materials with a wide range of potential applications including information storage, molecular spintronics, quantum computation, magnetic refrigeration and MRI.[3]

Our ongoing interest in this field has focused on the synthesis of Mn complexes with salicylaldoxime-based organic ligands (R-saoH_2; R = H, Me, Et, etc.), which has so far produced a set of compounds with the aforementioned magnetic properties.[4] Most notably this includes a family of hexanuclear SMMs of general formula $[Mn^{III}_6O_2(R\text{-}sao)_6(R'CO_2)_2(sol)_{4-6}]$ (R = H, Me, Et; R′ = various; sol = H_2O, MeOH, EtOH) for which a magnetostructural correlation could be established, and an SMM with the largest effective energy barrier to magnetization reversal.[5,6] The hexanuclear SMMs consists of two ferromagnetically coupled $[Mn^{III}_3O(R\text{-}sao)_3]^+$ triangles. The exchange interactions within the triangles could be varied from antiferromagnetic to ferromagnetic by twisting and structurally distorting the core of the complex upon substitution of the oximate and/or the carboxylate ligands. This induces a change in the Mn–N–O–Mn torsion angle (α) and consequently an increase or decrease in the pairwise exchange coupling and a change in the ground state spin of the complex. Qualitatively, α angles below ca. 30.4° were found to produce antiferromagnetic pairwise exchange and α angles above ca. 31.3° produced ferromagnetic pairwise exchange.[6]

Despite the fact that structure–property relations are now well understood for hexanuclear clusters, the case for the constituent $[Mn^{III}_3O(R\text{-}sao)_3]^+$ triangles (and related $[Mn_3O]^{7+}$ triangular complexes) has just started to crys-

---

[a] Department of Chemistry, University of Crete,
71003 Herakleion, Greece
E-mail: komil@chemistry.uoc.gr
[b] Department of Chemistry, University of Patras,
26504 Patras, Greece
[c] Faculty of Chemistry, University of Wroclaw,
Joliot-Curie 14, 50-383 Wroclaw, Poland
[d] School of Chemistry, The University of Edinburgh,
West Mains Road, EH9 3JJ, UK

Supporting information for this article is available on the WWW under http://dx.doi.org/10.1002/ejic.200900905.

tallize.[7–14] Magnetic studies for such compounds date back to 1950 when Kambe,[15] studying the "basic" metal carboxylates $[\mathrm{Mn^{III}}_3\mathrm{O}(\mathrm{RCO_2})_6\mathrm{L}_3]^{n+}$ (R = various, L = terminal ligand), was able to predict the molecular structures of such compounds long before they were solved crystallographically.[16] In all cases these triangles display dominant antiferromagnetic pairwise exchange interactions.[17]

The first example of a ferromagnetic Mn triangle was reported in 2002: the complex $[\mathrm{Mn^{III}}_3\mathrm{O(bamen)_3}]^+$ [bamenH_2 = 1,2-bis(biacetylmonoximeimino)ethane],[18] contains six diatomic Mn–N–O–Mn oximate bridges rather than the six triatomic Mn–O–C–O–Mn carboxylate bridges present in the "basic" Mn carboxylates. The second example was reported some three years later in 2005: $[\mathrm{Mn^{III}}_3\mathrm{O}(\mathrm{MeCO_2})_3(\mathrm{mpko})_3]^+$ (mpkoH = methyl-2-pyridyl ketone oxime) consists of three triatomic Mn–O–C–O–Mn carboxylate bridges and three diatomic Mn–N–O–Mn oximate bridges, each of which bridges two Mn atoms on the same edge of the triangle.[19] Other examples in which the Mn–O–C–O–Mn bridges have been replaced with monoatomic (Mn–O–Mn) bridges, for example in the complex $[\mathrm{Mn^{III}}_3\mathrm{O(5\text{-}Br\text{-}sap)_3(H_2O)_3}]^+$ [5-Br-sapH_2 = 2-(5-bromosalicylideneamino)-1-propanol],[20] have always produced complexes displaying dominant antiferromagnetic exchange.

The above suggests that a sensible route for "unlocking" ferromagnetic exchange pathways within $[\mathrm{Mn_3O}]^{7+}$-type complexes lies in the use of ligands bearing diatomic bridging compartments. However, this statement is only partially true. Attempts to prepare complexes with other diatomic ligands such as pyrazolates[21] and benzotriazolates[22] led to molecules with only antiferromagnetic interactions, perhaps due to the rigidity of the azolate (Mn–N=N–Mn) bridge compared to that of the oximate (Mn–N–O–Mn) bridge. Thus, we have been trying to prepare triangular complexes using oxime-base ligands, seeking to better understand the factors that govern the magnetic interactions within the $[\mathrm{Mn_3}]$ units, and we are now able to switch the pairwise exchange interactions from antiferromagnetic to ferromagnetic in a family of salicylaldoximate-base Mn triangles. We have previously reported the synthesis of several R-saoH_2-based Mn triangles involving carboxylate bridges with the general formula $[\mathrm{Mn^{III}}_3\mathrm{O(R\text{-}sao)_3(R'CO_2)(sol)_{3-4}}]$[7,10] as well as triangles of general formula $[\mathrm{Mn^{III}}_3\mathrm{O(R\text{-}sao)_3(XO_4)(sol)_3}]$[12] (X = Cl, Re) in which tetrahedral ligands cap one face of the cluster. Herein we report the synthesis of two new members of the family, namely, $[\mathrm{Mn^{III}}_3\mathrm{O(Et\text{-}sao)_3(HCO_2)(MeOH)_5}]$ (**1**) and $[\mathrm{Mn^{III}}_3\mathrm{O(Me\text{-}sao)_3(MeOH)_5}]\mathrm{Cl}$ (**2**), that do not incorporate any auxiliary bridging ligands other than the oximes.

Results and Discussion

Synthesis

Complex **1** was prepared by treating an alcoholic solution containing $\mathrm{Mn(ClO_4)_2{\cdot}6H_2O}$, Et-sao$H_2$ and $\mathrm{NEt_4OH}$ (a reaction mixture from which the complex $[\mathrm{Mn^{III}}_3\mathrm{O(Et\text{-}sao)_3(ClO_4)(MeOH)_3}]$ can be isolated[12]) with solid $[\mathrm{Ni(pao)_2(py)_2}]$.[23] The initial aim of the reaction was to perform an in situ replacement of the weakly bonded capping perchlorate with one or both of the oximate oxygen atoms of the metalloligand. Indeed, the $\mathrm{ClO_4^-}$ ion was removed but contrary to our ambitions it was replaced by two MeOH molecules and a terminally bonded formate ($\mathrm{HCO_2^-}$) ion – the result of a commonly observed oxidation of the solvent. The presence of the latter is required to balance the single positive charge of the $\{\mathrm{Mn^{III}}_3\mathrm{O(Et\text{-}sao)_3}\}^+$ core. Complex **2** was isolated from a similar reaction by adding DL-valine to a MeOH/EtOH mixture of $\mathrm{MnCl_2{\cdot}4H_2O}$, Me-sao$H_2$ and $\mathrm{NEt_4OH}$. Yet again, the obtained compound does not contain the added coligand; though clearly it still affects the identity of the final product. The terminal ligands above and below the $\mathrm{Mn_3}$ plane are again solvate MeOH molecules, whereas a weakly interacting chloride is present to counterbalance the charge of the $\{\mathrm{Mn^{III}}_3\mathrm{O(Me\text{-}sao)_3}\}^+$ core.

X-ray Crystal Structures

Selected interatomic distances and angles are listed in Table 1, and bond valence sum (BVS) calculations for the metal ions of the two complexes are given in Table 2. Crystallographic information for both complexes is presented in Table 3. In Figure 1 is presented the molecular structure of complex **1**. It crystallizes in the chiral orthorhombic $P2_12_12_1$ space group. It consists of three independent $\mathrm{Mn^{III}}$ ions held together by a central μ_3-$\mathrm{O^{2-}}$ ligand to form a scalene triangle (Mn1···Mn2 3.248 Å, Mn2···Mn3, 3.261 Å and Mn3···Mn1 3.278 Å). The central oxido bridge is located 0.033(1) Å above the $[\mathrm{Mn_3}]$ plane. The three oximate ligands provide peripheral support to the $\{\mathrm{Mn_3O}\}^{7+}$ core bridging across each edge of the triangle in a $\eta^1{:}\eta^1{:}\eta^1{:}\mu$ mode; chelating one Mn ion through N,O ligation forming a six-membered ring, and bridging a second Mn metal through the deprotonated oximate oxygen atom. The three ligands thus form a puckered $\{\mathrm{Mn{-}N{-}O{-}}\}_3$ ring. The oxide/oximate coordination saturates the equatorial plane of the distorted octahedra around each Mn ion, leaving the axial positions to be occupied by flexible monodentate ligands; these define the Jahn–Teller (JT) elongation axes for the three Mn sites. Five of these ligands are MeOH molecules, whereas the sixth is a monoatomically coordinated formate anion, leading to a chiral centre at the octahedron defined by Mn2. All three JT axes are approximately coparallel and perpendicular to the $\mathrm{Mn_3}$ plane. The torsion angles are: Mn1–N–O–Mn2 38.36(11)°, Mn2–N–O–Mn3 28.68(11)° and Mn3–N–O–Mn1 32.86(11)°, showing that the ring is somewhat distorted from planarity, with two angles being above the limiting window of 30.4–31.3° governing the magnetic exchange (vide infra).

Complex **2** (Figure 2) has a very similar structure. It crystallizes in the monoclinic $P2_1/c$ space group and possesses a $\{\mathrm{Mn^{III}}_3\mathrm{O}\}^{7+}$ core with the three metals in a triangular arrangement supported by three oximate $\eta^1{:}\eta^1{:}\eta^1{:}\mu$ ligands.

Table 1. Selected interatomic distances [Å] and angles [°] for complexes **1** and **2**.

1		**2**	
Mn1–O1	1.887(1)	Mn1–O1	1.899(2)
Mn1–O11	1.870(1)	Mn1–O11	1.866(1)
Mn1–O14	2.244(1)	Mn1–O14	2.242(1)
Mn1–O15	2.311(1)	Mn1–O15	2.287(1)
Mn1–O22	1.922(1)	Mn1–O22	1.932(1)
Mn1–N11	2.010(1)	Mn1–N11	2.004(1)
Mn2–O1	1.883(1)	Mn2–O1	1.883(1)
Mn2–O12	1.858(1)	Mn2–O12	1.871(1)
Mn2–O16	2.238(1)	Mn2–O16	2.261(1)
Mn2–O17	2.331(1)	Mn2–O17	2.306(1)
Mn2–O23	1.912(1)	Mn2–O23	1.918(1)
Mn2–N12	2.012(1)	Mn2–N12	2.022(1)
Mn3–O1	1.881(1)	Mn3–O1	1.873(1)
Mn3–O13	1.855(1)	Mn3–O13	1.850(1)
Mn3–O18	2.425(1)	Mn3–O18	2.204(1)
Mn3–O19	2.258(1)	Mn3···Cl	3.107(1)
Mn3–O21	1.928(1)	Mn3–O21	1.900(1)
Mn3–N13	2.012(1)	Mn3–N13	2.006(1)
Mn1–O22–N12–Mn2	38.36(11)	Mn1–O22–N12–Mn2	40.19(11)
Mn2–O23–N13–Mn3	28.68(11)	Mn2–O23–N13–Mn3	–28.93(12)
Mn3–O21–N11–Mn1	32.86(11)	Mn3–O21–N11–Mn1	37.25(11)
Mn1–O1–Mn2	118.95(5)	Mn1–O1–Mn2	120.16(6)
Mn1–O1–Mn3	120.88(5)	Mn1–O1–Mn3	119.72(5)
Mn2–O1–Mn3	120.08(5)	Mn2–O1–Mn3	120.03(6)

Table 2. BVS calculations for complexes **1** and **2**.

1	Mn^{2+}	Mn^{3+}	Mn^{4+}
Mn1	3.276069	3.0311	3.12608
Mn2	3.231719	2.990254	3.083651
Mn3	3.317408	3.068725	3.165883
2	Mn^{2+}	Mn^{3+}	Mn^{4+}
Mn1	3.273027	3.028977	3.122779
Mn2	3.259118	3.014491	3.110434
Mn3	3.193518	2.955968	3.046592

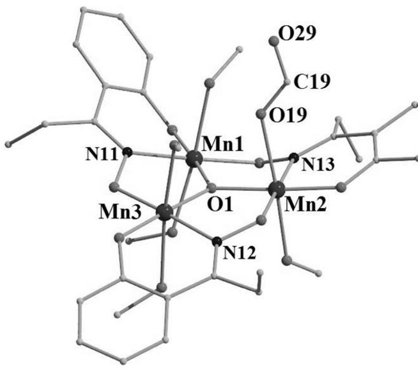

Figure 1. The molecular structure of complex **1**.

The central oxide is again 0.033(1) Å above the $[Mn_3]$ plane. Of the six axial coordination sites on the Mn atoms, five are occupied by MeOH ligands, with the sixth remaining "vacant", leading to a square pyramidal geometry around Mn3 [τ = 2.01 %].[24] The Cl^- counterion weakly interacts with Mn3, the Mn(3)–Cl distance is 3.107(2) Å. The torsion angles fall within the same range as those of **1**: Mn1–N–O–Mn2 40.19(11)°, Mn2–N–O–Mn3 28.93(12)° and Mn3–N–O–Mn1 37.25(11)°.

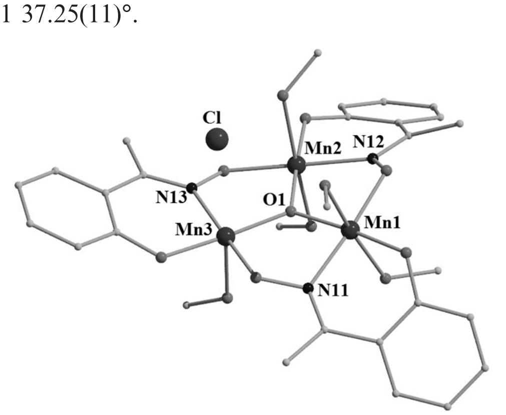

Figure 2. The molecular structure of complex **2**.

The presence of anions that can act as hydrogen-bond acceptors and MeOH and HCO_2^- molecules that can act as hydrogen-bond donors produces 1D networks of clusters in the crystals (Figure 3). In complex **1**, the two MeOH molecules sitting on the same face of the triangle as the formate ligand are H-bonded to the coordinated oxygen atom of the HCO_2^- ligand (O17), forming a bifurcated intramolecular H-bond. The noncoordinated oxygen atom of the HCO_2^- ligand (O27) is also H-bonded to two MeOH molecules originating from the opposite face of an adjacent triangle, forming a second bifurcated bond. The third MeOH molecule is H-bonded to one of the two involved in the intermolecular bonding, forming a single intramolecular H-bond.

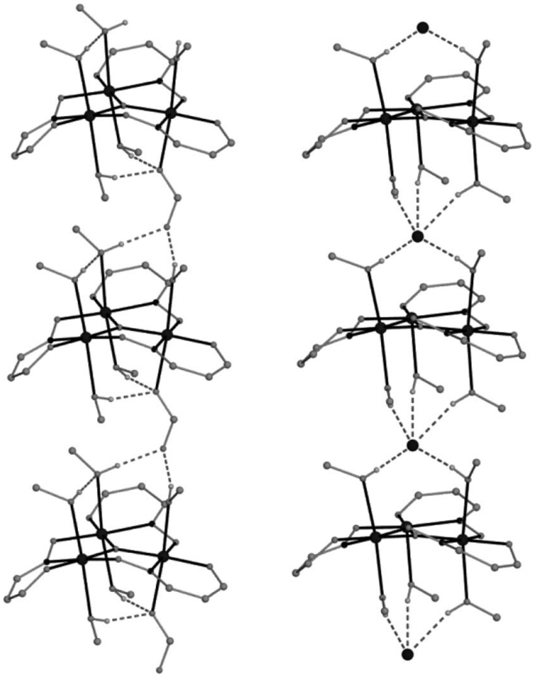

Figure 3. The supramolecular 1D structures of complexes **1** (left) and **2** (right) in the crystals. Only the methanolic hydrogen atoms are shown.

In complex **2**, the H-bonding pattern is even more spectacular: all five MeOH molecules are H-bonded to the Cl^- counterion, forming a quintuply furcated bond (Figure 3).

Magnetochemistry

DC Magnetic Susceptibility Studies

Variable-temperature dc magnetic susceptibility data were collected on powdered microcrystalline samples of **1** and **2** in the temperature range 5–300 K under an applied field of 0.1 T. The results are plotted as the $\chi_M T$ product vs. T in Figure 4. For complex **1**, the room-temperature $\chi_M T$ value is 7.95 $cm^3 mol^{-1} K$ slightly lower than the expected value of 9.00 $cm^3 mol^{-1} K$ for three uncoupled $S = 2$ spins with $g = 2$. Upon cooling, this value remains near constant until ca. 140 K, below which it starts to decrease, reaching a value of 3.97 $cm^3 mol^{-1} K$ at 5 K. The low-temperature value is indicative a small spin ground state of $S \approx 2$. Complex **2** displays almost identical behaviour. The room-temperature $\chi_M T$ value of 8.21 $cm^3 mol^{-1} K$ remains constant until ca. 130 K, below which it decreases to reach the value of 3.15 $cm^3 mol^{-1} K$ at 5 K. Both triangles are scalene (Figures 1 and 2), and thus, strictly speaking, there are three different exchange pathways between the metal ions. However, we were able to successfully simulate the magnetic data for both complexes employing the 2-J scheme shown in Figure 5, which assumes Mn–N–O–Mn bridges with similar torsion angles are equivalent. Using the program MAGPACK[25] and the spin Hamiltonian shown in Equation (1) afforded the parameters: $S = 2$, $J_1 = +0.5\ cm^{-1}$, $J_2 = -3.4\ cm^{-1}$, $g = 1.95$ and $S = 2$, $J_1 = +0.5\ cm^{-1}$, $J_2 = -4.2\ cm^{-1}$, $g = 1.98$ for complexes **1** and **2**, respectively. The first excited state for both complexes is $S = 3$, which lies 4.8 and 6.4 cm^{-1} above the ground state for **1** and **2**, respectively, consistent with the slightly stronger antiferromagnetic interaction present in **2**.

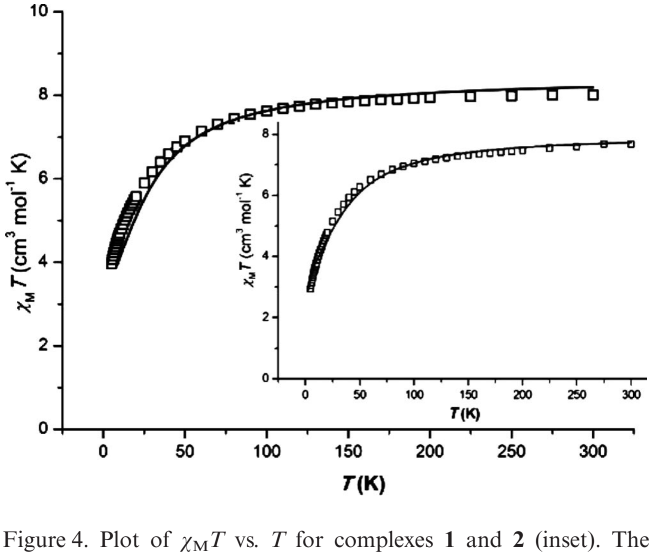

Figure 4. Plot of $\chi_M T$ vs. T for complexes **1** and **2** (inset). The solid lines represent the simulation of the experimental data in the temperature range 300–5 K (see text for details).

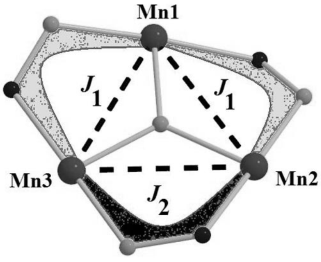

Figure 5. J coupling scheme for **1** and **2**. The grey-filled area represents torsion angles above the *magic area*, whereas the black-filled area shows the torsion angle below the *magic area*.

$$\hat{H} = -2J_1(\hat{S}_1\hat{S}_2 + \hat{S}_1\hat{S}_3) - 2J_2(\hat{S}_2\hat{S}_3) \qquad (1)$$

On the basis of our previous work,[5–7,10,12] we are able to interpret the values obtained from the simulation process in terms of the Mn–N–O–Mn torsion angle dependence. Thus, the ferromagnetic exchange pathway is assigned to the edges of the triangle that are bridged through the oximate ligands that form a torsion angle large enough to overcome the "*magic area*" of 30.4–31.3° (32.9 and 38.4° for **1** and 40.2 and 37.2° for **2**), whereas the antiferromagnetic interaction arises from the oxime pathway that has a torsion angle below the *magic area* (28.7° for **1** and 28.9° for **2**).

In an attempt to further verify the ground state of the complexes, variable-temperature and variable-field magnetization measurements were taken in the 1.8–7 K and 0.4–

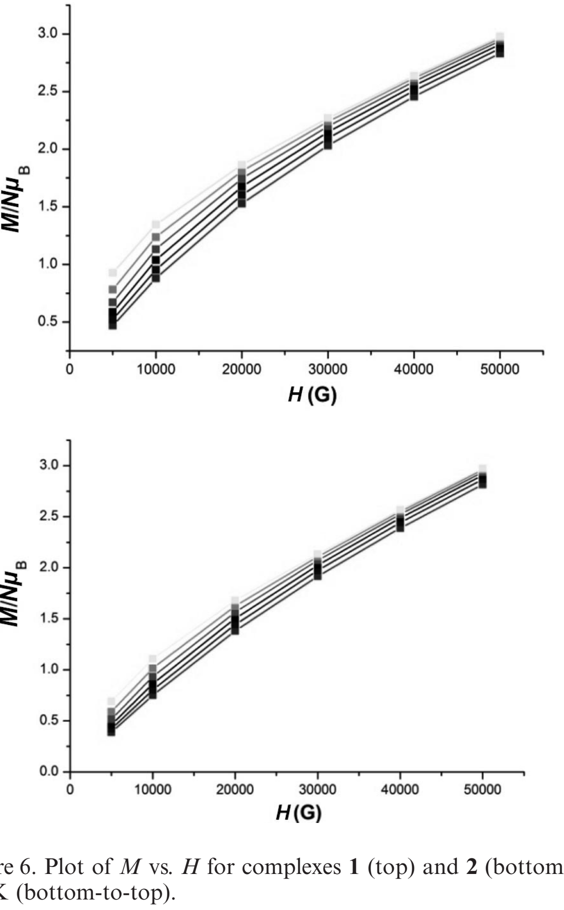

Figure 6. Plot of M vs. H for complexes **1** (top) and **2** (bottom) at 2–7 K (bottom-to-top).

5 T ranges. These are plotted in Figure 6. However, we were unable to satisfactorily fit the data, most probably due to the population of multiple low-lying excited states, which is a common problem in this family of complexes, and in all complexes in which the exchange interactions are extremely weak (weak exchange limit).[26] Indeed, the magnetization data increases only slowly with increasing field rather than abruptly reaching saturation as one would expect for an isolated ground state.

AC Magnetic Susceptibility Studies

Variable-temperature ac magnetic susceptibility data were collected on powdered microcrystalline samples of **1** and **2** in the temperature range 1.8–10 K in zero applied dc field and a 2.5 G ac field oscillating at 50, 250 and 1000 Hz.

For **1**, the in-phase signal (χ_M', plotted as $\chi_M'T$ vs. T in Figure 7) decreases upon cooling, indicating the presence of excited states with $S_{exc.} > S_{g.s.}$, consistent with the simulation of the dc data. Extrapolation of the curve to 0 K from ca. 4 K gives a $\chi_M'T$ value of ca. 3 $cm^3 mol^{-1}$ K, in excellent agreement with the $S = 2$ "ground state" found from dc data. No out-of-phase (χ_M'') signals were observed in this temperature range despite the appearance of some frequency dependence in the in-phase signal. Complex **2** displays essentially analogous behaviour (Figure S1, Supporting Information).

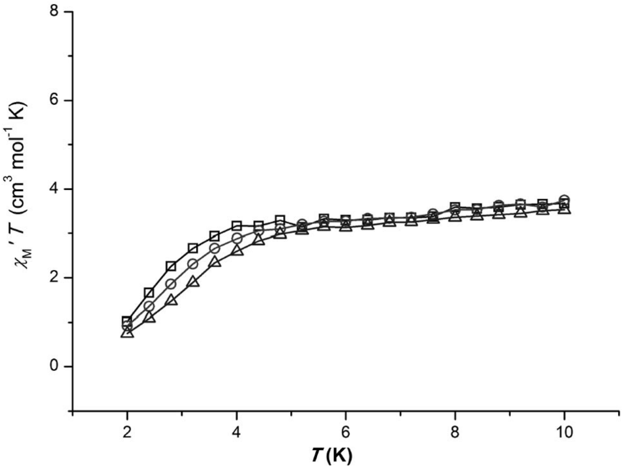

Figure 7. Plot of the in-phase (as $\chi_M'T$) ac susceptibility for **1** in the indicated temperature range, under a 2.5 G ac field oscillating at 50 Hz (squares), 250 Hz (circles) and 1000 Hz (triangles).

Discussion and Concluding Remarks

Complexes **1** and **2** represent two additional examples of compounds that follow the "*magic area*" rule of thumb, initially proposed and applied for 30 hexanuclear manganese salicylaldoximate (R-$saoH_2$) complexes.[6b] This rule has also been applied to successfully interpret the magnetic behaviour of two octanuclear manganese clusters[27] and, recently, was found to be valid for approximately 25 trinuclear manganese salicylaldoximate complexes.[28] According to this rule – and specific to salicylaldoxime-bridged Mn^{III} complexes – when a Mn–N–O–Mn torsion angle, α, is larger than ca. 31.3°, then $J > 0$ (F), and if $\alpha <$ ca. 30.4°, then $J < 0$ (AF). In all the cases reported so far, the ferro- or antiferromagnetic nature of the exchange interaction was (in the main) attributed to the distortion of the torsion angle induced by the substituted R-$saoH_2$ ligands, somewhat overlooking the contribution of the bridging/capping ligands. Complex **1** is the first example of a $[Mn_3]$ salicylaldoximate compound in which there is no bridging/capping ligand. The most important conclusion we can extract from the current result is that although the bridging/capping ligand has little *direct* effect on the magnitude of $|J|$, its presence is vital if one wants to isolate a more puckered triangle; that is, the presence of a capping ligand in combination with bulky R-$saoH_2$ ligands enables more distortion of the $[Mn_3]$ plane, which in turn leads to larger $|J|$. When a capping/bridging ligand is not present it appears the distortion imposed by the R-$saoH_2$ is, in itself, insufficient for all the Mn–N–O–Mn torsion angles to be larger than the ca. 31.3° required to produce ferromagnetic pairwise exchange interactions. In the above examples, two torsion angles are above the 31.3° limit, and one below it. The effect of the capping ligand becomes more profound if we consider the complex $[Mn^{III}_3O(Et\text{-}sao)_3(ClO_4)]$,[12] in which the presence of the "pincer-like" face-capping perchlorate, combined with equatorially bonding Et-sao^{2-} ligands, enforces huge distortions on the Mn–O–N–Mn torsion angles (all torsion angles are ca. 42°). Compound **2** is the first example of a "naked" $[Mn_3]$ compound, which does not contain any capping ligand, but rather a halide counterion – albeit one that occupies a position near the "vacant" coordination site of the Mn^{III} ion. Again, the methyl-derivatized oxime, Me-sao^{2-}, on its own, is incapable of "twisting" the torsion angles to the extent that ferromagnetic exchange occurs. It thus appears that the use of auxiliary face-capping ligands is beneficial in achieving maximal structural distortion.

Experimental Section

Physical Methods: All manipulations were performed under aerobic conditions using materials and solvents (Merck, Aldrich) as received. Infrared spectra (4000–400 cm^{-1}) were recorded from KBr pellets with a Perkin–Elmer PC 16 FTIR spectrometer. Magnetic susceptibility measurements were carried out for polycrystalline samples of **1** and **2** with a SQUID magnetometer operating in the 5–300 K temperature range under a constant 0.1 T magnetic field. Diamagnetic corrections were estimated from Pascals constants.

$[Mn^{III}_3O(Et\text{-}sao)_3(HCO_2)(MeOH)_5]$ (1): A solution of $Mn(ClO_4)_2\cdot 6H_2O$ (0.725 g, 2.00 mmol) and Et-$saoH_2$ (0.336 g, 2.00 mmol) in MeOH was treated whilst stirring with an ethanolic solution of NEt_4OH (6 mL, 0.1 M), leading to an intensely coloured green/black solution. To this was added solid $[Ni(pao)_2(py)_2]$ (0.458 g, 1.00 mmol) with no significant colour change. After 2 d, black needles started to precipitate, which were washed carefully with MeOH and dried in air. The yield was ca. 50%. $C_{33}H_{48}Mn_3N_3O_{14}$ (875.57): calcd. C 45.27, H 5.53, N 4.80; found C 45.12, H 5.28, N 4.97. IR (KBr pellet): $\tilde{\nu}$ = 1593 (s), 1537 (m), 1429 (m), 1387 (s), 1327 (s), 1296 (m), 1249 (w), 1220 (w), 1187 (w), 1068 (s), 963 (s), 824 (m), 804 (w), 752 (m), 699 (s), 666 (s), 632 (s), 502 (m) cm^{-1}.

$[Mn^{III}_3O(Me\text{-}sao)_3(MeOH)_5]Cl$ (2): A solution of $MnCl_2\cdot 4H_2O$ (0.495 g, 2.00 mmol) and Me-saoH_2 (0.312 g, 2.00 mmol) in MeOH was treated whilst stirring with an ethanolic solution of NEt_4OH (6 mL, 0.1 M), leading to an intensely coloured green/black solution. To this was added solid DL-valine (0.225 g, 2.00 mmol) with no significant colour change. After 1 d, black blocks started to precipitate from the portion of the solution left for slow evaporation. The crystals were collected by decantation, washed with a minimum amount of MeOH and dried in air. The yield was ca. 35%. $C_{29}H_{41}ClMn_3N_3O_{12}$ (823.92): calcd. C 42.28, H 5.02, N 5.10; found C 42.35, H 5.08, N 5.03. IR (KBr pellet): $\tilde{\nu}$ = 1601 (s), 1533 (m), 1439 (m) (s), 1337 (s), 1300 (m), 1253 (w), 1222 (w), 1190 (w), 1068 (s), 962 (s), 826 (m), 800 (w), 748 (m), 700 (s), 661 (s), 633 (s), 500 (m) cm^{-1}.

Crystallography: Diffraction data were collected with Mo-K_α radiation (λ = 0.71073 Å) with an Xcalibur PX diffractometer with CCD Onyx camera. The structures were solved by direct methods and refined by using the full-matrix least-squares method on F^2 with the use of SHELXL-97 software.[29] All non-hydrogen atoms were refined with anisotropic thermal parameters. All H atoms were placed in geometrically calculated positions and refined by using a riding model with U_{iso} set at $1.2U_{eq}$(C) for aromatic and formic H atoms, and $1.5U_{eq}$(C or O) for methyl and methanol H atoms. Crystallographic parameters for the crystal structures of complexes **1** and **2** are gathered in Table 3. CCDC-746270 (for **1**) and -746271 (for **2**) contain the supplementary crystallographic data for this paper. These data can be obtained free of charge from The Cambridge Crystallographic Data Centre via www.ccdc.cam.ac.uk/data_request/cif.

Table 3. Crystallographic parameters for the crystal structures of complexes **1** and **2**.

	1	**2**
Formula	$C_{33}H_{48}Mn_3N_3O_{14}$	$C_{29}H_{41}ClMn_3N_3O_{12}$
M (g mol^{-1})	875.56	823.92
Crystal system	orthorhombic	monoclinic
Space group	$P2_12_12_1$	$P2_1/c$
Dimensions (mm^{-1})	0.08 × 0.12 × 0.42	0.04 × 0.05 × 0.60
a (Å)	8.477(3)	17.592(6)
b (Å)	20.846(7)	7.785(3)
c (Å)	21.916(7)	25.100(8)
β (°)	90.00	95.74(3)
V (Å^3)	3873(2)	3420(2)
Z	4	4
T (K)	100(2)	120(2)
λ (Å)	0.71073[a]	0.71073[a]
$\rho_{calcd.}$ (g cm^{-3})	1.502	1.600
μ (mm^{-1})	1.031	1.233
Measd./independent (R_{int}) reflns.	36208/18082 (0.0393)	41877/15032 (0.0520)
Obsd. reflns. [$I > 2\sigma(I)$]	11614	8237
R_1[b]	0.0366	0.0404
wR_2[c]	0.0739	0.0952
GOF on F^2	1.011	1.004
$(\Delta\rho)_{max.,min.}$ (e Å^{-3})	059, –0.66	0.685, –0.495

[a] Mo-K_α radiation, graphite monochromator. [b] $R_1 = \Sigma(|F_o| - |F_c|)/\Sigma(|F_o|)$ for observed reflections. [c] $wR_2 = \{\Sigma[w(F_o^2 - F_c^2)^2]/\Sigma[w(F_o^2)^2]\}^{1/2}$ for all data.

Supporting Information (see footnote on the first page of this article): Plot of the in-phase (as $\chi_M'T$) ac susceptibility for **2** in the indicated temperature range under a 2.5 G ac field oscillating at 50, 250 and 1000 Hz.

Acknowledgments

C. J. M. would like to acknowledge BIOSOLENUTI (Bioinspired Solar Energy Utilization, REGPOT-2008-1, grant number 229927) for financial support. E. K. B. would like to thank the EPSRC for funding.

---

[1] T. Lis, *Acta Crystallogr., Sect. B* **1980**, *36*, 2042–2046.
[2] R. Sessoli, D. Gatteschi, A. Caneschi, M. A. Novak, *Nature* **1993**, *365*, 141–143.
[3] D. Gatteschi, R. Sessoli, J. Villain, *Molecular Nanomagnets*, Oxford University Press, Oxford, **2006**.
[4] C. J. Milios, S. Piligkos, E. K. Brechin, *Dalton Trans.* **2008**, 1809–1817.
[5] C. J. Milios, A. Vinslava, S. Moggach, S. Parsons, W. Wernsdorfer, G. Christou, S. P. Perlepes, E. K. Brechin, *J. Am. Chem. Soc.* **2007**, *129*, 2754–2755.
[6] a) C. J. Milios, R. Inglis, A. Vinslava, R. Bagai, W. Wernsdorfer, S. Parsons, S. P. Perlepes, G. Christou, E. K. Brechin, *J. Am. Chem. Soc.* **2007**, *129*, 12505 –12511; b) R. Inglis, L. F. Jones, C. J. Milios, S. Datta, A. Collins, S. Parsons, W. Wernsdorfer, S. Hill, S. P. Perlepes, S. Piligkos, E. K. Brechin, *Dalton Trans.* **2009**, 3403–3412.
[7] J. Cano, T. Cauchy, E. Ruiz, C. J. Milios, C. C. Stoumpos, T. C. Stamatatos, S. P. Perlepes, G. Christou, E. K. Brechin, *Dalton Trans.* **2008**, 234–240.
[8] H. B. Xu, B.-W. Wang, F. Pan, Z.-M. Wang, S. Gao, *Angew. Chem. Int. Ed.* **2007**, *46*, 7388–7393.
[9] C. J. Milios, P. A. Wood, S. Parsons, D. Foguet-Albiol, C. Lampropoulos, G. Christou, S. P. Perlepes, E. K. Brechin, *Inorg. Chim. Acta* **2007**, *360*, 3932–3940.
[10] R. Inglis, L. F. Jones, A. Collins, S. A. Moggach, S. Parsons, S. P. Perlepes, W. Wernsdorfer, E. K. Brechin, *Chem. Eur. J.* **2008**, *14*, 9117–9121.
[11] C. J. Milios, R. Inglis, L. F. Jones, A. Prescimone, S. Parsons, W. Wernsdorfer, E. K. Brechin, *Dalton Trans.* **2009**, 2812–2822.
[12] R. Inglis, L. F. Jones, G. Karotsis, A. Collins, S. Parsons, S. P. Perlepes, W. Wernsdorfer, E. K. Brechin, *Chem. Commun.* **2008**, 5924–5926.
[13] C. C. Stoumpos, R. Inglis, G. Karotsis, L. F. Jones, A. Collins, S. Parsons, C. J. Milios, G. S. Papaefstathiou, E. K. Brechin, *Cryst. Growth Des.* **2009**, *9*, 24–27.
[14] C. I. Yang, W. Wernsdorfer, K. H. Cheng, M. Nakano, G. S. Lee, H.-L. Tsai, *Inorg. Chem.* **2008**, *47*, 10184–10186.
[15] K. Kambe, *J. Phys. Soc. Jpn.* **1950**, *5*, 48–51.
[16] a) J. N. Van Niekerk, F. R. L. Schoening, *Acta Crystallogr.* **1953**, *6*, 227; b) B. N. Figgis, B. G. Robertson, *Nature* **1965**, *205*, 694.
[17] J. B. Vincent, H.-R. Chang, K. Folting, J. C. Huffman, G. Christou, D. N. Hendrickson, *J. Am. Chem. Soc.* **1987**, *109*, 5703–5711.
[18] S. G. Sreerama, S. Pal, *Inorg. Chem.* **2002**, *41*, 4843–4845.
[19] T. C. Stamatatos, D. Foguet-Albiol, C. C. Stoumpos, C. P. Raptopoulou, A. Terzis, W. Wernsdorfer, S. P. Perlepes, G. Christou, *J. Am. Chem. Soc.* **2005**, *127*, 15380–15381.
[20] M. Nihei, N. Hoshino, T. Ito, H. Oshio, *Chem. Lett.* **2002**, 1016–1017.
[21] M. Viciano-Chumillas, S. Tanase, I. Mutikainen, L. Jos de Jongh, J. Reedijk, *Inorg. Chem.* **2008**, *47*, 5919–5929.
[22] L. F. Jones, G. Rajaraman, J. Brockman, M. Murugesu, E. C. Sañudo, J. Raftery, S. J. Teat, W. Wernsdorfer, G. Christou, E. K. Brechin, D. Collison, *Chem. Eur. J.* **2004**, *10*, 5180–5194.
[23] R. A. Krause, D. H. Busch, *J. Am. Chem. Soc.* **1960**, *82*, 4830–4834.
[24] A. W. Addison, T. N. Rao, J. Reedijk, J. Van Rijn, G. C. Verschoor, *J. Chem. Soc., Dalton Trans.* **1984**, 1349.
[25] a) J. J. Borrás-Almenar, J.-M. Clemente, E. Coronado, B. S. Tsukerblat, *Inorg. Chem.* **1999**, *38*, 6081; b) J.-M. Clemente, E. Coronado, B. S. Tsukerblat, *J. Comput. Chem.* **2001**, *22*, 985.

[26] S. Caretta, T. Guidi, P. Santini, G. Amoretti, O. Pieper, B. Lake, J. van Slageren, F. El Hallak, W. Wernsdorfer, M. Russina, C. J. Milios, E. K. Brechin, *Phys. Rev. Lett.* **2008**, *100*, 157203.
[27] C. J. Milios, R. Inglis, L. F. Jones, A. Prescimone, S. Parsons, W. Wernsdorfer, E. K. Brechin, *Dalton Trans.* **2009**, 2812–2822.
[28] R. Inglis, S. M. Taylor, L. F. Jones, G. S. Papaefstathiou, S. P. Perlepes, S. Datta, S. Hill, W. Wernsdorfer, E. K. Brechin, *Dalton Trans.* **2009**, 9157.
[29] G. M. Sheldrick, *Acta Crystallogr., Sect. A* **2008**, *64*, 112–122.

Received: September 11, 2009